



HAL
open science

Quelle place pour les massifs cristallins externes des Alpes occidentales dans l'orogénèse varisque ?

Jean-Baptiste Jacob

► **To cite this version:**

Jean-Baptiste Jacob. Quelle place pour les massifs cristallins externes des Alpes occidentales dans l'orogénèse varisque ?. Sciences de la Terre. Université Grenoble Alpes [2020-..], 2022. Français. NNT : 2022GRALU001 . tel-03625732

HAL Id: tel-03625732

<https://theses.hal.science/tel-03625732v1>

Submitted on 31 Mar 2022

HAL is a multi-disciplinary open access archive for the deposit and dissemination of scientific research documents, whether they are published or not. The documents may come from teaching and research institutions in France or abroad, or from public or private research centers.

L'archive ouverte pluridisciplinaire **HAL**, est destinée au dépôt et à la diffusion de documents scientifiques de niveau recherche, publiés ou non, émanant des établissements d'enseignement et de recherche français ou étrangers, des laboratoires publics ou privés.

THÈSE

Pour obtenir le grade de

DOCTEUR DE L'UNIVERSITÉ GRENOBLE ALPES

Spécialité : **Terre Solide (CETSOL)**

Arrêté ministériel : 25 mai 2016

Présentée par

Jean-Baptiste Jacob

Thèse dirigée par **Stéphane Guillot**

et codirigée par **Émilie Janots**

préparée au sein de **Institut des Sciences de la Terre (Grenoble)**

et de l'école doctorale **Sciences de la Terre, de l'Environnement et des Planètes (STEP)**

Quelle place pour les Massifs Cristallins Externes des Alpes occidentales dans l'orogénèse varisque ?

Thèse soutenue publiquement le **28 janvier 2022**,

devant le jury composé de :

Julia De Sigoyer

Professeur des universités, Université Grenoble Alpes, Grenoble, Présidente

Olivier Vanderhaeghe

Professeur des universités, Université Paul Sabatier, Toulouse, Rapporteur

Pavla Štípská

Chercheuse, Service Géologique Thèque, Prague, Rép. Thèque, Rapportrice

Stéphanie Duchêne

Professeur des universités, Université Paul Sabatier, Toulouse, Examinatrice

Pierre Trap

Maître de Conférence, Université de Franche-Comté, Besançon, Examineur

Émilie Janots

Maître de Conférence, Université Grenoble Alpes, Grenoble, Co-Directrice de thèse

Stéphane Guillot

Directeur de Recherche, CNRS, Grenoble, Directeur de thèse

Michel Faure

Professeur Émérite, ISTO, Orléans, Invité

Florence Cagnard

Chercheuse, BRGM, Orléans, Invitée



Table des matières

I	Contexte Général	17
1	L'orogénèse varisque en Europe de l'ouest	21
1.1	Les terrains anté-varisques en Europe : un ensemble de blocs continentaux issus de la marge nord du Gondwana	22
1.1.1	Situation au Paléozoïque inférieur	22
1.1.2	Combien d'océans ouverts au Paléozoïque?	25
1.2	La chaîne varisque en Europe	28
1.2.1	Zonation générale de la chaîne	28
1.2.2	Les sutures varisques	31
1.2.3	Une évolution polyphasée	33
1.3	Des caractéristiques typiques d'un orogène chaud	37
1.4	Comparaison avec le système orogénique Himalaya–Tibet	40
1.5	Quelques points essentiels à retenir sur la chaîne varisque européenne	45
2	Les domaines varisques dans les Alpes	47
2.1	Organisation générale de la chaîne alpine	49

2.1.1	La géodynamique alpine	49
2.1.2	Structure générale de la chaîne alpine	50
2.1.3	Le métamorphisme alpin	52
2.1.4	Structure profonde de la chaîne alpine	55
2.2	Les domaines de socle anté-Mésozoïque dans les Alpes	56
2.2.1	Des domaines issus de la marge nord du Gondwana	57
2.2.2	L'orogénèse varisque dans les Alpes	59
2.2.3	Des enregistrements Paléozoïques contrastés, marqueurs de la zonéographie varisque	62
2.3	Focus sur les domaines externes de la marge européenne : les massifs cristallins externes (MCE)	64
2.3.1	Les événements alpins dans les MCE	64
2.3.2	Le socle varisque dans les MCE	67
2.3.3	Les différentes phases tectono-métamorphiques varisques dans les MCE	70
2.4	Questions en suspens	71
 II Étude structurale et pétrochronologique des reliques de haute pression varisques dans les MCE		75
 3 Les éclogites rétromorphosées des lacs de la Tempête (Belledonne NE)		79
3.1	Carboniferous high pressure metamorphism and deformation in the Belledonne Massif (Western Alps)	80
3.2	Données complémentaires sur le contexte structural	117
3.2.1	Contexte tectonique alpin	117

3.2.2	Étude structurale des formations métamorphiques des lacs de la Tempête	117
3.2.3	Une exhumation localisée des reliques de haute pression au sein de la zone de cisaillement est-varisque	120
4	Les granulites de haute pression de l'Oisans	123
4.1	Article #2 : HT overprint of HP granulites in the Oisans–Pelvoux massif : implications for the dynamics of the Variscan collision in the external Western Alps	125
4.1.1	Introduction	126
4.1.2	Geological setting and field description	128
4.1.2.1	General setting and Variscan evolution	128
4.1.2.2	Field description	131
4.1.3	Methods	133
4.1.3.1	Analytical methods	133
4.1.3.2	Thermobarometry	136
4.1.4	Petrographic description	137
4.1.4.1	La Lavey mafic HP granulites (JB-19-43, JB-19-56)	139
4.1.4.2	La Lavey garnet-free amphibolite (JB-19-55)	141
4.1.4.3	Peyre-Arguet mafic retrogressed granulites (JB-19-16; JB-19-18)	144
4.1.5	Bulk rock Geochemistry	144
4.1.6	Thermobarometry	147
4.1.6.1	Inverse thermobarometry and forward thermodynamic modeling	147

4.1.6.2	Zr-in-rutile (ZiR) thermometry	152
4.1.7	U-Pb Geochronology	154
4.1.7.1	Composition and internal textures of zircon and rutile	154
4.1.7.2	Zircon and rutile U-Pb dating	157
4.1.8	Discussion	159
4.1.8.1	Emplacement of the mafic protoliths	159
4.1.8.2	Metamorphic evolution of the HP mafic granulites	159
4.1.8.3	Timing of the metamorphic evolution	163
4.1.8.4	Evolution at the regional scale	164
4.1.8.5	Thermal state of the Variscan crust and possible geodynamic scenario	167
4.2	Données complémentaires sur le contexte structural	176
4.2.1	Déformation alpine dans le massif de l'Oisans–Pelvoux	176
4.2.2	Étude des structures varisques	178
4.2.2.1	Modélisation géologique 3D	178
4.2.2.2	Identification des structures	180
4.2.3	Mécanismes de déformation de la croûte inférieure	184
4.2.4	Mécanismes d'exhumation de la croûte profonde dans le massif de l'Oisans–Pelvoux	186
5	Géochimie et contexte de mise en place des protolithes magmatiques	189
5.1	Signature géochimique des protolithes	190
5.1.1	Un magmatisme prolongé au cours de l'Ordovicien	192
5.1.2	L'ophiolite de Chamrousse est elle bien cambrienne?	194

III Magmatisme mantellique et évolution du manteau varisque dans les MCE	197
6 Les péridotites orogéniques du massif de l'Oisans : implications sur la structure et la composition du manteau varisque	201
6.1 Introduction	203
6.2 Geological setting	204
6.2.1 General setting	204
6.2.2 Ultramafic rocks in the ECM	207
6.3 Samples and methods	211
6.3.1 Petrography and mineral analysis	211
6.3.2 Whole rock composition	212
6.3.3 Sr–Nd isotopes	213
6.4 Petrography	215
6.5 Mineral compositions	219
6.6 Whole rock geochemistry and Nd-Sr isotopes	224
6.6.1 Major elements	224
6.6.2 Trace elements	226
6.6.3 Sr–Nd Isotopes	227
6.7 Thermobarometry	230
6.8 Discussion	232
6.8.1 Consequences of crustal retrogression	232
6.8.2 A refractory mantle refertilized by melts and fluids	235

6.8.2.1	Early melt-depletion	235
6.8.2.2	Evidence for mantle metasomatism	236
6.8.2.3	Multiple types of metasomatism	236
6.8.2.4	Crustal isotopic signature	238
6.8.3	Implications for the Variscan evolution	239
6.9	Conclusion	241
7	Le magmatisme (ultra)-potassique des MCE	243
7.1	Introduction	245
7.2	Geological setting	247
7.2.1	General setting	247
7.2.2	Variscan magmatism in the ECM	249
7.3	Field description and structural analysis	250
7.3.1	The Olan plutonic formations	251
7.3.2	Mafic dykes and enclaves in granitoids	253
7.4	Petrographic description and mineral composition	255
7.4.1	Petrographic descriptions	256
7.4.2	Mineral compositions	257
7.5	Whole rock geochemistry and Sr-Nd isotopes	259
7.5.1	Major elements composition	262
7.5.2	Trace elements composition	266
7.5.3	Sr-Nd isotopes	267
7.6	U-Pb geochronology	270

7.7	Thermobarometry	272
7.7.1	Thermobarometry of rock forming minerals	273
7.7.2	Apatite and zircon saturation	275
7.7.3	Ti-in-zircon (TiZ) thermometry	276
7.8	Discussion	277
7.8.1	Emplacement of the Olan plutonic formation	277
7.8.1.1	Crystallization sequence and P-T conditions of emplacement	277
7.8.1.2	Age of emplacement	279
7.8.1.3	Tectonic setting of emplacement	280
7.8.2	A petrogenetic model for the durbachites in the ECM	281
7.8.2.1	Crust vs Mantle sources	281
7.8.2.2	Mechanism of mantle enrichment and geodynamic implications	283
7.9	Conclusion	284
8	Discussion Générale	289
8.1	Synthèse des données pétrologiques, géochronologiques et structurales	292
8.1.1	Enregistrement des roches métamorphiques de haute pression dans les MCE	292
8.1.2	Les péridotites orogéniques des MCE	294
8.1.3	Âge et nature du magmatisme varisque	296
8.2	Évolution géodynamique varisque dans les MCE	300
8.2.1	Signification géodynamique de la haute pression dans les MCE : sub- duction ou collision?	300

8.2.2	Y a-t-il une suture océanique dans les MCE?	303
8.2.3	Phases post-collisionnelles et exhumation des unités de HP dans les MCE	305
8.2.4	Magmatisme mantellique et évolution de la composition du manteau .	307
8.3	Place des MCE dans les système varisque	310
8.3.1	Domaine varisque occidental vs oriental	310
8.3.2	Place des MCE : une portion du domaine varisque oriental décallée par la tectonique décrochante tardi-varisque	314
8.3.3	Redéfinition de la branche sud-est varisque	317
	Conclusions et perspectives	321
	Bibliographie	323
A	Annexes	359
A.1	Article #1 : Paleozoic evolution and Variscan inheritance in the Alps	359
A.2	Article #2 : Crustal melting vs. fractionation of basaltic magmas – Parts 1 and 2	413

Introduction générale

La formation des ceintures orogéniques au niveau des zones de convergence est décrite schématiquement comme le résultat d'une subduction suivie de la collision entre deux masses continentales, de l'accrétion de blocs crustaux le long d'une marge active ou encore de l'inversion de petits bassins de type rift ou bassin marginal. Cependant, au-delà des modèles conceptuels, les systèmes orogéniques présentent fréquemment des géométries très complexes et peuvent être marqués par une évolution géodynamique polyphasée, impliquant plusieurs phases de subduction et de collision de vergences différentes, pouvant être entrecoupées par des phases d'extension et d'ouverture de bassins. La convergence Afrique-Eurasie et la formation des chaînes alpines péri-méditerranéennes (Jolivet et Faccenna, 2000; Jolivet et Brun, 2010) est un parfait exemple actuel illustrant la complexité des processus tectoniques pouvant se développer en contexte de convergence (Figure 1). La reconstitution des différentes phases tectoniques dans ces contextes est donc une tâche particulièrement difficile. Ceci est encore plus vrai dans les systèmes orogéniques anciens, où l'enregistrement géologique est en partie oblitéré : (i) par l'érosion des niveaux structuraux supérieurs, qui contiennent la plupart des unités ophiolitiques marquant les zones de suture ; (ii) par les remaniements tectoniques parfois important survenus après les phases de collision, soit par des décrochements tardi-orogéniques ou encore par une reprise éventuelle dans de nouveaux cycles orogéniques ultérieurs ; (iii) par la fusion partielle des domaines crustaux inférieurs lors des phases syn à post-collisionnelles, qui favorise le fluage de la croûte et la mise en place de batholites ou de dôme migmatitiques recoupant les structures plus anciennes ; (iv) par le dépôt de séries sédimentaires plus récentes, recouvrant en partie les anciens domaines

INTRODUCTION

orogéniques.

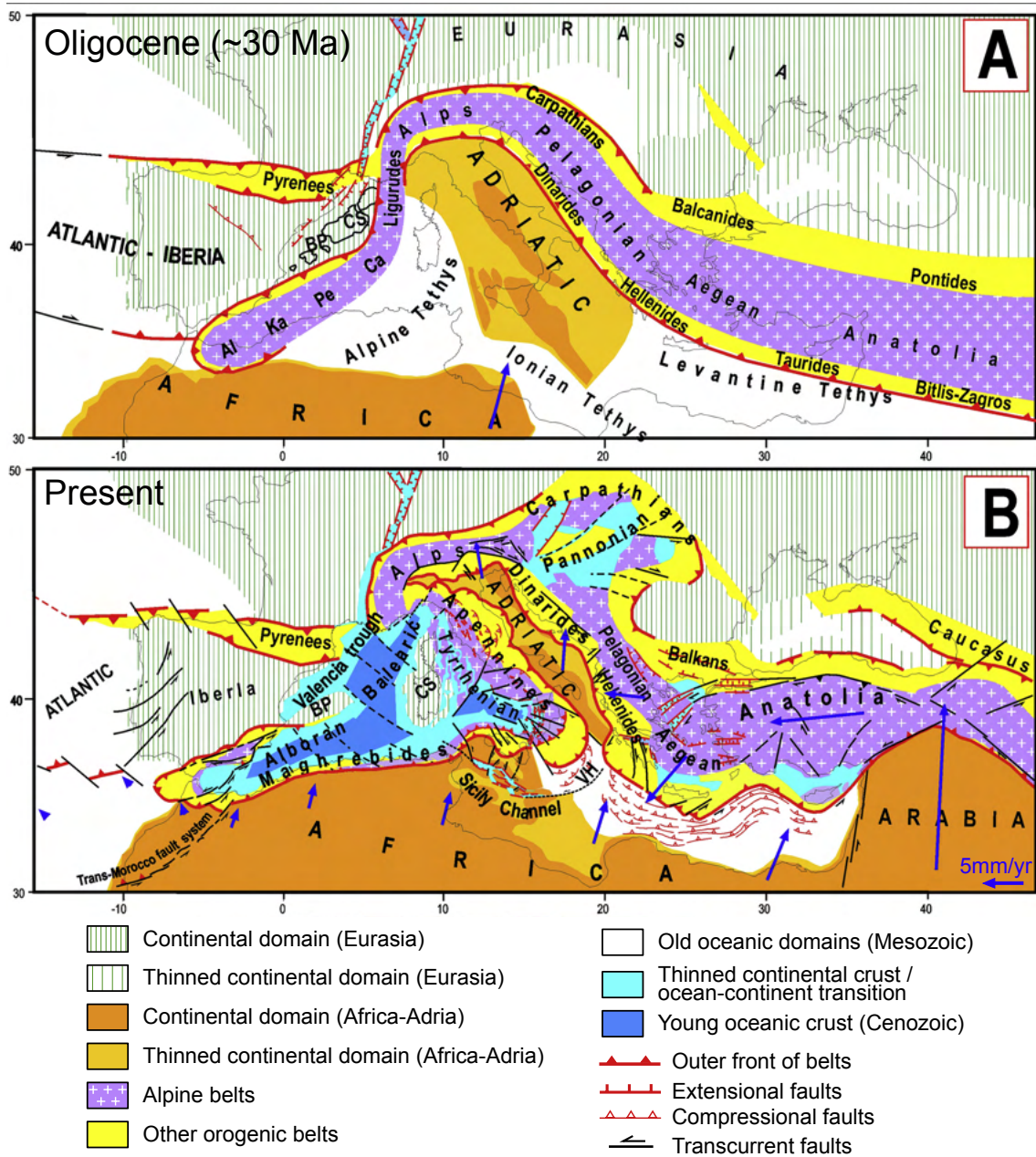


FIGURE 1 – Exemple de contexte géodynamique complexe développé en contexte de convergence : le domaine méditerranéen et les chaînes alpines. De manière schématique, ce domaine marque la convergence entre la plaque africaine et la plaque eurasiennne, et la fermeture de l'ancien domaine océanique téthysien. Dans le détail, on observe une évolution géodynamique extrêmement complexe, impliquant plusieurs slabs en subduction (alpin, dinarique, apennin, égéen), présentant des vergences différentes, plusieurs phases orogéniques, et l'ouverture de bassins océaniques en contexte de convergence. Figure extraite de [Mantovani et al. \(2020\)](#).

La chaîne varisque européenne représente un cas d'école. Cette chaîne résulte de la fermeture progressive de l'océan Rhéique et de plusieurs petits bassins océaniques ou de transition océan-continent au cours du Silurien et du Dévonien, entraînant la collision entre les continents Gondwana, Laurussia et plusieurs petits blocs intermédiaires à partir du Dévonien (Matte, 1986, 2001). L'orogénèse varisque affecte une grande partie des terrains paléozoïques du sud et de l'ouest de l'Europe, de la péninsule ibérique au sud de la Pologne, et a été étudiée depuis plus d'un siècle par de multiples générations de géologues (*e.g.* Suess, 1909; Kossmat, 1927; Matte, 1986; Franke, 2000; Martínez Catalán *et al.*, 2021). Malgré les milliers de travaux produits, il n'existe toujours pas à l'heure actuelle de réel consensus sur le nombre de blocs continentaux impliqués, le nombre et la taille des domaines océaniques refermés, ainsi que sur la position et la vergence des sutures. Néanmoins, de larges portions de socle varisque affleurent de manière continue dans plusieurs massifs, en particulier dans le massif de Bohême, le massif Central, le massif Armoricaïn, et sur la péninsule ibérique, ce qui a permis d'établir plusieurs coupes de référence (Ballèvre *et al.*, 2014; Faure *et al.*, 2009; Franke, 2000; Lardeaux *et al.*, 2014; Schulmann *et al.*, 2005; Simancas *et al.*, 2003) et d'établir des corrélations de grande échelle entre les principaux domaines lithotectoniques. La situation est en revanche plus complexe dans les domaines alpins et du sud-est de l'Europe. De nombreuses portions de socle varisque affleurent dans ces zones, qui forment une multitude de petits domaines plus ou moins affectés par la tectonique et le métamorphisme alpin, ce qui complique les corrélations avec le reste de la chaîne varisque. Une caractérisation précise des différentes phases tectono-métamorphiques et magmatiques varisques dans ces domaines peut néanmoins apporter des points de comparaison avec le reste de la chaîne, afin d'intégrer ces domaines dans les reconstitutions géodynamiques de l'orogénèse varisque.

Cette thèse se focalise sur les Massifs Cristallins Externes (MCE) des Alpes occidentales. Ces massifs représentent des portions exhumées du socle varisque impliqué dans la collision alpine. Ils sont localisés sur la marge européenne externe (dauphinoise-helvétique) de la

chaîne alpine, et ont été relativement peu affectés par le métamorphisme et la déformation alpine. Cependant, leur intégration au sein de la chaîne varisque reste difficile à établir en raison des importants mouvements décrochants tardi-varisques (Guillot *et al.*, 2009a) et la rotation de l'arc alpin. Par ailleurs, si des reliques de roches de haute pression (HP) varisques affleurent dans ces massifs, leur signification géodynamique et leur lien avec une possible zone de suture fait débat (Guillot et Ménot, 2009).

Le but de ce travail de thèse est de mieux contraindre l'évolution tectono-métamorphique et magmatique dans les MCE, en vue de proposer un modèle géodynamique cohérent permettant de les intégrer dans la chaîne varisque. Ce travail a été mené sur les massifs de Belledonne et de l'Oisans–Pelvoux, en parallèle d'une seconde thèse (Jonas Vanardois, univ. Franche-Comté) réalisée sur le socle des massifs du Mont Blanc et des Aiguilles-Rouges, dans le cadre du chantier RGF Alpes piloté par le BRGM. De nouvelles données structurales, thermobarométriques et géochronologiques ont été acquises sur les unités métamorphiques profondes préservant des reliques de HP. Un travail a aussi été réalisé sur le magmatisme (ultra)-potassique des MCE et sur des enclaves de péridotites découvertes dans le massif de l'Oisans–Pelvoux lors de ce travail de thèse, qui donnent des indications sur l'évolution du manteau varisque.

Le manuscrit se structure en quatre grandes parties.

- La Partie I présente le contexte géodynamique général associé au cycle orogénique varisque en Europe, et présente un travail de synthèse réalisé sur l'évolution paléozoïque des différents domaines de socle dans les Alpes et qui fait l'objet d'un chapitre sous presse (Jacob *et al.*, 2022) dans le livre *Geodynamics of the Alps*.
- La Partie II traite de la datation et de l'estimation des conditions P-T du métamorphisme varisque dans les MCE, avec un focus sur les reliques d'éclogites et de granulites de HP. Les résultats obtenus pour les éclogites de Belledonne sont publiés dans *Journal*

of *Metamorphic Geology* (Jacob *et al.*, 2021a), et ceux des granulites de HP de l'Oisans sont présentés dans une seconde publication en révision dans *Lithos*. En parallèle, une étude structurale des unités métamorphiques contenant ces reliques de HP a été réalisée, afin de contraindre le contexte structural et préciser les mécanismes d'exhumation de ces roches.

- La Partie III se focalise sur le magmatisme mantellique et l'évolution du manteau varisque dans les MCE, en couplant l'étude des séries magmatiques (ultra)-potassiques, à forte composante mantellique, et l'étude pétrographique et géochimique des enclaves de péridotites échantillonnées dans les domaines structuraux inférieurs. Ces travaux sont présentés sous la forme de deux publications en préparation.
- Enfin, la Partie IV est une partie de discussion générale, qui fait une synthèse des résultats obtenus, les intègre dans un modèle d'évolution géodynamique varisque des MCE, et replace ces massifs à l'échelle de la chaîne varisque européenne.

Première partie

Contexte Général

Une grande partie du socle paléozoïque européen a été structuré au cours de l'orogénèse varisque, entre le Dévonien et le Carbonifère (ca. 380–300 Ma). Cette orogénèse résulte de la convergence entre deux grandes masses continentales, le Gondwana au sud et la Laurussia au nord, ainsi que plusieurs microcontinents intermédiaires, et aboutit à la formation du supercontinent Pangée à la fin du Carbonifère (Matte, 2001). Les domaines varisques exposés en Europe ne représentent qu'une petite partie de ce grand système orogénique, qui s'étend sur plus de 8000 km du Caucase aux Appalaches (Matte, 1986), et est donc comparable en étendue à la chaîne alpino-himalayenne actuelle. La majeure partie du socle varisque européen est aujourd'hui recouverte par une couverture sédimentaire plus ou moins épaisse, déposée au cours du Mésozoïque et du Cénozoïque. L'étude du système orogénique varisque s'est donc concentrée principalement dans les massifs où le socle Paléozoïque affleure en surface, les principaux étant le Massif de Bohême, le Massif Central, le Massif Armoricain et le Massif Ibérique. La plupart des massifs varisques d'Europe de l'Ouest et d'Europe Centrale ont été relativement peu affectés par les événements tectoniques post-Permien, ce qui permet de corréler les principaux domaines tectoniques et les grandes structures varisques à l'échelle du continent (*e.g.* Ballèvre *et al.*, 2014; Edel *et al.*, 2018; Matte, 1986; Martínez Catalán *et al.*, 2020). La situation est en revanche plus compliquée dans un large quart sud-est de l'Europe, où de nombreux domaines de socle paléozoïque affleurent dans un contexte géodynamique extrêmement complexe, associé à la fermeture de la Téthys et à la formation des chaînes alpines (Jolivet et Faccenna, 2000). Ainsi, la reconstitution du puzzle varisque dans ces domaines affectés par la tectonique alpine demeure un problème ouvert, qui nécessite de comprendre l'organisation générale de la chaîne alpine et son évolution géodynamique depuis le Trias.

Cette première partie consacrée au contexte géologique général est donc découpée en deux chapitres. Le premier chapitre est consacré à l'organisation générale du système orogénique varisque en Europe, et présente une synthèse des connaissances actuelles sur la structure de

la chaîne et sur l'évolution géodynamique varisque et anté-varisque en Europe, du Néopro-
térozoïque à la fin du Permien. Le second chapitre se focalise sur l'évolution varisque des
domaines alpins. Ce chapitre présente une revue des différents domaines de socle Paléozoïque
exposés dans les Alpes, et discute de leur évolution géodynamique varisque et anté-varisque.
Un focus particulier est accordé aux domaines externes de la marge européenne (domaine
Helvétique), dans lesquels se trouvent les Massifs Cristallins Externes étudiés au cours de
cette thèse. Ce second chapitre reprend, avec quelques ajouts et modifications, un chapitre
écrit pour un ouvrage de synthèse sur la chaîne alpine (*Geodynamics of the Alps, in press*).

CHAPITRE 1

L'orogénèse varisque en Europe de l'ouest

Sommaire

1.1 Les terrains anté-varisques en Europe : un ensemble de blocs continentaux issus de la marge nord du Gondwana	22
1.1.1 Situation au Paléozoïque inférieur	22
1.1.2 Combien d'océans ouverts au Paléozoïque ?	25
1.2 La chaîne varisque en Europe	28
1.2.1 Zonation générale de la chaîne	28
1.2.2 Les sutures varisques	31
1.2.3 Une évolution polyphasée	33
1.3 Des caractéristiques typiques d'un orogène chaud	37
1.4 Comparaison avec le système orogénique Himalaya–Tibet	40
1.5 Quelques points essentiels à retenir sur la chaîne varisque européenne	45

1.1 Les terrains anté-varisques en Europe : un ensemble de blocs continentaux issus de la marge nord du Gondwana

1.1.1 Situation au Paléozoïque inférieur

Au Paléozoïque inférieur (Cambrien–Ordovicien), la plupart des futurs domaines varisques d'Europe étaient situés sur la marge nord du Gondwana (Matte, 2001; Stampfli *et al.*, 2011; Von Raumer *et al.*, 2002), faisant face à un domaine océanique Proto-Rhéique ou Iapetus (Figure 1.1). Cette marge continentale a été active durant une grande partie du Néoprotérozoïque, formant une zone d'accrétion associée à la subduction de l'océan Iapetus (Garfunkel, 2015). En Europe, cette période d'accrétion a culminé à la fin de l'Édiacarien (ca. 600–580 Ma) avec l'orogénèse Cadomienne, principalement préservée en Nord Bretagne et en Normandie (Ballèvre *et al.*, 2001; Chantraine *et al.*, 2001).

Au cours du Cambrien, ce contexte de marge active en convergence évolue progressivement vers un contexte extensif, associé à une subsidence généralisée de la marge nord du Gondwana (von Raumer and Stampfli, 2008). Cette extension entraîne la formation de petits bassins marginaux (*e.g.* l'océan de Chamrousse, Guillot *et al.*, 1992; Ménot *et al.*, 1988; Pin et Carme, 1987), et aboutit à l'Ordovicien inférieur à l'ouverture de l'océan Rhéique et à la séparation du microcontinent Avalonia (Linnemann *et al.*, 2007; Nance *et al.*, 2010), Figure 1.4. Plusieurs microcontinents au sud d'Avalonia (bloc Armoricain, Saxo-thuringien, zone d'Ossa-Morena) se retrouvent aussi séparés du Gondwana par de petits bras d'océans. Cette phase de rifting s'accompagne d'une activité magmatique importante, que l'on retrouve dans une grande partie des terrains anté-varisques en Europe (Figure 1.2). Il s'agit principalement de magmatisme bimodal caractérisé par des associations de basaltes alca-

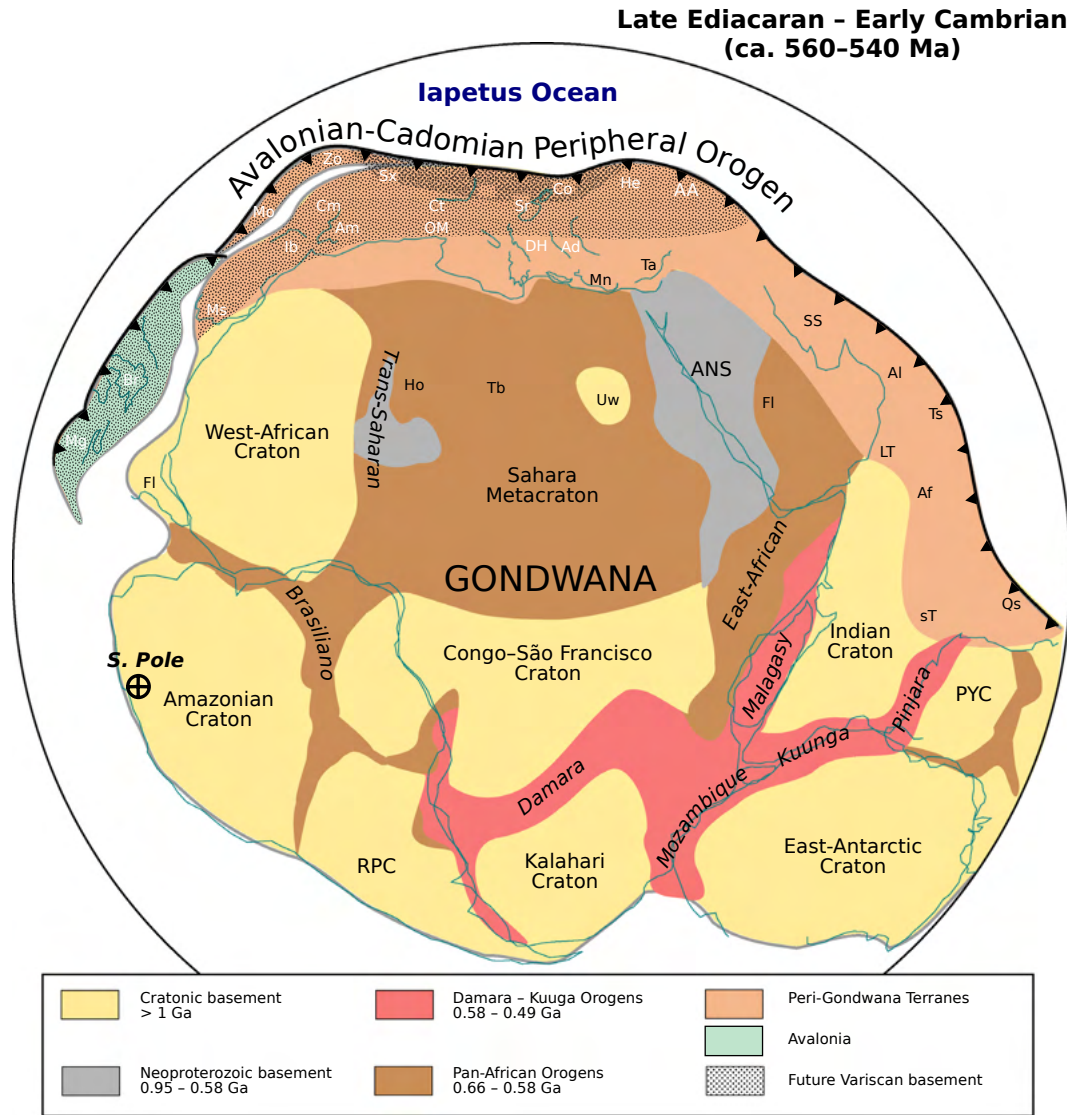


FIGURE 1.1 – Reconstitution paléogéographique du Gondwana au Cambrien inférieur. Modifié d’après *Avigad et al. (2018)*. Aa Afif, AA Austro-Alpin, Ad Adria, Af bloc Afghan, Al Alborz, Am Armorica, ANS Bouclier Arabo-Nubien (Arabian–Nubian Shield), Aq Aquitaine, Br Britannia, Cm Cadomia, Co Corse, Ct Cantabria, DH Dinarides–Helenides, Fl Floride, He Domaine Helvetique, Ho Hoggar, Ib terrains allochtones du NW de l’Espagne (Ibérie), Is Zone d’Istanbul, LT Lut-Tabas, Mg Meguma, Mn Menderes, Mo Moldanubien, Ms Meseta, OM Ossa–Morena, PYC Craton de Pilbara–Yilgarn, Qs sud Qinling, RPC Craton de Rio Plata, Sr Sardaigne, SS Sanandaj–Sirjan, sT sud-Tibet, Sx Saxo-Thuringien, Ta Taurus, Tb Tibesti, Ts sud Tarim, Uw Uweinat, Zo Zonguldak

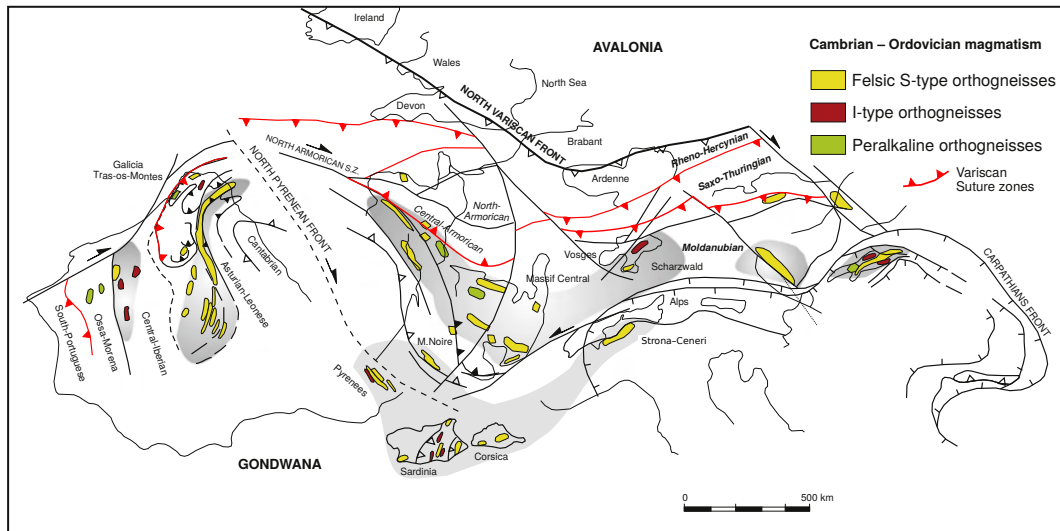


FIGURE 1.2 – Magmatisme Cambro-Ordovicien dans le socle varisque en Europe. D'après Villaseca *et al.* (2016).

lins à tholéitiques et de rhyolites alcalines à peralcalines (*e.g.* Crowley *et al.*, 2000; Pin et Marini, 1993). Ces associations sont communément associées à des corps ultramafiques, et pourraient correspondre à des anciens bassins océaniques ou à des zones de lithosphère hyperamincie de la transition océan-continent. De nombreux granitoïdes peralumineux (type S de Chappell et White, 2001) se forment aussi durant cette période (*e.g.* Couzinié *et al.*, 2017; Villaseca *et al.*, 2016; Zurbruggen, 2017), et marquent une fusion importante de croûte continentale riche en (méta)sédiments (Chelle-Michou *et al.*, 2017; Couzinié *et al.*, 2017).

Ainsi, le contexte géodynamique associé à l'ouverture de l'océan Rhéique reste débattu. Selon certains auteurs, la présence de nombreux granitoïdes d'âge Cambrien à Ordovicien, ainsi que les signatures d'arc de certains protolites mafiques (Figure 1.3) marquent un contexte d'arc et indiquent donc la présence d'une subduction active jusqu'à l'Ordovicien (*e.g.* Stampfli *et al.*, 2013; Zurbruggen, 2015, 2017). L'ouverture de l'océan Rhéique serait alors liée à de l'extension arrière-arc, provoquée par un retrait de la subduction (slab rollback), comme proposé par Stampfli *et al.* (2013) (Figure 1.4). Selon d'autres auteurs, la présence de séries magmatiques alcalines et tholéitiques marquent un contexte de rifting, et les signatures d'arc

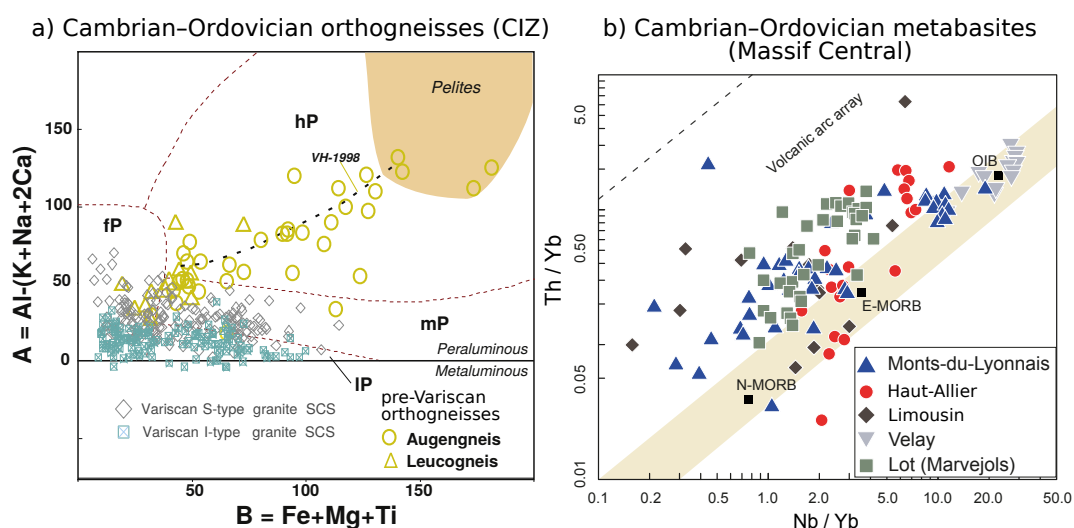


FIGURE 1.3 – Caractéristiques géochimiques du magmatisme Cambro-Ordovicien en Europe. a) Composition des orthogneiss peralumineux de la zone centrale-ibérique (CIZ), dans le diagramme B-A de [Debon et Le Fort \(1983\)](#) modifié par [Villaseca et al. \(1998\)](#). Une aluminosité (A) élevée, ainsi qu’une corrélation B-A positive sont des caractéristiques typiques des séries très peralumineuses, issues de la fusion de sédiments matures. b) Métabasites des unités métamorphiques allochtones du Massif Central (*Groupes Leptyno-Amphiboliques* [Santallier et al., 1988](#)) sur le diagramme Nb/Yb – Th/Yb de [Pearce \(2008\)](#). Modifié d’après [Couzinié \(2017\)](#). Les basaltes océaniques sont alignés sur l’axe MORB–OIB, alors que les basaltes ayant subi une contamination crustale durant leur mise en place, ou issus d’une source mantellique enrichie par des fluides de subduction pointent sur l’axe des arcs volcaniques.

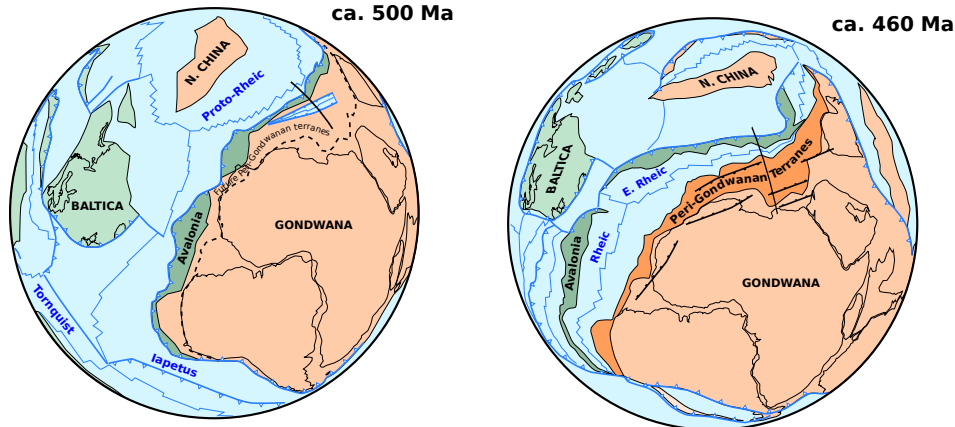
observées dans certaines roches mafiques [Figure 1.3](#) résulteraient de la fusion d’un manteau hétérogène enrichi par les fluides de subduction au cours du Néoprotérozoïque (*e.g.* [Ballèvre et al., 2012](#)). Ceci implique une transition d’un contexte de marge active à une marge passive au cours du Cambrien, potentiellement liée à une rupture de slab suivant la collision avec une paléo-ride océanique ([Linnemann et al., 2007](#)), ([Figure 1.4](#)).

1.1.2 Combien d’océans ouverts au Paléozoïque ?

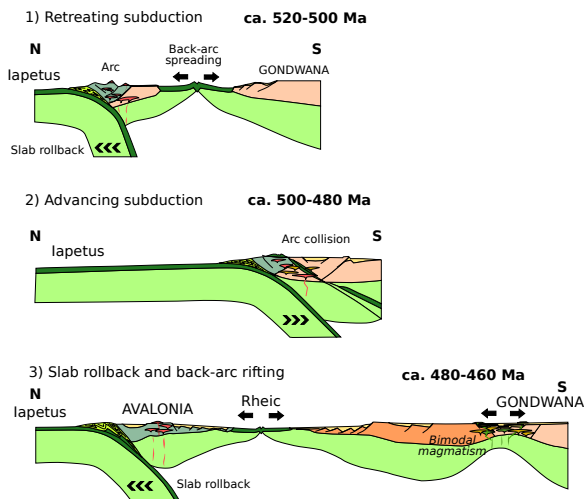
Il existe un débat concernant le nombre et l’étendue des domaines océaniques ouverts au Paléozoïque inférieur le long de la marge nord du Gondwana. Si la présence d’un large océan Rhéique (ca. 4000 km) séparant Avalonia du reste des domaines gondwaniens est attestée par de nombreuses données paléomagnétiques et paléobiogéographiques ([Cocks et Torsvik, 2002](#); [Nance et al., 2010](#)), la présence de domaines océaniques plus au sud est débattue.

L'OROGENÈSE VARISQUE EN EUROPE DE L'OUEST

a) Tectonic situation during the late Cambrian – Ordovician



b) Slab rollback and back-arc opening (Stampfli et al. 2013)



c) Passive margin rifting (Linnemann et al. 2007)

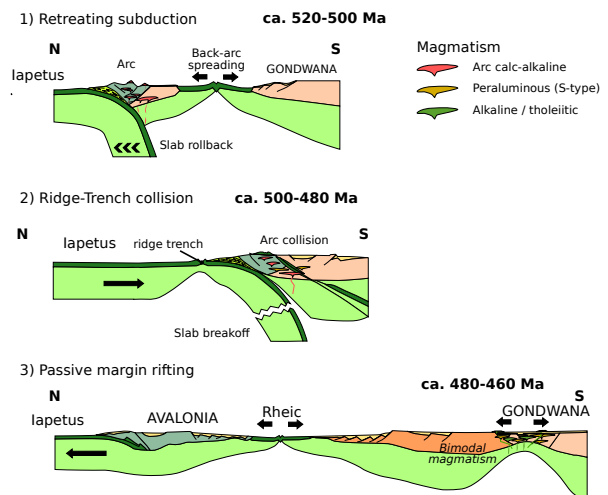


FIGURE 1.4 – Reconstitution paléogéographique de la marge nord du Gondwana entre la fin du Cambrien et l’Ordovicien (a), et différents modèles possibles pour l’ouverture de l’océan Rhéique : (b) Retrait de slab et ouverture en arrière-arc (Stampfli *et al.*, 2013) ; (c) Rupture de slab et transition vers une marge passive, suivie d’un épisode de rifting (Linnemann *et al.*, 2007). Cartes et coupes modifiées d’après Stampfli *et al.* (2013).

En effet, les registres paléoclimatiques et paléobiogéographiques ainsi que les enregistrements paléomagnétiques suggèrent plutôt l’absence de grands domaines océaniques au sud de l’océan Rhéique (Cocks et Torsvik, 2002; Fortey et Cocks, 2003; ?; Žák et Sláma, 2018). Cependant, les nombreuses reliques de roches de haute pression ainsi que la présence d’unités ophiolitiques au sud de la suture Rhéique, dans les domaines varisques d’Europe occidentale et centrale, suggèrent la présence d’anciens bassins fermés par subduction (Ballèvre *et al.*, 2009; Faure *et al.*, 2008; Guillot et Ménot, 2009; Lardeaux *et al.*, 2014). Par ailleurs, une

suture est clairement identifiable sur les profils géophysiques dans le massif de Bohême, entre les domaines Saxo-Thuringien et Teplà-Barrandien (Schulmann *et al.*, 2014), et des zones de suture sont bien identifiées au sud du massif Armoricaïn et en Espagne (Ballèvre *et al.*, 2009, 2014; Martínez Catalán *et al.*, 2020). Ainsi, certaines reconstitutions paléogéographiques suggèrent la présence d'un ou plusieurs microcontinents, séparés de Gondwana par des petits bassins océaniques analogues aux océans alpins (Franke *et al.*, 2017; Matte, 2001). A l'inverse, d'autres modèles suggèrent la présence d'une péninsule armoricaïne au nord du Gondwana, composée de noyaux continentaux épais séparés par des zones de lithosphère amincie (*e.g.* Kroner et Romer, 2013; Stephan *et al.*, 2019b). Enfin, le modèle proposé par Stampfli *et al.* (2013) suggère une séparation plus tardive des blocs péri-gondwaniens, associée à l'ouverture de la Paléotéthys à partir du Silurien (Figure 1.5).

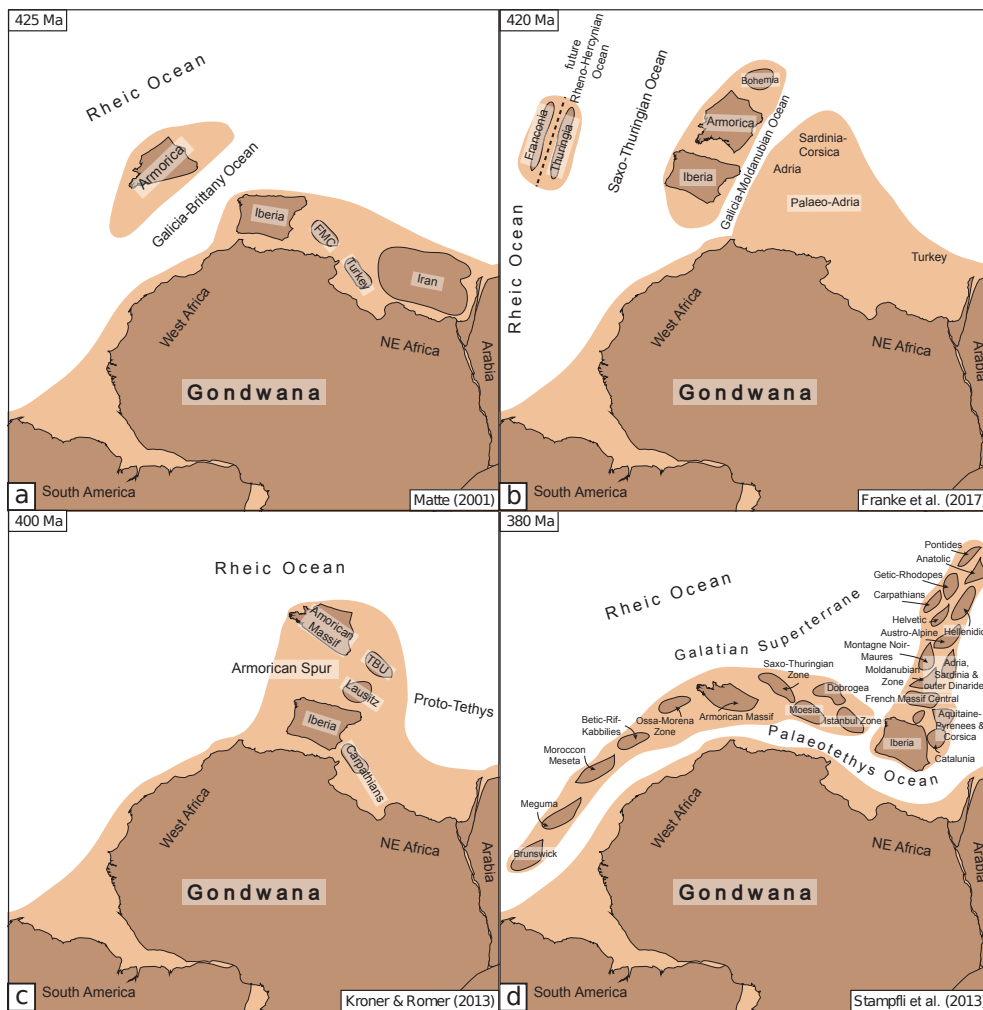


FIGURE 1.5 – Différentes configurations possibles de la marge nord du Gondwana et des blocs péri-gondwaniens après l'ouverture de l'océan Rhéique (Silurien). Figure tirée de [Stephan et al. \(2019a\)](#), d'après les reconstitutions paléogéographiques de [Matte \(2001\)](#); [Kroner et Romer \(2013\)](#); [Franke et al. \(2017\)](#); [Stampfli et al. \(2013\)](#).

1.2 La chaîne varisque en Europe

1.2.1 Zonation générale de la chaîne

Au premier ordre, la chaîne varisque d'Europe peut être vue comme un assemblage de plusieurs blocs péri-gondwaniens pincés entre les deux continents Gondwana et Laurussia. La forme générale de la chaîne n'est pas linéaire, mais apparaît au contraire fortement arquée, en particulier dans sa partie ouest au niveau de la syntaxe Ibéro-Armoricaine ([Figure 1.6](#)).

La chaîne est découpée en cinq grands domaines tectoniques, d'orientation générale NE–SW (Ballèvre *et al.*, 2014; Franke *et al.*, 2017; Kossmat, 1927; Martínez Catalán *et al.*, 2020; Matte, 1991, 2001) : le domaine Rhéno-Hercynien, le domaine Saxo-Thuringien, le domaine Armoricaïn, les nappes métamorphiques allochtones de la marge gondwaniennne (domaine *Moldanubien*), et les domaines autochtones et para-autochtones de la marge gondwaniennne. La chaîne varisque apparaît donc aux premiers abords comme grossièrement cylindrique. Cependant, des différences notables existent entre différents segments de la chaîne, qui est divisée en trois domaines séparés par de grandes zones de cisaillement décrochantes d'échelle lithosphérique, comme la zone de cisaillement du Pays de Bray (Edel et Weber, 1995; Matte, 1986) ou la zone de cisaillement sud-armoricaine (Ballèvre *et al.*, 2009) : le domaine nord-varisque, regroupant les massifs de Bohême, des Vosges – Forêt-Noire et le massif Rhénan ; le domaine central-varisque, regroupant le Massif Central, le massif Armoricaïn et le Sud de l'Angleterre ; le domaine sud-varisque, regroupant la péninsule Ibérique, le bloc Corso-Sarde et le massif des Maures-Tanneron dans le Sud de la France (Edel *et al.*, 2018).

Le domaine Rhéno-Hercynien forme la partie externe de la chaîne dérivée de la marge laurussienne. Elle se développe sur l'ancien microcontinent Avalonia, accreté à la Baltica et la Laurentia au Silurien lors de l'orogénèse Calédonienne. Elle est délimitée au nord par le front nord-varisque, qui passe par le sud de l'Irlande et de l'Angleterre et le nord de la Rhénanie, et marque la limite avec l'avant-pays non-déformé. Cette zone est corrélée avec la zone sud-portugaise dans le domaine sud-varisque (Ballèvre *et al.*, 2014). Elle est principalement formée de séries de flyschs d'âge Dévonien-Carbonifère reposant sur un socle Néoprotérozoïque (Franke, 2000; Matte, 1991), et formant un système de plis de vergence nord (vergence SW dans la zone sud-portugaise).

Les domaines Armoricaïns et Saxo-Thuringien correspondent à un ensemble de blocs péri-gondwaniens. Ces blocs sont marqués par un fort héritage Néoprotérozoïque, en particulier

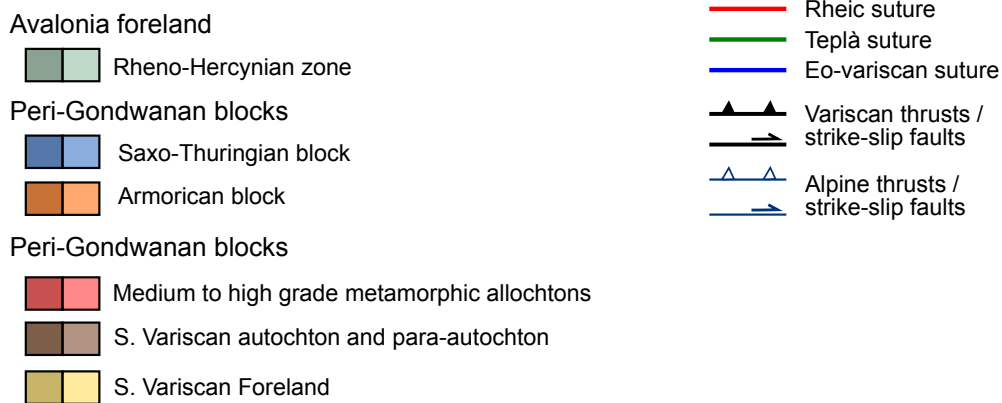
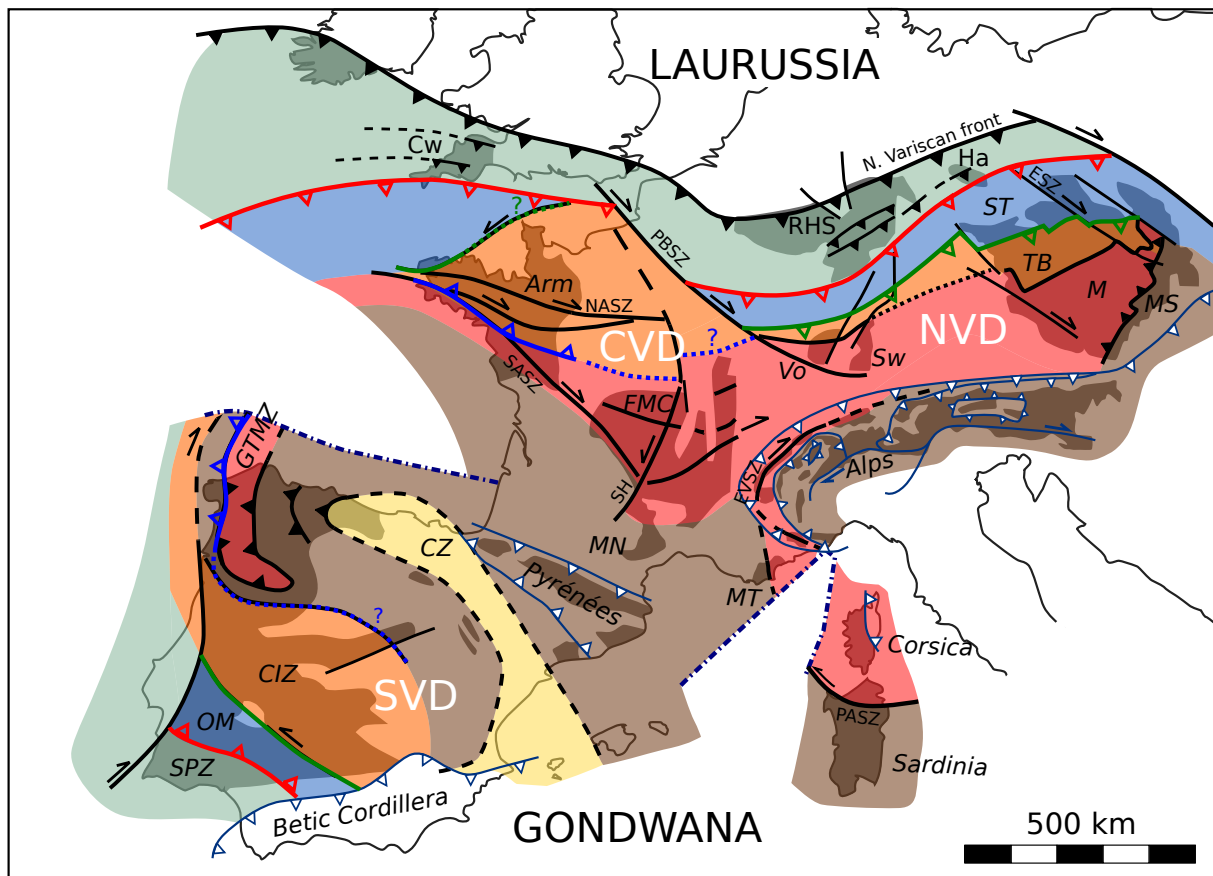


FIGURE 1.6 – Carte de la chaîne varisque en Europe, montrant la zonation de la chaîne et les principales sutures. Modifié d'après Ballèvre *et al.* (2014); Faure *et al.* (2005); Franke *et al.* (2017); Lardeaux *et al.* (2014) Arm Armorica, CIZ Central Iberian Zone, CZ Cantabrian Zone, Cw Cornwall, GTMZ Galicia-Trás-os-Montes Zone, Ha Harz, M Moldanubian, MN Montagne-Noire, MS Moravo-Silesian zone, MT Maures-Tanneron, OM Ossa-Morena, RHS Rheinische Schiefergebirge, SPZ South Portugese Zone, ST Saxo-Thuringian, Sw Schwarzwald, TP Teplà Barrandian. EVSZ East-Variscan Shear Zone, ESZ Elbe Shear Zone, NASZ N. Armorican Shear Zone, PASZ Posada-Asinara Shear Zone, PBSZ Pays de Bray Shear Zone, SASZ South Armorican Shear Zone, SH Sillon Houiller

dans le domaine Saxo-Thuringien du massif de Bohême et au nord du massif Armoricaïn, où des portions d’arcs magmatiques Cadomiens sont préservés (Ballèvre *et al.*, 2001; Chantraine *et al.*, 2001). Ces domaines de socle Néoprotérozoïque sont partiellement recouverts de séries sédimentaires Paléozoïques.

Le cœur de la chaîne est formé d’un ensemble d’unités métamorphiques allochtones dérivées de la marge gondwaniennne, et présentant des degrés de métamorphisme variables allant jusqu’à un métamorphisme de haut grade dans le faciès des granulites (O’Brien, 2000). Les unités les plus métamorphiques représentent des portions exhumées de croûte profonde formant l’ancienne racine crustale de la chaîne (Schulmann *et al.*, 2009). Elles sont composées principalement de gneiss et de migmatites, et contiennent fréquemment des reliques d’éclogites et de granulites de haute pression, avec parfois des fragments de péridotites et de serpentinites (Gardien *et al.*, 1990; Medaris *et al.*, 2005). Ces unités métamorphiques allochtones sont fréquemment recoupées par des granitoïdes d’âge Carbonifère, mis en place lors des stades syn à post-collisionnels.

Enfin, les domaines situés plus au sud représentent les domaines externes plus superficiels de la marge gondwaniennne, formés principalement de séries sédimentaires plissées. Ils laissent place au sud à des bassins d’avant-pays remplis de dépôts molassiques Carbonifères (Ballèvre *et al.*, 2014; Faure *et al.*, 2009; Martínez Catalán *et al.*, 2020).

1.2.2 Les sutures varisques

Plusieurs zones de suture sont indentifiées dans la chaîne varisque européenne. Cependant, la corrélation de ces sutures entre les différents segments de la chaîne n’est pas toujours bien établie, en raison des importants remaniements tectoniques de la chaîne ayant eu lieu au cours du Carbonifère.

Une première suture marque la limite entre les domaines Rhéno-Hercyniens et l'assemblage de blocs péri-gondwaniens des domaines Armoricaïn et Saxo-Thuringien. Elle est définie par la présence d'ophiolites Dévoniennes dans le Sud de l'Angleterre (Cap Lizard, [Shail et Leveridge, 2009](#)) et par la présence de séries magmatiques d'arc dans le sud du massif Rhénan ([Franke et al., 2017](#)). Elle est corrélée dans le domaine sud-varisque avec la suture sud-ibérique, marquant la limite entre la zone sud-portugaise et la zone d'Ossa-Morena ([Matte, 1991](#)). Cette suture marque vraisemblablement la fermeture de l'océan Rhéique. Cependant, selon [Franke et al. \(2017\)](#), la fermeture de l'océan Rhéique serait plus ancienne (420–400 Ma), et la suture observée aujourd'hui marquerait en fait la fermeture d'un bassin marginal Rhéno-Hercynien, ouvert le long de la marge laurussienne au cours du Dévonien supérieur (ca. 390-360 Ma). Cette suture Rhéno-Hercynienne serait alors superposée à une suture plus ancienne, marquant la fermeture de l'océan Rhéique au cours du Silurien / Dévonien inférieur (ca. 420-400 Ma).

Une seconde suture, la suture de Teplà, est bien identifiée dans le domaine nord-varisque (Bohême), sur la base de profils géophysiques ([Schulmann et al., 2014](#)). Cette suture marque la subduction vers le sud d'un océan ou d'une portion de lithosphère hyperamincie au cours du Dévonien moyen à supérieur (ca. 390-370 Ma [Schulmann et al., 2009](#)). Elle semble se prolonger au nord des Vosges. Au nord du Massif Central, la présence d'un magmatisme d'arc d'âge Dévonien moyen à supérieur (arc du Morvan) associé à l'ouverture contemporaine d'un bassin d'arrière arc (bassin de la Brévenne) pourrait marquer la subduction vers le sud de cet océan ([Faure et al., 2008, 2009](#); [Lardeaux et al., 2014](#)). Elle pourrait aussi être corrélée à la suture du Conquet au nord de la Bretagne, qui marque la limite entre le microcontinent Armoricaïn et le bloc du Léon sur la pointe nord-ouest de la Bretagne ([Ballèvre et al., 2009](#); [Faure et al., 2005](#)).

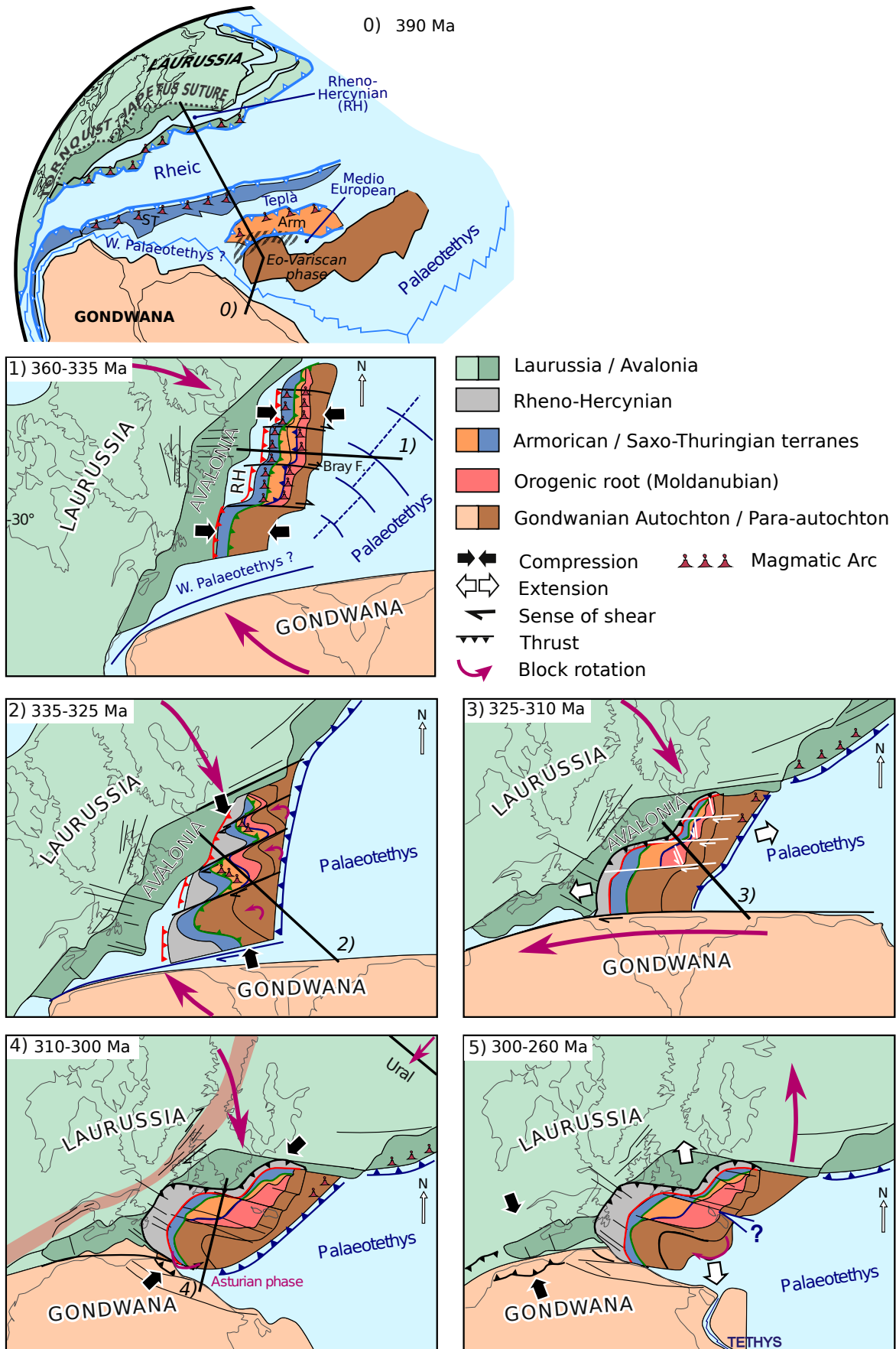
Enfin, une dernière suture *éo-varisque* est identifiée au sud du massif Armoricaïn (Ballèvre *et al.*, 2009; Burg et Matte, 1978; Girardeau *et al.*, 1986; Santallier *et al.*, 1988), qui marque la subduction vers le nord du domaine océanique *Médio-européen* entre le Silurien et le Dévonien inférieur (Faure *et al.*, 2005, 2008). Cette suture, est corrélée avec la suture de Galice dans la zone sud-varisque (Ballèvre *et al.*, 2014), mais sa prolongation vers l'Est est incertaine. Selon certains auteurs, les nombreuses reliques éclogitiques affleurant au coeur des unités métamorphiques allochtones du Massif Central et du massif de Bohême marqueraient une « suture cryptique », fortement remaniée par les événements tectono-métamorphiques postérieurs. (Lardeaux *et al.*, 2014; Schulmann *et al.*, 2014).

1.2.3 Une évolution polyphasée

La formation de la chaîne varisque est un processus long, qui s'étale sur près de 100 Ma entre le Dévonien et le Permien, et implique une succession de plusieurs phases tectoniques, associées à la fermeture diachrone de plusieurs bassins océaniques ou de lithosphère amincie. Une évolution en six étapes est proposée ici, qui se base sur une synthèse récente de Edel *et al.* (2018) compilant un large jeu de donnée paléomagnétiques, tectoniques, géochronologiques, magmatiques et métamorphiques. Une synthèse de l'évolution géodynamique de la chaîne varisque du Dévonien au Permien est présentée sur la Figure 1.7 et la Figure 1.8.

Étape 0 (> 380 Ma) : Une première phase de collision dite *éo-varisque* a lieu entre le Silurien et le Dévonien inférieur, associée à la fermeture du domaine océanique *Médio-européen*. L'âge Siluro-Dévonien de cette première phase repose sur des datations d'éclogites des unités métamorphiques allochtones du Massif Central et du Massif Armoricaïn, qui donnent des âges entre 420 et 400 Ma, interprétés comme l'âge du métamorphisme de haute pression (Berger *et al.*, 2010; Ducrot *et al.*, 1983; Paquette *et al.*, 1995). Cependant, la plupart de ces âges reposent sur des méthodes de datations anciennes, et des estimations

L'OROGENÈSE VARISQUE EN EUROPE DE L'OUEST



34

FIGURE 1.7 – Tentative de reconstitution de l'évolution géodynamique et paléogéographique des domaines varisques entre le Dévonien inférieur et le Permien, d'après les modèles de [Edel et al. \(2018\)](#) et [Stampfli et al. \(2013\)](#). La trace approximative des coupes de la [Figure 1.8](#) est figurée en noir. Voir description dans le texte. Arm Armorica, ST bloc Saxo-Thuringien

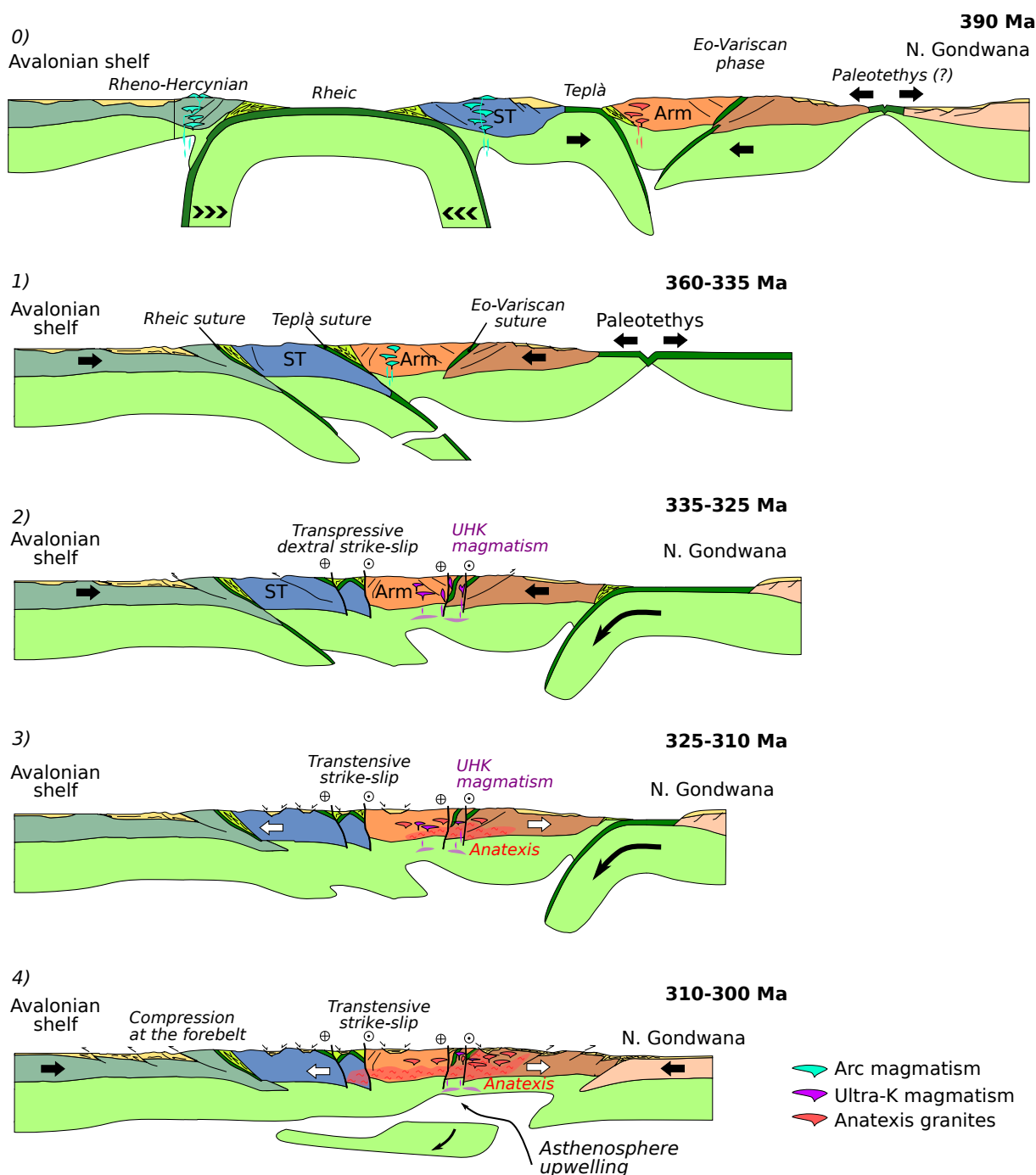


FIGURE 1.8 – Coupes synthétiques de l'évolution géodynamique de la chaîne varisque entre le Dévonien inférieur et le Permien, d'après les modèles de Edel *et al.* (2018) et Stampfli *et al.* (2013). Voir Figure 1.7 pour la légende et le code couleur. Arm Armorica, ST bloc Saxo-Thuringien

plus récentes semblent plutôt indiquer un âge dévonien (ca. 390-370 Ma) pour le stade de haute pression éo-varisque (Lotout *et al.*, 2018, 2020; Paquette *et al.*, 2017). À la suite de cette subduction, une phase d'extension arrière-arc liée à la subduction de l'océan rhéique provoque l'ouverture de petits bassins marginaux au cours du Dévonien moyen à supérieur, comme le bassin de la Brévenne au nord du Massif Central (Faure *et al.*, 2005), ou le domaine Rhéno-Hercynien le long de la marge avalonienne (Franke *et al.*, 2017). Les domaines au sud-est de la chaîne varisque sont par ailleurs affectés par l'ouverture de la Paléotéthys à partir du Silurien (Stampfli *et al.*, 2013). Cependant, l'extension de la Paléotéthys à la partie ouest de l'Europe, telle que proposée par (Stampfli *et al.*, 2011), est débattue, en raison de l'absence de traces de cet océan autour du bassin méditerranéen occidental. La Paléotéthys se terminerait plutôt en biseau quelque part au niveau de la Grèce et des Balkans (Pešić *et al.*, 1988; Zulauf *et al.*, 2015).

Étape 1 (360–335 Ma) : Entre le Dévonien supérieur et le Carbonifère inférieur (Tournaisien), un mouvement de convergence E–W entraîne la fermeture progressive du domaine Rhéique et la collision entre les différents blocs péri-gondwaniens. Dans la géométrie actuelle, cette phase de compression apparaît plutôt de direction NW–SE, et est à l'origine d'une tectonique de nappes bien enregistrée dans l'ensemble des massifs varisques (Ballèvre *et al.*, 2009, 2014; Faure *et al.*, 2009; Schulmann *et al.*, 2009; Shail et Leveridge, 2009).

Étape 2 (335–325 Ma) : Au cours du Viséen, la convergence change de direction et s'opère selon un axe général N–S à NE–SW. Ce changement de direction serait lié à la fermeture du domaine Rhéno-Hercynien, entraînant une relocalisation de la subduction sur la marge nord de la Paléotéthys (Edel *et al.*, 2018). Cette seconde phase de compression, presque orthogonale à l'ancienne, est à l'origine d'une tectonique décrochante dextre de direction NW–SE (Edel et Weber, 1995; Žák *et al.*, 2014), associée à une rotation anti-horaire de l'assemblage de blocs varisques.

Étape 3 (325–310 Ma) : Un épisode extensif majeur a lieu au Serpukhovien-Baskirien. Cette extension est accommodée par des décrochements dextres de direction NW–SE et par la formation de décrochements sénestres secondaires de direction NE–SW, découpant la chaîne en blocs grossièrement losangiques. Cette phase est associée à un métamorphisme de haute température dans le coeur de la chaîne, associée à une migmatisation intense des domaines de croûte inférieure et à un magmatisme post-collisionnel. (Faure, 1995; Moyen *et al.*, 2017; Talbot *et al.*, 2005; Žák *et al.*, 2014).

Étape 4 (310–300 Ma) : Une phase tardive de raccourcissement N–S à NE–SW a lieu au Carbonifère supérieur, provoquée par la collision du Gondwana avec l'assemblage de blocs péri-gondwaniens. Cette phase de raccourcissement est à l'origine de la formation de la syntaxe Ibéro-Armoricaine, donnant la forme arquée actuelle de la chaîne. Elle se développe principalement dans les domaines externes de la chaîne (Edel *et al.*, 2018).

Étape 5 (300–260 Ma) : Enfin, une phase d'extension tardive NNE–SSW a lieu entre le Carbonifère supérieur et le Permien, provoquant la formation de petits bassins continentaux sur l'ensemble de la chaîne (Faure, 1995). Dans la partie sud-est de la chaîne varisque (bloc Corso–Sarde, Italie), cette phase d'extension est particulièrement marquée, et est associée à un métamorphisme HT et à un magmatisme à dominance mantellique, marqué par la mise en place de séries d'andésites–dacites (Briançonnais), de gabbros (zone d'Ivrée), et de granitoïdes peralcalins (Corse) (Ballèvre *et al.*, 2018; Kunz *et al.*, 2018; Manzotti *et al.*, 2018; Rossi et Cocherie, 1991; Spalla *et al.*, 2014).

1.3 Des caractéristiques typiques d'un orogène chaud

L'orogénèse varisque se caractérise par un abondant magmatisme syn à post-collisionnel (Faure, 1995; Ledru *et al.*, 2001; Moyen *et al.*, 2017; Vanderhaeghe *et al.*, 2020), accompagné

d'un métamorphisme de haute à ultra-haute température (HT/UHT) dans les unités internes allochtones (O'Brien, 2000; Usuki *et al.*, 2017; Schantl *et al.*, 2019). Ce magmatisme est à l'origine d'une grande diversité de granitoïdes, allant de termes très peralumineux (types MPG et CPG de Barbarin, 1999), associés à la fusion de sources crustales riches en métasédiments, à des granitoïdes calco-alcalins à subalcalins potassiques, associés à de la fusion de roches crustales intermédiaires à mafiques et / ou à l'hybridation entre des sources crustales et mantelliques (Moyen *et al.*, 2017), (Figure 1.9). Dans les domaines internes (Massif Central, Vosges–Forêt-Noire, Alpes Externes, et zone Moldanubienne du massif de Bohême), les granites peralumineux sont associés à des séries métalumineuses potassiques à ultrapotassique. Ces roches forment la série des *Durbachites-Vaughnérites* (Janoušek *et Holub*, 2007; Janoušek *et al.*, 2019; Von Raumer *et al.*, 2014), et sont interprétées comme des produits de fusion d'un manteau métasomatisé. Le magmatisme syn à post-collisionnel varisque témoigne donc d'une fusion généralisée des domaines crustaux profonds de la zone interne, et d'une partie du manteau supérieur métasomatisé, probablement associée à des épisodes de remontées asthénosphériques, provoquée par la délamination de portions de manteau lithosphérique ou par des épisodes de rupture ou retrait de slab (Laurent *et al.*, 2017; Žák *et al.*, 2014).

La chaîne varisque présente en outre des caractéristiques rhéologiques atypiques en comparaison avec les orogènes « froids » modernes, comme les Alpes ou l'Himalaya, et présente certaines caractéristiques d'orogènes chauds (Figure 1.10). Elle se caractérise par une déformation très ductile dans les niveaux crustaux inférieurs, succédant à la phase d'épaississement par empilement de nappes (Chardon *et al.*, 2009). Ce type de tectonique est associé à un fluage généralisé de la croûte inférieure partiellement fondue (*e.g.* Cochelin *et al.*, 2017; Schulmann *et al.*, 2008). La présence de larges domaines partiellement fondus peu denses dans la croûte inférieure est susceptible de générer des instabilités de Rayleigh-Taylor, et ainsi de provoquer des remontées de matériel migmatitiques à des niveaux supérieurs de la

1.3 Des caractéristiques typiques d'un orogène chaud

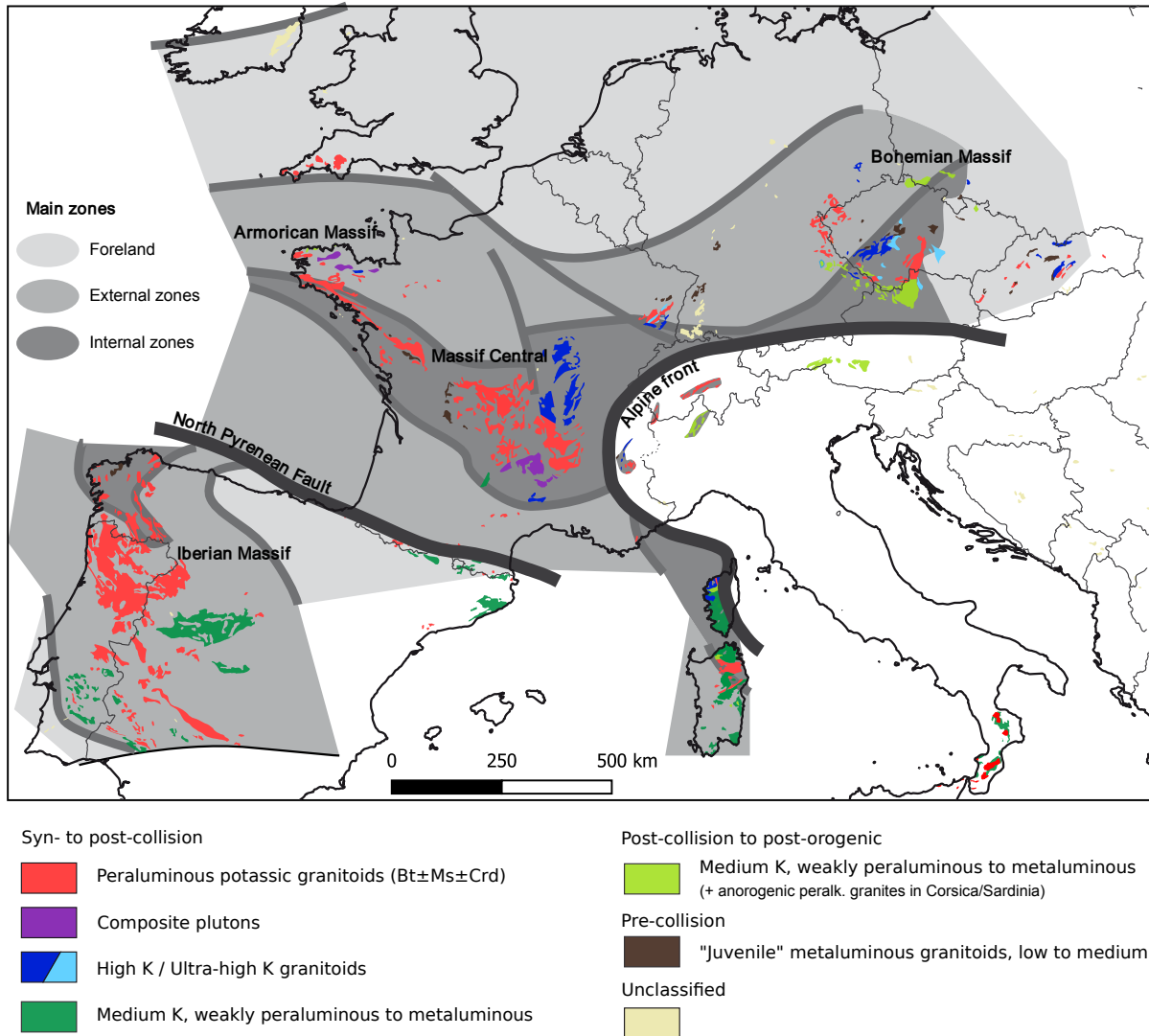


FIGURE 1.9 – Typologie des granitoïdes varisques, d'après *Jacob et al. (2021a)*

croûte, au sein de dômes migmatitiques ou de diapirs (*Schulmann et al., 2014; Vanderhaeghe et al., 2020*), (*Figure 1.10*).

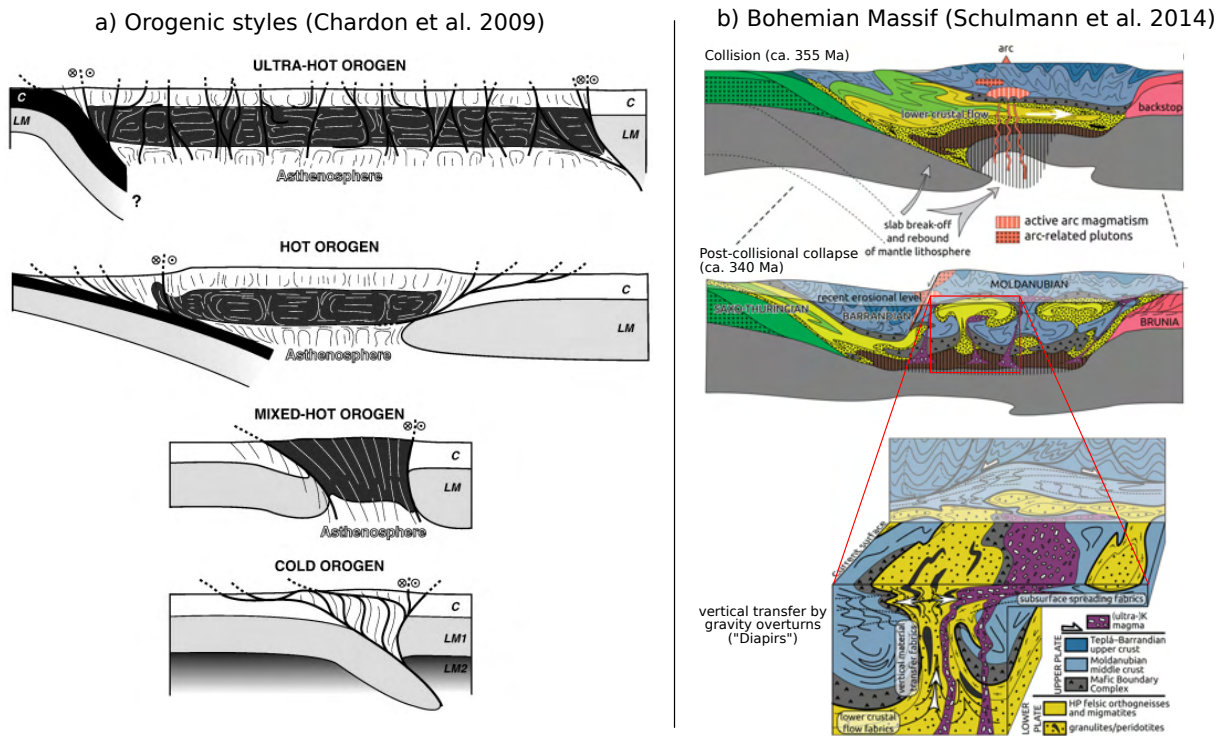


FIGURE 1.10 – Comparaison entre différents types orogéniques proposés par Chardon *et al.* (2009) (a) et interprétation des structures crustales dans le massif de Bohême d’après Schulmann *et al.* (2014) (b). Les structures observées en Bohême sont interprétées comme le résultat d’un fluage généralisé dans la croûte inférieure à intermédiaire. Des instabilités gravitaires apparaissent lors des stades post-collisionnels, provoquant des remontées de croûte inférieure migmatitique au seins de dômes ou de diapirs crustaux

1.4 Comparaison avec le système orogénique

Himalaya–Tibet

De par son étendue géographique et sa durée de mise en place, la chaîne varisque européenne est comparable au système orogénique Himalaya–Tibet. Les similitudes vont cependant plus loin qu’une simple équivalence de taille, et de nombreux autres points de comparaison existent entre ces deux ensembles (Maierová *et al.*, 2016; Matte, 1986).

Premièrement, la géométrie des deux systèmes est similaire : dans les deux cas, l’orogénèse résulte de la collision entre plusieurs petits blocs continentaux et une marge continentale active (blocs péri-gondwaniens le long de la Laurussia / terranes Cimmériens le long de

1.4 Comparaison avec le système orogénique Himalaya–Tibet

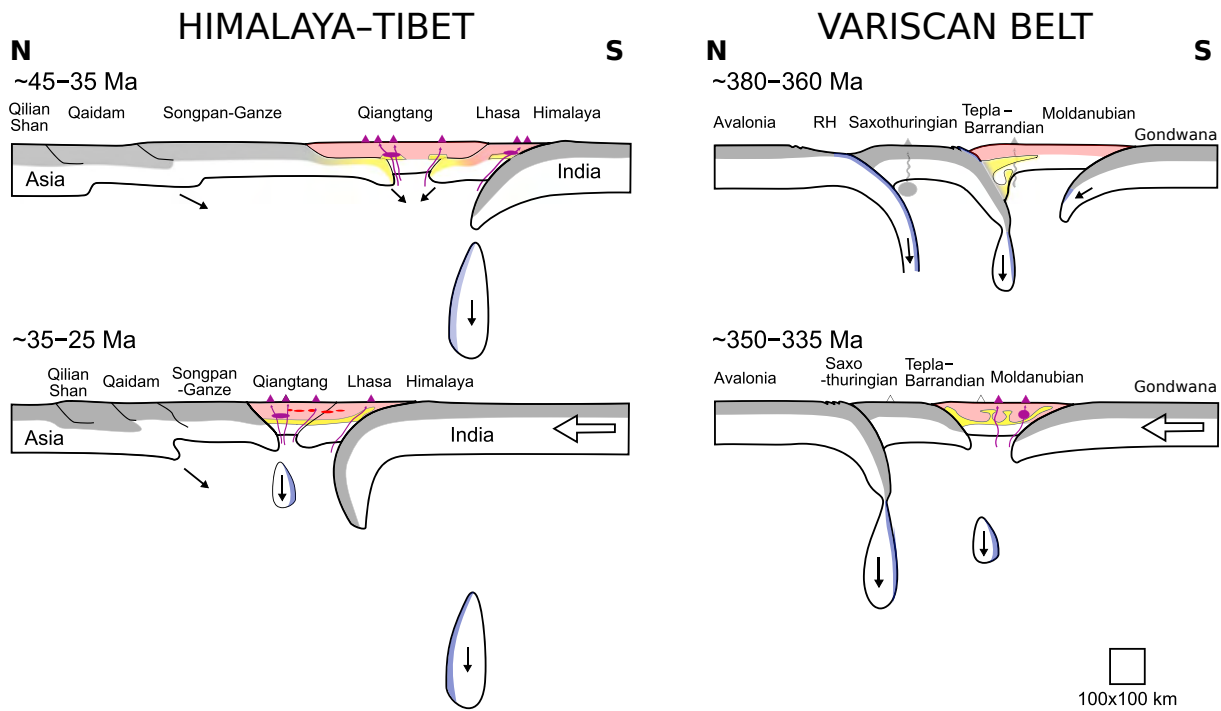


FIGURE 1.11 – Comparaison des scénarios géodynamiques de formation de la chaîne varisque (*d.*) et du système Himalaya–Tibet (*g.*), résultant de l'accrétion de plusieurs blocs continentaux. D'après [Maierová et al. \(2016\)](#)

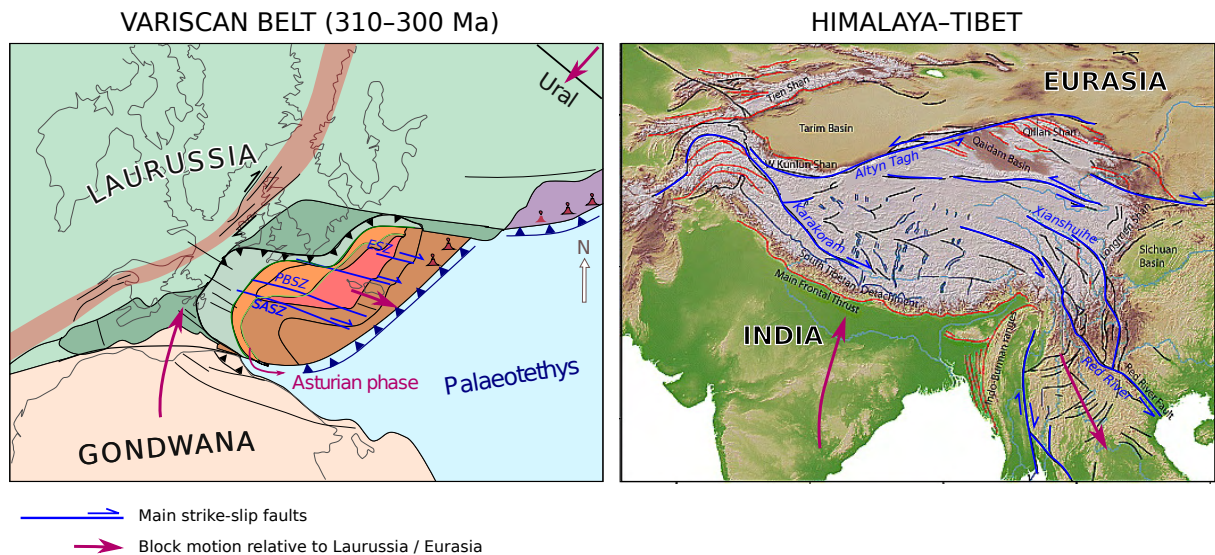
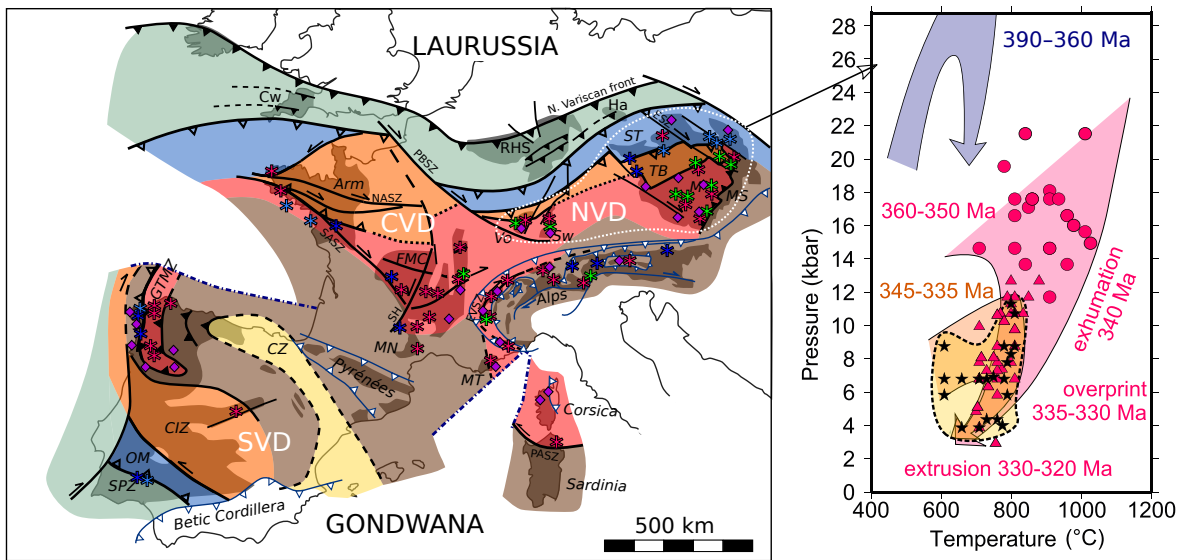


FIGURE 1.12 – Comparaison des systèmes orogéniques varisque *g.* et himalay-tibétain *d.*, mettant en évidence l'importance de la tectonique décrochante dans l'accommodement du raccourcissement, par extrusion latérale de matière selon le modèle de [Tapponnier et al. \(1982\)](#). Figures modifiées d'après [Cook et Royden \(2008\)](#); [Edel et al. \(2018\)](#)

a) Variscan Belt



b) Himalaya-Tibet

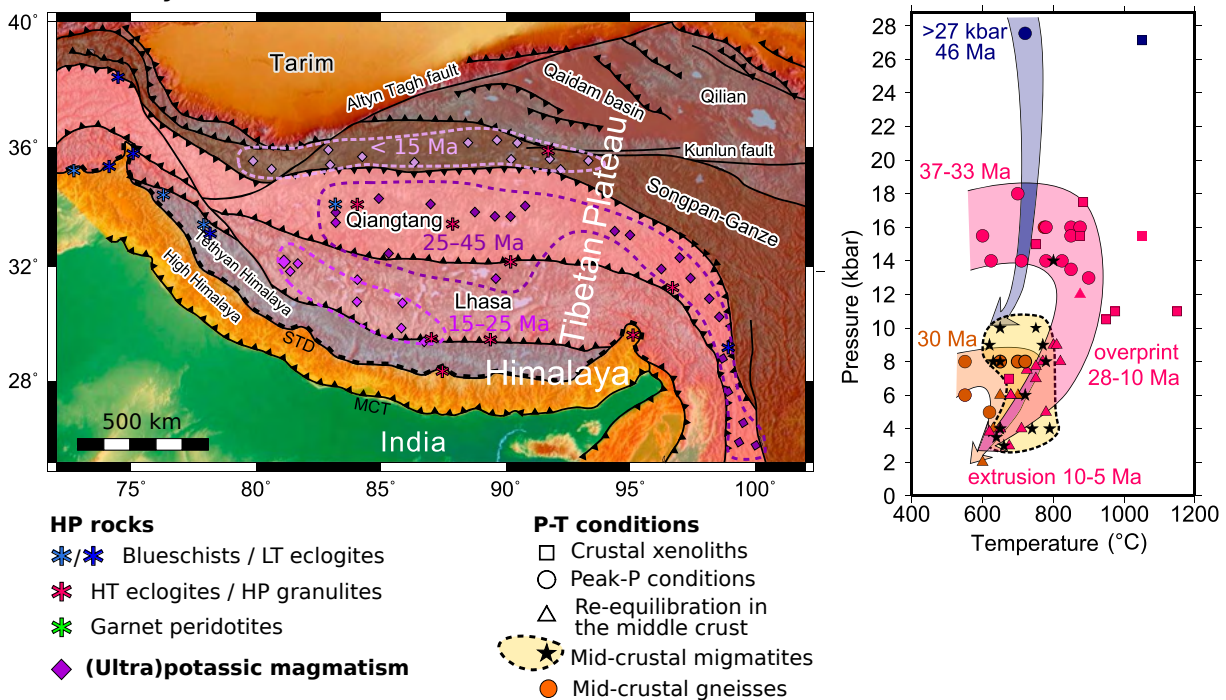


FIGURE 1.13 – Carte des reliques métamorphiques de haute pression (HP) au sein de la chaîne varisque et de la chaîne himalayano-tibétaine, et compilation des données P-T-t associées. Voir Figure 1.6 pour les légendes de la figure a). La distribution du magmatisme (ultra) potassique est indiquée en violet. On retrouve dans les deux chaînes (i) une phase HP-BT précoce, formant des schistes bleus et des éclogites BT rapidement exhumées au niveau des zones de suture (chemin bleu); (ii) une phase HP-HT plus tardive, formant des éclogites HT et des granulites HP, qui sont exhumées plus lentement et qui se ré-équilibrent partiellement dans la croûte intermédiaire (chemin rose). Le chemin orange montre l'évolution P-T-t des domaines crustaux intermédiaires, et les étoiles montrent les conditions P-T enregistrées au sein des migmatites. Modifié d'après Maierová *et al.* (2016).

l'Eurasie), suivie d'une collision terminale avec un bloc continental rigide (Gondwana / Inde) (**Figure 1.11**). La collision entre un bloc continental rigide formé de vieille croûte cratonique et un assemblage de terranes peu consolidés et séparés par des sutures entraîne une extrusion latérale de matière, selon le modèle de l'indenteur rigide proposé par **Tapponnier *et al.* (1982, 1986)**. Cette extrusion latérale est favorisée par la présence d'un bord libre à l'est (Paléotéthys / Océan Pacifique), et est accommodée par des décrochements d'échelle lithosphérique (**Figure 1.12**) : La faille de Bray, les zones de cisaillement Nord et Sud-Armoricaine pour la chaîne varisque (**Edel *et al.*, 2018; Matte, 1986**) ; la faille du Karakorum, de l'Altyn-Tagh, ou de l'Ailao Shan – fleuve rouge pour la chaîne himalayo-tibétaine (**Leloup *et al.*, 1995; Valli *et al.*, 2007**).

Ces deux ensembles présentent en outre des évolutions métamorphiques similaires, avec en particulier deux phases successives de métamorphisme de haute pression (HP) : (i) une phase HP–BT précoce, formant des schistes bleus et des éclogites BT, que l'on retrouve le long des anciens complexes de subduction marquant la fermeture de domaines océaniques ; (ii) une phase de HP – HT/UHT plus tardive, formant des éclogites HT et des granulites HP qui affleurent sporadiquement dans les zones internes, liée à la formation et au maintien sur une longue période d'une croûte orogénique sur-épaissie (jusqu'à 60–70 km), dont la portion inférieure est équilibrée dans le facies éclogitique / granulitique HP (**Guillot *et al.*, 2008; Maierová *et al.*, 2016; O'Brien, 2000, 2019**), (**Figure 1.13**).

Enfin, les deux systèmes sont marqués par la présence de séries magmatiques ultrapotassiques, mises en places lors des stades post-collisionnels, et caractérisées par des signatures géochimiques hybrides. Ces roches présentent en effet à la fois des caractéristiques marquant une source mantellique (Mg# élevé, fortes teneurs en Cr et Ni indiquant la fusion d'une source riche en olivine) et des caractéristiques de sources crustales (teneur élevée en K₂O, LREE et LILE, anomalies négatives en Ti, Nb et Ta, signatures isotopiques Sr-Nd

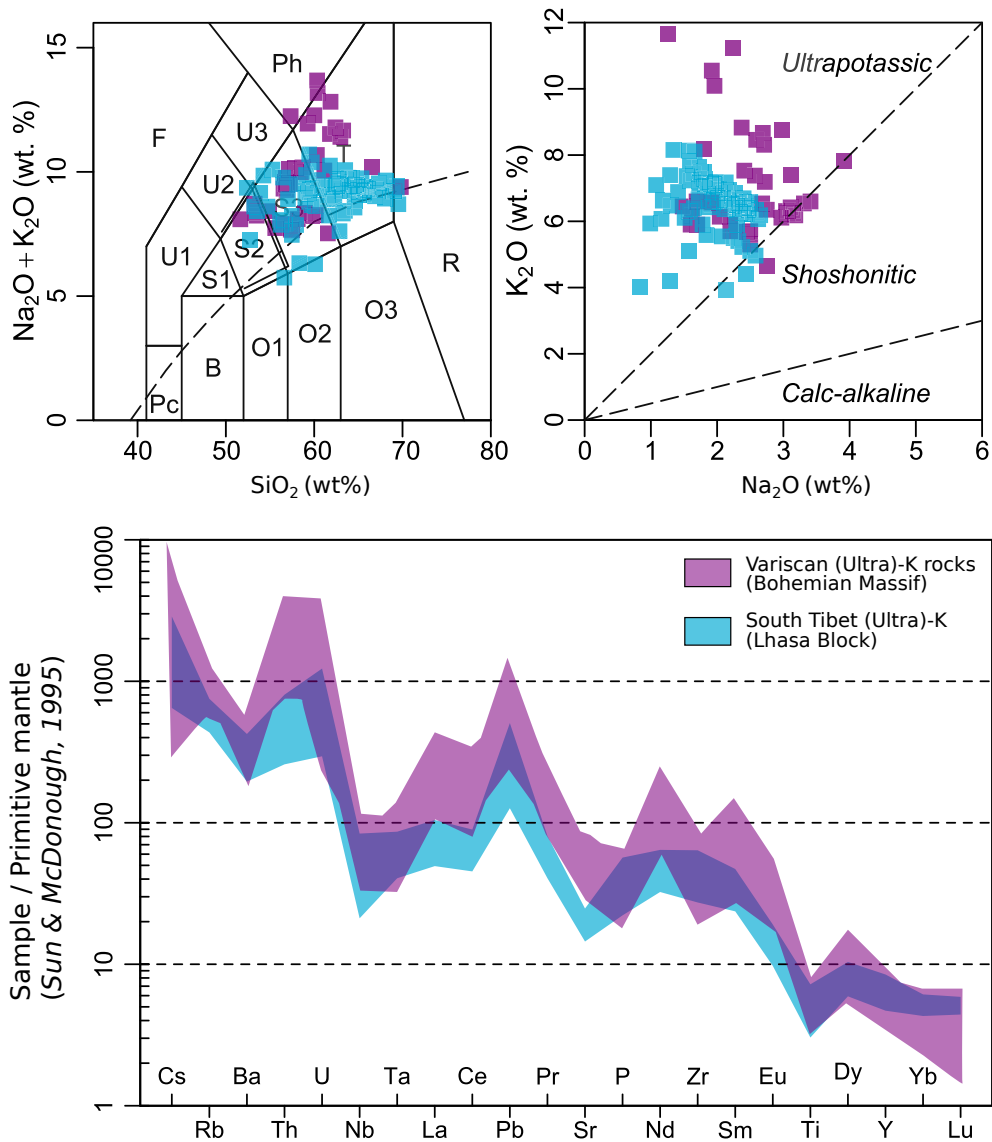


FIGURE 1.14 – Comparaison des caractéristiques géochimiques des roches (ultra)potassiques varisques (violet) et du Sud Tibet (bloc de Lhasa) (bleu). F = foidite, Pc = microbasalt, B = basalt, O1 = basaltic andesite, O2 = andesite, O3 = dacite, S1 = trachybasalt, S2 = basaltic trachyandesite, S3 = trachyandesite, T = trachyte/trachydacite, R = rhyolite, U1 = tephrite/basanite, U2 = phonotephrite, U3 = tephriphonolite, Ph = phonolite. Modifié d'après [Maierová et al. \(2016\)](#).

crustales) ([Figure 1.14](#)). Ce caractère dual est interprété comme le produit de la fusion d'un manteau lithosphérique métasomatisé par des fluides dérivé de croûte continentale mature, subduite dans le manteau lors de la collision ([Janoušek et Holub, 2007](#)). En revanche, les granitoïdes syn à post-collisionnels sont plutôt rares dans la chaîne himalayo-tibétaine, à l'exception des leucogranites himalayens. Cette différence marque le fait que les stades

post-collisionnels durant lesquels la majeure partie des granitoïdes varisques ont été produits n'ont pas encore eu lieu dans le cas de la collision Inde–Asie.

1.5 Quelques points essentiels à retenir sur la chaîne varisque européenne

- La chaîne varisque d'Europe résulte de la collision de plusieurs microcontinents périgondwaniens avec la Laurussia au cours du Dévonien, suivie de la collision terminale avec le Gondwana au Carbonifère.
- La géométrie du système orogénique varisque n'est pas parfaitement cylindrique, et différents segments de la chaîne ont pu connaître des évolutions assez différentes et diachrones (Lardeaux *et al.*, 2014). Par ailleurs, la continuité des sutures n'est pas toujours bien établie entre les différents segments de la chaîne, en particulier en ce qui concerne la suture éo-varisque.
- La tectonique décrochante a joué un rôle important dans la structuration de la chaîne à partir du Carbonifère supérieur. Ainsi, différents segments de la chaîne se retrouvent aujourd'hui séparés par de grandes failles décrochantes d'échelle lithosphérique.
- Les stades post-collisionnels sont caractérisés par un échauffement important et la fusion importante des domaines de croûte inférieure. Ceci entraîne un fluage important des domaines partiellement fondus, qui se retrouvent parfois exhumés au sein de dômes migmatitiques ou de diapirs. Outre l'accumulation de chaleur radiogénique au sein de la croûte épaissie, cet échauffement est aussi probablement lié à un flux de chaleur mantellique élevé, provoqué par des phénomènes de remontées d'asthénosphère lors d'épisodes de délamination lithosphérique. Ainsi, la chaîne varisque européenne présente des caractéristiques rhéologiques d'un orogène chaud (Chardon *et al.*, 2009).

- De par son étendue, sa géométrie et son histoire géodynamique, la chaîne varisque d'Europe est un bon analogue ancien de l'actuel système orogénique himalayo-tibétain, ce qui fait de ces deux ensembles des objets complémentaires dans l'étude des processus orogéniques associés à la collision.

CHAPITRE 2

Les domaines varisques dans les Alpes



Sommaire

2.1	Organisation générale de la chaîne alpine	49
2.1.1	La géodynamique alpine	49
2.1.2	Structure générale de la chaîne alpine	50
2.1.3	Le métamorphisme alpin	52
2.1.4	Structure profonde de la chaîne alpine	55
2.2	Les domaines de socle anté-Mésozoïque dans les Alpes	56
2.2.1	Des domaines issus de la marge nord du Gondwana	57
2.2.2	L'orogénèse varisque dans les Alpes	59
2.2.3	Des enregistrements Paléozoïques contrastés, marqueurs de la zono- néographie varisque	62
2.3	Focus sur les domaines externes de la marge européenne : les massifs cristallins externes (MCE)	64
2.3.1	Les événements alpins dans les MCE	64
2.3.2	Le socle varisque dans les MCE	67
2.3.3	Les différentes phases tectono-métamorphiques varisques dans les MCE	70
2.4	Questions en suspens	71

2.1 Organisation générale de la chaîne alpine

2.1.1 La géodynamique alpine

La chaîne alpine résulte de la fermeture de plusieurs petits bassins téthysiens (océan Liguro-Piémontais, bassin Valaisan, océan de Meliata–Maliac–Vardar) à partir du Crétacé, entraînant la collision entre le continent européen et la microplaque adriatique (ou apulienne) au cours du Cénozoïque (Handy *et al.*, 2010; Schmid *et al.*, 2004; van Hinsbergen *et al.*, 2019). Ces bassins correspondent à de petits domaines océaniques ou de lithosphère hyperamincie (transition océan-continent), ouverts à partir du Trias et faisant la jonction entre la Téthys à l'est et l'Océan Atlantique à l'ouest (Figure 2.1).

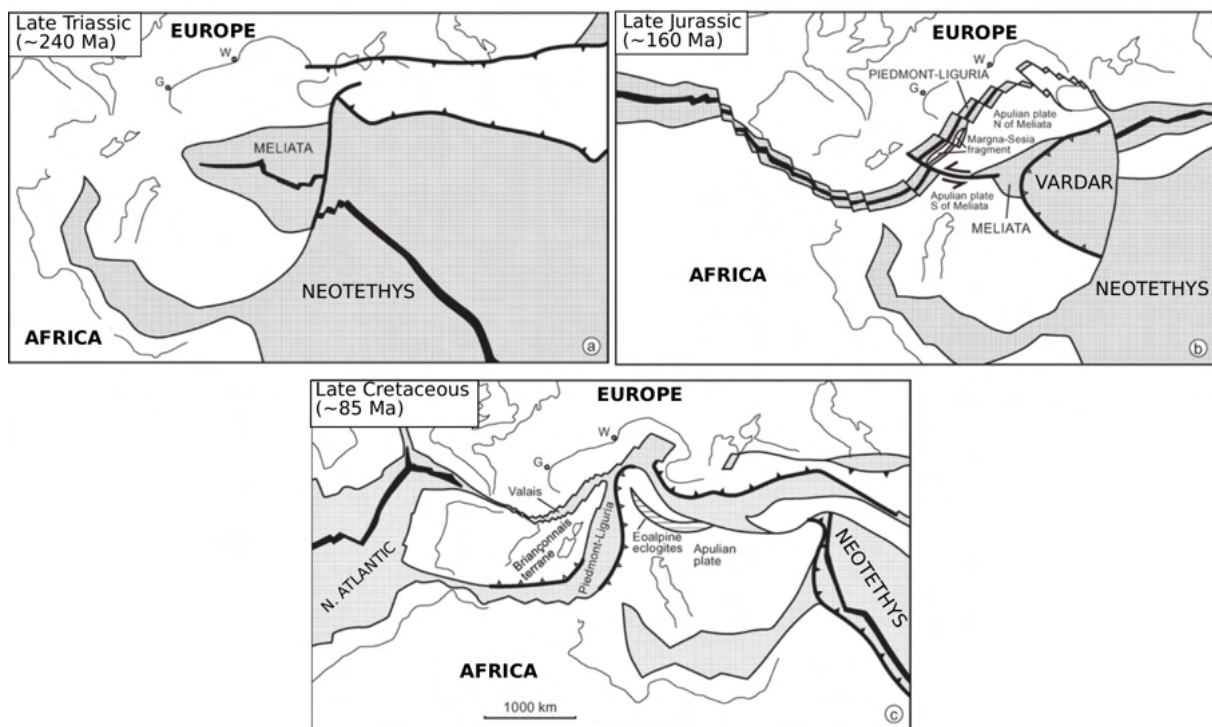


FIGURE 2.1 – Reconstitution paléogéographique des domaines alpins au Trias supérieur (a), au Jurassique supérieur (b) et au Crétacé supérieur (c). D'après Schmid *et al.* (2004).

L'orogénèse alpine comporte deux phases orogéniques bien distinctes (Figure 2.2) : (i) une première phase *éo-alpine* a lieu au Crétacé supérieur, et correspond à un épisode précoce de

subduction intra-continentale et d'empilement de nappes au sein des unités austro-alpines (Alpes orientales), selon une direction N–S. Cette phase est responsable de la formation des unités éclogitiques de Koralpe-Wölz, dont le stade de haute pression est daté à 90–95 Ma (Thöni *et al.*, 2008). (ii) La phase alpine *sensu stricto* débute à la fin de Crétacé (ca. 60 Ma), et correspond à la subduction des unités océaniques liguro-piémontaises, suivie de la collision entre la plaque européenne et la plaque adriatique à partir de l'Éocène (ca. 40 Ma). Un changement de direction de raccourcissement est observé au cours de l'Oligocène : d'abord N–S durant le Crétacé et le Paléocène, le raccourcissement prend une direction E–W dans les Alpes occidentales (Handy *et al.*, 2010; Malusà *et al.*, 2021; Schmid *et al.*, 2004; van Hinsbergen *et al.*, 2019).

2.1.2 Structure générale de la chaîne alpine

La chaîne alpine est séparée en plusieurs domaines lithotectoniques, représentés sur la **Figure 2.3**. Ces domaines correspondent aux unités autochtones et allochtones dérivées des plaques européenne et adriatique, ainsi qu'aux unités associées aux anciens bassins océanique (Bousquet *et al.*, 2008; Handy *et al.*, 2010; Schmid *et al.*, 2004). D'ouest en est (ou du nord au sud dans les Alpes centrales et orientales), on retrouve :

- les unités autochtones de la marge Européenne, qui forment le domaine *Helvétique* ;
- les unités distales allochtones de cette même marge, que l'on retrouve dans les Alpes centrales (domaine Lépointin, nappe d'Adula, massif du Gotthard) et qui apparaissent en fenêtre dans les Alpes orientales (Tauern) ;
- les unités de flysch associées au bassin *Valaisan* ;
- le domaine *Briançonnais*, qui dérive d'un microbloc détaché du continent européen lors de l'ouverture du bassin Valaisan, et affilié au bloc corso-sarde ;

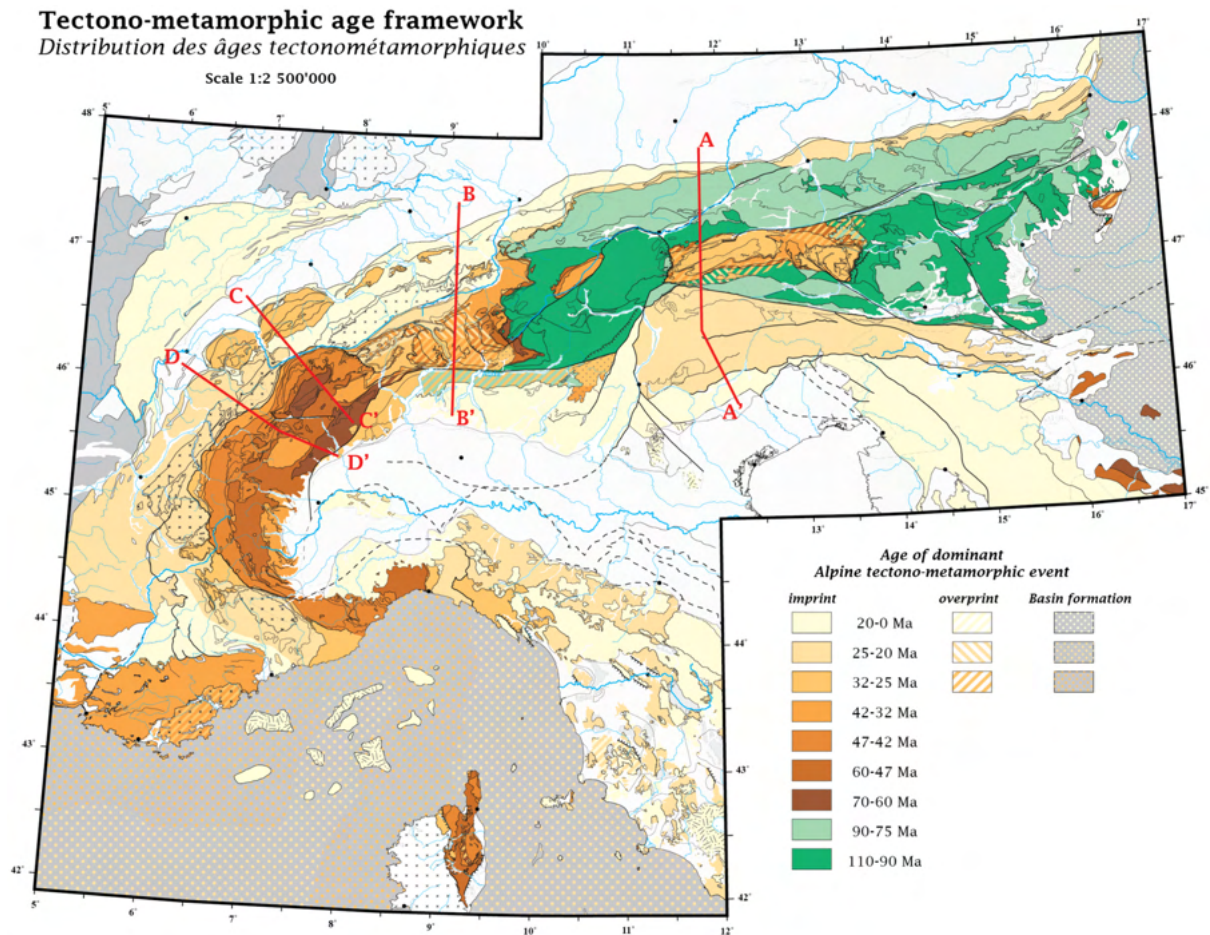


FIGURE 2.2 – Distribution des âges des principales phases tectono-métamorphiques dans les Alpes, d'après Bousquet *et al.* (2008). La phase Eo-alpine est marquée par un métamorphisme d'âge Crétacé dans les nappes Austro-alpine (Alpes orientales), alors que la phase alpine *s.s.* est marquée par un métamorphisme Paléogène (ca. 60–20 Ma).

- les unités ophiolitiques de l'océan *Liguro-Piémontais* et de l'ancien prisme d'accrétion formé lors de la subduction ;
- les nappes allochtones dérivées de la plaque adriatique, qui incluent les nappes du domaine *Austro-alpins* dans les Alpes orientales et la nappe de la Dent Blanche et la zone de Sesia dans les Alpes occidentales ;
- Les unités autochtones de la plaque adriatique, séparées des unités allochtones par la ligne insubrienne, qui forment le domaine *Sud-alpin*.

Les unités allochtones de la marge européenne, le domaine Briançonnais et les domaines

Valaisans et Liguro–Piémontais sont parfois regroupés ensemble sous le terme de *nappes penniques*, qui forment le cœur de la chaîne alpine. Cette dénomination est héritée de concepts tectoniques anciens (*e.g.* Argand *et al.*, 1911), selon lesquels la structure de la chaîne alpine est essentiellement cylindrique. L’ordre d’empilement actuel des unités refléterait ainsi la zonation paléogéographique Mésozoïque. Cependant, cette typonomie est trompeuse, car elle ne tient pas compte de la complexité des mouvements tectoniques associés au rifting (*e.g.* Masini *et al.*, 2013) et à la fermeture des domaines océaniques. Ainsi, le domaine pennique ne forme pas un ensemble cohérent mais regroupe différents domaines paléogéographiques très différents les uns des autres (Briançonnais et marge européenne distale en particulier).

2.1.3 Le métamorphisme alpin

Les différents domaines de la chaîne ont subi différents degrés de métamorphisme et de déformation lors des stades de subduction et de collision (Figure 2.4 et Figure 2.5). Les domaines externes autochtones Helvétique et Sud-alpin ont largement échappé au métamorphisme alpin. S’il y a bien eu enfouissement puis exhumation de la marge européenne à l’Eocène et à l’Oligocène, le métamorphisme associé est faible et n’excède pas le faciès des schistes verts (Bousquet *et al.*, 2008). En revanche, le métamorphisme et la déformation sont beaucoup plus marqués dans les domaines internes de la chaîne. On observe en fait deux stades successifs de métamorphisme : (i) un métamorphisme éclogitique HP-BT associé à la subduction océanique puis continentale, d’âge Crétacé supérieur à Paléocène (ca. 75–35 Ma, Brouwer *et al.*, 2005; Handy *et al.*, 2010; Rubatto *et al.*, 1999, 2008), qui atteint par endroit des conditions de ultra haute pression dans le champ de stabilité de la coésite (> 3.0 GPa, 650–720 °C, Chopin, 1984; Nowlan *et al.*, 2000); (ii) un métamorphisme barrovien MP-MT d’âge Eocène–Oligocène (ca. 35–20 Ma, Rubatto *et al.*, 2009), associé à la collision dans les Alpes centrales et orientales (Rubatto *et al.*, 2009; Todd et Engi, 1997), qui atteint les conditions du faciès amphibolite (ca. 0.5–0.7 GPa, 600–650 °C, Bousquet *et al.*, 2008; Todd et Engi, 1997).

2.1 Organisation générale de la chaîne alpine

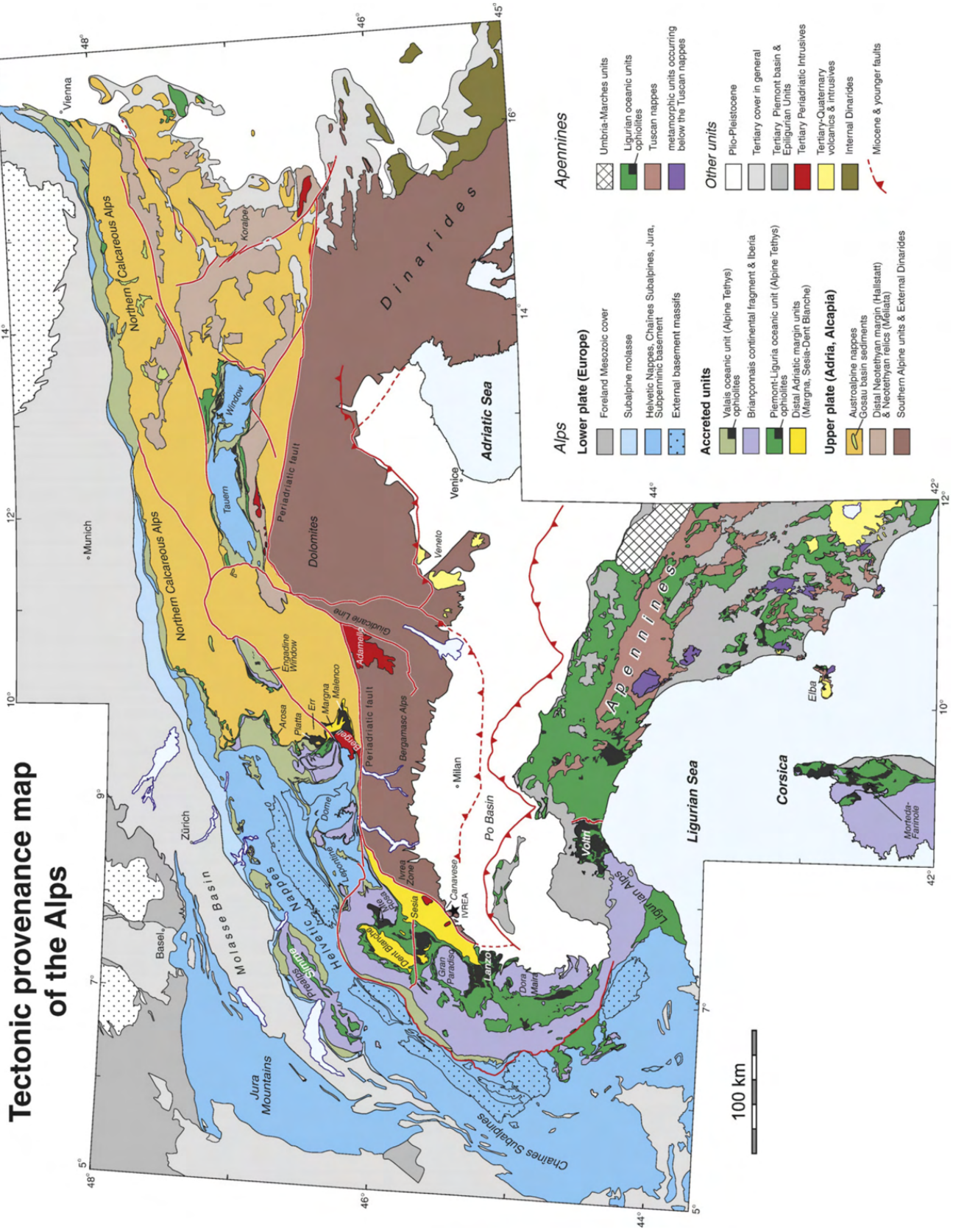


FIGURE 2.3 – Carte tectonique de la chaîne alpine, d'après Handy *et al.* (2010).

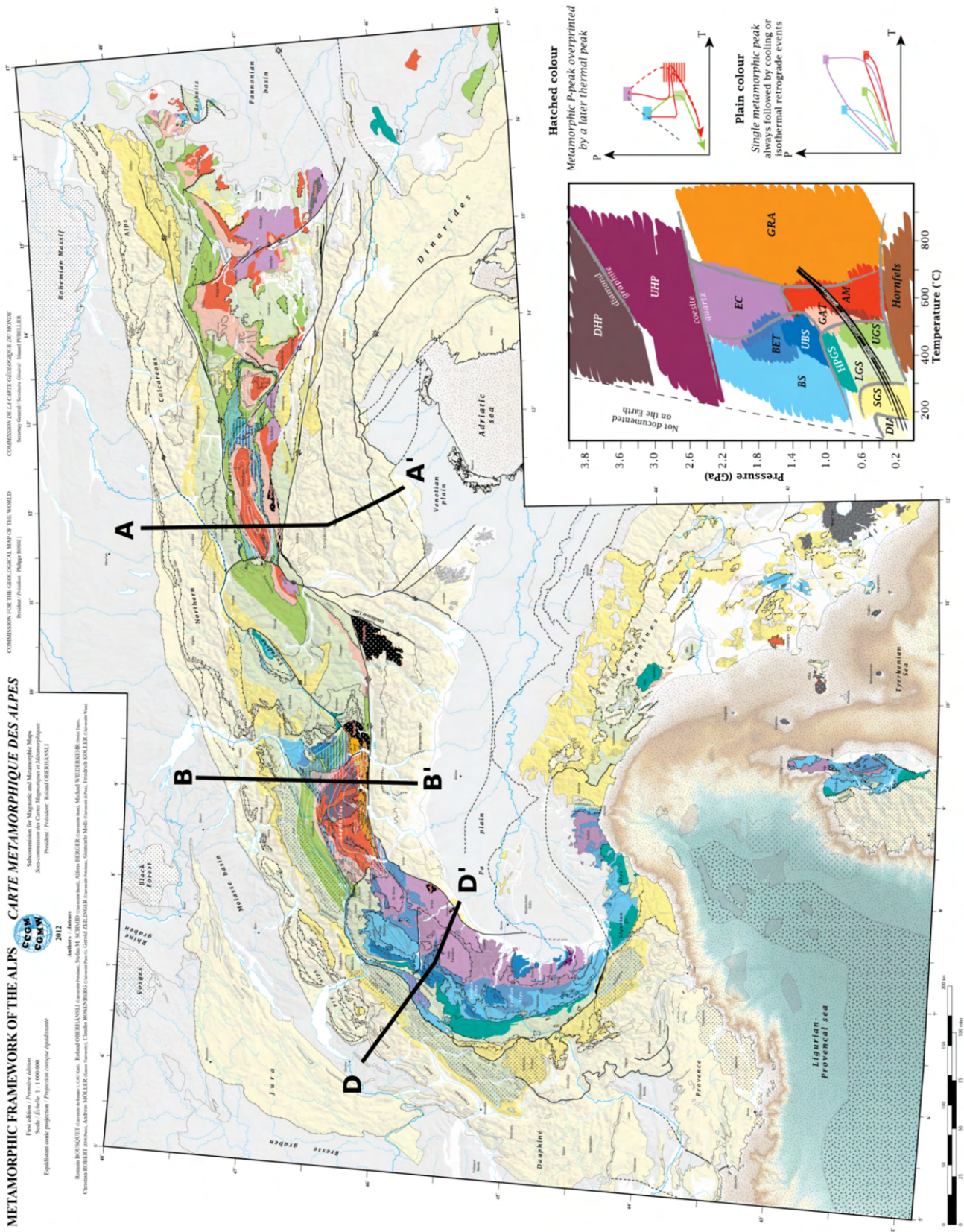


FIGURE 2.4 – Carte du métamorphisme dans les Alpes. D'après *Bouquet et al. (2008)*.

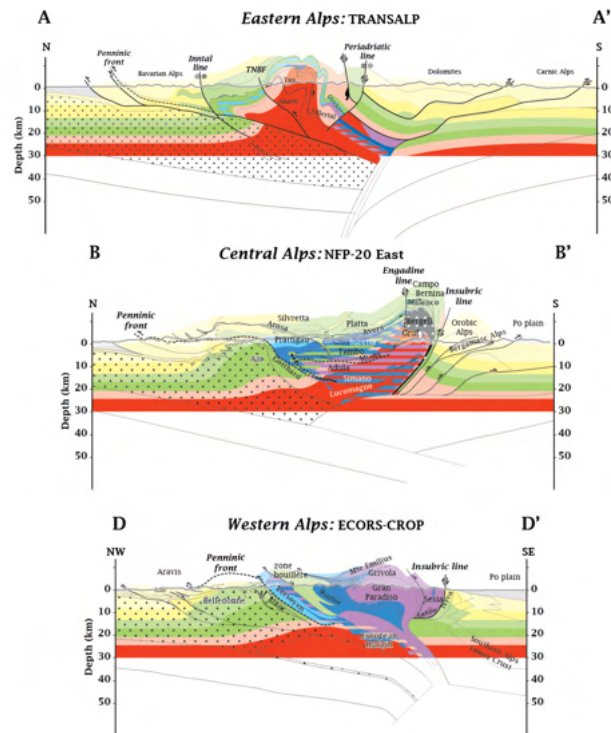


FIGURE 2.5 – Coupes métamorphiques de la chaîne alpine, interprétées à partir des différents profils sismiques TRANSALP, ECORS-CROP et NFP. La position des coupes est figurée sur la Figure 2.4. D’après Bousquet *et al.* (2008).

2.1.4 Structure profonde de la chaîne alpine

La structure crustale et mantellique profonde de la chaîne alpine a récemment fait l’objet de nombreuses études, suite au programme d’imagerie AlpArray mené sur l’ensemble de la chaîne, et aux deux profils sismiques CIFALPS réalisés dans les Alpes occidentales (Lyu *et al.*, 2017; Malusà *et al.*, 2021; Solarino *et al.*, 2018; Zhao *et al.*, 2015, 2016). Entre autres résultats majeurs, ces études ont permis d’imager en profondeur la géométrie des plaques plongeantes (slabs), subduites avant les phases de collision alpine (Figure 2.6). Ainsi, l’évolution tectonique de la chaîne alpine et des massifs voisins (Appenins, Dinarides) implique trois slabs différents, étroitement enchevêtrés : le slab alpin, qui plonge vers le sud-est sous la plaque adriatique, le slab appenin, qui plonge vers l’Ouest sous la mer Tyrrhénienne, et le slab dinarique, qui plonge vers le nord-est sous les Dinarides. Aucune rupture de ces

slabs n'a été mise en évidence, comme cela avait pu être suggéré pour expliquer le magmatisme Oligocène–Miocène des Alpes centrales (Davies et von Blanckenburg, 1995), et leur continuité est observée jusqu'à environ 600 km de profondeur, dans la zone de transition du manteau (Zhao *et al.*, 2016).

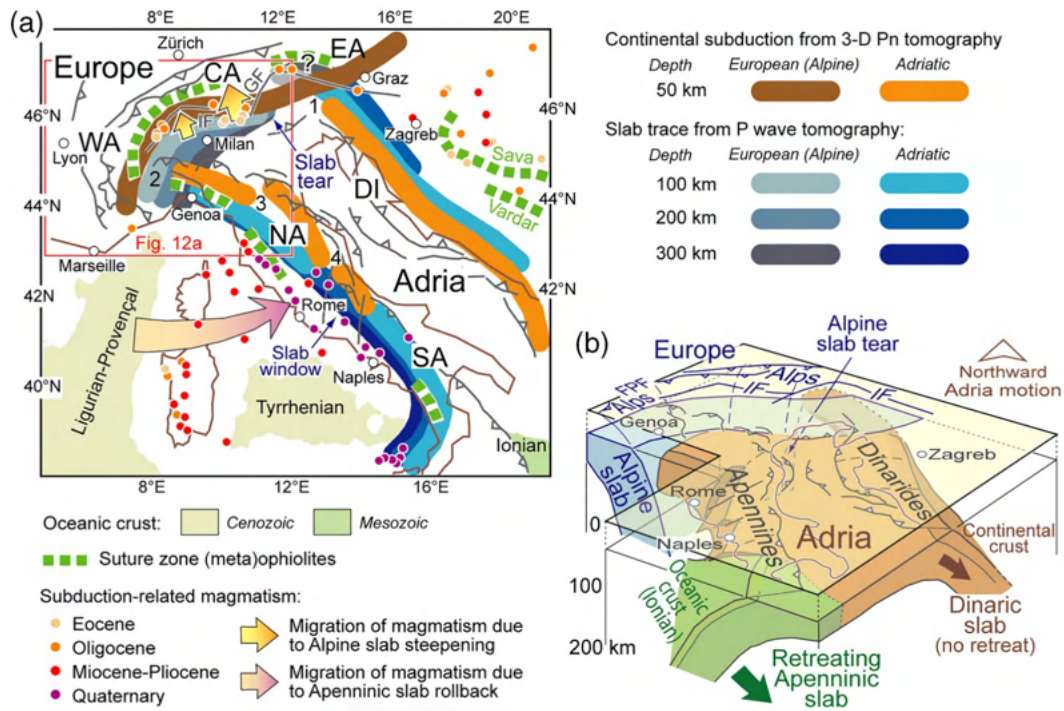


FIGURE 2.6 – Schéma tectonique interprétatif des relations entre les slabs dans la région alpine (a), et interprétation de la structure profonde des slabs obtenue à partir des études tomographiques récentes. D'après Malusà *et al.* (2021).

2.2 Les domaines de socle anté-Mésozoïque dans les Alpes

Le socle anté-triasique forme environ la moitié de la surface exposée au sein de la chaîne alpine (Von Raumer *et al.*, 2013), ce qui fait des Alpes l'un des principaux affleurements de socle Paléozoïque en Europe. Cependant, ce socle ne forme pas un unique bloc cohérent, mais est en fait un ensemble composite, formé de différentes unités agglomérées par la tectonique

alpine (Figure 2.7). Le socle alpin peut ainsi être découpé en quatre grands domaines : la marge européenne autochtone (Helvétique) et distale ; le microbloc Briançonnais ; les domaines allochtones issus de la plaque adriatique (Austro-alpin) ; les domaines autochtones au sud de la ligne insubrienne (Sud-alpin). Ces unités occupaient des positions anté-triasiques différentes, et échantillonnent donc différents domaines de la chaîne varisque. L'évolution anté-triasique des domaines de socle alpin et leur place dans la chaîne varisque européenne est discutée de manière plus exhaustive dans Jacob *et al.* (2022) (*sous presse*), et les principales conclusions sont résumées ci-dessous.

2.2.1 Des domaines issus de la marge nord du Gondwana

A l'instar d'une grand partie du sud et de l'ouest de l'Europe, le socle alpin présente des caractéristiques typiques des domaines issus de la marge nord du Gondwana, à savoir : (i) La prédominance de protolithes magmatiques et sédimentaires d'âge cambro-ordovicien, marquant la distension de la marge nord du Gondwana (Figure 2.8 et Figure 2.9). On retrouve de nombreuses traces de magmatisme alcalin et tholéiitique cambrien, avec plusieurs reliques ophiolitiques cambriennes (Ménot, 1986; Neubauer *et al.*, 1989). (ii) La prédominance de zircons néoprotérozoïques (550–650 Ma) dans les séries détritiques du Paléozoïque inférieur, marquant la proximité avec les anciens arcs magmatiques cadomiens (Chu *et al.*, 2016; Haas *et al.*, 2020; Manzotti *et al.*, 2016). On retrouve aussi une fraction subordonnée de zircons paléoprotérozoïques et archéens, marquant un apport sédimentaire depuis les cratons situés à l'intérieur du Gondwana (bouclier Arabo-Nubien, cratons Trans-Saharien et Ouest-Africain). Par ailleurs quelques portions de socle Néoprotérozoïque affleurent dans les nappes austro-alpines (Neubauer, 1989; Schaltegger *et al.*, 1997), et des orthogneiss néoprotérozoïques ont récemment été identifiés dans des écaillés de socle du domaine Briançonnais (*données non publiées, D. Thiéblemont*).

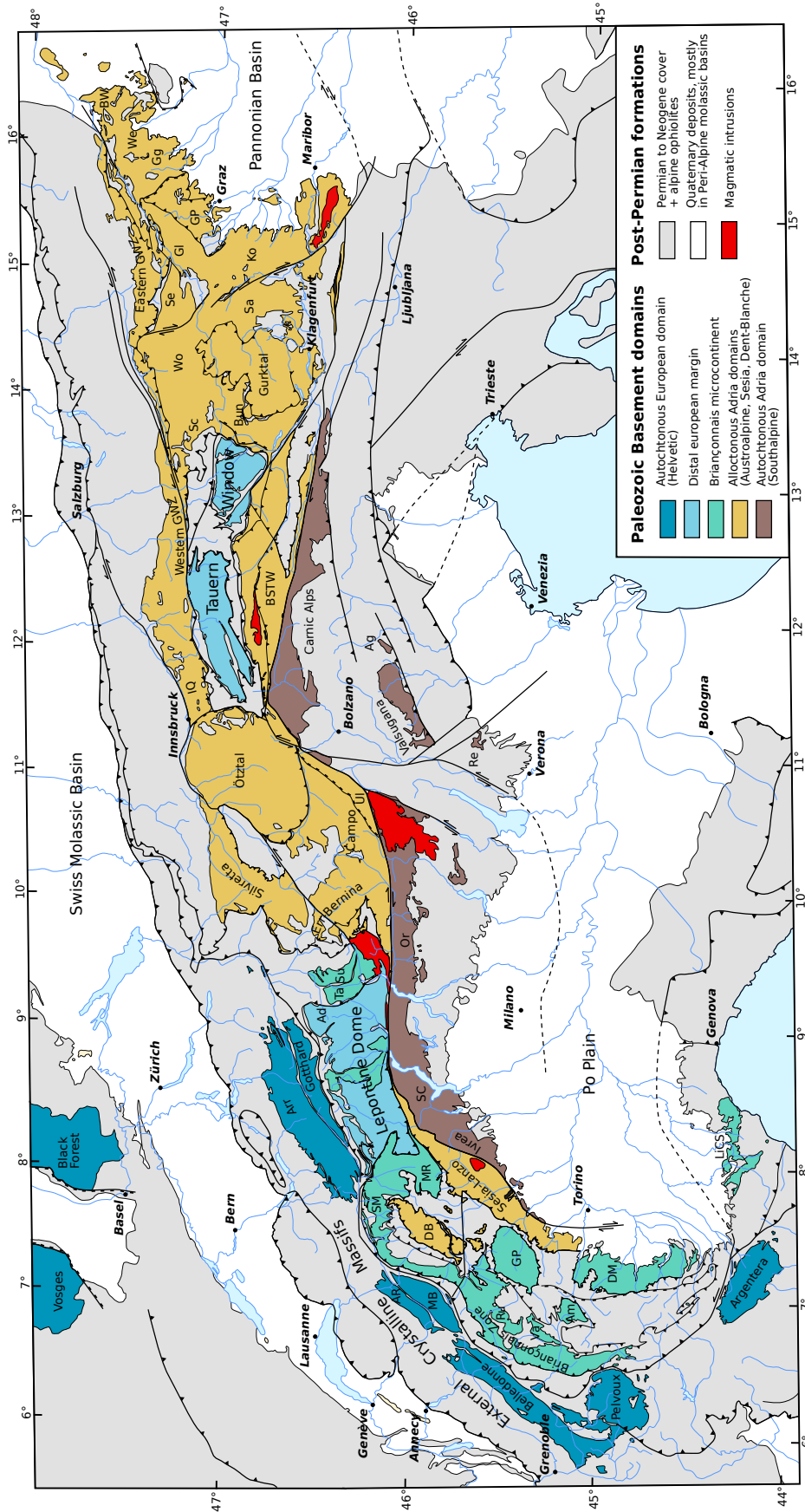


FIGURE 2.7 – Carte des différents domaines de socle anté-Mésozoïque dans les Alpes, modifié d'après Jacob et al., *accepté*.

2.2.2 L'orogénèse varisque dans les Alpes

Dans les domaines internes des Alpes, les phases tectono-métamorphiques varisques sont difficiles à caractériser à cause de la reprise du socle par la tectonique et le métamorphisme alpin. Les événements collisionnels varisques sont donc principalement caractérisés à partir des données thermobarométriques et géochronologiques obtenues sur les roches métamorphiques du socle, ainsi que par la distribution des âges détritiques (zircon, micas) dans les formations sédimentaires paléozoïques et mésozoïques (Chu *et al.*, 2016; Fréville *et al.*, 2018; Haas *et al.*, 2020; Manzotti *et al.*, 2016). L'intensité des épisodes tectono-métamorphiques varisques est variable selon les domaines, allant de très faible ou nul (< schistes verts) à un métamorphisme de faciès amphibolitique supérieur ou granulitique. Les domaines alpins présentent peu de traces d'une phase éo-varisque au Dévonien inférieur. Les principaux épisodes tectono-métamorphiques associés à la collision varisque ont lieu au Carbonifère entre 350 et 320 Ma, avec de petits décalages entre les différents domaines [Figure 2.9](#). On retrouve de nombreuses reliques d'un métamorphisme HP–MT Carbonifère (350–330 Ma), en particulier dans les domaines issus de la marge européenne et dans certaines nappes austroalpines ([Figure 2.8](#), Ladenhauf *et al.*, 2001; Liati *et al.*, 2009; Miller et Thöni, 1995; Rubatto *et al.*, 2010; Sandmann *et al.*, 2014; Tumiati *et al.*, 2003), auquel succède un métamorphisme barrovien à MP–MT/HT (Guillot et Menot, 1999; Von Raumer et Bussy, 2004). Enfin, une phase post-collisionnelle a lieu entre Carbonifère supérieur et le Permien inférieur (310-295 Ma), associée au désépaississement de la chaîne (Ballèvre *et al.*, 2018; Fernandez *et al.*, 2002; Guillot *et al.*, 2009a).

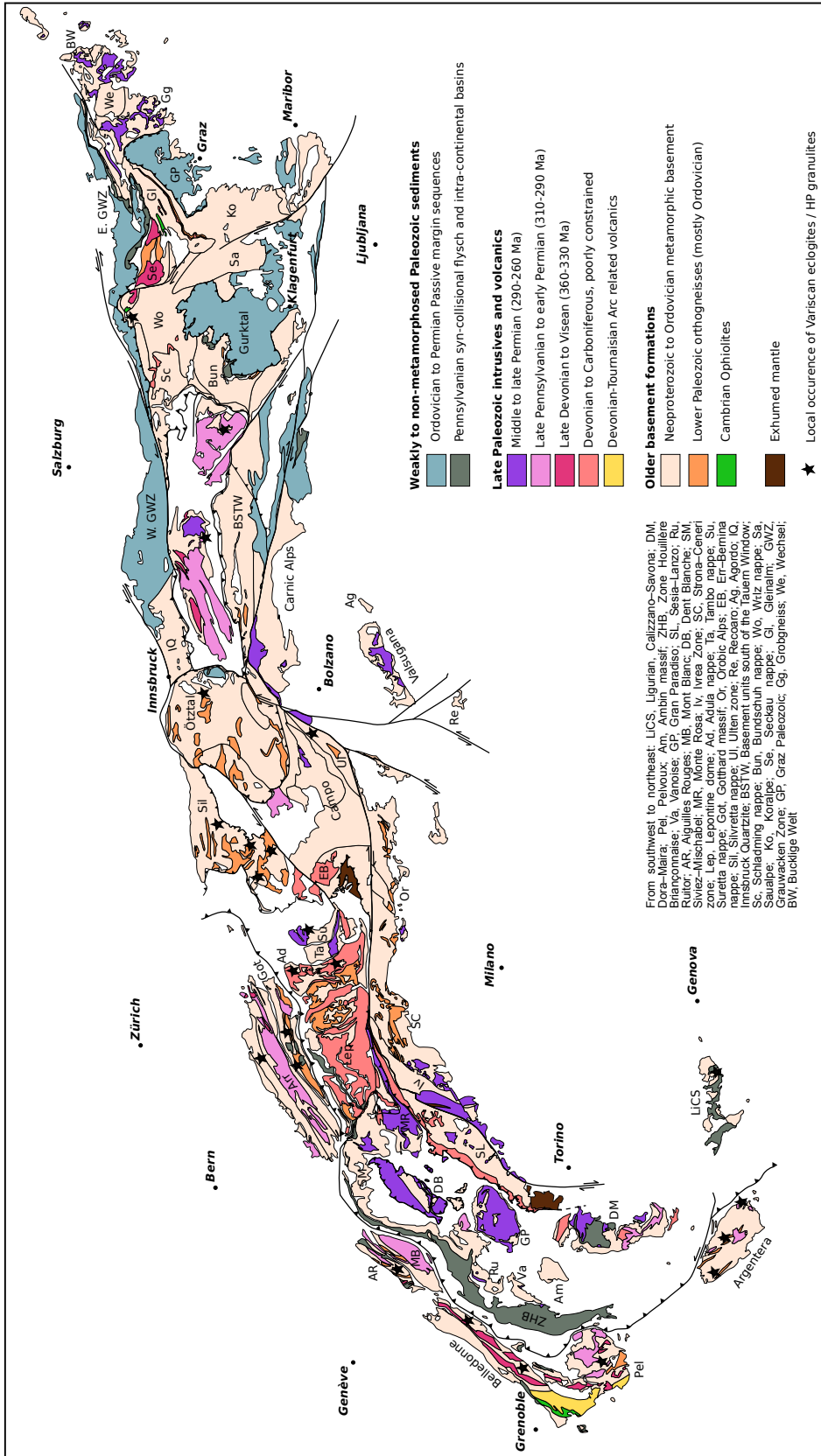


FIGURE 2.8 – Carte géologique simplifiée des unités lithologiques au sein du socle pré-Mésozoïque des Alpes. Du sud-ouest au nord-est : LiCS, Ligurie, Calizzano-Savona ; DM, Dora-Maira ; Pel, Pelvoux ; Am, Ambin ; ZHB, Zone Houillère Briançonnaise ; Va, Vanoise ; GP, Gran Paradiso ; SL, Sesia-Lanzo ; Ru, Ruitor ; AR, Aiguilles-Rouges ; MB, Mont Blanc ; DB, Dent Blanche ; SM, Siviez-Mischabel ; MR, Monte Rosa ; Iv, Zone d'Ivrée ; SC, Strona-Ceneri ; Lep, Lepontin ; Ad, nappe d'Adula ; Ta, nappe de Tambo ; Su, nappe de Suretta ; Or, Gotthard ; Or, Alpes Orobiques ; EB, nappe d'Err-Bermina ; Sil, nappe de Silvretta ; Ul, zone d'Ulten ; Re, Recoaro ; Ag, Agordo ; Ag, Agordo ; IQ, Quartzite d'Innsbruck ; BSTW, Unités de socle au sud de la fenêtre des Tauern ; Sc, nappe de Schladming ; Bun, nappe de Bundschuh ; Wo, nappe de Wölz ; Sa, Saualpe ; Ko, Koralpe ; Se, nappe de Seckau ; Gl, Gleinalm ; GWZ, Grauwacken Zone ; GP, Paléozoïque de Graz ; Gg, Grotgnneiss ; We, Wechsell ; BW, Bucklige Welt. D'après Jacob et al. (2021), accepté

2.2 Les domaines de socle anté-Mésozoïque dans les Alpes

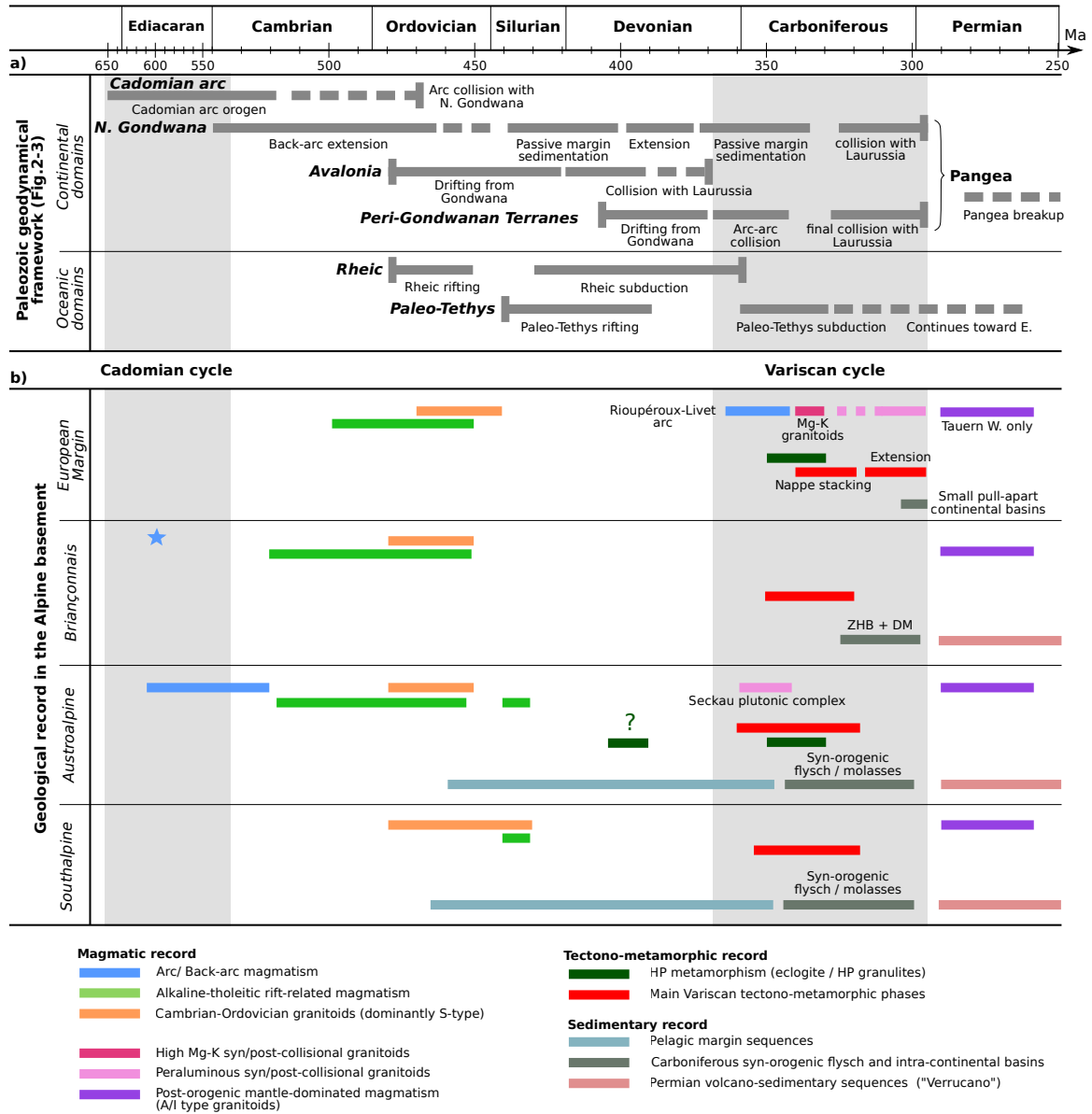


FIGURE 2.9 – Synthèse chronologique de l'évolution géodynamique des domaines varisques au cours du Paléozoïque. (a) Evolution générale des domaines varisques en Europe; (b) Evolution des différents domaines de socle dans les Alpes (marge Européenne, Briançonnais, Sud-alpin, Austro-alpin. D'après Jacob et al. (2021), accepté.

2.2.3 Des enregistrements Paléozoïques contrastés, marqueurs de la zonéographie varisque

Il existe des différences de premier ordre entre le socle varisque des domaines issus de la marge européenne et les domaines Briançonnais, Sud-alpin et Austro-alpin. Sur la marge européenne, le métamorphisme varisque est très marqué, et atteint ou dépasse fréquemment les conditions du faciès amphibolitique supérieur, alors qu'il est de manière générale beaucoup moins marqué dans les autres domaines, en particulier dans les domaines austro-alpin et sud-alpin, où les séries sédimentaires du Paléozoïque inférieur sont bien préservées (Haas *et al.*, 2020; Neubauer *et al.*, 2007).

Les domaines de la marge européenne sont marqués par une forte activité magmatique au Carbonifère, caractérisée par la mise en place de nombreux granitoïdes entre le Viséen et le Ghzélien (ca. 340–300 Ma), mais présentent peu ou pas d'activité magmatique permienne (Figure 2.9). A l'inverse, les autres domaines alpins sont caractérisés par un magmatisme Permien plus marqué, en particulier dans la zone d'Ivrée (Sud-alpin) et dans le Briançonnais, et sont peu marqués par le magmatisme Carbonifère. Par ailleurs, les domaines de la marge européenne sont marqués par la présence de roches métalumineuses (ultra)potassiques appartenant à la série des Durbachites–Vaugnérites (Janoušek et Holub, 2007), que l'on retrouve typiquement dans les domaines internes de la zone Moldanubienne (Jacob *et al.*, 2021b; Von Raumer *et al.*, 2014), alors que ces séries sont totalement absentes des autres domaines.

L'enregistrement sédimentaire paléozoïque est très contrasté entre les différents domaines (Figure 2.9). Les unités de la marge européenne ne présentent pas de grand bassins sédimentaires post-Ordovicien. On y retrouve en revanche des séries volcano-sédimentaires d'âge Dévonien (Fréville *et al.*, 2018; Ménot, 1987a) ainsi que de petits bassins houillers

continentaux pennsylvaniens (310–300 Ma), ouverts en transtension le long de zones de failles décrochantes tardi-varisques (Fernandez *et al.*, 2002). L’enregistrement sédimentaire dans le domaine Briançonnais contraste largement avec ces séries. On y retrouve en effet la zone houillère briançonnaise (Figure 2.8), mise en place entre le Sherpukhovien et le Ghzélien (325–300 Ma), qui malgré le raccourcissement alpin forme l’un des bassins houillers Carbonifère les plus étendus d’Europe (Ballèvre *et al.*, 2018). Par ailleurs, les dépôts d’âge Permien sont plus développés que sur la marge européenne. Ils sont composés de brèches rougeâtres riches en clastes rhyolitiques issus des formations volcaniques permienne (287–295 Ma, Ballèvre *et al.*, 2020). Ce faciès « Verrucano » très caractéristique et aussi présent en abondance dans le domaine Sud-alpin. Enfin, les domaines Sud-Alpin et Austro-alpin sont marqués par la présence de séries de marge passive d’âge ordovicien à dévonien (460–350 Ma), auxquelles se succèdent des séries de flysch viséens (345–325 Ma) et des dépôts molassiques pennsylvaniens (310–300 Ma) (Haas *et al.*, 2020; Neubauer *et al.*, 2007).

Ainsi, les domaines de socle de la marge européenne, marqués par métamorphisme MT à HT et un magmatisme syn à post-collisionnel important, sont plutôt caractéristiques des zones internes de la chaîne, et présentent certaines similitudes avec les unités métamorphiques allochtones du Massif Central ou des Vosges (Lardeaux *et al.*, 2014). A l’inverse, le domaine Briançonnais et les domaines issus de la plaque adriatique (Sud-alpin et Austro-alpin) présentent des caractéristiques des domaines externes de la chaîne, et sont vraisemblablement corrélés au bassin d’avant pays et aux unités autochtones et para-autochtones de la marge gondwaniennne.

2.3 Focus sur les domaines externes de la marge européenne : les massifs cristallins externes (MCE)

Les massifs cristallins externes (MCE) forment le socle des domaines les plus externes de la marge européenne impliquée dans la collision alpine. Ils regroupent, du nord-est au sud-ouest, les massifs de l'Aar-Gothard, du Mont-Blanc, des Aiguilles Rouges, de Belledonne, des Grandes-Rousses, de l'Oisans-Pelvoux et de l'Argentera-Mercantour (Figure 2.7).

2.3.1 Les événements alpins dans les MCE

En comparaison avec les zones internes des Alpes, les MCE ont été relativement peu affectés par les épisodes tectono-métamorphiques associés au cycle orogénique alpin. Les déformations alpines sont en général peu pénétratives dans le socle et le métamorphisme alpin n'excède pas le faciès des schistes verts, ce qui a permis la préservation des structures et assemblages métamorphiques varisques.

Au cours du Jurassique inférieur (200–165 Ma), une période de rifting associée l'ouverture de l'océan Liguro-Piémontais a entraîné la formation de grandes failles normales d'orientation N–N30°, qui ont découpé le socle et la mince couverture triasique en plusieurs blocs basculés, délimitant des bassins en demi-grabben (Lemoine *et al.*, 1986; Lemoine et Trümpy, 1987). Les premiers stades de la collision alpine ont lieu à partir de l'Eocène précoce à moyen (ca. 40 Ma), et correspondent à l'enfouissement au sous-charriage des domaines externes (Helvétique) sous les domaines internes (Briançonnais). L'exhumation des MCE débute à partir de l'Oligocène (ca. 27 Ma), et montre une accélération rapide vers 5–6 Ma (van der Beek *et al.*, 2010). Le taux de raccourcissement alpin dans les domaines externes a été estimé

2.3 Focus sur les Massifs Cristallins Externes (MCE)

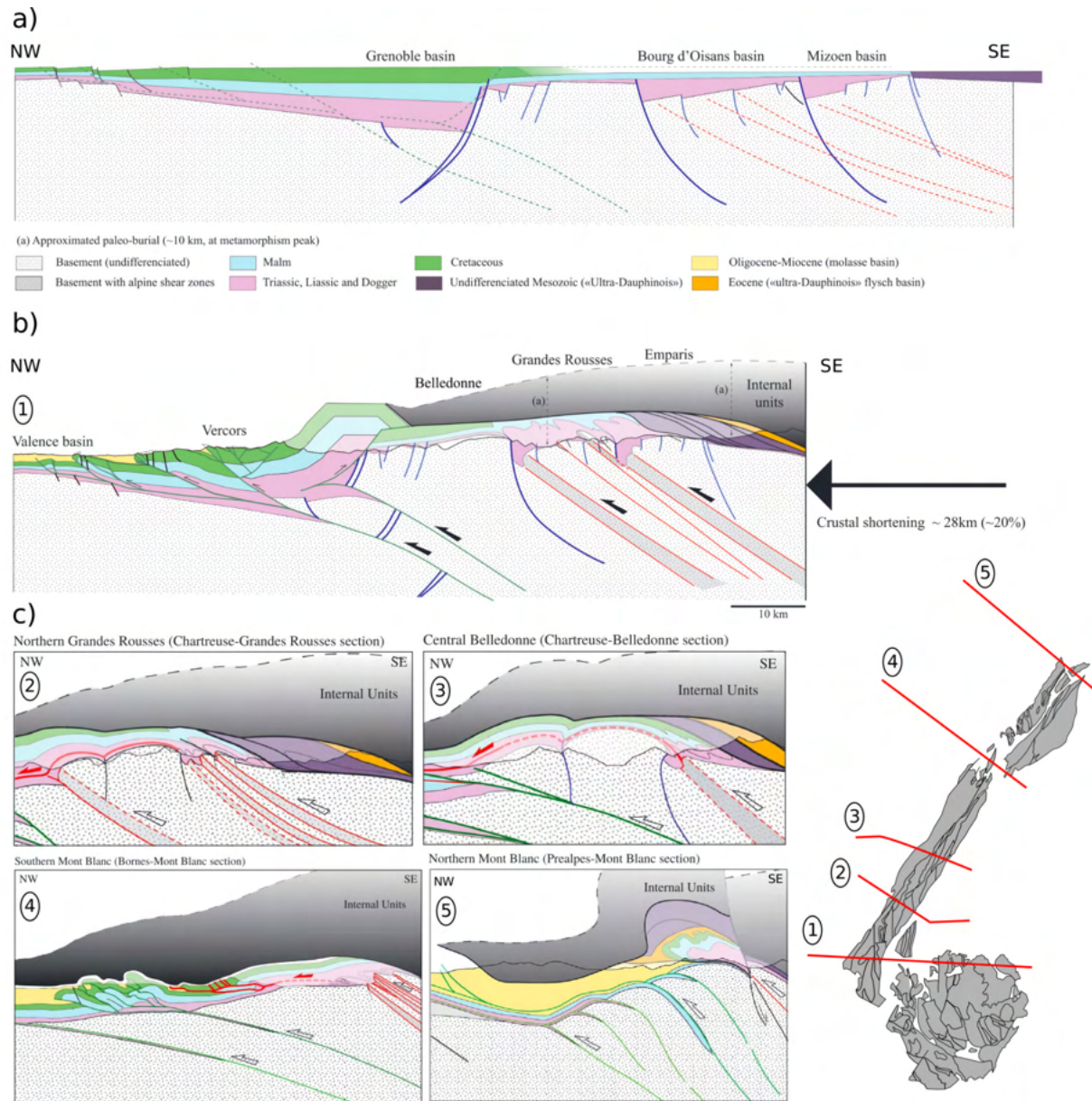


FIGURE 2.10 – Coupes structurales équilibrées à travers les Massifs Cristallins Externes (MCE), d'après Bellahsen *et al.* (2014). (a) Reconstitution de la structure de la marge passive au niveau de Bourg d'Oisans avant la collision alpine. (b) Coupes structurales montrant l'évolution de la déformation alpine dans les MCE du sud (Oisans–Pelvoux) vers le nord (Mont-Blanc). On observe un découplage mécanique entre le socle et la couverture sédimentaire Méso-Cénozoïque : alors que le socle se comporte comme un bloc rigide, dans lequel le raccourcissement est accomodé par des zones de cisaillement déca à hectométriques, la courvure se décolle du socle et se déforme de manière très ductile.

à environ 20–27%, ce qui correspond à un raccourcissement E–W total de 28 à 66 km du sud vers le nord (Bellahsen *et al.*, 2014). Cette déformation affecte de manière différente le socle et la couverture sédimentaire Mésozoïque (Figure 2.10). Cette dernière se décolle du socle, et accommode le raccourcissement par la formation d’un système de plis et de chevauchements d’axe NE–SW. Le socle présente quant à lui une déformation beaucoup moins pénétrative, caractérisée par le développement de zones de cisaillement ductiles-fragiles décamétriques à hectométriques, avec peu ou pas de réactivation en compression des structures extensives Jurassiques à fort pendage (Bellahsen *et al.*, 2012; Bellanger *et al.*, 2014; Bellahsen *et al.*, 2014; Marquer *et al.*, 2006). Le métamorphisme alpin est généralement limité à ces zones de cisaillement alpine, et atteint les conditions du faciès schistes verts inférieur (0.3–0.4 GPa, 300–350 °C, Bellanger *et al.*, 2015; Simon-Labric *et al.*, 2009).

Cependant, les déformations alpines dans les MCE sont plus complexes qu’un simple raccourcissement perpendiculaire à la chaîne. Dumont *et al.* (2011) identifie trois phases de déformations successives depuis l’Eocène : une phase D1 de compression N–S anté-priabonienne (> 40 Ma), coïncidant avec l’orogénèse Pyrénéo-Provençale ; une phase D2 entre l’Eocène et l’Oligocène (40–32 Ma), marquée par la formation d’un système de nappes de vergence nord-ouest, qui correspond à la propagation du prisme de collision vers le nord-ouest ; une phase D3 à partir de l’Oligocène (<32 Ma), marquée par la propagation vers l’ouest du système de nappes. Dans le massif de l’Oisans–Pelvoux, l’interférence entre les phases de raccourcissement D2 et D3 a entraîné la formation d’une structure en dôme, mise en évidence par les variations d’élévation de la paléosurface de la pénélaine triasique. Malgré cette superposition de déformations alpines, le socle varisque préserve encore bien les structures paléozoïques, et des corrélations sont possibles à l’échelle des différents chaînons formant les MCE (Guillot et Ménot, 2009; Ménot *et al.*, 1987; Vivier *et al.*, 1987).

2.3.2 Le socle varisque dans les MCE

Le socle des MCE est composé : (i) de diverses unités sédimentaires et magmatiques d'âge Paléozoïque inférieur, qui ont été métamorphosées et recoupées par des granitoïdes lors de l'orogénèse varisque au Carbonifère ; (ii) de sédiments non métamorphiques d'âge Carbonifère à Permien (310–300 Ma), déposés sur les séquences métamorphiques plus anciennes dans de petits bassins intracontinentaux (Figure 2.11). Le tout est recouvert en discordance par la couverture sédimentaire Mésozoïque–Cénozoïque. Le travail réalisé au cours de cette thèse se focalise sur les massifs de Belledonne et de l'Oisans–Pelvoux, qui forment avec les Grandes–Rousses la partie centrale des MCE. Cet ensemble présente une zonation générale d'ouest en est se subdivise en trois grands domaines structuraux, le *domaine occidental*, le *domaine central* et le *domaine oriental*, séparés par un ensemble de failles décrochantes tardi-varisques (Ménot, 1987a; Guillot *et al.*, 2009a; Vivier *et al.*, 1987).

Le domaine occidental est composé d'une série de micaschistes avec des intercalations de métaquartzites, formant la *Série Satinée* (Bordet et Bordet, 1963). Cette série dérive probablement d'anciens flyschs, formés par accumulation de séquences turbiditiques dans un bassin profond. La datation U-Pb des zircons détritiques de cette série (Fréville *et al.*, 2018) a donné des âges principalement édiacarien–cryogénien (550–700 Ma), avec des populations subordonnées de zircons mésoarchéens (2.8–3.1 Ga) et paléoprotérozoïques (2.0–2.2 Ga). La population la plus jeune donne des âges cambro–ordoviciens (540–463 Ma), ce qui contraint l'âge maximal de dépôt de cette série à l'Ordovicien moyen. La prédominance de zircons néoprotérozoïques suggère que cette série est principalement composée de matériel érodé provenant des ceintures Néoprotérozoïques péri-gondwaniennes (arcs *cadomiens*), avec une contribution mineure de matériel cratonique gondwanien venant de l'intérieur du continent.

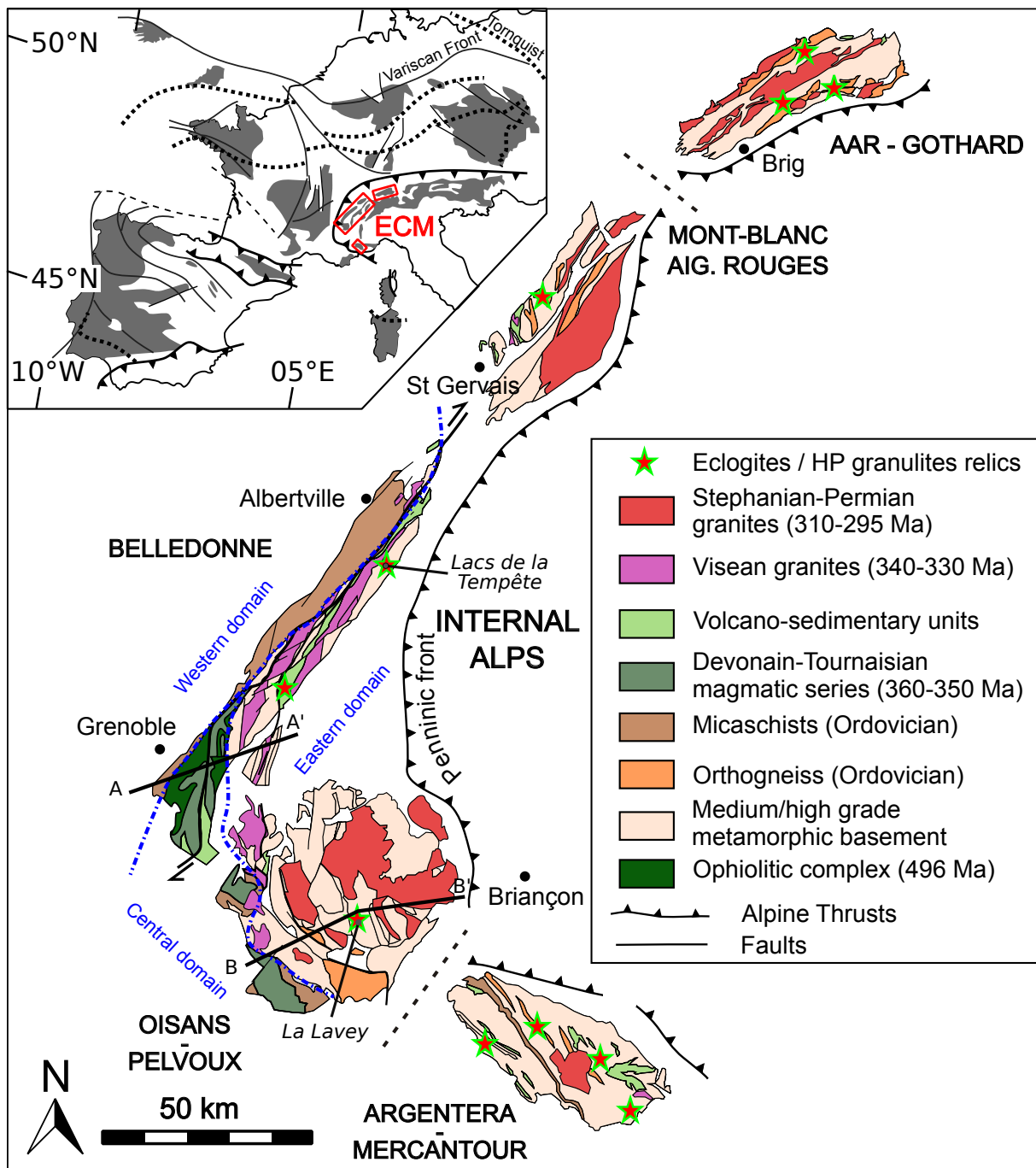


FIGURE 2.11 – Carte litho-tectonique du socle Paléozoïque des MCE. Modifié d'après Guillot et Ménot (2009); Ménot (1987a); Vivier *et al.* (1987). La localisation des principales reliques de haute pression varisques sont indiquées par des étoiles, et les noms des deux localités étudiées en détail est indiqué en italique.

Le domaine central est constitué d'un ensemble de nappes métamorphiques d'orientation est-ouest, mises en place lors de la collision varisque entre 350 et 325 Ma (Fréville *et al.*, 2018; Guillot et Ménot, 2009; Ménot *et al.*, 1987). De la plus supérieure à la plus inférieure, on retrouve : (i) une séquence de métaconglomérats du Dévonien moyen à supérieur (série du Taillefer) ; (ii) Le complexe ophiolitique cambrien de Chamrousse (ca. 500 Ma, Ménot *et al.*, 1988; Pin et Carme, 1987), considéré comme une relique d'un bassin marginal ouvert le long de la marge nord gondwaniennne (Guillot *et al.*, 1992) ; (iii) le complexe volcano-sédimentaire dévonien-tournaisien de Rioupéroux-Livet (Ménot, 1986, 1987a), composé de séries magmatiques bimodales mises en place vers 360–350 Ma, intercalées avec des micaschistes. Ce complexe est interprété comme un ancien bassin ouvert en arrière-arc le long de la marge gondwaniennne (Fréville *et al.*, 2018; Guillot et Ménot, 2009). (iv) Les gneiss migmatitiques de la série d'Allemont, qui forment la partie inférieure de l'empilement.

Enfin, le domaine oriental est principalement constitué de séquences métamorphiques de haut grade, composées de métasédiments, d'orthogneiss et d'amphibolites fréquemment migmatitiques. Des reliques d'éclogites et de granulites de haute pression (HP) affleurent au sein des unités migmatitiques (Paquette *et al.*, 1989). Ces séquences sont recoupées par des granitoïdes carbonifères. Deux générations principales de granitoïdes sont identifiées (Debon *et al.*, 1998; Debon et Lemmet, 1999) : une première série mise en place au Viséen (ca. 340–330 Ma), riche en enclaves mafiques lamprophyriques (*Vaughnérites*) et localisée plutôt dans la partie ouest (nord-est du massif de Belledonne, zone corticale du massif de l'Oisans-Pelvoux), et une série mise en place au Carbonifère supérieur – Permien inférieur (310–295 Ma), plus ferrifère et localisée dans la partie est (zone interne du massif de l'Oisans-Pelvoux). Les séquences métamorphiques anciennes dérivent vraisemblablement de protolithes sédimentaires et magmatiques d'âge Paléozoïque inférieur.

2.3.3 Les différentes phases tectono-métamorphiques varisques dans les MCE

L'orogénèse varisque dans les massifs de Belledonne et de l'Oisans–Pelvoux s'étale entre 350 et 295 Ma. Plusieurs phases tectono-métamorphiques successives se succèdent durant cette période (Fréville *et al.*, 2018; Guillot *et al.*, 2009a; Guillot et Ménot, 2009), que l'on peut regrouper en trois phases principales :

- Une phase d'épaississement crustal D1, associée à la formation d'un empilement de nappe d'orientation est-ouest et d'une foliation métamorphique S1 (Figure 2.12). Cette tectonique de nappe est principalement visible dans le domaine sud-ouest, et correspond à l'enfouissement des séries dévono-tournaisiennes. Elle s'accompagne d'un métamorphisme dans le faciès amphibolique à 600–700 °C et 0.6–0.9 GPa (Fréville *et al.*, 2018; Guillot et Menot, 1999). L'âge de cette phase est contraint à 345–325 Ma par la datation U-Pb sur monazite et Ar-Ar sur biotite (Fréville *et al.*, 2018; Fréville, 2016).
- Une phase de transpression D2, associée au développement d'une foliation subverticale S2 orientée N à N30°. Cette transpression correspond au développement d'une grande zone de cisaillement dextre, la zone de cisaillement est-varisque qui a été active entre 325 et 310 Ma (Guillot *et al.*, 2009a; Simonetti *et al.*, 2018, 2020).
- Une phase d'extension D3, associée à l'effondrement post-collisionnel. Cette phase a lieu en régime transtensif, est associée à la formation de petits bassins d'échelle hectométrique à kilométrique, ouverts en pull-apart le long de décrochements dextres ou bien en demi-graben le long de petites failles normales. Des études sédimentologiques et paléontologiques ont fourni des preuves de la sédimentation syntectonique entre le Moscovien et le Gzhélien (310–300 Ma, Ballèvre *et al.*, 2018).

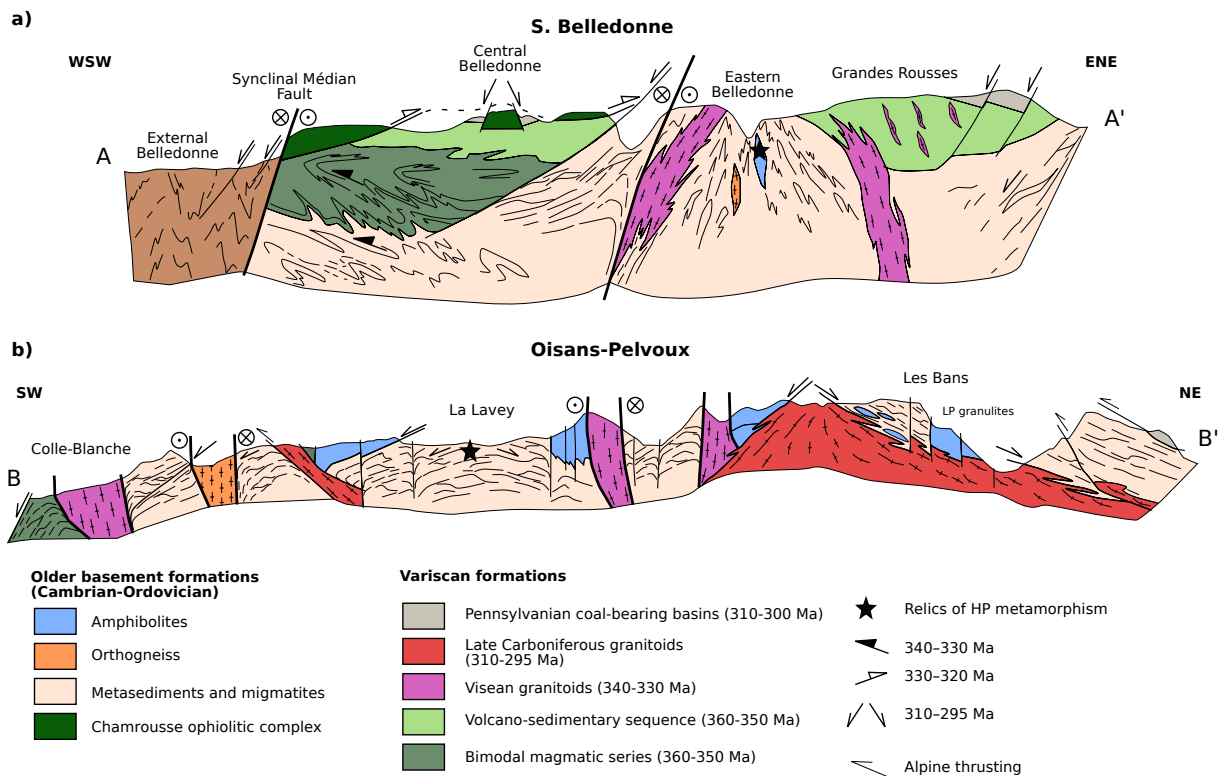


FIGURE 2.12 – Coupes tectoniques interprétatives à travers le massif de Belledonne (a) et le massif de l'Oisans-Pelvoux (b), montrant la succession des différents épisodes tectoniques varisques. Les épisodes d'empilement de nappes E–W correspondent à la phase D1 (D1-D2 dans Guillot et Ménot (2009)), les décrochements dextres à la phase D2 et l'extension à la phase D3. La position des coupes est figurée sur la Figure 2.11. Modifié d'après Guillot et Ménot (2009)

2.4 Questions en suspens

Si la composition du socle et la chronologie des différentes phases tectono-métamorphiques varisques commencent à être relativement bien contraintes dans les MCE, la place de ces massifs dans le système orogénique varisque est à l'heure actuelle mal connue. En particulier, la position des MCE par rapport aux grandes sutures varisques reste à préciser.

La présence d'unités ophiolitiques d'âge cambrien dans le sud du massif de Belledonne, ainsi que la présence de reliques éclogitiques jalonnant les différents massifs suggère la présence d'une ancienne suture le long des MCE. Cependant, ces massifs sont dans une position très méridionale dans l'édifice varisque, et semblent éloignés des grandes sutures (Rhéique

/ Teplà) situées plus au nord. Une hypothèse proposée par [Guillot et Ménot \(2009\)](#) fait des MCE la prolongation vers l'est de la suture éo-varisque, qui aurait été décalée vers le sud à la faveur de grands cisaillements au cours du Carbonifère supérieur. Cette proposition repose essentiellement sur un âge Dévonien (395 ± 2 Ma) obtenu par datation U–Pb de zircons extraits des éclogites du massif de Belledonne ([Paquette *et al.*, 1989](#)). Cependant, cet âge obtenu par datation d'une fraction multi-grain de zircon par dilution isotopique (ID-TIMS) est sujet à caution, en raison d'un mélange possible entre différentes populations de zircons métamorphiques et/ou magmatiques. Il n'est ainsi pas exclu que l'âge Dévonien obtenu par [Paquette *et al.* \(1989\)](#) soit en réalité un âge de mélange sans signification géodynamique particulière, comme cela s'est révélé être le cas sur certaines éclogites du massif Armoricain ([Paquette *et al.*, 2017](#)). Il est donc important de dater de manière fiable le stade HP dans les MCE.

En outre, les conditions P-T du stade métamorphique HP ne sont pas contraintes, ce qui pose la question de la signification géodynamique du métamorphisme de haute pression. En effet, seules les éclogites de basse températures et les schistes bleus, équilibrés sur un gradient géothermique froid (< 10 °C.km⁻¹) sont des indicateurs fiables d'un contexte de subduction. En contexte de collision, un épaissement de la croûte continentale supérieur à 50–60 km implique que de larges portions de croûte inférieure se trouvent équilibrées dans le faciès éclogitique ou dans le faciès granulitique HP ([O'Brien et Rötzler, 2003](#)). Des portions de cette croûte inférieure éclogitique peuvent se retrouver exhumées lors des stades post-collisionnels, rendant ainsi ambiguë l'interprétation des reliques de HP affleurant en surface : s'agit-il de reliques de subduction, ou bien des marqueurs de l'épaississement crustal ? Des données thermobarométriques robustes sont nécessaires pour pouvoir trancher entre ces deux scénarios.

Un troisième point concerne la découverte au cours de ce travail de thèse de péridotites préservées au sein des unités internes du massif de l'Oisans–Pelvoux. Ces péridotites forment des enclaves décimétriques à métriques dans des domaines fortement mobilisés de la croûte inférieure migmatitique, et présentent des traces d'un métasomatisme mantellique. Plusieurs questions se posent concernant : 1) l'origine et la nature des agents métasomatiques impliqués ; 2) l'âge du métasomatisme ; et 3) les mécanismes d'exhumation et d'incorporation des enclaves de péridotites dans la croûte inférieure.

Enfin, un dernier point important concerne le magmatisme varisque dans les MCE. Le dernier travail de synthèse sur ce sujet date d'il y a plus de vingt ans (Debon et Lemmet, 1999). De nombreuses données géochronologiques, géochimiques et isotopiques ont été acquises depuis (Fréville, 2016), et les idées et concepts associés au magmatisme varisque (source des magmas, mécanismes pétrogénétiques, lien avec la géodynamique varisque) ont évolué, notamment grâce aux nombreux travaux réalisés dans les autres massifs varisques (Couzinié *et al.*, 2021; Janoušek *et al.*, 2019; Laurent *et al.*, 2017; Moyen *et al.*, 2017; Vanderhaeghe *et al.*, 2020). En particulier, il existe dans les MCE de nombreuses traces d'un magmatisme ultra-potassique (De Boisset, 1986; Laurent, 1992; Le Fort, 1971), bien connu dans les zones internes varisques du massif de Bohême, des Vosges et du Massif Central (Guillot *et al.*, 2020; Janoušek et Holub, 2007; Moyen *et al.*, 2017; Von Raumer *et al.*, 2014), mais qui n'a fait l'objet d'aucune étude récente dans les MCE. L'âge de ce magmatisme et sa signature géochimique et isotopique restent donc mal contraints dans les MCE, alors qu'il s'agit d'un marqueur géodynamique clé de la collision varisque (Janoušek et Holub, 2007).

Le travail réalisé au cours de cette thèse a pour but de répondre aux questions soulevées ci-dessus. Les [chapitre 3](#) et [chapitre 4](#) présentent les résultats acquis sur les reliques de HP varisques dans les MCE. Deux localités ont été examinées en détail : les reliques éclogitiques des lacs de la Tempête, au nord du massif de Belledonne, et les formations granulitiques de HP

de la Lavey en Oisans, découvertes durant la campagne de terrain de l'été 2019 ([Figure 2.11](#)). Un travail de caractérisation structurale et pétrographique, associé à des datations U-Pb sur zircon et rutile ont été réalisés sur ces formations, afin de contraindre l'évolution P-T-t des reliques HP varisques dans les MCE et de relier les différents stades métamorphiques aux grandes phases de déformations identifiées à l'échelle régionale. Bien que l'essentiel des travaux réalisés sur ces roches porte sur le métamorphisme varisque, les données acquises apportent des informations sur l'origine et la nature des protolithes de ces roches. Ces données sont présentées dans un court chapitre annexe ([chapitre 5](#)). Le [chapitre 6](#) présente les résultats d'un premier travail exploratoire de caractérisation pétrographique et géochimique réalisé sur les enclaves de péridotites du massif de l'Oisans–Pelvoux. Le [chapitre 7](#) présente une étude menée sur le magmatisme ultrapotassique (série des "Durbachites") en Oisans. Cette étude se focalise principalement sur les formations de l'Olan, décrites par ([Le Fort, 1971](#)), et apporte des nouvelles données structurales, pétrographiques, géochronologiques et géochimiques sur ces formations. Enfin, un dernier chapitre de discussion ([chapitre 8](#)) intègre toutes ces données dans un cadre géodynamique plus général, et propose un modèle pour l'évolution varisque des MCE et leur place dans le système orogénique varisque.

Deuxième partie

Étude structurale et
pétrochronologique des reliques de
haute pression varisques dans les
MCE

Les reliques d'éclogites et de granulites HP représentent des marqueurs clés de l'évolution géodynamique des chaînes de collision. Elles enregistrent les stades métamorphiques précoces, qui peuvent correspondre à la subduction d'unités océaniques, d'unités continentales, ou encore à des phases d'écaillage crustal conduisant à l'épaississement et à la croissance du prisme orogénique. Dans les MCE, des reliques de ces roches métamorphiques affleurent de manière sporadique dans les unités internes (domaine oriental), sous forme de lentilles métriques à hectométriques, fréquemment rétro-morphosées. Ces reliques ont été longtemps considérées comme des témoins d'une paléo-suture éo-varisque (Fréville *et al.*, 2018; Guillot *et al.*, 2009a; Paquette *et al.*, 1989). Toutefois, une quantification rigoureuse des conditions P-T enregistrées ainsi que l'âge du métamorphisme doit permettre de préciser le contexte de formation de ces roches.

Deux de ces formations ont été étudiées en détail : les éclogites rétro-morphosées des lacs de la Tempête, dans le NE du massif de Belledonne, et les granulites HP de La Lavey, dans le massif de l'Oisans–Pelvoux (Figure 2.11), qui sont présentées dans les chapitres 3 et 4. Alors que les éclogites des lacs de la Tempête sont connues depuis longtemps (Gros, 1974), les granulites HP La Lavey ont été découvertes dans le cadre de ce travail de thèse, lors des campagnes de terrain de 2019 et 2020. Une étude pétrochronologique a été menée sur des échantillons de ces deux formations, dans le but de caractériser l'évolution pression-température-temps (P-T-t) de ces roches, et en particulier contraindre (1) le stade métamorphique HP, et (2) les chemins d'exhumation suivant le stade HP. En parallèle, une étude structurale de détail a été menée, afin de préciser le contexte structural dans lequel affleurent ces reliques HP et relier les différents stades métamorphiques identifiés dans ces roches aux principales phases de déformation décrites à l'échelle des MCE (Fréville *et al.*, 2018; Guillot et Ménot, 2009). L'étude pétrochronologique des formations des lacs de la Tempête et de La Lavey a fait l'objet de deux articles, un premier publié dans *Journal of Metamorphic Geology* et un second accepté à *Lithos*. Ces deux publications étant focalisées

sur la datation et l'estimation des conditions P-T du métamorphisme, l'étude structurale et l'étude géochimique des protolithes y sont présentées de manière relativement succincte. Une discussion plus détaillée des structures dans les deux domaines étudiés est donc présentée sous forme de données additionnelles à la suite de chaque article. Enfin, un court chapitre additionnel (**chapitre 5**) est dédié à la caractérisation géochimique des protolithes et discute de leur âge et de leur contexte de mise en place.

CHAPITRE 3

Les éclogites rétro-morphosées des lacs de la Tempête (Belledonne NE)



Les lacs de la Tempête vus depuis la face sud du Grand Mont.



Sommaire

3.1 Carboniferous high pressure metamorphism and deformation in the Belledonne Massif (Western Alps)	80
3.2 Données complémentaires sur le contexte structural	117
3.2.1 Contexte tectonique alpin	117
3.2.2 Étude structurale des formations métamorphiques des lacs de la Tempête	117
3.2.3 Une exhumation localisée des reliques de haute pression au sein de la zone de cisaillement est-varisque	120

3.1 Article #1 : Carboniferous high pressure metamorphism and deformation in the Belledonne Massif (Western Alps)

Jean-Baptiste Jacob, Stéphane Guillot, Daniela Rubatto, Émilie Janots,
Jérémy Melleton, Michel Faure

Carboniferous high-*P* metamorphism and deformation in the Belledonne Massif (Western Alps)

Jean-Baptiste Jacob¹  | Stéphane Guillot¹ | Daniela Rubatto^{2,3}  | Emilie Janots¹ | Jérémie Melleton⁴ | Michel Faure⁵

¹Univ. Grenoble Alpes, Univ. Savoie Mont Blanc, CNRS, IRD, Univ. Gustave Eiffel, ISTerre, Grenoble, France

²Institute of Geological Sciences, University of Bern, Bern, Switzerland

³Institut des Sciences de La Terre, University of Lausanne, Lausanne, Switzerland

⁴Bureau de Recherches Géologiques et Minières, Orléans, France

⁵Institut des Sciences de la Terre d'Orléans, Université d'Orléans, CNRS, Orléans, France

Correspondence

Jean-Baptiste Jacob, Univ. Grenoble Alpes, Univ. Savoie Mont Blanc, CNRS, IRD, Univ. Gustave Eiffel, ISTerre, 38000 Grenoble, France.
Email: jean-baptiste.jacob@univ-grenoble-alpes.fr

Funding information

Bureau de Recherches Géologiques et Minières, Grant/Award Number: RGF Alpes

Editor: Julia Baldwin

Abstract

The age and *P–T* conditions of Variscan high-*P*(HP) metamorphism in the Palaeozoic basement of the western Alps remain poorly constrained, but is nevertheless crucial to build a consistent tectonic scenario for the southeastern domain of the Variscan Belt. We report here the results of a structural, petrological, thermobarometric, and geochronological investigation of an eclogite-bearing unit exposed in the northeastern part of the Belledonne Massif (France). This unit is mostly composed of meta-sediments that are locally migmatized and contain decametre- to hectometre-scale lenses of orthogneiss and amphibolites. SIMS U–Pb dating of magmatic zircon cores in two retrogressed ecogites yields ages at 456 ± 4 Ma and 448 ± 6 Ma, which are interpreted to date the emplacement of the magmatic protoliths. The peak pressure stage in the retrogressed ecogites is estimated to be >1.4 GPa at 690–740°C, and was followed by decompression from 1.4 to ca. 1.0 GPa at 700–800°C. By contrast, the investigated migmatitic metasediment does not present any trace of HP metamorphism, but instead preserves prograde evolution from sub-solidus conditions (ca. 0.8–1.1 GPa and 600–700°C) to supra-solidus conditions (1.1–1.4 GPa and 700–780°C). A later stage of retrogression below ca. 0.5–0.8 GPa and 570–610°C is recorded in both lithologies, and is taken to indicate cooling and exhumation to upper crustal levels. Metamorphism was roughly coeval in the retrogressed ecogites and in the migmatitic metasediment. Metamorphic zircon rims yield U–Pb dates scattering between 340 and 310 Ma in both lithologies. In the migmatitic metasediment, a distinct younger age at 306 ± 3 Ma is interpreted to represent late stages of melt crystallization. In the retrogressed ecogites, zircon zoning and chemical composition (Th/U and REE) indicate initial crystallization of the rims during the HP stage followed by protracted growth during decompression to granulitic/amphibolitic conditions. Rutile U–Pb dating in one eclogite sample yields an age of 340 ± 11 Ma similar to the oldest zircon ages and is interpreted to approximate the age of the peak pressure metamorphism. Retrogression in the amphibolite facies is correlated with the development of a penetrative, N30° subvertical mylonitic S2 foliation. Regionally, this deformation occurs in a dextral transpressive corridor interpreted to represent a crustal-scale shear zone active during the mid-late Carboniferous. We therefore

suggest that this structure has driven the exhumation of eclogites from the lower crust and their mixing with mid-crustal felsic lithologies devoid of HP assemblages.

KEYWORDS

external crystalline massifs, high-*p* metamorphism, phase equilibria modelling, U–Pb geochronology, variscan orogeny

1 | INTRODUCTION

High-*P* (HP) metamorphic rocks, namely eclogites and HP granulites, are widespread in the Variscan Belt of Europe (Faure et al., 2009; Catalán et al., 2009; Paquette et al., 2017; Schulmann et al., 2009). They are exposed in the Saxo-Thuringian zone and in the high-grade metamorphic domains of the allochthonous Galicia-Moldanubian zone, which forms the core of the belt and exposes deep portions of the orogenic crust. These rocks only form minor portions of the exposed high-grade units, but they are nevertheless important geodynamical markers, which provide crucial information to reconstruct the dynamics of the Variscan Belt. They are commonly associated with small ultramafic bodies, and may represent dismembered meta-ophiolites, which could possibly mark suture zones formed by the closure of an oceanic basin or a domain of hyperextended continental crust, as it has been inferred for the ‘Leptyno-amphibolic complexes’ in the French Massif Central and in the Armorican Massif (Ballèvre et al., 2009; Faure et al., 2009; Lardeaux et al., 2014). Alternatively, some eclogite-bearing units may also represent deep portions of the orogenic lower crust extruded during the collision, as it has been inferred for the ultra high temperature (UHT)–HP granulites in the Bohemian Massif (Schulmann et al., 2008) or in the eclogites from the Montagne Noire Axial Zone (Roger et al., 2020; Whitney et al., 2020).

Independently of their origin, thermobarometric and geochronological information recorded in these HP rocks is crucial to constrain relevant parameters such as exhumation rates, age of peak pressure, and maximal pressure and temperature reached during the collision. The ability to test different geodynamical scenarios with thermomechanical models strongly depends on the quality of the pressure–temperature (*P–T*) and geochronological data (time) obtained from these HP rocks. However, constraining the *P–T*–time (*P–T–t*) evolution in complex metamorphic rocks such as eclogites is far from being trivial. Analytical developments made over the past few decades have significantly improved the ability to extract geologically meaningful information from the metamorphic rocks. In particular, the development of high spatial resolution techniques (particularly secondary ion mass spectrometry (SIMS), laser ablation inductively coupled plasma mass spectrometry (LA-ICP-MS), and to a

lesser extent electron microprobe) has allowed microscale dating and trace elements analyses on mineral domains to be performed, which can then be used to obtain multiple ages from one single sample and to correlate them with particular magmatic or metamorphic stages. Prior petrological and geochronological studies of eclogites, which did not benefit from these analytical improvements, are less likely to provide geologically accurate age information. In particular, many ages on high-grade metamorphic samples obtained by ID-TIMS bulk zircon dating are likely a mix between metamorphic and inherited components. This has been for example shown in the recent study of Paquette et al., (2017) for the eclogites and blueschists from the Armorican massif. In the Massif Central, Silurian–Devonian ages (ca. 400–420 Ma) inferred for the HP stage in eclogites have recently been re-estimated at ca. 360–385 Ma by Lu–Hf dating and in situ U–Pb dating of zircon (Benmammour et al., 2020; Lotout et al., 2018, 2020). Many eclogites in the Variscan Belt still lack recent petrological investigation in order to solidly anchor geodynamic models that are based on possibly outdated constraints (e.g. Regorda et al., 2019).

In the Alpine domain, numerous bodies of Variscan eclogites and HP granulites are exposed in the Palaeozoic basement, especially in the external crystalline massifs (ECMs), which form the exposed parts of the basement in the external Western Alps (Von Raumer et al., 2013). Most of the geochronological data available for the HP rocks of the ECM were obtained by multigrain ID-TIMS dating of zircon (e.g. Paquette et al., 1989; Schaltegger, 1993; Schaltegger et al., 2003), which constrained the age of emplacement of the magmatic protoliths to the early-mid Ordovician (ca. 480–450 Ma) and the age of HP metamorphism to the early Devonian (ca. 395–425 Ma). These age constraints have been used in several tectonic studies (Fréville et al., 2018; Guillot & Ménot, 2009; Von Raumer et al., 2009) to argue for the existence of a Devonian oceanic suture across the ECMs, possibly marking the southern prolongation of the Saxo-Thuringian suture (Guillot & Ménot, 2009). However, in the southernmost ECM of Argentera, more recent studies have re-estimated the age of the HP stage to the early-mid Carboniferous (ca. 340 Ma, Jouffray et al., 2020; Rubatto et al., 2010), questioning the previous geodynamic interpretation. Similar studies are lacking for the northern part of the ECM and remain crucial for informing tectonic models. This

study aims to provide new thermobarometric and geochronological data on HP rocks and contiguous metasediments exposed in the northeastern Belledonne massif. A detailed structural investigation of the eclogite-bearing unit has also been undertaken in order to better constrain the tectonic setting associated with exhumation of these rocks.

2 | GEOLOGICAL SETTING

2.1 | The external crystalline massifs

The ECMs represent exposed portions of the European Palaeozoic basement involved in the Alpine Orogeny. They form a discontinuous arcuate alignment of massifs along the central and western external Alps, and consist, from the northeast to the south, in the massifs of Aar-Gothard, Mont-Blanc, Aiguilles Rouges, Belledonne, Grandes-Rousses, Oisans-Pelvoux, and Argentera-Mercantour (Figure 1). They are composed of (i) various early to mid-Palaeozoic units, which were metamorphosed and intruded by granitoids during the Carboniferous and the early Permian, and (ii) non-metamorphic late Carboniferous to Permian sediments deposited over the older metamorphic sequences in small intracontinental basins. The basement is unconformably

covered by a thick sedimentary sequence deposited between the Triassic and the Palaeogene along the European margin of the Piemonte–Liguria Ocean (Lemoine et al., 1986). The ECM and their post-Permian cover were deformed and metamorphosed during the Alpine collision. Post-Permian deformation in the basement is generally localized. Stretching and thinning of the crust during the lower Jurassic rifting sliced the ECM basement into tens of kilometres wide tilted blocks, separated by kilometre-scale SW–NE-trending normal faults (Lemoine et al., 1986; Lemoine & Trümpy, 1987). The Alpine collision in the external domain was accompanied by ca. 20% to 27% shortening from South to North (Bellahsen et al., 2014). This shortening was accommodated by buckle folding and thrusting in the sedimentary cover and by the development of an anastomosing network of decametre- to hectometre-scale shear zones in the basement, with only little tectonic reactivation of older structures (Bellahsen et al., 2012, 2014; Bellanger et al., 2014; Marquer et al., 2006). These shear zones delimit low-strain domains in which Palaeozoic structures remained largely preserved. The Alpine metamorphic overprint is mild: metamorphic conditions recorded in Alpine shear zones range from the lower greenschist facies (0.3–0.4 GPa, 300–350°C, Simon-Labric et al., 2009) in Oisans-Pelvoux to the upper greenschist facies in the Aar-Gothard Massif (0.6 GPa, 400–450°C, Challandes et al., 2008).

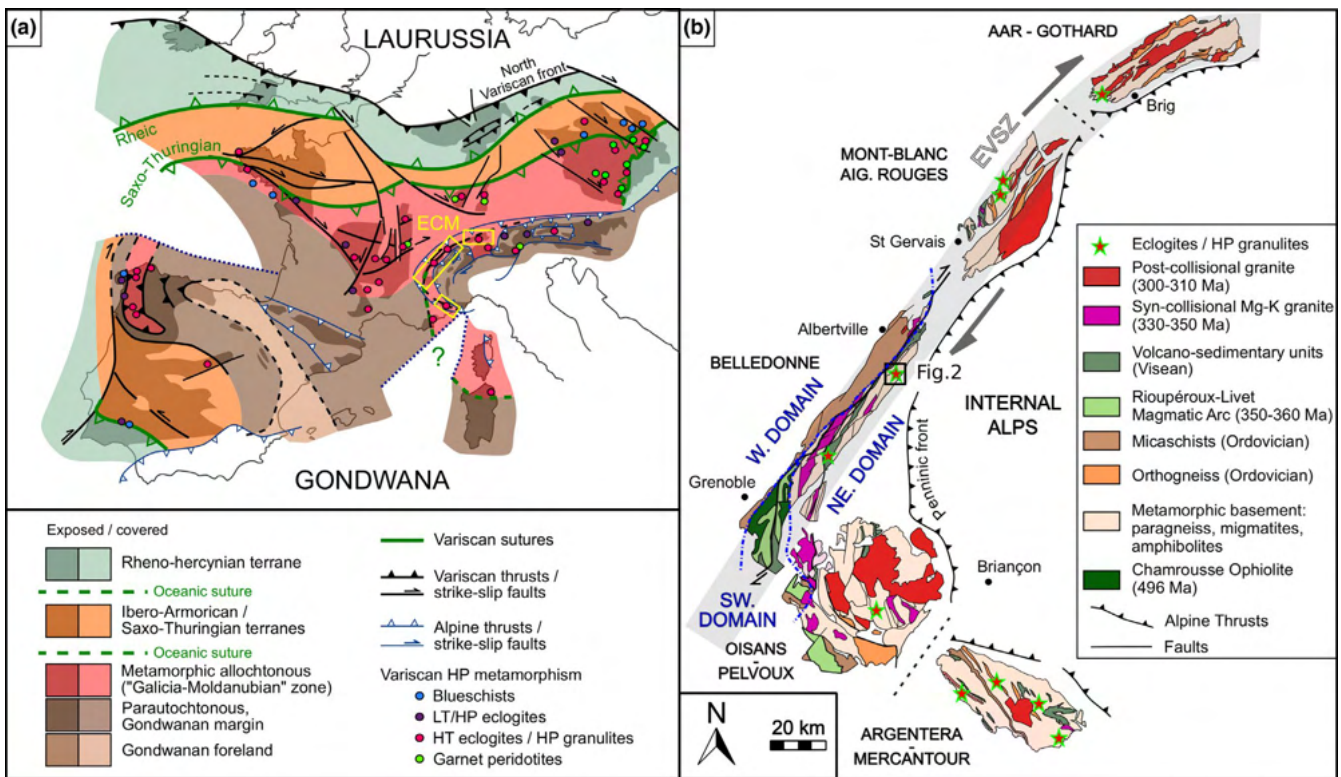


FIGURE 1 (a) Tectonic map of the Variscan belt of Europe, with marked the main position of the External Crystalline Massifs (ECM) and the main exposures of HP rocks (dots). (b) Geological map of the Palaeozoic basement in the External Crystalline massifs, with marked the main locations where HP rocks are exposed (red stars). Modified from Guillot and Ménot (2009)

2.2 | The Belledonne massif

The Belledonne massif forms a 15–20 km wide strip of crustal basement, which extends over more than 100 km from the southwest to the northeast (Figure 1b). Petrographic and structural investigation carried out since the 1950s (e.g. Bordet, 1961; Bordet & Bordet, 1963; Gros, 1974; Ménot, 1987; Ménot et al., 1987; Verjat, 1981; Vivier et al., 1987) has led to subdivide this massif into three distinct tectono-stratigraphic domains, namely the western, the southwestern, and the northeastern domains, separated by late Palaeozoic strike-slip faults (Guillot et al., 2009). The western domain is composed of a series of medium to low-grade micaschists with minor intercalations of metasandstones ('Série Satinée', Bordet & Bordet, 1963), interpreted as deriving from a thick sequence of deep-sea turbiditic sediments. U–Pb dating of detrital zircons from this series (Fréville et al., 2018) yielded mostly Ediacaran–Cryogenian ages (ca. 550–700 Ma), with subordinate populations of Mesoarchean (ca. 2.8–3.1 Ga) and Palaeoproterozoic (ca. 2.0–2.2 Ga) zircons and a youngest population of late Cambrian–Ordovician age (540–463 Ma), which places the maximal deposition age for this series to middle–lower Ordovician. The prevalence of Neoproterozoic zircons suggests this series is mostly composed of material eroded from the peri-Gondwanan Neoproterozoic 'Cadomian' belts, with minor contribution of cratonic Gondwanan material.

The southwestern domain consists of different nappes stacked during the Variscan collisional stages (ca. 350–330 Ma, Fréville et al., 2018; Guillot & Ménot, 2009; Ménot et al., 1987) and capped by a sequence of mid-late Devonian metaconglomerates (Taillefer series, Fréville et al., 2018). The uppermost unit is composed of the Chamrousse ophiolitic complex, a well-preserved witness of Cambrian oceanic lithosphere (ca. 500 Ma, Ménot, Peucat, Scarenzi, et al., 1988; Pin & Carme, 1987), and regarded as the relic of a short-lived marginal basin that opened in a back-arc setting (Guillot et al., 1992). It is thrust over the late Devonian–Tournaisian magmatic complex of Rioupéroux–Livet (Ménot, 1986, 1987) composed of a mafic–felsic bimodal suite of volcanic and plutonic rocks emplaced at ca. 360–350 Ma and attributed to continental extension in a back-arc setting (Fréville et al., 2018; Guillot et al., 2009). This magmatic complex overlies the migmatitic gneisses of the Allemont series. The lower series (Rioupéroux–Livet–Allemont) have been metamorphosed to amphibolite facies during the Variscan nappe stacking events, with peak temperature conditions increasing from ca. 0.6 GPa and 600°C in the upper series to ca. 0.8 GPa and 680°C in the lower migmatitic series (Fernandez et al., 2002; Fréville et al., 2018; Guillot & Ménot, 2009).

Finally, the northeastern domain mostly consists of high-grade metamorphic sequences composed of metasediments, orthogneisses, and amphibolites, with sporadic occurrence of retrogressed eclogites that are the main focus of this study. These sequences are intruded by Carboniferous granitoids and overlain by low-grade volcano-sedimentary sequences that post-date the granitoids (Vivier et al., 1987). Two main generations of granitoids are identified (Debon et al., 1998; Debon & Lemmet, 1999): a Mg–K-rich suite emplaced during Visean (ca. 340–330 Ma) and a ferriferous low-Mg suite emplaced during upper Carboniferous–early Permian (ca. 310–295 Ma). The Mg–K series predominates in Belledonne (Figure 1b), and forms the largest Sept Laux, Saint-Colomban, and Lauzière plutons emplaced syn-tectonically in strike-slip shear zones (Guillot & Ménot, 2009). Little is known about the old metamorphic sequences. The metasediments presumably derive from a lower Palaeozoic series in which mafic and felsic intrusives were emplaced during the Ordovician. The metamorphic evolution is also poorly constrained. The eclogite relics formed at HP were overprinted by high-*T* metamorphism, which culminated with partial melting of the most fertile metasedimentary and metaigneous protoliths. However, no quantitative thermobarometry has been carried so far to constrain more precisely this *P–T* evolution in NE Belledonne.

2.3 | Structural evolution in the Belledonne massif

The Variscan collision in Belledonne occurred at ca. 350–295 Ma and is characterized by a succession of different tectono-metamorphic stages, which have been summarized in Guillot and Ménot (2009) and more recently in Fréville et al., (2018). These authors use different labelling for the successive tectono-metamorphic stages, which partly overlap, and also partly disagree between each other. The choice has been made here to group them into four different stages D0 to D3.

- D0 (Dx in Fréville et al., 2018) is poorly constrained and corresponds to the early thrusting of the Chamrousse ophiolitic unit, which presumably occurred during the Devonian (ca. 360–380 Ma). D1 is an early collisional stage which formed E–W directed nappes, mainly visible in the southwestern domain, and was associated with the development of amphibolite facies assemblages (garnet ± kyanite ± staurolite) at ca. 600–700°C and 0.6–0.9 GPa (Fréville et al., 2018; Guillot et al., 2009). The age of D1 is constrained between ca. 350 and 330 Ma by U–Pb dating on monazite and K/Ar–Ar dating on mica and amphibole (Fréville, 2016; Fréville et al., 2018; Ménot et al., 1987). Following D1, D2 is a transpressive

phase associated with the development of N-N30 oriented strike-slip shear zones, which formed a penetrative steeply dipping foliation S2, mostly visible in the northeastern domain. It has been correlated in the ECMs as well as in the Maures-Tanneron massif and corresponds to a regional-scale dextral shear zone system known as the East Variscan Shear Zone (EVSZ; Corsini & Rolland, 2009; Guillot et al., 2009; Rossi et al., 2009; Simonetti et al., 2018, 2020). Deformation in the EVSZ started from ca. 320 Ma under amphibolite facies conditions, and lasted at least for 10–15 Ma (Simonetti et al., 2018, 2020). Finally, a stage of D3 extension occurred at ca. 310–295 Ma, associated with the development of SW–NE oriented ductile–brittle normal faults and shear zones (Fernandez et al., 2002). It resulted in the opening of kilometer- to ten-kilometre-scale coal-bearing half-graben and pull-apart basins, which preserved sedimentological and paleontological evidence for syntectonic sedimentation during the late Westphalian–Stephanian (Ballèvre et al., 2018, and references therein).

3 | FIELD DESCRIPTION AND STRUCTURAL ANALYSIS

3.1 | Field description

The area investigated in this study is located North of the Isère Valley, in the high-grade metamorphic formations of the northeast Belledonne massif (Figure 1b). It mostly consists of a ca. 2–3 km thick series composed of biotite-poor metagreywackes with intercalated orthogneisses and amphibolites, which form decametre- to hectometre-scale lenses elongated along the main foliation (Figure 2a) (Gros, 1974). Migmatization occurs mostly in the central part of the domain, and is confined to the most fertile lithologies. This metamorphic formation is cut by a kilometer-scale intrusive complex composed of microgranites and rhyolites (Grand Mont intrusive complex). It forms steeply dipping sheets oriented parallel to the main foliation and crossed by N30° oriented shear bands, which argues for a strong tectonic control of the emplacement. The retrogressed eclogites are only found in a hectometre-scale amphibolite body exposed near the Lacs de la

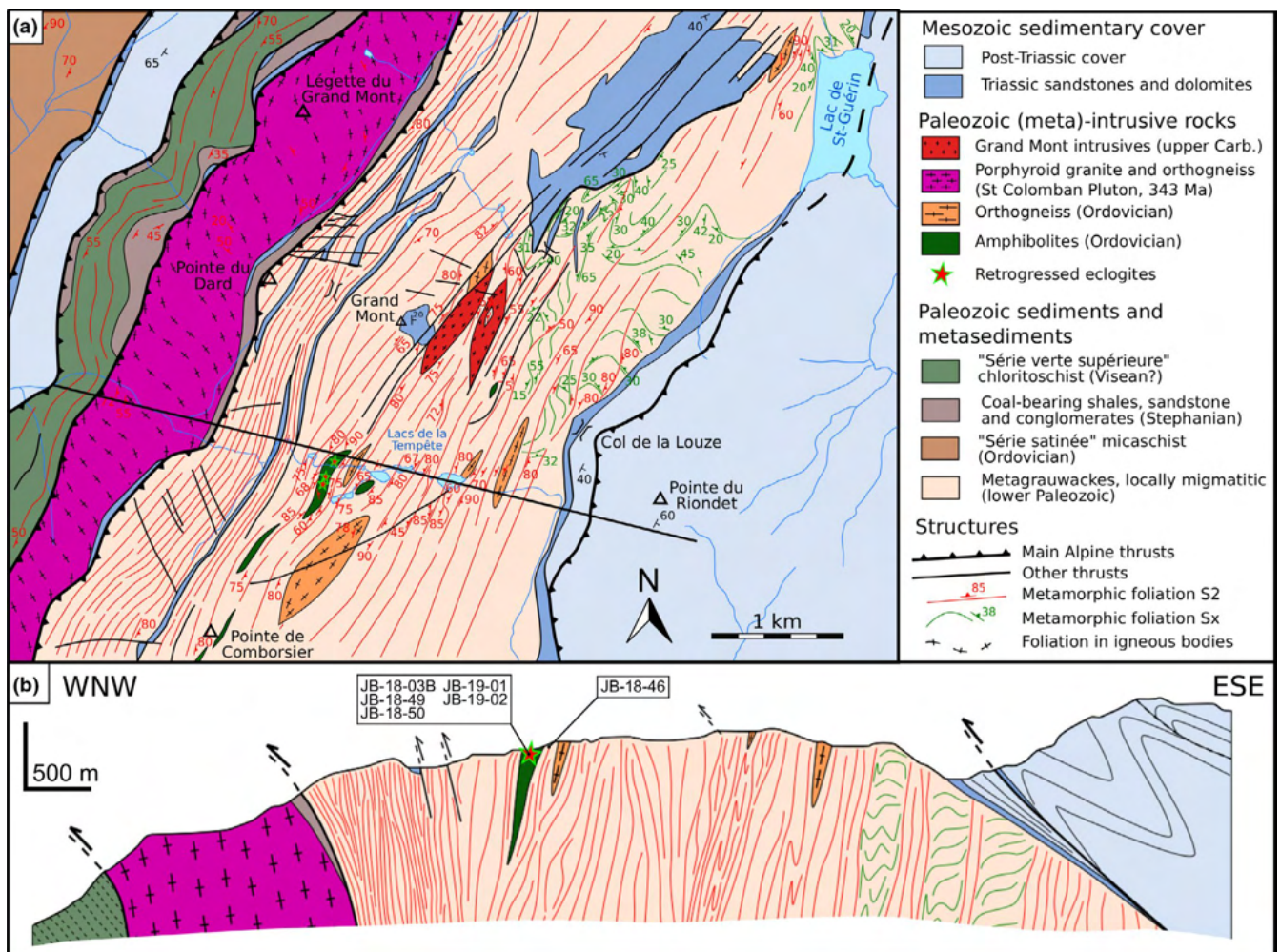


FIGURE 2 (a) Geological map of the studied area (modified from Gros (1974), showing the direction of planar structures and relationship between the early metamorphic foliation Sx and the steep S2 fabric. Position of the interpretative profile is also indicated. (b) Structural cross-section showing the deformation in the metamorphic basement and its relationship with the Mesozoic cover

Tempête (Figure 2a,b). They form unfoliated metre-size *boudins* preserved in the main metamorphic foliation. The geochemical and geochronological study (ID-TIMS bulk zircon dating) of the eclogites from the ECM done by Paquette et al., (1989) included samples from the Lacs de la Tempête body (reported as samples B7751 to B7755 in the original paper). According to this study, this amphibolite body derives from N/E-MORB like tholeiites emplaced at 473 ± 28 Ma in a thinned continental crust, and metamorphosed to HP (>1.4 GPa) at 395 ± 2 Ma. Regarding the mode of exposure of eclogites (isolated lenses within felsic lithologies devoid of HP assemblages) and the geochemical signature and age of the mafic magmatic protoliths, the investigated metamorphic unit presents striking similarities with other Variscan eclogite-bearing units in the Massif Central and the

Armorican Massif, commonly referred as ‘Leptyno-Amphibolite Complexes’ (Ballèvre et al., 2009; Faure et al., 2009; Lardeaux et al., 2014; Ménot, Peucat, & Paquette, 1988; Ménot, Peucat, Scarenzi, et al., 1988; Santallier et al., 1988). New U–Pb data presented in this paper will precise both the age of the protolith and the peak of metamorphism.

3.2 | Structural analysis

Careful investigation of structures in the field allows the identification of two generations of metamorphic foliation and two main episodes of deformation. The foliation trajectories were mapped and are reported in Figure 2. Field photos

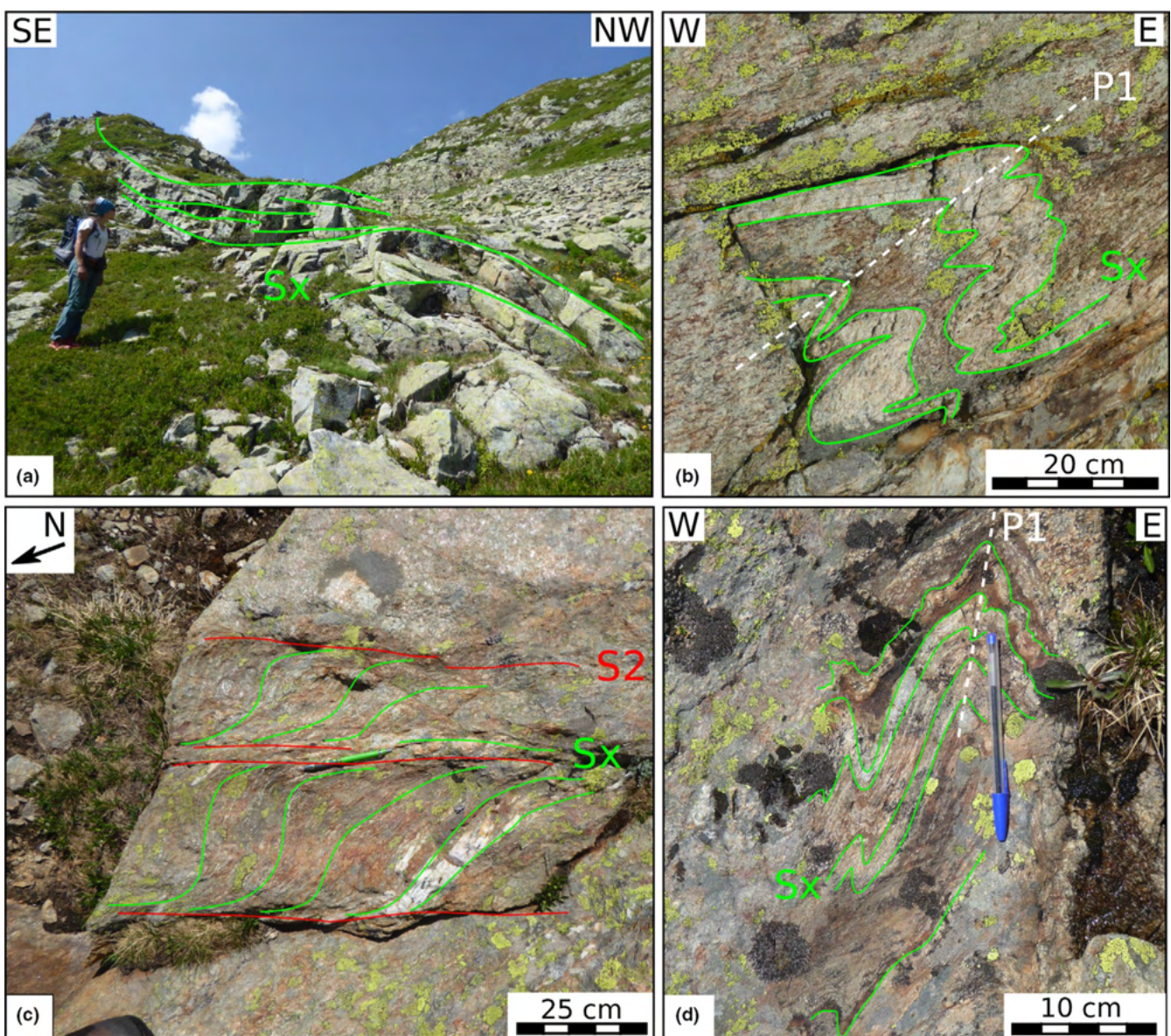


FIGURE 3 Field photographs illustrating typical structural features of the early metamorphic foliation S_x . (a) low angle open folds in S_x ; (b) East-verging P_1 folds deforming S_x ; (c) Deformation of the early foliation S_x by D_2 dextral shearing, resulting in the formation of a second S_2 planar fabric; (d) P_1 upright fold

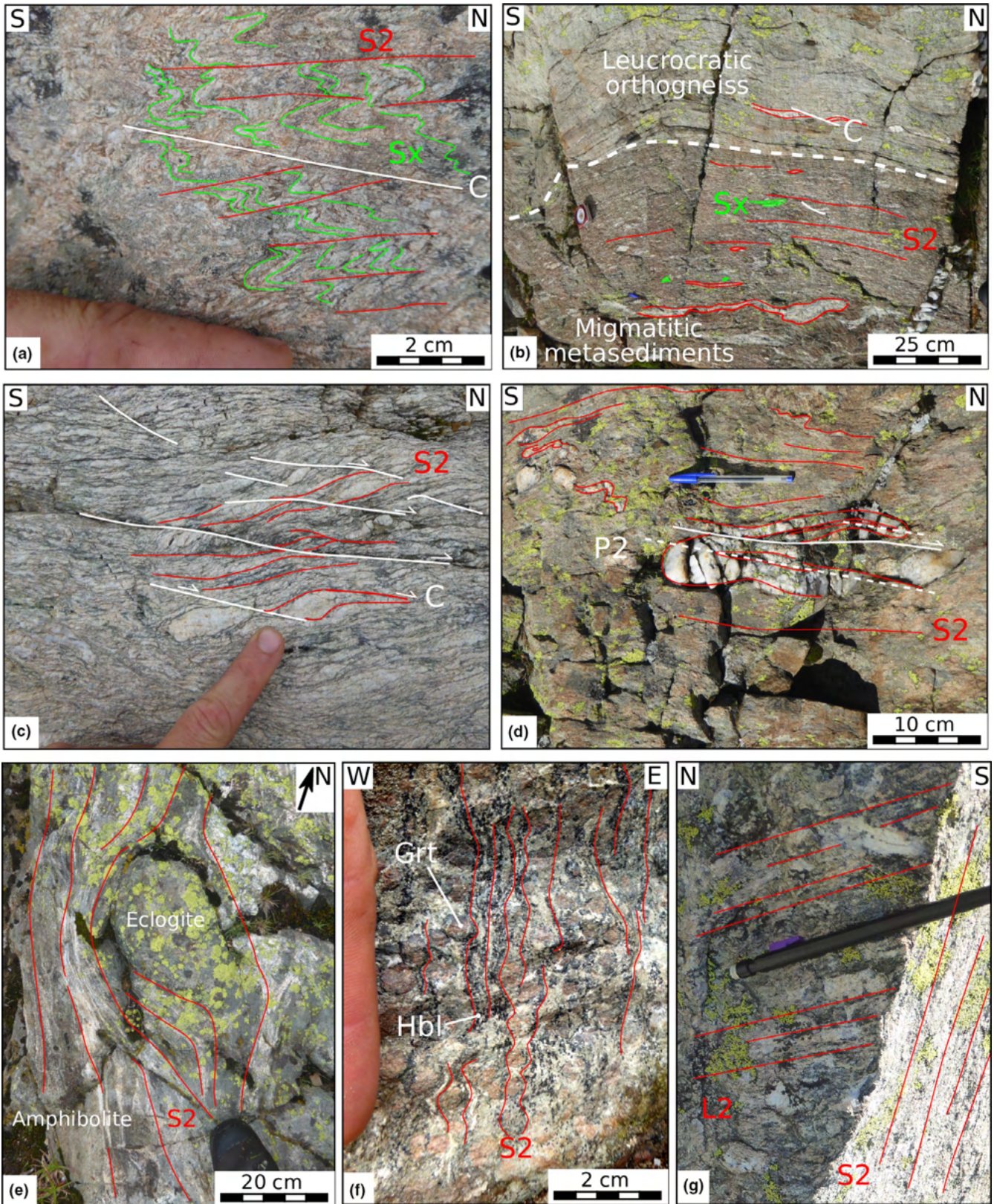


FIGURE 4 Field photographs illustrating typical structural features of the metamorphic foliation S2. (a) Sx relics between S2 planes; (b) contact between a leucocratic orthogneiss layer and migmatitic metasediments. The metasediments contain sheared leucosomes indicating a dextral strike-slip kinematics; (c)-(d) S/C fabrics and P2 drag folds associated with D2 dextral shearing; (e) preserved eclogitic boudin surrounded by foliated amphibolites; (f) S2 fabrics in a deformed retrogressed eclogite. Hornblende growth is syn-D2, while garnet is ante-kinematic; (g) L2 stretching lineation in a mylonitic orthogneiss

of the main structural features are shown in Figures 3 and 4. Labelling reflects our interpretations about how the different structures and deformation stages correlate with the general tectonic framework presented in Section 2.3.

The earliest foliation S_x is a low-angle ($< 30^\circ$) North-dipping foliation (Figure 3a), which is interpreted to be pre-D1. It is only preserved in decametre to hectometre wide low-strain domains, which are mostly exposed in the northeastern part of the investigated zone (Figure 2a). Due to the poor preservation of the structures, the deformation that generated S_x could not be precisely characterized. Gros (1974) reported evidence of cross laminated sedimentary structures, which suggests S_x developed at low-grade metamorphic conditions. S_x is impacted by decimetre- to metre-scale P1 folding (Figure 3b,d), which did not generate any new foliation, but formed tight upright to slightly overturned folds oriented N-N15°, with axes slightly plunging to the North ($< 20^\circ$). The general E–W orientation of folding, and the presence of overturned E-vergent folds are consistent with the D1 nappe stacking phase. However, it cannot be excluded that these folds may be the result of shortening during the transpressive phase D2.

The second foliation S_2 is a pervasive, steeply dipping, N15–30° trending foliation that affects the largest part of the metamorphic sequence (Figure 2) and largely overprints the former S_x , that we associate with D2 dextral strike-slip shearing. In the northeastern part of the field area, D2 is not pervasive and mostly formed localized brittle faults cutting through the low-strain domains. Towards the west, it becomes increasingly intense and pervasive. In the felsic gneisses, it formed the blastomylonitic S_2 foliation that totally obliterated the former structures, which only persist as small lenses and microfold relics (Figures 3c and 4ab). In the mafic lenses, S_2 is associated with the amphibolitization of the eclogite assemblages, which only persist in undeformed metre-scale *boudins* (Figure 4e). Near subhorizontal stretching lineations L2 on S_2 planes (Figure 4g), shear bands, and deformed clasts (Figure 4a–c) clearly indicate a dominant dextral strike-slip kinematics. The presence of syn-folial P2 folds (Figure 4d) with a steeply plunging axis, that developed parallel to S_2 , is also consistent with this kinematics. Deformation probably initiated at high temperature in the amphibolite facies, as indicated by: (i) the pervasive ductile deformation that affected a several kilometres wide unit; (ii) the development of hornblende oriented parallel to S_2 planes in the amphibolites (Figure 4f); (iii) the presence of sheared leucosomes in the migmatites (Figure 4b), which suggest migmatization occurred just prior to or during shearing. D2 strike-slip shearing then localized in decametre to hectometre wide brittle fault zones during the latest stages of deformation. These fault zones are well visible in the western part of the metamorphic unit and near the Grand Mont summit (Figure 2).

4 | METHODS

4.1 | Mineral and whole-rock analyses

Backscattered electron images were acquired at ISTERre Grenoble with a Tescan Vega 3 scanning electron microscope operated with an accelerating voltage of 16 kV and a beam current of 10 nA.

Mineral compositions were measured by electron probe microanalysis (EPMA) using a JEOL JXA-8230 electron microprobe at ISTERre Grenoble. Different protocols were used for garnet and the other silicates. Garnet analyses were performed with a 15 kV accelerating voltage, a 20 nA beam current and a counting times of 60s for the peak and 30s for the background. The other silicates were analysed with a 15 kV accelerating voltage, a 10 nA beam current and counting times of 30s for the peak and 15s for the background. The spot size was set to 1–3 μm depending on the size of minerals and the presence of volatile elements. X-ray element maps were acquired with a 15 kV accelerating voltage, a 100 nA beam current, and a 100 ms counting time per pixel. Natural minerals and synthetic glass were used for standardization, and the ZAF matrix procedure was applied for data reduction. X-ray maps were processed using the XmapTools software (Lanari et al., 2018, 2014). Details of abbreviations used for the mineral end-members are given in Table S1 in the online supplements. The concentration of Zr and other trace elements (Nb, Fe, Cr) in the rutile were measured in situ with an electron microprobe at ISTERre Grenoble. The instrument was operated with an acceleration voltage of 20 kV, a beam current of 600 nA, and a total counting time of 600s, with spot size set to 1–3 μm . Standardization was done using a synthetic TiO_2 glass. Accuracy check was done on standard rutile R632 (Axelsson et al., 2018), which returned accurate Zr concentrations within $\pm 3\%$ interval. This uncertainty is consistent with counting error statistics returned by the JEOL microprobe software for the rutile analyses (R632 and unknowns), which varies between 2% and 8% and converts into an absolute uncertainty below 40 ppm in most of the cases. A conservative estimate of ± 50 ppm is therefore retained for electron microprobe analyses (EMPAs) of rutile. This propagates to a ca. $\pm 10^\circ\text{C}$ uncertainty for Zr in rutile temperatures, which is lower than the calibration uncertainty of the thermometer equation ($\pm 30^\circ\text{C}$, Tomkins et al., 2007). In addition, trace element analyses were performed by LA-ICP-MS on separated rutile grains, some of which were subsequently dated (see below). Whole-rock compositions were obtained on representative rock powders at the SARM laboratory (CNRS-CRPG) in Nancy, using a Thermo Fisher iCap6500 ICP-OES and an iCapQ ICP-MS.

4.2 | U–Pb dating and LA-ICP-MS trace element analyses

Zircon and rutile were separated using conventional rock crushing and heavy liquids. Crystals were mounted in epoxy resin and polished to expose the grain centre for analysis. Charge contrast (CC) images of zircon grains were obtained with a ZEISS EV050 scanning electron microscope at the Institute of Geological Sciences, University of Bern, at low vacuum conditions (18 Pa), 12 kV, a beam current of 100 mA and a working distance of 9.5 mm. It has been previously demonstrated that CC images correlate exactly with cathodoluminescence (Watt et al., 2000), as also confirmed by checks in the Bern laboratory. Backscattered electron images of separated rutile grains were obtained at Isterre Grenoble using the same instrument and analytical conditions as described above (section 4-1).

Trace element spot analysis of separated zircon and rutile was performed with a RESolution Laser System coupled to an Agilent 7,900 quadrupole ICP-MS at the Institute of Geological Sciences (University of Bern). A He–H₂ gas mixture was used as the aerosol transport gas. Zircon trace element analyses were performed with laser beam diameters of 24 and 20 µm, rutile with a diameter of 38 µm. The laser was set to 5 Hz repetition rate and an energy density on the sample of 4 J/cm². Oxide interferences were reduced by maintaining ThO/Th < 0.2. Sample analyses were calibrated using NIST SRM 612 (Jochum et al., 2011). Accuracy was monitored using the reference material GSD-1G (Jochum et al., 2005) and zircon 91,500 (Wiedenbeck et al., 2004), and was assessed to be better than 10% for all elements. Data reduction was performed using the software Iolite (Paton et al., 2011).

U–Pb dating of rutile was performed with the same LA-ICP-MS system at the University of Bern with the laser operating at a repetition rate of 5 Hz and an energy density on the sample of 3.5 J/cm². The count rate ratio for Th/U was 98–97 and the ThO/Th < 0.2. Measurements consisted of 30s background and 30s signal acquisition sweeping through the masses ²⁰⁶Pb, ²⁰⁷Pb, ²⁰⁸Pb, ²³²Th, and ²³⁸U. Spot size was 50µm with a pre-cleaning with a 60µm beam. U–Pb ratios were standardized to rutile R10 (1,091.6 ± 3.5 Ma, Luvizotto et al., 2009), whereas secondary reference material was rutile R632 (496 ± 2 Ma, Axelsson et al., 2018) which returned an average ²⁰⁶Pb/²³⁸U of 496 ± 11 Ma. Data reduction was performed using the software Iolite (Paton et al., 2011) running the DRS VizualAge_UcomPbine (Chew et al., 2014), although no common Pb correction was applied to the data of either standards or unknown. The single spot 2σ standard error external on the primary standard was 7.5% and propagated in full to the unknowns.

U–Th–Pb geochronology of zircon was carried out with the SwissSIMS Cameca IMS 1280-HR at Université de Lausanne, which is equipped with an high-brightness Hyperion H201

RF plasma oxygen ion source. Basic instrument set up parameters were 6–8 nA, 20 µm O₂- primary beam, mass resolution M/ΔM ~ 5,000, energy window = 40 eV. Data were acquired in mono-collection, peak-hopping mode. U–Pb–Th data were standardized to TEM2 zircon (417 Ma, Black et al., 2003) and accuracy was checked with zircon standard Plešovice (337.17 ± 0.37 Ma, Sláma et al., 2008) which were cast in the same epoxy mount as the unknowns. Data were collected over four analytical sessions in which the Plešovice standard returned average ages between 335.7 ± 2.6 and 338.5 ± 3.6 Ma. Uncertainties on standard ²⁰⁶Pb/²³⁸U–UO₂/U calibration were between 1.0% and 1.8% for each session and were propagated to the data. Common Pb correction was based on the measured ²⁰⁴Pb signal (when significant relative to background) assuming the present-day model terrestrial Pb composition of Stacey and Kramers (1975). Radiogenic ratios and single ages were calculated using the CIPS program compiled by Martin Whitehouse. Age calculations use the decay constant recommendations of Steiger and Jäger (1977). The IsoplotR package (Vermeesch, 2018) was employed to plot the diagrams and calculate concordia and weighted average ages. Individual uncertainties are quoted at 1σ level and the confidence level for weighted average is 95%.

4.3 | Thermobarometry

The *P–T* evolution of the retrogressed eclogites and the migmatitic metasediments has been assessed using a combination of Zr-in-rutile thermometry and forward thermodynamic modelling with PerpleX 6.8.4 (Connolly, 2005, 2009). Zr-in-rutile temperatures were calculated using the calibration of Tomkins et al., (2007). Isochemical *P–T* phase diagrams were computed using the thermodynamic database of Holland and Powell (2011). The solution models used are from Fuhrman and Lindsley (1988); Green et al., (2007), Green et al., (2016); Holland and Powell (1998, 2011); Newton et al., (1980); White et al., (2000), White et al., (2014). A detailed list of the solution models used to compute each phase diagram and the associated references is given in Table S3 in the online supplements. Input compositions used in PerpleX were determined either by ICP-OES analysis of the bulk rock, or on a local domain using the mineral compositions measured with the electron microprobe and mineral volume proportions estimated by point counting on the thin section. The method and composition used for each calculation are summarized in Table S3. Because Perplex inputs are specific to each sample, details about chemical systems, input composition, and adjustments of fluid content and Fe³⁺/Fe_{tot} ratios are specified for each calculation in the Thermobarometry section.

Phase assemblage stability fields and mineral composition have been used to assess the equilibrium *P–T* conditions of the different mineral assemblages. Predicted mineral

compositions on the whole P – T grid have been extracted using the *werami* script (PerpleX) and compared with EPMA measurements. The match between observed and modeled mineral composition has been quantitatively assessed by introducing a misfit function $\delta(P,T)$, which measures the distance between observed and predicted composition over the entire P – T grid. Considering p composition parameters $(1, \dots, p)$, the misfit $\delta(P, T)$ for a given mineral is defined as:

$$\delta(P, T) = 100 \sqrt{\sum_{i=1}^n \left[\frac{x_{\text{measured}}^i - x_{P,T}^i}{x_{\text{measured}}^i} \right]^2}$$

where x_{measured}^i and $x_{P,T}^i$ correspond respectively to the measured (EPMA) and predicted (PerpleX) values at given pressure and temperature for the composition parameter i . For instance, the composition parameters considered for garnet are the proportions of almandine, pyrope grossular, and spessartine (when MnO is included in the calculation) end-members. Detail of all composition variables used for each mineral is given in Table S3 in the online supplements. A panel of $\delta(P,T)$ maps is given on Figure 10.

5 | PETROGRAPHY AND MINERAL COMPOSITION OF THE METAMORPHIC SAMPLES

Seven samples of retrogressed eclogite and one sample of migmatitic metasediment were collected for petrological investigation and U–Pb dating, after careful field investigation to select only the least retrogressed domains. The seven retrogressed eclogites (JB-18-03(A-F), JB-18-06, JB-18-49, JB-18-50, JB-19-01 and JB-19-02) come from the large amphibolic body near the Lacs de la Tempête. (Figure 2). The garnet-bearing migmatitic metasediment JB-18-46 was collected in the immediate vicinity of this mafic body. Location and main petrological features are summarized in Table 1. Electron probe mineral analyses data are available in Table S2 in the online supplements.

5.1 | Retrogressed eclogites

The retrogressed eclogites are composed of garnet, clinopyroxene, amphibole, plagioclase, and quartz, with accessory epidote–clinozoisite, actinolite, chlorite, rutile, titanite, ilmenite, and rare zircon. The collected samples display various degrees of retrogression, and only sample JB-18-50 preserved a complete eclogitic assemblage, in a small centimetre-size fine-grained domain (Figure 5a-f). Petrographic descriptions are therefore focused on this sample. Mineral compositions given below are only valid for this sample, except when

stated otherwise. The complete set of mineral analyses for all the investigated samples is represented in various diagrams in Figure 7 and is also available in Table S2 in the online supplementary data.

Garnet forms millimetre- to centimetre-size grains, which have been partly resorbed. Two generations of garnet, Grt-1 and Grt-2, are identified based on composition and texture (Figures 5d,e and 7b). Grt-1 forms the core of the grains, and has a composition of $\text{Alm}_{52-56}\text{Prp}_{15-18}\text{Grs}_{25-31}\text{Sp}_{01-02}$. It contains various inclusions of quartz, rutile and omphacite, titanite, ilmenite, hornblende, and rare zircon. Titanite, ilmenite, and hornblende inclusions are commonly connected with cracks and may therefore not be primary inclusions, but would have rather developed during the subsequent metamorphic stages. In contrast, quartz, rutile, omphacite, and zircon inclusions are generally isolated within garnet and are therefore unambiguously primary inclusions that grew together with garnet. Grt-2 forms Ca-rich inclusion-poor rims around Grt-1. It has a composition of $\text{Alm}_{49-51}\text{Prp}_{15-16}\text{Grs}_{32-34}\text{Sp}_{01}$ and presents multiple concentric growth zones. The irregular boundary between Grt-1 and Grt-2 (Figure 5e) suggests that resorption of Gt-1 occurred before the development of Grt-2 rims.

Several generations of clinopyroxene are identified (Figures 5d,f and 7a). Primary clinopyroxene (Cpx-1) is an omphacite (Jd_{22-26}), with a $\text{Mg}/(\text{Mg} + \text{Fe}^{2+})$ ratio (Mg#) between 0.71 and 0.75. It was generally destabilized following the reaction $\text{Omph} + \text{Qtz} \rightarrow \text{Di} + \text{Pl}$, and formed plagioclase + diopside (+ amphibole) symplectites. It is nevertheless preserved as relics in the fine-grained domain and as inclusions in garnet cores (Grt-1). Clinopyroxene formed by destabilization of the primary omphacite occurs in the symplectites, and has been subdivided into two groups, Cpx-2 and Cpx-3, based on its jadeite content (Cpx-2: Jd_{10-20} , $\text{Mg}\# = 0.70\text{--}0.78$, Cpx-3: Jd_{03-08} , $\text{Mg}\# = 0.70\text{--}0.78$). This subdivision is somewhat artificial, as there is a continuous trend from omphacite to diopside measured in the symplectites (Figure 6a), but it allows identification of successive stages of re-equilibration during the retrogression.

Amphibole occurs in different textural positions in the retrogressed eclogites (Figure 5a,b,d,h). It mainly forms large millimetre- to centimetre-size grains associated with plagioclase, which grow in replacement of the symplectites. Amphibole–plagioclase assemblages also develop in coronas around resorbed garnet grains, and amphibole occurs as inclusions in garnet. There is no significant variation in Si–Al, Fe^{2+} –Mg, and Na–K composition within the same sample, but variation is more significant between different samples (Figure 7e). Amphibole is a magnesian hastingsite in samples JB-18-50 and JB-18-06, whereas it mostly plots in the magnesian hornblende field in samples JB-18-03(A-F). Ti concentration varies over quite a large range. High Ti concentration ($\text{Ti} > 0.15$ atom per formula) is generally correlated with the

TABLE 1 List of collected samples, with summary of age and P - T data

Sample	JB-18-03 (A-F)	JB-18-06	JB-18-49	JB-19-01	JB-19-02	JB-18-50	JB-18-46
Lithology	Retrogressed Eclogites						
Field Relations	Core of an eclogite boudin	Core of an eclogite boudin	Core of an eclogite boudin	not in place	not in place	Core of an eclogite boudin	Migmatitic Metasediment Border of the large Amphibolitic lense
Coordinates	Long °	6.53014	6.52928	6.52928	6.53014	6.52928	6.52975
WGS84	Lat °	45.62189	45.62131	45.62131	45.62189	45.62131	45.62069
	Alt (m)	2026	2051	2051	2026	2051	2013
Mineralogy	I – eclogitic assemblage: Grt-1+Omp+Qtz+Rt (+Hbl) II – HT amphibolitic/granulitic assemblage: Grt-2+Cpx-2+Hbl+Pl+Ilm/Ttn (+Rt) III – retro-morphic greenschist assemblage: Act+Ep+Chl+Ab+Ttn Accessory minerals: Zrc, Ap						
U-Pb ages (Ma)	Zrc core	-	-	448 ± 6	456 ± 4	-	-
	Zrc rim	-	311 ± 7	314–335	-	332 ± 19	317–343 305 ± 3
	Rt	340 ± 11	-	-	-	-	-
P - T Estimates	Prograde	-	-	-	-	-	0.8–1.1 GPa 600–700°C
	Peak pressure	-	-	-	-	>1.4 GPa 690–740°C	Same as peak T
	Peak temperature	-	-	-	-	0.8–1.4 GPa 700–800°C	1.1–1.4 GPa 700–780°C

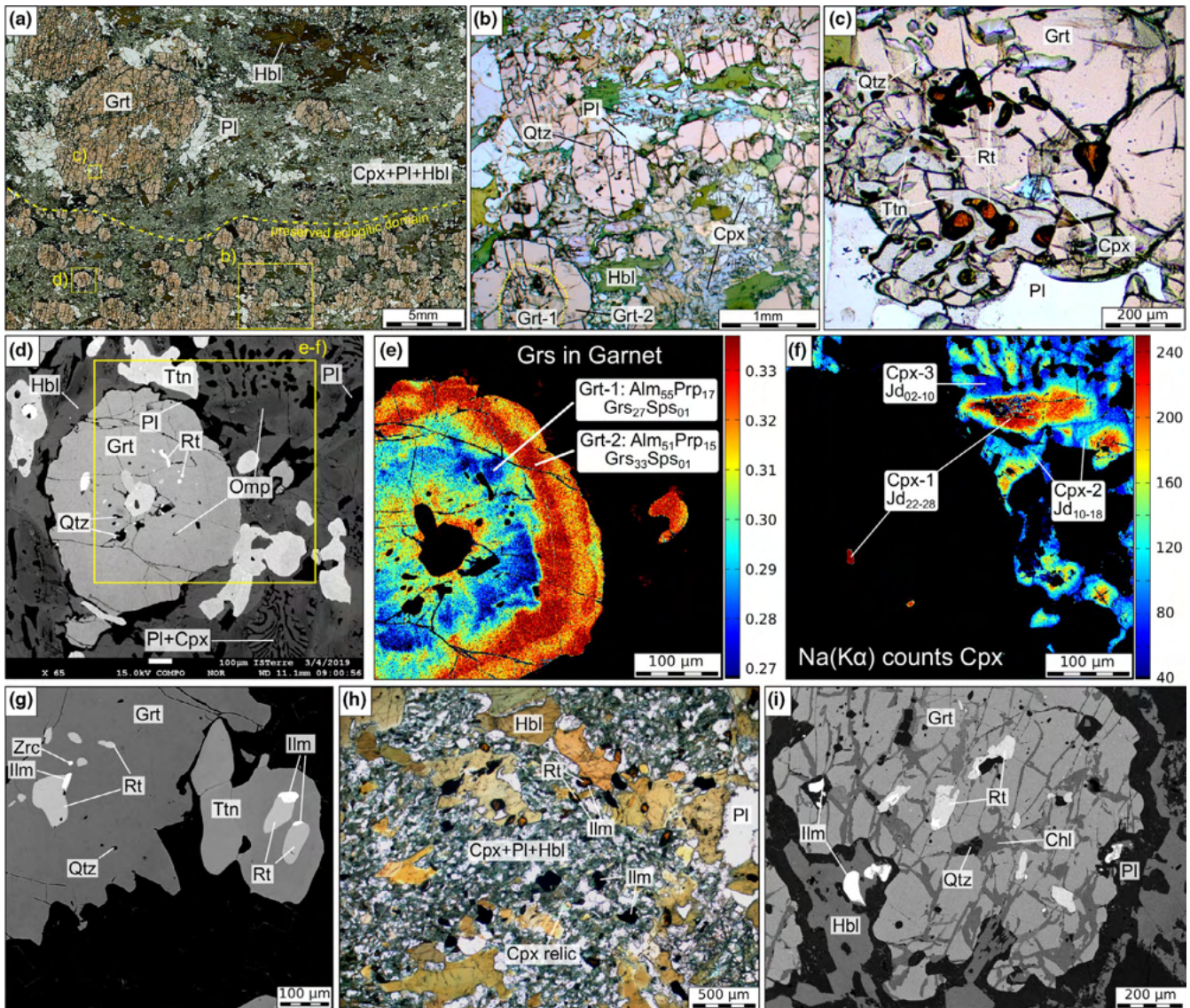


FIGURE 5 Petrological features of the retrogressed eclogite samples JB-18-50 (a–g) and JB-18-03B (h–i). (a) Scan image of a thin section of sample JB-18-50, which displays two textural domains; (i) a retrogressed coarse-grained domain and (ii) a fine-grained domain which preserved the relics of an eclogitic assemblage; (b) Microscope photograph in the fine-grained domain; (c) Garnet grain containing numerous inclusions of quartz, omphacite and rutile. Rutile is partially resorbed and replaced by titanite; (d) Backscattered electron image taken in the thin-grained eclogitic domain. Coarse grain omphacite is partially replaced by clinopyroxene–plagioclase–(hornblende) symplectites. Garnet contains numerous inclusions (see text for description); (e) X-ray map of grossular content in garnet, which shows the distinction between the Ca-poor inclusion-rich garnet core and the Ca-rich garnet rim. Additional X-ray maps for other elements are available in the online supplements (Figures S1–3); (f) X-ray map of Na in clinopyroxene, which shows the distinction between coarse-grained Na-rich omphacite and Na-poor augite in the symplectites; (g) Backscattered electron image showing rutile grains in different textural positions, enclosed in garnet and in the matrix. Ilmenite and titanite developed at the expense of rutile during retrogression; (h) Microscope photograph of the matrix in retrogressed eclogite sample JB-18-03B. Primary omphacite has almost been completely resorbed and replaced by the symplectites. Rutile is being replaced by titanite; – (i) Backscattered electron image of a garnet grain with large rutile inclusions

presence of Ti-rich minerals (titanite, rutile) bounding the amphibole grains, whereas Ti-poor grains are mostly in the symplectites. Actinolite is present in the most retrogressed samples and generally occurs in cracks together with other with greenschist facies minerals (chlorite, epidote, and albite).

Plagioclase occurs mostly in the symplectites and as millimetre- to centimetre-size grains associated with amphibole

(Figure 5a,b,d,h). It also forms thin rims around garnet. It displays a trend of composition in the range An_{10-25} in sample JB-18-50, and over a wider range (from An_{25} to pure albite) in the other samples (Figure 7f).

Rutile is the main Ti-bearing phase in the retrogressed eclogites. It forms grains of various sizes ranging from a few tens of micrometres to 200 μm (Figure 5c,d,g,h,i). It forms

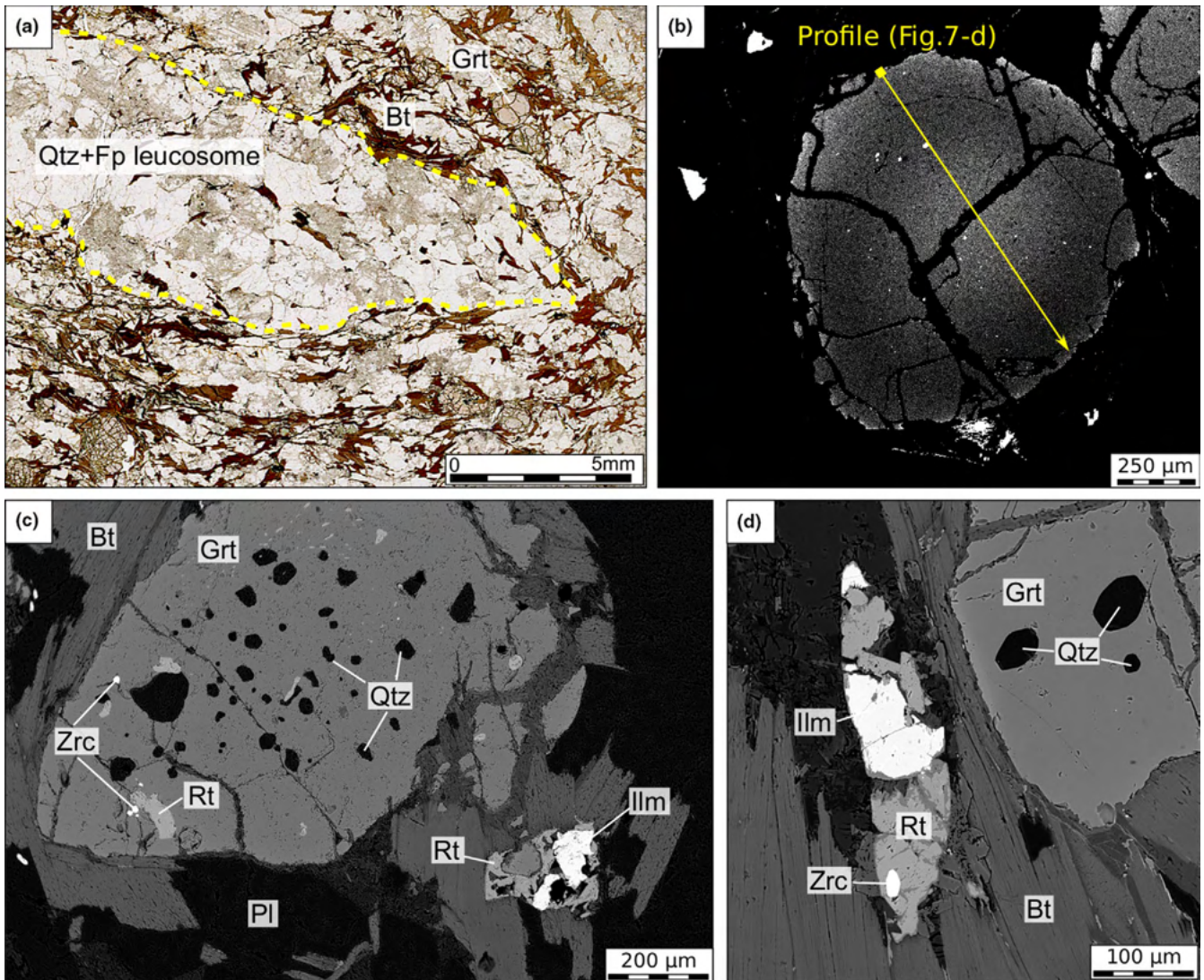


FIGURE 6 Petrological features of the migmatitic metasediment JB-18-46. (a) Thin section scan of the migmatitic metasediment. The quartz-feldspar rich domain in the centre is interpreted as a leucosome, and biotite-rich surrounding domains form the mesosome; (b) Backscattered electron image of a garnet grains. Contrast has been increased to reveal internal zoning; (c) Backscattered electron image of garnet containing inclusions of quartz and rutile; (d) Backscattered electron image of a rutile grain in the matrix, which grows over ilmenite

inclusions in garnet, and it is also found as inclusion in omphacite and amphibole, and within the symplectites. Rutile was partly replaced by titanite and ilmenite during retrogression. In samples JB-18-03A-F, ilmenite is the dominant retrogressive Ti-bearing phase (Figure 5h,i), and partially replaces rutile, especially in the matrix. In sample JB-18-50 ilmenite is rare and titanite is the main retrogressive phase, which grows forming coronas around rutile (Figure 5c). In the latter sample, some rutile grains are partly replaced by ilmenite, and the whole is surrounded by a corona of titanite, which gives the following sequence for the stability of Ti-bearing phases during retrogression: $Rt \rightarrow Ilm \rightarrow Ttn$.

Zircon is rare in the eclogites, and not all samples provided enough zircon grains for U–Pb dating. It forms grains of various sizes ranging from $<10 \mu\text{m}$ to $>200 \mu\text{m}$, which are

found as inclusions in different minerals (garnet, omphacite, and hornblende) and within the symplectites. Detailed description of zircon internal textures is provided in Section 7 (U–Pb geochronology).

In summary, minerals observed in the retrogressed eclogites define three successive parageneses: (i) a relict eclogitic assemblage, (ii) a secondary amphibolite/granulitic assemblage that forms the majority of the rocks, and (iii) a later retrograde assemblage composed of greenschist facies minerals. The eclogitic assemblage consists of garnet cores (Grt-1), omphacite (Cpx-1), quartz, and rutile. Amphibole was possibly stable during this stage, but extensive recrystallization which occurred during retrogression makes the identification of possible relicts of HP amphibole difficult. The amphibolitic/granulitic assemblage consists of garnet rims (Grt-2),

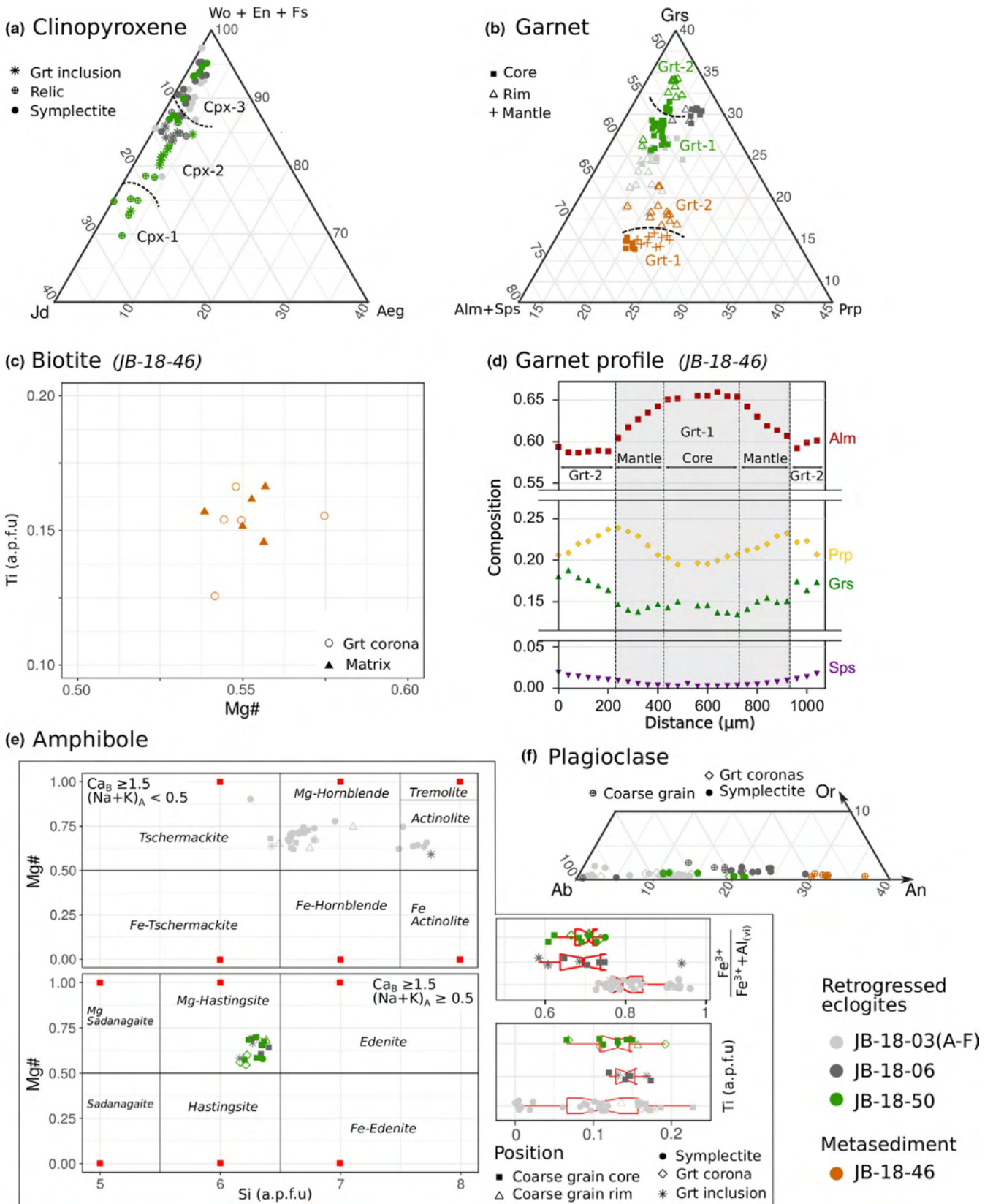


FIGURE 7 Mineral composition in the retrogressed eclogites and in the migmatitic metasediment

amphibole (hornblende/hastingsite), plagioclase, and diopside (Cpx-2–3) + plagioclase symplectites. It is associated with resorption of rutile (although it was still probably stable

at the onset of decompression) and development of ilmenite and then titanite. Finally, the late retrograde paragenesis was formed at greenschist facies conditions and consists of

actinolite, epidote, chlorite, albite, and titanite. In the least retrogressed sample (JB-18-50), this assemblage is restricted to small cracks in garnet, and to the development of pure albite at the expense of plagioclase in symplectites, while it pervasively replaces all the previous assemblages in the most retrogressed samples.

5.2 | Migmatitic metasediment

Sample JB-18-46 is a migmatitic metasediment mostly composed of quartz, feldspar, and biotite, with millimetre-size garnet and accessory rutile and ilmenite (Figure 6). Centimetre-size domains interpreted as leucosomes are mainly composed of quartz and feldspar.

Garnet presents a complex zoning, revealed by composition profiles and backscattered electron images (Figure 6b and Figure 7d). Three domains are identified, that are from core to rim: (i) a ca. 300 μm wide core domain with nearly flat Ca–Fe profiles; (ii) a ca. 200 μm wide mantle domain with Fe–Mg zoning and flat Ca profile; and (iii) a 200 μm wide rim with a flat Fe profile and Ca–Mg zoning. This zoning is interpreted as the successive growth of two garnet generations: Grt-1 forms the core ($\text{Alm}_{60-65}\text{Prp}_{19-24}\text{Grs}_{14-15}\text{Sps}_{0-1}$) and the mantle of the grains, and Grt-2 ($\text{Alm}_{57-60}\text{Prp}_{21-24}\text{Grs}_{17-19}\text{Sps}_{1-2}$) forms the rim (Figure 7d).

Biotite does not present major compositional variation. Most of the analysed grains display Mg# of 0.54–0.56 and Ti concentration of 0.15–0.17 atom per formula (Figure 8c). Feldspar is an andesine (An_{30-37}). No K-feldspar was identified in this sample.

Rutile is observed both as inclusions in garnet, associated with quartz inclusions (Figure 6a), and in the matrix, where it grows in replacement of ilmenite (Figure 6c,d).

6 | THERMOBAROMETRY

6.1 | Thermodynamic modelling

6.1.1 | Retrogressed eclogite (JB-18-50)

Isochemical phase diagrams for the retrogressed eclogites have been calculated in the chemical system NCFMASHTO. K_2O has not been included because it represents a very minor proportion of the bulk rock (ca. 0.3 wt% K_2O in the bulk rock) and is concentrated in alteration phases. Clinopyroxene stoichiometry indicates the presence of small amounts of Fe^{3+} (up to 5% aegirine end-member, Figure 7a), which could possibly affect the pressure estimation given by the proportion of the jadeite end-member in omphacite. A small amount of excess O_2 (0.15 mol%) has therefore been added, which has been adjusted so that Fe^{3+} in modelled clinopyroxene fits with the

amount estimated by stoichiometric balance of EMPAs. This converts into a $\text{Fe}^{3+}/\text{Fe}_{\text{tot}}$ ratio of 0.047. The reactive bulk composition has been estimated on a small (5x20 mm) texturally homogeneous eclogitic domain which preserves relicts of omphacite (Figure 5a). For most of the major elements, the composition estimated for this local domain is not significantly different from the bulk rock composition measured by ICP-OES (Table 2). It only appears to be slightly richer in Al and Ca and poorer in Si and Ti, which suggests it contains slightly more garnet than the bulk rock. The absence of strong chemical variation between the different grains cores (garnet and omphacite) suggests that thermodynamic equilibrium was reached at the scale of the local domain during the eclogitic stage. During the retrogression stages, many disequilibrium textures such as symplectites, coronas around garnet, and mineral core-rim zoning appeared by destabilization of the eclogitic assemblage, so the assumption of thermodynamic equilibrium for the bulk domain cannot be assumed. Two different phase diagrams have therefore been computed, respectively for the prograde and the retrograde evolution.

The prograde P – T diagram has been computed using the composition of the local domain as the reactive bulk composition, and assuming fluid-saturated conditions to model progressive dehydration of the protolith during prograde metamorphism. Concerning the retrograde evolution, the modification of the reactive volume due to garnet fractionation has been partly taken into account by removing the garnet cores (Grt-1) from the reactive composition, but other disequilibrium may persist, especially regarding the destabilization of omphacite in plagioclase + diopside symplectites. H_2O has been constrained to a fixed amount to prevent complete resorption of garnet and clinopyroxene during regression. This amount has been adjusted on a P – $M_{\text{H}_2\text{O}}$ diagram (Figure S2 in the supplements online) to fit with the observed modal proportions of amphibole, which is the main OH-bearing phase in the system.

The prograde evolution is characterized by progressive dehydration of the protolith and replacement of hydrous minerals (chlorite, epidote–clinozoisite) by garnet and omphacite. The observed plagioclase-free eclogitic assemblage with co-existing garnet, omphacite, quartz, and rutile is only stable above ca. 1.4 GPa and 600°C (black contour on Figure 8a). Small amounts of amphibole and epidote/zoisite are predicted in the lower P – T part of this domain. Considering uncertainties due to the calibration of solution models and to unconstrained assumptions concerning the fluid (assumption of fluid saturation during the prograde evolution is only a working hypothesis and not a constrained observation), the possible range of P – T conditions for the HP assemblage has been extended to the hornblende–epidote-bearing fields. Moreover, the presence of these minerals in the eclogitic assemblage cannot be completely ruled out based on petrographic observations (see section 5). At eclogitic conditions

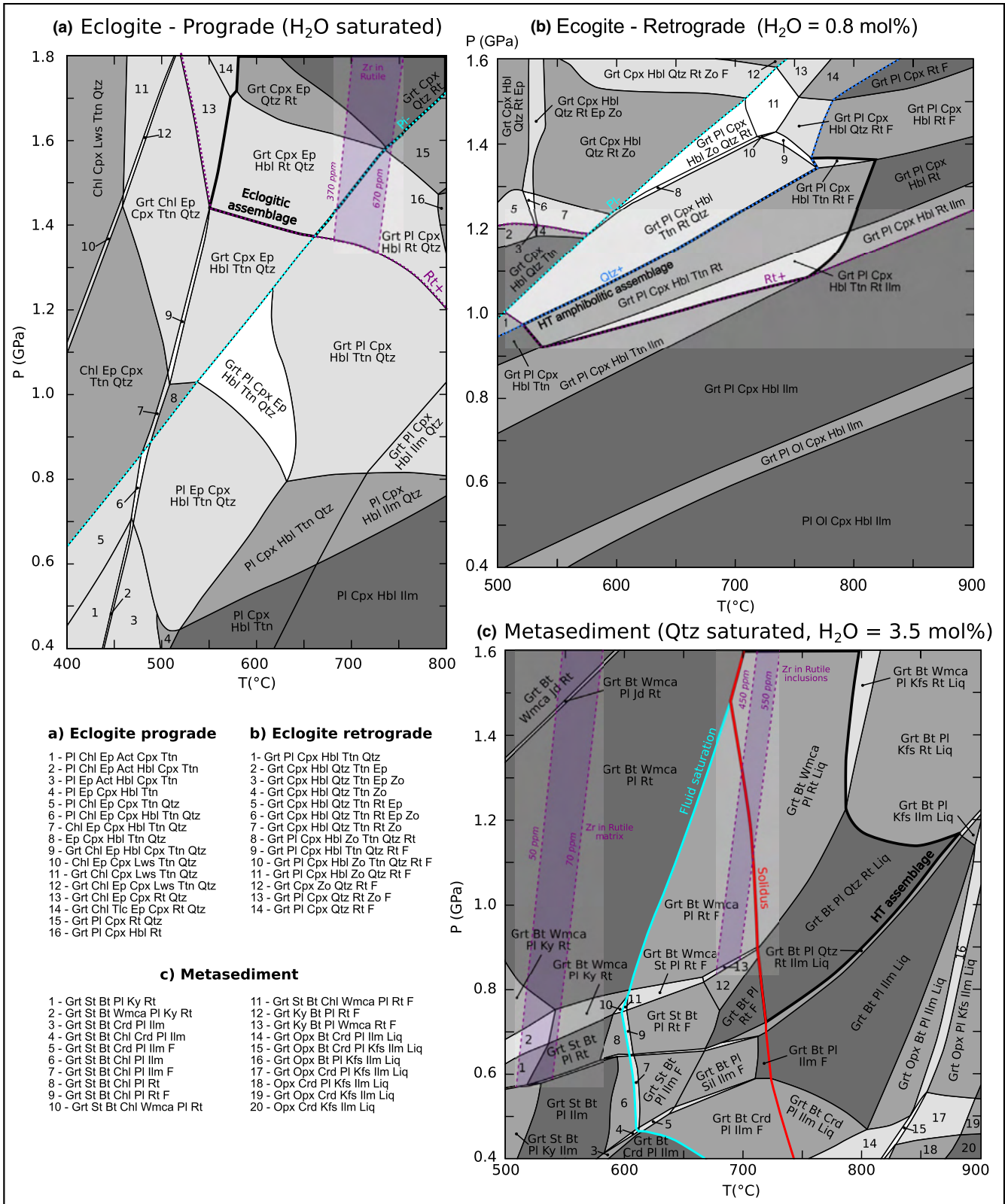


FIGURE 8 Isochemical P - T phase diagrams computed with *PerpleX* for the prograde stage in the eclogites (a), the retrograde stage in the eclogites (b) and the metasediment (c); Grey tones represent the variance within each field. The P - T domain corresponding to the observed assemblage is highlighted with a bold line contour. Temperature range obtained from Zr-in-Rutile thermometry is highlighted in purple

TABLE 2 Bulk compositions measured by ICP-OES on the bulk rock and determined by re-integration of electron microprobe analyses on a local domain, in oxide weight %

Sample	JB-18-50	JB-18-50	JB-18-50	JB-18-46
Domain	Bulk rock	Microdomain (Figure 5a)	Microdomain (Figure 5a) Without Grt1	Bulk rock
Method	ICP-OES	EPMA	EPMA	ICP-OES
Measured compositions (wt %)				
SiO ₂	48.85	46.79	49.91	62.34
TiO ₂	1.95	1.15	1.58	0.96
Al ₂ O ₃	13.47	14.84	12.52	15.10
FeO	13.61	14.65	10.61	7.09
MnO	0.26	0.30	0.21	0.13
MgO	6.60	6.50	7.15	3.78
CaO	11.00	13.49	14.99	2.67
Na ₂ O	2.13	2.18	2.95	2.55
K ₂ O	0.28	0.08	0.08	2.67
P ₂ O ₅	0.14	not analysed	not analysed	0.18
L.O.I.	0.32	not analysed	not analysed	1.50
Total	98.61	99.99	100.00	98.97
Perplex input (mol%)				
SiO ₂	-	49.14	51.22	65.11
TiO ₂	-	0.91	1.22	0.75
Al ₂ O ₃	-	9.18	7.57	9.29
FeO	-	12.87	9.11	6.19
MnO	-	excluded	excluded	0.11
MgO	-	10.18	10.94	5.89
CaO	-	15.18	16.48	2.99
Na ₂ O	-	2.22	2.94	2.58
K ₂ O	-	excluded	excluded	1.78
P ₂ O ₅	-	excluded	excluded	excluded
H ₂ O	-	excess	0.80	3.50
O ₂	-	0.15	0.15	excluded

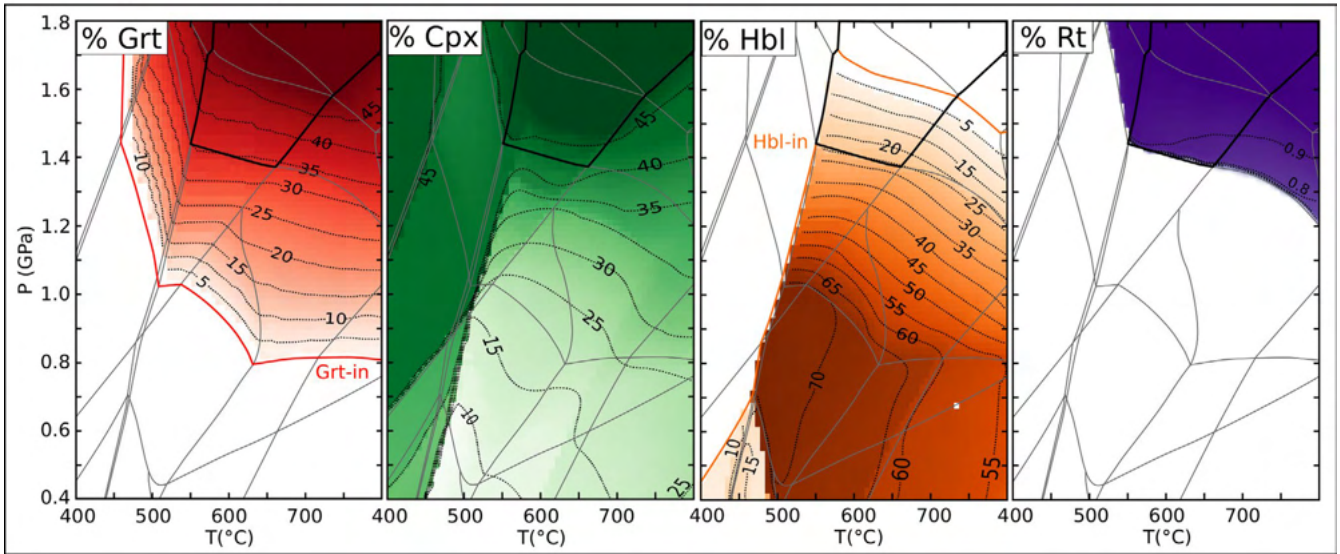
Compositions used as input in PerpleX are given below in oxide mole %.

and with $T > 600^{\circ}\text{C}$, garnet and omphacite are predicted to form respectively ca. 35–50 vol% and ca. 45–50 vol% of the assemblage, the rest being composed of quartz, rutile, and possibly hornblende and epidote/clinozoisite (Figure 9a). The volume fraction of omphacite is in agreement with the observations (Table S4), assuming that the symplectites represent destabilized grains of omphacite (35% symplectites + 15% omphacite on the thin section = ca. 50% omphacite at HP). Predicted garnet fraction is higher than the fraction actually measured (35%), but this discrepancy probably results from resorption of garnet during retrogression.

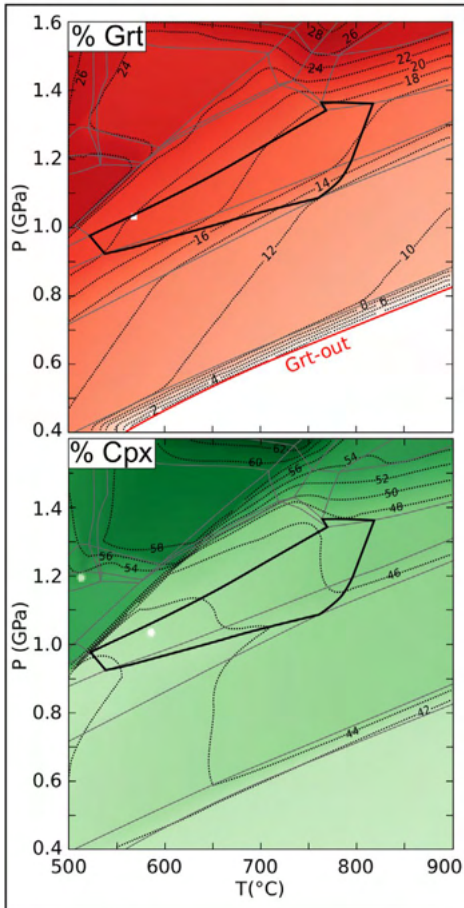
At eclogite facies conditions, garnet composition varies very smoothly with pressure and temperature, and it is therefore not a sensitive thermobarometer. There are two local

minima for the misfit, one outside of the eclogitic domain which can be excluded, and the other one at ca. 600°C and 1.7 GPa (Figure 10). However, the compositional isolines relatively widely spaced in the HP domain and do not allow precise P – T estimation. The composition of omphacite depends on its textural position, and inclusions in garnet tend to be more jadeitic than the grains in the matrix. The most jadeite-rich grain, which corresponds to a small inclusion in garnet has a composition consistent with equilibration in the eclogitic domain at $T > 550$ – 600°C (Figure 10). Taking the average of omphacite analyses, which includes relic grains in the matrix, the misfit becomes higher in the eclogitic facies and is minimal just below the PI-out line. However, omphacite grains in the matrix show internal Na–Al/Ca–Fe–Mg

(a) Eclogite - Prograde



(b) Eclogite - Retrograde



(c) Metasediment

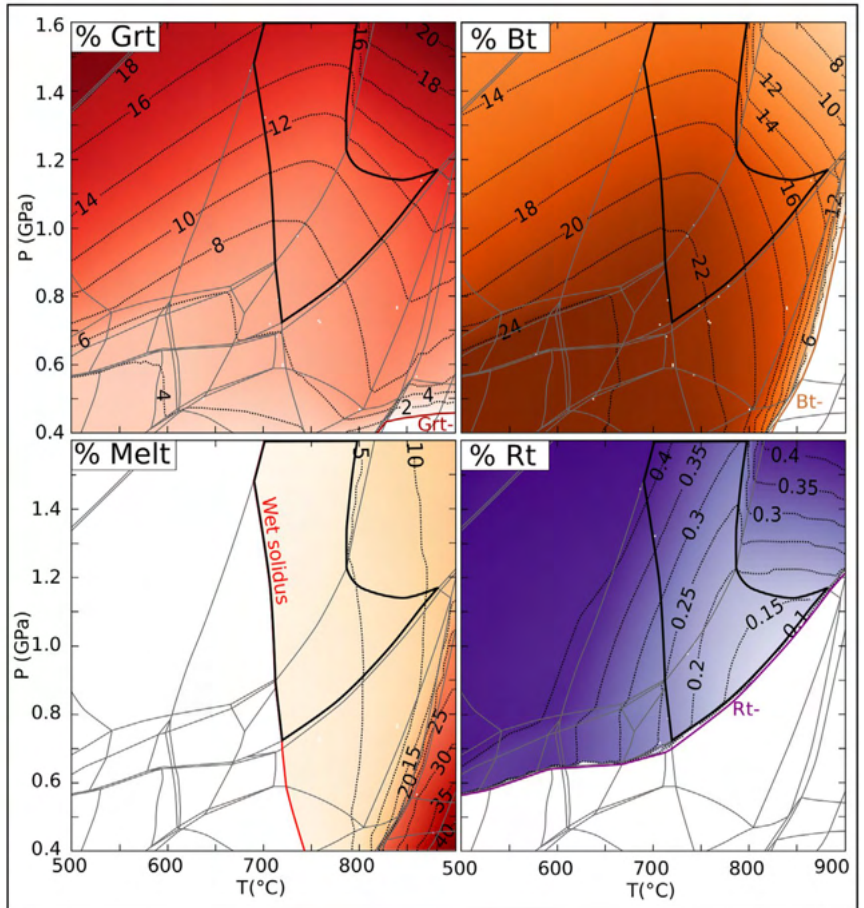
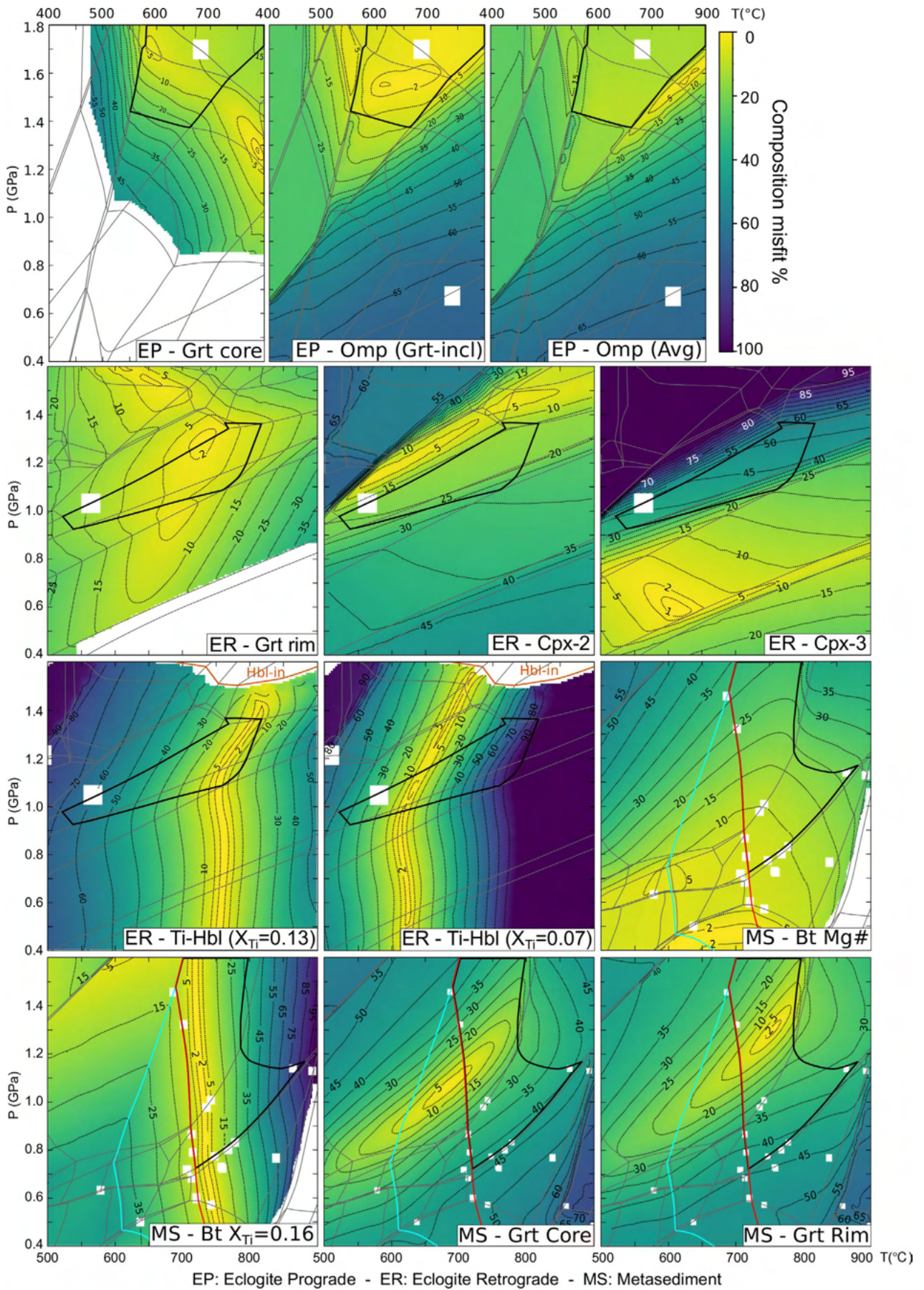


FIGURE 9 Phase proportions computed with PerpleX for the P - T diagrams on Figure 8. Contour labels indicate the volume proportion (%) of the phase present in the system. Colour scales also give a qualitative indication on the amount of the phase stable (the darker the tone, the greater amount of the phase). On each panel, the P - T domain corresponding to the observed assemblage is highlighted with a bold line contour

FIGURE 10 Misfit $\delta(P,T)$ between observed and predicted mineral composition for the P - T phase diagrams on Figure 8. Yellow corresponds to good fit with the measured composition, blue to poor fit. On each panel, the P - T domain corresponding to the observed assemblage is highlighted with a bold line contour. EP: Eclogite Prograde (Figure 8a); ER: Eclogite Retrograde (Figure 8b); MS: Metasediment (Figure 8c). End-members considered in the calculation are given in Table S3 in the online supplements



zoning which may be due to post peak pressure diffusion, and the most Al-rich cores are commonly replaced by very thin Pl + Cpx symplectites (Figure 5e,f). The composition of omphacite at peak pressure is therefore rarely preserved in the matrix grains. The Jd-rich inclusions are taken to provide a more reliable estimation of the peak pressure composition of omphacite.

The retrograde evolution is characterized by progressive resorption of garnet, clinopyroxene and quartz, and the development of hornblende and plagioclase. Rutile is also destabilized at lower pressure and is replaced by titanite and ilmenite at high temperature. However, the degree of retrogression and the stability field of Ti phases are strongly controlled by the amount of fluid in the system: more fluid results in larger resorption of garnet and clinopyroxene and larger development of hornblende and plagioclase. The stability field of rutile at low pressure and ilmenite at low temperature is also reduced at the expense of titanite for fluid-rich compositions.

The retrograde assemblage composed of garnet 2, clinopyroxene 2, hornblende, plagioclase, titanite, rutile, rare ilmenite, and without quartz appears only below 1.3–1.0 GPa and 800°C (black contour on Figure 8b). The match between the observed and the modelled mineral proportions must be assessed considering that garnet cores (garnet 1) were excluded from the reactive composition. The recalculated mineral proportions are given in Table S4. The correspondence is not totally perfect, except for hornblende, which has been used to adjust the amount of H₂O. The amount of garnet predicted is too low (ca. 15% instead of 25%) and the amounts of clinopyroxene and plagioclase are slightly too high in comparison with the measured proportions (respectively 45% and 20%–25% predicted instead of 40% and 20% for the observed proportions, Figure 9b and Table S4). These discrepancies may result from uncertainties in the estimation of the proportion of plagioclase versus clinopyroxene in the symplectites, and the proportion of core versus rim in garnet. Moreover, the retrogressed eclogites present disequilibrium textures (symplectites) and were probably not in a perfect state of thermodynamic equilibrium during retrogression.

The optimal fit for garnet composition (Grt-2) is obtained at ca. 1.3 GPa and 730°C, but the modelled garnet composition remains compatible with the measured values for a large range of *P*–*T* conditions between ca. 650–800°C and 0.9–1.4 GPa (Figure 10). Clinopyroxene Cpx-2 and Cpx-3 correspond to different stages of retrogression. Composition of Cpx-2 is compatible with a formation at relatively HP (ca. 1.3–1.4 GPa assuming *T* ~ 730°C), and has probably developed together with Grt-2 during the early stages of retrogression. Composition of Cpx-3 (late symplectites) is only compatible with much lower pressure and temperature (ca. 0.5–0.8 GPa and 550–650°C). Ti in hornblende is strongly temperature dependent and can therefore be used as a thermometer. X(Ti) in coarse grain hornblende ranges between 0.11 and 0.14

(Figure 7d), excluding abnormally Ti-rich grains in contact with rutile or titanite. This converts into a temperature range between ca. 740 and 810°C assuming *p* = 1.3 GPa, consistent with the temperature estimated for Grt-2. Some hornblende in the symplectites contains much less Ti (X(Ti)~0.06–0.07), which corresponds to *T* ~ 570–610°C, consistent with the *P*–*T* conditions estimated for Cpx-3.

6.1.2 | Migmatitic metasediment (JB-18-46)

The *P*–*T* phase diagram for sample JB-18-46 has been computed in the chemical system MnNCKFMASHT. The addition of O₂, even in small amount, results in unrealistic stabilization of ilmenite towards high pressure (>1.0 GPa) at the expense of rutile, which is not supported by the petrographic observations (in particular, garnet contains numerous inclusions of rutile but no inclusions of ilmenite). This component has therefore been excluded. The reactive composition corresponds to the bulk rock composition measured in sample JB-18-46. This sample is taken from a portion of the migmatite that is predominantly composed of mesosome and only contains minor portions of leucosome (<5%). Fractionation due to possible melt extraction has therefore been neglected. H₂O has been adjusted on a T-M_{H₂O} section (Figure S4 in the supplements) to fit with the observed amount of biotite (15–20 vol%), which is the main hydrous phase in the system. In contrast with the eclogites, the metasediment does not present significant disequilibrium textures. Garnet cores represent an insignificant proportion of the whole rock (3% of the rock volume for total garnet, probably < 1% for the garnet cores), so fractionation due to garnet growth has been neglected.

The presence of a small amount of granitic liquid formed by muscovite-breakdown reactions and the absence of K-feldspar constrains temperature between 700 and 800°C (Figure 8c). The composition of the garnet cores is consistent with sub-solidus growth ca. 1.0–1.15 GPa and 650–700°C, while the composition of the garnet rims is more consistent with supra-solidus formation at ca. 1.1–1.4 GPa and 720–780°C (Figure 10). The Ti concentration in biotite indicates temperatures between 720 and 740°C consistent with those estimated for the garnet rims. However, the Mg/Fe ratio in biotite (Mg# = 0.54–0.56) is inconsistent with these *P*–*T* conditions, which may be due to diffusional resetting during retrogression. The modelled stable assemblage at peak temperature conditions is composed of garnet, plagioclase, quartz, biotite, white mica, and rutile, in equilibrium with ca. 5% of granitic liquid (Figure 8c). The small amount liquid predicted is consistent with the presence of centimetre-size leucosomes observed on the thin section. White mica has not been observed, but is predicted to be present only in small amounts (<5 vol%) at peak temperature conditions, and

disappears from the stable assemblage below 0.6–1.0 GPa. It may therefore have been completely resorbed during retrogression. The amount of garnet predicted to be stable at peak temperature conditions (~8–12 vol%, Figure 9c) is greater than the amount actually observed in the sample (~3–4 vol%). This may result from strong resorption of garnet during retrogression. Alternatively, it may also be due to different proportions of garnet in the thin section and in the whole rock. Finally, the presence of ilmenite in the matrix indicates that the rock experienced decompression down to ca. 0.6–0.7 GPa following the HP stage (Figure 8c).

6.2 | Zr-in-rutile (ZiR) thermometry

The retrogressed eclogites contain rutile in two different textural settings, either as inclusions in the eclogitic garnet 1 or in the matrix. In situ analyses of rutile grains performed with the electron microprobe show a distinction in Zr concentration between these two populations (Figure 11a). The rutile inclusions contain between 370 and 500 ppm Zr (Table S5), while matrix rutile contains more Zr (550–670 ppm). In sample JB-18-50, a few analyses of rutile inclusions in one garnet grain yield higher Zr concentrations, closer to those of matrix rutile. The composition of rutile grains recovered as mineral

separates and analysed by LA-ICP-MS is significantly different from matrix rutile and present Zr concentrations closer to the rutile included in garnet. The calibration of Tomkins et al., (2007) of the Zr-in-rutile thermometer was used to calculate temperatures, with an assumed pressure of 1.6 GPa constrained by the stability of the eclogitic assemblage. Calculated temperatures are in the range 690–730°C for the rutile inclusions and the separated grains, and in the range 720–740°C for the matrix rutile (Figure 11b). Instrumental uncertainty for Zr concentration is below 10 ppm for LA-ICP-MS analyses and below 50 ppm for EMPAs. This propagates to an insignificant temperature uncertainty of ±1–2°C for LA-ICP-MS data and ±10°C for electron microprobe data, which is in any case lower than the ±30°C uncertainty derived from the calibration of Tomkins et al., (2007). Considering a realistic uncertainty of ±30°C, the temperature estimates for rutile inclusions and rutile in the matrix are thus indistinguishable and plot between 690 and 740°C.

In the metasediment, the two rutile populations (rutile inclusions in garnet and matrix rutile associated with ilmenite) present much larger compositional differences than in the retrogressed eclogites. Rutile inclusions contain ca. 450–550 ppm Zr, while matrix rutile is much poorer in Zr (ca. 50–70 ppm Zr). This yields temperatures in the range 695–715°C for the rutile inclusions and in the range

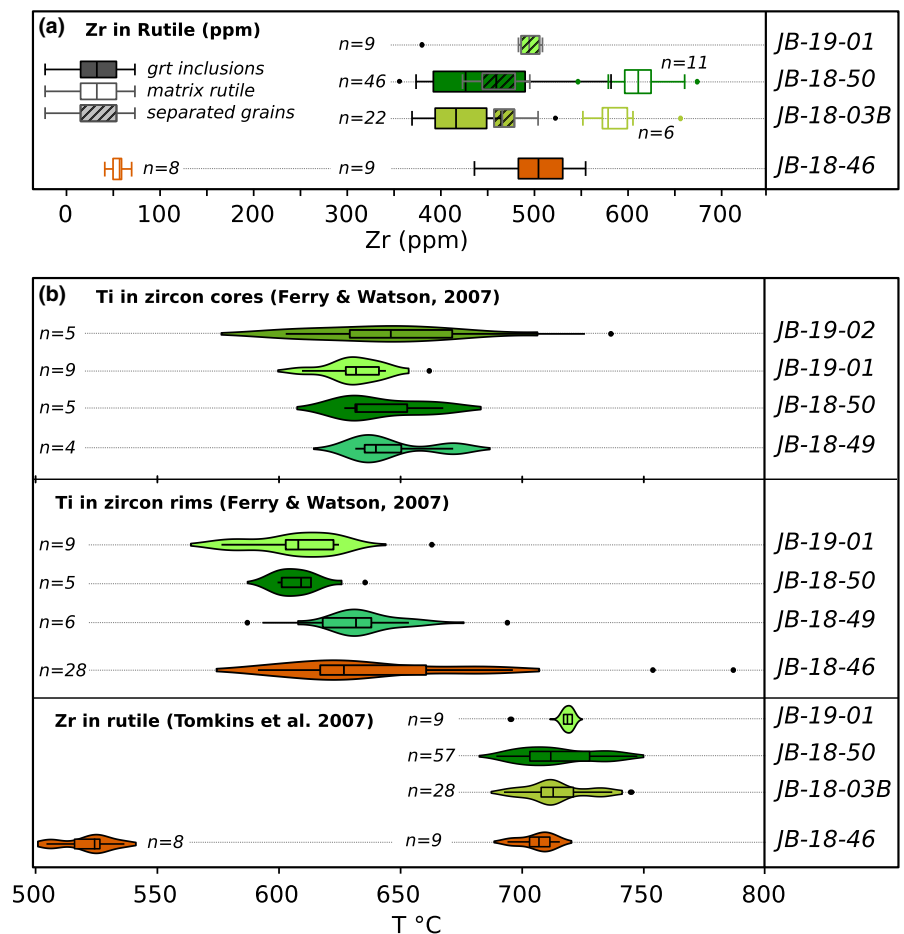


FIGURE 11 Distribution of Zr concentration measured in rutile (a) and Ti-in-zircon and Zr-in-rutile temperatures (b), estimated with the calibration of Ferry and Watson (2007) for zircon and Tomkins et al., (2007) for rutile. Eclogites are figured with green tones, and the metasediment in orange. Considering the calibration uncertainty of the Zr-in-rutile thermometer (±30°C), the calculated temperature is indistinguishable for the different populations in the eclogites, which have therefore been merged together

515–545°C for the matrix rutile, assuming $p = 1.3$ GPa for the rutile inclusions and $p = .8$ GPa for the matrix rutile. For the Zr-poor rutile in the matrix, The ± 50 ppm on the Zr measurement translates into a temperature uncertainty larger than $\pm 30^\circ\text{C}$ (up to $\pm 70^\circ\text{C}$), especially for the lower bound due to the logarithmic relation between Zr and T.

7 | U–Pb GEOCHRONOLOGY

7.1 | Zircon and rutile description

The zircon grains from the retrogressed eclogites are typically 100–150 μm in size and have a slightly rounded

shape (Figure 12a). Most of the grains present a CC-dark core surrounded by a CC-brighter, 10–30 μm wide rim. Grain cores can present oscillatory zoning, but most crystals are characterized by broad sector or fir-tree zoning. Metasediment JB-18-46 contains zircon crystals that vary in size (<100 to 400 μm) and shapes from rounded to euhedral (Figure 12b). CC imaging reveals a variety of zoning patterns, with mainly rounded cores with sector or oscillatory zoning that are surrounded by multiple CC-bright overgrowths. Rutile separated for U–Pb dating forms 100–250 μm wide homogeneous grains devoid of ilmenite exsolution and containing rare inclusions of omphacite (Figure 12c). Grains are often bordered by titanite and plagioclase.

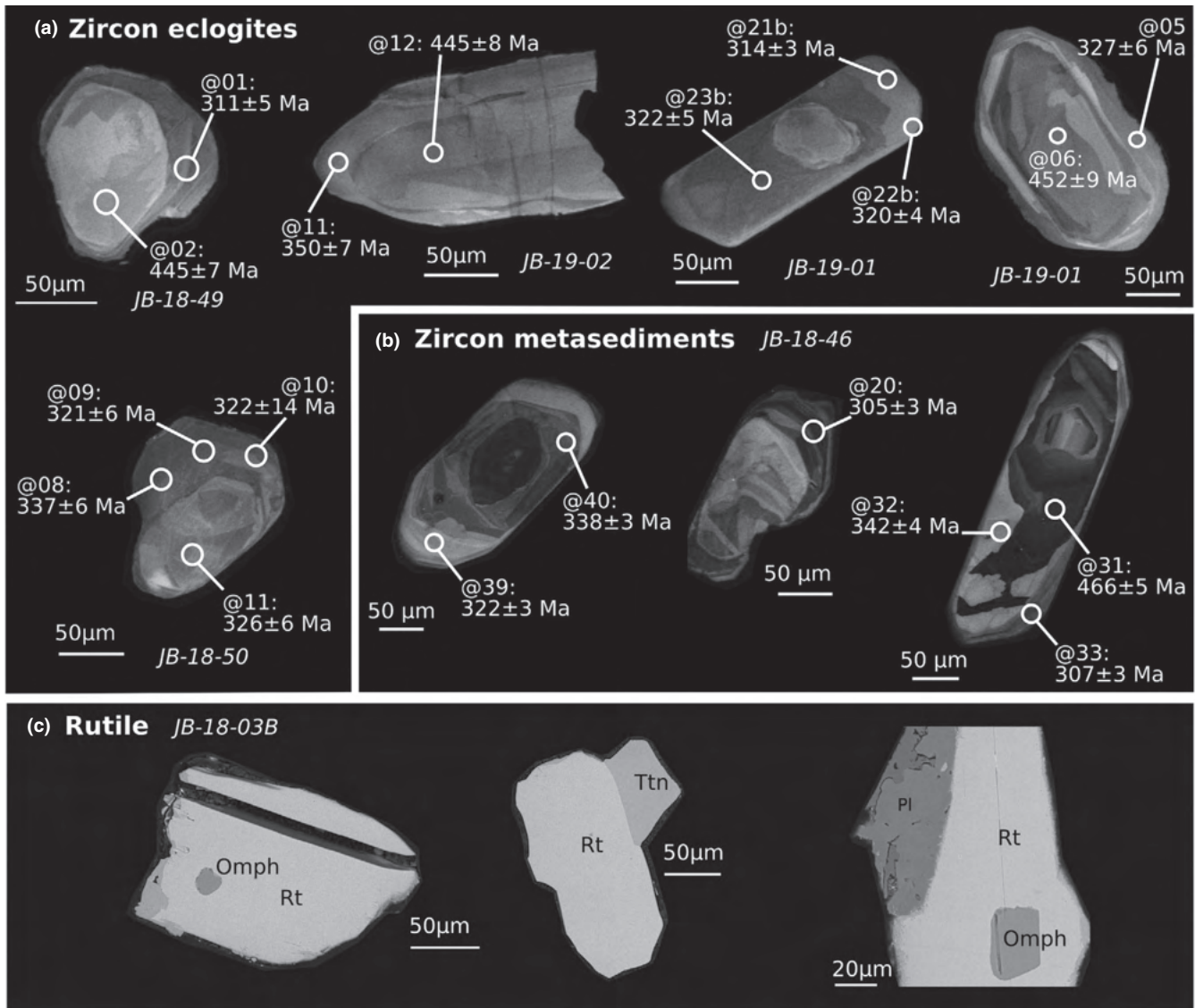


FIGURE 12 CC images of representative zircon grains separated from the retrogressed eclogites (a) and from the metasediment (b). (c) Backscattered electron images of representative rutile grains separated from the retrogressed eclogites and analysed for trace elements and U–Pb isotopes

7.2 | Zircon composition

Thorium and Uranium content were measured during SIMS analysis and values are generally consistent with LA-ICP-MS data measured on the same domain, considering the different volume sampled. In the retrogressed eclogites, grain cores generally have high U concentrations of 50–900 ppm and Th/U ratios >0.1, while rims generally contain 1–50 ppm U and show various Th/U ratios, from <0.01 to 0.5 (Figure 13a, Table S6 in the online supplements). Some grain cores with low U and Th/U ratios yield U–Pb dates similar to the rims,

and can be considered as belonging to the same population. In metasediment JB-18-46, zircons are richer in U than in the metabasic rocks. Zircon rims were targeted as a priority in order to date the metamorphic events. They contain 100–2000 ppm U with low Th/U ratios in the range 0.001–0.03. Only a few inherited cores yielded higher Th/U ratios.

Some of the zircons analysed for trace elements by LA-ICP-MS present an unusually high concentration of Ti (Table S6), probably due to the sampling of micro-inclusions of rutile or other Ti-bearing phases, and these analyses were therefore discarded. The remaining data were then sorted

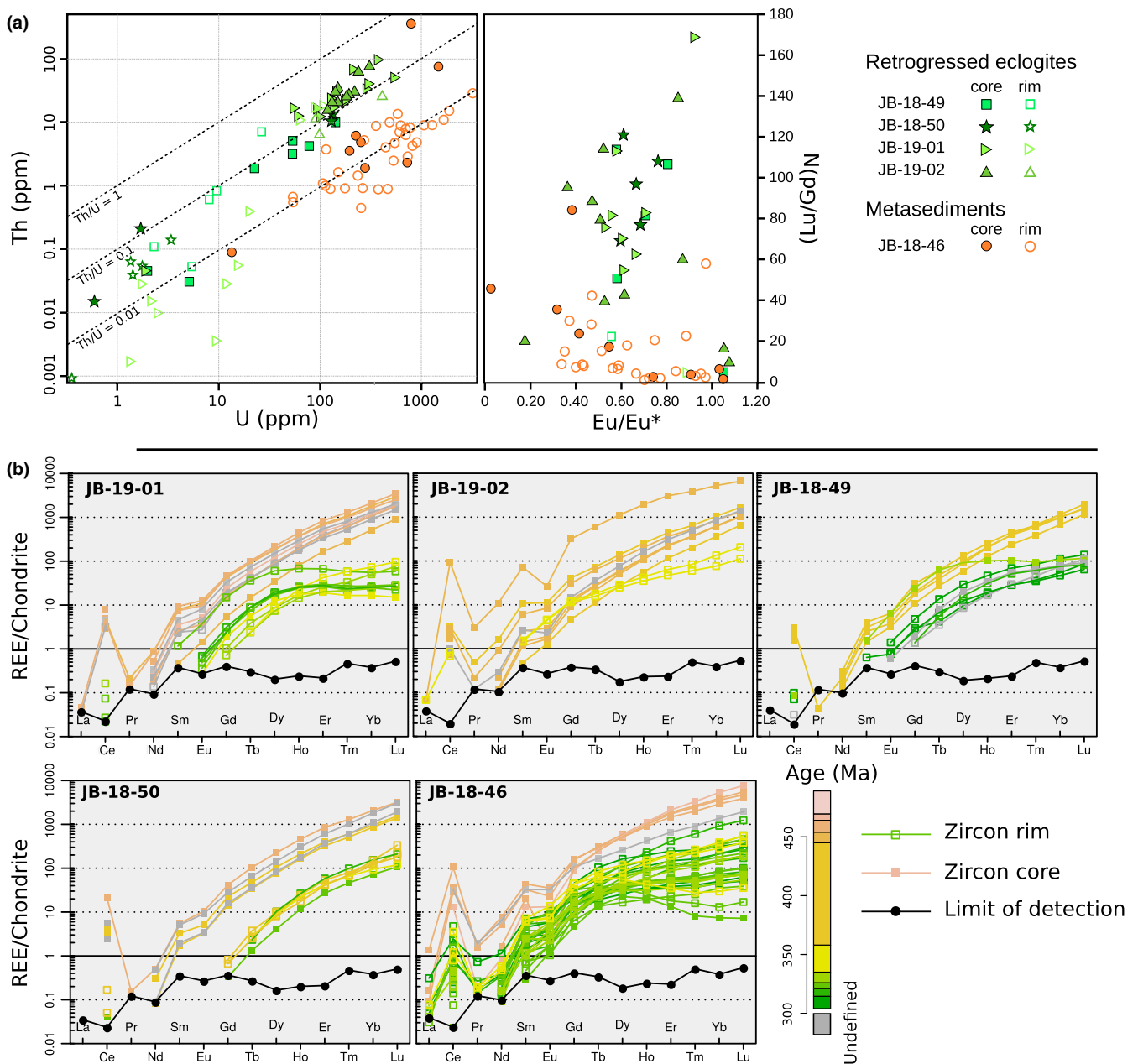


FIGURE 13 Th–U and REE composition of zircon cores and rims in both rock types. (a) plots of Th versus U and $(Lu/Gd)_N$ versus Eu anomaly in analysed zircon cores and rims. (b) Chondrite normalized patterns for REE in zircon. The colour scale indicates the common Pb corrected $^{206}Pb/^{238}U$ date obtained by SIMS dating of the same domain

by $^{206}\text{Pb}/^{238}\text{U}$ dates and sampling domain (core or rim). Chondrite normalized (Palme and O'Neill 2004) REE patterns are presented on Figure 13b. Eu anomaly ($\text{Eu}/\text{Eu}^* = \text{Eu}_\text{N}/(\text{Sm}_\text{N}^*\text{Gd}_\text{N})^{1/2}$) and $(\text{Lu}/\text{Gd})_\text{N}$ are used as proxies to discriminate between different zircon populations (Figure 13a). A summary of trace element data in zircon is available in Table S6 in the online supplements.

In the four samples of retrogressed eclogites, a clear distinction based on REE concentration exists between the old zircon domains (>400 Ma, mostly zircon cores) and the younger ones (300–350 Ma, mostly zircon rims): the younger zircon domains are generally poorer in REE than the older domains and have a flatter REE patterns (Figure 13b). Zircon cores across samples are similar in REE composition. They have a negative Eu anomaly ($\text{Eu}/\text{Eu}^* = 0.5\text{--}0.8$) and are enriched in HREE, with Lu–Yb concentrations close to 1,000 times chondrite and a steep positive slope of the HREE pattern ($(\text{Lu}/\text{Gd})_\text{N} = 40\text{--}120$). By contrast, zircon rims present more significant variation between samples. Zircon rims from sample JB-19-01 display flat or nearly flat HREE profiles at around 10–100 times chondrite composition, with moderated enrichment in HREE relative to MREE ($(\text{Lu}/\text{Gd})_\text{N} = 4\text{--}12$ for the majority of analyses). Eu/Eu^* could not be calculated because Sm is below detection, but the smooth slope between Eu and Tb suggests the Eu anomaly is weak or absent. Zircon rims from the other retrogressed eclogites (JB-19-02, JB-18-49, JB-18-50) display steeper HREE profiles ($(\text{Lu}/\text{Gd})_\text{N} > 20$, and up to 270 in sample JB-18-50) and have a higher content in HREE (Lu–Yb concentrations >100 times chondrite). When it could be calculated, Eu/Eu^* is close to 1 (>0.8).

In metasediment JB-18-46, inherited zircon cores also have a distinctly different REE composition with respect to the rims (Figure 13b). They zircon cores are ~1 order of magnitude richer in REE than the rims, present a pronounced Eu anomaly ($\text{Eu}/\text{Eu}^* = 0.03\text{--}0.55$) and are strongly enriched in HREE (Lu–Yb concentration up to 5,000 times chondrite). Zircon rims display important variations, with REE profiles ranging from flat HREE with a low Eu anomaly ($(\text{Lu}/\text{Gd})_\text{N} < 10$, Lu–Yb ~ 10 times chondrite concentration and $\text{Eu}/\text{Eu}^* > 0.5$) to enriched HREE with a more pronounced Eu anomaly ($(\text{Lu}/\text{Gd})_\text{N} = 10\text{--}60$, Lu–Yb concentration = 50–100 times chondrite, $\text{Eu}/\text{Eu}^* < 0.6$). There is no clear relation between the U–Pb age and the shape of REE profiles for the rims.

The Ti content in zircon ranges between 1.8–4.2 ppm for the cores and 1.3–5.0 ppm for the rims, with no significant difference between samples (Table S6). Using the calibration of Ferry and Watson (2007), this yields a temperature range of 600–680°C for the cores and 560–680°C for the rims (Figure 11b). These temperatures are significantly lower than those given by Zr-in-rutile thermometry and those estimated for the crystallization of the main metamorphic assemblages. Possible explanations for these discrepancies are reviewed in the discussion.

7.3 | Zircon U–Pb dating

7.3.1 | Retrogressed eclogites

Most of the U–Pb analyses of zircon cores are more than 95% concordant and yielded $^{206}\text{Pb}/^{238}\text{U}$ dates in the range 440–465 Ma (Figure 14a,b and Table S7). A few analyses yielded younger dates around 400–430 Ma, which have been excluded from further calculation since they are significantly discordant (up to 20% discordance) and may have been partially reset during metamorphism. Fourteen zircon cores analyses from samples JB-19-01 and 10 core analyses from sample JB-19-02 allowed to define two $^{206}\text{Pb}/^{238}\text{U}$ weighted mean ages at respectively 456 ± 4 Ma and 448 ± 6 Ma, which are within uncertainty the same as the concordia ages.

Zircon rims were more challenging to analyse, because the U content is generally low (down to 1–2 ppm, Table S7) and rims are thin and difficult to target without overlapping with the core. The position of the SIMS spot has been checked after analysis and mixed analyses between core and rim have been discarded. Some of the remaining data show significant common Pb content, especially in sample JB-18-50. For this sample, uncorrected ratios are presented in a Tera-Wasserburg diagram, where the age is defined by a regression line anchored to the common Pb composition predicted by the model of Stacey and Kramers (1975) at 0 Ma ($^{207}\text{Pb}/^{206}\text{Pb} = 0.8356$). Given the relatively low per cent of initial Pb ($f_{206} < 10\%$), the choice of initial Pb composition has little bearing on the age. Five analyses define an intercept age at 332 ± 19 Ma (Figure 14c). Zircon rims from samples JB-18-49 and JB-19-01 contain a lower percent of common Pb, so corrected ratios are presented in Wetherill concordia diagrams. The zircon rim analyses from sample JB-18-49 define a weighted mean $^{206}\text{Pb}/^{238}\text{U}$ age of 311 ± 7 Ma (Figure 14f). Analyses from sample JB-19-01 are over-dispersed between 314 Ma and 335 Ma (MSWD = 3.6) and therefore a meaningful average age cannot be calculated. (Figure 14d,e). Finally, only two rims from sample JB-19-02 could be analysed. They are slightly discordant (~5% discordance) and yield $^{206}\text{Pb}/^{238}\text{U}$ dates of 350 ± 7 Ma and 351 ± 7 Ma (Table S7). However, two concordant data points are not enough to define a statistically robust population, and more analyses would be needed to confirm this date.

7.3.2 | Migmatitic metasediment

Zircon rims in sample JB-18-46 yield $^{206}\text{Pb}/^{238}\text{U}$ dates scattered between ca. 305 and 345 Ma (Figure 14g,h + Table S8). A few inherited cores have older concordant dates at ca. 466 Ma and one younger rim analysis is discordant. The $^{206}\text{Pb}/^{238}\text{U}$ dates of the zircon rims that are more than 95% concordant do not define a statistically consistent population but rather form three

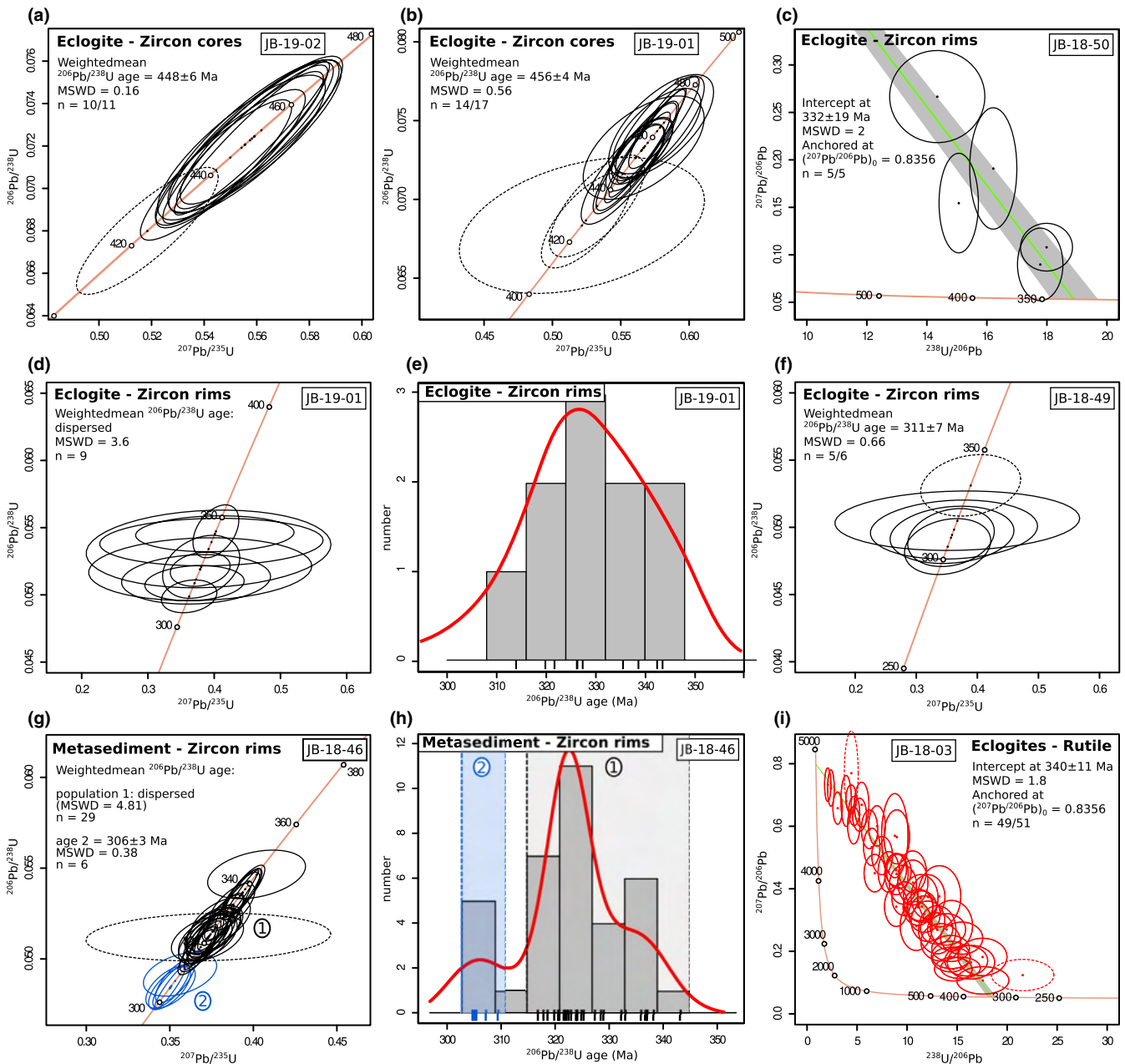


FIGURE 14 Summary of U–Pb analyses in zircon and rutile plotted on Wetherill and Tera-Wasserburg (ratios uncorrected for common Pb) diagrams using the IsoplotR R package (Vermeesch, 2018); (a)–(b) eclogite zircon cores; (c), (d), (f) eclogite zircon rims; (g) metasediment; (e), (h) probability distribution and histogram of $^{206}\text{Pb}/^{238}\text{U}$ dates in zircon rims from eclogite JB-19-01 (e) and metasediment JB-18-46 (h); (i) rutile from the retrogressed eclogite JB-18-03B. In the Tera-Wasserburg diagram of (c), the regression is forced to the $^{207}\text{Pb}/^{206}\text{Pb}$ value of present-day common Pb according to Stacey and Kramers (1975). Analyses excluded from age calculation are shown with dotted contours

groups centred at ca. 305, 325, and 335 Ma (Figure 14h). The six youngest dates are from rims with distinct CC that grew over older rims (Figure 12b). We therefore consider them as a distinct population with an age at 306 ± 3 Ma. On the other hand, the dates between 317 ± 3 and 343 ± 3 Ma are from domains that are similar in CC zoning and in REE composition (Figure 13b). In the lack of any criteria to define any sub-group, we consider these analyses as a dispersed population, that does not form a statistically

homogeneous group and for which a geologically meaningful average age cannot be calculated.

7.4 | Rutile U–Pb dating

The retrogressed eclogites derive from Fe–Ti rich tholeiites which are rather poor in U, and consequently the U content in rutile is generally low (<1 ppm). Only the rutile

from sample JB-18-03B contained enough U (up to 3 ppm) to be dated (Table S9). The U–Pb analyses contain significant common Pb, so the U–Pb age has been assessed using a linear regression of the uncorrected U–Pb ratios plotted on a Tera–Wasserburg diagram (Figure 14i). Two data points were excluded as they plot far from the regression line. The unconstrained regression and the regression anchored to the common Pb composition predicted by the model of Stacey and Kramers (1975) at 0 Ma yield identical ages within the uncertainty at 340 ± 11 Ma (MSWD = 1.8).

8 | DISCUSSION

8.1 | Conditions of metamorphism and P – T evolution

8.1.1 | Zircon in rutile temperatures

The Zr-in-rutile (ZiR) thermometer has demonstrated to be resistant to diffusion resetting, and has proven its ability to retain UHT conditions above 900°C in granulitic terranes (e.g. Kooijman et al., 2012; Luvizotto & Zack, 2009). Therefore, the measured Zr concentration is interpreted to reflect accurately the actual amount of Zr incorporated in rutile at formation. In the retrogressed eclogites, rutile is stable only at HP (>1.4 GPa under water-saturated conditions, Figure 8a). The ZiR thermometer is therefore taken to indicate temperature during the eclogitic stage. The rutile inclusions in garnet contain about 150 ppm less Zr than the matrix rutile. This difference may be due to the early entrapment of the rutile inclusions in garnet during the prograde to peak evolution. Such inclusions would have then been protected from further re-equilibration, whereas matrix rutile continued to equilibrate after peak pressure during decompression. The higher Zr concentration in matrix

rutile may thus result either from equilibration at higher temperature, lower pressure or lower a_{SiO_2} , all of these changes resulting in more Zr being incorporated in the rutile. The difference induced by these effects on the calculated ZiR temperature is small (+30°C at constant pressure or –0.5 GPa at constant temperature), and is close to the uncertainty of the calibration ($\pm 30^\circ\text{C}$, Tomkins et al., 2007). The temperature range between 690 and 740°C obtained by grouping all the rutiles together is taken to indicate conditions close to the peak pressure, from the late prograde evolution to the onset of decompression.

In the metasediments, the ZiR T for the rutile inclusions in garnet is estimated between 695 and 715°C, and is within uncertainty the same as temperature obtained with Ti-in-biotite and garnet thermobarometry for the supra-solidus stage. The ZiR T is interpreted as the peak temperature during the P – T evolution of the metasediment. In contrast, matrix rutile, which grows by replacement of ilmenite (Figure 5i), records $T < 550^\circ\text{C}$. At low temperature, the stability field of rutile extends down to 0.6 GPa in the metasediment (Figure 11). The partial resorption of ilmenite and its replacement by low- T rutile in the matrix has therefore occurred during the late cooling stage, and is a retrograde feature.

8.1.2 | Possible P – T paths

The thermobarometric estimates obtained by ZiR thermometry and forward thermodynamic modelling indicate that the retrogressed eclogites and the metasediments underwent different P – T evolutions (Figure 15). The retrogressed eclogites experienced HP metamorphism during the lower-mid Carboniferous (see below), with minimal peak pressure conditions $p > 1.4$ GPa and 690–740°C. This stage was followed by decompression from 1.4 to 1.0 GPa at 700–800°C, associated with the resorption of the eclogitic assemblage and the

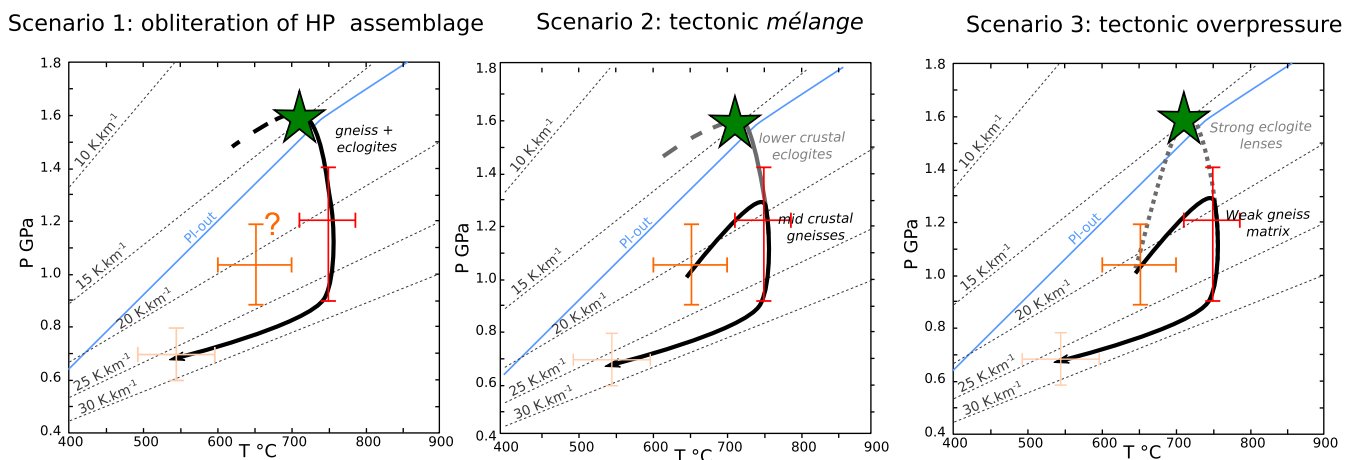


FIGURE 15 Possible P – T evolution for the eclogitic lenses and the surrounding gneisses corresponding to the three presented scenarios. See discussion in text

development of the secondary amphibolite/granulite facies assemblage. In contrast, the investigated metasediment does not show any trace of a HP stage at eclogite facies. It records instead prograde evolution from sub-solidus conditions (0.8–1.1 GPa and 600–700°C) to supra-solidus conditions (1.1–1.4 GPa and 700–780°C) in upper amphibolite/HP granulite facies, roughly coeval with the HP stage in the eclogites (see below). A later stage of retrogression in the amphibolite facies is recorded in both lithologies, associated with the development of Na-poor clinopyroxene and Ti-poor hornblende in the eclogites at ca. 0.5–0.8 GPa and 570–610°C, and with retrograde replacement of ilmenite by rutile in the matrix of the metasediment below 550°C and 0.6–0.7 GPa.

In gneiss units that host eclogite relics, it is quite common for the host rock to record lower pressure than that of the enclosed eclogite lenses (Godard, 2001). Possible explanations for this discrepancy include: (i) the obliteration of the former HP assemblage in the host gneiss during retrogression, (ii) mixing of different crustal components with their own P – T history in a tectonic *mélange* zone, or (iii) tectonic overpressure caused by a difference in strain rates between the weak host gneiss and the stronger mafic bodies (Figure 15).

(i) The obliteration of the HP assemblage in the host gneiss is quite plausible, especially considering the important strain rate associated with D2 dextral shearing, which affected the weak metasediments more intensely than the stronger mafic lenses (Figure 4). Moreover, the HP stage would not have been characterized by a readily identifiable mineral assemblage in the metasediments (Figure 8), which makes the identification of possible HP relics even more difficult. However, the metasediments record a prograde evolution from P – T conditions in the mid amphibolite facies that is roughly coeval (see below) with the development of HP assemblages in the retrogressed eclogite, which is not explained by this scenario.

(ii) The model of tectonic *mélange* provides a more consistent explanation to the absence of HP relics and the preservation of prograde evolution at lower pressure in the metasediments. The mafic protoliths would represent deep portions of the lower crust metamorphosed at eclogite facies conditions, while the felsic protoliths would represent portions of the middle crust metamorphosed at lower pressure. These two different crustal fragments would have come together in the middle crust during the HP amphibolite stage, before being exhumed to the upper crust.

(iii) Finally, it is possible that the recorded pressure difference between the retrogressed eclogites and the surrounding metasediments results from local tectonic overpressure in the mafic lenses. In terms of rheology, the Lacs de la Tempête unit is composed of a weak metasedimentary matrix containing strong elliptical bodies of amphibolite, which underwent pervasive strike-slip shearing during the D2 tectonic phase. A simple mechanical model which applies to this situation

has been proposed by Moulas et al., (2014), which shows that significant deviation from the lithostatic pressure (up to 1 GPa) can occur, both in the strong bodies and in the surrounding matrix. The pressure excess in the eclogites relative to the metasediments is lower than 0.5–0.6 GPa and is therefore achievable with this process. However, this model implies that HP metamorphism in the strong mafic *boudins* is coeval with D2 dextral shearing, which is not supported by petrographic observations. Indeed, garnet in the retrogressed eclogites is clearly ante-kinematic, while hornblende is syn-D2 (Figure 4f). D2 is therefore not associated with the development of the garnet-bearing HP assemblage, and more likely took place at amphibolite facies conditions.

We therefore consider that mixing of HP lower crustal metabasic rocks with mid-crustal felsic gneisses in a tectonic *mélange* zone is the most likely scenario to explain the absence of an HP assemblage in the investigated metasediment.

8.2 | Timing of the geological evolution

8.2.1 | Ordovician mafic intrusions

The Ordovician zircon cores in the eclogites present typical features of magmatic zircon. They generally display oscillatory, broad sector or fir-tree zoning on CC images and contain more U than the rims, and present high Th/U typical of magmatic zircon (Corfu et al., 2003; Hoskin & Schaltegger, 2003). The steep REE patterns are consistent with crystallization from a gabbroic melt (Hoskin & Schaltegger, 2003). The magmatic cores present only a weak Eu anomaly typically observed in zircon from metagabbros (e.g. Kaczmarek et al., 2008). The calculated TiZ for the magmatic zircon cores are around 650°C, which are significantly lower than what is expected for the crystallization of a tholeiitic melt. This apparent temperature underestimation may be partly due to crystallization in a TiO₂ undersaturated melt. However, assuming $a_{\text{TiO}_2} = 0.5$ if ilmenite is the main stable Ti-bearing phase, results in an increase of only ca. 50°C in the calculated temperature with the equation of Ferry and Watson (2007). Low TiZ temperatures been documented in other gabbroic rocks (e.g. Kaczmarek et al., 2008), and are attributed to the fact that in such systems, zircon is a late crystallizing phase, and its Ti content reflects the composition of the residual melt rather than that of the original magma. Decrease in Ti concentration in zircon correlated with melt fractionation has for instance been documented in MORB series from the Atlantic Ocean (Grimes et al., 2009), where Ti concentration in zircon decreases from 80–100 ppm in the least evolved rocks down to 5–10 ppm in the most differentiated ones, which results in TiZ temperatures as low as 700°C in magmatic zircons.

The Ordovician ages of 456 ± 4 Ma and 448 ± 6 Ma are interpreted as the age of crystallization of the gabbroic

magmatic protolith. These ages are consistent with the previous estimates at 473 ± 28 Ma obtained by Paquette et al., (1989) using bulk ID-TIMS analysis for the same mafic body, and remain in the typical range of ages measured for Ordovician magmatism in the External western Alps (ca. 450–480 Ma, Bussy et al., 2011; Rubatto et al., 2001; Schaltegger & Gebauer, 1999). Similar Ordovician tholeiitic magmatism is commonly observed in all parts of the Variscan basement (Pin & Marini, 1993), and is generally attributed to a widespread extensional event which affected the northern part of Gondwana and resulted in the rifting of the Rheic and Saxo-Thuringian Oceans during the early-mid Ordovician (Linnemann et al., 2007).

8.2.2 | Carboniferous metamorphism

Geochronological data on zircon rims indicate that crystallization took place over an extended period of time. Mid-Carboniferous ages between 340 and 300 Ma are recorded both in the metasediments and in the retrogressed eclogites, which shows that metamorphism is roughly coeval in the two lithologies. In the metasediments, geochronological data in zircon rims can be, however, deconvoluted in three stages of crystallization with an early crystallization at around 340 Ma, a main growth stage at 320 Ma and a late stage at around 305 Ma. Geochronological data were interpreted based on trace element compositions. Three of the retrogressed eclogites (JB-18-49, JB-18-50, and JB-19-01) contain zircon rims that are weakly zoned, have low Th/U below 0.1, low U and Th concentrations and contain 10–100 times less REE than the cores. The zircon rims from metasediment JB-18-46 display similar features (Th/U < 1, low REE concentration) but with higher Th and U concentrations. These are typical features of metamorphic zircons in mafic rocks and metasediments (Hoskin & Schaltegger, 2003; Rubatto, 2017). However, zircon rims display a large range of REE patterns. The flat HREE patterns with weak or absent Eu anomaly (JB-19-01, plus one profile in JB-18-49) are characteristic of growth in presence of garnet and in a plagioclase-poor reactive bulk (Rubatto, 2002), which suggests that the zircon rims developed in a HP assemblage. Other REE patterns (JB-18-50, JB-18-49) display an enrichment in HREE and a more pronounced negative Eu anomaly, which is more consistent with a growth during garnet-breakdown reactions in presence of plagioclase. In the metasediment JB-18-46, REE patterns also display similar variations (flat to steep HREE, weak to strong negative Eu anomaly), although complete resorption of plagioclase is not expected in the metasediment even at HP (Figure 8c), and garnet is stable within a larger P - T range than the eclogite. The coronitic and poorly equilibrated textures of the investigated samples may have prevented trace element re-equilibration at the sample scale, thus producing

variable REE patterns in zircon rims that have grown (even at the same time) in different textural positions. Dispersion in REE composition of metamorphic zircon has been described in other coronitic metabasic HP rocks (Lotout, 2017; Phillips et al., 2015). The zircons which display HP signature would have crystallized in textural domains which contain a preserved eclogitic assemblage, while the other zircons would have crystallized in more retrogressed plagioclase-rich domains. Following this interpretation, zircon rims are considered to start growing near peak pressure in the eclogite (U–Pb dates at 342 ± 3 Ma) and then continue during decompression under granulitic/amphibolitic conditions. The lower temperature obtained by TiZ thermometer compared to those obtained with other thermobarometers, may be due to the pressure dependence of the TiZ thermometer (estimated to be around $\pm 50^\circ\text{C}/\text{GPa}$, Ferry & Watson, 2007), but more importantly to reduced TiO_2 and SiO_2 activities in the reactive bulk that can underestimate temperature of up to 50°C . This effect is especially relevant for the eclogites, in which quartz is unstable below 1.2–1.3 GPa and rutile unstable below 1.0–1.4 GPa, depending on H_2O activity. In the metasediment, the three distinct age populations suggest rather for episodic zircon growth than continuous protracted growth. The distinct younger event at 306 ± 3 Ma was constrained by analyses of distinct metamorphic rims that grew over older rims (Figure 12). The boundary between the two rims is sharp and shown embayments, suggesting that the older rims were partly resorbed, likely in a melt dominated environment, before the external rim grew. Therefore the younger age of 306 ± 3 Ma from the external zircon rim is attributed to the final crystallization of melt during cooling.

Rutile U–Pb dating yielded an age at 340 ± 11 Ma, which overlaps within uncertainty with the age of the oldest metamorphic zircon (<329 Ma), but is surprisingly older than most of zircon analyses. The phase diagrams computed for the eclogites (Figure 8a) indicate that rutile grows at $P > 1.4$ GPa and is resorbed with decreasing pressure. The peak temperature obtained for the HP stage and the following decompression is $>700^\circ\text{C}$ and lasted over an extended period of time possibly exceeding 20 Ma, based on zircon ages. At these conditions, significant Pb diffusion in rutile is expected (Cherniak, 2000; Kooijman et al., 2010; Zack & Kooijman, 2017). Rutile U–Pb ages should therefore record cooling and thus be younger than in zircon, which instead constrains HP metamorphism. Given the small amount of U in the dated rutile, it is possible that the ± 11 Ma uncertainty has been underestimated, and that the rutile age is within uncertainty of that of most metamorphic zircon. However, the similarity between rutile and zircon ages indicate that Pb diffusion in rutile was significantly inhibited. There is a possibility that rutile has retained the age of crystallization because it is shielded in garnet. Diffusion calculations assume that the matrix around the crystal acts as a homogeneous

infinite reservoir for the diffusing species. This assumption becomes unrealistic if the crystal is enclosed in another mineral, in which Pb diffusion is slow. In this case, Pb loss in the inclusion would be limited by the slow diffusion of Pb in the shielding mineral. In the retrogressed eclogites, many grains of rutile are enclosed in garnet (Figure 5c). EMPA of rutile grains in their textural position has shown that inclusions in garnet and matrix grains have distinct Zr contents (Figure 10a). Almost all the separated rutile analysed by LA-ICP-MS have a Zr content of rutile inclusion indicating that they were enclosed in garnet. This preferential separation of rutile inclusions was probably favoured by partial replacement of rutile by ilmenite and titanite in the strongly retrogressed matrix (Figure 5). Pb diffusion in garnet has been recognized to be slow to insignificant below 800°C (Burton et al., 1995; Mezger et al., 1989, 1991). It is therefore possible that shielding by garnet has prevented Pb loss from the rutile inclusions, which would thus date the HP crystallization, even if other case studies have shown that this principle is not systematic (Zhou et al., 2020). Similar effects were found for preservation of REE primary compositions (magmatic and granulitic) for apatite shielded as inclusions in ilmenite-hematite and garnet from the Bergen eclogite in Norway (Janots et al., 2018).

8.3 | *P–T–t* evolution and tectonic interpretation

The eclogite *boudins* and the host felsic gneisses record distinct *P–T* evolutions, which are roughly coeval between 340 and 310 Ma. In the eclogites, rutile sealed in HP garnet and the oldest metamorphic zircon rims have yielded ages at 340 ± 11 Ma, interpreted to date the HP stage at eclogite facies (>1.4 GPa, 690–740°C) and the onset of decompression under granulitic conditions. At the same time, the migmatitic metasediments underwent prograde metamorphism at lower pressure in the amphibolite facies. The two lithologies were amalgamated together between ca. 335 and 310 Ma at amphibolite/granulite facies conditions (ca. 1.0–1.4 GPa, 700–780°C) in the middle crust, and were subsequently exhumed to upper crustal levels. During this time interval, partial melting occurred in the most fertile metasediments and produced small amounts of leucogranite, some of which may have been extracted from the source to form the small granite plutons emplaced syn-tectonically in the upper crust (Figure 2a). The younger age at 306 ± 3 Ma recorded in the migmatitic metasediment likely corresponds to the final crystallization of melt during cooling, and is contemporaneous with emplacement of the ferriferous low-Mg granitoids in the ECMs (Debon & Lemmet, 1999). The penetrative metamorphic foliation S2, which formed by dextral strike-slip shearing, is correlated with amphibolitization of the

eclogitic assemblage in the mafic *boudins* and partial melting in the metasediment. Exhumation therefore occurred in transpression during the D2 tectonic phase. Because of poor preservation of the older structures, it is difficult to correlate them with the *P–T–t* evolution. E–W folding during D1 may be a relic of the main collision and nappe stacking phase, which took place during the early Carboniferous (D1 phase between ca. 350–330 Ma). The late Carboniferous D2 phase of transpressive dextral shearing has been recognized in the entire ECM, from Argentera-Mercantour to the Mont-Blanc and Aiguilles Rouges massifs (Corsini & Rolland, 2009; Guillot et al., 2009), and is associated with the orogen-wide East-Variscan shear zone, which was active during the late Carboniferous (ca. 330–310 Ma, Simonetti et al., 2018, 2020). This shear zone was probably rooted in the lithospheric mantle and controlled the emplacement of several granitoid plutons (Bussy et al., 2000; Guillot et al., 2009) in the ECM, including the Mg–K rich granitoid series in the Belledonne massif, which partially derives from a subcontinental mantle source (Debon & Lemmet, 1999). This shear zone may therefore have driven exhumation and mixing of various lithologies from different crustal levels, including the lower crustal eclogite *boudins* and the mid crustal gneisses exposed in the Lacs de la Tempête unit.

8.4 | Geodynamic significance of the Carboniferous HP metamorphism in the ECM

The Variscan eclogites and HP granulites exposed in the other ECM of Argentera-Mercantour and Aiguilles-Rouges display remarkably similar features as those of the Belledonne eclogites presented here. They all derive from normal to enriched MORB-type tholeiites emplaced during the Ordovician between ca. 480 and 450 Ma (Jouffray et al., 2020; J. L. Paquette et al., 1989; Rubatto et al., 2010; Von Raumer & Bussy, 2004), presumably in a thinned continental crust during the opening of the Rheic and Saxo-Thuringian oceans. Peak pressure is constrained between 1.3–1.8 GPa and 650–750°C (Ferrando et al., 2008; Liégeois & Duchesne, 1981; Vanardois et al., 2020; this work), and is followed by near-isothermal decompression to ca. 1.0–0.8 GPa and later cooling in the amphibolite facies below 600°C and 0.6–0.7 GPa. The age of the HP stage is consistently recorded around 340 Ma by U–Pb chronometers (Rubatto et al., 2010; this work). Exhumation is constrained between 340 and 310 Ma, coeval with migmatization in the felsic hosts (Fréville et al., 2018; Jouffray et al., 2020; Rubatto et al., 2010; Von Raumer & Bussy, 2004).

The Carboniferous age recorded for the HP is consistent with that of other Variscan HP rocks in the basement of the Central and Eastern Alps, where the HP stage is constrained between ca. 350 and 330 Ma by Lu–Hf and

U–Pb geochronology (Ladenhauf et al., 2001; Miller & Thöni, 1995; Sandmann et al., 2014; Thöni, 2006; Tumiati et al., 2003). In the more eastern Bohemian Massif, early-mid Carboniferous ages are also reported for the HP rocks of the Moldanubian domain and MORB-derived eclogites in the Erzgebirge (Bröcker et al., 2009; Schmädicke et al., 1995; Schulmann et al., 2005). The Carboniferous HP rocks are widespread in the Variscan Belt, especially in the high-grade metamorphic allochthonous domains of the Galicia-Moldanubian zone, and are typically equilibrated at HP–HT/UHT conditions of ca. 700–1000°C and 1.4–2.2 GPa (Maierová et al., 2016; O’Brien, 2000). The Carboniferous eclogites contrast with the scarce mid-late Devonian (400–360 Ma) eclogites that are exposed in the Saxo-Thuringian zone of the Bohemian Massif (Collett et al., 2018; Konopásek et al., 2019; Kryza & Fanning, 2007; Scherer et al., 2002), in the southern Armorican Massif (Bosse et al., 2000; Paquette et al., 2017), or in the Cabo Ortegal and upper allochthon in Iberia (Martínez Catalán et al., 2020). The latter are typically LT–MT eclogites associated with blueschists (Figure 1a) and are interpreted as the relics of subduction complexes along the Saxo-Thuringian suture (e.g. Ballèvre et al., 2009; Franke, 2000).

Due to their equilibration at HP–HT/UHT conditions, the Carboniferous HP rocks of the European Variscan Belt rarely preserve prograde metamorphic evolution and only record exhumation from deep crustal levels (O’Brien, 2000). A possible interpretation is that these HP rocks represent deep portions of orogenic lower crust equilibrated at eclogitic/HP granulitic conditions during the main crustal thickening phases, which were then exhumed during the later stages of the collision and the post-orogenic collapse. In the Bohemian massif, a combination of active buckling and gravity-driven extrusion in diapir-like structures is proposed as a mechanism for exhumation, which may favour the mixing of eclogites and migmatites (Schulmann et al., 2005, 2009, 2014; Štípská et al., 2004). The setting in the Western Alps is somewhat different, as no UHT nor dome-like structures have been recognized. We speculate that the lower crust was probably too cold to produce gravity-driven diapirs, and exhumation was more probably driven by active deformation in a transpressive setting, presumably within the lithospheric scale East-Variscan shear zone. In this regard, eclogites exposed in the Montagne Noire Axial Zone (French Massif Central) may be a good analogue. Indeed, they present particularly young zircon U–Pb ages (ca. 310–315 Ma) and record HP conditions at moderate temperature (ca. 1.5 GPa and 700°C, Whitney et al., 2015, 2020), which is consistent with equilibration in the orogenic lower crust, and similar to the *P–T* conditions recorded in the ECM eclogites. The mechanism that drove exhumation of lower and mid crustal lithologies in the Montagne Noire Axial Zone is still debated, and could correspond either to bulk extension or compression, but it has

been recognized that non-coaxial deformation in a large dextral shear zone played an important role (Rabin et al., 2015).

The evolution of the ECM eclogites prior to exhumation is not constrained, as no prograde assemblage has ever been identified. These eclogites, equilibrated in the lower crust, may initially derive from dismembered portions of a subducting slab. Deciphering the early prograde history will require additional geochronological constraints, possibly by Sm–Nd and Lu–Hf garnet dating of the eclogites.

9 | CONCLUSION

The eclogite-bearing amphibolite lenses exposed at the Lacs de la Tempête, in northeast Belledonne, derive from Ordovician mafic protoliths emplaced at ca. 450 Ma. They preserve evidence of Carboniferous HP metamorphism under eclogitic conditions (>1.4 GPa and 690–740°C), followed by decompression from 1.4 to 1.0 GPa at 700–800°C. In contrast, the associated migmatitic metasediments are devoid of HP mineral assemblages, but records instead prograde evolution from sub-solidus conditions (0.8–1.1 GPa and 600–700°C) to supra-solidus conditions (1.1–1.4 GPa and 700–780°C). Metamorphism was roughly coeval in the two lithologies, and occurred between 340 and 310 Ma. Zircon zoning and chemical composition (Th/U and REE) indicate initial crystallization during the HP stage followed by protracted growth during decompression under granulitic/amphibolitic conditions. Rutile in one eclogite sample yields a U–Pb age of 340 ± 11 Ma, interpreted as the age of the HP stage, assuming that diffusion was inhibited by its textural position as garnet inclusion. Retrogression is correlated with the development of a penetrative, N30° subvertical mylonitic S2 foliation, which is associated with the development of the orogen-wide East-Variscan shear zone during the mid-late Carboniferous. We therefore speculate that this shear zone has driven exhumation of the eclogites from the lower crust and their incorporation into felsic gneisses in the middle crust. Due to the absence of preserved prograde assemblages, it was only possible to constrain the exhumation path of the eclogites. The early pre-340 Ma history of these rocks therefore remains unclear. Additional petrochronological investigation is needed in order to better constrain this early evolution.

ACKNOWLEDGEMENTS

This work was supported by the BRGM through the Référentiel Géologique de la France program (RGF). J-B Jacob was funded by a doctoral grant from the ENS de Lyon. Dr. Caroline Lotout and Dr. Stephen Collett are thanked for their insightful reviews, which greatly improved the quality of the final manuscript. We also thank Alex Bisch, a Bachelor student who was involved in the project during the summer 2018 and greatly helped with the field work. Finally, this work would not have been possible

without the involvement of many technicians and engineers, who were of great help in the preparation of the samples and the operation of the various analytical instruments. We wish to thank Valérie Magnin and Valentina Batanova at Isterre in Grenoble for operating the electron microprobe, and Anne-Sophie Bouvier at the university of Lausanne for her help with the SwissSIMS instrument.

ORCID

Jean-Baptiste Jacob  <https://orcid.org/0000-0002-2783-4756>
Daniela Rubatto  <https://orcid.org/0000-0002-7425-7904>

REFERENCES

- Axelsson, E., Pape, J., Berndt, J., Corfu, F., Mezger, K., & Raith, M. M. (2018). Rutile R632 - A new natural reference material for U-Pb and Zr determination. *Geostandards and Geoanalytical Research*, 42(3), 319–338. <https://doi.org/10.1111/ggr.12213>
- Ballèvre, M., Bosse, V., Ducassou, C., & Pitra, P. (2009). Palaeozoic history of the Armorican Massif: Models for the tectonic evolution of the suture zones. *Comptes Rendus Geoscience*, 341(2), 174–201. <https://doi.org/10.1016/j.crte.2008.11.009>
- Ballèvre, M., Manzotti, P., & Piaz, G. V. D. (2018). Pre-alpine (Variscan) inheritance: A key for the location of the future Valaisian Basin (Western Alps). *Tectonics*, 37(3), 786–817. <https://doi.org/10.1002/2017TC004633>
- Bellahsen, N., Jolivet, L., Lacombe, O., Bellanger, M., Boutoux, A., Garcia, S., Mouthereau, F., Le Pourhiet, L., & Gumiaux, C. (2012). Mechanisms of margin inversion in the external Western Alps: Implications for crustal rheology. *Tectonophysics*, 560–561, 62–83. <https://doi.org/10.1016/j.tecto.2012.06.022>
- Bellahsen, N., Mouthereau, F., Boutoux, A., Bellanger, M., Lacombe, O., Jolivet, L., & Rolland, Y. (2014). Collision kinematics in the western external Alps. *Tectonics*, 33(6), 1055–1088. <https://doi.org/10.1002/2013TC003453>
- Bellanger, M., Bellahsen, N., Jolivet, L., Baudin, T., Augier, R., & Boutoux, A. (2014). Basement shear zones development and shortening kinematics in the Ecrins Massif. *Western Alps Tectonics*, 33(2), 84–111. <https://doi.org/10.1002/2013TC003294>
- Benmammour, A., Berger, J., Triantafyllou, A., Duchene, S., Bendaoud, A., Baele, J.-M., Bruguier, O., & Diot, H. (2020). Pressure-temperature conditions and significance of Upper Devonian eclogite and amphibolite facies metamorphisms in southern French Massif central. Evolution pression-température et implications des métamorphismes amphibolitique et élogitique du Dévonien supérieur dans le sud du Massif central français. *Bulletin de La Société Géologique de France*, 191(1), <https://doi.org/10.1051/bsgf/2020033>
- Black, L. P., Kamo, S. L., Allen, C. M., Aleinikoff, J. N., Davis, D. W., Korsch, R. J., & Foudoulis, C. (2003). TEMORA 1: A new zircon standard for Phanerozoic U-Pb geochronology. *Chemical Geology*, 200(1), 155–170. [https://doi.org/10.1016/S0009-2541\(03\)00165-7](https://doi.org/10.1016/S0009-2541(03)00165-7)
- Bordet, C. (1961). *Recherches géologiques sur la partie septentrionale du Massif de Belledonne (Alpes françaises)*. <https://hal-insu.archives-ouvertes.fr/insu-00720441>
- Bordet, P., & Bordet, C. (1963). Belledonne-Grandes Rousses et Aiguilles Rouges-Mont Blanc: quelques données nouvelles sur leurs rapports structuraux. *Mém. H.s. Soc. Géol. Fr.*, 2, 309–316. Scopus.
- Bosse, V., Feraud, G., Ruffet, G., Ballèvre, M., Peucat, J.-J., & De Jong, K. (2000). Late Devonian subduction and early-orogenic exhumation of eclogite-facies rocks from the Champtoceaux Complex (Variscan belt, France). *Geological Journal*, 35(3–4), 297–325.
- Bröcker, M., Klemd, R., Cosca, M., Brock, W., Larionov, A. N., & Rodionov, N. (2009). The timing of eclogite facies metamorphism and migmatization in the Orlica-Šnieżnik complex, Bohemian Massif: Constraints from a multimethod geochronological study. *Journal of Metamorphic Geology*, 27(5), 385–403. <https://doi.org/10.1111/j.1525-1314.2009.00823.x>
- Burton, K. W., Kohn, M. J., Cohen, A. S., & O'Nions, R. K. (1995). The relative diffusion of Pb, Nd, Sr and O in garnet. *Earth and Planetary Science Letters*, 133(1–2), 199–211. [https://doi.org/10.1016/0012-821X\(95\)00067-M](https://doi.org/10.1016/0012-821X(95)00067-M)
- Bussy, F., Hernandez, J., & Von Raumer, J. (2000). Bimodal magmatism as a consequence of the post-collisional readjustment of the thickened Variscan continental lithosphere (Aiguilles Rouges-Mont Blanc Massifs, Western Alps). *Earth and Environmental Science Transactions of the Royal Society of Edinburgh*, 91(1–2), 221–233. <https://doi.org/10.1017/S0263593300007392>
- Bussy, F., Péronnet, V., Ulianov, A., Epard, J. L., & von Raumer, J. (2011). Ordovician magmatism in the external French Alps: Witness of a peri-Gondwanan active continental margin. In J. C. Gutiérrez-Marco, I. Rábano, & D. García-Bellido (Eds.), *The Ordovician of the world* (Vol. 14, pp. 75–82). Instituto Geológico y Minero de España, Cuadernos del Museo Geominero.
- Challandes, N., Marquer, D., & Villa, I. M. (2008). P-T-t modelling, fluid circulation, and ³⁹Ar-⁴⁰Ar and Rb-Sr mica ages in the Aar Massif shear zones (Swiss Alps). *Swiss Journal of Geosciences*, 101(2), 269–288. <https://doi.org/10.1007/s00015-008-1260-6>
- Cherniak, D. J. (2000). Pb diffusion in rutile. *Contributions to Mineralogy and Petrology*, 139(2), 198–207. <https://doi.org/10.1007/PL00007671>
- Chew, D. M., Petrus, J. A., & Kamber, B. S. (2014). U-Pb LA-ICPMS dating using accessory mineral standards with variable common Pb. *Chemical Geology*, 363, 185–199. <https://doi.org/10.1016/j.chemgeo.2013.11.006>
- Collett, S., Štípská, P., Schulmann, K., Peřestý, V., Soldner, J., Anczkiewicz, R., Lexa, O., & Kylander-Clark, A. (2018). Combined Lu-Hf and Sm-Nd geochronology of the Mariánské Lázně Complex: New constraints on the timing of eclogite- and granulite-facies metamorphism. *Lithos*, 304–307, 74–94. <https://doi.org/10.1016/j.lithos.2018.02.007>
- Connolly, J. A. D. (2005). Computation of phase equilibria by linear programming: A tool for geodynamic modeling and its application to subduction zone decarbonation. *Earth and Planetary Science Letters*, 236(1–2), 524–541. <https://doi.org/10.1016/j.epsl.2005.04.033>
- Connolly, J. A. D. (2009). The geodynamic equation of state: What and how. *Geochemistry, Geophysics, Geosystems*, 10(10), n/a-n/a. <https://doi.org/10.1029/2009GC002540>
- Corfu, F., Hanchar, J. M., Hoskin, P. W., & Kinny, P. (2003). Atlas of zircon textures. *Reviews in Mineralogy and Geochemistry*, 53(1), 469–500. <https://doi.org/10.2113/0530469>
- Corsini, M., & Rolland, Y. (2009). Late evolution of the southern European Variscan belt: Exhumation of the lower crust in a context of oblique convergence. *Comptes Rendus Geoscience*, 341(2), 214–223. <https://doi.org/10.1016/j.crte.2008.12.002>
- Debon, F., Guerrot, C., & Ménot, R. P. (1998). Late Variscan granites of the Belledonne massif (French Western Alps): An Early Visean magnesian plutonism. *Schweizerische Mineralogische und Petrographische Mitteilungen*, 78, 67–85.

- Debon, F., & Lemmet, M. (1999). Evolution of Mg/Fe ratios in late Variscan plutonic rocks from the external crystalline Massifs of the Alps (France, Italy, Switzerland). *Journal of Petrology*, *40*(7), 1151–1185. <https://doi.org/10.1093/ptro/40.7.1151>
- Faure, M., Lardeaux, J.-M., & Ledru, P. (2009). A review of the pre-Permian geology of the Variscan French Massif Central. *Comptes Rendus Geoscience*, *341*(2–3), 202–213. <https://doi.org/10.1016/j.crte.2008.12.001>
- Fernandez, A., Guillot, S., Ménot, R.-P., & Ledru, P. (2002). Late Paleozoic polyphased tectonics in the SW Belledonne massif (external crystalline massifs, French Alps). *Geodinamica Acta*, *15*(2), 127–139. <https://doi.org/10.1080/09853111.2002.10510746>
- Ferrando, S., Lombardo, B., & Compagnoni, R. (2008). Metamorphic history of HP mafic granulites from the Gesso-Stura terrain (Argentera Massif, western Alps, Italy). *European Journal of Mineralogy*, *20*(5), 777–790. <https://doi.org/10.1127/0935-1221/2008/0020-1891>
- Ferry, J. M., & Watson, E. B. (2007). New thermodynamic models and revised calibrations for the Ti-in-zircon and Zr-in-rutile thermometers. *Contributions to Mineralogy and Petrology*, *154*(4), 429–437. <https://doi.org/10.1007/s00410-007-0201-0>
- Franke, W. (2000). The mid-European segment of the Variscides: Tectonostratigraphic units, terrane boundaries and plate tectonic evolution. *Geological Society, London, Special Publications*, *179*(1), 35–61. <https://doi.org/10.1144/GSL.SP.2000.179.01.05>
- Fréville, K. (2016). *L'orogénèse varisque dans les massifs cristallins externes de Belledonne et du Pelvoux (Alpes occidentales françaises) : rôle de la fusion partielle et du plutonisme dans la structuration de la croûte continentale* [PhD Thesis, Université d'Orléans]. <https://tel.archives-ouvertes.fr/tel-01968058/document>
- Fréville, K., Trap, P., Faure, M., Melleton, J., Li, X.-H., Lin, W., Blein, O., Bruguier, O., & Poujol, M. (2018). Structural, metamorphic and geochronological insights on the Variscan evolution of the Alpine basement in the Belledonne Massif (France). *Tectonophysics*, *726*, 14–42. <https://doi.org/10.1016/j.tecto.2018.01.017>
- Fuhrman, M. L., & Lindsley, D. H. (1988). Ternary-feldspar modeling and thermometry. *American Mineralogist*, *73*(3–4), 201–215.
- Godard, G. (2001). Eclogites and their geodynamic interpretation: A history. *Journal of Geodynamics*, *32*(1), 165–203. [https://doi.org/10.1016/S0264-3707\(01\)00020-5](https://doi.org/10.1016/S0264-3707(01)00020-5)
- Green, E., Holland, T., & Powell, R. (2007). An order-disorder model for omphacitic pyroxenes in the system jadeite-diopside-hedenbergite-acmite, with applications to eclogitic rocks. *American Mineralogist*, *92*(7), 1181–1189. <https://doi.org/10.2138/am.2007.2401>
- Green, E. C. R., White, R. W., Diener, J. F. A., Powell, R., Holland, T. J. B., & Palin, R. M. (2016). Activity–composition relations for the calculation of partial melting equilibria in metabasic rocks. *Journal of Metamorphic Geology*, *34*(9), 845–869. <https://doi.org/10.1111/jmg.12211>
- Grimes, C. B., John, B. E., Cheadle, M. J., Mazdab, F. K., Wooden, J. L., Swapp, S., & Schwartz, J. J. (2009). On the occurrence, trace element geochemistry, and crystallization history of zircon from in situ ocean lithosphere. *Contributions to Mineralogy and Petrology*, *158*(6), 757. <https://doi.org/10.1007/s00410-009-0409-2>
- Gros, Y. (1974). *Etude pétrologique et structurale du Beaufortin (Nord de Belledonne). Alpes françaises*. [Theses, Université Scientifique et Médicale de Grenoble]. <https://tel.archives-ouvertes.fr/tel-00556510>
- Guillot, S., di Paola, S., Ménot, R.-P., Ledru, P., Spalla, M. I., Gosso, G., & Schwartz, S. (2009). Suture zones and importance of strike-slip faulting for Variscan geodynamic reconstructions of the External Crystalline Massifs of the western Alps. *Bulletin de La Société Géologique de France*, *180*(6), 483–500. <https://doi.org/10.2113/gssgfbull.180.6.483>
- Guillot, S., & Ménot, R.-P. (2009). Paleozoic evolution of the External Crystalline Massifs of the Western Alps. *Comptes Rendus Geoscience*, *341*(2–3), 253–265. <https://doi.org/10.1016/j.crte.2008.11.010>
- Guillot, S., Ménot, R.-P., & Lardeaux, J.-M. (1992). Tectonique intra-océanique distensive dans l'ophiolite paléozoïque de Chamrousse (Alpes occidentales). *Bulletin de la Société Géologique de France*, *163*, 229–240.
- Holland, T. J. B., & Powell, R. T. J. (1998). An internally consistent thermodynamic data set for phases of petrological interest. *Journal of Metamorphic Geology*, *16*(3), 309–343. <https://doi.org/10.1111/j.1525-1314.1998.00140.x>
- Holland, T. J. B., & Powell, R. (2011). An improved and extended internally consistent thermodynamic dataset for phases of petrological interest, involving a new equation of state for solids. *Journal of Metamorphic Geology*, *29*(3), 333–383. <https://doi.org/10.1111/j.1525-1314.2010.00923.x>
- Hoskin, P. W. O., & Schaltegger, U. (2003). The composition of zircon and igneous and metamorphic petrogenesis. *Reviews in Mineralogy and Geochemistry*, *53*(1), 27–62. <https://doi.org/10.2113/0530027>
- Janots, E., Austrheim, H., Spandler, C., Hammerli, J., Trepmann, C. A., Berndt, J., Magnin, V., & Kemp, A. I. S. (2018). Rare earth elements and Sm-Nd isotope redistribution in apatite and accessory minerals in retrogressed lower crust material (Bergen Arcs, Norway). *Chemical Geology*, *484*, 120–135. <https://doi.org/10.1016/j.chemgeo.2017.10.007>
- Jochum, K. P., Nohl, U., Herwig, K., Lammel, E., Stoll, B., & Hofmann, A. W. (2005). GeoReM: A new geochemical database for reference materials and isotopic standards. *Geostandards and Geoanalytical Research*, *29*(3), 333–338. <https://doi.org/10.1111/j.1751-908X.2005.tb00904.x>
- Jouffray, F., Spalla, M. I., Lardeaux, J. M., Filippi, M., Rebay, G., Corsini, M., Zononi, D., Zucali, M., & Gosso, G. (2020). Variscan eclogites from the Argentera-Mercantour Massif (External Crystalline Massifs, SW Alps): A dismembered cryptic suture zone. *International Journal of Earth Sciences*, *109*(4), 1273–1294. <https://doi.org/10.1007/s00531-020-01848-2>
- Kaczmarek, M.-A., Müntener, O., & Rubatto, D. (2008). Trace element chemistry and U-Pb dating of zircons from oceanic gabbros and their relationship with whole rock composition (Lanzo, Italian Alps). *Contributions to Mineralogy and Petrology*, *155*(3), 295–312. <https://doi.org/10.1007/s00410-007-0243-3>
- Konopásek, J., Anczkiewicz, R., Jeřábek, P., Corfu, F., & Žáčková, E. (2019). Chronology of the Saxothuringian subduction in the West Sudetes (Bohemian Massif, Czech Republic and Poland). *Journal of the Geological Society*, *176*(3), 492–504. <https://doi.org/10.1144/jgs2018-173>
- Kooijman, E., Mezger, K., & Berndt, J. (2010). Constraints on the U-Pb systematics of metamorphic rutile from in situ LA-ICP-MS analysis. *Earth and Planetary Science Letters*, *293*(3), 321–330. <https://doi.org/10.1016/j.epsl.2010.02.047>
- Kooijman, E., Smit, M. A., Mezger, K., & Berndt, J. (2012). Trace element systematics in granulite facies rutile: Implications for Zr geothermometry and provenance studies. *Journal of Metamorphic Geology*, *30*(4), 397–412. <https://doi.org/10.1111/j.1525-1314.2012.00972.x>
- Kryza, R., & Fanning, C. M. (2007). Devonian deep-crustal metamorphism and exhumation in the Variscan Orogen: Evidence from SHRIMP zircon ages from the HT-HP granulites and migmatites of

- the Góry Sowie (Polish Sudetes). *Geodinamica Acta*, 20(3), 159–175. <https://doi.org/10.3166/ga.20.159-175>
- Ladenhauf, C., Armstrong, R., Konzett, J., & Miller, C. (2001). The timing of pre-Alpine high pressure metamorphism in the Eastern Alps: Constraints from U-Pb SHRIMP dating of eclogite zircons from the Austroalpine Silvretta nappe. *Journal of Conference Abstracts*, 6, 600.
- Lardeaux, J. M., Schulmann, K., Faure, M., Janoušek, V., Lexa, O., Skrzypek, E., Edel, J. B., & Štípská, P. (2014). The moldanubian zone in the French Massif Central, Vosges/Schwarzwald and Bohemian Massif revisited: Differences and similarities. *Geological Society, London, Special Publications*, 405(1), 7–44. <https://doi.org/10.1144/SP405.14>
- Lemoine, M., Bas, T., Arnaud-Vanneau, A., Arnaud, H., Dumont, T., Gidon, M., Bourbon, M., de Graciansky, P.-C., Rudkiewicz, J.-L., Megard-Galli, J., & Tricart, P. (1986). The continental margin of the Mesozoic Tethys in the Western Alps. *Marine and Petroleum Geology*, 3(3), 179–199. [https://doi.org/10.1016/0264-8172\(86\)90044-9](https://doi.org/10.1016/0264-8172(86)90044-9)
- Lemoine, M., & Trümpy, R. (1987). Pre-oceanic rifting in the alps. *Tectonophysics*, 133(3), 305–320. [https://doi.org/10.1016/0040-1951\(87\)90272-1](https://doi.org/10.1016/0040-1951(87)90272-1)
- Liégeois, J.-P., & Duchesne, J.-C. (1981). The Lac Cornu retrograded eclogites (Aiguilles Rouges massif, Western Alps, France): Evidence of crustal origin and metasomatic alteration. *Lithos*, 14(1), 35–48. [https://doi.org/10.1016/0024-4937\(81\)90035-9](https://doi.org/10.1016/0024-4937(81)90035-9)
- Linnemann, U., Gerdes, A., Drost, K., & Buschmann, B. (2007). The continuum between Cadomian orogenesis and opening of the Rheic Ocean: Constraints from LA-ICP-MS U-Pb zircon dating and analysis of plate-tectonic setting (Saxo-Thuringian zone, northeastern Bohemian Massif, Germany). *Special Papers - Geological Society of America*, 423, 61.
- Lotout, C. (2017). *Âge, durée et enregistrement du métamorphisme de haute pression dans le massif Central* [PhD Thesis].
- Lotout, C., Pitra, P., Poujol, M., Anczkiewicz, R., & Van Den Driessche, J. (2018). Timing and duration of Variscan high-pressure metamorphism in the French Massif Central: A multimethod geochronological study from the Najac Massif. *Lithos*, 308–309, 381–394. <https://doi.org/10.1016/j.lithos.2018.03.022>
- Lotout, C., Poujol, M., Pitra, P., Anczkiewicz, R., & Van Den Driessche, J. (2020). From burial to exhumation: Emplacement and metamorphism of mafic eclogitic terranes constrained through multimethod petrochronology, case study from the Lévézou Massif (French Massif Central, Variscan Belt). *Journal of Petrology*, 61(4), <https://doi.org/10.1093/petrology/egaa046>
- Luvizotto, G. L., & Zack, T. (2009). Nb and Zr behavior in rutile during high-grade metamorphism and retrogression: An example from the Ivrea-Verbano Zone. *Chemical Geology*, 261(3), 303–317. <https://doi.org/10.1016/j.chemgeo.2008.07.023>
- Luvizotto, G. L., Zack, T., Meyer, H. P., Ludwig, T., Triebold, S., Kronz, A., Munker, C., Stockli, D. F., Prowatke, S., Klemme, S., Jacob, D. E., & von Eynatten, H. (2009). Rutile crystals as potential trace element and isotope mineral standards for microanalysis. *Chemical Geology*, 261(3), 346–369. <https://doi.org/10.1016/j.chemgeo.2008.04.012>
- Maierová, P., Schulmann, K., Lexa, O., Guillot, S., Štípská, P., Janoušek, V., & Čadek, O. (2016). European Variscan orogenic evolution as an analogue of Tibetan-Himalayan orogen: Insights from petrology and numerical modeling: Variscan and Himalayan Orogenies. *Tectonics*, 35(7), 1760–1780. <https://doi.org/10.1002/2015TC004098>
- Marquer, D., Calcagno, P., Barfety, J.-C., & Baudin, T. (2006). 3D modeling and kinematics of the external zone of the French Western Alps (Belledonne and Grand Châtelard Massifs, Maurienne Valley, Savoie). *Eclogae Geologicae Helveticae*, 99(2), 211–222. <https://doi.org/10.1007/s00015-006-1183-z>
- Martínez Catalán, J. R., Arenas, R., Abati, J., Martínez, S. S., García, F. D., Suárez, J. F., Cuadra, P. G., Castiñeiras, P., Barreiro, J. G., Montes, A. D., Clavijo, E. G., Pascual, F. J. R., Andonaegui, P., Jeffries, T. E., Alcock, J. E., Fernández, R. D., & Carmona, A. L. (2009). A rootless suture and the loss of the roots of a mountain chain: The Variscan belt of NW Iberia. *Comptes Rendus Geoscience*, 341(2–3), 114–126. <https://doi.org/10.1016/j.crte.2008.11.004>
- Martínez Catalán, J. R., Collett, S., Schulmann, K., Aleksandrowski, P., & Mazur, S. (2020). Correlation of allochthonous terranes and major tectonostratigraphic domains between NW Iberia and the Bohemian Massif, European Variscan belt. *International Journal of Earth Sciences*, 109(4), 1105–1131. <https://doi.org/10.1007/s00531-019-01800-z>
- Ménot, R.-P. (1986). Les formations plutono-volcaniques dévoniennes de Rioupéroux-Livet (Massifs cristallins externes des Alpes Françaises): Nouvelles définitions lithostratigraphique et pétrographique. *Les Formations Plutono-Volcaniques Dévoniennes de Rioupéroux-Livet (Massifs Cristallins Externes Des Alpes Françaises): Nouvelles Définitions Lithostratigraphique et Pétrographique*, 66(1–2), 229–258.
- Ménot, R.-P. (1987). Magmatismes et structuration orogénique paléozoïques de la chaîne de Belledonne (Massifs cristallins externes alpins). Le domaine sud - occidental. *Magmatismes et Structuration Orologénique Paléozoïques de La Chaîne de Belledonne (Massifs Cristallins Externes Alpins). Le Domaine Sud - Occidental*, 63, 55–93.
- Ménot, R.-P., Bonhomme, M. G., & Vivier, G. (1987). Structuration tectono-métamorphique carbonifère dans le massif de Belledonne (Alpes Occidentales françaises), apport de la géochronologie K/Ar des amphiboles. *Schweizerische Mineralogische Und Petrographische Mitteilungen*, 67(3), 273–284.
- Ménot, R., Peucat, J., & Paquette, J. (1988). Les associations magmatiques acide-basique paléozoïques et les complexes leptyno-amphiboliques: Les corrélations hasardeuses. Exemples du massif de Belledonne (Alpes occidentales). *Bulletin de la Société Géologique de France*, 8, 917–926.
- Ménot, R.-P., Peucat, J. J., Scarenzi, D., & Piboule, M. (1988). 496 My age of plagiogranites in the Chamrousse ophiolite complex (external crystalline massifs in the French Alps): Evidence of a Lower Paleozoic oceanization. *Earth and Planetary Science Letters*, 88(1–2), 82–92. [https://doi.org/10.1016/0012-821X\(88\)90048-9](https://doi.org/10.1016/0012-821X(88)90048-9)
- Mezger, K., Hanson, G. N., & Bohlen, S. R. (1989). U-Pb systematics of garnet: Dating the growth of garnet in the late Archean Pikwitonei granulite domain at Cauchon and Natawahunan Lakes, Manitoba, Canada. *Contributions to Mineralogy and Petrology*, 101(2), 136–148. <https://doi.org/10.1007/BF00375301>
- Mezger, K., Rawnsley, C. M., Bohlen, S. R., & Hanson, G. N. (1991). U-Pb garnet, sphene, monazite, and rutile ages: Implications for the duration of high-grade metamorphism and cooling histories, Adirondack Mts., New York. *The Journal of Geology*, 99(3), 415–428. <https://doi.org/10.1086/629503>
- Miller, C., & Thöni, M. (1995). Origin of eclogites from the Austroalpine Ötztal basement (Tirol, Austria): Geochemistry and SmNd vs. RbSr isotope systematics. *Chemical Geology*, 122(1), 199–225. [https://doi.org/10.1016/0009-2541\(95\)00033-1](https://doi.org/10.1016/0009-2541(95)00033-1)
- Moulas, E., Burg, J.-P., & Podladchikov, Y. (2014). Stress field associated with elliptical inclusions in a deforming matrix: Mathematical

- model and implications for tectonic overpressure in the lithosphere. *Tectonophysics*, 631, 37–49. <https://doi.org/10.1016/j.tecto.2014.05.004>
- Newton, R. C., Charlu, T. V., & Kleppa, O. J. (1980). Thermochemistry of the high structural state plagioclases. *Geochimica et Cosmochimica Acta*, 44(7), 933–941. [https://doi.org/10.1016/0016-7037\(80\)90283-5](https://doi.org/10.1016/0016-7037(80)90283-5)
- O'Brien, P. J. (2000). The fundamental Variscan problem: High-temperature metamorphism at different depths and high-pressure metamorphism at different temperatures. *Geological Society, London, Special Publications*, 179(1), 369–386. <https://doi.org/10.1144/GSL.SP.2000.179.01.22>
- Paquette, J.-L., Ballèvre, M., Peucat, J.-J., & Cornen, G. (2017). From opening to subduction of an oceanic domain constrained by LA-ICP-MS U-Pb zircon dating (Variscan belt, Southern Armorican Massif, France). *Lithos*, 294–295, 418–437. <https://doi.org/10.1016/j.lithos.2017.10.005>
- Paquette, J. L., Menot, R. P., & Peucat, J. J. (1989). REE, Sm-Nd and U-Pb zircon study of eclogites from the Alpine External Massifs (Western Alps): Evidence for crustal contamination. *Earth and Planetary Science Letters*, 96(1–2), 181–198. [https://doi.org/10.1016/0012-821X\(89\)90131-3](https://doi.org/10.1016/0012-821X(89)90131-3)
- Paton, C., Hellstrom, J., Paul, B., Woodhead, J., & Hergt, J. (2011). Iolite: Freeware for the visualisation and processing of mass spectrometric data. *Journal of Analytical Atomic Spectrometry*, 26(12), 2508–2518. <https://doi.org/10.1039/C1JA10172B>
- Phillips, G., Offler, R., Rubatto, D., & Phillips, D. (2015). High-pressure metamorphism in the southern New England Orogen: Implications for long-lived accretionary orogenesis in eastern Australia. *Tectonics*, 34(9), 1979–2010. <https://doi.org/10.1002/2015TC003920>
- Pin, C., & Carme, F. (1987). A Sm-Nd isotopic study of 500 Ma old oceanic crust in the Variscan belt of Western Europe: The Chamrousse ophiolite complex, Western Alps (France). *Contributions to Mineralogy and Petrology*, 96(3), 406–413. <https://doi.org/10.1007/BF00371258>
- Pin, C., & Marini, F. (1993). Early Ordovician continental break-up in Variscan Europe: Nd-Sr isotope and trace element evidence from bimodal igneous associations of the Southern Massif Central, France. *Lithos*, 29(3), 177–196. [https://doi.org/10.1016/0024-4937\(93\)90016-6](https://doi.org/10.1016/0024-4937(93)90016-6)
- Rabin, M., Trap, P., Carry, N., Fréville, K., Cenki-Tok, B., Lobjoie, C., Goncalves, P., & Marquer, D. (2015). Strain partitioning along the anatectic front in the Variscan Montagne Noire massif (southern French Massif Central): Anatectic Front and Strain Partitioning. *Tectonics*, 34(8), 1709–1735. <https://doi.org/10.1002/2014TC003790>
- Regorda, A., Lardeaux, J.-M., Roda, M., Marotta, A. M., & Spalla, M. I. (2019). How many subductions in the Variscan orogeny? Insights from numerical models. *Geoscience Frontiers*, 11(3), 1025–1052. <https://doi.org/10.1016/j.gsf.2019.10.005>
- Roger, F., Teyssier, C., Whitney, D. L., Respaut, J.-P., Paquette, J.-L., & Rey, P. F. (2020). Age of metamorphism and deformation in the Montagne Noire dome (French Massif Central): Tapping into the memory of fine-grained gneisses using monazite U-Th-Pb geochronology. *Tectonophysics*, 776, 228316. <https://doi.org/10.1016/j.tecto.2019.228316>
- Rossi, P., Oggiano, G., & Cocherie, A. (2009). A restored section of the “southern Variscan realm” across the Corsica-Sardinia microcontinent. *Comptes Rendus Geoscience*, 341(2–3), 224–238. <https://doi.org/10.1016/j.crte.2008.12.005>
- Rubatto, D. (2002). Zircon trace element geochemistry: Partitioning with garnet and the link between U-Pb ages and metamorphism. *Chemical Geology*, 184(1), 123–138. [https://doi.org/10.1016/S0009-2541\(01\)00355-2](https://doi.org/10.1016/S0009-2541(01)00355-2)
- Rubatto, D. (2017). Zircon: The metamorphic mineral. *Reviews in Mineralogy and Geochemistry*, 83(1), 261–295. <https://doi.org/10.2138/rmg.2017.83.9>
- Rubatto, D., Ferrando, S., Compagnoni, R., & Lombardo, B. (2010). Carboniferous high-pressure metamorphism of Ordovician protoliths in the Argentera Massif (Italy). *Southern European Variscan Belt. Lithos*, 116(1–2), 65–76. <https://doi.org/10.1016/j.lithos.2009.12.013>
- Rubatto, D., Schaltegger, U., Lombardo, D., Colombo, F., & Compagnoni, R. (2001). Complex Paleozoic magmatic and metamorphic evolution in the Argentera massif (Western Alps), resolved with U-Pb dating. *Schweizerische Mineralogische Und Petrographische Mitteilungen*, 81, 213–228.
- Sandmann, S., Nagel, T. J., Herwartz, D., Fonseca, R. O. C., Kurzwaski, R. M., Munker, C., & Froitzheim, N. (2014). Lu-Hf garnet systematics of a polymetamorphic basement unit: New evidence for coherent exhumation of the Adula Nappe (Central Alps) from eclogite-facies conditions. *Contributions to Mineralogy and Petrology*, 168(5), 1075. <https://doi.org/10.1007/s00410-014-1075-6>
- Santallier, D., Briand, B., Menot, R. P., & Piboule, M. (1988). Les complexes leptyno-amphiboliques (CLA): Revue critique et suggestions pour un meilleur emploi de ce terme. *Bulletin de La Société Géologique de France*, 4(1), 3–12.
- Schaltegger, U. (1993). The evolution of the polymetamorphic basement in the Central Alps unravelled by precise U-Pb zircon dating. *Contributions to Mineralogy and Petrology*, 113(4), 466–478. <https://doi.org/10.1007/BF00698316>
- Schaltegger, U., Abrecht, J., & Corfu, F. (2003). The Ordovician orogeny in the Alpine basement: Constraints from geochronology and geochemistry in the Aar Massif (Central Alps). *Swiss Bulletin of Mineralogy and Petrology*, 83(2), 183–239.
- Schaltegger, U., & Gebauer, D. (1999). Pre-Alpine geochronology of the central, western and southern Alps. *Schweizerische Mineralogische Und Petrographische Mitteilungen*, 79, 79–87.
- Scherer, E. E., Mezger, K., & Munker, C. (2002). Lu-Hf ages of high pressure metamorphism in the Variscan fold belt of southern Germany. *Geochimica et Cosmochimica Acta*, 66, A677.
- Schmädicke, E., Mezger, K., Cosca, M. A., & Okrusch, M. (1995). Variscan Sm-Nd and Ar-Ar ages of eclogite facies rocks from the Erzgebirge, Bohemian Massif. *Journal of Metamorphic Geology*, 13(5), 537–552. <https://doi.org/10.1111/j.1525-1314.1995.tb00241.x>
- Schulmann, K., Catalán, J.-R.-M., Lardeaux, J.-M., Janoušek, V., & Oggiano, G. (2014). The Variscan orogeny: Extent, timescale and the formation of the European crust. *Geological Society, London, Special Publications*, 405(1), 1–6. <https://doi.org/10.1144/SP405.15>
- Schulmann, K., Konopásek, J., Janoušek, V., Lexa, O., Lardeaux, J.-M., Edel, J.-B., Štípská, P., & Ulrich, S. (2009). An Andean type Palaeozoic convergence in the Bohemian Massif. *Comptes Rendus Geoscience*, 341(2), 266–286. <https://doi.org/10.1016/j.crte.2008.12.006>
- Schulmann, K., Kröner, A., Hegner, E., Wendt, I., Konopásek, J., Lexa, O., & Štípská, P. (2005). Chronological constraints on the pre-orogenic history, burial and exhumation of deep-seated rocks along the eastern margin of the Variscan Orogen, Bohemian Massif. *Czech Republic. American Journal of Science*, 305(5), 407–448. <https://doi.org/10.2475/ajs.305.5.407>

- Schulmann, K., Lexa, O., Štípská, P., Racek, M., Tajčmanová, L., Konopásek, J., Edel, J.-B., Peschler, A., & Lehmann, J. (2008). Vertical extrusion and horizontal channel flow of orogenic lower crust: Key exhumation mechanisms in large hot orogens? *Journal of Metamorphic Geology*, 26(2), 273–297. <https://doi.org/10.1111/j.1525-1314.2007.00755.x>
- Simonetti, M., Carosi, R., Montomoli, C., Cottle, J. M., & Law, R. D. (2020). Transpressive deformation in the Southern European Variscan Belt: New Insights From the Aiguilles Rouges Massif (Western Alps). *Tectonics*, 39(6), e2020TC006153. <https://doi.org/10.1029/2020TC006153>
- Simonetti, M., Carosi, R., Montomoli, C., Langone, A., D'Addario, E., & Mammoliti, E. (2018). Kinematic and geochronological constraints on shear deformation in the Ferriere-Mollières shear zone (Argentiera-Mercantour Massif, Western Alps): Implications for the evolution of the Southern European Variscan Belt. *International Journal of Earth Sciences*, 107(6), 2163–2189. <https://doi.org/10.1007/s00531-018-1593-y>
- Simon-Labric, T., Rolland, Y., Dumont, T., Heymes, T., Authemayou, C., Corsini, M., & Fornari, M. (2009). $^{40}\text{Ar}/^{39}\text{Ar}$ dating of Penninic Front tectonic displacement (W Alps) during the Lower Oligocene (31–34 Ma). *Terra Nova*, 21(2), 127–136. <https://doi.org/10.1111/j.1365-3121.2009.00865.x>
- Sláma, J., Košler, J., Condon, D. J., Crowley, J. L., Gerdes, A., Hanchar, J. M., Horstwood, M. S. A., Morris, G. A., Nasdala, L., Norberg, N., Schaltegger, U., Schoene, B., Tubrett, M. N., & Whitehouse, M. J. (2008). Plešovice zircon — A new natural reference material for U-Pb and Hf isotopic microanalysis. *Chemical Geology*, 249(1), 1–35. <https://doi.org/10.1016/j.chemgeo.2007.11.005>
- Stacey, J., & Kramers, J. (1975). Approximation of terrestrial lead isotope evolution by a two-stage model. *Earth and Planetary Science Letters*, 26(2), 207–221. [https://doi.org/10.1016/0012-821X\(75\)90088-6](https://doi.org/10.1016/0012-821X(75)90088-6)
- Steiger, R. H., & Jäger, E. (1977). Subcommission on geochronology: Convention on the use of decay constants in geo- and cosmochronology. *Earth and Planetary Science Letters*, 36(3), 359–362. [https://doi.org/10.1016/0012-821X\(77\)90060-7](https://doi.org/10.1016/0012-821X(77)90060-7)
- Štípská, P., Schulmann, K., & Kröner, A. (2004). Vertical extrusion and middle crustal spreading of omphacite granulite: A model of syn-convergent exhumation (Bohemian Massif, Czech Republic). *Journal of Metamorphic Geology*, 22(3), 179–198. <https://doi.org/10.1111/j.1525-1314.2004.00508.x>
- Thöni, M. (2006). Dating eclogite-facies metamorphism in the Eastern Alps—approaches, results, interpretations: A review. *Mineralogy and Petrology*, 88(1–2), 123–148. <https://doi.org/10.1007/s00710-006-0153-5>
- Tomkins, H. S., Powell, R., & Ellis, D. J. (2007). The pressure dependence of the zirconium-in-rutile thermometer. *Journal of Metamorphic Geology*, 25(6), 703–713. <https://doi.org/10.1111/j.1525-1314.2007.00724.x>
- Tumiati, S., Thöni, M., Nimis, P., Martin, S., & Mair, V. (2003). Mantle-crust interactions during Variscan subduction in the Eastern Alps (Nonsberg–Ulten zone): Geochronology and new petrological constraints. *Earth and Planetary Science Letters*, 210(3–4), 509–526. [https://doi.org/10.1016/S0012-821X\(03\)00161-4](https://doi.org/10.1016/S0012-821X(03)00161-4)
- Vanardois, J., Trap, P., Roger, F., Barou, F., Lanari, P., Marquer, D., Paquette, J.-L., Melleton, J., & Fréville, K. (2020). *New deformation, metamorphic and geochronological data on the Aiguilles-Rouges massif (Alpine External Crystallin massifs, France). A Reappraisal of the Variscan tectono-metamorphic Evolution in the Alpine Western External Crystallin Massifs*, 22, 8143. <http://adsabs.harvard.edu/abs/2020EGUGA.22.8143V>
- Verjat, J. L. (1981). *Etude pétrologique et structurale des terrains cristallins du sud-est de Belledonne, à l'ouest du col du Glandon - Alpes françaises*. <https://tel.archives-ouvertes.fr/tel-00547453>
- Vermeesch, P. (2018). Statistical models for point-counting data. *Earth and Planetary Science Letters*, 501, 112–118. <https://doi.org/10.1016/j.epsl.2018.08.019>
- Vivier, G., Ménot, R.-P., & Giraud, P. (1987). Magmatismes et structuration orogénique Paléozoïques de la chaîne de Belledonne (Massifs cristallins externes alpins). Le Domaine nord-oriental. *Géologie Alpine (Grenoble)*, 63, 25–53.
- Von Raumer, J. F., Bussy, F., Schaltegger, U., Schulz, B., & Stampfli, G. M. (2013). Pre-Mesozoic Alpine basements—their place in the European Paleozoic framework. *Bulletin*, 125(1–2), 89–108. <https://doi.org/10.1130/B30654.1>
- Von Raumer, J. F., Bussy, F., & Stampfli, G. M. (2009). The Variscan evolution in the External massifs of the Alps and place in their Variscan framework. *Comptes Rendus Geoscience*, 341(2–3), 239–252. <https://doi.org/10.1016/j.crte.2008.11.007>
- Von Raumer, J. F., & Bussy, F. (2004). Mont Blanc and Aiguilles Rouges geology of their polymetamorphic basement (external massifs, Western Alps, France-Switzerland). In *Mémoires de Géologie (Lausanne)* (Vol. 42, pp. 1–210).
- Watt, G. R., Griffin, B. J., & Kinny, P. D. (2000). Charge contrast imaging of geological materials in the environmental scanning electron microscope. *American Mineralogist*, 85(11–12), 1784–1794. <https://doi.org/10.2138/am-2000-11-1221>
- White, R. W., Powell, R., Holland, T. J. B., Johnson, T. E., & Green, E. C. R. (2014). New mineral activity–composition relations for thermodynamic calculations in metapelitic systems. *Journal of Metamorphic Geology*, 32(3), 261–286. <https://doi.org/10.1111/jmg.12071>
- White, R. W., Powell, R., Holland, T. J. B., & Worley, B. A. (2000). The effect of TiO_2 and Fe_2O_3 on metapelitic assemblages at greenschist and amphibolite facies conditions: Mineral equilibria calculations in the system $\text{K}_2\text{O}-\text{FeO}-\text{MgO}-\text{Al}_2\text{O}_3-\text{SiO}_2-\text{H}_2\text{O}-\text{TiO}_2-\text{Fe}_2\text{O}_3$. *Journal of Metamorphic Geology*, 18(5), 497–511.
- Whitney, D. L., Hamelin, C., Teyssier, C., Raia, N. H., Korchinski, M. S., Seaton, N. C. A., Bagley, B. C., von der Handt, A., Roger, F., & Rey, P. F. (2020). Deep crustal source of gneiss dome revealed by eclogite in migmatite (Montagne Noire, French Massif Central). *Journal of Metamorphic Geology*, 38(3), 297–327. <https://doi.org/10.1111/jmg.12523>
- Whitney, D. L., Roger, F., Teyssier, C., Rey, P. F., & Respaut, J.-P. (2015). Syn-collapse eclogite metamorphism and exhumation of deep crust in a migmatite dome: The P–T–t record of the youngest Variscan eclogite (Montagne Noire, French Massif Central). *Earth and Planetary Science Letters*, 430, 224–234. <https://doi.org/10.1016/j.epsl.2015.08.026>
- Wiedenbeck, M., Hanchar, J. M., Peck, W. H., Sylvester, P., Valley, J., Whitehouse, M., Kronz, A., Morishita, Y., Nasdala, L., Fiebig, J., Franchi, I., Girard, J.-P., Greenwood, R. C., Hinton, R., Kita, N., Mason, P., Norman, M., Ogasawara, M., Piccoli, P. M., ... Zheng, Y.-F. (2004). Further characterisation of the 91500 zircon crystal. *Geostandards and Geoanalytical Research*, 28(1), 9–39. <https://doi.org/10.1111/j.1751-908X.2004.tb01041.x>
- Zack, T., & Kooijman, E. (2017). Petrology and geochronology of rutile. *Reviews in Mineralogy and Geochemistry*, 83(1), 443–467. <https://doi.org/10.2138/rmg.2017.83.14>

Zhou, T., Li, Q., Klemm, R., Shi, Y., Tang, X., Li, C., & Liu, Y. (2020). Multi-system geochronology of North Dabie eclogite: Ineffective garnet 'shielding' on rutile inclusions under multi-thermal conditions. *Lithos*, 368–369, 105573. <https://doi.org/10.1016/j.lithos.2020.105573>

SUPPORTING INFORMATION

Additional supporting information may be found online in the Supporting Information section.

Figure S1. X-ray element maps of garnet in retrogressed eclogite JB-18-50.

Figure S2. X-ray element maps of clinopyroxene in retrogressed eclogite JB-18-50.

Figure S3. X-ray element maps of amphibole and plagioclase in retrogressed eclogite JB-18-50.

Figure S4. P-MH₂O diagram for eclogite JB-18-50 and T-MH₂O diagram for metasediment JB-18-46, computed with the same bulk composition as diagrams on Figure 8 (main text). Modal proportions (vol%) of hornblende and biotite are displayed on the right.

Figure S5. P–T diagram with mineral isopleths for the prograde stage in the eclogites.

Figure S6. P–T diagram with mineral isopleths for the retrograde stage in the eclogites.

Figure S7. P–T diagram with mineral isopleths for the

migmatitic metasediment.

Table S1. Abbreviations used for mineral end-members.

Table S2. Mineral EPMA data for the retrogressed eclogites and metasediment JB-18-46. (a) Garnet; - (b) Clinopyroxene; - (c) Amphibole; (d) Feldspar.

Table S3. Settings and solution models used in PerpleX to compute the phase diagrams.

Table S4. Observed mineral proportions (vol%).

Table S5. Summary of rutile analyses and zircon-in-rutile temperatures calculated with the calibration of Tomkins et al., (2007).

Table S6. Summary of trace element analyses in zircon, with Ti-in-zircon temperatures calculated with the calibration of Ferry and Watson (2007).

Table S7. SIMS U–Pb analyses of zircon in eclogites.

Table S8. SIMS U–Pb analyses of zircon in metasediment.

Table S9. LA-ICP-MS U–Pb analyses of rutile.

How to cite this article: Jacob J-B, Guillot S, Rubatto D, Janots E, Melleton J, Faure M. Carboniferous high-*P* metamorphism and deformation in the Belledonne Massif (Western Alps). *J Metamorph Geol.* 2021;00:1–36. <https://doi.org/10.1111/jmg.12600>

3.2 Données complémentaires sur le contexte structural

L'ensemble des mesures structurales réalisées dans les formations métamorphiques du nord-est du massif de Belledonne a permis d'établir plusieurs coupes, représentées sur la **Figure 3.2**, qui montrent les caractéristiques principales des déformations varisques et alpines.

3.2.1 Contexte tectonique alpin

Les anciens blocs basculés formés lors du rifting jurassique apparaissent nettement dans la topographie, en particulier sur les sommets du Grand Mont et du Grand Rognoux, dont les flancs orientaux présentent une morphologie en plateau basculé de 10 à 25° vers le sud-est. Ces plateaux sont jalonnés d'affleurements de grès et de dolomies triasiques, marquant la position de la paléosurface triasique, qui a par endroit été décalée par des failles normales décamétriques à hectométriques (**Figure 3.1**). Ainsi, en dehors des zones de faille marquant la limite entre différents blocs basculés et des zones de cisaillement déca à hectométriques développées lors de la compression alpine, la structure générale du socle varisque semble avoir été relativement peu affectée par la tectonique alpine, et se trouve simplement basculée vers le sud-est de 10 à 25°.

3.2.2 Étude structurale des formations métamorphiques des lacs de la Tempête

Les mesures structurales mettent bien en évidence l'existence de deux populations de foliations : une ancienne foliation S_x peu pentée, préservée essentiellement dans la partie nord-est de la zone étudiée, et une foliation S₂ fortement pentée, d'orientation N10° à

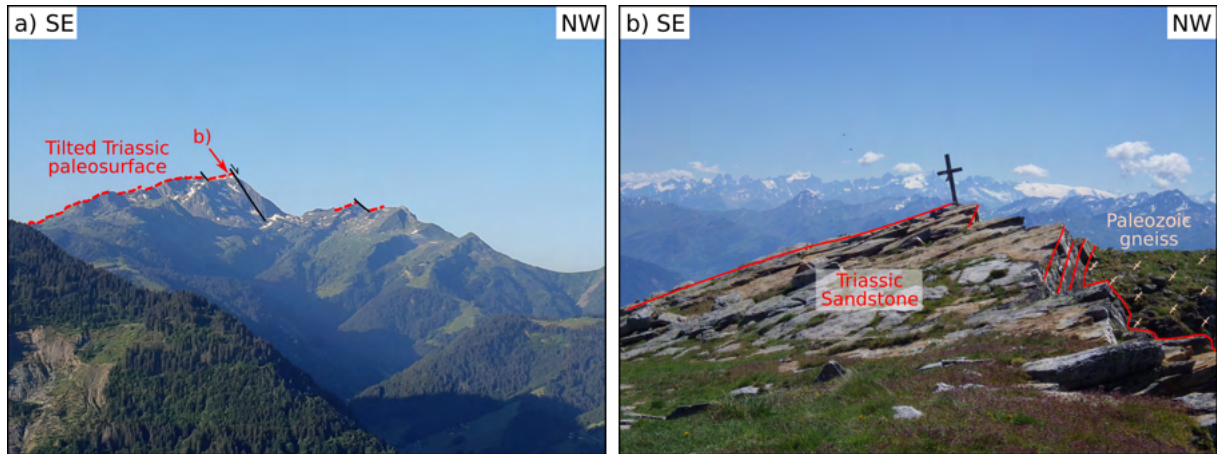


FIGURE 3.1 – a) Vue du massif du Grand Mont prise depuis le nord-est (Montagne d’Outray). Le flanc est, peu penté, représente l’ancienne surface triasique basulée lors du rifting Jurassique. Le flanc ouest, beaucoup plus raide, marque vraisemblablement une ancienne faille normale. b) Affleurement de grès triasiques au sommet du Grand Mont, déposés en discordance sur les gneiss paléozoïques.

$N40^\circ$ (Figure 3.2), qui recoupe nettement S_x . S_x porte quelques linéations d’étirement qui semblent indiquer un mouvement de direction N-S. Les plans S_2 portent des linéations L_2 (étirement et minérales) peu pentées ($<30^\circ$), qui marquent une composante décrochante dominante. Les différents critères de cisaillement, incluant les relations S_2-C_2' et les clastes asymétriques mettent en évidence une cinématique dextre, similaire à celle observée dans les Aiguilles Rouges (Simonetti *et al.*, 2020). Les plis P_1 orientés $N10^\circ$ à $N30^\circ$, qui affectent S_x , pourraient correspondre soit à des reliques de la tectonique de nappe (D_1) observée dans le sud-ouest du massif de Belledonne (Fréville *et al.*, 2018), soit à un raccourcissement NW-SE syn- D_2 , lié à une composante en cisaillement pur (tectonique transpressive). Une étude de vorticité réalisée par Simonetti *et al.* (2020) dans des formations similaires du massif des Aiguilles Rouges indique en effet une forte composante en cisaillement pur (raccourcissement NW-SE) lors de la phase D_2 . La présence de petits bassins sédimentaires d’âge Carbonifère supérieur (310–300 Ma, Ballèvre *et al.*, 2018), ouverts en pull-apart le long des zones de faille, marque la transition vers un contexte transtensif dextre à la fin du Carbonifère (D_3).

3.2 Données complémentaires sur le contexte structural

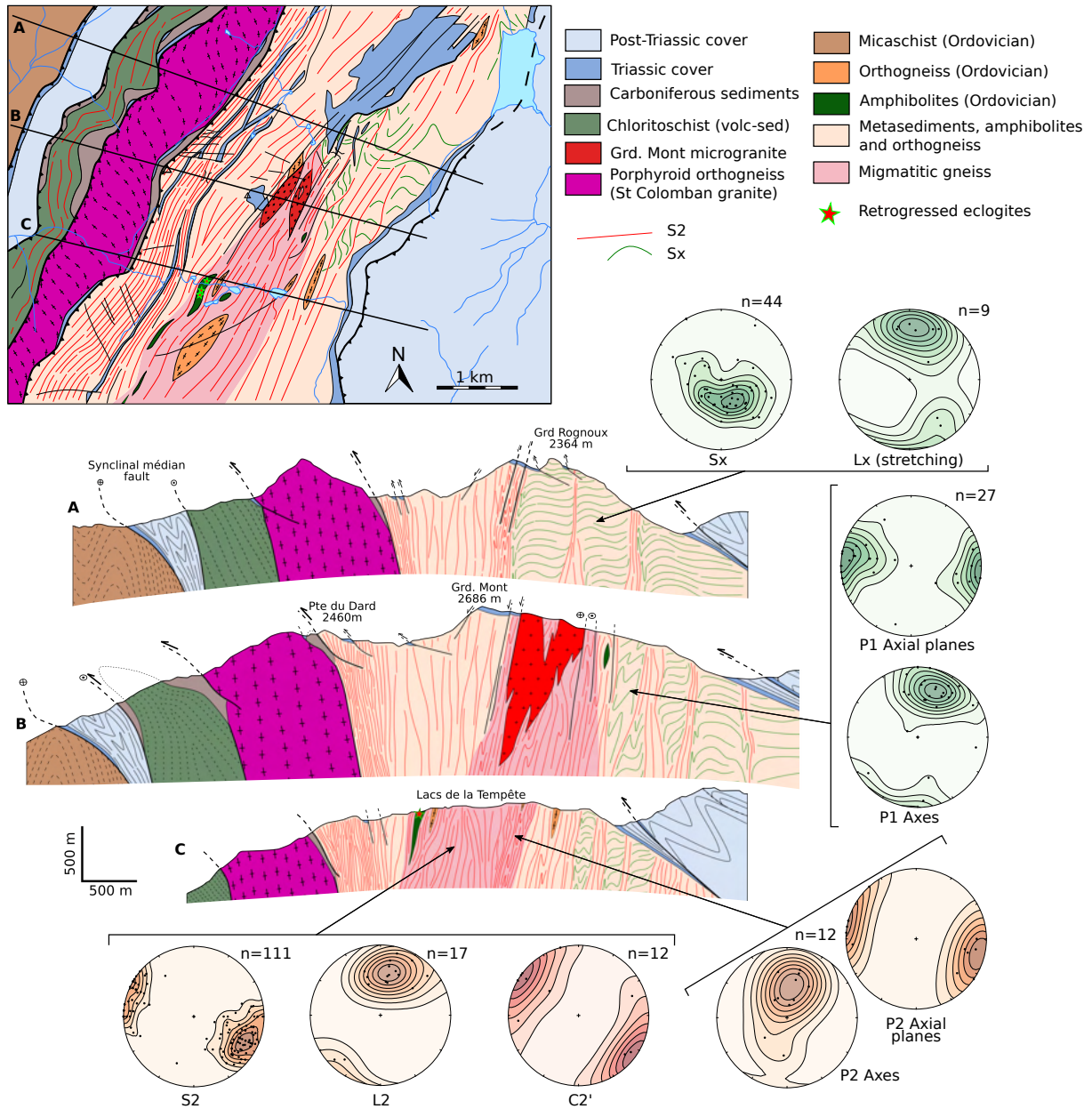


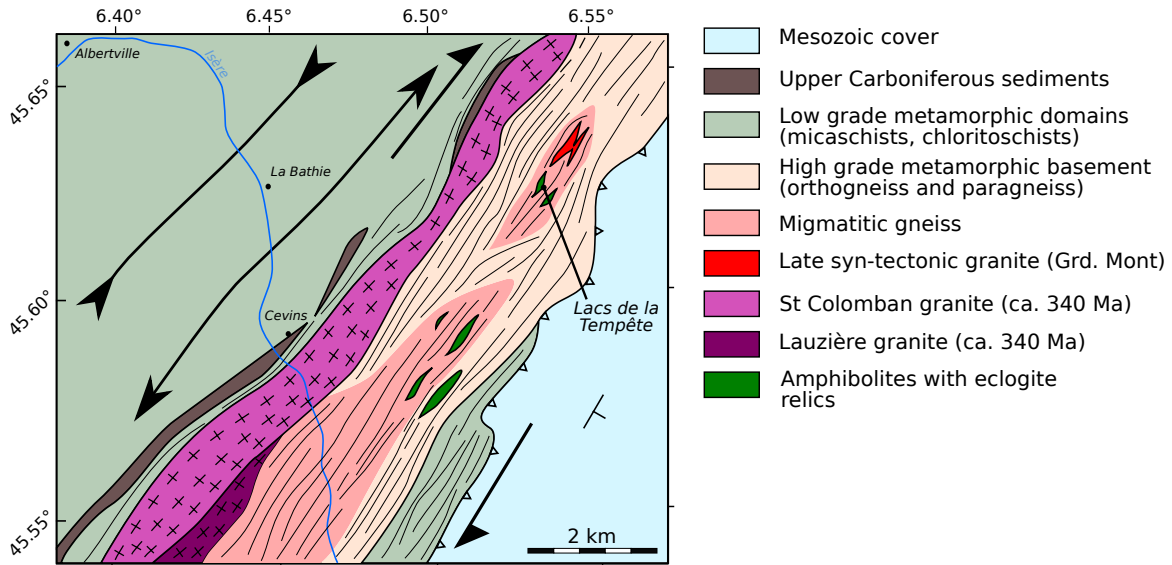
FIGURE 3.2 – Carte et coupes géologiques de la zone étudiée (Lacs de la Tempête, Beaufortain), montrant les relations entre les différentes structures varisques et alpines. Les mesures structurales des différentes fabriques ainsi que l'orientation des plis sont reportées sur des projections stéréographiques (projection sur demi-sphère inférieure).

3.2.3 Une exhumation localisée des reliques de haute pression au sein de la zone de cisaillement est-varisque

Une vue d'ensemble de la partie nord du massif de Belledonne, incluant la série satinée (domaine occidental) ainsi que des domaines exposés au sud-est des lacs de la Tempête, fait clairement apparaître une zonation métamorphique d'axe NW–SE, orthogonale à l'orientation générale de S2 et des intrusions granitiques (Figure 3.3-a) : les roches métamorphiques de plus haut grade (migmatites et reliques éclogitiques) et les granitoïdes varisques affleurent uniquement dans une bande centrale large de 2 à 4 km, fortement déformée, entourée de roches métamorphiques de plus bas grade : à l'ouest, les micaschistes de la série satinée (Bordet et Bordet, 1963), et des chloritoschistes représentant d'anciennes formations volcano-sédimentaires peu métamorphiques (Vivier *et al.*, 1987) ; à l'est, les formations de la « série satinée interne », composée de séricito-schistes feldspatiques et de métaconglomérats (Vivier *et al.*, 1987). On observe par ailleurs un gradient E–W de déformation D2, plus intense dans les formations de haut grade que dans les micaschistes de la série satinée. Cette disposition est typique des grands systèmes décrochants (e.g. Cao et Neubauer, 2016; Leloup *et al.*, 1995; Valli *et al.*, 2008). Les unités de haut grade contenant les reliques HP correspondraient donc au coeur de la zone de cisaillement est-varisque (EVSZ, chapitre 2), dans laquelle affleure du matériel crustal équilibré dans la croûte intermédiaire à inférieure.

Cette disposition peut s'expliquer par une extrusion localisée de matériel crustal profond associée à la tectonique transpressive. En effet, plusieurs études suggèrent que les zones de cisaillement transpressives sont des lieux favorables à l'exhumation active de croûte inférieure par extrusion, qui est d'autant plus efficace que la composante en cisaillement pur de la déformation est grande (Schulmann *et al.*, 2008; Štípská *et al.*, 2004; Thompson *et al.*, 1997; Tikoff et Teyssier, 1994). Des portions de manteau lithosphérique peuvent même être exhumées au sein de ces zones, comme par exemple au niveau de la faille de San Andreas en

a) Simplified structural map of the northeastern Belledonne massif



b) Interpretative 3D sketch of the Variscan deformation pattern

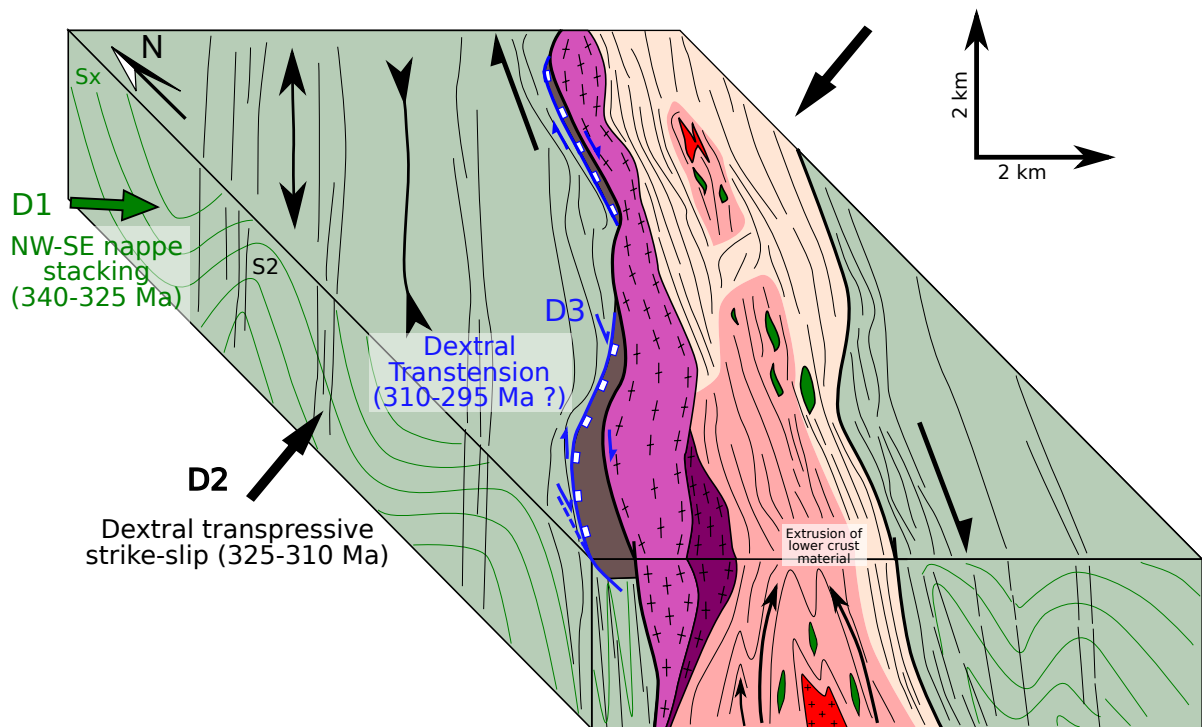


FIGURE 3.3 – (a) Schéma structural de la partie nord-est du massif de Belledonne; (b) Bloc diagramme interprétatif montrant la superposition des différentes phases de déformation varisque, suivant le schéma D1-D2-D3 présenté dans le chapitre 2. La phase D1 (empilement de nappes E-W) apparaît de manière relictuelle. La phase transpressive D2, qui est la plus marquée dans ce domaine, se caractérise notamment par l'extrusion localisée de matériel crustal profond au sein de la zone centrale de l'EVSZ. La phase D3 (transtension) est responsable de la formation de bassins houillers kilométriques.

Californie, qui est jalonnée de massifs kilométriques de serpentinites, exhumées au sein de la zone de cisaillement (Kirby *et al.*, 2014; Guillot *et al.*, 2015). Ce mécanisme d'exhumation étant plus rapide qu'une combinaison érosion – réajustement isostatique, la relaxation thermique n'a pas le temps d'opérer. Ceci se traduit par des chemins d'exhumation isothermes ou avec un faible réchauffement durant la décompression (Thompson *et al.*, 1997), ce qui est cohérent avec les estimations thermobarométriques réalisées sur les éclogites des lacs de la Tempête. Ainsi, il est possible que la zone centrale de l'EVSZ contrôle l'exhumation localisée de matériel crustal profond par un mécanisme d'extrusion lié à la tectonique transpressive (Figure 3.3-b). Cette zone centrale formerait ainsi une zone de mélange, dans laquelle seraient extrudées des roches provenant de différents niveaux structuraux, équilibrées à des pressions et températures différentes, incluant des lentilles éclogitiques et les gneiss migmatitiques équilibrés à plus basse pression.

CHAPITRE 4

Les granulites de haute pression de l'Oisans



L'Olan (*d.*) et la cime du Vallon (*g.*), vus depuis le lac des Rouies, dans le Vallon de la Lavey.

Sommaire

4.1 Article #2 : HT overprint of HP granulites in the Oisans–Pelvoux massif : implications for the dynamics of the Variscan collision in the external Western Alps	125
4.1.1 Introduction	126
4.1.2 Geological setting and field description	128
4.1.3 Methods	133
4.1.4 Petrographic description	137
4.1.5 Bulk rock Geochemistry	144
4.1.6 Thermobarometry	147
4.1.7 U-Pb Geochronology	154
4.1.8 Discussion	159
4.2 Données complémentaires sur le contexte structural	176
4.2.1 Déformation alpine dans le massif de l'Oisans–Pelvoux	176
4.2.2 Étude des structures varisques	178
4.2.3 Mécanismes de déformation de la croûte inférieure	184
4.2.4 Mécanismes d'exhumation de la croûte profonde dans le massif de l'Oisans–Pelvoux	186

4.1 Article #2 : HT overprint of HP granulites in the Oisans–Pelvoux massif : implications for the dynamics of the Variscan collision in the external Western Alps

Jean-Baptiste Jacob, Émilie Janots, Stéphane Guillot, Daniela Rubatto, Jérémie Melleton, Michel Faure

Abstract

The Oisans–Pelvoux massif, belonging to the Paleozoic basement of the External western Alps has undergone high temperature (HT) metamorphism associated with intense migmatization during the syn to post-collisional stages of the Variscan orogeny. Most of prior metamorphic assemblages have been obliterated and the early collision stages remained so far unconstrained. Field investigation has led to identify new bodies of high pressure (HP) mafic granulites, which preserved relics of the prograde evolution up to HP conditions. Relics of Mn-rich garnet cores containing inclusions of epidote, titanite, chlorite and rare white micas constrain an early prograde stage at 460–550°C and 0.4–1.0 GPa. The HP assemblage consists in garnet + clinopyroxene + quartz + rutile ± plagioclase ± amphibole ± biotite and yield peak-P conditions at 650–730°C and 1.5–1.7 GPa. Decompressional evolution was associated with heating to HT granulite-facies conditions at 800–870°C and 0.6–0.9 GPa, which led to the development of granoblastic polycrystalline mosaics over the resorbing HP assemblage. The U–Pb dating of magmatic zircon cores constrains the emplacement age of the mafic protoliths at 479±5 Ma. Timing of the prograde to HP evolution is estimated around 345–330 Ma based on rutile U–Pb dating, which is contemporaneous with HP recorded in

the other crystalline massifs of the western Alps. The U-Pb dating of zircon metamorphic rims yields U–Pb dates scattering between 337 and 294 Ma, which are interpreted to have crystallized during broad decompression and heating to the HT granulite-facies. Metamorphic conditions during the early prograde stage precludes scenarios involving subduction of a cold passive margin and are better reconciled with thickening of an orogenic wedge during collision. In contrast with other Variscan HP relics of the external Alps, the HP rocks of the Oisans–Pelvoux massif record heating to HT granulitic conditions during decompression, which may result from longer residence time in the lower crust before the exhumation.

4.1.1 Introduction

High pressure (HP) metamorphic rocks are important geodynamical markers of lithospheric processes, which provide information about pressure-temperature (P-T) conditions and timing of the metamorphic evolution of crustal units, which can be in turn interpreted in terms of geodynamic environment (Thompson et England, 1984). In collapsed and eroded orogens such as the Variscan belt of Europe, these HP relics form relatively minor portions of the exposed metamorphic units. Furthermore, thermobarometric and geochronological information about the prograde and HP stages has often been blurred, in particular for those exposed in HT migmatitic domains, in which metamorphic reaction rates are dramatically increased by temperature and the presence of melts (White et al., 2001). Hence, the geodynamic significance of these HP relics remains ambiguous, and they may be interpreted either as relics of a former subduction (e.g. Pitra et al., 2021) or represent exhumed portions of thickened lower crust equilibrated at eclogitic or HP granulitic conditions (e.g. O'Brien et Rötzler, 2003; Whitney et al., 2020). Rare samples preserving relics of the prograde evolution are therefore invaluable and provide key geodynamical constraints.

We present here a case-study from the Variscan basement of the external western Alps, in the Oisans–Pelvoux massif. This massif has been recognized as a portion of orogenic middle-to-lower crust, which has undergone HT metamorphism and intense migmatization during the syn to post-collisional stages of the Variscan orogeny (Grandjean *et al.*, 1996). This HT migmatitic stage has obliterated most of the pre-HT metamorphic history, and no indisputable evidence of an earlier HP metamorphic stage had been recognized so far in this massif. This metamorphic record strongly contrasts with that of the other basement massifs in the external western Alps, which present several relics of Variscan eclogites and HP granulites (Jacob *et al.*, 2021a; Jouffray *et al.*, 2020; Paquette *et al.*, 1989; Rubatto *et al.*, 2010), but are comparatively less affected by the HT migmatitic event. Thus, the early stages of the Variscan collision remained unconstrained in the Oisans–Pelvoux massif. Our recent field investigation of high-grade metamorphic domains has identified mafic HP granulite bodies that contain a relict garnet-clinopyroxene HP assemblage overprinted by a HT granulitic assemblage. These granulites are the first documented Variscan HP rocks in the Oisans–Pelvoux massif, and they represent a unique opportunity to constrain the complete metamorphic evolution from collisional to post-collisional stages. The HP granulite bodies were investigated using a multi-method approach, which combined petrologic and microstructural observations, phase equilibrium modeling and Zr-in-rutile thermometry to constrain the P-T evolution, and U-Pb dating of zircon and rutile to constrain the timing of metamorphism. This contribution aims to present the results of these detailed investigations, and discuss the implications for the Variscan geodynamic evolution of the Oisans–Pelvoux massif. In particular, preservation of early prograde stages of the metamorphic evolution provides important constraints regarding the thermal state of the middle and the lower crust during the early stages of the collision.

4.1.2 Geological setting and field description

4.1.2.1 General setting and Variscan evolution

The Oisans-Pelvoux massif is a roughly rounded massif about 35 km wide located in the French western Alps, which exposes high grade metamorphic domains of the Variscan orogenic root (Figure 4.1). It belongs to the External Crystalline Massifs (ECM), which form exposed portions of the Variscan basement in the external western and central Alps (Guillot *et Ménot*, 2009; Von Raumer *et al.*, 2009). This basement is mainly composed of various early to mid-Paleozoic units, which were metamorphosed and intruded by granitoids during the Variscan orogeny. The whole is capped by non-metamorphic sediments deposited in small pull-apart basins between the late Carboniferous and the early Permian (Fernandez *et al.*, 2002; Guillot *et Ménot*, 2009). The Paleozoic basement was only mildly affected by post-Permian deformation and metamorphism. The Alpine collision has occurred from the early-mid Eocene (ca. 40 Ma), during which the basement was buried and developed greenschist-facies metamorphic assemblages (Bellanger *et al.*, 2015), which are mostly concentrated in Alpine compressional and strike-slip shear zones (Bellahsen *et al.*, 2014; Marquer *et al.*, 2006). The pre-Variscan protoliths derive from a variety of sedimentary and igneous rocks mostly emplaced during the Cambrian–Ordovician period (Fréville *et al.*, 2018; Paquette *et al.*, 1989; Von Raumer *et al.*, 2013). Volcano-sedimentary and bimodal plutonic series of Devonian–Tournaisian age (ca. 370–350 Ma, Fréville *et al.*, 2018; Guillot *et Ménot*, 2009; Ménot, 1987a), presumably emplaced in an arc or back-arc setting, are exposed in the western part of the massif (Figure 4.1). They are strongly affected by Variscan tectono-metamorphic events, and their formation therefore predates the main Variscan collision stages.

4.1 HT overprint of HP granulites in the Oisans–Pelvoux massif

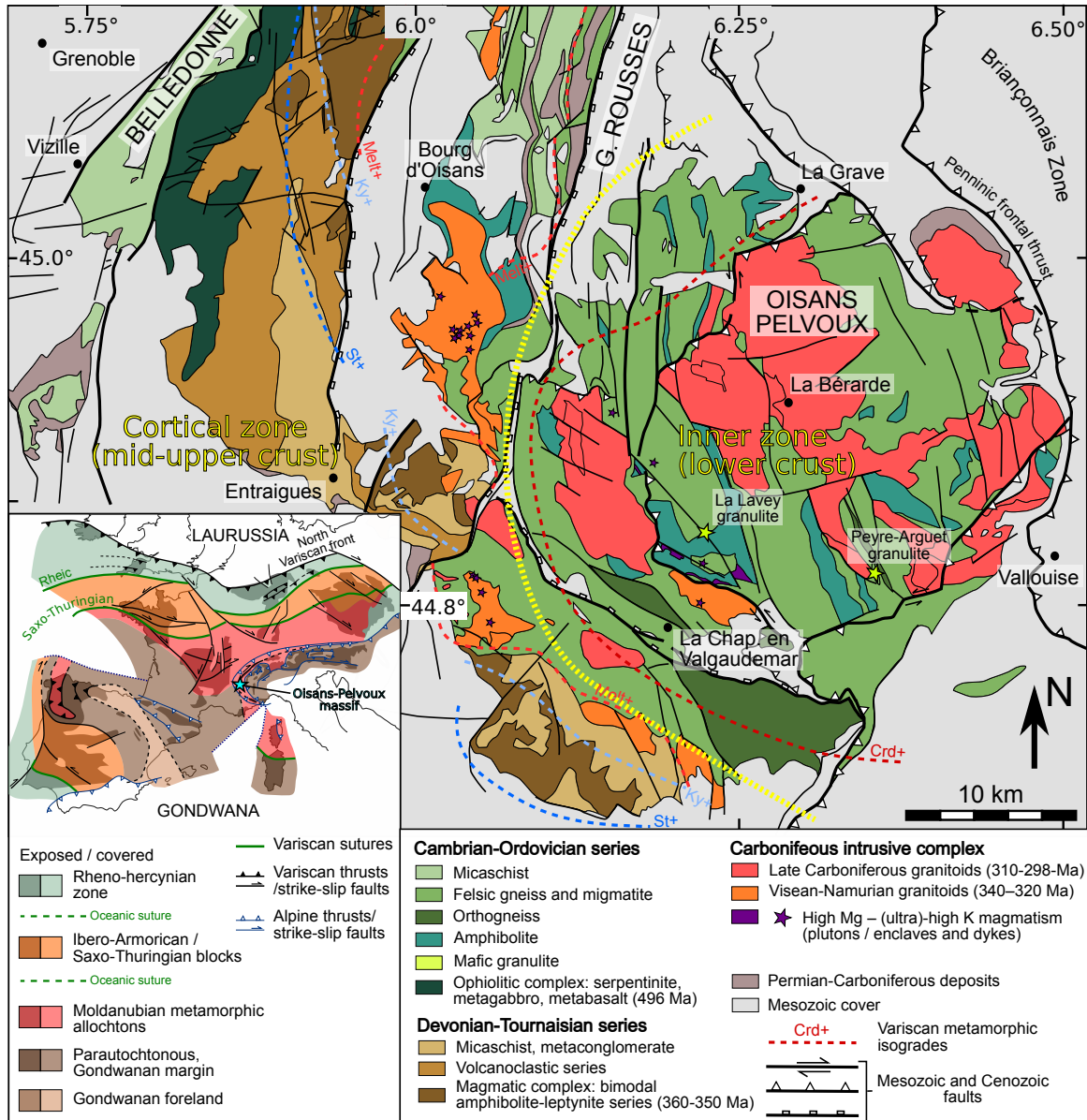


FIGURE 4.1 – Simplified geological map of the Paleozoic basement of the Oisans-Pelvoux, southern Belledonne and southern Grandes-Rousses Massifs in the external western Alps, redrawn from the BRGM 1 :50 000 geological maps. Location of these domains in the Variscan Belt, shown in the bottom left insert. Zonation of the Variscan Belt modified from (Ballèvre *et al.*, 2014)

The Variscan Orogeny in the ECMs occurred from ca. 350 to 295 Ma (Fréville *et al.*, 2018; Guillot *et Ménot*, 2009). The general tectono-metamorphic evolution during this period is summarized here in three main phases :

1. An early Carboniferous (Visean) collisional phase associated with nappe stacking and crus-

tal thickening, which formed E–W vergent nappes. These nappes are mainly visible in the south of the Belledonne massif and are associated with burying of the Devonian–Tournaisian series and the development of amphibolite-facies assemblages (garnet \pm kyanite \pm staurolite) at ca. 600–700°C and 0.6–0.9 GPa (Fréville *et al.*, 2018; Guillot et Menot, 1999). The age of this phase is constrained at ca. 345–330 Ma by U–Pb dating on monazite and Ar–Ar dating on micas (Fréville *et al.*, 2018, 2022). U–Pb dating of zircon and rutile from eclogite relics exposed in northeast Belledonne and in the other ECMs yields the same age (Jacob *et al.*, 2021a; Rubatto *et al.*, 2010), and the development of HP assemblages is therefore correlated with this nappe stacking phase.

2. A phase of transpression, associated with the formation of penetrative, steeply dipping fabrics. In the massifs of Belledonne and Grandes–Rousses, these fabrics form a ten-kilometer-wide high-strain corridor marked by dextral shearing, which extends in the other ECM and is thought to represent a crustal-scale dextral shear zone, which was active from ca. 325 Ma (Guillot *et al.*, 2009a; Rossi *et al.*, 2009; Simonetti *et al.*, 2018, 2020). In the Oisans–Pelvoux massif, steep metamorphic fabrics rather display sinistral shearing (Fréville *et al.*, 2022) and may represent antithetic shear zones developed during transpression.

3. Transpression progressively evolved toward transtension during the late Carboniferous (ca. 310–300 Ma), which resulted in the formation of SW–NE oriented ductile-brittle normal faults and dextral shear zones controlling the opening of kilometer to ten-kilometer scale half-graben and pull-apart basins (Fernandez *et al.*, 2002). Sedimentological and paleontological studies have provided evidence for syntectonic sedimentation during the Moscovian to Gzhelian (ca. 310–300 Ma, Ballèvre *et al.*, 2018, and references therein).

The older (pre-Carboniferous) metamorphic sequences are intruded by numerous Variscan granitoids, which form about 25% of the exposed area in the Oisans–Pelvoux massif. These granitoids were emplaced from the Viséan to the late Carboniferous – early Permian (ca. 345–295 Ma), with two dominant production peaks around 345–330 Ma and 310–295 Ma

(Debon et Lemmet, 1999; Fréville, 2016).

4.1.2.2 Field description

The investigated area is located in the inner part of the Oisans–Pelvoux massif and mainly exposes high-grade gneiss and amphibolites (Figure 4.22) identified locally as the Lavey series (Le Fort, 1971), which are intruded by Carboniferous granitoids (Figure 4.1). Early foliation S1 associated with the nappe stacking phase (1) was only observed as relics and is better preserved further west in upper structural levels. Two groups of metamorphic foliations have been observed in the investigated area : (i) flat-lying fabrics (S2h), which display shear criteria and mineral lineations consistent with roughly N–S directed flow (Figure 4.2-a,g); steeply-dipping fabrics striking N140° to N160° (S2v), which display sinistral shear criteria (Figure 4.2-b,g). Development of both fabrics initiated at supra-solidus or HT sub-solidus conditions, as evidenced by the presence of sheared leucosomes and sheared amphibolite boudins (Figure 4.2-a,b).

Both felsic and mafic lithologies underwent significant partial melting and display various migmatitic textures ranging from metatexites to diatexites (Figure 4.22 in the supplements). None of the collected felsic samples preserved any pre-HT assemblage. Cordierite develops sporadically in aluminous metasediments, which testifies to the high temperature of melting, probably associated with biotite-breakdown reactions above 800°C (Vielzeuf et Holloway, 1988). By contrast, some of the mafic bodies display little evidence of partial melting, and may exceptionally preserve HP granulitic assemblages. HP granulites are extremely rare in the Oisans–Pelvoux massif, since most of them have been partly or completely retrogressed by reaction with anatectic melts or fluids released during crystallization of these melts. A first occurrence of mafic granulite was found by Pecher (1970) in the eastern part of the massif and reported as the Peyre-Arguet granulites (Figure 4.1), but early HP stages remained controversial and were disregarded (Grandjean *et al.*, 1996; Pecher, 1970). In this study, a

LES GRANULITES DE HAUTE PRESSION DE L'OISANS

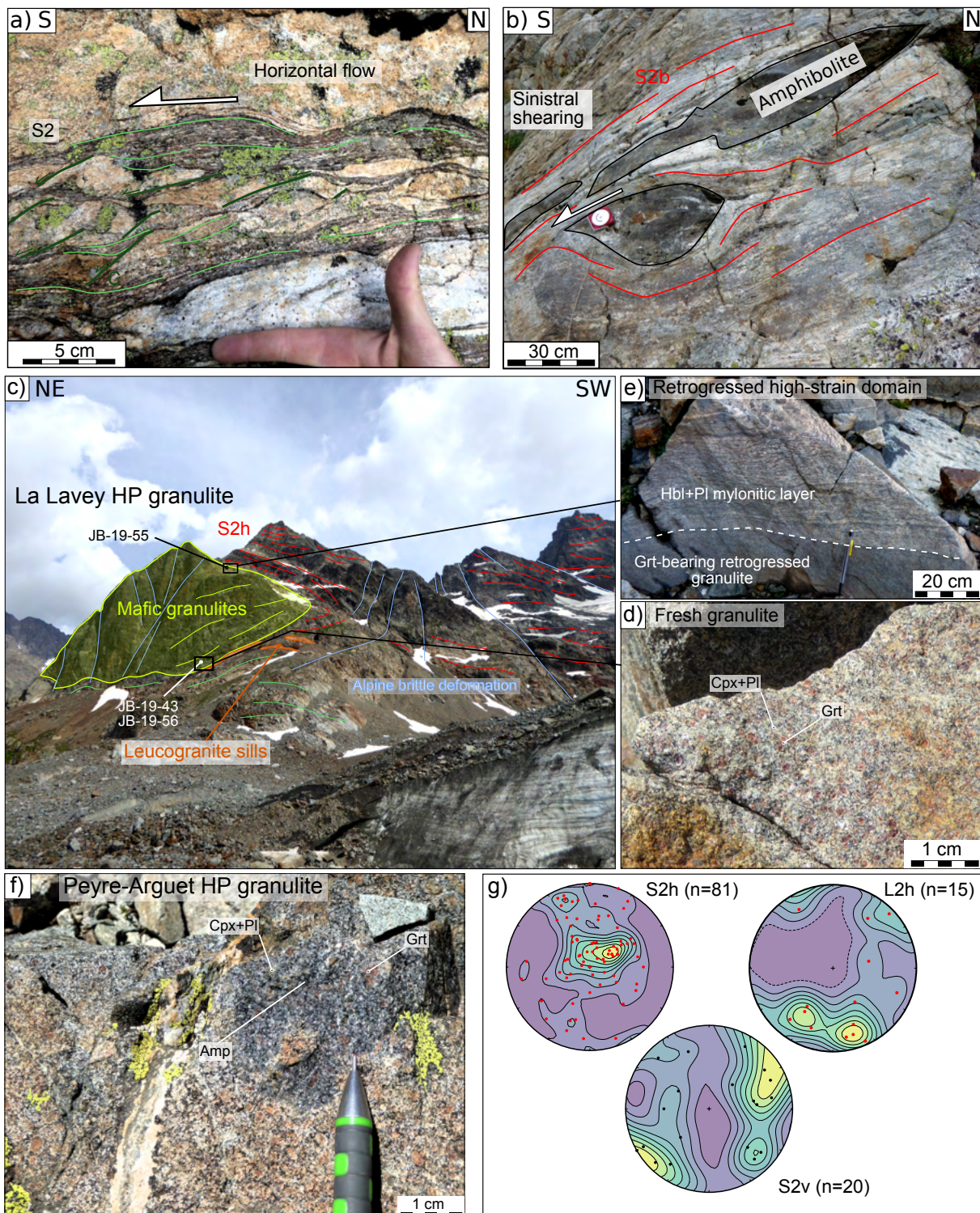


FIGURE 4.2 – Field photographs of the investigated area and main lithologies. (a) – S2h flat-lying foliation in felsic migmatites, with sheared leucosomes marking top-to-the-South shearing. (b) – S2v steeply-dipping foliation in the sub-vertical migmatitic shear zones. Deformed amphibolite boudins mark a sinistral kinematics. (c) – View on the granulitic formation of La Lavey, which consist in a hectometer-wide lens inserted in the flat-lying S2h. (d) – High-strain domain consisting of a mylonitic amphibole-plagioclase-rich layer alternating with retrogressed garnet-bearing granulites. (e) – Close up view of a massive, non-retrogressed garnet-clinopyroxene-bearing mafic HP granulite. (f) – Close-up view on a retrogressed mafic HP granulite from Peyre-Arguet. (g) – Poles of S2h and S2v foliations and mineral lineations measured on S2h.

newly discovered body of HP mafic granulites was found in La Lavey valley in the central part of the massif (Figure 4.1). It forms a hectometer-wide body embedded in flat-lying migmatitic S2h (Figure 4.2-c). The Peyre-Arguet body lies in a N150° oriented mylonitic shear zone (S2v), and shows more intense overprinting by amphibolite-facies assemblages than the Lavey granulites. The mafic granulite in the Lavey body shows variable degrees of retrogression and deformation (Figure 4.2-d-e). Some portions are composed of massive, weakly to non-foliated HP mafic granulites (Figure 4.2-d), whereas others portions present a layered texture parallel to S2h, with alternating centimetric to metric layers of granulites and garnet-free amphibolites (Figure 4.2-e). The plagioclase-amphibole rich layers generally display a highly strained texture, while the garnet-bearing layers are much less deformed.

4.1.3 Methods

4.1.3.1 Analytical methods

Backscattered electron images were acquired at ISTERre Grenoble with a Tescan Vega 3 scanning electron microscope operated with an accelerating voltage of 16 kV and a beam current of 10 nA. Mineral compositions were measured using a JEOL JXA-8230 electron microprobe at ISTERre Grenoble. Garnet analyses were performed with a 15 kV accelerating voltage, a 20 nA beam current and a counting times of 60s for the peak and 30s for the background. The other silicates were analyzed with a 15 kV accelerating voltage, a 10 nA beam current and counting times of 30s for the peak and 15s for the background. The spot size was set to 1–3 μm depending on the size of minerals and the presence of volatile elements. X-Ray element maps were acquired with a 15 kV accelerating voltage, a 100 nA beam current and a 100 ms counting time per pixel. Natural minerals and synthetic glass were used for standardization, and the ZAF matrix procedure was applied for data reduction. X-Ray maps were processed using the XMapTools software (Lanari *et al.*, 2014, 2018).

Zr and other trace elements (Nb, Fe, Cr) in rutile were measured in thin section on the JEOL JXA-8230 electron microprobe at ISTERre Grenoble. The instrument was operated with an accelerating voltage of 20 kV, a beam current of 600 nA, and a total counting time of 600s, with spot size set to 1–3 μm . Standardization was done on synthetic and natural standards of TiO_2 , ZrO_2 , Cr_2O_3 , Fe_2O_3 and Nb. Accuracy check was done on standard rutile R632 (Axelsson *et al.*, 2018), which returned Zr concentrations between 2 and 5% of the reference value. This uncertainty is consistent with counting error statistics returned by the JEOL microprobe software for rutile analysis and corresponds to an absolute uncertainty below 40 ppm in most of the cases. A conservative estimate of ± 50 ppm is therefore assigned for electron microprobe analyses of rutile. In addition, trace element analyses were performed by LA-ICPMS on separated rutile grains from sample JB-19-56, which were subsequently dated (see below).

Zircon and rutile were separated using conventional rock crushing and heavy liquids. Crystals were mounted in epoxy resin and polished to expose the grain center for analysis. Charge contrast (CC) images of zircon grains were obtained with a ZEISS EV050 scanning electron microscope at the Institute of Geological Sciences, University of Bern, at low vacuum conditions (18 Pa), 12 kV, a beam current of 100 mA and a working distance of 9.5 mm. It has been previously demonstrated that CC images correlate exactly to cathodoluminescence (Watt *et al.*, 2000). Backscattered electron images of separated rutile grains were obtained at ISTERre Grenoble using the same instrument and analytical conditions as described above. Trace element spot analysis of separated zircon and rutile was performed with a RESOLUTION Laser System coupled to an Agilent 7900 quadrupole ICP-MS at the Institute of Geological Sciences (University of Bern). A He-H₂ gas mixture was used as the aerosol transport gas. The laser spot diameter was 24 and 20 μm for zircon, and 38 μm for rutile. The laser was set to 5 Hz repetition rate and an energy density on the sample of 4 $\text{J}\cdot\text{cm}^{-2}$. Oxide interferences were reduced by maintaining $\text{ThO}/\text{Th} < 0.2$. Sample analyses were calibrated using NIST

SRM 612 (Jochum *et al.*, 2011). Accuracy was monitored using the reference material GSD-1G (Jochum *et al.*, 2005) and zircon 91500 (Wiedenbeck *et al.*, 2004), and was assessed to be better than 10% for all elements. Data reduction was performed using the software Iolite (Paton *et al.*, 2011).

U–Pb dating of rutile was performed with the same LA-ICP-MS system at the University of Bern with conditions of 5 Hz and 3.5 J/cm². The count rate ratio for Th/U was 98–97 and the ThO/Th < 0.2. Measurements consisted of 30s background and 30s signal acquisition sweeping through the masses ²⁰⁶Pb, ²⁰⁷Pb, ²⁰⁸Pb, ²³²Th and ²³⁸U. Spot size was 50 μm with a pre-cleaning with a 60 μm beam. U–Pb ratios were standardized to rutile R10 (1091.6 ± 3.5 Ma, Luvizotto *et al.*, 2009), whereas secondary reference material was rutile R632 (496 ± 2 Ma, Axelsson *et al.*, 2018), which returned an average ²⁰⁶Pb/²³⁸U age of 496 ± 11 Ma. Data reduction was performed using the software Iolite (Paton *et al.*, 2011) running the DRS VizualAge UcomPbine (Chew *et al.*, 2014), although no common Pb correction was applied to the data of either standards or unknown. The single spot 2σ standard error external on the primary standard was 7.5% and propagated in full to the unknowns. U–Pb geochronology of zircon was carried out with the SwissSIMS Cameca IMS 1280-HR at Université de Lausanne, which is equipped with an high-brightness Hyperion H201 RF plasma oxygen ion source. Basic instrument set up parameters were 6–8 nA, 20 μm O²⁻ primary beam, mass resolution M/M = 5000, energy window = 40 eV. Data were acquired in mono-collection, peak-hopping mode. U–Pb–Th data were standardized to TEM2 zircon (417 Ma, Black *et al.*, 2003) and accuracy was checked with zircon standard Plešovice (337.17 ± 0.37 Ma, Sláma *et al.*, 2008), which were cast in the same epoxy mount as the unknowns and returned an age at 337.7 ± 3.5 Ma. The uncertainty on standard ²⁰⁶Pb/²³⁸U – UO₂/U calibration was 1.0 and was propagated to the data. Common Pb correction was based on the measured ²⁰⁴Pb signal (when significant relative to background) assuming the present-day model terrestrial Pb composition of Stacey *et al.* (1975). Radiogenic ratios and single ages were calculated

using the CIPS program compiled by Martin Whitehouse. Age calculations use the decay constant recommendations of [Steiger et Jäger \(1977\)](#). The IsoplotR package ([Vermeesch, 2018](#)) was employed to plot the diagrams and calculate concordia and weighted average ages. Individual uncertainties are quoted at 1 level and the confidence level for weighted average is 95%.

Whole rock geochemical analyses were performed at the SARM in Nancy, using a Thermo Fischer iCap6500 ICP-OES for major oxides and an iCapQ ICP-MS for minor and trace elements. Details about the analytical procedures for whole rock geochemical analyses are described in [Carignan *et al.* \(2001\)](#). In addition, FeO was measured by wet titration in sample JB-19-43 in order to constrain the Fe³⁺/Fe²⁺ balance in the mafic granulites.

4.1.3.2 Thermobarometry

Zr-in-rutile temperatures were calculated using the calibration of [Kohn \(2020\)](#), constrained with combined experimental and natural datasets. In addition, two samples of garnet-bearing mafic granulites (JB-19-43 and JB-19-56) were selected for more comprehensive P-T estimations using a combination of forward phase equilibrium modeling with PerpleX 6.9.0 ([Connolly, 2005, 2009](#)) and inverse thermobarometry on plagioclase-amphibole pairs using the edenite-richterite exchange thermometer of [Holland et Blundy \(1994\)](#). Inverse thermobarometry was performed directly on quantitative X-Ray map using the P-T spot add-ons implemented in XMapTools. Phase equilibrium models were computed in the compositional space MnNCKFMASHTO, using the TC-DS622 thermodynamic database of Thermocalc ([Holland et Powell, 2011](#)), with a set of solution models from [Fuhrman et Lindsley \(1988\)](#); [Green *et al.* \(2007, 2016\)](#); [Holland et Powell \(1998, 2011\)](#); [White *et al.* \(2000, 2014\)](#). Reactive bulk compositions used as input in PerpleX were obtained by re-integration of X-Ray maps using XMapTools 3.4.0 and by ICP-OES whole rock analyses. Fe³⁺ inferred by difference between ICP-OES and wet titration measurements in sample JB-19-43 was taken as a

maximum value, and was then adjusted iteratively using the meemum function of PerpleX, by modifying incrementally the amount of O₂ until a good fit is obtained for Fe³⁺/Fetot in garnet and clinopyroxene. No evidence of C-S-bearing volatile species have been observed, so fluid was considered as pure H₂O ($a_{H_2O}(\text{Fluid}) = 1$). P-T conditions of equilibration for the different mineral assemblages were assessed by comparing predicted stable assemblages with petrographic observations, and by plotting selected mineral isopleths. In addition, we used the approach described in [Duisterhoeft et Lanari \(2020\)](#), which allows a more rigorous assessment of the match between predicted and measured mineral composition than the standard isopleth approach. It relies on a set of quality factors, which are computed over the whole P-T grid and take values between 0 and 1, 0 meaning very poor fit and 1 meaning that predicted and measured composition are indistinguishable within uncertainty.

4.1.4 Petrographic description

Two well-preserved samples of HP granulite (JB-19-43 and JB-19-56) have been collected in a massive, weakly to non-foliated domain of the Lavey granulite. Another sample (JB-19-55) was collected in a ca. 50 cm thick, highly strained layer retrogressed to amphibolite-facies conditions ([Figure 4.2-c](#)). In addition, two mafic granulite samples (JB-19-16 and JB-19-18) were collected in the Peyre-Arguet granulite body but are generally more retrogressed and do not preserve the early prograde and HP stages. The well-preserved HP granulite samples from La Lavey have been used to constrain the P-T evolution, and mineral assemblage and compositional zoning have been investigated in detail. The granulites from Peyre-Arguet are generally described more briefly. Summary of sample locations and main petrographic features is provided in [Table 4.1](#).

LES GRANULITES DE HAUTE PRESSION DE L'OISANS

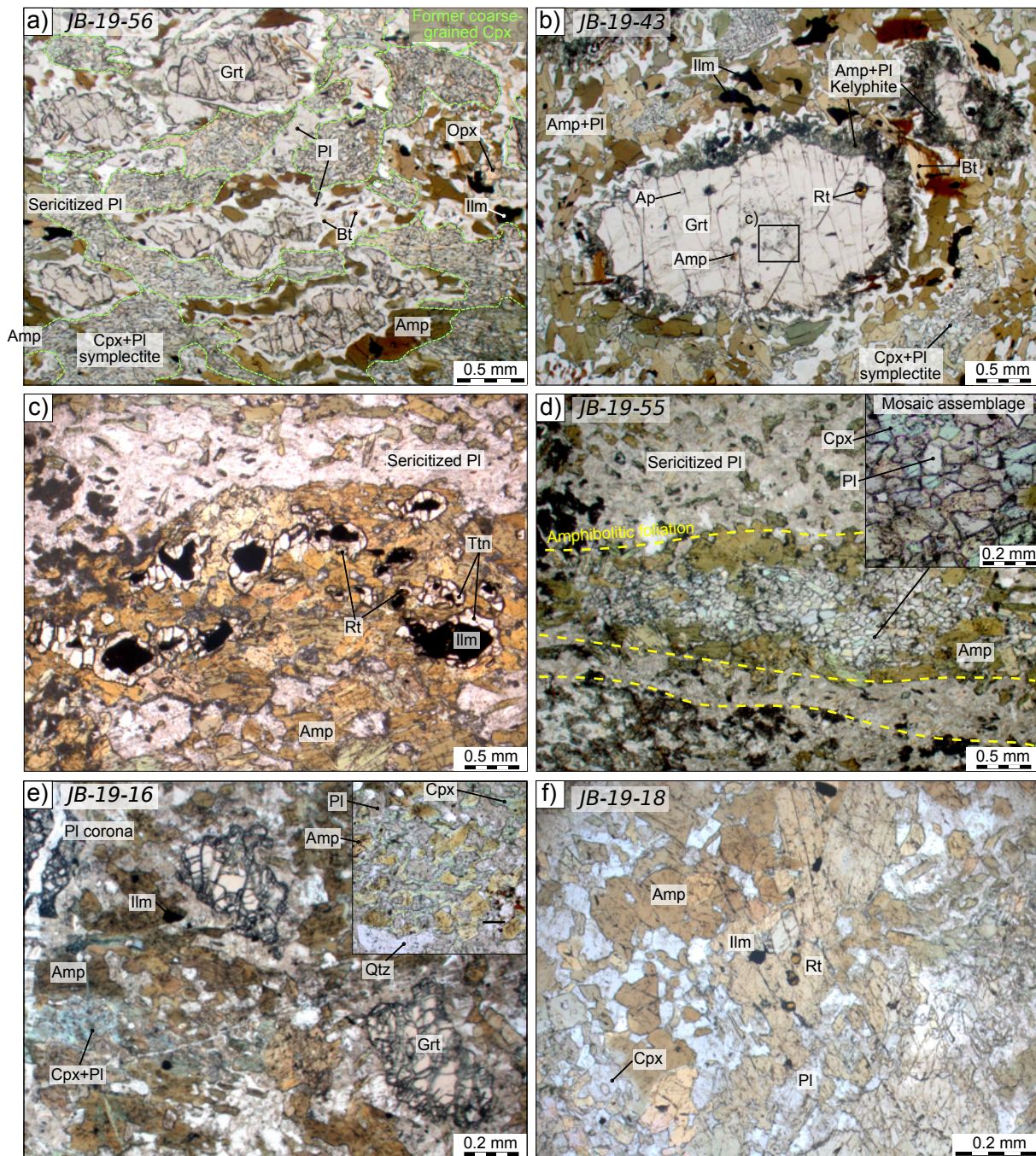


FIGURE 4.3 – Microscope photographs of the granulite samples. (a) – Large field view on the mineral assemblage in sample JB-19-56 (La Lavey), which shows the resorbed garnet and the destabilized clinopyroxene forming the relict HP assemblage. The coarse-grained HT assemblage composed of plagioclase+amphibole+biotite+orthopyroxene develops mainly around the resorbed garnet grains. (b) – Large garnet grain in sample JB-19-43, partly destabilized and surrounded by a kelyphite of plagioclase and amphibole. (c) – Alternating amphibole-rich and feldspar-rich layers in sample JB-19-55. Patches composed of a mosaic of fine-grained (<100 μm) euhedral to sub-euhedral clinopyroxene and plagioclase are preserved in the amphibole-rich layers, and interpreted as relics of the HT granulitic assemblage. (d) – Ilmenite rimmed by titanite in sample JB-19-55. (e) – Mineral assemblage in retrogressed granulite sample JB-19-16. The matrix is mainly composed of plagioclase and amphibole with relict clinopyroxene, and garnet grains are partly resorbed and surrounded by a rim of plagioclase. Former symplectites have partly recrystallized into a mosaic assemblage of plagioclase + clinopyroxene amphibole. (f) – Mineral assemblage in garnet-free sample JB-19-18. Mineral abbreviation follow IUGS recommandation.

4.1 HT overprint of HP granulites in the Oisans–Pelvoux massif

Sample	JB-19-16	JB-19-18	JB-19-43	JB-19-55	JB-19-56
Locality	Peyre-Arguet	Peyre-Arguet	La Lavey	La Lavey	La Lavey
Long°	6.35414	6.35463	6.2199	6.22303	6.21990
Lat°	44.84356	44.84292	44.86604	44.86517	44.86604
Alt (m)	2708	2674	2488	2731	2488
Rock type	Grt-bearing mafic granulite	Grt-free mafic granulite	Grt-bearing mafic granulite	Cpx-bearing amphibolite	Grt-bearing mafic granulite
Main minerals	Amp, Pl, Grt, Qtz, Cpx (relics)	Amp, Cpx, Pl	Grt, Pl, Cpx, Opx, Amp, Bt, Qtz	Amp, Cpx, Pl (sericitized), Kfs	Grt, Pl, Cpx, Opx, Amp, Bt, Qtz
Accessory mineral	Ilm, Zrc, Rt (grt incl. only)	Ilm, Zrc, rare Rt	Ilm, Rt (grt incl. + matrix), Zrc	Ilm, Ttn, rare Rt	Ilm, Rt (grt incl. only), Zrc

TABLE 4.1 – Localization and mineral composition of the investigated samples

4.1.4.1 La Lavey mafic HP granulites (JB-19-43, JB-19-56)

The two HP granulites contain an assemblage of garnet, clinopyroxene, plagioclase, calcic amphibole, quartz and biotite, with accessory rutile, apatite, ilmenite and zircon (Figure 4.3-a,b). Garnet in both samples contain inclusions of quartz and rutile. In addition, garnet of sample JB-19-43 contains inclusions of epidote, chlorite, titanite, amphibole and plagioclase (Figure 4.15). Rare white mica inclusions, which do not present evidence of phengite substitution, have also been observed in garnet. Epidote, chlorite and titanite are absent in the matrix.

Garnet forms 0.5–3 mm wide grains, which are variably resorbed. The most common resorption texture consists in replacement by granoblastic polycrystalline coronas rich in plagioclase (Figure 4.4-b and Figure 4.5-b). Kelyphite with plagioclase + amphibole also occur in sample JB-19-43. Selected grains were imaged by X-Ray mapping in both samples, and compositional variations were quantitatively assessed on 1D profiles (Figure 4.4). In both samples, garnet displays complex internal zoning. The large garnet grain in sample JB-19-43 is considered to preserve prograde zoning, possibly affected by later diffusion (Figure 4.4-a). Two domains are distinguished : a Ca-Mn-rich core (Grt-1 : $\text{Alm}_{48-49}\text{Prp}_{14-16}\text{Grs}_{29-32}\text{Sps}_{04-08}$) and a Mg-rich rim (Grt-2 : $\text{Alm}_{49}\text{Prp}_{25}\text{Grs}_{25}\text{Sps}_{01}$), separated by a broad transitional zone with smoothed compositional gradient attributed to diffusion. Within Grt-1, there is a gradual concentric increase in Ca and Mg correlated with a decrease in Fe and Mn. Concentric

oscillations in Ca observed within Grt-1 are interpreted to result from growth-related processes. Garnet grains in sample JB-19-56 are smaller and more resorbed than in sample JB-19-43 (Figure 4.4-b). They display a broad Ca-rich core domain (Grt-1 : $\text{Alm}_{45-47}\text{Prp}_{24}\text{Grs}_{28-30}\text{Sps}_{01}$) surrounded by a Mg-richer and Ca-poorer domain (Grt-2 : $\text{Alm}_{49}\text{Prp}_{26}\text{Grs}_{24}\text{Sps}_{01}$). Grt-1 displays patchy Ca-zoning, which may be relics of an initial concentric zoning as observed in sample JB-19-43. Grt-1 and Grt-2 are surrounded by a thin Fe-Mn-richer domain (Grt-3 : $\text{Alm}_{52}\text{Prp}_{25}\text{Grs}_{21}\text{Sps}_{02}$), which has no equivalent in sample JB-19-43.

Clinopyroxene is a Na-poor augite ($\text{Na} < 0.03$, $\text{Ca} = 0.85-0.90$ per formula unit (p.f.u), $\text{Mg}\# = 0.66-0.76$, Figure 4.5). It crystallizes in symplectites of plagioclase + clinopyroxene, which replaced an earlier generation of coarse-grained Na-richer clinopyroxene, that is however not preserved. An estimate of the composition of primary coarse-grains clinopyroxene has been obtained by re-integrating the composition over a ca. 400 μm -wide symplectite domain in sample JB-19-56 (Figure 4.5-a). The obtained mineral formula normalized to 6 oxygens is consistent with clinopyroxene ($\text{Si} = 1.97$ p.f.u, sum of cations = 3.93 p.f.u) containing $20 \pm 3\%$ jadeite (Figure 4.5-c). Orthopyroxene is an enstatite ($\text{Mg}\# = 0.50-0.60$) with an Al content between 0.02–0.05 p.f.u. It forms anhedral to sub-euhedral 100–500 μm large grains, and also occurs in small proportions in the symplectites.

Plagioclase mainly crystallizes as fine-grained, granoblastic polycrystalline coronas around resorbed garnet (Figure 4.3-a,b and Figure 4.5-b). Smaller amount of plagioclase is also found in symplectites with clinopyroxene, which have grown by replacement of primary coarse-grained clinopyroxene. Plagioclase composition present a large scattering from Na-rich ($\text{An}_{18}\text{Ab}_{79}\text{Or}_{03}$ for the Na-richest grains) to Ca-rich ($\text{An}_{48}\text{Ab}_{51}\text{Or}_{01}$ for the Ca-richest grains) composition. Na-rich plagioclase is found in the core of the grains in the granoblastic domains as well as in the symplectites, while Ca-rich plagioclase is restricted to thin coronas around garnet and at grain boundaries (Figure 4.3-b,c).

Calcic amphibole is a magnesian and slightly titanian hastingsite ($\text{Al}_{iv} = 1.5-1.9$ p.f.u,

Mg# = 0.55–0.67, Ti = 0.16–0.27 p.f.u, $\text{Fe}^{3+}/(\text{Fe}^{3+}+\text{Al}_{vi}) > 0.5$). It forms sub-millimetric euhedral to sub-euhedral prismatic grains, which crystallize in the matrix around garnet or associated with plagioclase in thin kelyphites in sample JB-19-43. Compositional variations are related to textural position : amphibole in contact with Na-rich plagioclase is poorer in Al ($\text{Al}_{iv} = 1.5\text{--}1.7$) than amphibole in contact with Ca-rich plagioclase ($\text{Al}_{iv} = 1.8\text{--}1.9$).

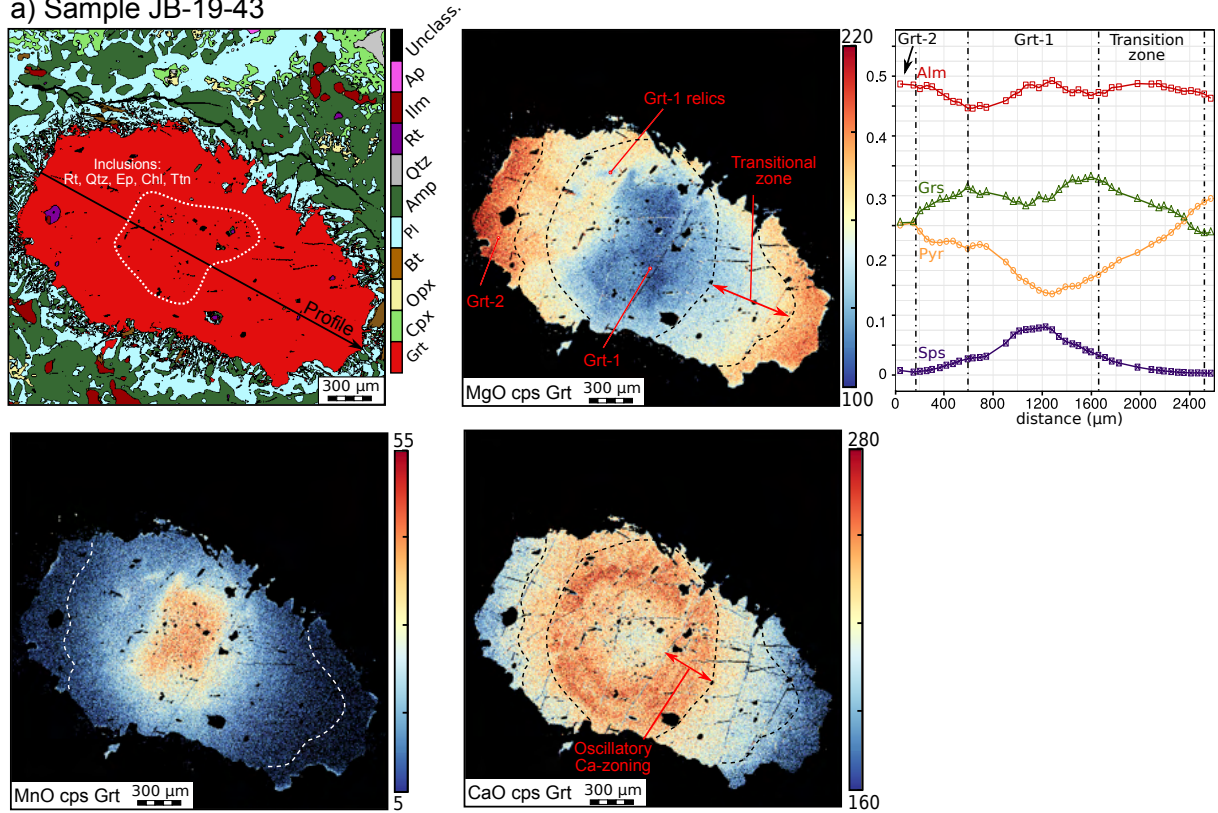
Biotite has Mg# between 0.48 and 0.57 contain about 0.17–0.27 p.f.u Ti. It forms thin 100–200 μm long rods and coarser flakes (up to 1 millimeter-long), which are frequently grouped in patches associated with amphibole and plagioclase around garnet (Figure 4.3-b). Quartz occurs as small (10–20 μm) inclusions in garnet and also forms larger grains (100–500 μm) in the matrix (Figure 4.4).

Rutile and ilmenite occur in both samples. Ilmenite is the main Ti-bearing phase and forms 100–500 μm long grains, mainly located outside of garnet (Figure 4.3-a,b and Figure 4.4). Rutile is mainly preserved as inclusions in garnet, where it forms grains up to 100 μm long, which occasionally display partial replacement by ilmenite and/or contain ilmenite exsolutions (Figure 4.5-c and Figure 4.6-a). In sample JB-19-43 small (generally < 50 μm) grains of rutile also occur outside of garnet, either in inclusion in amphibole or within the symplectites (Figure 4.6-b). No rutile was observed outside of garnet in sample JB-19-56. Zircon is ubiquitous in the mafic granulites, and occurs either as inclusions in garnet porphyroclasts or in the matrix.

4.1.4.2 La Lavey garnet-free amphibolite (JB-19-55)

In contrast with the HP granulites, garnet-free sample JB-19-55 is strongly deformed, with alternating millimeter-wide layers of calcic amphibole and sericitized feldspar. It contains 1–5 mm wide patches composed of a mosaic of equant, fine-grained (<100 μm) euhedral to sub-euhedral clinopyroxene and plagioclase, which are mainly concentrated in the amphibole-rich layers (Figure 4.3-d). Clinopyroxene is a diopside ($\text{Ca} = 0.9\text{--}0.95$ p.f.u, Mg#

a) Sample JB-19-43



b) Sample JB-19-56

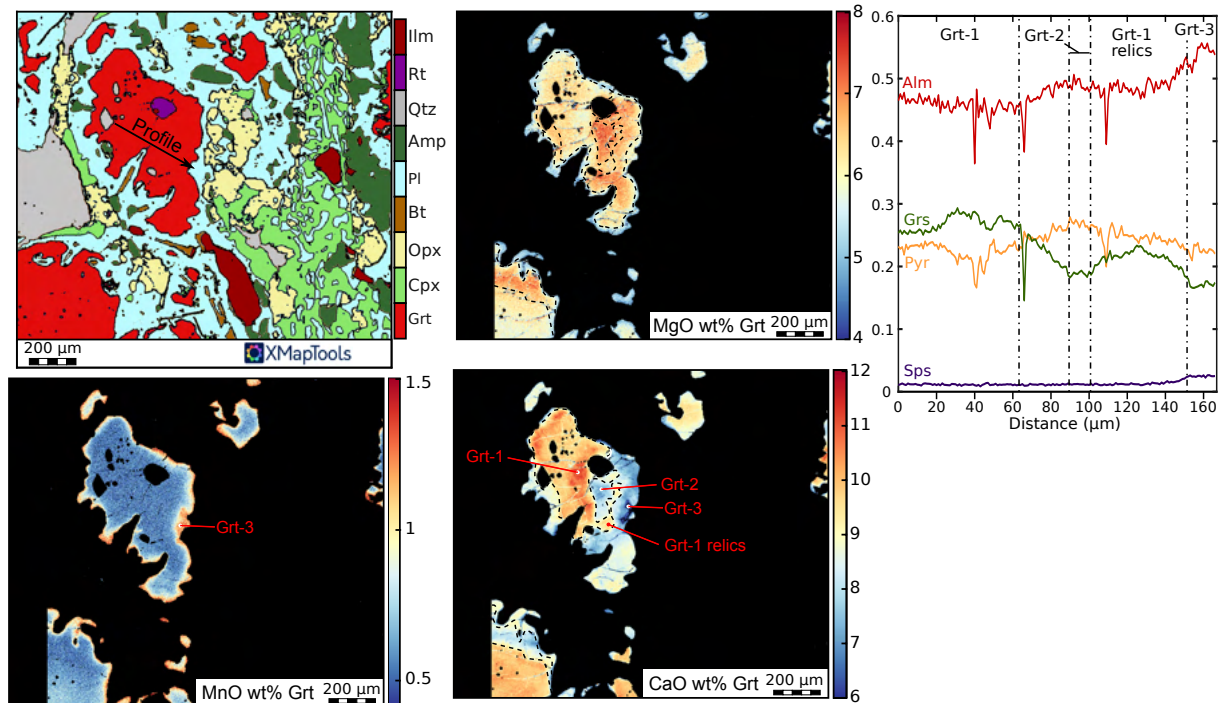


FIGURE 4.4 – (a) – X-Ray map and composition profiles of garnet in samples JB-19-43 (a) and JB-19-56 (b), processed with XMapTools (Lanari *et al.*, 2014). X-Ray maps in sample JB-19-56 were processed using the internal standardization approach of Lanari *et al.* (2018), and are therefore fully quantitative, while EDS map of sample JB-19-43 is only qualitative.

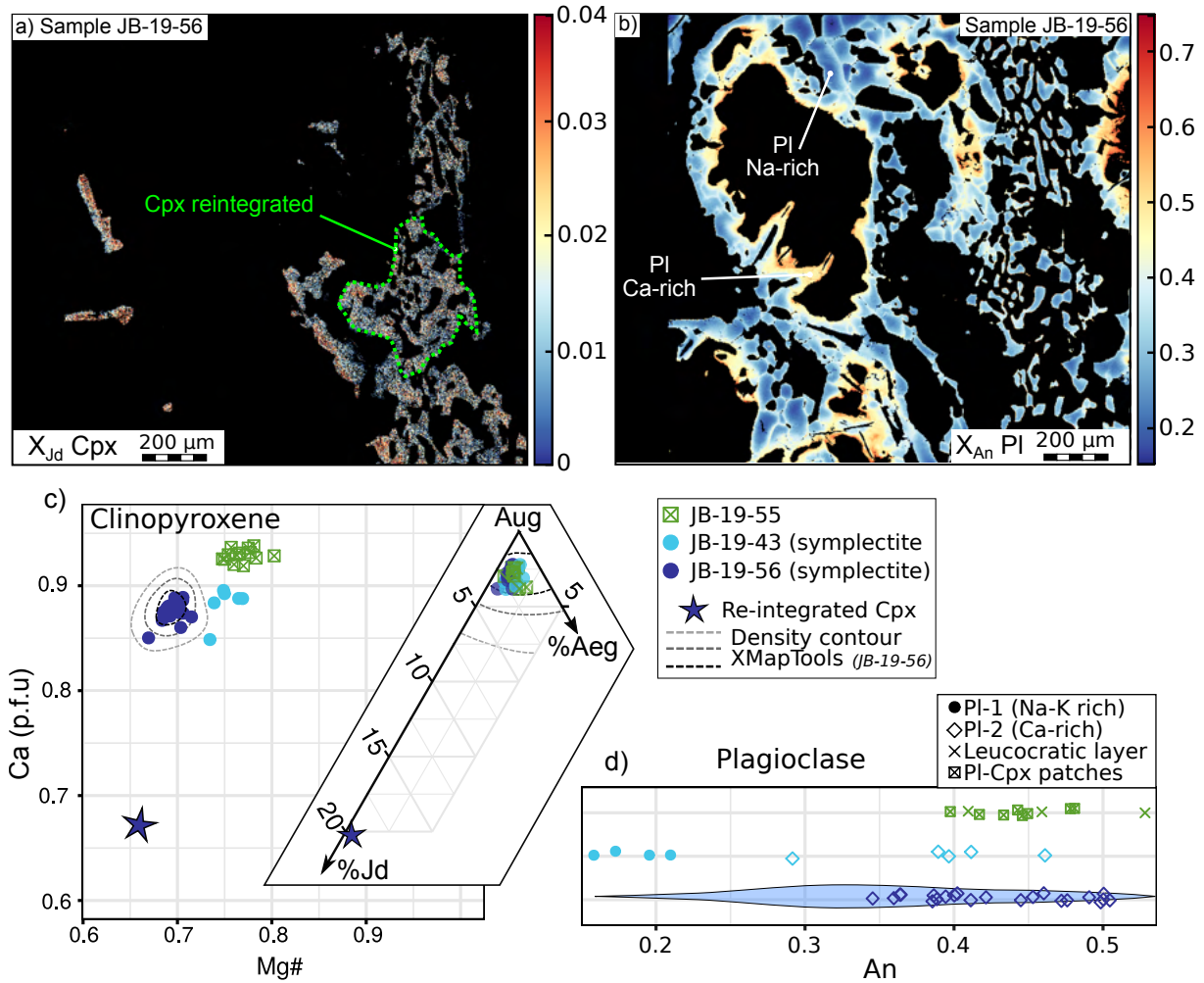


FIGURE 4.5 – Quantitative X-Ray maps of clinopyroxene (a) and plagioclase (b) in sample JB-19-56, processed with XMapTools. The maps correspond to the same domain as in Figure 4-b). (c) – (d). Summary of clinopyroxene (c) and plagioclase (d) electron microprobe analyses in the three samples from La Lavey (JB-19-43, JB-19-55, JB-19-56). Composition of the re-integrated Na-rich clinopyroxene in sample JB-19-56 is shown with a blue star. Distribution of pixel composition on the X-Ray map, obtained by processing with XMapTools, is represented with density contours.

= 0.75–0.80). Plagioclase composition ranges between An_{39-52} , with no significant difference between the larger sericitized grains in leucocratic layers and the plagioclase + clinopyroxene mosaics (Figure 4.5-c). Amphibole is mainly a Ti-poor pargasitic hornblende ($Al_{iv} = 1.41-1.66$, $Mg\# = 0.63-0.68$, $Ti = 0.12-0.17$ p.f.u.). A few grains of actinolite are also found ($Al_{iv} = 0.30-0.75$, $Mg\# = 0.71-0.75$, $Ti = 0.02-0.06$ p.f.u.). Ilmenite is the dominant Ti phase and forms 100–500 μm grains, which are partly resorbed and commonly surrounded by titanite coronas. Rutile is rare and forms small grains (<50 μm), that are commonly

rimmed by titanite (Figure 6-c). Tiny grains (5–20 μm) of late rutile (Rt-II) also crystallized in association with titanite over ilmenite (Figure 6-f).

4.1.4.3 Peyre-Arguet mafic retrogressed granulites (JB-19-16 ; JB-19-18)

Sample JB-19-16 is mainly composed of calcic amphibole, garnet, plagioclase, quartz, with relics of clinopyroxene in symplectites, accessory rutile and ilmenite, and zircon (Figure 4.3-e). No orthopyroxene has been observed. Garnet occurs as partly resorbed, 0.5–2 mm-wide grains surrounded by a corona of sericitized plagioclase (Figure 4.3-e). Clinopyroxene occurs in coarse-grained symplectites, which locally display recrystallization textures in mosaics. In this sample, rutile has only been preserved in garnet where it forms up to 200 μm -large inclusions (Figure 4.6-e).

Sample JB-19-18 contains the same mineral assemblage as sample JB-19-16, except that it completely lacks of garnet, which has been entirely resorbed. It is mainly composed of a granoblastic amphibole and sericitized plagioclase (Figure 4.3-f), with relics of coarse-grained symplectites of clinopyroxene + plagioclase. Ilmenite is the dominant Ti-bearing phase, but rare, small grains of rutile (<50 μm) are found in inclusion in feldspar and amphibole, or in the plagioclase + clinopyroxene symplectites (Figure 4.6-f).

4.1.5 Bulk rock Geochemistry

Whole rock major and trace element compositions (Table S3 and Figure 6) were obtained on the three samples from La Lavey (JB-19-43,55,56) and on one sample from the Peyre-Arguet body (JB-19-16). All samples except sample JB-19-55 display major element composition of Fe-Ti-rich tholeiitic basalts ($\text{Na}_2\text{O}+\text{K}_2\text{O} = 3\text{--}4 \text{ wt}\%$, $\text{SiO}_2 = 48\text{--}50 \text{ wt}\%$, $\text{TiO}_2 = 1.9\text{--}2.3 \text{ wt}\%$, molar $\text{Mg}/(\text{Mg}+\text{Fe}^{2+}) = 0.39\text{--}0.44$). Trace element patterns normalized to N-MORB (composition from Gale *et al.*, 2013) indicate significant enrichment in

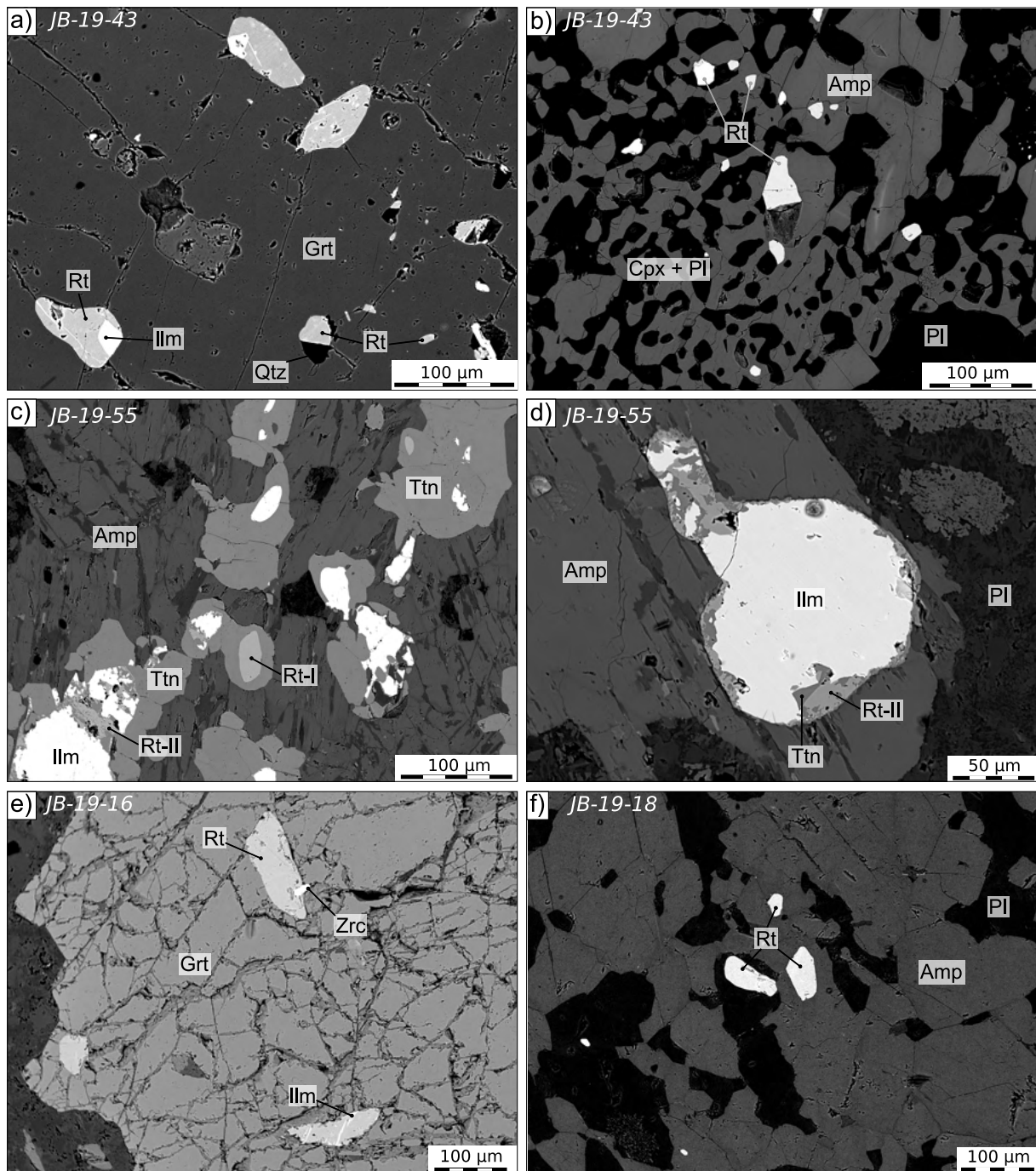


FIGURE 4.6 – Representative BSE images of rutile analyzed in different textural settings. (a) – (b) Rutile inclusions in garnet and matrix rutile in sample JB-19-43. Some rutile inclusions on image (a) display partial replacement by ilmenite; (c) – (d) primary rutile surrounded by titanite and secondary rutile growing over ilmenite in sample JB-19-55. (e) – Rutile inclusions in garnet of sample JB-19-16. (f) – Matrix rutile in sample JB-19-18.

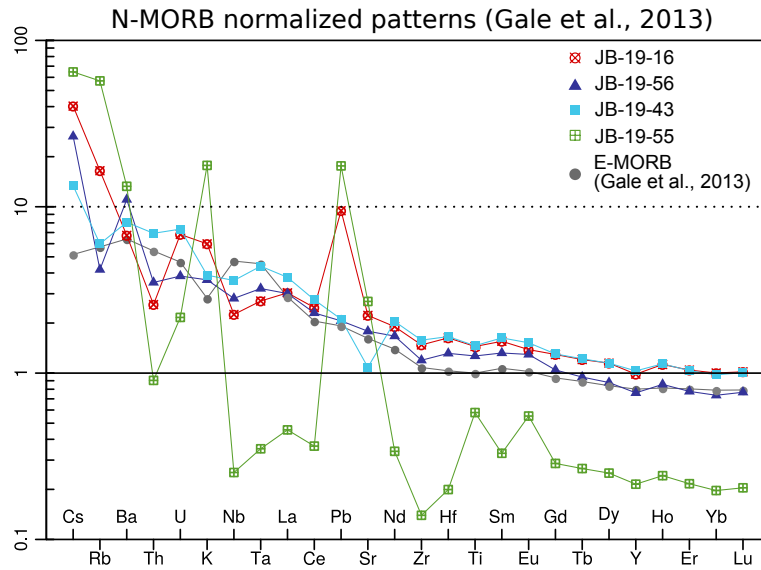


FIGURE 4.7 – Trace element composition of the (retrogressed) mafic granulites, normalized to the composition of N-MORB from Gale *et al.* (2013). E-MORB composition is shown for comparison.

LREE and other incompatible elements $(La/Yb)_N = 3.34\text{--}4.26$, $(Th/Yb)_N = 2.58\text{--}7.09$ (Figure 4.7). Enrichment relative to N-MORB can reach high values for elements highly mobile in fluids (Cs, Rb, U, Pb), especially in sample JB-19-16, which presents strong spikes in Pb, U and Cs. There are no significant Eu anomalies $(Eu/Eu^*)_N = 0.98\text{--}1.04$, with $(Eu/Eu^*)_N = Eu_N / (Sm_N \cdot Gd_N)^{1/2}$ and Nb–Ta anomalies are weak $((Th/Nb)_N = 1.15\text{--}1.92)$.

Sample JB-19-55 has a distinct composition both in major and trace elements. It is much richer in K_2O , Al_2O_3 and MgO ($Mg\# = 0.56$) than other samples. It roughly follows the same LREE/HREE fractionation as observed in the other samples $((La/Yb)_N = 2.56)$, but REE concentrations are one order of magnitude lower than that of other mafic granulites. It presents extreme enrichment in fluid-mobile elements, in particular Cs, Rb, Ba and Pb, positive anomalies in Eu $(Eu/Eu^*)_N = 1.74$, Sr, Ti and negative anomalies in Nb and Ta $((Th/Nb)_N = 3.58)$. The overall low REE, the strong positive Eu anomalies in Eu, Sr and Pb suggest plagioclase-rich cumulates as protolith. The high K_2O content and the large enrichment in fluid-mobile elements in this sample suggest pervasive interaction with crustal fluids during metamorphism.

4.1.6 Thermobarometry

4.1.6.1 Inverse thermobarometry and forward thermodynamic modeling

The P-T evolution of the Lavey granulitic body has been inferred using the three samples JB-19-43, JB-19-56 and JB-19-55. These samples preserve different stages of the P-T evolution and were therefore used to constrain different portions of the P-T path. Sample JB-19-43 contains garnet with the most complete zoning, and preserved evidence of an early prograde phase characterized by the formation of Mn-rich garnet cores containing inclusions of epidote, chlorite, titanite and white mica. It has therefore been used to constrain the early prograde evolution. Sample JB-19-56 has then been used to constrain peak-P / post peak-P decompression at HT based on quantitative X-Ray mapping. Finally, sample JB-19-55 is heavily retrogressed in the amphibolite-facies and has been used to constrain retrogression to lower T using inverse thermobarometry.

Inclusions of OH-bearing minerals such as epidote or chlorite in garnet of sample JB-19-43 suggest that garnet growth initiated under H₂O-rich conditions. This is further supported by the Mn-rich composition of the garnet cores, which could only be reproduced in PerpleX by adding a high amount of H₂O close to fluid-saturation in the reactive bulk. The P-T phase diagram for sample JB-19-43 was therefore computed using the bulk rock composition measured by ICP-OES and assuming saturation in H₂O (Figure 4.8-a). Garnet becomes stable over ca. 0.4–0.6 GPa, and combined presence of chlorite, epidote, titanite and white mica indicates equilibration at T between 460 and 550°C and P between 0.4 and 1.0 GPa. Then, presence of rutile and amphibole inclusions mark progressive increase in P and T over 550°C and 0.8 GPa. This relatively mild T is in line with the preservation of Ca-Mn-rich garnet core (Grt-1). Ca–Mn isopleths indicate P–T conditions around 550–600°C and 0.8–1.1 GPa for Grt-1. Smoothed zoning on X-Ray maps indicate post-growth diffusion, in

particular in Mg. Therefore, it is likely that garnet composition has been partially reset by diffusion exchange and P–T conditions for Mn-rich core are thus maximal estimates. Increase in Mg-content between Grt-1 and Grt-2 is consistent with increasing T and P during prograde to peak-P evolution, but precise quantitative estimations are hampered by post-growth diffusion and fractionation of components in garnet cores.

The HP stage in sample JB-19-56 has been modeled using a local composition extracted from the X-Ray map. H₂O was treated as a standard thermodynamic component with a fixed amount, which was adjusted to fit with the observed proportion of OH-bearing phases (biotite and amphibole) in the local domain. The mineral mode match criterion (Q_{vol}) of [Duesterhoeft et Lanari \(2020\)](#) indicates reasonably good fit between observed and predicted modal composition ($Q_{vol} > 80\%$) over a wide domain between 0.5 and 1.5 GPa ([Figure 4.17](#)). The local composition used in input is therefore considered to be appropriate within this range. The HP stage assemblage is inferred as Grt-2–Cpx–Qtz–Rt, possibly with plagioclase, amphibole and/or biotite. Although Na-rich clinopyroxene is no longer present, its composition was inferred from compositional mapping through the Cpx–Pl symplectite, indicating a reintegrated composition of ca. 20% Jd. Phase diagrams computed for samples JB-19-56 and JB-19-43 ([Figure 4.8](#)) both predict presence of OH-bearing minerals, either amphibole + biotite or phengite, up to HT conditions. Some inclusions of amphibole are present in garnet of sample JB-19-43. Therefore, it is likely that amphibole, and possibly biotite were part of the peak-P assemblage, but no phengite has been observed. The stability field of the HP assemblage corresponds to a broad domain between 600–800°C and 1.0–1.8 GPa ([Figure 4.8-b](#)). Composition quality factors (Q_{cmp}) computed for Grt-2 yields the best match at 650–730°C and 1.5–1.7 GPa. This P–T range is consistent with the jadeite content in Cpx estimated by re-integration, which constrains P around 1.55–1.65 GPa for the same range of T.

Two HT decompression stages (stages 3 and 4) are distinguished from mineral zoning and assemblages in JB-19-56. Decompression is associated with resorption of garnet and clinopyroxene, which are replaced by plagioclase, Na-poor clinopyroxene, amphibole, and then orthopyroxene below ca. 1.0 GPa. Biotite and quartz are also part of this assemblage. Most of the plagioclase in the symplectites and the granoblastic coronas around resorbed garnet is Na-rich (An_{18-30}), which according to our thermodynamic calculations indicates that most of the resorption occurred at relatively high-P between 1.0 and 1.3 GPa (Figure 4.8-c). Temperature during this first stage of decompression (stage 3) is thought to have been relatively high, as evidenced by relatively K-rich plagioclase cores (Or_{03}), which indicates T around 750–800°C, and high Ti-content in biotite (> 0.2 p.f.u), which implies equilibration between 780 and 820°C. These temperatures are consistent with those estimated with Na-rich plagioclase – Al-poor amphibole pairs, which yield an average $T = 764 \pm 27^\circ\text{C}$ (assuming $P = 1.2$ GPa), both in the granoblastic coronas and in the symplectites.

The formation of the thin Ca-rich plagioclase rims around garnet and at grain boundaries (An_{40-48}) indicates a second stage of decompression to 0.6–0.9 GPa (stage 4). This stage is associated with the formation of the thin garnet rims (Grt-3) in sample JB-19-56, which presents an increase in Mn relative to Grt-2 that can only be reconciled with growth at low-P close to the Grt-out boundary. Q_{cmp} computed for Grt-3 yields a good fit between 0.7 and 1.0 GPa and over a wide range of T (650–900°C). The edenite-richterite thermometer applied to Al-rich amphibole in contact with Ca-rich plagioclase yields high T at $833 \pm 34^\circ\text{C}$ (assuming $P = 0.8$ GPa). Thus, sample JB-19-56 records decompression from HP conditions at 650–730°C and 1.5–1.7 GPa to 0.7–1.0 GPa and 800–870°C, which corresponds to an increase in T of ca. 100–200°C during decompression.

Retrogression to lower T is mostly visible in sample JB-19-55, which has been heavily retrogressed to the amphibolite-facies. We used plagioclase-amphibole pairs located at the interface between amphibole and plagioclase-rich layers to constrain T. These minerals pre-

Sample	Domain	n pairs	P(GPa)	T(°C)	$\pm 1\sigma(^{\circ}\text{C})$
JB-19-56	granoblastic coronas (Na-rich Pl)	52600	1.2	763	25
JB-19-56	Symplectites (Na-rich Pl)	23400	1.2	764	27
JB-19-56	Garnet rim (Ca-rich Pl)	12340	0.8	833	35
JB-19-55	Amp-Pl layers (Hornblende)	13	0.4	656	34
JB-19-55	Amp-Pl layers (Actinolite)	3	0.4	573	44

TABLE 4.2 – Summary of results of plagioclase-amphibole inverse thermometry (Holland et Blundy, 1994). For each sample, reported T is an average of results obtained on multiple plagioclase-amphibole pairs. Number of pairs (n) is given for each sample, and 1-sigma standard deviation is reported as a measure of dispersion. Results of sample JB-19-56 were obtained directly on the X-Ray map using the P-T spot add-on of XMapTools.

sumably crystallized during retrogression at lower P than the HT stage 4, and therefore temperature estimates are reported for an assumed pressure of 0.4 GPa. Pargasitic hornblende – plagioclase pairs yield an average T at $656\pm 34^{\circ}\text{C}$ (13 pairs), while actinolite – plagioclase pairs yield an average T at $573\pm 44^{\circ}\text{C}$ (3 pairs).

In contrast with the La Lavey HP granulites, The Peyre-Arguet granulite is more retrogressed, and samples JB-19-16 and JB-19-18 are therefore less suitable to determine P-T path, particularly on the prograde or HP stages. Given petrographic retrogression similarities with the La Lavey samples (e.g. plagioclase corona around garnet in JB-19-16, and conspicuous clinopyroxene–plagioclase symplectite relics), they are nevertheless assumed to have also undergone a HP stage followed by HT decompression. This HT metamorphism was here independently confirmed by the Zr-in rutile thermometry.

4.1 HT overprint of HP granulites in the Oisans–Pelvoux massif

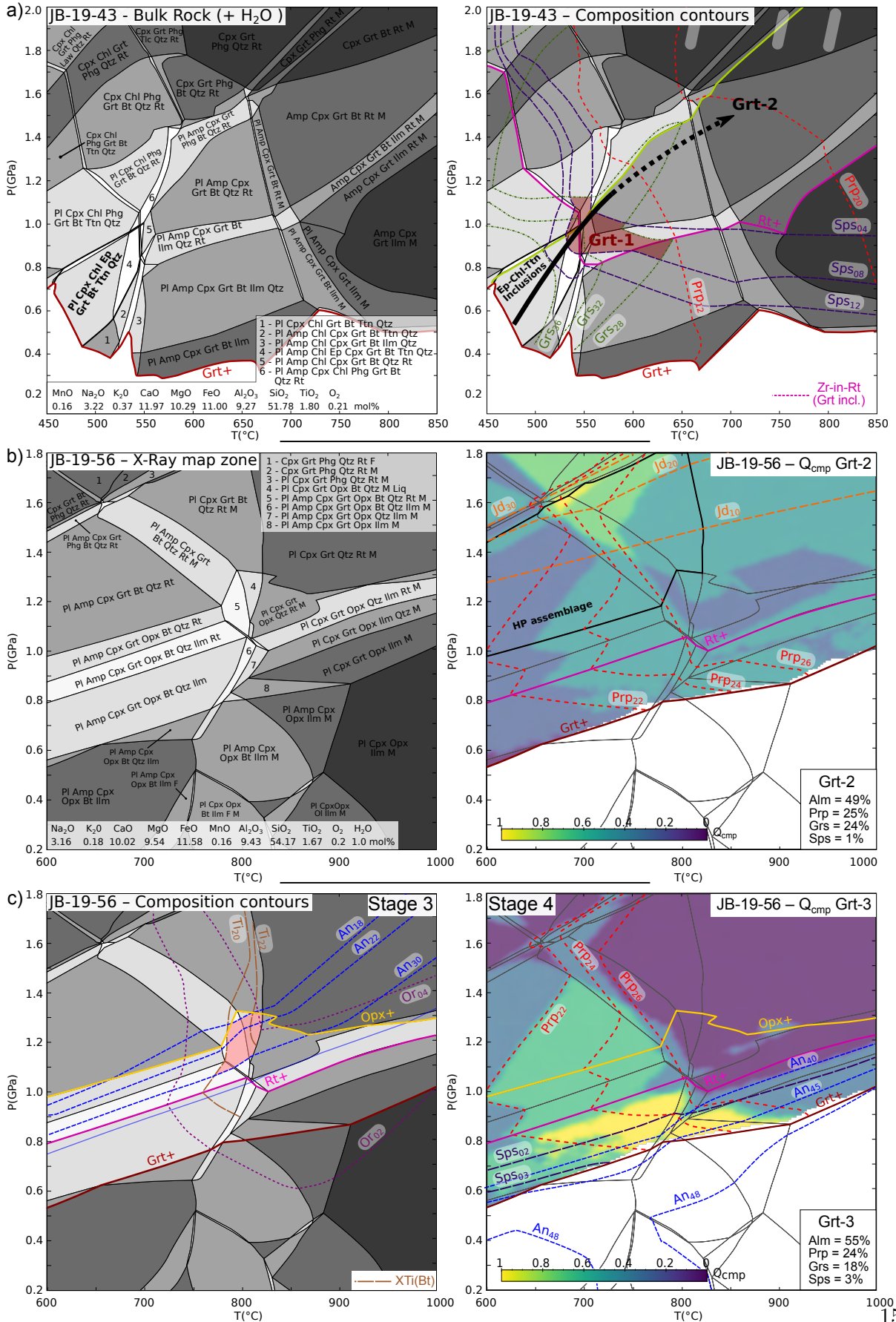


FIGURE 4.8 – Phase diagrams computed with PerpleX and P–T constraints for the early prograde stage (a), the HP stage (b) and HT decompression (c). See description in text.

4.1.6.2 Zr-in-rutile (ZiR) thermometry

Rutile was analyzed in different textural settings in the five samples from La Lavey and Peyre-Arguet to spot possible relation with composition in Zr and other trace elements. Several grains were analyzed in multiple spots to check possible core-rim zoning. Variation in Zr-content within a single grain are generally small to insignificant, which rules out significant loss of Zr by diffusion in the rims.

Several populations of rutile are distinguished based on Nb-Zr systematics (Figure 4.9-a). Rutile inclusions in garnet generally display low Nb content (<1000 ppm, except a few grain in sample JB-19-43 with higher Nb) and large scattering in Zr (304–1119 ppm in sample JB-19-43 and 355–1298 ppm in sample JB-19-16). In sample JB-19-43, highest Zr-content are observed in rutile inclusions which display partial replacement by ilmenite, but such a relation is not observed in sample JB-19-16. Several grains are located close to or in contact with zircon but do not display significant difference in Zr with other grains. In contrast, matrix grains display important scattering in Nb (470–2350 ppm in sample JB-19-43, 180–2310 ppm in sample JB-19-55 and 800–3750 ppm in sample JB-19-18), and high Zr content (851–1291 ppm in sample JB-19-43, 803–1223 ppm in sample JB-19-55 and 1147–1593 ppm in sample JB-19-18). Rutile grains separated from sample JB-19-56 and analyzed by LA-ICPMS form a cluster of Nb–Zr poor analyses (Nb = 500–890 ppm, Zr = 220–342 ppm) similar to that of rutile inclusions in garnet. No matrix rutile was observed in the petrographic thin section of sample JB-19-56, and therefore it is very likely that the separated grains were initially included in garnet. Finally, late rutile found around ilmenite in sample JB-19-55 displays very low Zr and Nb content (Nb = 28–124 ppm and Zr = 41–78 ppm).

Temperatures were obtained using the calibration of [Kohn \(2020\)](#), which has a dependence in P of ca. $+50^{\circ}\text{C.GPa}^{-1}$. According to phase diagrams computed for samples JB-19-43 and JB-19-56, rutile may have equilibrated anywhere between 0.8 and 1.6 GPa during the prograde or the retrograde evolution. A central value of 1.2 GPa was used for all the grains, except for the late rutile in sample JB-19-55, which is assumed to have formed during late retrogression and for which P was set to 0.4 GPa. Applying a nominal P of 1.2 GPa yields to slightly underestimate or overestimate T if rutile formed respectively at higher or lower P. Considering the possible range of P for rutile growth, this uncertainty is at most of $\pm 20^{\circ}\text{C}$. There are no P estimates for rutile of the Peyre-Arguet samples, but considering the strong similarities in composition and mineral assemblages with the samples from La Lavey, these rocks may have evolved approximately within the same range of P. Therefore, uncertainties related to unknown P during rutile growth are within the same range of $\pm 20^{\circ}\text{C}$. Quartz is stable over the whole stability field of rutile ([Figure 4.8](#)) and zircon seems to have been reactive over a large part of the P–T evolution, as suggested by the large scattering of U–Pb dates in metamorphic zircon rims (see below). We therefore assume that rutile has grown under SiO_2 and ZrO_2 saturated conditions.

Zr-poor separated grains (JB-19-56), consistently yield low T between 611°C and 650°C ([Figure 4.9-b](#)). The large spread of Zr content in rutile inclusions (samples JB-19-43 and JB-19-16) translates into a spread in temperature from 637 to 775°C in sample JB-19-43 and from 654 to 793°C in sample JB-19-16. In contrast, matrix rutile yields T clustered between 743°C and 792°C in sample JB-19-43, between 737 and 785°C in sample JB-19-55 and between 778 and 818°C in sample JB-19-18. Finally, low-Zr rutile in sample JB-19-55 yields low T between 457 and 499°C , although with large uncertainty (ca. 40 – 60°C), due to poor precision on the Zr measurements.

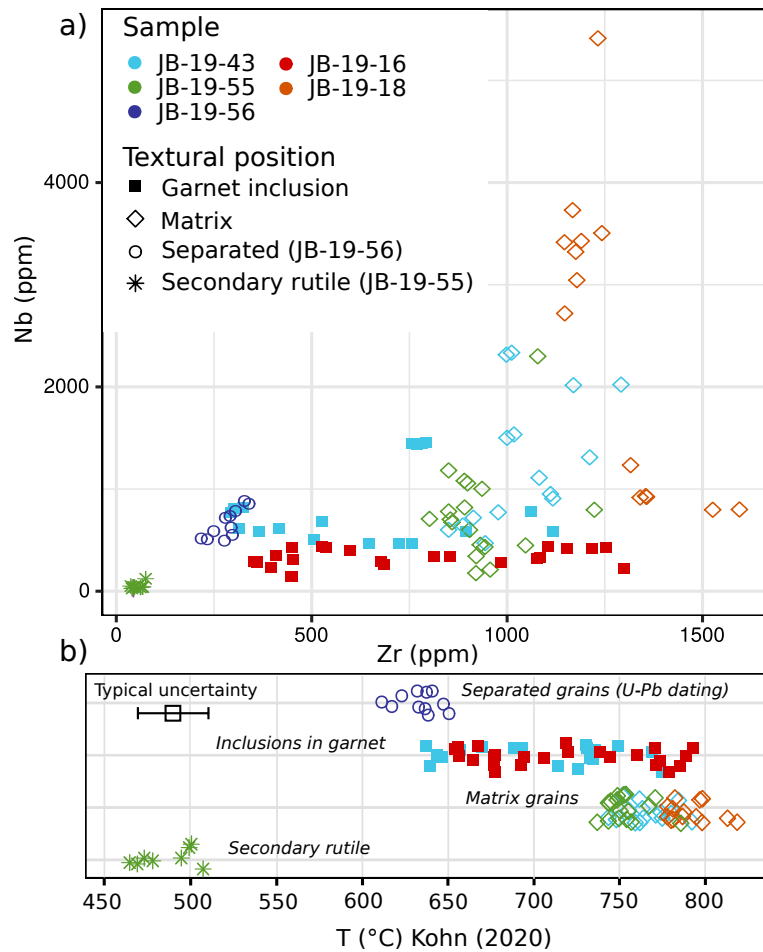


FIGURE 4.9 – a) – Zr–Nb content in rutile measured in-situ by electron microprobe and on separated grains by LA-ICPMS. (b) – Zr temperatures computed using the calibration of [Kohn \(2020\)](#), assuming $P = 1.2$ GPa (0.4 GPa for secondary rutile in sample JB-19-55). A typical uncertainty of ± 20 °C is inferred combining analytical and calibration uncertainties.

4.1.7 U-Pb Geochronology

4.1.7.1 Composition and internal textures of zircon and rutile

The garnet-bearing mafic HP granulite JB-19-56 was selected for U-Pb dating of zircon and rutile. The zircon grains are typically 100–200 μm in size and are rounded to sub-euhedral ([Figure 4.10-a](#)). They present CC-dark cores with frequent oscillatory or broad sector zoning. Most of the zircon cores present homogeneous CC-bright rims of variable width (10–50 μm), which display embayments. Rutile grains separated for U-Pb dating are

100–250 μm in diameter and are devoid of ilmenite exsolutions and/or replacement.

Thorium and U contents in zircon were measured during SIMS analysis and values are generally consistent with LA-ICPMS data measured on the same domain, considering the different volumes sampled. LA-ICPMS trace element analyses of zircon grains were filtered by monitoring P, Y, Sr, Ti and Nb, and analyses presenting an unusually high concentration of these elements were discarded, as they are likely sampling micro-inclusions. REE patterns normalized to chondrite composition (Palme et O’Neill, 2004), Eu anomaly Eu/Eu^* and Th/U ratios are used as proxies to discriminate between different zircon populations (Figure 4.10-b). The zircon cores are older (>400 Ma) with respect to the rims (<350 Ma) and have a distinct Th–U and REE systematic. Grain cores generally contain 50–900 ppm U and display Th/U ratios in the range 0.28–0.99, while rims contain 2–40 ppm U and display Th/U ratios generally lower than 0.2. The zircon cores are around one or two orders of magnitude richer in REE than the younger zircon rims, they present slight to strong negative Eu anomalies ($\text{Eu}/\text{Eu}^* = 0.17\text{--}0.47$) and are enriched in HREE with respect to the L–MREE (Lu–Yb concentrations 1000 times chondrite and $(\text{Lu}/\text{Gd})_N = 17\text{--}40$). The zircon rims are poorer in REE with a variety of patterns ranging from flat to strongly enriched in HREE ($(\text{Lu}/\text{Gd})_N$ ranging from 1.4 to 614). Eu anomaly ranges from weakly negative to positive ($\text{Eu}/\text{Eu}^* = 0.88\text{--}1.53$). There is no clear relationship between the U–Pb dates and the shape of REE profiles for the rims.

The Ti content of zircon ranges from 4.6 to 9.9 ppm in the cores, and from 1.1 to 10 ppm in the rims, excluding one outlier. Using the Ti-in-zircon (TiZ) thermometer of Ferry et Watson (2007) assuming TiO_2 and SiO_2 saturation, this converts to T ranging from 677 to 745°C for the cores and from 575 to 746°C for the rims. Assuming TiO_2 activity reduced to 0.5 if ilmenite was the stable Ti phase during zircon crystallization increases T estimates by ca. 70°C (737–814°C for the cores and 622–815°C for the rims).

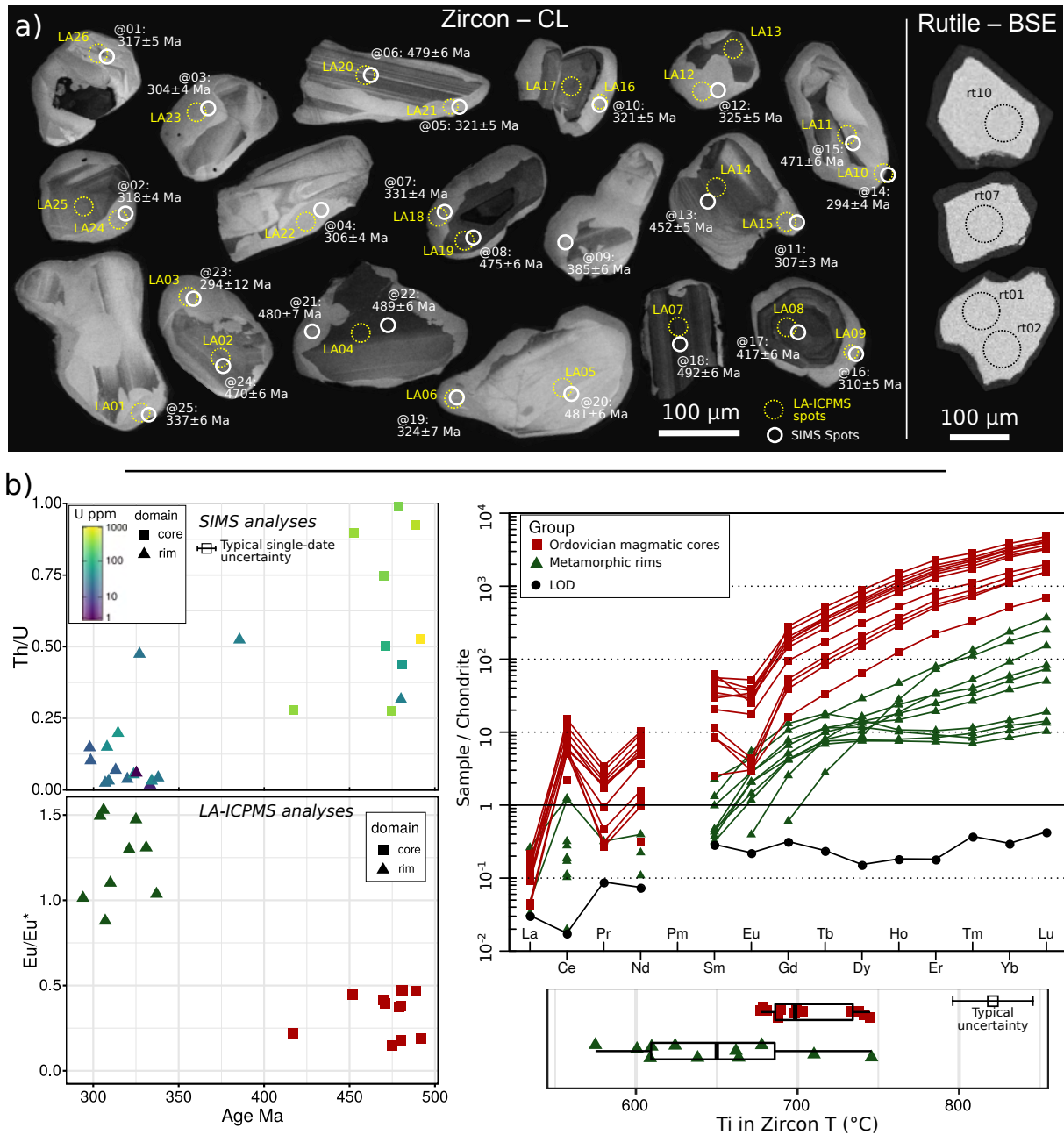


FIGURE 4.10 – (a) – Charge Contrast (CC) images of dated zircon grains and BSE images of representative rutile in sample JB-19-56, with reported positions of SIMS and LA-ICPMS spot analyses. (b) – REE profiles and trace element proxies used to identify the different zircon populations. Ti-in-zircon temperatures calculated using the calibration of [Ferry et Watson \(2007\)](#) are reported in the bottom right panel.

4.1.7.2 Zircon and rutile U-Pb dating

Most of U-Pb analyses of zircon cores are concordant (more than 95%) and yield $^{206}\text{Pb}/^{238}\text{U}$ dates in the range 470–492 Ma (Figure 4.11-a), with the exclusion of three younger outliers. The $^{206}\text{Pb}/^{238}\text{U}$ weighted mean age of 479 ± 5 Ma is calculated from eight zircon cores analyses, which is within uncertainty the same as the concordia age. Zircon rims analyses contain more common Pb (f206 up to 6%) and are best displayed in the Tera-Wasserburg diagram (Figure 4.10-c). Analyses corrected for common Pb assuming present day $^{207}\text{Pb}/^{206}\text{Pb}$ value according to Stacey et Kramers (1975) display $^{206}\text{Pb}/^{238}\text{U}$ dates scattering between 294 and 337 Ma (Figure 4.10-b). Zircon U–Pb dates present a bimodal distribution, with two clusters around 318–326 Ma and 303–310 Ma. There is no discernible correlation between U–Pb dates and composition or internal texture of the zircon rims.

The rutile extracted from sample JB-19-56 contains significant common Pb, 43 analyses from 34 different grains define a linear regression in the Tera-Wasserburg diagram (Figure 11-c). The intercept age is 337 ± 7 Ma (MSWD=1.3) with a free upper intercept for $^{207}\text{Pb}/^{206}\text{Pb}$ of 0.80 ± 0.04 . This value is within uncertainty that of the present-day value predicted by the Stacey et Kramers (1975) model.

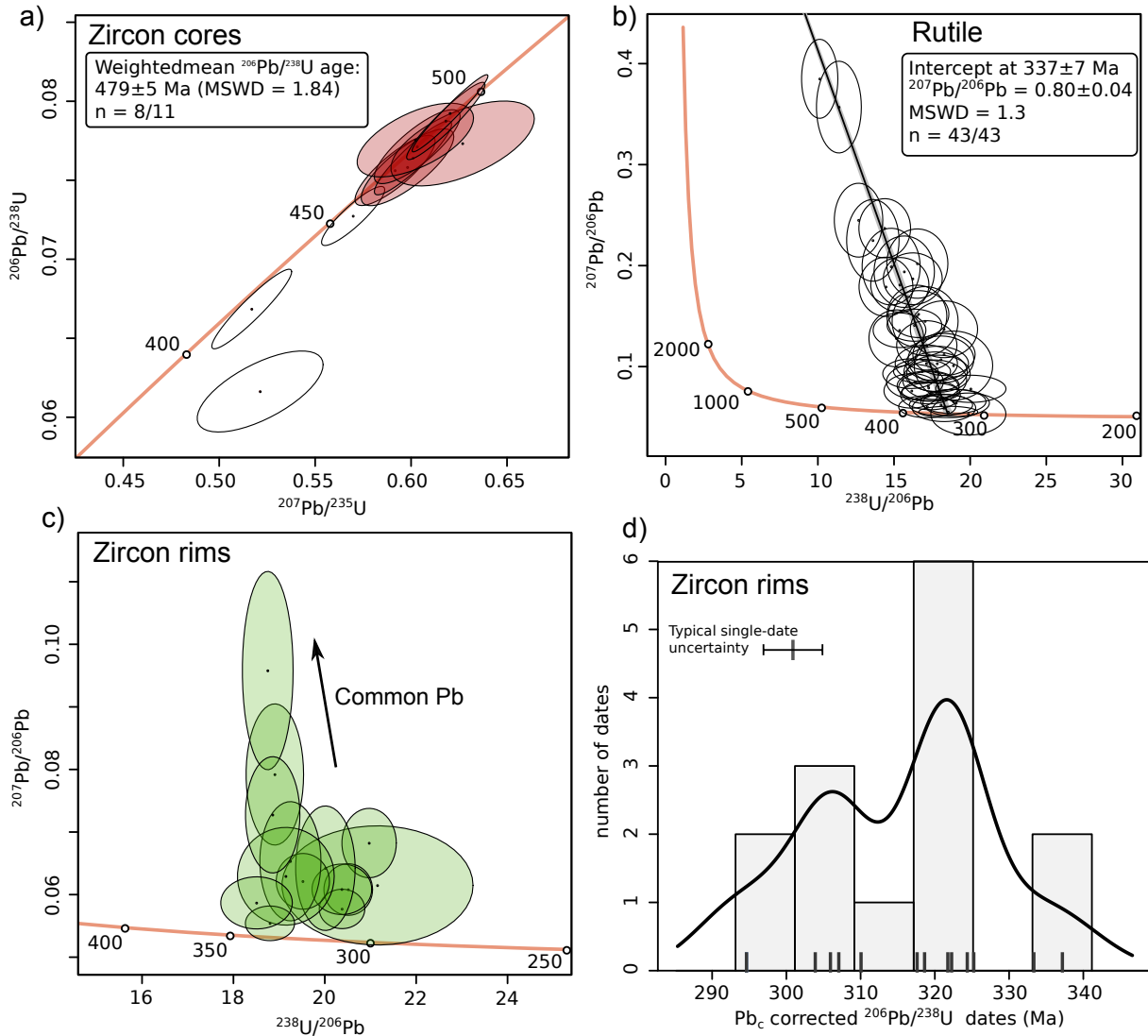


FIGURE 4.11 – U-Pb zircon and rutile dating of sample JB-19-56. (a) – Zircon core analyses defining the age of the protolith; data uncorrected for common Pb. (b) – Tera-Wasserburg diagram of rutile U-Pb analyses, uncorrected for common Pb. (c) – Tera-Wasserburg diagram of zircon rim analyses uncorrected for common Pb. The black arrow points to the $^{207}\text{Pb}/^{206}\text{Pb}$ value of present-day common Pb according to [Stacey et Kramers \(1975\)](#). (d) – Kernel density estimate and histogram of $^{206}\text{Pb}/^{238}\text{U}$ dates in zircon rims, corrected for common Pb according to the $^{207}\text{Pb}/^{206}\text{Pb}$ present-day value of the model of [Stacey et Kramers \(1975\)](#).

4.1.8 Discussion

4.1.8.1 Emplacement of the mafic protoliths

The zircon cores in the dated mafic granulite sample (JB-19-56) present typical features of magmatic zircon. They generally display oscillatory or broad sector zoning, are richer in U than the rims and present high Th/U typical of magmatic zircon (Corfu *et al.*, 2003; Hoskin *et Schaltegger*, 2003). The steep REE patterns and the negative Eu anomalies are consistent with crystallization from a basaltic melt fractionating plagioclase (Hoskin *et Schaltegger*, 2003). The Ordovician age of 479 ± 5 Ma of the zircon cores is therefore interpreted as the crystallization age of the magmatic protolith. This age is within uncertainty the same as that obtained for zircon in a sample from the Peyre-Arguet granulite at 471 ± 5 Ma (Fréville *et al.*, 2022), which suggests that these two bodies were emplaced during the same magmatic event. This Ordovician age is consistent with the regional record in the ECM, where most of igneous mafic protoliths yield ages between 450 and 480 Ma (Jacob *et al.*, 2021a; Paquette *et al.*, 1989; Rubatto *et al.*, 2010). Cambrian–Ordovician magmatism is widespread in the Variscan basement of Europe (Pin *et Marini*, 1993), and is generally attributed to a regional extensional event that affected all the northern part of Gondwana and resulted in the rifting of the Rheic and Saxo-Thuringian Oceans during the Early-mid-Ordovician.

4.1.8.2 Metamorphic evolution of the HP mafic granulites

P–T evolution of La Lavey granulitic body

Inverse thermobarometry and forward modeling in the samples from La Lavey provide reliable constraints for five different metamorphic stages, which allow to reconstruct a comprehensive P–T path from the early prograde (stage 1) to the late retrograde phases (stage 5). The early prograde phase (stage1) is constrained by Mn-rich garnet cores (Grt-1) in sample JB-19-43, which contain inclusions of epidote, chlorite, titanite and white mica. Thermo-

dynamic modeling indicates conditions of the amphibolite-facies during stage 1 (460–550°C and 0.4–1.0 GPa), which rules out possible evolution along a low-T geotherm at blueschist-facies conditions typical of subduction environments. Then, progressive increase in T and P is marked by increasing modal proportion of garnet, entrapment of rutile inclusion and progressive increase in Mg associated with decrease in Ca from Grt-1 to Grt-2. The pressure peak (stage 2) is constrained at 650–730°C and 1.5–1.7 GPa based on composition of Mg-rich garnet (Grt-2) and estimation of the highest jadeite content in clinopyroxene by reintegration of the symplectites.

Decompression following the pressure peak is associated with resorption of garnet and coarse-grained clinopyroxene, which are replaced respectively by a polycrystalline, plagioclase-rich granoblastic corona and by plagioclase + clinopyroxene symplectites. Recrystallization of the symplectites into a mosaic assemblage of plagioclase and clinopyroxene is observed, in particular in relict granulitic domains in sample JB-19-55. These annealing textures are indicative of HT conditions during decompression. They contrast with fine-grained (vermicular) symplectites commonly observed in retrogressed eclogites or HP granulites, in particular in those from the other ECM of Belledonne, Aiguilles–Rouges and Argentera ([Jacob *et al.*, 2021a](#); [Jouffray *et al.*, 2020](#); [Vanardois *et al.*, 2021](#)). Two stages of decompression are identified (stages 3 and 4), which correspond to different compositions of plagioclase (Na-rich or Ca-rich) and amphibole (Al-poor or Al-rich). They occurred at HP to MP conditions (stage 3 : 1.0–1.3 GPa and 730–800°C; stage 4 : 0.6–0.9 GPa and 800–870°C). According to the amount of Na vs Ca-rich plagioclase, most of the retrogression has occurred during stage 3, while stage 4 is more discrete and produced only a stealth overprint around garnet and between the plagioclase grain boundaries ([Figure 4.4-a](#)). Stage 4 is associated with the formation of a thin garnet rim enriched in Mn (Grt-3) in contact with Ca-rich plagioclase. Garnet overgrowth during decompression may result from local enrichment in Mn around the resorbing garnet grains.

Finally, stage 5 corresponds to late retrogression and cooling at amphibolite-facies conditions. It is associated with pervasive rehydration (metasomatism) and intense deformation, which resulted in development of a layered plagioclase-amphibole assemblage, which almost completely overprint the former HT granulitic assemblage. The latter is only preserved as relics in the plagioclase + clinopyroxene mosaic domains. This retrogression occurred over a large range of T from the HT amphibolite-facies ($656\pm 33^\circ\text{C}$) to the LT amphibolite-facies ($573\pm 44^\circ\text{C}$) based on plagioclase–amphibole thermometry.

Interpretation of Zr-in-rutile temperatures

Rutile temperatures in samples from La Lavey are consistent with this P–T evolution. Rutile inclusions in garnet yield T scattering between 611 and 775°C (assuming that separated rutile from sample JB-19-56 comes from former inclusions). The lower end of this range is consistent with prograde entrapment of rutile in garnet between stage 1 and stage 2, while the higher end yields approximately the same T as matrix rutile and indicates equilibration during heating under decompression. Most of HT rutile inclusions display textures indicative of partial replacement by ilmenite and/or exsolution, which suggests rutile re-equilibrated at HT conditions in the stability field of rutile + ilmenite (ca. 1.0 GPa). However, it is not excluded that high Zr content result from the lack of Zr incorporation into ilmenite replacing rutile, as observed by [Whitney *et al.* \(2015\)](#). The large dispersion of Zr-content in rutile inclusions may reflect either protracted growth and entrapment in garnet from the early prograde to the HT decompression stages (stages 1 to 3), or it may be a mixing trend between a prograde population formed around $600\text{--}650^\circ\text{C}$ and a Zr-rich population formed during decompression at HT ($730\text{--}775^\circ\text{C}$).

Matrix rutile in samples JB-19-43 and JB-19-55 yields HT conditions ($737\text{--}792^\circ\text{C}$) consistent with equilibration during HT decompression. Highest ZiR T is ca. 40°C lower than peak-T estimated by amphibole-plagioclase thermometry ($833\pm 35^\circ\text{C}$). We do not interpret this discrepancy as the result of post peak-T diffusion, first because there is no evidence of

diffusion zoning in the rutile grains, and second because several studies have demonstrated that the Zr-in-rutile thermometer is robust to diffusive re-equilibration up to ultra-high T conditions (*e.g.* Ewing *et al.*, 2013; Kooijman *et al.*, 2012; Pape *et al.*, 2016). We suggest instead that peak-T occurred in the stability field of ilmenite, and is therefore not recorded by rutile, which rather constrains T during the last step of equilibration above the Rt-out line between stages 3 and 4 (Figure 4.8-b). Finally, late rutile in sample JB-19-55, which grows together with titanite in replacement of ilmenite, yields low T between 457 and 499°C, which is ca. 50–70°C lower than T estimated for plagioclase–actinolite pairs (stage 5) and marks late retrogression to the lower amphibolite-facies.

P–T evolution of the mafic retrogressed granulites from Peyre-Arguet

Despite generally more pervasive retrogression, the samples from Peyre-Arguet share similarities with the mafic HP granulites from La Lavey. In particular, widespread occurrence of granoblastic mosaic assemblages rather than vermicular symplectites marks decompression at HT conditions following the HP stage. Textures in sample JB-19-16 correspond to an intermediate state of retrogression between well-preserved HP granulites (JB-19-43;56) and highly retrogressed sample JB-19-55. Rutile in samples from Peyre-Arguet displays similar features as rutile in samples from La Lavey, with high ZiR T in matrix grains (778–818 °C) and large scattering of T in rutile inclusions in garnet (654–793°C). Consequently, the Peyre-Arguet retrogressed granulites have probably undergone a similar P–T evolution as the Lavey HP granulites, with a prograde to HP evolution at relatively moderate T (ca. 650–750°C), followed by heating to >800°C during decompression. However, Zr-content in rutile is generally higher in samples from Peyre-Arguet than in samples from La Lavey. For the same textural position (matrix or inclusions), the distribution of ZiR data is shifted by ca. 50–300 ppm toward higher values in Peyre-Arguet, which may reflect slightly higher peak-P (+0.4 GPa) and/or peak-T (+20°C) conditions.

4.1.8.3 Timing of the metamorphic evolution

Rutile dated in sample JB-19-56 yielded an age at 337 ± 7 Ma, which is older than most of U–Pb dates obtained in zircon rims of this study and predates by 30 to 40 Ma the widespread HT migmatitic event recorded in the inner zone of the Oisans–Pelvoux massif (Fréville *et al.* (2022), see compilation of U–Pb data on Figure 4.12). We therefore interpret the age at 337 ± 7 Ma as an early stage of the metamorphic evolution which predates HT decompression, rather than a cooling age after the thermal peak, which would be inconsistent with the regional geochronological record.

Preservation of an old rutile age is unexpected, given that Pb diffusion in rutile is considered to be fast over 600–650°C (Cherniak, 2000; Zack *et al.*, 2017). This is not an isolated observation. Rutile preserving old crystallization ages despite subsequent evolution at relatively HT conditions (700–750°C during >10 Ma) has also been reported in retrogressed Variscan eclogites from the neighboring massifs of Belledonne (Jacob *et al.*, 2021a) and Aiguilles–Rouges (Vanardois *et al.*, 2021). Low Zr-content and lack of ilmenite exsolution or replacement in dated grains (Figure 4.9-a and Figure 4.10-a) indicate lack of re-equilibration during HT decompression, probably due to shielding in garnet. Therefore, we tentatively attribute the unusual preservation of old rutile ages to the shielding effect of garnet, which may prevent both fluid access to the rutile inclusions and diffusional Pb-loss (Dahl, 1997).

Zircon rims generally display low U and low Th/U ratios, they are depleted in REE with respect to the zircon cores and they form homogeneous CC bright domains, which are typical features of metamorphic zircon formed under sub-solidus conditions (Hoskin *et al.*, 2003; Rubatto, 2017). U–Pb dates present a large scattering between 294 and 337 Ma, with two main clusters at 326–318 Ma and 310–303 Ma, which does not fit with one single age population. This suggests that zircon rims have crystallized during a protracted period, either continuously or during multiple episodic pulses. Large variety of zircon REE

patterns, which do not correlate with U-Pb dates, suggests chemical disequilibrium for REE at the microscopic scale during zircon growth. Flat HREE patterns are indicative of growth in a garnet-rich bulk, which fractionates HREE (Rubatto, 2002), while enrichment in HREE rather indicates zircon growth associated with garnet-breakdown. The HREE-enriched rims would therefore have grown in portions of the rock where the garnet-bearing HP assemblage was resorbing and releasing HREE, while the HREE-flat rims would have grown in non-resorbing portions of the rock. Correspondingly, the lack of a significant negative Eu anomaly in the zircon rims is not taken to signify lack of plagioclase in the assemblage, but rather disequilibrium growth (*e.g.* Lotout *et al.*, 2018).

Ti-in-zircon thermometry yields scattering T, that are uncorrelated with U-Pb date and are broadly 50°C lower than Zr-in-rutile T in the same sample. This shift suggests rutile and zircon growth are decorrelated and that zircon rims have formed under reduced a_{TiO_2} conditions, either at lower P in the stability field of ilmenite, or due to local TiO₂ undersaturation resulting from chemical disequilibrium at the microscopic scale. Overall, our small geochronological dataset combined with non-systematic trace elements patterns is limited to assign precise conditions but indicate a metamorphic zircon growth between ca. 337 and 294 Ma, broadly under decompression as attested by some HREE-enriched rims.

4.1.8.4 Evolution at the regional scale

Comparison of the zircon rims U-Pb dates from this study with data from the surrounding metamorphic rocks provide an interesting insight into the metamorphic evolution of the Oisans–Pelvoux massif. A summary of geochronological data from the study of Fréville *et al.* (2022) is presented on Figure 4.12. The data were split by domains between the widely migmatized inner Oisans-Pelvoux zone and the lower grade cortical zone in the western part of the massif (Figure 4.1). The distribution of zircon and monazite U–Pb dates in the high grade inner zone marks three distinct peaks corresponding to the Viséan (ca. 340–325

Ma), the Late Carboniferous – Early Permian (ca. 310–295 Ma) and the mid-Permian (ca. 285–270 Ma). Only the Visean peak is recorded in the lower grade cortical zone, which does not display any trace of younger events.

Excluding the late mid-Permian stage, the regional timing of metamorphism is consistent with that recorded in the HP granulites : the rutile age at 337 ± 7 Ma plots in the older end of the Visean peak and zircon rims U–Pb dates spread from the Visean to the late Carboniferous – early Permian peak. Dated rutile yields low ZiR/T consistent with the prograde evolution and zircon rims are interpreted to have formed during broad decompression and heating to HT conditions (stages 3 and 4 of the metamorphic evolution). Therefore, we correlate the Visean peak with the period of nappe stacking and crustal thickening (D1 regional phase), during which upper and mid-crustal units of both the inner and the cortical zone were buried to depth. The upper Carboniferous – early Permian peak is in turn interpreted to date heating to HT conditions during exhumation, which is only recorded in the inner zone of the Oisans–Pelvoux massif and match with the emplacement age of most of granite intrusions in this domain (Fréville, 2016).

Interestingly, nearly all zircon of the younger populations (late Carboniferous and Permian) display high $Th/U > 0.1$ (Figure 4.12-b), while older zircons display more scattered Th/U between 0.001 and 1. High Th/U are generally indicative of crystallization in equilibrium with a melt (Hoskin et Schaltegger, 2003), and therefore the lack of low Th/U zircon in the late Carboniferous population, comparatively with older zircon, is another indication of a HT migmatitic environment during this period. This strongly suggests that HT decompression observed in the HP granulites, emplacement of granitoids and migmatization of the inner Oisans–Pelvoux zone occurred during the same late Carboniferous – early Permian (ca. 310–295 Ma) HT event.

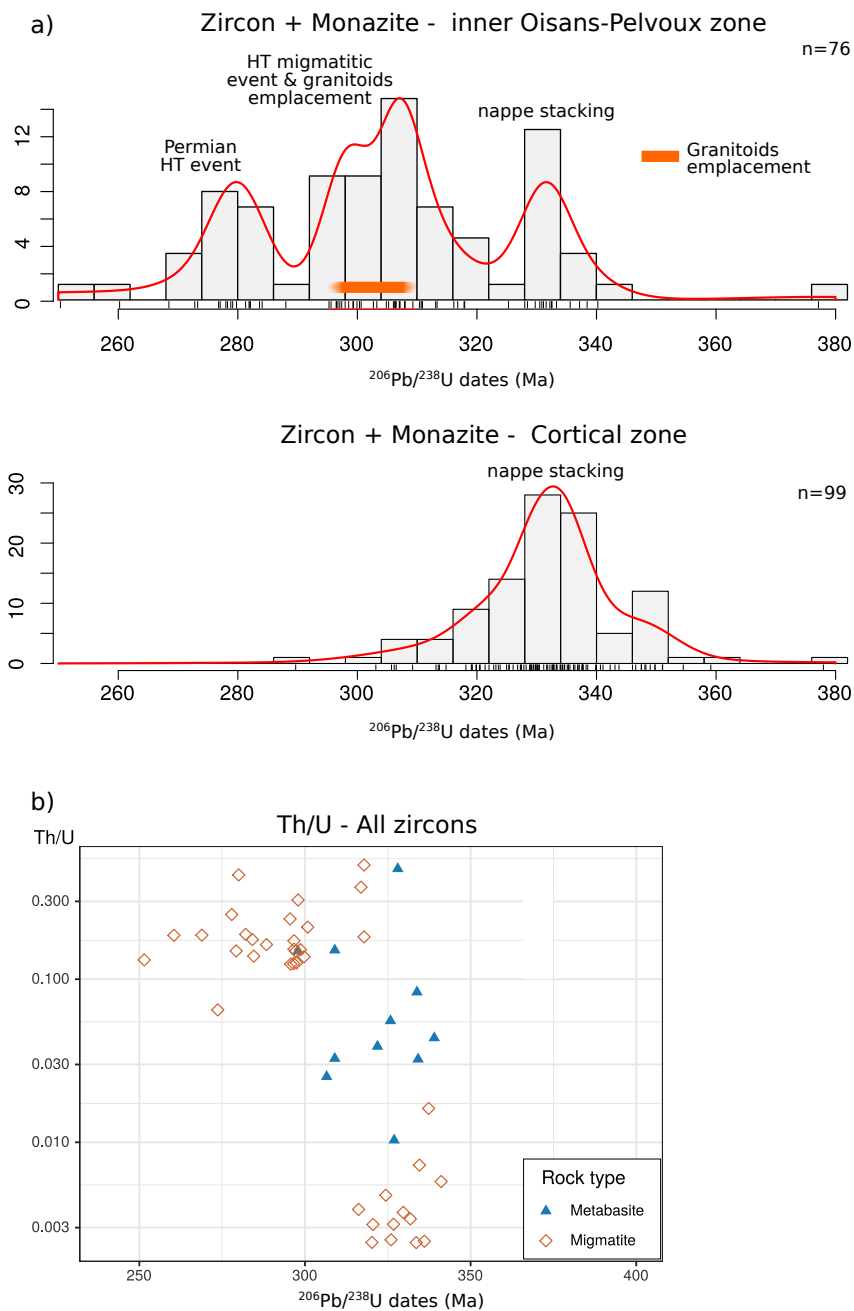


FIGURE 4.12 – Compilation of metamorphic zircon and monazite data from the Oisans–Pelvoux massif, taken from Fréville *et al.* (2022) and this work. (a) Distribution of Variscan zircon and monazite $^{206}\text{Pb}/^{238}\text{U}$ dates, obtained after filtering for the most discordant analyses ($-5\% < \text{disc} < 10\%$), where discordance is expressed as the relative difference between the $^{206}\text{Pb}/^{238}\text{U}$ and the $^{207}\text{Pb}/^{235}\text{U}$ dates). Distinction between the intensely migmatized inner domain (East) and the Cortical domain (West) devoid of HT overprint is shown on Figure 4.1. (b) Plot of Th/U vs $^{206}\text{Pb}/^{238}\text{U}$ dates in zircon. Not all U–Pb zircon analyses plotted in (a) are shown here because they lack corresponding value for Th.

4.1.8.5 Thermal state of the Variscan crust and possible geodynamic scenario

Metamorphic P–T conditions estimated for the mafic HP granulites from La Lavey allow to constrain the local geotherm during the different stages of the metamorphic evolution (Figure 4.13). Assuming a crustal density of 2800 kg.m^{-3} , we estimate that early burial of the mid-crustal metamorphic nappes (stage 1) occurred along a relatively mild local geothermal gradient (ca. $12\text{--}19^\circ\text{C.km}^{-1}$). Peak-P conditions (stage 2) were reached at ca. 55–60 km depth along a mean gradient of $12\text{--}13^\circ\text{C.km}^{-1}$. Then, exhumation and heating (stages 3 and 4) mark progressive re-equilibration along a much warmer geotherm (ca. $25\text{--}38^\circ\text{C.km}^{-1}$).

Thus, it clearly appears that prograde metamorphism did not occur along a low-T metamorphic gradient. Early prograde stage 1 occurred in a middle crust that was already at upper greenschist-facies conditions, which then reached conditions of the HP granulite-facies during stage 2. Timing of the prograde to HP evolution and peak-P conditions are similar to those estimated for eclogites in the other ECM of Aiguilles–Rouges, Argentera and Belledonne (Jacob *et al.*, 2021a; Jouffray *et al.*, 2020; Rubatto *et al.*, 2010; Vanardois *et al.*, 2021). This timing also match with that of the barrovian metamorphic sequence observed in the southern Belledonne massif and the cortical zone of the Oisans–Pelvoux massif, which corresponds to burying of the Devonian–Tournaisian arc/back-arc series to ca. 0.6–0.9 GPa and $650\text{--}700^\circ\text{C}$ (Fréville *et al.*, 2018; Guillot *et Menot*, 1999). Therefore, the HP stage marks a regional MT/HP event at the scale of the ECM, that we correlate to the regional D1 nappe stacking.

Relatively high T in the middle crust during the onset of collision is inconsistent with subduction of a cold passive margin, which would generate much cooler gradient ($< 10^\circ\text{C/km}$, Maruyama, 1996). This result is in line with early emplacement of granitoids during the Viséan (345–335 Ma), which implies that the crust was already hot and prone to melting

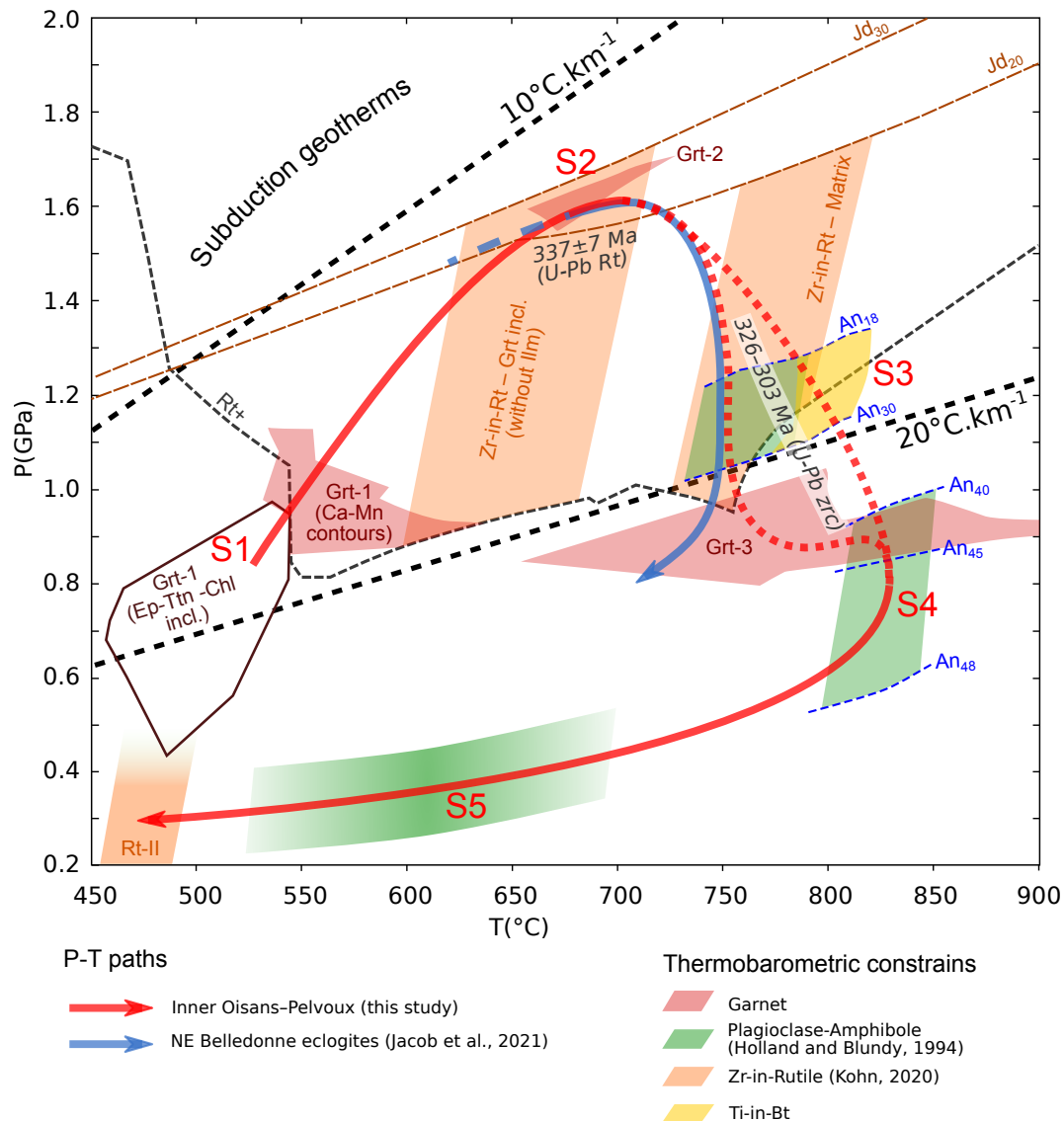


FIGURE 4.13 – Synthetic P-T-t evolution inferred for the mafic HP granulites from La Lavey (red path). Dotted lines indicate the two possible scenarios for decompression from stage 2 to stage 4 (see discussion in text). P-T path of retrogressed eclogites in northeast Belledonne (Jacob *et al.*, 2021a) is shown in blue for comparison.

during the early collisional stages. This initial thermal anomaly may be inherited from Devonian arc/back-arc magmatism, which was active from ca. 370 to 350 Ma in the ECM (Fréville *et al.*, 2018; Guillot et Ménot, 2009; Ménot, 1987a). We therefore suggest that the regional phase D1 corresponds to the inversion of a Devonian continental back-arc during collision, which resulted in HP metamorphism at MT/HT conditions.

Post peak-P heating to HT granulite-facies conditions (>800°C) during the late Car-

boniferous is only recorded in the inner zone of the Oisans–Pelvoux massif. In contrast, peak-T conditions in metamorphic series exposed in the cortical Oisans–Pelvoux zone and in the southern Belledonne massif (Figure 4.1) do not exceed 650–700°C at 0.6–0.9 GPa (Fréville *et al.*, 2018, 2022; Guillot *et Menot*, 1999). All the other eclogites relics in the ECM (Belledonne, Argentera, Aiguilles–Rouges) reached peak-T 700–750°C. Furthermore, the geochronological record in the cortical zone of Oisans–Pelvoux does not reveal any sign of a late Carboniferous HT overprint (Figure 4.12-a). We interpret the lack of HT overprint in these domains as the result of relatively rapid exhumation to upper structural levels after peak-P. In contrast, the inner zone of the Oisans–Pelvoux massif has remained in the lower crust until the late Carboniferous (310–300 Ma), where it has been heated to HT conditions. Our thermobarometric estimations indicate that peak-T was reached in the lower crust (ca. 20–30 km ; 0.6–0.9 GPa), but HT conditions above 800°C have probably persisted during exhumation to $P < 0.6$ GPa, since cordierite is observed in Al-rich metasedimentary protoliths (Figure 4.22).

Heating could have occurred progressively during decompression from stage 2 to stage 4, due to thermal maturation of the lower crust. However, given the relatively stealth overprint of the HP granulites during stage 4 and the episodic growth of zircon and monazite in the metamorphic basement, we suggest that the HT overprint was relatively short-lived and occurred after a first step of decompression from high to middle-P conditions. These two possible exhumation paths are shown with dotted lines on Figure 4.13.

The sharp increase of T (ca. 100–200°C) between stage 2 (peak-P) and stage 4 (peak) requires important heat input, especially when considering that a significant part of the additional thermal energy has been pumped out in melting reactions to form the large volumes of granite (Moyen, 2019). Part of this thermal energy comes from internal radiogenic heat production in the thickened orogenic crust. However, the metamorphic pile in the Oisans–Pelvoux massif contains large amounts of amphibolite and amphibolitic gneiss poor in

radioactive elements, and the ca. 30 Ma interval between peak-P and peak-T may have therefore been too short to produce this thermal overprint accounting only for internal crustal heat sources (Bea, 2012; Clark *et al.*, 2011; England et Thompson, 1984). Mantle-derived (ultra)-potassic magmatic rocks akin to the durbachites and vaugnerites series (Von Raumer *et al.*, 2014) are ubiquitous in the basement (Figure 4.1) and may have contributed to heating, either by underplating below the lower crust or by intruding directly in the lower crust. Finally, upwelling of hot asthenospheric mantle in response of slab rollback or lithospheric delamination during the post-collisional stages may be a possible source for additional heating, as suggested in the French Massif Central or the Bohemian Massif (*e.g.* Vanderhaeghe *et al.*, 2020; Žák et Sláma, 2018).

Conclusion

High-pressure mafic granulite that were newly identified in the Oisans–Pelvoux massif represents an invaluable material to infer the P-T-t evolution of this widely migmatized massif that records the highest metamorphic conditions in the external crystalline massifs of the French Alps. The mafic HP granulites derive from ordovician tholeiitic protoliths emplaced at 479 ± 5 Ma. They preserve the relicts of multiple Variscan metamorphic stages, from an early prograde phase at $460\text{--}550^\circ\text{C}$ and $0.4\text{--}1.0$ GPa to peak P conditions at $650\text{--}730^\circ\text{C}$ and $1.5\text{--}1.7$ GPa. The HP assemblage was then destabilized at HT conditions during decompression and peak T of $800\text{--}870^\circ\text{C}$ was reached at $0.6\text{--}0.9$ GPa. In the best-preserved mafic HP granulites, lack of strong fluid-input during cooling allowed preservation of the HP and HT assemblages, and no subsequent retrogression stage is recorded. In contrast, the most retrogressed samples have undergone pervasive deformation and metasomatism that were associated with crystallization of an amphibolitic assemblage from ca. 690°C to 450°C .

The timing of the Variscan metamorphic evolution is constrained by a U-Pb age on rutile at 337 ± 7 Ma and by U-Pb dates of metamorphic zircon rims scattered between 337

and 294 Ma. Most of zircon rims have crystallized during decompression, and therefore the older rutile age is interpreted to date prograde or HP stages. The timing and P–T conditions of prograde to HP evolution are comparable with those of other HP rocks in the ECM, and correspond to burying of continental units along a medium-T geothermal gradient (ca. 12–13°C.km⁻¹). Upper greenschist-facies conditions during the early prograde stage are inconsistent with subduction of a cold passive margin. We therefore ascribe the prograde to HP evolution to thickening of a relatively hot continental crust, presumably caused by inversion of a Devonian back-arc during the collision.

The HP rocks of the Oisans–Pelvoux massif are the only ones in the ECM to record heating to HT granulitic conditions during decompression. Therefore, we suppose that unlike most other HP relics in the ECM, these mafic HP granulites remained stored in the lower crust for a longer period, and recorded a late heating stage possibly triggered by a combination of underplating and /or intrusion of hot mantle magmas and increased basal conductive heat flux caused by asthenospheric upwelling.

Acknowledgements

This work was supported by the BRGM through the Référentiel Géologique de la France program (RGF). J-B Jacob was funded by a doctoral grant from the ENS de Lyon. We wish to thank all the technical staff at ISTERre in Grenoble, UNIL in Lausanne and at the University of Bern, who greatly helped for the preparation of samples and during the multiple analytical sessions. This manuscript also benefited from interesting and constructive reviews by Julien Berger and an anonymous reviewer, and from editorial handling and advices from Nadia Malaspina. Most of the field investigations were carried out in the central zone of the Ecrins National park, in which collecting rock samples is usually strictly forbidden. We therefore wish to thank the administration staff of the Ecrins National park, who gave us authorization to collect the samples and followed with great interest the advancement of

this work.

Supplementary material

This section groups figures that are not included in the main text of the article but are provided as supplements.

4.1 HT overprint of HP granulites in the Oisans–Pelvoux massif

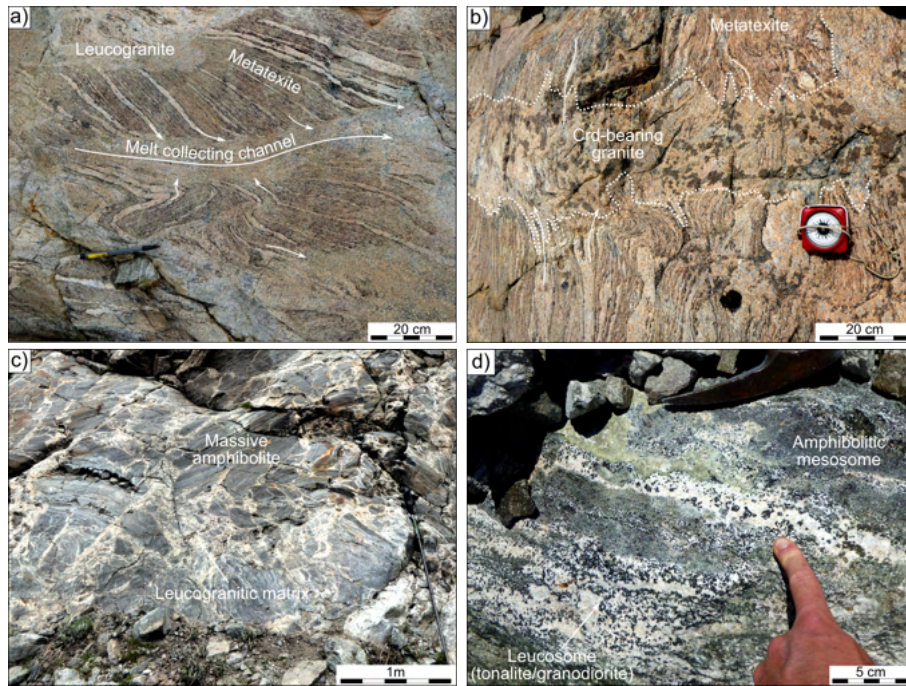


FIGURE 4.14 – Field pictures of migmatitic textures in the felsic (a–b) and intermediate / mafic (c–d) protoliths in the inner Oisans–Pelvoux zone.

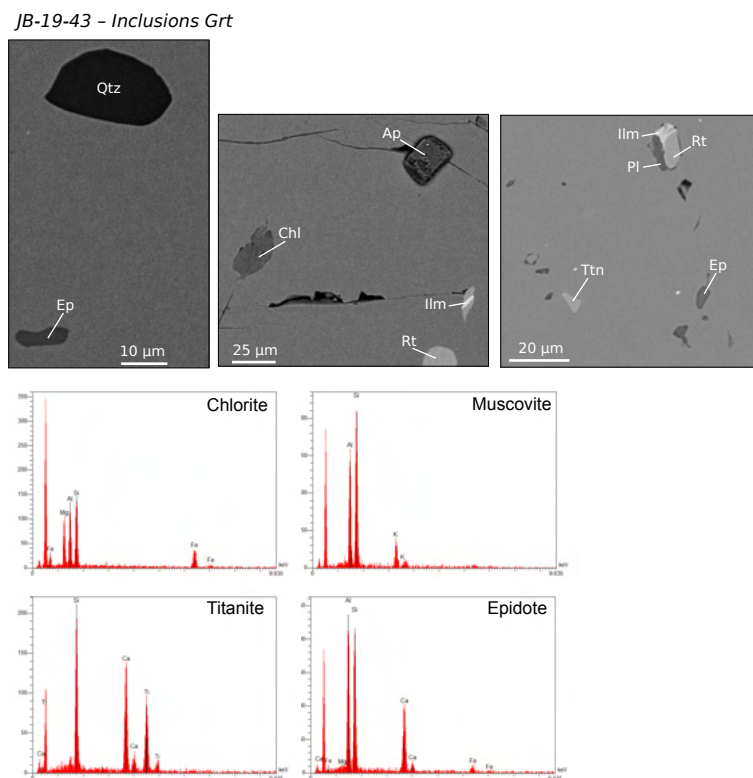


FIGURE 4.15 – Backscattered electron images and EDS spectra of mineral inclusions in garnet of sample JB-19-43.

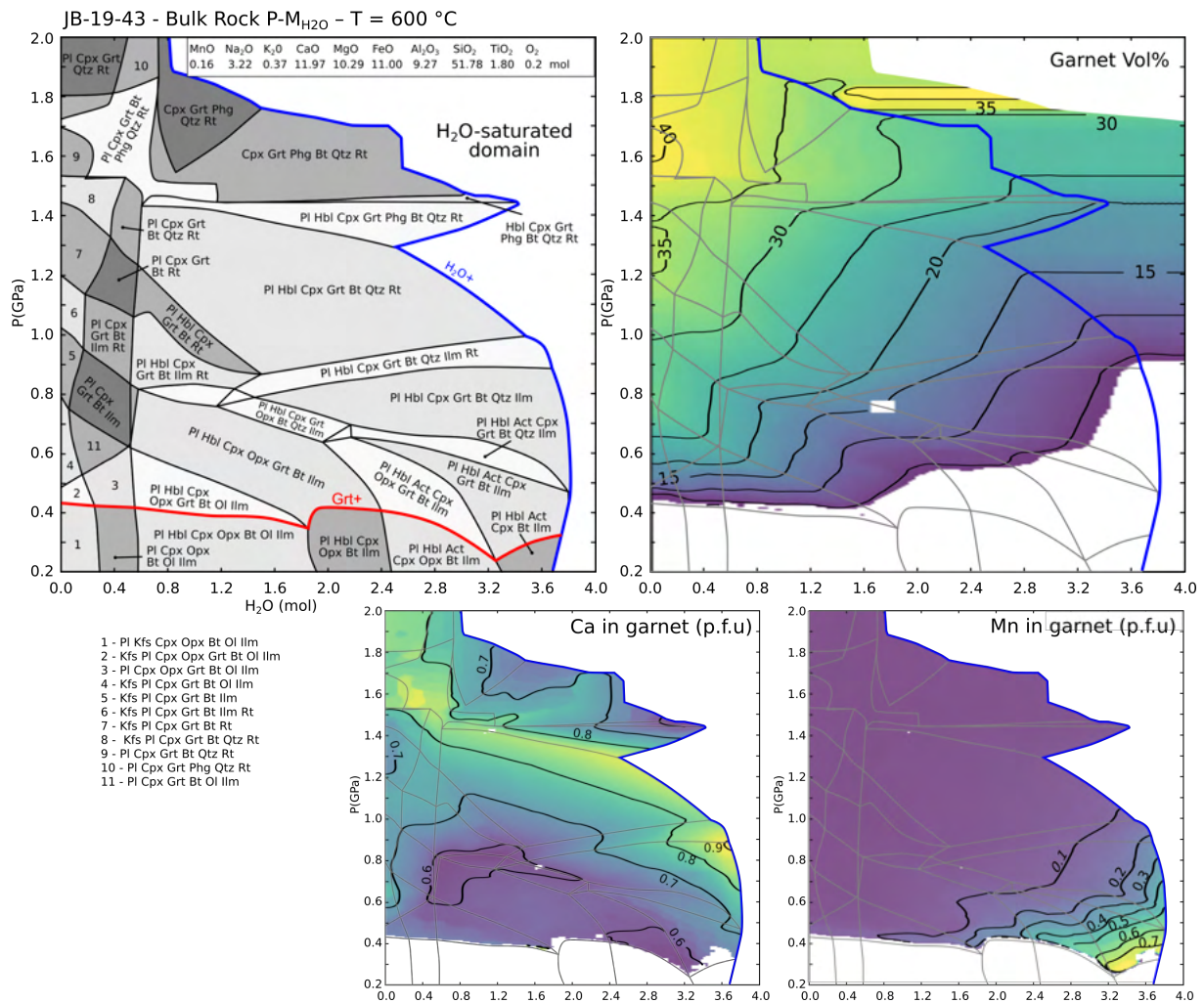


FIGURE 4.16 – P-H₂O phase diagram computed with the composition of garnet-bearing mafic granulite (JB-19-43) and associated garnet isopleths. Ca-Mn-rich garnet can only grow at low P (<0.8 GPa) and for composition close to the fluid saturation.

4.1 HT overprint of HP granulites in the Oisans–Pelvoux massif

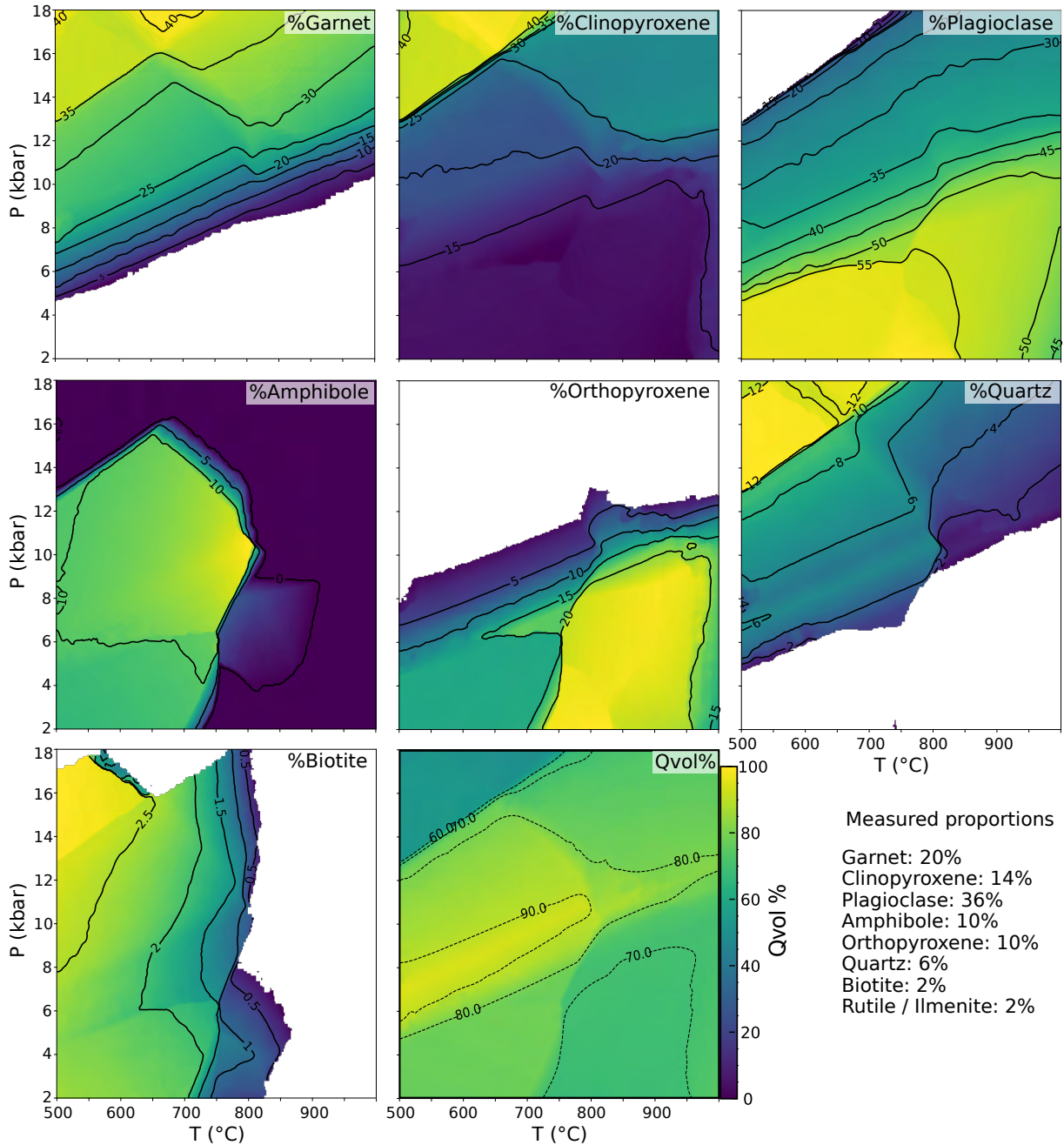


FIGURE 4.17 – Modal proportion of minerals (vol%) modeled with PerpleX for the local X-Ray map domain in sample JB-19-56. Comparison between observed and modeled mineral proportions is assessed using the Q_{vol} criterion of [Duisterhoeft et Lanari \(2020\)](#).

4.2 Données complémentaires sur le contexte structural

4.2.1 Déformation alpine dans le massif de l'Oisans–Pelvoux

Le socle paléozoïque du massif de l'Oisans–Pelvoux est découpé en une série de blocs tectoniques, séparés par les anciennes failles normales issues du rifting jurassique et par un ensemble de zones de cisaillement formées lors de la compression alpine. Les formations étudiées se situent dans le bloc de la Meije, délimité à l'ouest et au sud par la faille de l'Olan (Figure 4.18), et qui se prolonge au nord vers le chevauchement de la Meije (Bellanger *et al.*, 2014). Au sud, cette zone de faille forme une bande phylliteuse de 10 à 30 m de large, d'orientation N110–120° et présentant un fort pendage (>70°) vers le nord. Les sigmoïdes C/S indiquent une cinématique sénestre (Figure 4.19). A l'ouest du sommet de l'Olan, la zone de faille s'oriente vers le nord, diminue en pendage (40-50° E) et évolue vers un système chevauchant top vers l'ouest (Figure 4.18 et Figure 4.19). Quelques failles secondaires traversent le bloc de la Meije. Elles sont en général fortement pentées, d'orientation N150–N180°.

4.2 Données complémentaires sur le contexte structural

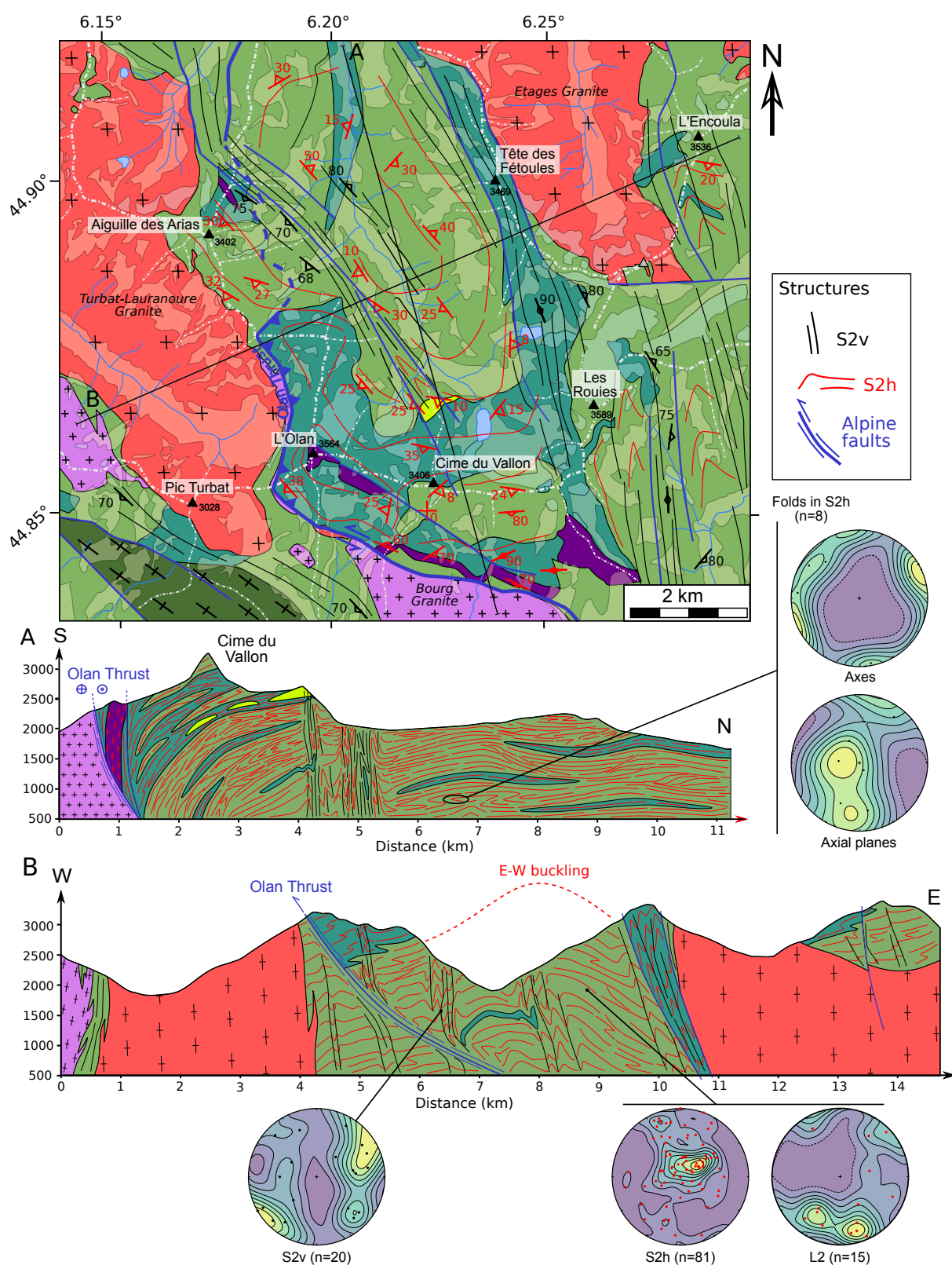


FIGURE 4.18 – Carte des formations de la Lavey (zone interne du massif de l’Oisans–Pelvoux). Les caractéristiques structurales des foliations varisques S2h (rouge) et S2v (noir) sont représentées sur des coupes N-S et E-W. Les couleurs utilisées sont identiques à celles de la Figure 1 de l’article soumis à Lithos.

Olan Thrust (La Chapelle en Valgaudemar)

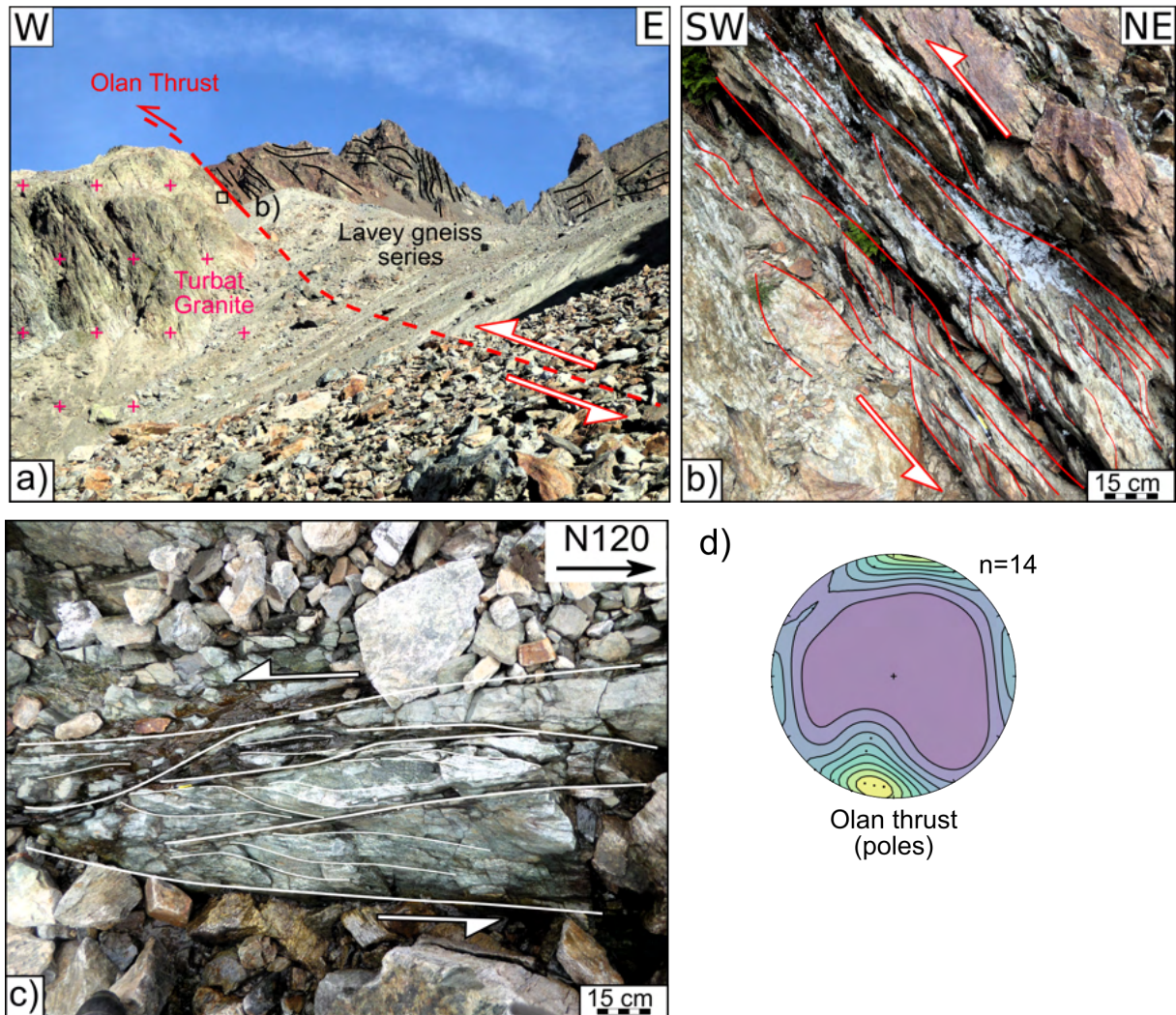


FIGURE 4.19 – Caractéristiques structurales de la faille de l’Olan. Dans sa partie ouest, la faille fonctionne en chevauchement top vers l’ouest et fait chevaucher les formations de la Lavey sur le granite de Turbat (a–b). Vers le sud, elle se verticalise et fonctionne en faille décrochante sénestre (c–d).

4.2.2 Étude des structures varisques

4.2.2.1 Modélisation géologique 3D

La géométrie des structures métamorphiques varisques a fait l’objet d’une étude de détail, centrée sur un rectangle d’environ 8x10 km² dans la zone interne du massif, fortement migmatisée, correspondant à l’emprise de la carte sur la [Figure 4.18](#). Les plans de foliations,

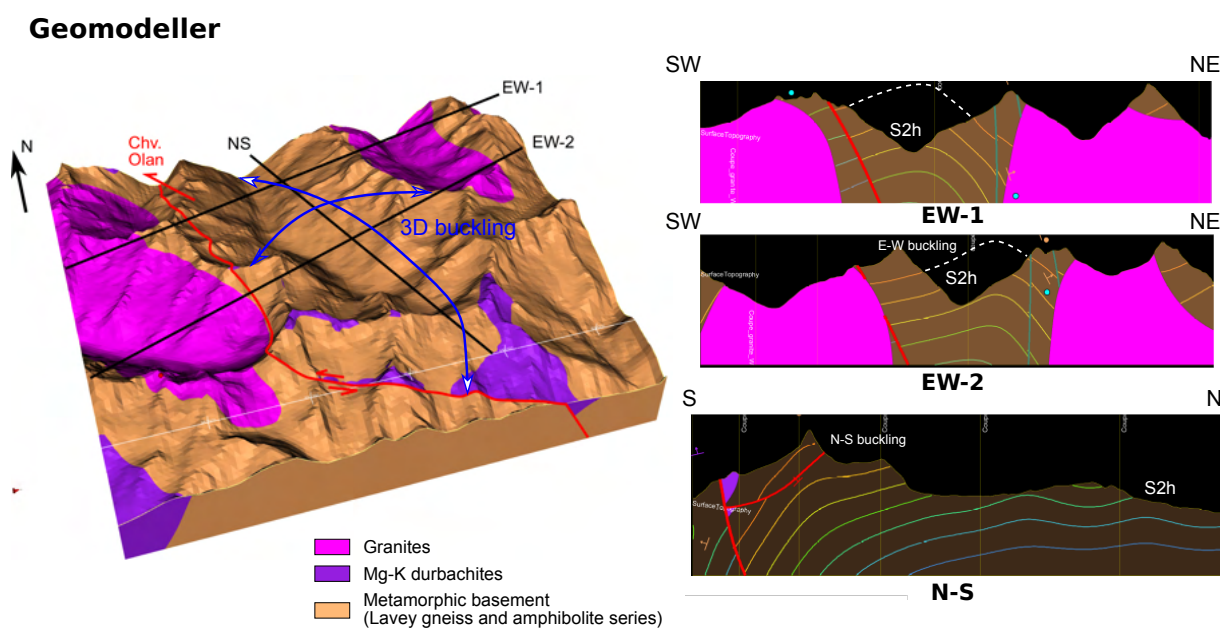


FIGURE 4.20 – Bloc diagramme du modèle 3D réalisé sur la zone centrale du massif de l’oisans–Pelvoux à l’aide de *Geomodeller*.

ainsi que les linéations d’étirement et minérales ont été mesurées sur plus d’une centaine de stations réparties sur l’ensemble de la zone, afin d’identifier les différentes générations de fabriques planaires et leur relations chronologiques. En parallèle, un travail de modélisation 3D des structures a été mené à l’aide du logiciel de modélisation géologique 3D *Geomodeller* développé au BRGM. Une visualisation en bloc diagramme du modèle 3D réalisé ainsi que plusieurs coupes structurales obtenues à partir du modèle sont représentées sur la [Figure 4.20](#). En raison des relations géométriques complexes entre les différentes fabriques métamorphiques, ce travail n’a pas abouti à un résultat final propre. En particulier, l’enracinement des formations intrusives en profondeur reste mal contraint. Néanmoins, le modèle 3D réalisé reste même utile pour visualiser les trajectoires de foliations métamorphiques à l’échelle du bloc crustal étudié, et a servi de base pour la réalisation des coupes synthétiques représentées sur la [Figure 4.18](#). En particulier, le modèle 3D permet de mettre en évidence un bombement des structures d’échelle kilométrique à pluri-kilométrique.

4.2.2.2 Identification des structures

En faisant abstraction des structures alpines, plusieurs fabriques métamorphiques sont visibles au sein du massif. La première n'est préservée que de manière relictuelle, et n'est pas cartographiée à l'échelle du massif. Elle semble correspondre à l'équivalent de la S1 observée par *Fréville et al.* (2018) dans le sud du massif de Belledonne, qui est mieux préservée plus à l'ouest dans le bloc du Rochail. Au niveau du camping du Plan du Lac (St Christophe en Oisans), cette S1 présente un pendage vers l'ouest et comporte des boudins amphiboliques cisailés qui indiquent une cinématique inverse top vers l'est avec un axe d'allongement maximal N80-N90° (Figure 4.22). Cette cinématique semble cohérente avec la phase D1 identifiée dans le sud du massif de Belledonne (*Fréville et al.*, 2018).

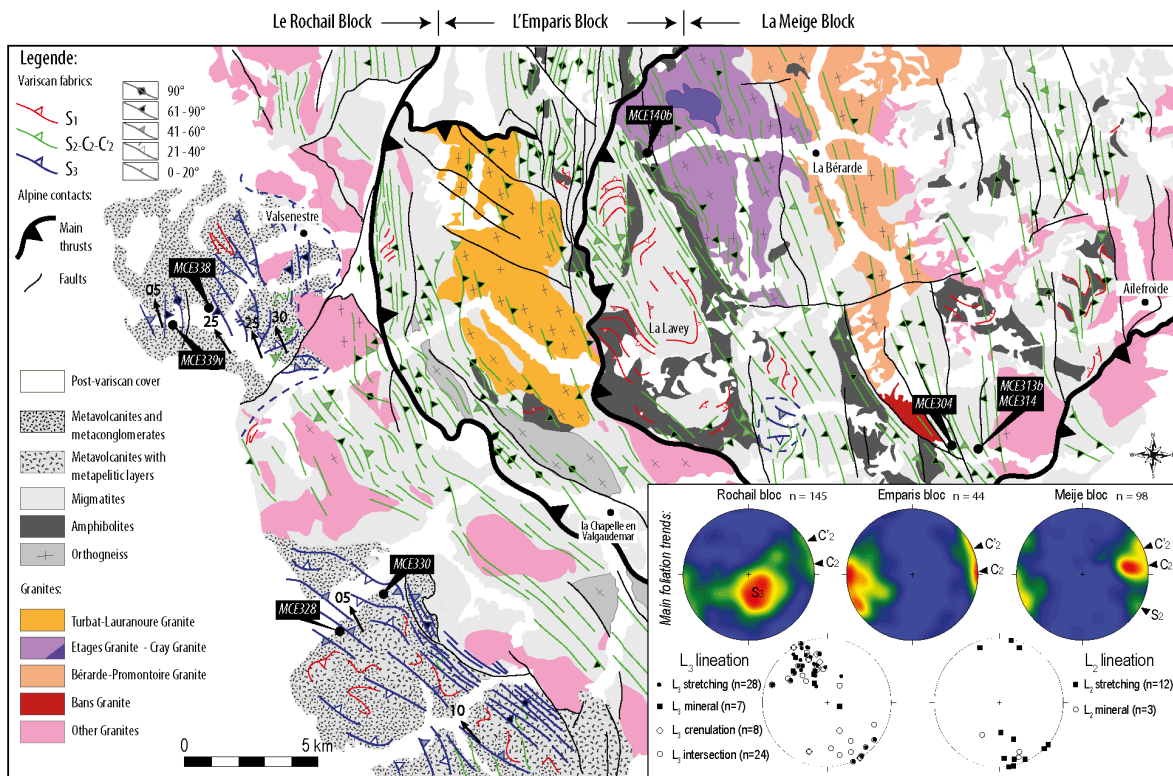
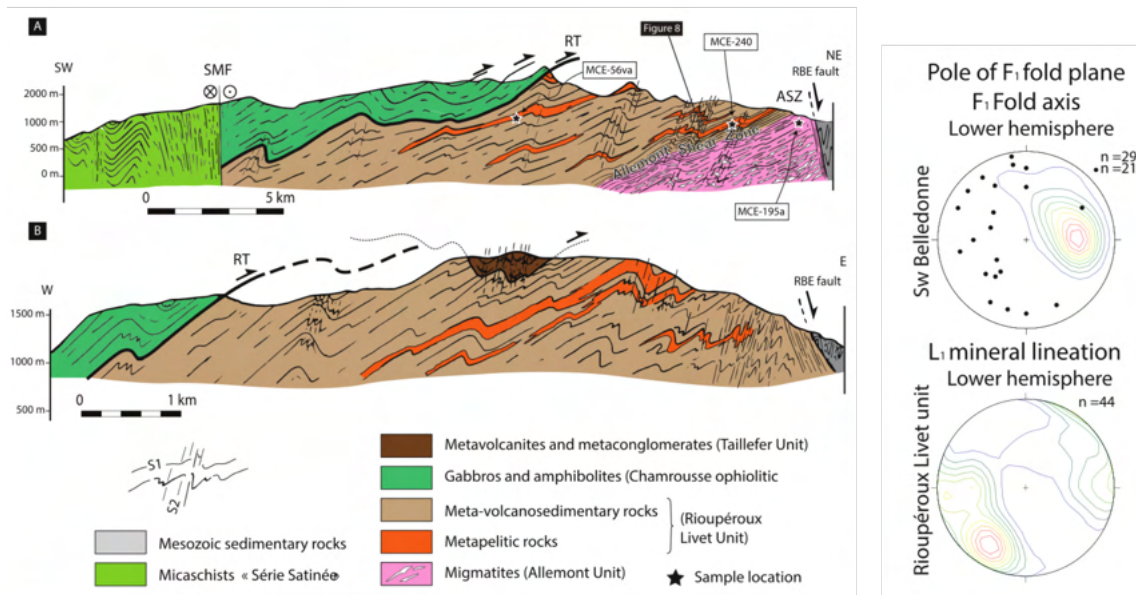


FIGURE 4.21 – Carte structurale du massif de l’Oisans–Pelvoux issue de *Fréville et al.* (2022), faisant apparaître différentes fabriques métamorphiques à l’échelle du massif. Les S1 et S2 de *Fréville et al.* (2022) correspondent respectivement à S2h et S2v dans ce travail de thèse. La foliation S3 identifiée par *Fréville et al.* (2022) dans le bloc du Rochail n’est pas présente dans la zone interne du massif.

4.2 Données complémentaires sur le contexte structural

L'ancienne S1 est oblitérée par deux populations de plans, qui apparaissent nettement sur la cartographie structurale faite à l'échelle du massif (Figure 4.21), ainsi que sur une cartographie plus localisée centrée sur le vallon de la Lavey (Figure 4.18). La première forme une foliation métamorphique peu pentée S2h, de pendage généralement $<45^\circ$, qui forme des ondulations d'échelle (pluri)-kilométrique à l'échelle du massif (Figure 4.20). La seconde

a) SE Belledonne (Fréville et al., 2018)



b) Plan du Lac (St-Christophe en Oisans)

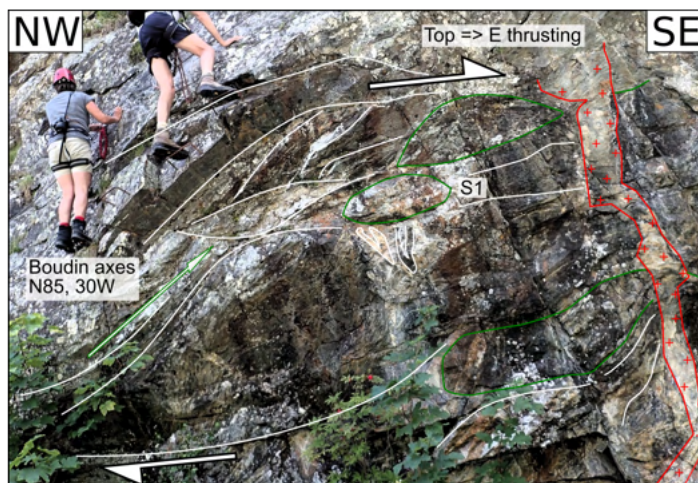


FIGURE 4.22 – (a) Caractéristiques de la déformation D1 dans le sud du massif de Belledonne, d'après Fréville *et al.* (2018). (b) Boudins amphibolitiques cisillés marquant une cinématique inverse top vers l'est, qui pourraient correspondre à l'équivalent de la D1 dans le massif de l'Oisans. (WGS84 : N44.96140°, E6.16589°).

forme une foliation subverticale S2v, d'orientation N140° à N170°, qui apparaît au sein de bandes de cisaillements recoupant S2h. Les fabriques S2v sont dominantes à l'échelle du massif, mais S2h reste relativement bien préservée dans plusieurs domaines, en particulier dans le vallon de la Lavey, sur lequel est centrée l'étude structurale.

Les plans de foliation S2h affectent des formations migmatitiques, et présentent de nombreux indices de déformation ductile, comme la présence de leucosomes cisillés ou de plis anisopaques, ce qui implique une déformation à haute température en condition supra-solidus ou proche du solidus. Les sigmoïdes C/S et les plis asymétriques subhorizontaux (plis d'entraînement) témoignent d'un fluage horizontal le long de ces plans (Figure 4.23). Les linéations d'étirement mesurées sur les plans S2h et les axes des plis asymétriques indiquent une direction préférentielle de fluage N150 à N180°. Quelques bandes de cisaillement conjuguées semblent marquer localement une composante en aplatissement vertical (Figure 4.23-c). Ces structures extensives pourraient être liées au plissement (pluri)-kilmétrique de S2h, qui induit un amincissement vertical au niveau des extradors des plis. Ainsi, la formation de S2h semble être associée à une déformation à forte composante constrictionnelle, avec un allongement horizontal selon un axe N150–180°.

S2v forme des corridors subverticaux orientés N140° à N170° (Figure 4.18). Cette foliation présente elle aussi des caractéristiques d'une déformation ductile à haute température (Figure 4.24), qui évolue vers une déformation plus froide localisée le long de bandes de cisaillement ductiles/fragiles lors des phases les plus tardives. Quelques boudins cisillés et sigmoïdes C/S indiquent une cinématique apparente sénestre, cohérente avec celle identifiée par Fréville *et al.* (2022). Les linéations sont difficilement observables. Fréville *et al.* (2022) reportent néanmoins plusieurs mesures de linéations d'étirement, toutes de faible pendage, qui indiquent donc une forte composante décrochante. La déformation comporte par ailleurs une composante compressive, marquée par le pincement de S2h, qui forme des plis décimétriques à métriques d'axe parallèle à S2v (Figure 4.24). De plus, le bombement

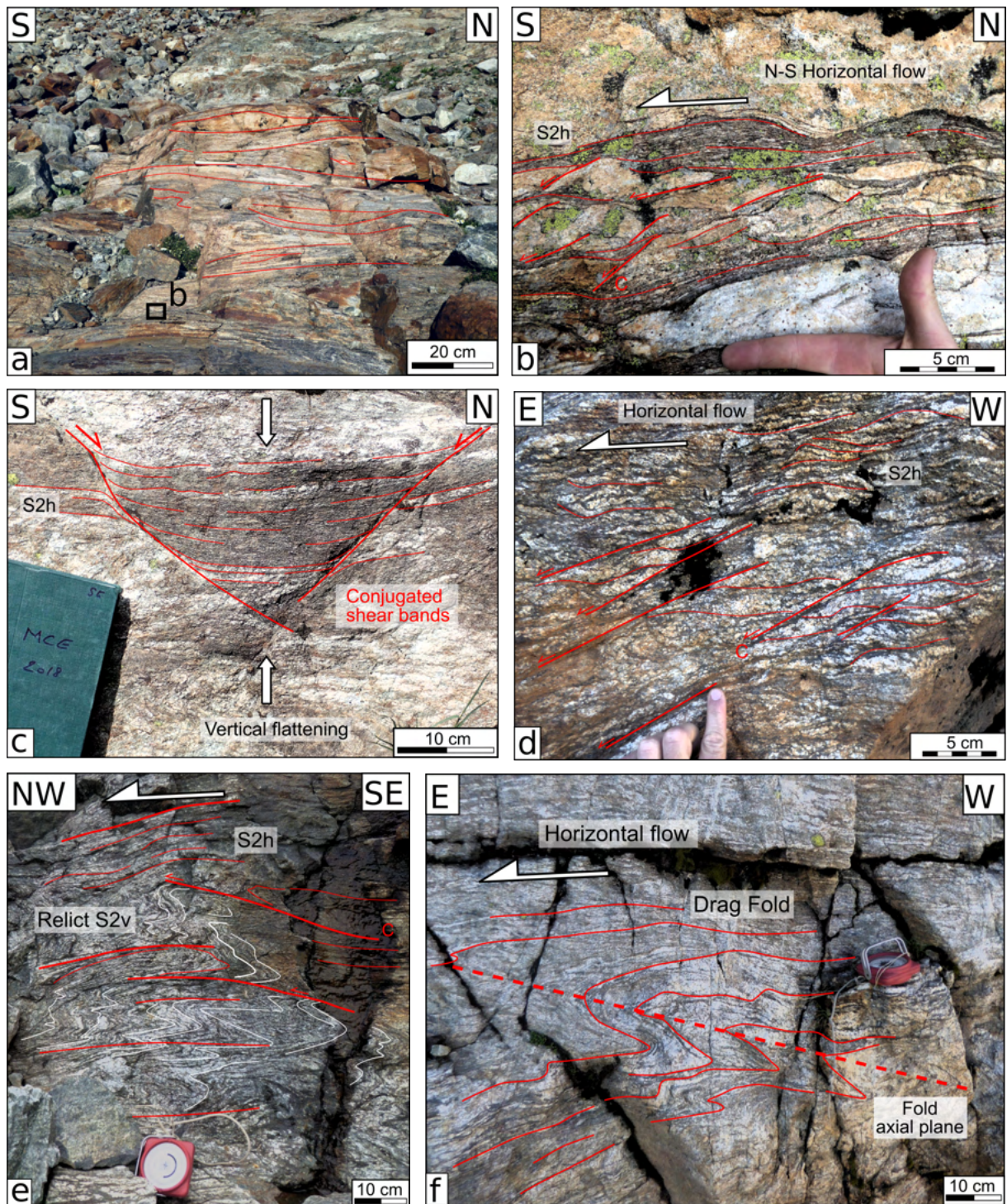


FIGURE 4.23 – Caractéristiques de la foliation S2h dans les formations de la Lavey. (a,b) Plans de foliation S2h dans des gneiss migmatitiques. Les leucosomes cisailés marquent une direction de fluage vers le sud. (c) Bandes de cisaillement conjuguées, marquant une composante en aplatissement vertical. (d) Leucosomes cisailés dans un gneiss migmatitique. (e,f) Plis asymétriques déversés, marquant un cisaillement horizontal de S2h.

La Lavey (St Christophe en Oisans)

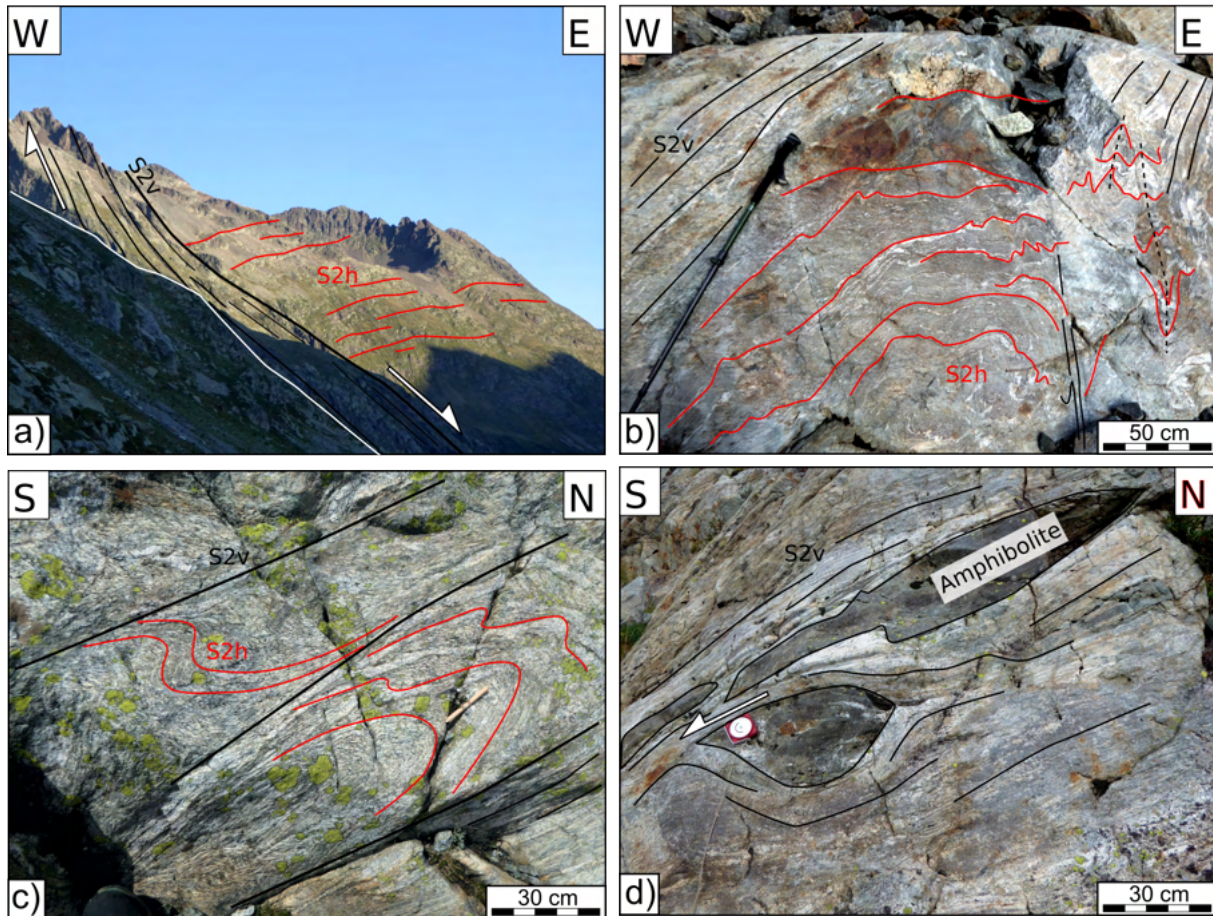


FIGURE 4.24 – Caractéristiques de la foliation S2v dans les formations de la Lavey. (a) Dans le paysage, les bandes de cisaillement subverticales formées par S2v apparaissent clairement, recoupant S2h. (b,c) Reliques de S2h préservées au sein de S2v, formant des plis décimétriques à métriques. (d) Boudin amphibolique cisailé, marquant une cinématique décrochante sénestre.

antiforme de S2h observé à l'échelle kilométrique se fait selon le même axe (Figure 4.18), et résulte donc probablement de cette composante compressive. La formation des structures S2v est donc associée à une déformation en régime transpressif sénestre, qui accommode un raccourcissement E–W à NW–SE.

4.2.3 Mécanismes de déformation de la croûte inférieure

De manière générale, on observe une reprise de la foliation S2h par les plans S2v, en particulier dans les zones où S2v présente des caractéristiques de déformation de plus basse

température (Figure 4.24). Néanmoins, dans les domaines très migmatitiques au cœur du vallon de la Lavey, on peut observer localement une reprise des plans S2v par le fluage horizontal associé à S2h. Ainsi, les plans S2h et S2v se recoupent mutuellement, et semblent donc avoir fonctionné en partie de manière synchrone lors d'une phase précoce de la déformation. Les directions de fluage mesurées sur les plans S2h sont par ailleurs compatibles avec le raccourcissement E-W à NW-SE associé aux cisaillements S2v. La déformation s'est par la suite localisée le long des plans de cisaillement verticaux S2v, entraînant l'oblitération des structures S2h sur une partie importante du massif. Cette interprétation contraste donc avec celle de Fréville *et al.* (2022), qui identifie les structures horizontales comme une S1 associée à D1, et les structures verticales comme un ensemble S2-C2-C2' associée à D2 (Figure 4.21). Ainsi, les structures S2h et S2v semblent être associées à une même phase de déformation en contexte transpressif sénestre, qui s'initie à relativement haute température et affecte des formations partiellement fondues. Cette déformation intervient donc après la phase D1, qui se fait en conditions relativement froides (<650 °C, Fréville *et al.*, 2018; Guillot et Menot, 1999), incompatibles avec un fort degré de fusion partielle. J'associe donc cette phase transpressive à la phase D2 observée à l'échelle des MCE.

Le fonctionnement synchrone des plans S2h et S2v lors des stades précoces de D2 marquerait un partitionnement de la déformation au sein de la croûte partiellement fondue, entre des chenaux de fluage horizontaux (S2h) et des bandes de cisaillement verticales (Figure 4.25), similaire au modèle proposé par Cagnard *et al.* (2006) ou Chardon *et al.* (2011) pour la déformation de la croûte inférieure en contexte orogénique chaud. Dans ce type de contexte, la présence de grands domaines partiellement fondus rend la croûte inférieure peu compétente. La déformation n'est plus localisée le long de grandes zones de cisaillement, mais se fait de manière plus diffuse et tend alors à se partitionner entre différents types de fabriques verticales et horizontales, qui accommodent des composantes différentes de la déformation. Dans les séries de la Lavey, les plans S2v et S2h sont cohérentes avec un échappement latéral de matière, en réponse à un raccourcissement général E-W à NW-SE

(Figure 4.25).

4.2.4 Mécanismes d'exhumation de la croûte profonde dans le massif de l'Oisans–Pelvoux

La zone centrale du massif de l'Oisans–Pelvoux expose en surface des domaines équilibrés dans des conditions caractéristiques de la croûte inférieure (ca. 30 km, 0.8–1.1 GPa), et contenant des reliques de granulites HP équilibrées à des profondeurs de l'ordre de 50 à 60

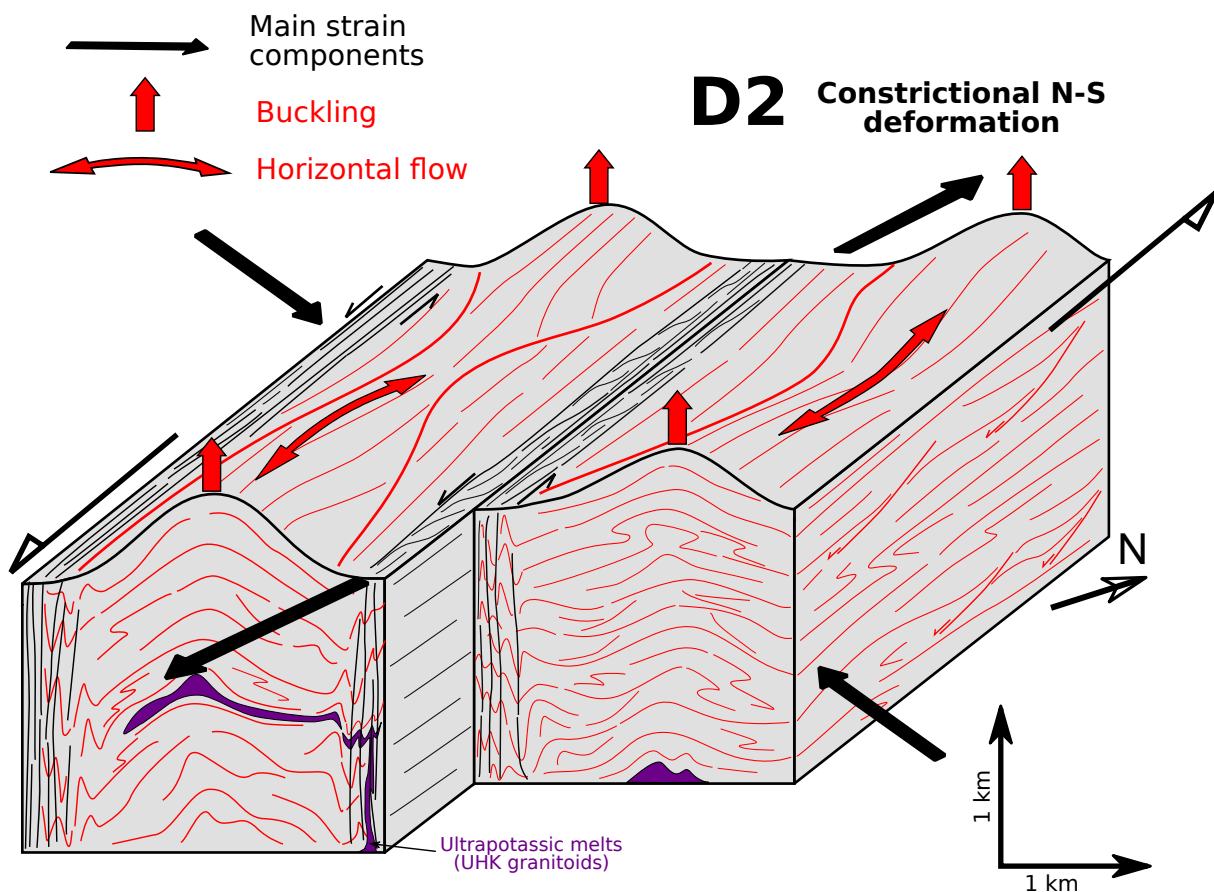


FIGURE 4.25 – Bloc diagramme schématique montrant les caractéristiques la déformation transpressive D2 dans la zone interne de l'Oisans–Pelvoux. Cette déformation a lieu en condition supra-solidus dans la croûte inférieure (ca. 30 km ; 0.8 GPa, d'après les estimations thermobarométriques obtenues dans les granulite de la Lavey). La composante décrochante est accomodée par les cisaillements sénestres (S2v), alors que la composante compressive est accomodée par un fluage latéral de matière perpendiculaire à la compression, produisant des fabriques horizontales (S2h). Les granitoïdes ultrapotassiques visibles sur la Figure 4.18 sont contemporains de cette phase de déformation.

km (1.5–1.6 GPa). La question des mécanismes d'exhumation de ces roches profondes se pose donc. Le contexte tectonique lors de l'exhumation est fondamentalement décrochant, avec une évolution progressive d'un régime transpressif (D2) vers un régime transtensif (D3) le long de l'EVSZ. Plusieurs mécanismes d'exhumation existent en contexte décrochant, qui peuvent se combiner (Cao et Neubauer, 2016). Une partie de l'exhumation pourrait être liée à une cinématique légèrement oblique le long des décrochements (Figure 4.26-a), qui conduirait à une exhumation du bloc Est (Oisans–Pelvoux, Grandes-Rousses) par rapport au bloc Ouest (Belledonne) (Figure 2.11), mais ce mécanisme semble très insuffisant pour expliquer les 30 km d'exhumation constatés. Les mécanismes les plus plausibles sont donc : (1) l'extrusion de croûte inférieure en régime transpressif, en réponse au raccourcissement perpendiculaire à la zone de cisaillement (Figure 4.26-d) ; (2) l'exhumation gravitaire de domaines de croûte inférieure partiellement fondue peu dense, localisée le long de la zone de cisaillement (Figure 4.26-e).

Les structures extensives observées se limitent aux failles normales délimitant les petits bassins Carbonifères dans les domaines crustaux supérieurs (Fernandez *et al.*, 2002), et jusqu'à présent aucune zone de détachement majeure n'a été identifiée de manière certaine. Les structures S3 peu pentées, identifiées par Fréville et al (2021) dans la partie ouest du massif de l'Oisans–Pelvoux (Figure 4.21), pourraient être associées à un détachement, mais les directions de linéations observées sur ces plans sont peu compatibles avec un mouvement extensif associé à l'exhumation d'un dôme. L'exhumation par extrusion en régime transpressif semble donc être le mécanisme dominant, même si les forces gravitaires ont pu jouer un rôle dans la remontée de croûte inférieure migmatitique peu dense. Ce type d'exhumation en contexte transpressif est relativement répandu dans les zones périphériques de la chaîne varisque, en particulier en Montagne Noire (Rabin *et al.*, 2015), dans le massif des Maures (Gerbault *et al.*, 2018) ou encore dans la zone axiale des Pyrénées (Cochelin *et al.*, 2021).

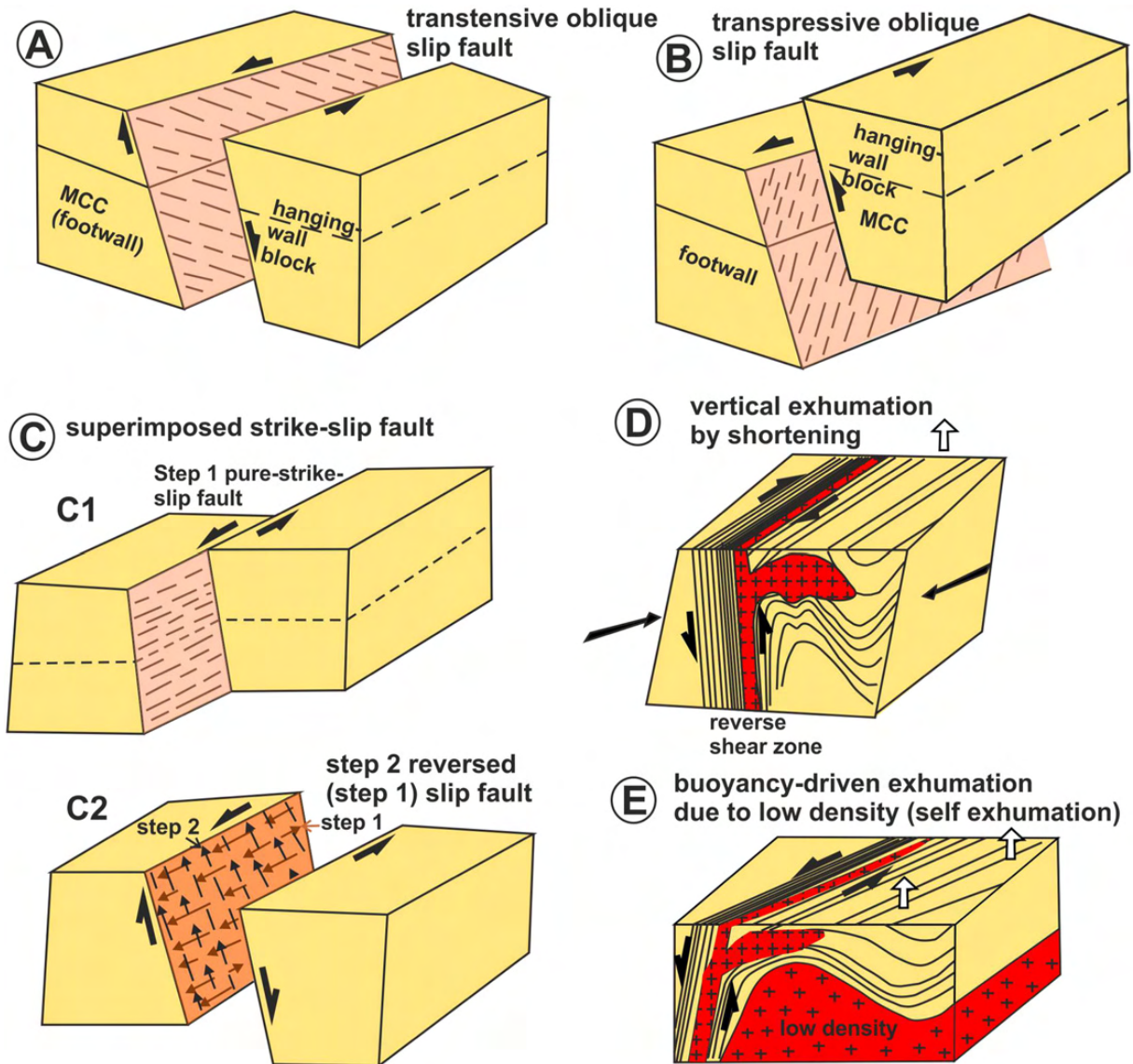


FIGURE 4.26 – Modèles d'exhumation de domaines profonds le long des grands systèmes décrochants, d'après Cao et Neubauer (2016). A,B – Exhumation par mouvement oblique le long d'une zone de cisaillement transpressive (A) et transpressive (B). C – Exhumation en deux stades, par superposition d'une composante en décrochement pur suivie d'une composante en extension. D – Exhumation par extrusion verticale de croûte inférieure ductile en régime transpressif, canalisée le long de la zone de cisaillement. E – Exhumation gravitaire passive de croûte inférieure peu dense en contexte transensif.

CHAPITRE 5

Géochimie et contexte de mise en place des protolithes magmatiques



Bloc d'amphibolite dans une migmatite – Vallon du Gioberney, Valgaudemar.

Sommaire

5.1	Signature géochimique des protolithes	190
5.1.1	Un magmatisme prolongé au cours de l'Ordovicien	192
5.1.2	L'ophiolite de Chamrousse est elle bien cambrienne?	194

L'étude des reliques HP et des roches métamorphiques environnantes est focalisée sur les épisodes métamorphiques varisques. Néanmoins, les données géochronologiques et géochimiques acquises sur ces roches fournissent aussi des indications sur l'origine et la mise en place des différents protolithes magmatiques. Cette partie vise à présenter ces données, et discuter succinctement le contexte de mise en place de ces roches. Les protocoles d'analyse (géochimie et datations) sont détaillés dans les sections Méthodologie des deux articles publiés. Par ailleurs, les résultats d'une datation additionnelle réalisée sur un échantillon d'orthogneiss des lacs de la Tempête est reportée ici.

5.1 Signature géochimique des protolithes

Les éclogites et les granulites HP dérivent toutes de protolithes magmatiques, marqués en particulier par la présence de zircons magmatiques ayant plus ou moins recristallisé lors du métamorphisme. La composition en éléments majeurs et traces a été obtenue sur plusieurs échantillons des lacs de la Tempête et des échantillons du massif de l'Oisans–Pelvoux, incluant les granulites de la Lavey et celles de Peyre-Arguet ([Figure 5.1](#)). Ces roches présentent toutes des compositions de basalte / gabbro tholéitique ferro-titané ($\text{SiO}_2 = 48\text{--}50$ wt%, $\text{Na}_2\text{O}+\text{K}_2\text{O} = 2\text{--}4$ wt%, $\text{TiO}_2 = 1.5\text{--}2.3$ wt%, ratio molaire $\text{Mg}/(\text{Fe}+\text{Mg}) = 0.45\text{--}0.50$), sans variations significatives entre les différents lieux d'échantillonnage. Les teneurs en éléments traces diffèrent en revanche quelque peu. Les échantillons des lacs de la Tempête présentent une composition en REE proche de N-MORBs, avec des ratios (La_N/Sm_N) inférieurs à 1 (0.77–0.87), alors que les autres échantillons présentent un enrichissement en LREE ($\text{La}_N/\text{Sm}_N = 1.98\text{--}2.31$) similaire à une signature de MORB enrichis (E-MORB, [Gale *et al.* \(2013\)](#)) ou de tholéïtes continentales. Les anomalies en Nb et Ta sont faibles, et tous les échantillons se situent sur l'axe MORB–OIB dans le diagramme de [Pearce \(2008\)](#), ce qui

exclut une interaction prolongée du manteau source avec des fluides issus de la déshydratation de lithosphère en subduction. En revanche, on observe un enrichissement important en éléments incompatibles et/ou mobiles dans les fluides (Ba, Rb, Th, U, Pb), qui marquent une contamination par une composante crustale. Cette contamination aurait pu se faire soit lors de la mise en place des magmas, ce qui impliquerait une mise en place en domaine continental, soit lors du métamorphisme varisque, en particulier lors des phases de rétro-morphoses, associées à une réhydratation des éclogites et des granulites. La présence de nombreux orthogneiss dérivant de granitoïdes contemporains des protolithes mafiques plaide néanmoins en faveur d'une mise en place de ces derniers en contexte continental.

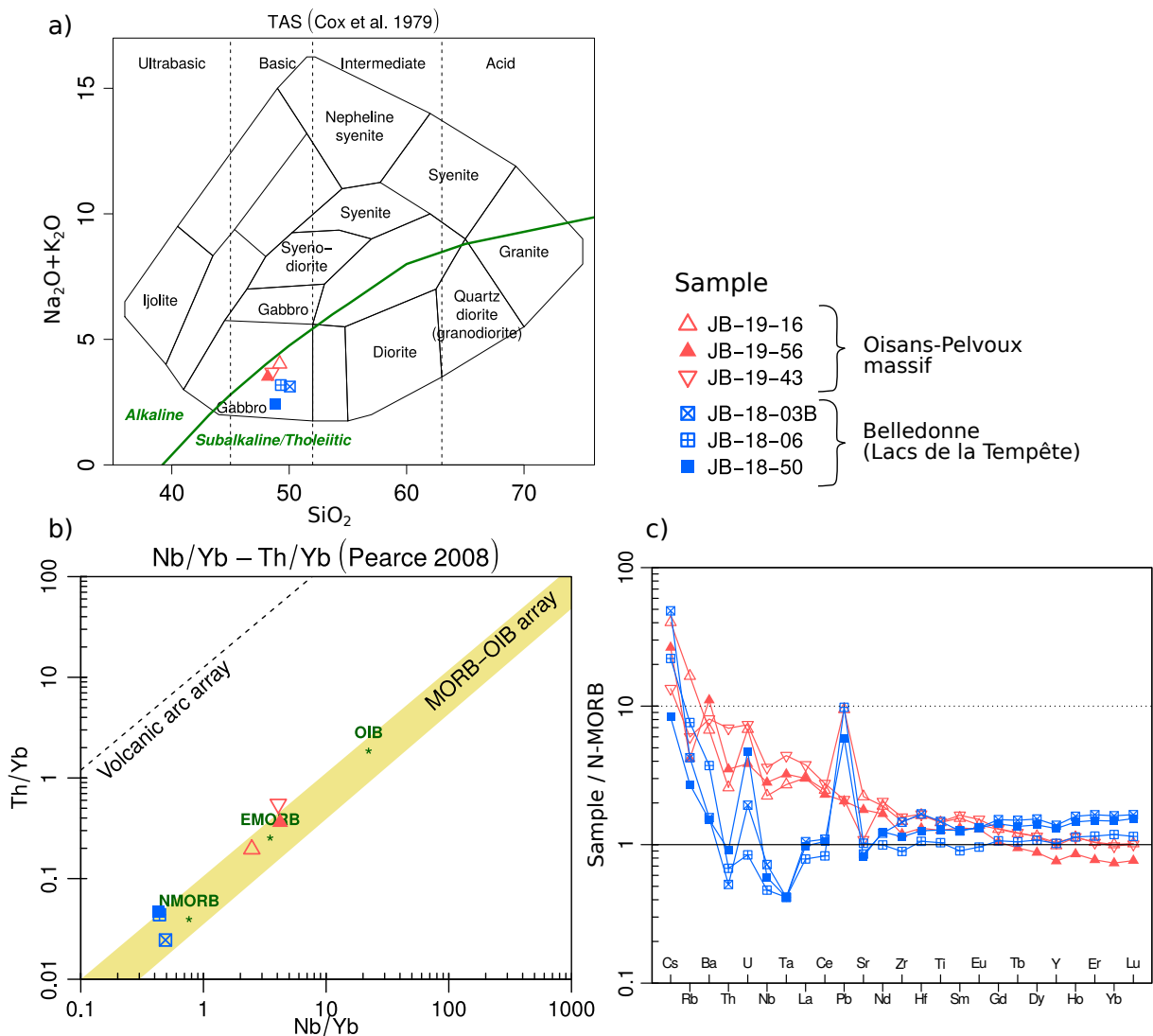


FIGURE 5.1 – Caractéristiques géochimiques des protolithes mafiques des reliques HP des massifs de Belledonne (bleu) et de l’Oisans-Pelvoux (rouge). (a) Diagramme TAS, permettant de discriminer les séries tholéitiques (subalcalines) des séries alcalines. (b) Le diagramme Th/Yb – Nb/Yb de (Pearce, 2008) permet de discriminer les basaltes océaniques, qui forment un alignement sur l’axe MORB-OIB, des basaltes contaminés par une source crustale ou dont la source mantellique a été métasomatisée par des fluides issus de la déshydratation d’une lithosphère en subduction. (c) Spectres d’éléments traces normalisés à la composition moyenne des N-MORB (Gale *et al.*, 2013).

5.1.1 Un magmatisme prolongé au cours de l’Ordovicien

Les âges U-Pb obtenus sur les cœurs de zircon magmatiques permettent de dater la mise en place des protolithes magmatiques. Le détail des datations des protolithes mafiques est fourni dans les deux articles précédents. Une datation additionnelle d’un échantillon

d'orthogneiss (JB-18-08) est présentée ici : Il s'agit d'un orthogneiss à grains fins (<3mm) prélevé à proximité des lacs de la Tempête (WGS84 : N45,62261° ; E6,53253°). Il est composé principalement d'un assemblage de quartz et feldspaths, avec du mica blanc (muscovite) et de la chlorite, qui se développe en remplacement de la biotite. Les zircons séparés après broyage de la roche sont généralement automorphes, et présentent des sections allongées de 200 à 400 μm . Sur les images réalisées au MEB en contraste de charge (voir article #1 pour le protocole), les zircons montrent fréquemment une zonation oscillatoire concentrique. La recristallisation des bordures lors du métamorphisme varisque est faible à inexistante (**Figure 5.2**). Les concentrations en U sont élevées (>100 ppm), avec des ratios Th/U entre 0.05 et 0.6. Les analyses isotopiques U-Pb réalisées à la microsonde ionique sont toutes concordantes, et donnent des âges $^{238}\text{U}/^{206}\text{Pb}$ entre 447 et 475 Ma. En excluant trois analyses significativement plus jeunes que les autres, la population principale composée de 18 grains donne un âge $^{238}\text{U}/^{206}\text{Pb}$ moyen à 464 ± 4 Ma (MSWD=1.71), équivalent à l'âge concordia dans la gamme d'incertitude. Les zonations oscillatoires, les ratios Th/U élevés et le caractère très homogène de la population de zircons sont plutôt des marqueurs indiquant une origine magmatique (**Corfu et al., 2003**). Cet âge est donc interprété comme l'âge de cristallisation du protolithe granitique.

La compilation des données géochronologiques acquises sur les protolithes magmatiques indique des âges d'emplacement étalés entre 445 et 485 Ma (**Figure 5.3**), similaires à la gamme d'âges obtenus sur les protolithes des massifs des Aiguilles Rouges (**Bussy et al., 2011**) et de l'Argentera (**Rubatto et al., 2001, 2010**), qui s'étalent entre 480 et 450 Ma. Par ailleurs, ces âges sont cohérent avec la distribution des âges de zircons hérités dans les roches métamorphiques et les granitoïdes varisques des massifs de Belledonne, des Grandes Rousses et de l'Oisans–Pelvoux, représentée à gauche sur la **Figure 5.3** (voir la légende pour les détails). Les zircons étant des minéraux se développant principalement en context magmatique ou métamorphique de moyen à haut grade (**Hoskin et Schaltegger, 2003; Rubatto, 2017**),

JB-18-08 - Orthogneiss (Lacs de la Tempête)

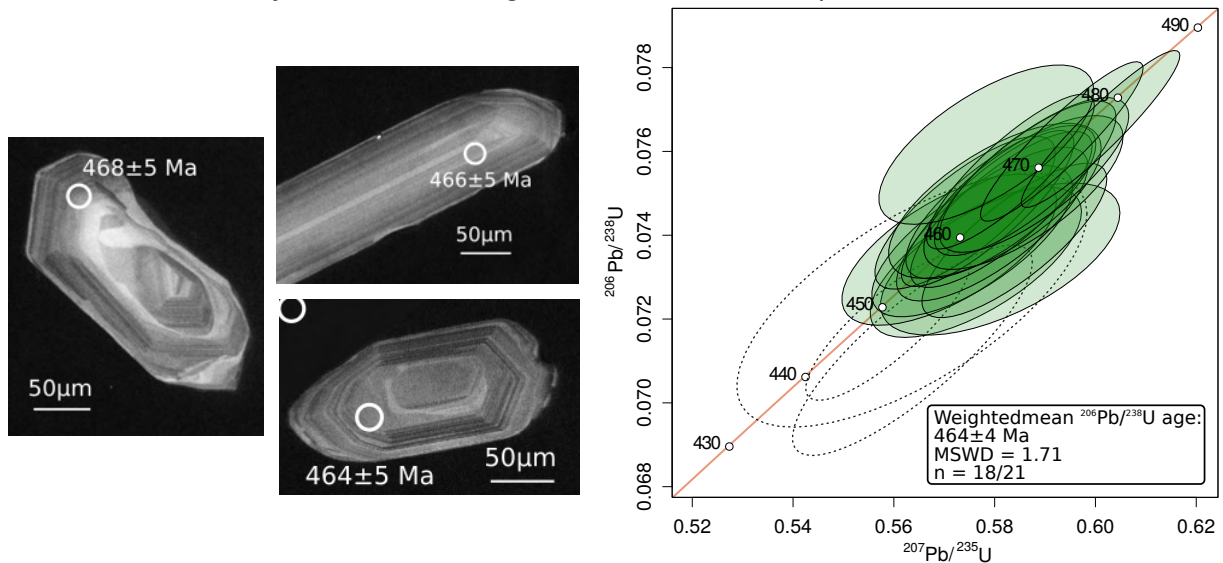


FIGURE 5.2 – Résultats des analyses U-Pb sur zircon d'un échantillon d'orthogneiss des lacs de la Tempête (Belledonne NE), obtenue à la microsonde ionique (SIMS). Les ellipses représentent les incertitudes à 2 sur chaque analyse, et les ellipses en pointillé représentent les points de données exclus dans le calcul de l'âge. Les textures internes (imagerie MEB par contraste de charge) de zircons représentatifs de la population analysée sont figurées à gauche, avec en blanc la position des points d'analyse.

cette distribution reflète l'activité magmatique et métamorphique au cours du temps dans le socle Paléozoïque. On observe une majorité de zircons entre 490 et 440 Ma, marquant un pic d'activité à l'Ordovicien. Un pic plus jeune est visible vers 420 Ma, mais il représente probablement des âges de mélange sans signification géologique, car aucun épisode magmatique n'est connu à cette époque dans les MCE. Ce magmatisme est équivalent au magmatisme bimodal Cambro-ordovicien enregistré de manière généralisée dans les domaines varisques en Europe, et correspond à la phase d'extension associée à l'ouverture des océans Paléozoïques ([chapitre 1](#)).

5.1.2 L'ophiolite de Chamrousse est elle bien cambrienne ?

L'ophiolite de Chamrousse, datée à environ 500 Ma ([Ménot *et al.*, 1988](#); [Pin et Carme, 1987](#)), est couramment interprétée comme une relique d'un bassin océanique ouvert lors de la phase d'extension Cambro-ordovicienne ([Fréville *et al.*, 2018](#); [Guillot et Ménot, 2009](#); [Pin](#)

et Carme, 1987). Cependant, la compilation des données géochronologiques existantes dans les MCE fait planer quelques doutes sur la validité de cet âge. En effet, on constate que le pic de magmatisme associé à l'extension dans les MCE a lieu entre 490 et 440 Ma, et est donc au minimum 10 Ma plus jeune que l'âge estimé de l'ophiolite. On n'observe en revanche aucun signal associé à l'ouverture du bassin de Chamrousse vers 500 Ma, alors qu'il s'agit d'un événement magmatique majeur. L'ouverture de cet océan n'est donc pas enregistrée dans le socle des MCE, ce qui peut s'expliquer de deux manières :

- L'ophiolite de Chamrousse correspond à un domaine exotique, qui a été charrié sur les domaines varisques des MCE lors des phases précoces de la collision au Carbonifère inférieur.
- Le domaine de Chamrousse s'est bien mis en place *in situ* dans les MCE, mais l'âge estimé à 500 Ma est incorrect. Les datations réalisées par Pin et Carme (1987) et Ménot *et al.* (1988) sont anciennes, et reposent sur des méthodes peu précises et sujettes à caution : isochrone Sm-Nd sur un ensemble de roches supposées cogenétiques pour la première, datation U-Pb d'une population de zircons par ID-TIMS pour la seconde.

Des travaux sont en cours, afin de préciser l'âge et le contexte du magmatisme à Chamrousse. Les premiers résultats d'imagerie en cathodoluminescence réalisés sur des zircons extraits de tonalites de Chamrousse montrent des zonations complexes résultant de plusieurs épisodes de dissolution / précipitation. Il apparaît donc assez vraisemblable que les fractions de zircon datées par Ménot *et al.* (1988) ne correspondent pas à une population homogène, mais à un mélange de populations d'âges différents. L'âge obtenu à 496 ± 6 Ma serait donc un âge de mélange sans signification géologique particulière (*comm. pers. C. Cordier*).

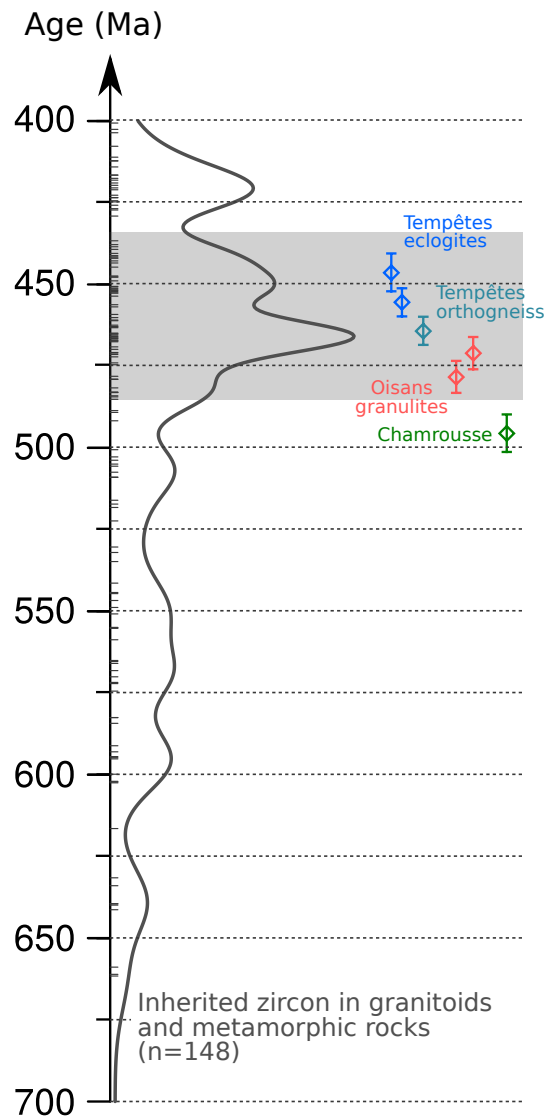


FIGURE 5.3 – Distribution des âges U-Pb sur zircon hérités dans les granitoïdes varisques et dans les formations métamorphiques des massifs de Belledonne, des Grandes Rousses et de l’Oisans–Pelvoux. Seuls les données entre 700 et 400 Ma sont représentée, afin de se focaliser uniquement sur le magmatisme Néoproterozoïque et Paléozoïque inférieur. Un filtre a été appliqué pour conserver uniquement les âges concordants (discordance < 5%). Les âges obtenus sur différents protolithes magmatiques (reliques HP, orthogneiss et complexe ophiolitique de Chamrousse) sont représentés avec leur barre d’incertitude. Données issues de Fréville *et al.* (2018, 2022); Ménot (1986) et de ce travail de thèse.

Troisième partie

Magmatisme mantellique et évolution du manteau varisque dans les MCE

Les processus orogéniques sont associés à des perturbations importantes du manteau sous-jacent. Les phénomènes de subduction, de retrait/rupture de slab, ou encore de délamination lithosphérique induisent en effet des perturbations importantes de la structure thermique du manteau (Maierová *et al.*, 2018; Sizova *et al.*, 2019). En parallèle, la déshydratation ou la fusion du matériel crustal enfouis lors de la subduction génère des fluides ou liquides silicatés, qui, en interagissant avec les péridotites du manteau, sont à l'origine de transformations métasomatiques (Zheng, 2019). La conjonction de ces deux phénomènes aboutit à la fusion partielle de certaines portions du manteau, générant ainsi un flux magmatique mantellique associé à la collision. Une meilleure compréhension de ces processus mantelliques passe par l'étude des séries magmatiques syn à post-collisionnelles et de leur distribution spatiale et temporelle, qui peut permettre d'identifier des phénomènes à l'œuvre dans le manteau, comme des épisodes de retrait/rupture de slab ou de délamination (*e.g.* Laurent *et al.*, 2017; Vanderhaeghe *et al.*, 2020). Par ailleurs, la présence de rares portions de manteau exhumées avec les domaines orogéniques profonds permet un échantillonnage direct et offre la possibilité d'étudier *in-situ* les processus de fusion partielle ou de métasomatisme mantellique.

Dans le contexte varisque européen, le magmatisme syn à post-orogénique est abondant et marqué principalement par de la fusion crustale, mais présente néanmoins un pôle mantellique bien identifiable et largement distribué à l'échelle de la chaîne (Couzinié *et al.*, 2016; Jacob *et al.*, 2021b; Janoušek *et al.*, 2019; Moyen *et al.*, 2017). Par ailleurs, les domaines profonds exhumés dans les MCE contiennent fréquemment des enclaves mantelliques, affleurant sous la forme de lentilles de serpentinites ou bien de péridotites aux compositions minéralogiques variées. Ces caractéristiques se retrouvent dans les massifs cristallins externes des Alpes. Les séries magmatiques Mg–K à fort caractère mantellique (série magnésienne, forte proportion de termes mafiques à intermédiaires, teneur élevée en Cr et Ni) y sont connues depuis longtemps (*e.g.* Banzet, 1987; Schaltegger et Corfu, 1992). La découverte lors de ce

travail de thèse d'enclaves de péridotites dans les domaines de croûte inférieure exhumée vient compléter l'éventail des péridotites orogéniques varisques, décrites en particulier dans le massif de Bohême (Medaris *et al.*, 2015; Naemura *et al.*, 2009), des Vosges (Altherr et Kalt, 1996; Kalt et Altherr, 1996), du Massif Central (Gardien *et al.*, 1990) ou encore dans la nappe Austro-alpine d'Ulten dans le socle varisque des Alpes orientales (Godard *et al.*, 1996; Tumiati *et al.*, 2003; Scambelluri *et al.*, 2006).

Cette partie est divisée en deux chapitres, présentés sous forme d'articles en cours de préparation. Le **chapitre 6** présente un travail préliminaire de caractérisation pétrographique et géochimique des péridotites et serpentinites. Les premières données obtenues sont encourageantes, mais nécessiteraient néanmoins une étude plus poussée, incluant des analyses géochimiques et isotopiques in-situ sur les différents minéraux, afin de s'abstraire des effets liés à la rétrogression et au métasomatisme crustal. Le **chapitre 7** présente les résultats d'une étude structurale, pétrographique, géochimique et isotopique des formations intrusives de l'Olan, une ancienne intrusion magmatique Mg–K mise en place dans le domaine interne du massif de l'Oisans–Pelvoux. En parallèle, une compilation des données géochimiques existantes sur les roches de la série Mg–K des MCE de Belledonne, des Grande-Rousses et de l'Oisans–Pelvoux a été réalisée, en vue de discuter des mécanismes pétrogénétiques associés à cette série magmatique.

CHAPITRE 6

Les péridotites orogéniques du massif de l'Oisans : implications sur la structure et la composition du manteau varisque



Relique de grenat dans une lherzolite, entourée d'une kelyphite à Opx+Spl(+Cpx).

Sommaire

6.1	Introduction	203
6.2	Geological setting	204
6.2.1	General setting	204
6.2.2	Ultramafic rocks in the ECM	207
6.3	Samples and methods	211
6.3.1	Petrography and mineral analysis	211
6.3.2	Whole rock composition	212
6.3.3	Sr–Nd isotopes	213
6.4	Petrography	215
6.5	Mineral compositions	219
6.6	Whole rock geochemistry and Nd–Sr isotopes	224
6.6.1	Major elements	224
6.6.2	Trace elements	226
6.6.3	Sr–Nd Isotopes	227
6.7	Thermobarometry	230
6.8	Discussion	232
6.8.1	Consequences of crustal retrogression	232
6.8.2	A refractory mantle refertilized by melts and fluids	235
6.8.3	Implications for the Variscan evolution	239
6.9	Conclusion	241

6.1 Introduction

Continental collision zones are complex settings in which a combination of tectonic, metamorphic and magmatic processes occur, which affect the whole lithosphere and upper asthenospheric mantle. These processes are generally well documented in the crust, which is exposed at various structural levels in internal and external zones of active and former orogenic belts, allowing detailed field-based structural, petrological and geochemical investigations. By contrast, the evolution of mantle lithosphere and asthenosphere during collisional orogenies is much less understood due to the scarcity of mantle outcrops. Mantle-derived magmas have been for long used as proxies to derive information on petrological and geochemical processes in the mantle in various geodynamic settings (Elliott *et al.*, 1997; Pearce, 1982). However, these magmatic proxies have strong limitations in collisional settings, in which the thick continental crust leaves wide space for crust/magma interactions, which partially obliterate the mantle signal. This is especially the case during the post-collisional stages of an orogeny, when the collapse of the orogenic belt drives significant melting in the lower crust and hence facilitates hybridization processes between mantle-derived magmas and the partially molten crust, which makes the interpretation of geochemical and isotopic signature of mantle-derived magmas strongly ambiguous (Jacob *et al.*, 2021b; Moyen *et al.*, 2017). Mantle peridotite xenoliths and orogenic peridotites sparsely distributed in orogenic domains are therefore particularly interesting, as they represent direct sampling of the mantle and are less likely to be affected by crustal contamination than hot mafic melts. They provide a wealth of information about metamorphic, metasomatic and magmatic processes which occur in the upper mantle from subduction to post-collisional stages (*e.g.* Grégoire *et al.*, 2003; Malaspina *et al.*, 2009; Scambelluri *et al.*, 2006).

In this contribution, we document the discovery of these rare but invaluable mantle rocks in the External Crystalline Massifs of the western Alps (ECM). These massifs represent

exposed portions of Paleozoic basement involved in the Variscan orogeny, which occurred from ca. 350 Ma to 295 Ma (Fréville *et al.*, 2018; Guillot *et Ménot*, 2009), following a period of calc-alkaline magmatism during the Devonian (ca. 370-350 Ma, Ménot, 1987a; Pin *et Carme*, 1987). Collision was associated with the emplacement of peculiar series of Mg-K rich granitoids and lamprophyres (Debon *et al.*, 1998; Laurent, 1992; De Boisset, 1986), akin to the vaugnerites and durbachites exposed in large parts of the Variscan Belt of Europe (Soder *et Romer*, 2018; Von Raumer *et al.*, 2014) and interpreted to derive primarily from a metasomatized mantle source (Janoušek *et Holub*, 2007). Therefore, the sub-continental mantle is thought to have experienced a complex evolution during the Devonian and the Carboniferous, involving multiple episodes of metasomatism and partial melting associated with the subduction of oceanic and continental lithosphere.

The investigated rocks were found as enclaves in lower crustal domains of the Oisans–Pelvoux massif, in the French Western Alps. They partly escaped serpentinization and preserved their initial mineral assemblages. In particular, they represent the first known occurrence of garnet peridotites in the ECM. We have undertaken petrographic, mineralogical and geochemical investigations of these peridotites in order to constrain their metamorphic evolution and document possible metasomatic events that occurred in the mantle.

6.2 Geological setting

6.2.1 General setting

The External Crystalline Massifs (ECM) represent exposed portions of Variscan basement located along the former European margin of the Mesozoic Piemonte-Liguria Ocean (Figure 6.1). The Alpine collision has occurred from the early-mid Eocene (ca. 40 Ma), during which the basement was buried and developed greenschist-facies metamorphic as-

semblages (Bellanger *et al.*, 2015). This low-grade metamorphism is mostly concentrated in Alpine compressional and strike-slip shear zones formed during the collision (Bellahsen *et al.*, 2014; Marquer *et al.*, 2006). Undeformed basement domains between these shear zones preserve the former Variscan structures and metamorphic assemblages.

The ECM contain high-grade metamorphic units with high pressure (HP) relics (Jacob *et al.*, 2021a; Liégeois et Duchesne, 1981; Rubatto *et al.*, 2010; Paquette *et al.*, 1989). They are therefore correlated with the internal "Moldanubian" zone of the Variscan Belt, which exposes deep crustal domains derived from the Gondwana continent, below which small oceanic basins and continental blocks were subducted during the Devonian and the lower Carboniferous (Lardeaux *et al.*, 2014; Schulmann *et al.*, 2009, 2014). This study is focused on the massifs of Oisans–Pelvoux and Belledonne (Figure 6.1-b). The Variscan basement in these massifs is mostly composed of lower Paleozoic (Cambrian–Ordovician) protoliths metamorphosed during the Variscan Orogeny and intruded by granitoids. In the southern part of Belledonne and the western part of the Oisans–Pelvoux massif, volcano-clastic and magmatic bimodal series of Devonian–Tournasian age (ca. 370–350 Ma) are observed, which present a calc-alkaline or arc tholeiitic signature and were presumably emplaced in a continental back-arc or arc setting (Carme et Pin, 1987; Fréville *et al.*, 2018; Guillot et Ménot, 2009; Ménot, 1987a). A general W–E zoning is observed, with low-grade mid-to-upper crustal domains exposed in the western part and high grade lower crustal domains in the eastern parts (Guillot *et al.*, 2009a). The eastern part of the Belledonne massif has been affected by a lithospheric-scale dextral shear zone known as the East-Variscan shear zone (EVSZ), which was active from the mid-to upper Carboniferous (ca. 325–295 Ma, Guillot *et al.*, 2009a; Simonetti *et al.*, 2018, 2020). It exposes HP eclogitic relics in its central domain and is therefore thought to have driven exhumation of deep-seated rocks (Jacob *et al.*, 2021a).

The Oisans–Pelvoux massif is located east of this shear zone, and exposes high-grade lower crustal domains composed of highly migmatized gneiss and amphibolite series (Fréville

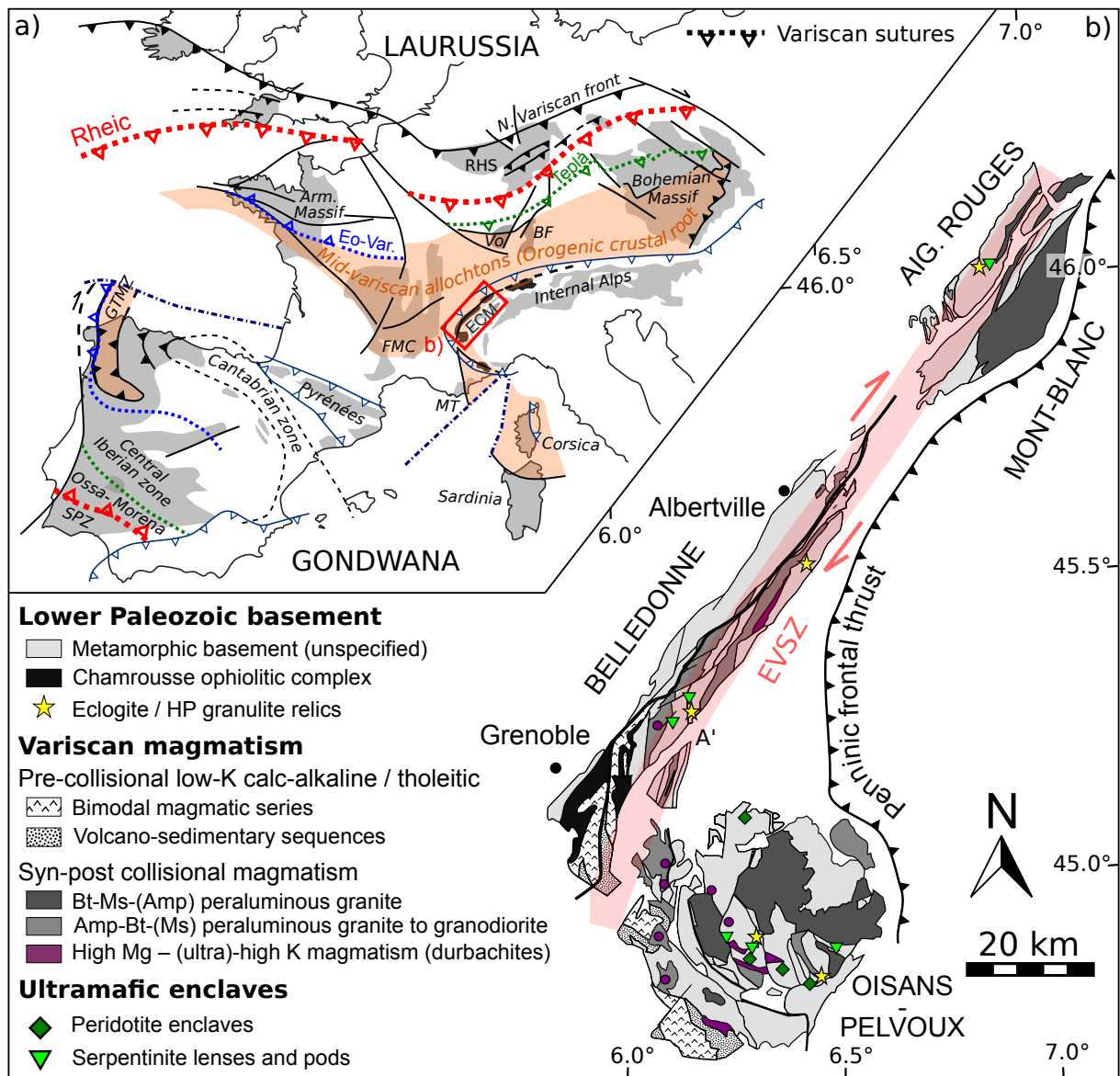


FIGURE 6.1 – a) Simplified tectonic map of the Variscan Belt of Europe, with position of the main suture zones and localization of the External Crystalline Massifs. Modified after Ballèvre *et al.* (2014). BF – Black Forest; ECM – External Crystalline Massifs; FMC – French Massif Central; GTMZ – Galicia-Trás-os-Montes; MT – Maures-Tanneron; RHS – Rheinische schiefergebirge; SPZ – South Portugese Zone; Vi – Vosges. b) Geological map of the External Crystalline Massifs of Belledonne, Oisans-Pelvoux, Mont-Blanc and Aiguilles-Rouges, with marked the position of main localities where high pressure relics and enclaves of peridotite / serpentinite have been observed. The core domain of the dextral East-Variscan Shear Zone (EVSZ) is shown by the light red stripe. Modified after Guillot *et Ménot* (2009).

et al., 2022; Le Fort, 1971). A few hectometer-scale lenses of mafic HP granulites have been identified in the massif (Chapter 4). They preserve the relics of a Visean HP event (1.5–1.7 GPa and 650–730 °C) dated at 337 ± 11 Ma, which was overprinted by HT granulite-facies

metamorphism (800–870 °C, 0.6–0.9 GPa) during the upper Carboniferous between ca. 310 and 295 Ma (Chapter 4). This HT overprint affected a large portion of the massif and triggered extensive migmatization of the metamorphic series.

The metamorphic basement is intruded by moderately peraluminous, medium to high-K alkali-calcic granitoids, deriving from crustal melting with subordinate contribution of an enriched mantle source (Debon *et al.*, 1998). In the massif of Belledonne and the western part of the Oisans–Pelvoux massif, these granitoids were mostly emplaced during the Viséan (345–335 Ma), while most of the granitoids in the eastern Oisans–Pelvoux massif were emplaced during the upper Carboniferous (308–298 Ma, Debon *et Lemmet*, 1999; Fréville, 2016). Finally, a suite of metaluminous, high Mg-K mafic to intermediate magmatic rocks is regionally ubiquitous, although in small volume (Figure 6.1). It occurs as enclaves in the granitoids, lamprophyric dykes intruding the basement or kilometer-scale intrusive bodies (De Boisset, 1986; Debon *et Lemmet*, 1999; Laurent, 1992). This series is akin to the durbachite and vaugnerite series known in different parts of the Variscan Belt (Hora *et al.*, 2021; Janoušek *et al.*, 2019; Moyen *et al.*, 2017; Soder *et Romer*, 2018), which displays dual geochemical characteristics combining high-Mg composition and strong enrichment in K₂O and mantle-incompatible trace elements (Ba, Sr, Th, U, Pb in particular).

6.2.2 Ultramafic rocks in the ECM

Different types of ultramafic rocks of different origins are exposed in the ECM. The largest outcrop is represented by the ophiolitic complex of Chamrousse (Figure 6.1-b), a slice of Cambrian oceanic lithosphere, which was presumably obducted during the early stages of the Variscan orogeny (Fréville *et al.*, 2018; Guillot *et Ménot*, 2009; Ménot, 1987a; Pin *et Carme*, 1987). This ophiolitic sequence is only found in the southwestern Belledonne massif, where it forms the top of the Variscan metamorphic nappe pile. The ultramafic units

in this ophiolite are mostly composed of serpentized cumulates with pods of chromite, which are overlain by cumulative gabbros, the whole being cross-cut by a dyke complex composed of several generations of metabasalts, metadolerites and metatonalites (Ménot *et al.*, 1988). This ophiolite is both structurally and geochemically unrelated to the other ultramafic bodies exposed in the ECM, which are located in deeper structural domains and do not present characteristics of a cumulate sequence.

In the eastern Belledonne massif, serpentinites and pyroxenites are found in high-strain domains of the EVSZ (Barféty *et al.*, 2000), where they form decameter to hectometer-scale lenses elongated along the main foliation (Figure 6.2-a). Serpentinite lenses are also reported in a similar setting in the Aiguilles Rouges Massifs (Von Raumer *et Bussy*, 2004), which represents the northern prolongation of the Belledonne massif. These rocks presumably represent portions of the sub-continental lithospheric mantle, which were exhumed in the high-strain domains of the lithospheric-scale EVSZ, where they have been completely serpentized.

Finally, peridotites and serpentinites are exposed in the high-grade domains of the Oisans–Pelvoux massif. The serpentinites form decameter-size pods and lenses, which are either concordant with the Variscan metamorphic foliation or tectonically transposed in Alpine brittle fault zones (Figure 6.2-b). The peridotites are found as decimeter-to-meter size enclaves widely distributed in scree slopes over a large part of the massif (Figure 6.1). These enclaves were first described by Pecher (1970) and Le Fort (1971), but due to the intense retrogression experienced by their samples, these authors did not recognize them as peridotites. They have been found in-place in a few outcrops, where they appear as nests of enclaves embedded in migmatites, and display various shapes ranging from rounded to angular (Figure 6.2-c-f). This disposition suggests the enclaves represent pieces of larger peridotite bodies, possibly of decameter-size, which have been fractured by injection of granitic

magmas and dismembered into smaller blocks. Melt/fluid – rock interaction at contact with migmatites is evidenced by spectacular coronas composed of radially-oriented biotite and/or tremolite, which rim some enclaves (Figure 6.2-e). Outside of these domains the peridotites generally look fresh and weakly to non-affected by these interactions.

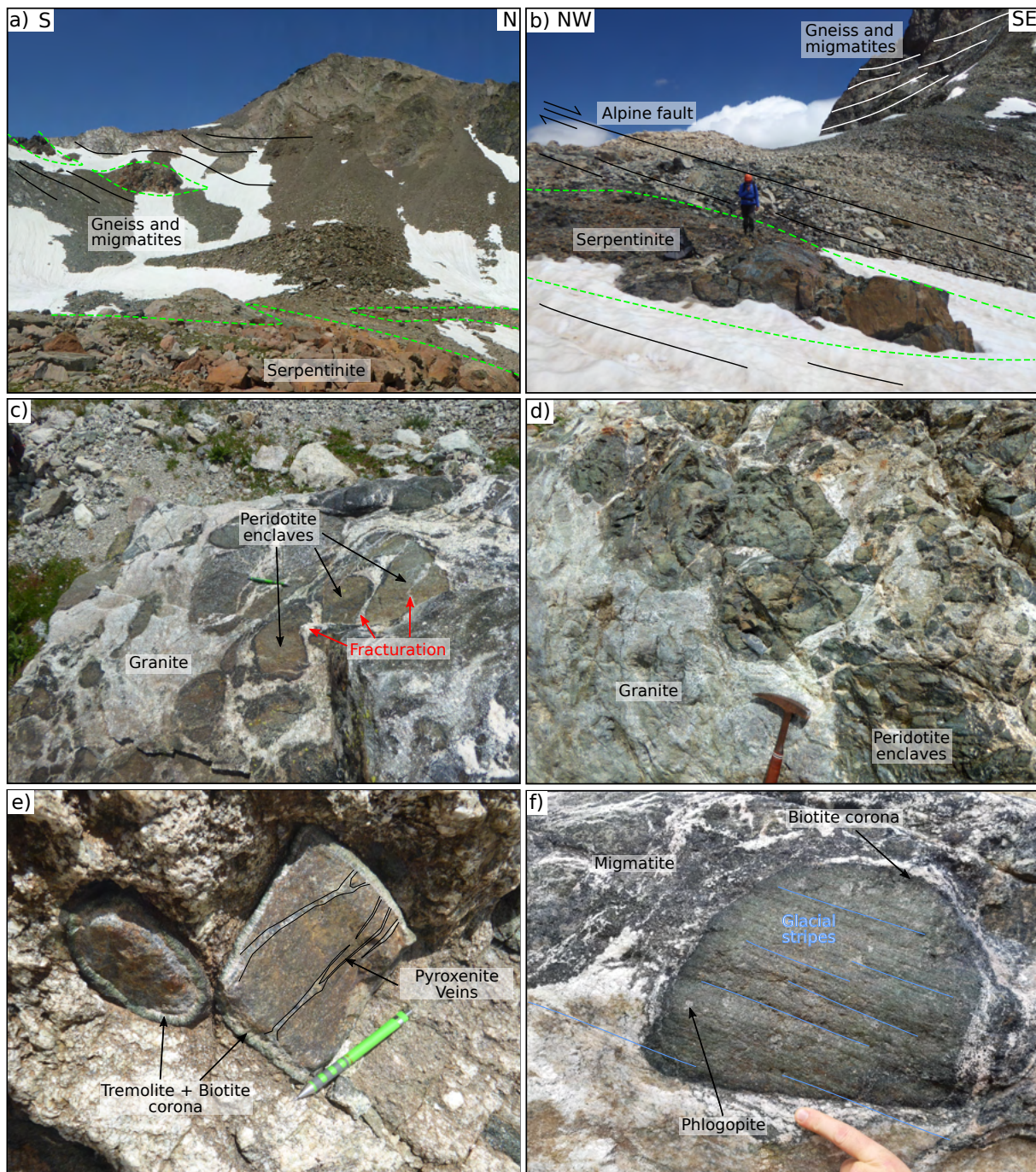


FIGURE 6.2 – Field pictures showing the different types of ultramafic outcrops in the ECM. (a) – decameter-size lenses of serpentinite exposed at Col de l'Amiante (eastern Belledonne) and embedded within the main gneiss foliation. (b) Serpentinite lense exposed at Col des Sellettes (Oisans) and transposed in an alpine brittle fault oblique to the main gneiss foliation. (c), (d) – Decimeter-to meter-scale enclaves of peridotite exposed within highly mobilized portions of a migmatite in the Oisans–Pelvoux massif. Note the fracturation of enclaves into smaller angular blocks caused by injection of granitic liquid. These enclaves display either sharp, reactionless contact with the surrounding granite, or present a thin corona rich in biotite. e) – Rounded enclaves of harburgite surrounded by a 2-3cm-wide corona of tremolite + biotite (Bans Valley, Oisans–Pelvoux massif). The core of enclaves is crossed by centimeter-wide veins of pyroxenite. f) Phlogopite-bearing enclave in a migmatite (Bans Valley, Oisans–Pelvoux massif). Bright shiny patches in the core of the enclaves are phlogopite crystals, whose color contrast with the dark biotite of the corona.

6.3 Samples and methods

11 samples of peridotites and 4 samples of serpentinites were collected at several locations separated from a few km to tens km in the Oisans-Pelvoux massif and Belledonne massifs, for petrographic study and whole rock geochemical and isotopic analysis. Sampling coordinates and petrographic types of each sample are summarized in Table 6.1.

6.3.1 Petrography and mineral analysis

Backscattered electron (BSE) images were acquired at ISTERre Grenoble with a Tescan Vega 3 scanning electron microscope equipped with an energy dispersive spectrometer (EDS) for semi-quantitative analysis. It was operated with an accelerating voltage of 16 kV and a beam current of 10 nA. Mineral compositions were measured using a JEOL JXA-8230 electron probe microanalyzer (EPMA) at ISTERre Grenoble, which is equipped with five wavelength dispersive spectrometers (WDS) and an additional EDS. All silicates except olivine were analyzed using standard EPMA protocols, with an accelerating voltage of 15 kV (amphibole, phlogopite) to 20 kV (garnet, pyroxenes), a beam current of 10 nA (amphibole, phlogopite) to 20 nA (garnet, pyroxenes), and a counting time per element of 30 to 60 s for peak and both background positions. Natural minerals and synthetic glass were used for standardization, and the ZAF matrix procedure was applied for data reduction. The spot size was set to 1–3 μm depending on the size of minerals and the presence of volatile elements.

The composition of olivine was analyzed following high-precision method for major (Si, Mg, Fe), minor (Ni, Mn) and trace (Al, Ca, Cr, Ti, P) elements (Batanova *et al.*, 2015, 2019) at an acceleration voltage of 20 kV, beam current of 900 nA and beam diameter of 2 microns. Total analysis time of each point was 7.2 minutes. MongOl sh11-2 olivine reference material

(Batanova *et al.*, 2019) was used as primary standard to verify precision and accuracy. Deviation from the reference measured during the analytical session was between 2 and 13 ppm for trace elements, between 10 and 85 ppm for minor elements and between 0.01 and 0.06 wt.% for major oxides, which is in all cases below the 2-sigma uncertainties reported in Batanova *et al.* (2019) for these respective elements.

The composition of Cr-spinel was measured at 20 kV and 50 nA beam current. Counting time was adapted to element content and was between 60 to 120 s for each element (for peak and both background positions). The standardization was made using a synthetic oxide standard set (P&H Developments Ltd., Calibration Standards for Electron Probe Microanalysis, Standard Block GEO) for all elements except Mn (on rhodonite). Ferric iron in spinel was calculated assuming perfect stoichiometry. Repeated measurements of the chromite USNM 117075 (Jarosewich *et al.*, 1980) standard and spinel samples Bar 8601-10 and Dar 8502-2, whose $\text{Fe}^{3+}/\text{Fe}_{total}$ ratio had been measured by Mossbauer spectroscopy (Ionov *et Wood*, 1992) have shown that the selected method provides $\text{Fe}^{3+}/\text{Fe}_{total}$ ratios accurate within the measurement error. Spinel Bar 8601-10 (Ionov *et Wood*, 1992) was used as a primary standard and was analyzed multiple times during the session to verify precision and accuracy. Deviation from the reference value measured during the session was below 50 ppm for most of trace elements (Ti, V, Mn, Ni) and bit higher for Zn (66 ppm) and Si (86 ppm). For major oxides, deviation from the reference value was about 0.64 wt.% for Al_2O_3 and 0.06 wt.% for FeO and MgO.

6.3.2 Whole rock composition

Samples were cut to remove the outer gangue formed at the contact with the migmatites, and domains devoid of large veins were carefully selected to keep only the least retrogressed part of the rocks. They were then crushed in a jaw crusher and pulverized into a 70–80

μm powder using an agate crusher. Whole rock geochemical analyses were performed at the SARM in Nancy, using a Thermo Fischer iCap6500 ICP-OES for major oxides and an iCapQ ICP-MS for minor and trace elements, following the procedures described in Carignan *et al.* (2001). Samples display high loss on ignition between 7 and 13 wt.% due to serpentinization, and therefore the analyses were recalculated on an anhydrous basis to allow comparison between samples. Raw analyses are provided in the supplements. The R-based GCDKit software (Janoušek *et al.*, 2016) was used for statistical analysis and plotting of whole rock geochemical data.

6.3.3 Sr–Nd isotopes

Nine samples were selected for Sr–Nd isotope analyses. Due to low Nd concentration, only five of them were analyzed for Nd isotopes. Isotopic measurements were also carried out at the SARM in Nancy. 100 to 200 mg of pulverized samples were dissolved into a mixture of concentrated HNO_3 and HF heated to 115 °C during 24 to 48h, followed by concentrated HCl at 125 °C during 24h. Sr and Nd were isolated via ion-exchange chromatography using Sr.Spec, Tru.Spec and Ln.spec resins, following the procedure described in Pin *et al.* (1994) and Pin et Zalduegui (1997). Sr and Nd isotopes were analyzed by thermal ionization mass spectrometry (TIMS), using respectively a Triton Plus and a Neptune Plus instrument operated in static multi-collection mode. The $^{87}\text{Sr}/^{86}\text{Sr}$ ratios were corrected for mass bias assuming $^{86}\text{Sr}/^{88}\text{Sr} = 0.119400$, and $^{143}\text{Nd}/^{144}\text{Nd}$ ratios were corrected to $^{146}\text{Nd}/^{144}\text{Nd} = 0.721900$ (Luais *et al.*, 1997). Internal standards NBS 987 and JNdi-1 (Tanaka *et al.*, 2000) were used respectively for Sr and Nd. The decay constants applied to age-correct the isotopic ratios are from Steiger et Jäger (1977) for Sr and Lugmair et Marti (1978) for Nd. The ϵNd_i values were obtained using Bulk Earth parameters of Bouvier *et al.* (2008).

Sample	Type	Position (WGS84)		wt.% oxides											Mg#	Cr#
		Long°	Lat°	SiO ₂	TiO ₂	Al ₂ O ₃	FeO	MnO	MgO	CaO	Na ₂ O	K ₂ O	P ₂ O ₅			
JB-19-20	<i>Grt Lrz</i>	6.35604	44.83521	45.11	0.11	3.29	8.14	0.12	40.70	2.33	0.20	< D.L	< D.L	0.90	0.07	
JB-19-23	<i>Grt Lrz</i>	6.34905	44.83562	48.19	0.06	2.20	8.67	0.12	39.16	1.41	0.14	0.05	< D.L	0.89	0.11	
JB-19-31	<i>Grt Lrz</i>	6.22290	44.84258	46.52	0.15	3.72	8.15	0.10	38.11	2.69	0.26	0.29	< D.L	0.89	0.06	
JB-19-33	<i>Grt Lrz</i>	6.20450	44.84665	45.33	0.15	3.62	8.52	0.11	39.46	2.58	0.23	< D.L	< D.L	0.89	0.06	
JB-19-34	<i>Grt Lrz</i>	6.20450	44.84665	45.71	0.13	3.41	8.29	0.08	40.23	2.02	0.13	< D.L	< D.L	0.90	0.07	
JB-20-06	<i>Grt Lrz</i>	6.20309	44.84967	46.06	0.11	2.78	8.30	0.08	40.54	1.93	0.16	0.04	< D.L	0.90	0.08	
JB-20-12	<i>Grt Lrz</i>	6.20473	44.84611	45.98	0.15	3.80	8.33	0.08	38.71	2.65	0.27	0.04	< D.L	0.89	0.07	
JB-20-13	<i>Grt Lrz</i>	6.20319	44.84945	45.22	0.17	4.49	8.29	0.11	38.60	2.84	0.22	0.06	< D.L	0.89	0.06	
JB-20-14	<i>Grt Lrz</i>	6.20274	44.84982	45.72	0.05	2.20	8.09	0.11	41.98	1.62	0.08	0.15	< D.L	0.90	0.11	
JB-19-21	<i>Phl Hrz</i>	6.33910	44.83612	45.98	0.10	1.03	8.45	0.10	43.21	0.36	< D.L	0.64	0.13	0.90	0.35	
JB-19-22	<i>Spl Hrz</i>	6.33910	44.83612	44.69	0.03	1.63	8.79	0.10	42.94	1.42	0.08	0.33	< D.L	0.90	0.14	
JB-18-27	<i>Srp</i>	6.39256	44.87250	45.01	< D.L	1.22	9.11	0.11	44.15	0.39	< D.L	< D.L	< D.L	0.90	0.20	
JB-19-45	<i>Srp</i>	6.23450	44.86690	46.66	< D.L	1.26	8.17	0.08	42.75	0.79	< D.L	0.29	< D.L	0.90	0.18	
JB-19-48	<i>Srp</i>	6.10814	45.23891	46.20	0.04	1.59	8.98	0.07	42.86	0.28	< D.L	< D.L	< D.L	0.89	0.15	
JB-19-49	<i>Srp</i>	6.11245	45.23940	46.20	< D.L	0.84	8.84	0.05	43.63	0.43	< D.L	< D.L	< D.L	0.90	0.24	

TABLE 6.1 – List of collected samples with localization (WGS84), petrographic type and bulk rock major element composition normalized to 100 wt.%. < D.L : Values below detection limit. Grt Lrz – Garnet Lherzolite; Spl Hrz – Spinel Harzburgite; Phl Hrz – Phlogopite Harzburgite; Srp – Serpentine

6.4 Petrography

Four different petrographic types are recognized among the collected samples : retrogressed garnet lherzolite, spinel harzburgite, phlogopite-chromite harzburgite and serpentinite (Figure 6.3). The samples are variously retrogressed, and serpentinization ranges from very scarce in the best-preserved peridotites to complete in the serpentinites. Petrographic descriptions are focused on the peridotites, which preserved their primary mineral assemblage. Serpentinites are mostly composed of serpentine (antigorite) and Fe-oxides, and occasionally preserved relics of primary minerals (olivine, orthopyroxene, spinel).

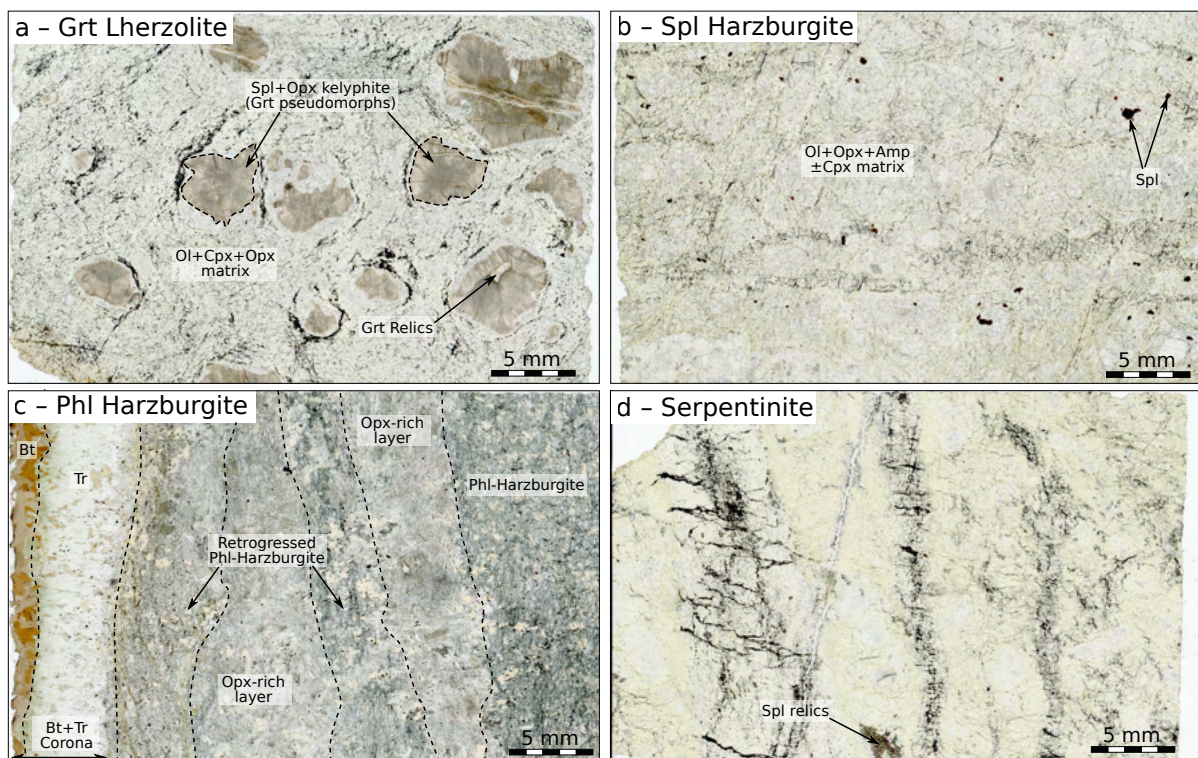


FIGURE 6.3 – Thin section scans of selected samples representative of the four different petrographic types identified (Garnet Lherzolite, Spinel Harzburgite, Phlogopite-Chromite Harzburgite and Serpentinite).

The garnet lherzolites display millimeter-to centimeter-size retrogressed garnet grains surrounded by a finer-grained olivine, orthopyroxene and clinopyroxene assemblage (Figure 6.3-

a). Clinopyroxene is abundant in this latter assemblage (ca. 10-15 vol.% of the olivine-pyroxenes assemblage) and forms 100–200 μm wide grains. This assemblage is generally well preserved (Figure 6.4-a) and olivine has been only mildly affected by serpentinization. In contrast, garnet has almost been completely retrogressed, and only a few relics were identified (Figure 6.3-a). In most samples it has been totally transformed into a kelyphite composed of micrometer-sized intergrowth of spinel and orthopyroxene, with a few larger grains (10–20 μm) of clinopyroxene (Figure 6.4-b). This kelyphite is surrounded by a coarse-grained corona composed of orthopyroxene and clinopyroxene. In most of samples, the thin kelyphite has started to recrystallize into a coarser-grained symplectite of orthopyroxene + spinel \pm clinopyroxene \pm amphibole, which eventually evolves toward a coarse-grained granoblastic assemblage of the same minerals (Figure 6.4-c). The few garnet relics which escaped destabilization are surrounded by a thin symplectite composed of plagioclase + amphibole + Cr-rich spinel (Figure 6.4-b). These rare garnet relics contain small inclusions (ca. 20 μm wide) of orthopyroxene, which themselves contain tiny, dark rounded inclusions of graphite (Figure 6.5).

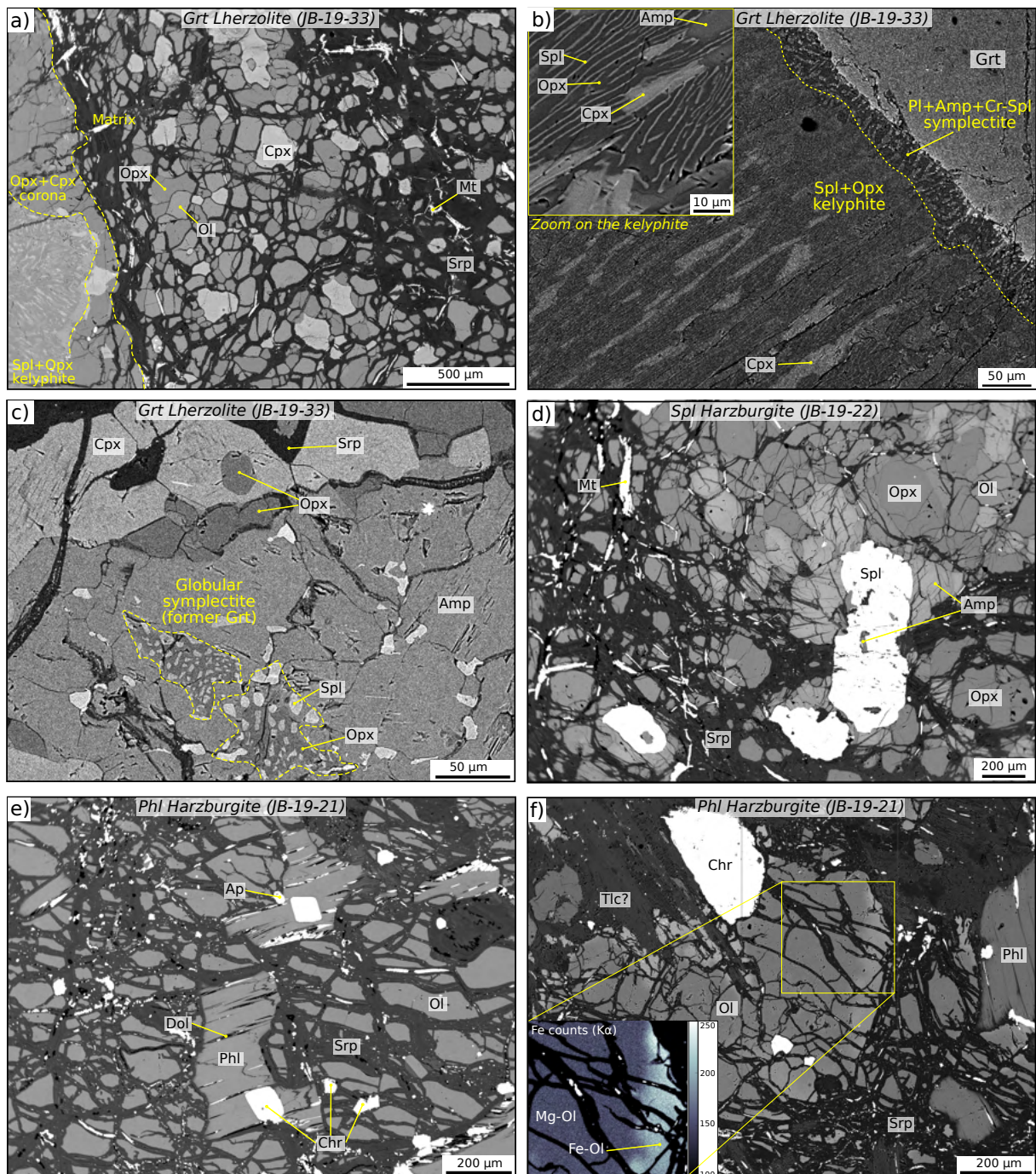


FIGURE 6.4 – Backscattered electron images (BSE) showing important petrographic features in the different peridotite groups. (a) – Mineral assemblage in a garnet lherzolite. Retrogressed garnet (bottom left) has been replaced by a kelyphite surrounded by a coarse-grained corona of clinopyroxene + orthopyroxene. (b) – orthopyroxene + spinel + clinopyroxene kelyphite surrounding a retrogressed garnet grain (top-right). A thin 20–50 μm wide symplectite of amphibole + plagioclase \pm Cr-spinel has developed at the contact with the garnet relics during a later stage of retrogression. (c) – Advanced stage of annealing of a former kelyphite, which has been replaced by an coarse-grained assemblage of amphibole, orthopyroxene, clinopyroxene and Cr-spinel. Relics of a globular spinel + orthopyroxene symplectite is visible in the centre. (d) – Mineral assemblage in a spinel harzburgite. This sample is rich in pargasite, which occurs as 100–200 μm grains and as inclusions in spinel. (e) – Mineral assemblage in a harzburgitic domain of the phlogopite-chromite harzburgite. Chromite is ubiquitous and occurs as inclusion in phlogopite. Olivine is unzoned and variably serpentinized. (f) – zoned olivine close to an orthopyroxenite layer. The rim of the grain has been replaced by BSE-brighter Fe-Mn-rich olivine. X-ray mapping of Fe reveals an irregular boundary between the Mg-rich and Fe-rich olivine. Note that this zoning is cut by the serpentine network, which indicates serpentinization postdates development of Fe-Mn-rich olivine.

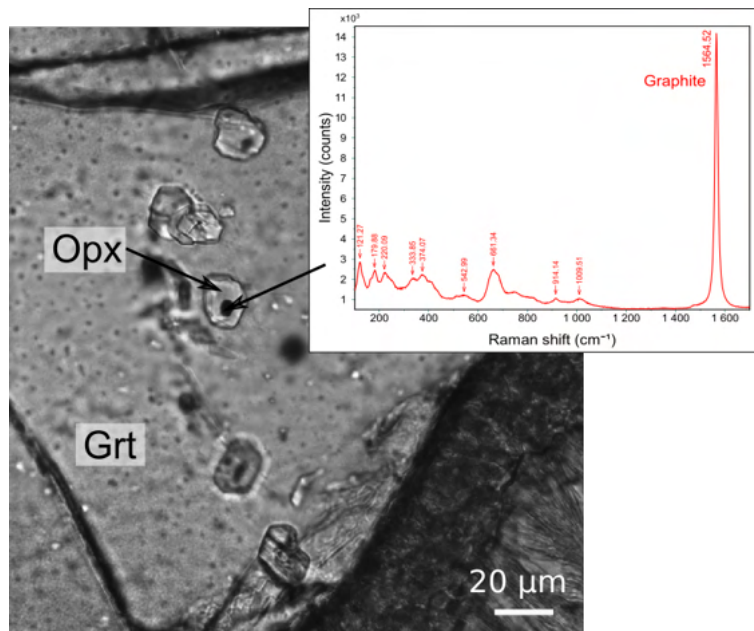


FIGURE 6.5 – Close-up view on orthopyroxene inclusions in a garnet relics of sample JB-19-33 (optical microscopy). Raman spectroscopy on the dark tiny inclusions in orthopyroxene reveals the presence of graphite, indicated by the strong peak around 1566–1575 cm^{-1} (Beyssac *et al.*, 2002).

The spinel harzburgite (sample JB-19-22) is mostly composed of olivine, orthopyroxene, pargasitic amphibole and spinel, with rare clinopyroxene and phlogopite, and accessory magnetite (Figure 6.3-b and Figure 6.4-d). No kelyphites nor mosaic assemblages of clinopyroxene and orthopyroxene formed after garnet have been identified, which indicates that garnet was absent from the primary assemblage. Spinel forms 200–500 μm wide grains that contain inclusions of pargasitic amphibole (Figure 6.4-d). Olivine forms 50–200 μm wide grains, which have been partly serpentinized. Orthopyroxene is abundant and forms large grains up to 500 μm wide. By contrast, clinopyroxene is rare and forms <100 μm grains. Phlogopite is scarce and generally found in association with pargasite.

Finally, the phlogopite-chromite harzburgite contains an assemblage of olivine, orthopyroxene, phlogopite, chromite and accessory apatite, and is completely devoid of clinopyroxene (Figure 6.4-e,f). Minor amount of dolomite is found between the cleavages of phlogopite. The sample investigated in detail (JB-19-21) is an enclave surrounded by a corona of biotite and

tremolite formed at the contact with the migmatite (Figure 6.3-c). Some portions of the rock are highly retrogressed and serpentized, while the core of the sample contains well-preserved harzburgite. In this domain, olivine forms 200–500 μm , partly serpentized grains. Orthopyroxene and phlogopite form large grains up to 1 mm-wide. Chromite is ubiquitous, and forms subeuhedral grains ranging from 10 μm to >100 μm (Figure 6.4-e). It has been found in particular in inclusion in phlogopite and olivine. Apatite and dolomite are closely associated with phlogopite : dolomite crystallized in veins opened within the cleavages of phlogopite, and small grains of apatite (<50 μm) are generally found close to phlogopite (Figure 4-e). Harzburgitic domains are cut by centimeter-wide veins of orthopyroxenite, which are mainly composed of large grains of orthopyroxene (up to 3 mm wide), with subordinate olivine, phlogopite and chromite (Figure 6.3-c). Partial replacement of Mg-rich primary olivine by BSE-brighter Fe-rich secondary olivine is commonly observed in olivine grains located close to or within these orthopyroxenite veins (Figure 6.4-f).

6.5 Mineral compositions

Mineral compositions have been investigated in three samples : a garnet lherzolite (JB-19-33), a spinel harzburgite (JB-19-22) and a phlogopite-chromite harzburgite (JB-19-21). A set of selected representative analyses is provided in Tables 6.2 and 6.3. The complete set of electron microprobe analyses is provided in the supplements.

In all samples, olivine displays high Mg# (molar ratio $\text{Mg}/(\text{Mg}+\text{Fe}^{2+})$) between 0.88 and 0.91, high Ni (2700–4200 ppm) and moderate Mn (1000–1300 ppm) content, with Ni/Mn between 2.1 and 3.3 (Figure 6.6-a), which is typical of olivine in mantle peridotite (Wang *et al.*, 2021). Other trace elements (Ca, Ti, Al, P, Cr) are present in much lower concentration, below 50 ppm for Ti and Al and below 200 ppm for Ca, Cr and P. In sample JB-19-21 (phlogopite-chromite harzburgite), some olivine grains located within or close to

Mineral Label	JB-19-21				JB-19-22				JB-19-33			
	<i>Opx-02</i> core	<i>Phl-04</i> core	<i>Bt-11</i> Corona	<i>Amp-5</i> Corona	<i>Opx-04</i> core	<i>Amp-1</i> core	<i>Grt-12</i> core	<i>Grt-01</i> rim	<i>Opx-07</i> Matrix Core	<i>Opx-08</i> Grt Corona	<i>Cpx-11</i> Grt Corona	<i>Cpx-06</i> Matrix Core
wt% oxides												
SiO ₂	57.57	41.27	38.32	55.29	56.02	44.74	41.32	41.45	55.71	55.01	52.99	53.49
TiO ₂	0.06	1.15	2.02	0.03	0.03	0.39	0.63	0.61	0.07	0.07	0.34	0.31
Al ₂ O ₃	0.15	12.96	14.50	1.23	2.12	12.73	21.45	21.64	1.91	3.57	3.99	3.42
Cr ₂ O ₃	0.05	1.03	0.19	0.24	0.32	1.49	1.33	1.30	0.28	0.09	0.76	0.87
FeO	6.06	2.45	15.93	7.58	6.78	3.63	8.65	11.69	7.27	7.26	2.04	2.75
MnO	0.16	0.00	0.21	0.42	0.17	0.06	0.28	0.70	0.20	0.18	0.09	0.11
MgO	35.94	25.39	15.15	19.96	34.01	18.25	20.57	18.25	33.73	33.35	16.33	18.05
CaO	0.12	0.00	0.00	11.46	0.21	12.34	4.41	4.31	0.43	0.25	22.39	19.55
Na ₂ O	0.00	0.15	0.20	0.26	0.00	1.76	0.00	0.02	0.00	0.00	1.04	1.03
K ₂ O	na	9.60	9.36	0.13	na	0.99	na	na	na	na	na	na
Total	100.10	93.99	95.87	96.61	99.67	96.39	98.63	99.96	99.61	99.78	99.95	99.57
Oxygen Cation												
Si	1.98	2.94	2.85	7.69	1.94	6.36	2.99	3.00	1.94	1.91	1.92	1.94
Ti	0.00	0.06	0.11	0.00	0.00	0.04	0.03	0.03	0.00	0.00	0.01	0.01
Al	0.01	1.09	1.27	0.20	0.09	2.13	1.83	1.85	0.08	0.15	0.17	0.15
Cr	0.001	0.06	0.01	0.03	0.009	0.17	0.076	0.074	0.008	0.002	0.022	0.025
Fe ²⁺	0.17	0.15	0.99	0.86	0.20	0.43	0.52	0.71	0.21	0.21	0.06	0.08
Fe ³⁺	-	-	-	0.02	-	0.00	-	-	-	-	-	-
Mn	0.005	0.00	0.01	0.05	0.005	0.01	0.017	0.043	0.006	0.005	0.003	0.003
Mg	1.84	2.69	1.68	4.14	1.76	3.87	2.22	1.97	1.75	1.73	0.88	0.97
Ca	0.00	0.00	0.00	1.71	0.01	1.88	0.34	0.33	0.02	0.01	0.87	0.76
Na	0.00	0.02	0.03	0.07	0.00	0.49	0.00	0.00	0.00	0.00	0.07	0.07
K	-	0.87	0.89	0.02	-	0.18	-	-	-	-	-	-
Total cation	4.01	7.87	7.85	16.80	4.01	17.56	8.03	8.01	4.01	4.01	4.01	4.01
Mg#	0.91	0.95	0.63	1.00	0.90	1.00	0.81	0.74	0.89	0.89	0.93	0.92
Cr#	0.20	0.05	0.01	0.12	0.09	0.07	2.83	2.85	0.09	0.02	0.11	0.15
(Na+K)tot	-	-	-	0.09	-	0.66	-	-	-	-	-	-

TABLE 6.2 – Representative analyses of garnet, orthopyroxene, clinopyroxene, amphibole and phlogopite. na : not analyzed

<i>Mineral Label Position</i>	JB-19-21				JB-19-22	
	<i>Chr Spl-09 core</i>	<i>Spl Spl-01 core</i>	<i>Ol Ol-07 core</i>	<i>Ol Ol-18 rim</i>	<i>Ol Ol-06 core</i>	<i>Ol Ol-07 core</i>
wt% oxides						
SiO ₂	0.02	0.00	40.83	39.29	40.80	40.58
TiO ₂	0.93	0.06	0.0035	0.0016	0.0010	0.0028
Al ₂ O ₃	4.38	37.75	0.0000	0.0000	0.0000	0.0018
Cr ₂ O ₃	58.96	28.98	0.0268	0.0110	0.0022	0.0028
V ₂ O ₃	0.17	0.12	na	na	na	na
FeO	29.47	18.10	8.79	17.27	9.66	10.78
MnO	0.87	0.18	0.1308	0.7278	0.1455	0.1669
MgO	3.77	14.75	49.54	42.36	48.98	48.11
CaO	na	na	0.0091	0.0052	0.0133	0.0133
P ₂ O ₅	na	na	0.0214	0.0779	0.0136	0.0100
NiO	0.07	0.16	0.4256	0.2446	0.3731	0.3590
ZnO	0.64	0.40	na	na	na	na
Total	99.29	100.50	99.78	99.99	100.00	100.02
Oxygen Cation	4	4	4	4	4	4
Si	-	-	1.02	0.97	1.01	1.01
Ti	0.025	0.001	-	-	-	-
Al	0.184	1.268	-	-	-	-
Cr	1.661	0.653	-	-	-	-
Fe ²⁺	0.752	0.343	0.36	0.71	0.40	0.44
Fe ³⁺	0.127	0.089	-	-	-	-
Mg	0.200	0.627	1.60	1.35	1.57	1.54
Total cation	2.95	2.98	2.98	3.03	2.99	2.99
Mg#	0.90	0.34	0.91	0.81	0.90	0.89
Cr#	0.21	0.65	-	-	-	0.61
Trace ppm						
Ni	586	1259	3344	1922	2932	2821
Mn	6766	1365	1013	5637	1127	1293
Cr	-	-	183	75	15	19
V	1155	840	-	-	-	-
Ca	-	-	65	37	95	95
Ti	5570	357	21	10	6	17
Si	90	0	-	-	-	-
Al	-	-	-	-	-	10
P	-	-	93	340	59	44
Zn	5158	3213	-	-	-	-
Ni/Mn	0.09	0.92	3.30	0.34	2.60	2.18

TABLE 6.3 – Representative analyses of spinel, chromite and olivine. na : not analyzed

the orthopyroxenite layers have been partially replaced by less magnesian, Fe-Mn-rich olivine (Mg# = 0.81–0.86, Mn = 2000–5800 ppm), with low Ni/Mn between 0.32 and 1.74. This replacement has mostly occurred in the rims and along cracks, leaving the olivine cores unmodified (Figure 6.4-f). Composition variations are observed between samples. In particular, there is a consistent increase in Ni/Mn correlated with increasing Mg#, from the least magnesian clinopyroxene-garnet lherzolites (Ni/Mn = 2.1–2.3) to the more magnesian clinopyroxene-free phlogopite-chromite harzburgite (Ni/Mn = 3.0–3.3).

Orthopyroxene displays high Mg# between 0.89 and 0.91. As for olivine, Mg# in orthopyroxene increases while Mn decreases from the garnet lherzolite to the phlogopite-chromite

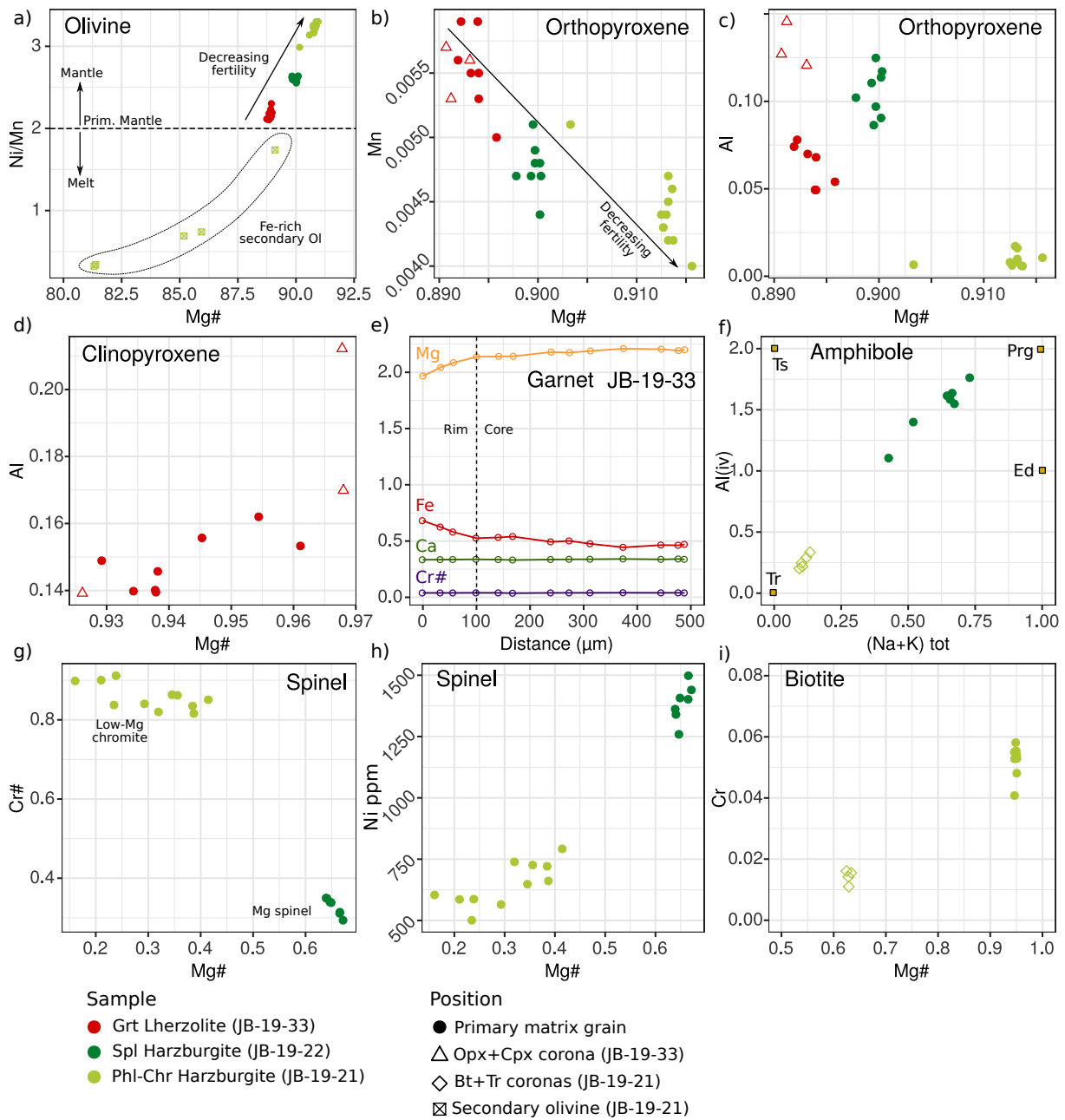


FIGURE 6.6 – Selected mineral plots showing important features of mineral compositions in the different peridotite groups. Note in particular the correlation between Mg# and Ni–Mn content in olivine and orthopyroxene. Distinction between mantle and cumulative (melt) olivine is after Wang *et al.* (2021).

harzburgite (Figure 6.6-b). Al content of orthopyroxene is very low in the phlogopite-chromite harzburgite (ca. 0.01 p.f.u) and higher in the spinel harzburgite and the garnet lherzolites (respectively 0.09–0.13 and 0.05–0.08 p.f.u, Figure 6.6-c). Orthopyroxene that recrystallized in the coronas around kelyphites displays higher Al-content up to 0.15 p.f.u.

Clinopyroxene and garnet were analyzed only in the garnet lherzolite. Clinopyroxene has high Mg# (0.92–0.94 p.f.u) and variable Al (0.14–0.17 p.f.u Al). Clinopyroxene in the coronas contains slightly more Al and slightly less Cr than the matrix clinopyroxene (Figure 6.6-d). Garnet is a slightly chromian pyrope, with Cr# = 0.04–0.05 (where Cr# is the molar ratio Cr/(Cr+Al)) and Mg# = 0.74–0.84. It displays Fe-Mg zoning from core to rim (Figure 6.6-e), with higher Mg-content in the core (Prp₇₃Alm₁₅) than in the rim (Prp₆₅Alm₂₃). No zoning is observed in Ca nor in Cr.

Amphibole was analyzed only in the spinel / phlogopite-chromite-bearing harzburgites (Figure 6.6-f). In sample JB-19-22 (spinel harzburgite), amphibole is a slightly chromian pargasite, with Cr = 0.15–0.19 p.f.u, Mg# >0.94 and Al_{iv} = 1.40–1.76 p.f.u. In sample JB-19-21 (phlogopite-chromite harzburgite), amphibole was only observed in the corona that rim the peridotite enclave. It is a nearly pure tremolite (Mg# > 0.95, Al_{iv} = 0.20–0.33).

Spinel in sample JB-19-22 is slightly chromian, with Mg# = 0.63–0.66 and Cr# = 0.29–0.35. It is quite rich in Ni (1250–1500 ppm, Figure 6.5-h) and poor in Mn (1240–1365 ppm), Zn (2700–3200 ppm), V (820–950 ppm) and Ti (300–400 ppm). By contrast, sample JB-19-21 contains ferroan chromite (Mg# = 0.15–0.40, Cr# = 0.81–0.91). It is poorer in Ni (500–740 ppm) and richer in Zn (up to 7400 ppm), V (1000–1250 ppm), Mn (2600–10050 ppm) and Ti (4500–6200 ppm) than spinel of sample JB-19-22 (Figure 6.6-g,h).

Finally, mica was only analyzed in sample JB-19-21. The preserved harzburgite in the core of the enclave contains nearly pure phlogopite (Mg# = 0.95), with 0.05–0.06 p.f.u Ti and 0.06 p.f.u Cr. This contrasts with biotite from the corona, which is less magnesian (Mg# = 0.62–0.63), contains less Cr (Cr < 0.02) and more Ti (Ti = 0.11 p.f.u) than the core phlogopite (Figure 6.6-i).

6.6 Whole rock geochemistry and Nd-Sr isotopes

6.6.1 Major elements

All the samples have been serpentinized to various degrees during retrogression, but this process is generally considered to induce no or very minor changes in major element composition, and preserves in particular $\text{Al}_2\text{O}_3/\text{SiO}_2$ and MgO/SiO_2 ratios (Deschamps *et al.*, 2013). Formation of talc during serpentinization may nevertheless be associated with strong modification of the initial composition, notably by SiO_2 enrichment (Paulick *et al.*, 2006). Apart from highly retrogressed or altered domains which have been removed before crushing, no talc has been observed in the samples. Therefore, the measured compositions renormalized to to an anhydrous basis (Table 6.1) are considered as representative of the initial whole rock compositions before serpentinization. Normalizing to dry composition may induces a bias for the phlogopite / pargasite-bearing samples, which were not anhydrous before serpentinization. This bias is however considered to be small considering the very high loss on ignition (8–10 wt.%), which is likely dominated by water serpentine minerals, and does anyway not affect element ratios.

The peridotites and serpentinites display variations in major elements composition. In the $\text{Al}_2\text{O}_3/\text{SiO}_2$ – MgO/SiO_2 diagram of Paulick *et al.* (2006), all samples plot close to – albeit slightly below – the terrestrial array (Figure 6.7-a), which represents the expected compositional evolution resulting from partial melting of primitive mantle (Jagoutz *et al.*, 1979). The clinopyroxene-rich garnet lherzolites are particularly fertile and are characterized by high $\text{Al}_2\text{O}_3/\text{SiO}_2 > 0.04$, low MgO/SiO_2 (0.81–0.91), and high CaO (1.41–2.69 wt.%), which is typical of lherzolites (Deschamps *et al.*, 2013). By contrast, the serpentinites and the spinel and phlogopite-chromite harzburgites display low $\text{Al}_2\text{O}_3/\text{SiO}_2 < 0.04$, high MgO/SiO_2 (0.91–0.96) and low CaO (0.28–1.42 wt.%), which is more typical of residual harzburgitic

mantle that has experienced some extent of partial melting (Figure 6.7). The phlogopite-chromite harzburgite JB-19-21 is also enriched in K_2O (0.63 wt.%) and P_2O_5 (0.12 wt.%) relative to the other samples (Table 6.1), which all contain less than 0.35 wt.% K_2O and P_2O_5 below detection limit (<0.1 wt.%).

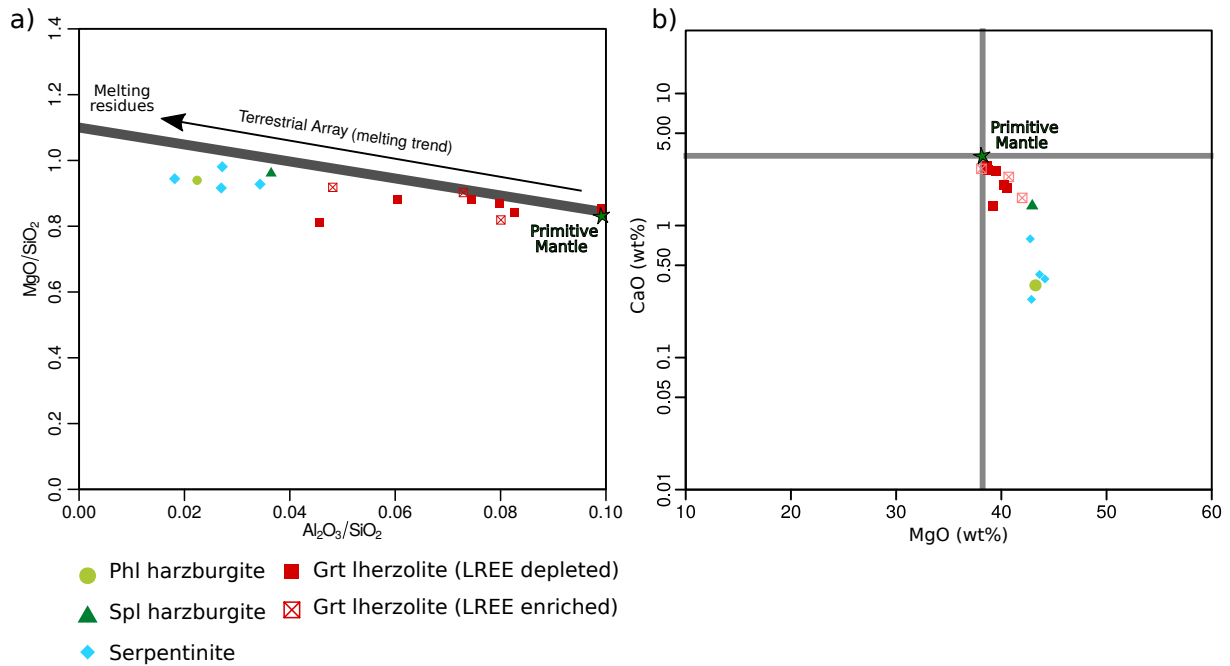


FIGURE 6.7 – Whole rock composition of collected peridotites and serpentinites plotted on the Al_2O_3/SiO_2 – MgO/SiO_2 diagram of Paulick *et al.* (2006) (a) and on a CaO – MgO diagram (b). All the samples align slightly below the terrestrial mantle melting array (Jagoutz *et al.*, 1979).

Variation in major element composition reflects the mineralogical composition of the peridotites. In particular, the trend in the Al_2O_3/SiO_2 – MgO/SiO_2 diagram is consistent with composition of olivine and orthopyroxene, which display lower Mg# in the most fertile garnet lherzolite and higher Mg# in the most refractory harzburgites (Figure 6.6). Furthermore, higher CaO and Al_2O_3 in the lherzolites is consistent with the abundance of – retrogressed – garnet and clinopyroxene, and higher K_2O and P_2O_5 in sample JB-19-21 is consistent with the presence of phlogopite and apatite.

6.6.2 Trace elements

Large variability is observed in trace element composition, and three main groups are identified based on REE and Th content (Figure 6.8). The first group includes most of the garnet lherzolites, which present LREE-depleted patterns ($(La/Yb)_N = 0.46 - 0.9$), with HREE content close to or slightly below that of the primitive mantle ($Yb_N = 0.5 - 1.1$). Samples from this group display no or slightly positive Eu anomaly ($Eu/Eu^* = 1.0-1.2$, where $Eu/Eu^* = Eu_N / (Sm_N \cdot Gd_N)^{1/2}$), and are not particularly enriched in Th, in contrast to the other groups. The second group includes the spinel and the phlogopite harzburgites, plus three samples of garnet lherzolite which present similar REE patterns. They display a HREE content similar to samples of the first group ($Yb_N = 0.4-1.2$), but they are strongly enriched in LREE and Th ($(La/Yb)_N = 1.3-8.7$, $(Th/Yb)_N = 6.8-26.7$) and present a negative Eu anomaly ($Eu/Eu^* = 0.46-0.85$). The third group consists of serpentinites. They are all strongly depleted in HREE relative to the primitive mantle ($Yb_N = 0.08-0.28$). They are slightly enriched both in LREE and Th ($(La/Yb)_N = 1.8-9.8$, $(Th/Yb)_N = 3.6-16.8$), and display either U-shaped REE patterns, with depletion in MREE relative to HREE and LREE, or continuous enrichment from HREE to LREE. With one exception, all the analyzed serpentinites have a positive Eu anomaly (Eu/Eu^* up to 3.2).

These three groups share in common a strong enrichment in fluid-mobile elements (Cs, Rb, U, Pb) and strongly negative anomalies in high-field strength elements (HFSE), in particular in Nb and Ta, independently of their mineral composition or REE and Th content (Figure 6.8-b). Nb anomalies Nb/Nb^* ($Nb/Nb^* = Nb_N / (Th_N \cdot La_N)^{1/2}$) range between 0.04 and 0.39, except for one serpentinite outlier with $Nb/Nb^* = 0.85$.

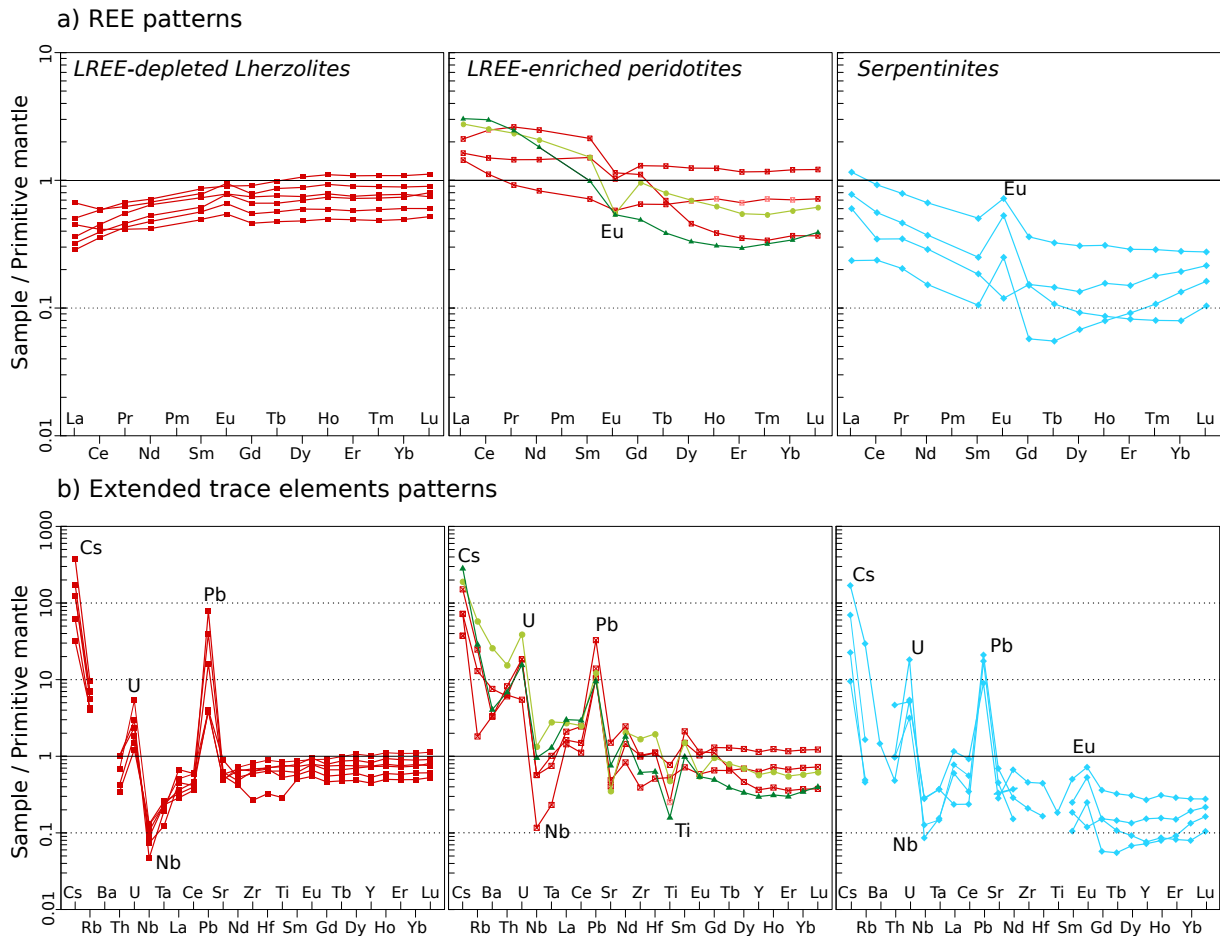


FIGURE 6.8 – Trace element composition of collected samples, normalized to the composition of primitive mantle after McDonough et Sun (1995). Three groups are identified based on their trends in rare earth elements (see description in text). Legend is the same as on Figure 6.7.

6.6.3 Sr–Nd Isotopes

Sr isotopic composition was measured on nine samples from the three groups identified above (Table 6.4). However, due to very low Nd content, no Nd isotopic data has been acquired for samples from the LREE-depleted group. Initial $(^{87}\text{Sr}/^{86}\text{Sr})_i$ ratio and ϵNd_i have been recalculated at 330 Ma, which corresponds roughly to the age of ultrapotassic magmatism and Variscan HP metamorphism in the ECM. Variation of a few 10 Ma has little effect on Nd isotopic composition but can strongly modify the Sr isotopic composition in Rb-rich phlogopite-bearing samples. To show the effect of age variations on Sr isotopic composition,

initial isotopic ratios $(^{87}\text{Sr}/^{86}\text{Sr})_i$ recalculated at 350 Ma and 310 Ma have been added in brackets on Table 6.4. Strong variations are observed both in Sr and Nd isotopic composition, and samples are globally more isotopically enriched than ocean island basalts. ϵNd_{330} ranges from slightly positive to strongly negative (-8.12 to +0.59), and $(^{87}\text{Sr}/^{86}\text{Sr})_{330}$ ranges from 0.69985 to 0.71727. There is no correlation between Sr and Nd isotopes, as strongly negative ϵNd_{330} are not necessarily associated with high $(^{87}\text{Sr}/^{86}\text{Sr})_{330}$. The highest values for Sr isotopes are observed in serpentinites, which suggests these high values are related to fluid-addition during serpentinitization.

Sample	Type	Composition (ppm)						Sr isotopes				Nd isotopes			
		Rb	Sr	Nd	Sm	$\frac{87Rb}{86Sr}$	$\frac{87Sr}{86Sr}$	$\frac{87Sr}{86Sr}$	$\frac{87Sr}{86Sr}$	$\frac{87Sr}{86Sr}$ [350–300]	$\frac{147Sm}{144Nd}$	$\frac{143Nd}{144Nd}$	$\frac{143Nd}{144Nd}$	ϵNd_{330}	
JB-19-20	Grt Lrz	1.09	9.7	1.039	0.291	0.32445	0.70895	0.70743	[0.70733; 0.70752]	0.16938	0.51261	0.51261	0.59		
JB-19-33	Grt Lrz	2.38	10.0	0.807	0.298	0.68983	0.70440	0.70116	[0.70096; 0.70136]	-	-	-	-		
JB-20-12	Grt Lrz	4.24	11.6	0.839	0.317	1.05645	0.71017	0.70520	[0.70490; 0.70550]	-	-	-	-		
JB-20-13	Grt Lrz	2.52	9.6	0.895	0.353	0.75968	0.70572	0.70215	[0.70193; 0.70236]	-	-	-	-		
JB-20-14	Grt Lrz	7.76	29.9	3.067	0.859	0.75138	0.71442	0.71089	[0.71068; 0.71111]	0.16924	0.51216	0.51216	-8.12		
JB-19-21	Plt Hrz	34.93	7.0	2.577	0.615	14.4460	0.76771	0.69985	[0.69573 ; 0.70397]	0.14426	0.51224	0.51224	-5.64		
JB-19-22	Spl Hrz	17.31	15.2	2.266	0.402	3.30482	0.72185	0.70633	[0.70539 ; 0.70727]	0.10713	0.51230	0.51230	-2.78		
JB-19-48	Srp	0.29	5.6	0.833	0.204	0.15114	0.71727	0.71656	[0.71652; 0.71661]	0.14816	0.51246	0.51246	-1.37		
JB-19-49	Srp	0.28	6.6	0.464	0.101	0.12105	0.71783	0.71727	[0.71723; 0.71730]	-	-	-	-		

TABLE 6.4 – Whole rock Sr-Nd isotopic compositions. Initial $^{87}Sr/^{86}Sr$ and ϵNd have been recalculated at 330 Ma, which corresponds to the climax of the Variscan collision in the ECM. Initial ratios may be highly sensitive to the age at which they are calculated, in particular if the sample presents high Rb/Sr or Sm/Nd. This sensitivity has been tested by recalculating isotopic compositions at 350 Ma and 300 Ma (values in bracket). Highlighted bold values indicate high uncertainty in initial $^{87}Sr/^{86}Sr$ due to high Rb/Sr ratio in the bulk rock, which makes the initial isotopic ratio very sensitive to even small age variation.

6.7 Thermobarometry

Garnet lherzolites contain garnet, clinopyroxene and orthopyroxene, which allow the use of classical thermobarometers based on equilibrium between these three phases (Nimis et Grütter, 2010). However, they have gone through multiple stages of metamorphic re-equilibration, and mineral compositions used for P–T estimates must therefore be chosen carefully. P-T conditions have been estimated on sample JB-19-33, which preserved the most complete mineral assemblage. The Mg-richest garnet core has been selected, combined with representative core compositions of orthopyroxene and clinopyroxene from the matrix, which are assumed to represent the primary assemblage. A temperature has also been calculated using an orthopyroxene-clinopyroxene pair in the coarse-grained coronas around kelyphites to constrain the retrogression path. The Al-in-Opx barometer (Nickel et Green, 1985) has been used, combined with the two-pyroxene thermometer of Taylor (1998) and the Ca-in-opx thermometer of Brey et Köhler (1990), as recommended in Nimis et Grütter (2010).

For the primary assemblage, the combination of two-pyroxene and Al-in-Opx thermobarometers yields $P = 3.0$ GPa and $T = 973$ °C (Figure 6.9). Uncertainty can realistically be assumed to be in the order of ± 0.5 GPa for P and ± 50 °C for T (Nimis et Grütter, 2010). However, assuming the same pressure, the Ca-in-Opx thermometer yields higher T around 1130°C. The orthopyroxene-clinopyroxene pairs in the coronas yield consistent T of 827 ± 50 °C for the two-pyroxene thermometer and 803 ± 50 °C for the Ca-in-Opx thermometer assuming $P = 1.0$ GPa, which indicates good equilibration of these domains.

Conventional thermobarometry has been completed by thermodynamic modeling with PerpleX 6.9.0 (Connolly, 2009), using the thermodynamic database of Holland et Powell (2011) and the set of solution models from Jennings et Holland (2015) developed for phase relations in peridotite in the composition space NaO-CaO-FeO-MgO-Al₂O₃-SiO₂-Cr₂O₃.

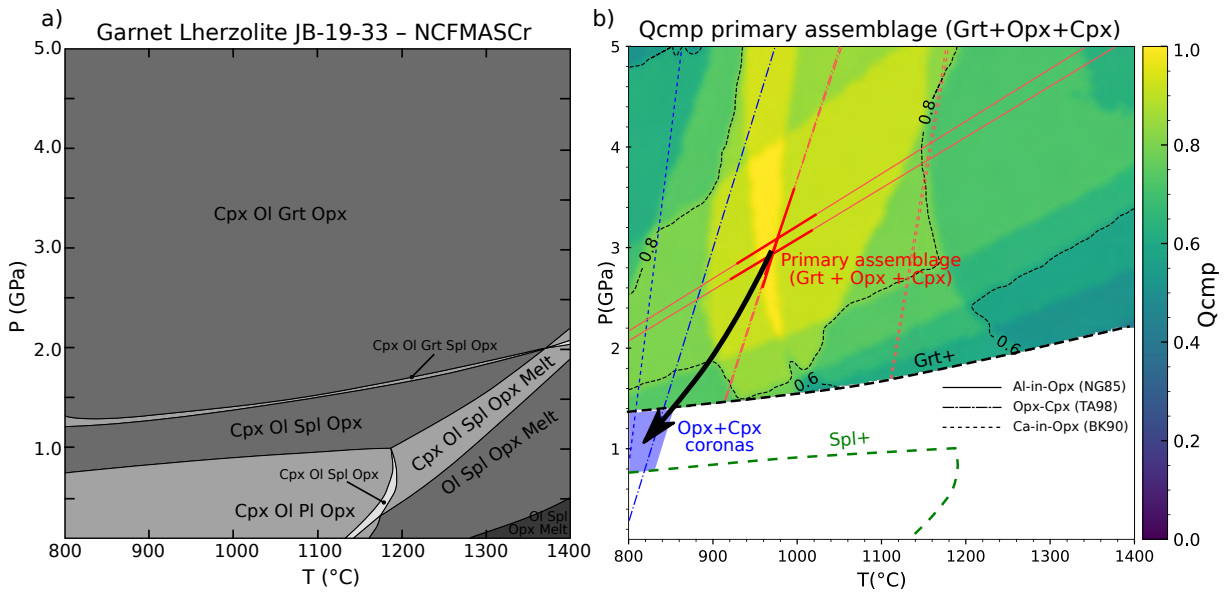


FIGURE 6.9 – a) Isochemical phase diagram computed with PerpleX 6.9.0 (Connolly, 2009). b) Composition quality factor Q_{cmp} (Duesterhoeft et Lanari, 2020) mapped over the P–T grid for the primary garnet + clinopyroxene + orthopyroxene assemblage. Best fit between modeled and measured composition (Q_{cmp} close to 1, yellow shades) is obtained around 940–980°C and 2–4 GPa, and is consistent with inverse thermobarometry results (red lines). Inverse thermobarometry on the clinopyroxene+orthopyroxene coronas around garnet indicate lower temperature of equilibration around 800–850°C (blue lines). TA98 – Taylor (1998); BK90 – Brey et Köhler (1990); NG85 – Nickel et Green (1985)

All iron was assumed to be ferrous (no Fe^{3+}), and the bulk composition of sample JB-19-33 recalculated on an anhydrous basis was used in input. The computed phase diagram is shown on Figure 6.9-a. The primary assemblage is stable over a large P-T range above 1.3–2.0 GPa. Equilibration between garnet, clinopyroxene and orthopyroxene has been tested for the primary assemblage by computing the composition quality factor Q_{cmp} of Duesterhoeft et Lanari (2020) over the whole P–T grid (Figure 6.9-b). Q_{cmp} gives the match between modeled and measured mineral composition in function of P and T, using the same mineral compositions as those used for conventional thermobarometry. The closer Q_{cmp} is to 1 (yellow shades on the diagram), the better the match. The best fit between observed and measured compositions is obtained for P between 2.0 and 4.0 GPa and T between 940 and 980°C, which is consistent with the P–T conditions estimated with the Al-in-Opx – Two-pyroxene thermobarometers.

By contrast with the lherzolites, spinel / phlogopite-chromite harzburgites lack of garnet and clinopyroxene, which prevents the use of classical thermobarometers. Moreover, these samples have been deeply affected by metasomatic reactions, which makes the identification of equilibrium assemblages particularly difficult. Therefore, no P–T estimates have been obtained on these samples. Lack of garnet nevertheless indicates they were equilibrated below the spinel / garnet transition. In the lherzolites, this transition occurs around 1.3–1.4 GPa for T between 800 and 1000°C (Figure 6.9-a), but it may be shifted up to 2.0–2.5 GPa in Cr-rich depleted harzburgites (Ziberna *et al.*, 2013). Therefore, we conclude that the harzburgite samples equilibrated below 2.0–2.5 GPa. T remains unconstrained but is assumed to be lower than in the garnet lherzolites, given that the latter equilibrated at higher P, presumably along the same local geotherm.

6.8 Discussion

6.8.1 Consequences of crustal retrogression

The investigated peridotites and serpentinites have been incorporated as enclaves in migmatites, and may have therefore undergone significant compositional, mineralogical and textural transformation due to metamorphic or metasomatic reactions involving melts or fluids derived from the migmatites. It is therefore important to assess to what extent the enclaves have been modified during and after their incorporation into the crust, in order to identify what relevant information can be extracted about the mantle.

Metamorphic textures indicate that the peridotites have partially recrystallized at crustal conditions. This is particularly obvious in the retrogressed garnet lherzolites, in which former garnet has almost been completely destabilized into kelyphite. These features are very common in retrogressed garnet peridotites, and result from reaction between garnet and olivine in the spinel stability field, following the reaction $\text{Grt} + \text{Ol} \rightarrow \text{Opx} + \text{Cpx} + \text{Spl}$ (Obata, 2011),

which occurred between ca. 1.3 and 0.8 GPa according to our thermodynamic calculations (Figure 6.9). The orthopyroxene-clinopyroxene coronas developed concomitantly with the kelyphite, and constrain T between ca. 800 and 850°C during this phase of retrogression. Finally, the formation of plagioclase-bearing symplectites around garnet relics indicate further decompression in the plagioclase stability field during a later stage of retrogression below 0.8 GPa.

Recrystallization of the kelyphite into coarser symplectites and eventually into a granuloblastic assemblage of pyroxene and amphibole is a process indicative of relatively high-T conditions >800°C (Obata, 2011). Resulting textures are very similar to annealing textures observed in garnet-clinopyroxene-bearing HP granulites of the Oisans – Pelvoux massif (Chapter 4, which have experienced an overprint at similar P-T conditions (0.6–0.9 GPa; 800–870°C) during the late stages of the Variscan orogeny around 310–295 Ma. These textures therefore mark an overprint due to protracted evolution of the peridotites at T > 800°C in the lower crust. Despite this overprint, the peridotites have preserved domains devoid of intense textural and mineralogical transformation, as supported 1) by thermobarometry on the garnet-orthopyroxene-clinopyroxene assemblage, which yielded high P–T conditions inconsistent with crustal re-equilibration, and 2) by Mg# and Ni–Mn composition of olivine and orthopyroxene, which vary consistently with the bulk rock fertility, which suggests that these minerals preserved their primary composition and were not further re-equilibrated by diffusional exchange. Recrystallization was hence mostly restrained to the kelyphites, which are particularly favorable sites due to their very fine-grained texture, which creates a high surface of exchange between minerals.

Interaction with the felsic migmatites may have potentially altered mineral and whole rock compositions. Such migmatite-peridotite interactions are exemplified by the spectacular biotite-tremolite radial coronas formed around some enclave (Figure 6.2-e). However, such

reactions did not affect all the enclaves, and many of them are completely devoid of such coronas, or are surrounded only by a thin biotite-rich layer (Figure 6.2-c,d,f). Formation of tremolite requires significant addition of H₂O to the relatively dry harzburgitic assemblage dominated by olivine and orthopyroxene, and occurs at P–T conditions of the amphibolite to greenschist-facies (Spear, 1981; Spear et Spear, 1995). Therefore, we interpret these coronas are relatively late features, which formed by reaction of the Mg-rich enclaves either with hydrous fluids released during crystallization of the granitic liquids or with some residual silicic melts enriched in H₂O. Enclaves that were not in contact with these residual melts or fluids hence remained unaffected by such reactions.

Retrogression to lower T and fluid input resulted in variable degrees of serpentinization, which partially obliterated the former mineral assemblages. In sample JB-19-21, serpentinized veins have formed across olivine grains and cut through the previous zonation without modifying it (Figure 6.4-f), which indicates it did not alter mineral compositions. However, fluid input in the crust may have been associated with enrichment of the whole rock in fluid-mobile elements. Strong enrichment in these elements is indeed observed in all samples, independently of their petrographic type (serpentinite, lherzolite, harzburgite) or REE signature (Figure 6.8-b). However, we do not believe it results from serpentinization and retrogression only. Indeed, there is no systematic increase in U/Th associated with increasing loss on ignition (Figure 6.10-a), which is considered here as a proxy for the degree of rehydration during retrogression (mostly due to serpentinization, but other reactions may be involved). Some serpentinites nevertheless display higher U/Th, which may indicate significant enrichment in some highly retrogressed samples. Furthermore, this enrichment is coupled with strongly negative anomalies in HFSE (Nb-Ta) and low Nb content below that of the primitive mantle ($Nb_N = 0.05-1.34$). Nb and Ta are relatively immobile in aqueous fluids, especially at greenschist-facies conditions (Elliott *et al.*, 1997; Hastie *et al.*, 2007), and it is therefore unlikely that they have leaked out during serpentinization in the crust.

They could have even been slightly enriched, given that the Nb-Ta content in the continental crust is about sixteen times higher than in the primitive mantle (Taylor et McLennan, 1995). Therefore, these anomalies – and the coupled enrichment in fluid-mobile elements – probably already existed before the incorporation of the mantle rocks into the crust.

6.8.2 A refractory mantle refertilized by melts and fluids

6.8.2.1 Early melt-depletion

Multiple lines of evidence indicate that the peridotites and serpentinites investigated in this study have experienced various degrees of partial melting. First, whole rock compositions in major elements (in particular Al_2O_3 and MgO) reveal large variations in fertility among the different groups, from the more fertile garnet lherzolites to the more refractory harzburgites, which may result from various degrees of partial melting and melt extraction. These variations are consistent with the composition of olivine and orthopyroxene, which present higher Mg# in the more refractory samples. There is furthermore a correlation between Mg# and compatible/incompatible elements content in minerals, in particular Ni and Mn : both olivine and orthopyroxene display decreasing Mn content with increasing Mg#, and olivine displays an increase in highly compatible Ni (Le Roux *et al.*, 2011) with increasing Mg#. Finally, LREE-depletion observed in most of garnet lherzolites probably results from partial melting. We therefore interpret these data as evidence that the different peridotite groups have undergone partial melting at various degrees. The serpentinites have not preserved primary minerals that could be analyzed, but they present high MgO/SiO_2 and low $\text{Al}_2\text{O}_3/\text{SiO}_2$ similar to the harzburgites, which suggests they also derive from a refractory mantle source.

6.8.2.2 Evidence for mantle metasomatism

A striking feature of the investigated samples is that their incompatible trace element composition is completely decoupled from the variations in major elements. Most of the fertile garnet lherzolites are indeed depleted in LREE, while the more residual harzburgitic samples are all strongly enriched in LREE and other incompatible elements like Th (Figures 6.7 and 6.8). Furthermore, the presence of phlogopite and pargasite in the harzburgites is inconsistent with high degree of melt-depletion. These contradictory features can only be explained by involving refertilization of the peridotites by one or multiple metasomatic events involving fluids and/or melts, which have re-enriched the mantle in incompatible elements. In the harzburgites, metasomatism is clearly modal, since it has produced phlogopite and/or pargasite. In the lherzolites, hydrous minerals are found (pargasite), but it is not excluded that they formed during retrogression in the crust. However, metasomatism in these rocks is evidenced 1) by the very fertile whole rock composition of these samples, which is inconsistent with LREE depletion, and 2) by the presence of tiny graphite-bearing inclusions in garnet relics (Figure 6.5), which marks the presence of C-O-H fluids during garnet crystallization.

6.8.2.3 Multiple types of metasomatism

The dichotomy between LREE-depleted and LREE-enriched samples suggests that two different types of metasomatism are recorded. Indeed, only the (serpentinized) harzburgites and some lherzolites are enriched in incompatible LREE and Th, while all the samples are variably enriched in fluid-mobile elements (Cs, Rb, U, Pb) and depleted in immobile HFSE (Nb-Ta), independently of their enrichment in LREE. This dichotomy appears more clearly when plotting Th/Nb against Th/Yb (Figure 6.10). The LREE-depleted lherzolite samples are aligned along a very steep trend, which indicates increasing Nb anomalies (increasing Th/Nb) at nearly constant Th/Yb. In contrast, the LREE-enriched samples are generally

more scattered and define a much shallower trend, which indicates significant Th enrichment at constant or slightly increasing Nb anomalies. Similar trends are observed when replacing Th by La or Th/U by Ce/Pb. We interpret these two different trends as the superposition of two different types of metasomatism, (respectively type I and type II), which have variously affected the different groups. Type I affected all samples at various degrees and resulted in enrichment in fluid-mobile elements and depletion in HFSE. Type II affected only the LREE-rich samples and resulted in strong enrichment in incompatible LREE and Th.

The nature of metasomatic agent(s) responsible for selective enrichment in fluid-mobile elements and depletion in HFSE is poorly constrained, due to the lack of a comprehensive dataset of *in-situ* trace element data for the different rock-forming and accessory minerals. In particular, it is currently impossible to estimate which proportion of enrichment is due to contamination in the crust and which part is due to metasomatism in the mantle. Given the presence of graphite-bearing inclusions in garnet, we speculate that the fertile composition of the garnet lherzolites results from metasomatism by C-O-H fluids, which carried a trace element signature enriched in fluid-mobile elements and depleted in HFSE. However, trace element analyses of clinopyroxene and garnet and more detailed investigation of the graphite-bearing inclusions are required to support this hypothesis.

In contrast, the second type of metasomatism associated with enrichment in incompatible LREE is better constrained by mineral compositions and petrographic observations in the phlogopite-chromite harzburgite (sample JB-19-21), which is one of the most enriched samples. This sample presents indeed several features indicative of percolation by mantle melts. First, it is rich in chromite with low Mg#, low Ni and high Ti and Mn content (Figure 6.6-g,h). This is unexpected in a depleted harzburgite, given that Ni is strongly compatible and preferentially fractionates into spinel during partial melting ($D_{Ni}^{Spl/Melt} = 6.1-22$), while Ti and Mn are more compatible ($D_{Ti} = 0.06-0.2$, $D_{Mn} = 0.2-0.9$) and fractionate

into the melt (Wijbrans *et al.*, 2015). Then, this sample contains veins of orthopyroxenite, around which primary olivine has been partially replaced by secondary olivine displaying typical magmatic features, such as low Mg# and low Ni/Mn < 2 (Wang *et al.*, 2021). These orthopyroxenite layers may therefore represent former melt-migrating channels, in which olivine was dissolved and replaced by orthopyroxene following the reaction $\text{Ol} + \text{Liq}_1 \rightarrow \text{Opx} + \text{Liq}_2$. In order to dissolve olivine and crystallize orthopyroxene, the percolating liquid had to be relatively rich in SiO_2 . It appears therefore likely that incompatible elements enrichment was driven by a silicate melt, which migrated either pervasively by porous melt flow through the mantle (*e.g.* Dijkstra *et al.*, 2003), or via channelized flow as evidenced by the orthopyroxenite layers in the phlogopite-chromite harzburgite. This melt-driven metasomatism resulted in crystallization of phlogopite and/or pargasite. Apatite is commonly found in association with phlogopite, and has also probably crystallized from the melt. This latter was therefore enriched in K_2O and P_2O_5 in addition to incompatible trace elements. All of this indicates involvement of continental crustal material in the source of the melt.

6.8.2.4 Crustal isotopic signature

The peridotites and serpentinites display highly variable Sr–Nd isotopic signatures, which are dominated by negative ϵNd_{330} and high $^{86}\text{Sr}/^{87}\text{Sr}_{330}$. Sr isotopic signature is difficult to interpret due to the large uncertainty on initial isotopic ratios resulting from strong enrichment in Rb in some samples. Highest values in $^{86}\text{Sr}_{330}$ are observed in the serpentinites, which suggests these high values are related to fluid-addition during serpentinization. Serpentinization was however not associated with peculiar enrichment in Nd and Sm (Figure 6.8). The Nd isotopic composition has thus probably been less affected than Sr by interaction with fluids in the crust, and is hence considered to provide more reliable information about the isotopic composition of the mantle. With one exception, all samples for which Nd-isotope data are available contain unradiogenic Nd ($\epsilon\text{Nd}_{330} < 0$), which again argues for contami-

nation of the mantle source by continental material. Large scattering in ϵNd_{330} among the analyzed samples suggests that the portion of mantle sampled by the ultramafic enclaves is highly heterogeneous, probably due to different extent of metasomatic interactions.

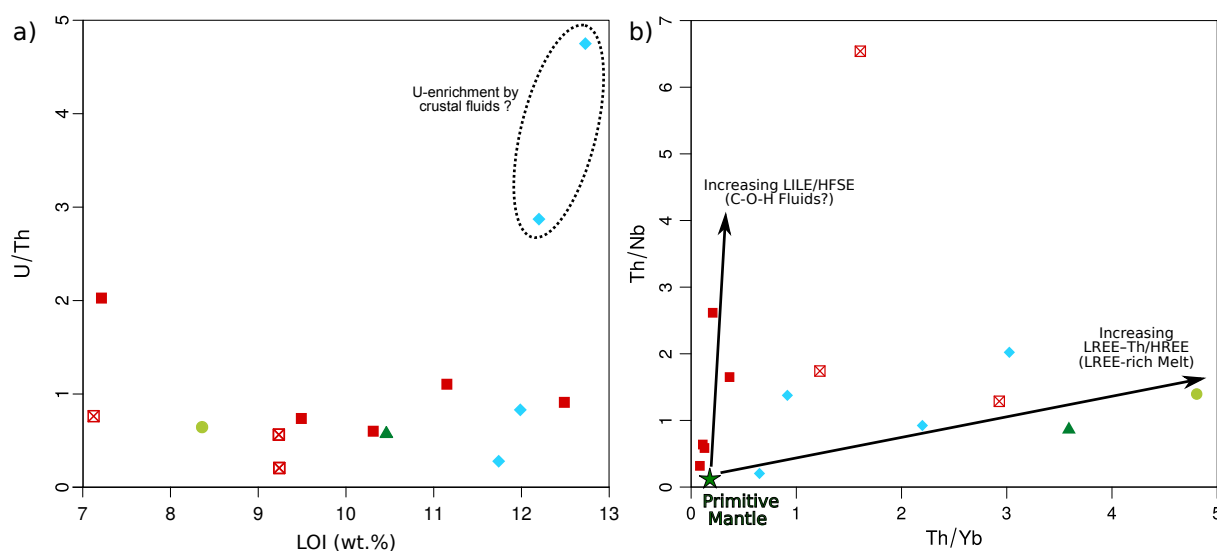


FIGURE 6.10 – a) evolution of U/Th in function of the loss of ignition (LOI). The LOI is considered here as a proxy for retrogression reactions (serpentinization in particular) occurring in the crust, while U/Th is a proxy for enrichment in fluid-mobile incompatible elements relative to less mobile incompatible elements. Excepted for two serpentinites with high U/Th, no significant variation of U/Th is observed with increasing LOI. b) Th/Yb – Th/Nb diagram indicating different trends of metasomatism. Increasing Th/Nb marks increasing anomaly in Nb, while increasing in Th/Yb marks enrichment in incompatible elements relative to more compatible HREE. Two different trends are observed, respectively for the LREE-depleted garnet lherzolites and the other samples. Legend is the same as on [Figure 6.7](#)

6.8.3 Implications for the Variscan evolution

The trace element and isotopic composition of the mantle enclaves display dual characteristics, which indicate refertilization of a refractory, melt-depleted mantle by aqueous fluids or melts carrying a crustal signature (enrichment in LILE, LREE, K_2O and P_2O_5 , negative HFSE anomalies, negative ϵNd_i), which certainly derived from dehydration and/or melting of subducted continental material ([Hermann et Rubatto, 2009](#); [Zheng, 2019](#)). This material was probably subducted during the Devonian or the lower Carboniferous, shortly preceding the Variscan collision in the ECM. Indeed, older magmatic record in the ECM does not show any evidence of an enriched mantle source. The Ordovician magmatic event

(ca. 480-450 Ma) recorded all across the ECM is characterized by emplacement of tholeiitic basalts with N/E-MORB-like signatures and positive ϵNd_i ($+6 < \epsilon\text{Nd}_i < +8$) characteristic of a depleted mantle source (Bussy *et al.*, 2011; Jacob *et al.*, 2021a; Paquette *et al.*, 1989; Rubatto *et al.*, 2010). It is difficult to envisage that pre-existing metasomatized mantle would have escaped this widespread magmatic event, especially considering that such a metasomatized mantle would be particularly prone to melting. Therefore, metasomatism necessarily postdates the Ordovician magmatism. Consequently, we attribute the early depletion of the mantle to this Ordovician magmatic event and the subsequent metasomatism to Variscan subduction and/or collision during the Devonian and the Carboniferous.

Metasomatism may be related either to subduction of sediments together with an oceanic slab prior to the collision (Devonian-Tournaisian), or to the subduction of continental units during the early collisional stages. In the first scenario, mantle metasomatism would be related to the arc/back-arc calc-alkaline magmatism recorded in the western part of ECM (Figure 6.1), while in the second scenario, it would be related to syn/post-collisional Mg-K magmatism. Petrographic and geochemical characteristics of the phlogopite-bearing harzburgite present striking similarities with that of Variscan Mg-K rocks (durbachites-vaugnerites, Von Raumer *et al.* (2014)), which suggests that at least the type II metasomatism is related to Mg-K magmatism. In particular, strong enrichment in incompatible elements (LILE, LREE Th), pervasive occurrence of apatite associated with phlogopite and unradiogenic Nd isotopic signature (negative ϵNd_i) are typical. Given the multiple evidence of pervasive interaction with a K_2O -rich melt, we do not regard this sample as representative of the mantle source of the durbachites-vaugnerites, but rather as a part of the subcontinental mantle that was percolated by these Mg-K rich magmas and reacted with them.

In any case, the peridotite enclaves must be derived from the mantle wedge or the overlying lithosphere, where the mantle has interacted with fluids or melts rising from the subducting

slab. Thermobarometric estimations suggest that the garnet lherzolites derive from the upper mantle wedge (ca. 80–130 km, assuming a crustal thickness of 40 km and a density of 3300 kg.m⁻³ for the mantle and 2800 kg.m⁻³ for the crust), while the harzburgites probably derive from shallower mantle (<80 km). This argues for a position of the ECM on the overlying plate, relatively far from the plate interface. Indeed, assuming a dip angle of the subducting slab between 30° and 50°, a distance of 100 to 220 km from the subduction front is necessary to open a mantle wedge wider than 130 km. The situation of the ECM may therefore be analogue to that of the Moldanubian zone of the Bohemian massif, which is located several hundreds of kilometers south of the Saxo-Thuringian subduction front and exposes high-grade lower crustal domains with embedded orogenic peridotites and Mg-K magmatic intrusions. In this massif, clear link has been established between metasomatism of the mantle and this (ultra)-potassic magmatism, which both resulted from relamination of the overlying lithosphere by continental material derived from the subducting Saxo-Thuringian plate (Janoušek et Holub, 2007; Kotková et al., 2011; Lexa et al., 2011; Maierová et al., 2021; Schulmann et al., 2014). Such a model seems plausible in the ECM, but further investigation of peridotite enclaves and Mg-K magmatic rocks is needed to make a stronger case.

6.9 Conclusion

Enclaves of peridotites and serpentinites discovered in exhumed lower and mid-crustal domains in the Oisans-Pelvoux and Belledonne massif provide insight into the composition and evolution of the Variscan mantle in the external zones of the Western Alps. Although information carried by these mantle rocks has been partially altered due to protracted stay in the migmatitic lower crust and subsequent serpentinization, they preserved information about their metamorphic evolution and record successive steps of melting and refertilization by melts or aqueous fluids in the mantle. Thermobarometric estimations indicate provenance of these enclaves in the upper mantle wedge or the overlying lithospheric mantle. Refrac-

tory compositions characterized in particular by high MgO/SiO_2 and low $\text{Al}_2\text{O}_3/\text{SiO}_2$ in the whole rock and high Mg# and Ni-content in olivine mark an early melt-depletion event, presumably related to the widespread Ordovician magmatism recorded in the European Variscan basement. Variably depleted mantle domains were refertilized by melts and/or fluids, which produced an enrichment in fluid mobile elements relative to immobile ones (LILE vs HFSE), together with the development of a pronounced Nb-Ta negative anomaly observed in all the collected samples. Strong enrichment in incompatible LREE relative to HREE and modification of the modal composition (crystallization of phlogopite and/or pargasite with accessory chromite and apatite) in some samples is attributed to percolation by K_2O - P_2O_5 -rich melts, presumably derived from a subducted continental slab. These geochemical characteristics are in line with whole rock Nd isotopic compositions, which indicates enrichment of the mantle by a continental crust component. Metasomatism is attributed to Variscan subduction and collision during the Devonian–Carboniferous period, but further work is needed to constrain the precise timing of metasomatic events and establish correlations with the magmatic and tectono-metamorphic record in the ECM.

CHAPITRE 7

Le magmatisme (ultra)-potassique des MCE



FIGURE 7.1 – Bloc de durbachite provenant d’une enclave hectométrique dans le granite du Rochail (Oisans)

Sommaire

7.1	Introduction	245
7.2	Geological setting	247
7.2.1	General setting	247
7.2.2	Variscan magmatism in the ECM	249
7.3	Field description and structural analysis	250
7.3.1	The Olan plutonic formations	251
7.3.2	Mafic dykes and enclaves in granitoids	253
7.4	Petrographic description and mineral composition	255
7.4.1	Petrographic descriptions	256
7.4.2	Mineral compositions	257
7.5	Whole rock geochemistry and Sr-Nd isotopes	259
7.5.1	Major elements composition	262
7.5.2	Trace elements composition	266
7.5.3	Sr-Nd isotopes	267
7.6	U-Pb geochronology	270
7.7	Thermobarometry	272
7.7.1	Thermobarometry of rock forming minerals	273
7.7.2	Apatite and zircon saturation	275
7.7.3	Ti-in-zircon (TiZ) thermometry	276
7.8	Discussion	277
7.8.1	Emplacement of the Olan plutonic formation	277
7.8.2	A petrogenetic model for the durbachites in the ECM	281
7.9	Conclusion	284

7.1 Introduction

The syn-to post-collisional stages of the Variscan orogeny in Europe were marked by the emplacement of peculiar series of highly magnesian, (ultra)-potassic (Mg–K) igneous rocks, locally referred to as durbachites, vaugnerites or redwitzites. They are ubiquitous in the high-grade granulite/eclogite-bearing metamorphic units derived from the former crustal root of the orogen, which spreads from the Moldanubian zone of the Bohemian Massif to Galicia and includes the Vosges – Black Forest massif, the French Massif Central, the southern Armorican Massif and also Variscan domains exposed in the External Crystalline Massifs of the Alps (ECM) and in Corsica (Couzinié *et al.*, 2016; Janoušek *et Holub*, 2007; Rossi *et Cocherie*, 1991; Soder *et Romer*, 2018; Tabaud *et al.*, 2015; Von Raumer *et al.*, 2014). In the following, they will be referred to as the durbachite series.

The durbachite series display dual geochemical characteristics combining strong enrichment in LILE and other incompatible elements (Cs, Ba, Rb, Sr, Th, U in particular) with highly magnesian composition and high content in compatible transitional metals (Cr, Ni). The most common interpretation of this dual character is that these Mg–K rocks were primarily produced by melting of a metasomatized mantle source (*e.g.* Couzinié *et al.*, 2016; Janoušek *et Holub*, 2007; Lexa *et al.*, 2011), although subsequent fractionation, mixing with anatectic magmas and contamination in the lower crust did probably occur at various extents. Variscan durbachites mostly emplaced within a short period between 345 and 335 Ma, coeval with or shortly following (ultra)-high-P metamorphism of the continental crust (Janoušek *et Holub*, 2007). Younger pulses however occurred until the early Permian (Laurent *et al.*, 2017; Soder *et Romer*, 2018). It is therefore an important geodynamic marker of the Variscan collision, and determining the spatial and temporal distribution of Mg–K magmatism at the scale of the orogen is a key element in the reconstruction of the Variscan geodynamic history. Variation in geochemical and isotopic composition of the durbachite

series with space and time can provide useful information about the compositional evolution and spatial variability in the mantle, which may allow to constrain mantle processes and/or discriminate different geotectonic domains (*e.g.* Hora *et al.*, 2021; Laurent *et al.*, 2017; Soder *et Romer*, 2018).

A large number of geochemical and geochronological studies of the durbachites have been conducted recently in the Bohemian Massif, in the Vosges–Black-Forest massif and in the Massif Central (Couzinié *et al.*, 2016; Janoušek *et al.*, 2019; Hora *et al.*, 2021; Laurent *et al.*, 2017; Tabaud *et al.*, 2015). In contrast, numerous magmatic bodies with durbachite affinity have been identified for long in the External Crystalline Massifs (ECM) of the Western Alps (*e.g.* Banzet, 1987; Bussy *et al.*, 2000; Debon *et al.*, 1998; Le Fort, 1971; Schaltegger *et Corfu*, 1992; Vittoz, 1987), which have remained comparatively understudied. In the Aar-Gothard massif, zircons extracted from a series of shoshonitic-ultrapotassic intrusive bodies have yielded an age of 334 ± 2.5 Ma and $\epsilon_{\text{Hf}(t)}$ scattered between 0 and -8 (Schaltegger *et Corfu*, 1992). In the Aiguilles-Rouges massif, U-Pb dating of durbachitic monzonites yielded similar ages between 330 and 335 Ma (Bussy *et al.*, 2000). In the more southern massifs of Belledonne and Oisans-Pelvoux, no isotopic nor geochronological data are available for the durbachites, apart from questionable Rb-Sr and K-Ar dating on biotite (Banzet, 1987; Demeulemeester, 1982). Overall, geochemical data are old and generally lack of analyses in REE and other key trace elements (HFSE, Th, U). This lack of data induces strong limitation in our understanding of the magmatic framework in the ECM, and hampers broader comparison with surrounding Variscan domains of the Bohemian Massif, Vosges or Massif Central. In order to fill this gap, we have undertaken new petrographic, geochemical and isotopic investigations of durbachitic rocks in the ECM. In particular, detailed study of the Olan plutonic formations exposed in the inner part of the Oisans–Pelvoux massif (Le Fort, 1971) provides new constraints about the age, the P-T conditions of emplacement and relationship with the Variscan tectono-metamorphic framework in the ECM.

7.2 Geological setting

7.2.1 General setting

The Variscan basement of the external Western Alps is a tectonic assemblage composed of medium to high-grade metamorphic units deriving from lower Paleozoic protoliths and intruded by syn-to post-collisional granitoids (Figure 7.2), over which non-metamorphic sediments were deposited in small pull-apart basins during the upper Carboniferous and the early Permian (Fréville *et al.*, 2018; Guillot et Ménot, 2009; Ménot, 1987a; Vivier *et al.*, 1987). Relics of eclogites and high-pressure (HP) granulites occur sporadically in the lower crustal domains, as well as decimeter-to meter-size enclaves of peridotites and serpentinites (Figure 7.2). Hence, it is interpreted as a portion of the medium-to high-grade mid-Variscan allochthons (Ballèvre *et al.*, 2014; Martínez Catalán *et al.*, 2021), forming the internal zone of the Variscan Belt.

The Variscan Orogeny has occurred from ca. 350 Ma to 295 Ma in the ECM, and consisted in : (1) an early Carboniferous (350-330 Ma) collisional phase associated with E-W directed nappe stacking and HP metamorphism, with peak-P conditions estimated at ca. 1.4-1.8 GPa and 650-730°C (Jacob *et al.*, 2021a); (2) a phase of transpression, associated with the development of a large, N-N30° oriented dextral wrenching system, which was active from ca. 325 Ma to 295 Ma (Fréville *et al.*, 2022; Jacob *et al.*, 2021a; Simonetti *et al.*, 2018, 2020; Vanardois *et al.*, 2021). It progressively evolved toward transtension during the upper Carboniferous (ca. 310–300 Ma), which was associated with the opening of small half-graben and pull-apart basins in the upper crustal levels (Ballèvre *et al.*, 2018; Fernandez *et al.*, 2002). The Variscan basement has only been mildly reworked by Alpine tectonics. An anastomosed network of ductile/brittle shear zones has developed during the Alpine collision (Bellanger *et al.*, 2014; Marquer *et al.*, 2006), which delineate crustal blocks devoid of strong

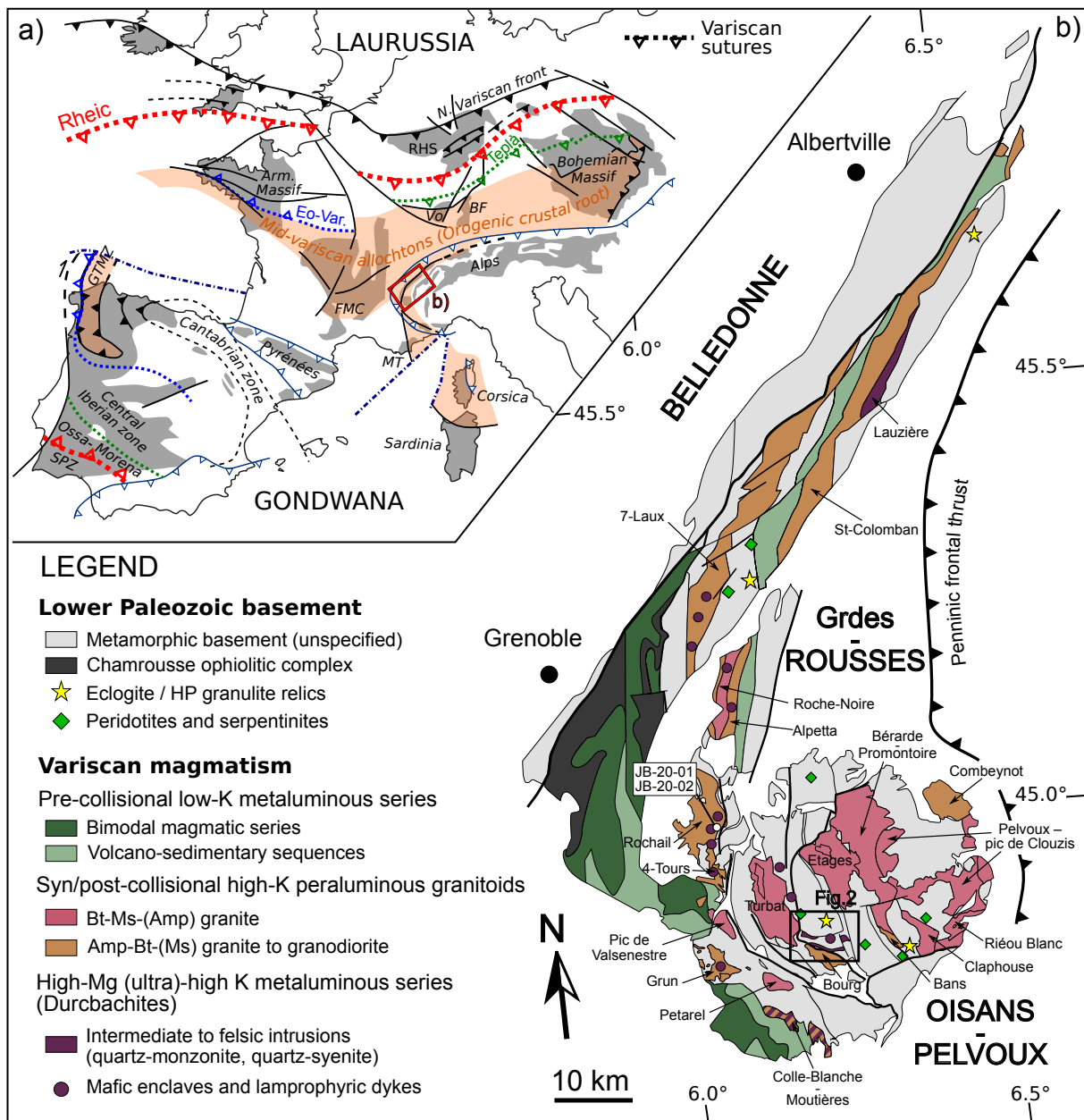


FIGURE 7.2 – a) Simplified tectonic map of the Variscan Belt of Europe, with position of the main suture zones and localization of the External Crystalline Massifs. Modified after [Ballèvre et al. \(2014\)](#). BF – Black Forest; FMC – French Massif Central; GTMZ – Galicia-Trás-os-Montes; MT – Maures-Tanneron; RHS – Rheinische schiefergebirge; SPZ – South Portugese Zone; Vi – Vosges. b) Map of the Variscan basement in the massifs of Belledonne, Grandes-Rousses and Oisans-Pelvoux, with the pre-collisional and syn/post-collisional magmatic series shown in color.

Alpine deformation and metamorphic overprint, in which the former Variscan structures and metamorphic or magmatic assemblages are preserved.

7.2.2 Variscan magmatism in the ECM

Magmatic activity is recorded from the pre-collisional stages (upper Devonian) to post-collisional stages during the late Carboniferous and the early Permian (ca. 370-295 Ma). We present here a brief review of Variscan magmatism in the ECM. The different magmatic series are shown in colour on [Figure 7.2](#).

The oldest Variscan magmatic rocks in the ECM are bimodal plutonic and volcano-sedimentary sequences with a low-K calc-alkaline to tholeiitic composition. They were presumably emplaced in an arc or back-arc setting ([Pin et Carme, 1987](#)), similar to the Brévenne unit in the northeastern Massif Central ([Faure *et al.*, 2009](#); [Pin et Paquette, 1997](#)) or the southern Bohemian Massif ([Schulmann *et al.*, 2009](#)). These series have been strongly overprinted by the Variscan collision during the Visean (350-330 Ma). The emplacement age is constrained between ca. 370 and 350 Ma by U-Pb dating of trondhjemitic sills and K-Ar dating on amphibole ([Fréville *et al.*, 2018](#); [Guillot et Ménot, 2009](#); [Ménot *et al.*, 1987](#)). The youngest age recorded in these formation at 352 ± 1 Ma ([Fréville *et al.*, 2018](#)) provides a lower boundary for the onset of the Variscan collision in the ECM.

The collisional and post-collisional stages were associated with the emplacement of large volumes of granitoids together with the subordinate mafic to intermediate rocks of the durbachite series. Review of granitic magmatism in the ECM by [Debon et Lemmet \(1999\)](#) has identified two sub-series based on age and composition : (1) an older (340-330 Ma), high Mg# series composed of amp-bt quartz-monzonites and granodiorites rich in mafic enclaves ; (2) a younger (305-295 Ma), lower Mg# series composed of (amp)-bt-ms quartz-monzonites and granites poorer in mafic enclaves. However, apart from the difference in Mg#, these two series are very similar and fall into a broad group of K-rich, alkali-calcic granitoids (defined as the "sub-alkaline potassic series" in [Debon et Lemmet \(1999\)](#)), which are common in the

internal zones of the Variscan Belt and are interpreted to derive from various degrees of hybridization between crustal and mantle sources (Moyen *et al.*, 2017).

Recent U-Pb *in situ* dating of zircon in granitoid intrusions in the Belledonne and Oisans-Pelvoux massifs (Fréville, 2016) confirms the presence of two magmatic peaks during the Viséan and the upper Carboniferous – early Permian, but it also indicates that the period between these two peaks was not completely devoid of magmatic activity, and plutons with intermediate ages have been identified. Furthermore, these data show that the two magmatic peaks identified by Debon et Lemmet (1999) do not perfectly coincide with the emplacement of a high Mg# and a low Mg# series, as some granites with high Mg# were emplaced until the upper Carboniferous.

7.3 Field description and structural analysis

Mg–K rocks of the durbachite series are widespread in the ECM. They form either small intrusive bodies composed of amp-bt-rich quartz-monzonite, mela-(quartz)-syenite and melagranite with K-feldspar megacrysts, or they occur as microgranular mafic enclaves (MME) in syn/post-collisional granitoids (Von Raumer *et al.*, 2014). In addition, they form countless dykes of lamprophyric affinity (minettes and vogesites) intruding the metamorphic basement (Laurent, 1992). These rocks have been investigated in the massifs of Oisans–Pelvoux, Belledonne and Grandes Rousses (Figure 7.2), with a strong focus on the Olan plutonic formations exposed in the internal zone of the Oisans–Pelvoux massif (Figure 7.3). These latter present indeed a diverse mineral assemblage, allowing estimation of P-T conditions of emplacement. In addition, structural relationships with the older metamorphic basement have been investigated.

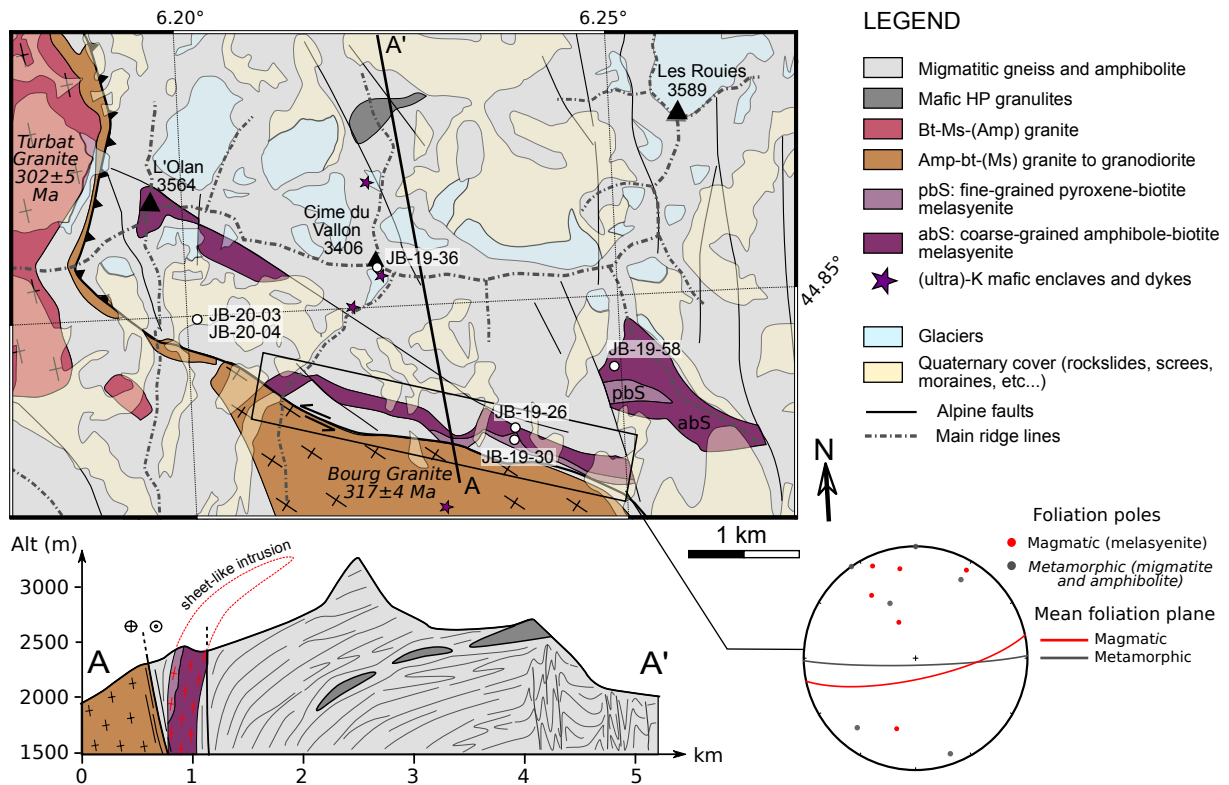


FIGURE 7.3 – Geological map of the Olan plutonic formations in the internal zone of the Oisans–Pelvoux massif. Position of collected samples is shown with white dots. A N–S cross section shows the structural relations with the surrounding metamorphic series. Foliations measured in the black rectangle are reported on a stereographic projection : in red, the foliation poles in the Olan plutonic formations ; in grey, foliation poles in the surrounding metamorphic basement.

7.3.1 The Olan plutonic formations

The Olan plutonic formations represent the main exposure of ultrapotassic rocks in the Oisans-Pelvoux massif. They were first described by [Le Fort \(1971\)](#) and are known locally as the *Olan amphibolic augen orthogneiss*. They form mesocratic to melanocratic igneous rocks containing large (1–3 cm) K-feldspar megacrysts ([Figure 7.4](#) and [Figure 7.6](#)), which classify as quartz-syenite following [Debon et Le Fort \(1983\)](#). They have commonly been strongly deformed and now appear as augen gneiss. Two different facies are recognized in the field : (1) coarse-grained amphibole-biotite porphyritic quartz-syenites (abS), which contain some relics of clinopyroxene (augite) ; (2) fine-grained clinopyroxene-biotite quartz-syenites (pbS), which are poorer in amphibole and richer in biotite than the coarse-grained

abS and contains better-preserved clinopyroxene. The coarse-grained facies forms the largest part of the intrusion, while the fine-grained facies was only observed in its southern flank (Figure 7.3). Enclaves are rare and consist in small (3-10 cm) ultramafic xenoliths, which are partially or completely retrogressed to hornblende (Figure 7.4-d).

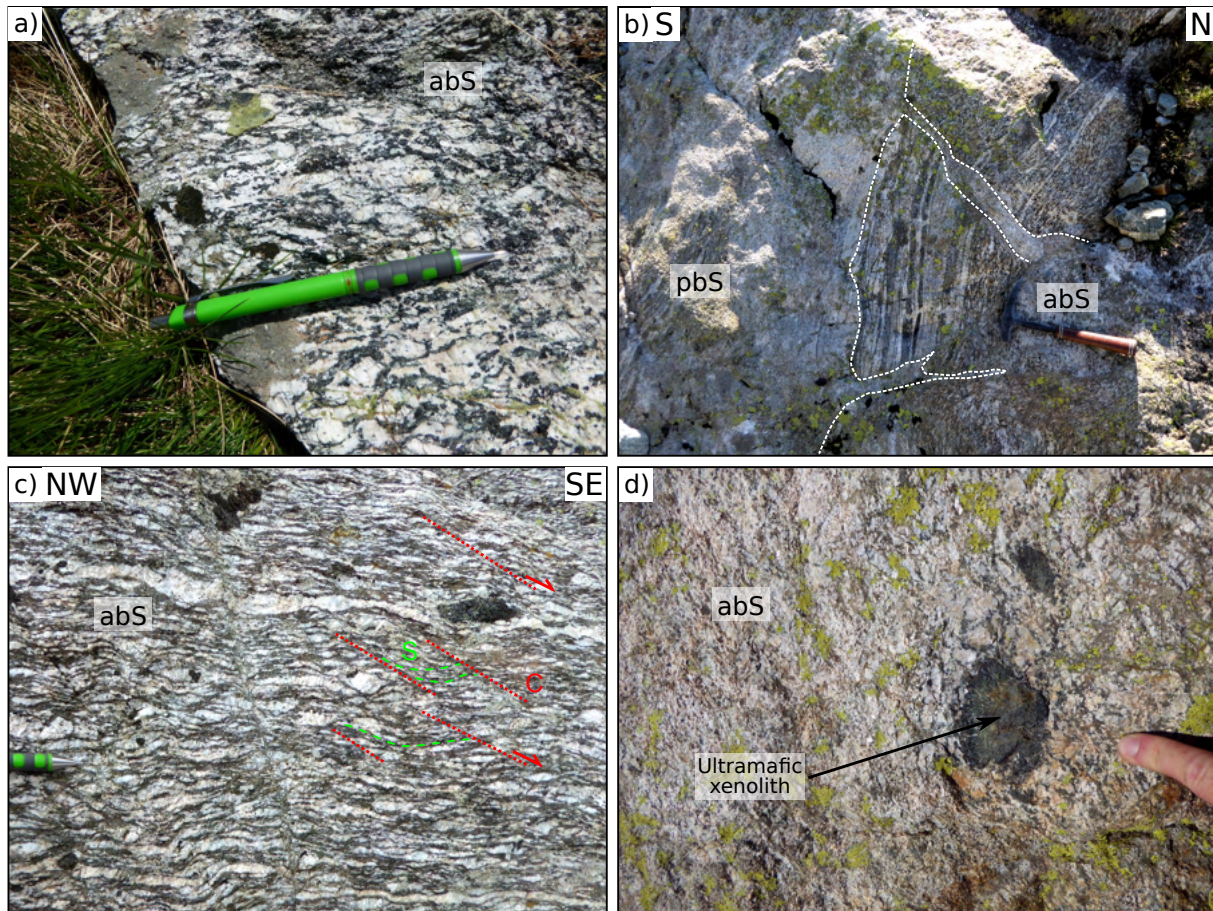


FIGURE 7.4 – Field pictures of the Olan quartz-syenites. Scale is given by the pencil / finger / hammer on each picture. a) close-up view on a sample of the coarse-grained amp-bt facies, showing K-feldspar megacrysts. b) cross-cutting relationships between two different magmatic batches, composed respectively of amphibole-biotite (abS) and pyroxene-biotite (pbS) quartz-syenite. Foliation in the abS facies is clearly crosscut by a younger intrusion of pbS facies. c) Foliation in the abS facies, with S-C relationships. A deformed sigmoidal enclave is visible on the top right. d) Ultramafic xenolith, partially retrogressed to hornblende.

Contact with the surrounding metamorphic sequence has often been blurred by subsequent migmatization. Field mapping reveals the Olan formations form a 100 to 200-meter thick elongated body concordant with the high-grade metamorphic foliation, which extends dis-

continuously over ca. 5 km from west to east ([Figure 7.3](#)). It has been cross cut by several brittle faults, which are either related to the Alpine collision or to late Variscan strike-slip tectonics. These formations have been strongly deformed and present a foliation characterized by stretching of dark minerals and K-feldspar, with common sigma clasts and S-C sigmoides ([Figure 7.4](#) and [Figure 7.6-f](#)), which suggest development at solid-state conditions. Foliation planes are steeply-dipping (70-90°) to the south and display similar orientation to the surrounding metamorphic foliation ([Figure 7.3](#)). This metamorphic foliation corresponds to the sub-horizontal S2h described in [Chapter 4](#), which forms in this part of the massif the southern flank of a kilometer-scale E-W oriented antiform, and therefore appears strongly tilted to the south. Some highly strained domains are crosscut by younger, less deformed magmatic injections ([Figure 7.4-b](#)), which indicates syn-tectonic emplacement. The Olan plutonic formations are therefore interpreted as a former laccolith inserted within the metamorphic series, which was emplaced syn-tectonically by accumulation of multiple batches of magma cross-cutting each others.

7.3.2 Mafic dykes and enclaves in granitoids

High Mg–K mafic enclaves are abundant in the older Visean granitoids (340-330 Ma), especially in the Sept-Laux, Grun and Rochail granites ([Figure 7.2](#)). They are less common in younger granites, but have nevertheless been observed in the Roche-Noire granite dated at 310 ± 5 Ma ([Fréville, 2016](#)) and are described further north in the Mont-Blanc granite dated at $304\pm$ Ma ([Bussy, 1990](#); [Debon et Lemmet, 1999](#)). They form either large decameter to hectometer size bodies, especially in the Rochail granite ([De Boisset, 1986](#)), or they occur as swarms of decimeter-to meter-size enclaves elongated parallel to the granite foliation ([Figure 7.5](#)). Detailed field studies have shown that these swarms of enclaves were formed by fragmentation of larger mafic bodies and subsequent stretching of the fragments, either in the magma or at HT solid-state conditions ([De Boisset, 1986](#)). Some enclaves display digitated

shapes with darker rims, or complex internal textures suggesting mechanical mingling and chemical mixing with the host granite (Figure 7.5-b,c).

Finally, countless occurrences of mafic durbachites are found in the metamorphic basement. They form either dykes, which can be followed over tens to hundreds of meters (Laurent, 1992), or occur as scattered 0.1–1m lenses within highly deformed – migmatitic – domains, which are transposed within the metamorphic foliation (Figure 7.5-d). These lenses presumably represent former dykes or sills, which have been highly strained and completely dismembered by injection of anatectic melts and deformation of the metamorphic series.

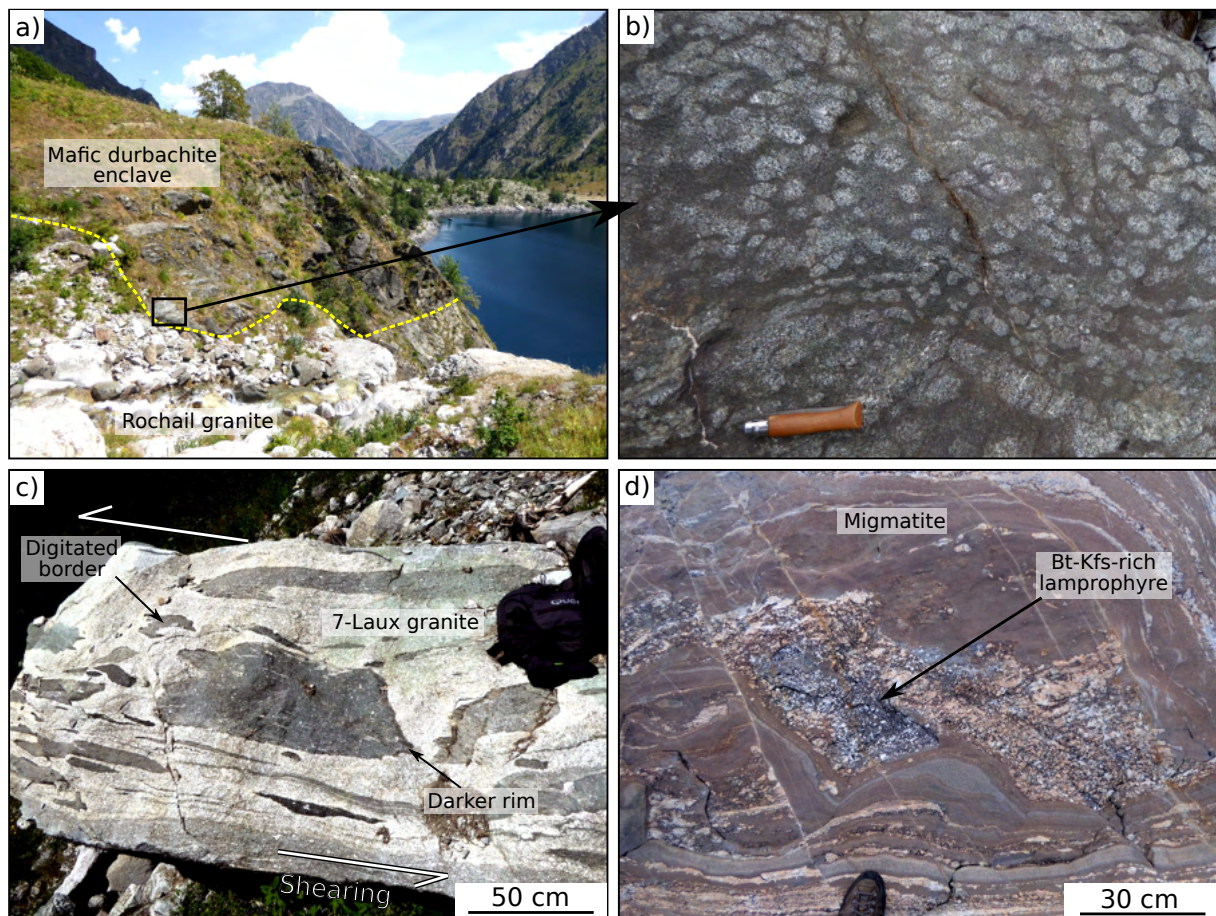


FIGURE 7.5 – Field pictures of the mafic durbachite enclaves. a) Hectometer-size durbachite in the Rochail granite (Figure 7.2). b) close-up view on a boulder from this enclave, which displays peculiar textures composed of mesocratic feldspar-biotite-(amphibole) patches surrounded by melanocratic, biotite-rich domains (biotite). c) Decimeter-to meter-size enclaves in the Sept-Laux granite (boulder not in place). Enclaves are sheared and elongated parallel to the granitic foliation. Digitated borders and darker rims indicate chemical interaction between the enclaves and the granite. d) Boudinage structures in mafic lamprophyres embedded in a migmatite (inner Oisans–Pelvoux massif). The lamprophyres are composed of K-feldspar phenocrysts in a dark, biotite-rich matrix. The boudins have been later cross-cut by brittle faults.

7.4 Petrographic description and mineral composition

Eight samples have been investigated in total. Five were collected in the two different facies of the Olan intrusive formations. In addition, two mafic enclaves were sampled in the Rochail granite, and a last sample was collected in a lense of biotite-rich lamprophyre

(minette) in the migmatitic series of the inner Oisans-Pelvoux massif. Sampling localities are reported on [Figure 7.2](#) and [Figure 7.3](#), and precise GPS coordinates are indicated in [Table 7.2](#).

7.4.1 Petrographic descriptions

The Olan amphibole-biotite (mela)-quartz-syenite (abS)

The amphibole-rich facies is characterized by a porphyritic assemblage rich in hornblende and large K-feldspar megacrysts (1-3 cm), with subordinate plagioclase, biotite and quartz ([Figure 7.6-a](#)). Clinopyroxene is occasionally preserved as relics. Secondary phases formed during retrogression include chlorite and actinolite. Chlorite commonly occur in replacement of biotite, while actinolite grows in replacement of hornblende and/or clinopyroxene. Apatite and titanite are ubiquitous and form euhedral crystals. In some samples, presence of shear bands localizing deformation in the (chloritized) biotite-rich layers marks post-crystallization, solid-state deformation.

The Olan pyroxene-biotite (mela)-quartz-syenite (pbS)

The pyroxene-biotite facies is generally finer-grained than the amphibole-biotite facies and does not present large K-feldspar megacrysts. It contains an assemblage rich in biotite, K-feldspar and clinopyroxene, with subordinate plagioclase, quartz, and hornblende ([Figure 7.6-b,e](#)). Secondary actinolite and chlorite occur, but this facies is generally drier and less retrogressed than the amphibole-biotite facies. Clinopyroxene is also better preserved and occasionally contains inclusions of biotite ([Figure 7.6-e](#)). This facies is rich in apatite, zircon and titanite, which are concentrated in the biotite-clinopyroxene-rich domains.

The mafic/intermediate enclaves in granite

Enclaves in granites display strong variations of facies between melanocratic, biotite-rich do-

main and mesocratic domains, which range from mafic to intermediate in composition. They contain a mineral assemblage similar to the pbS facies of the Olan formations (biotite–K-feldspar–hornblende– plagioclase–clinopyroxene–quartz–chlorite–actinolite, with accessory apatite, titanite and zircon), but are richer in Fe-Mg minerals and display different textures. Biotite forms elongated (2-5mm long) rods without any preferential orientation ([Figure 7.6-c](#)), that are commonly retrogressed to chlorite. Relics of clinopyroxene occur but are generally strongly retrogressed. Apatite is ubiquitous and forms elongated prisms and needles up to 500 μm long. Relics of euhedral titanite occurs, which has been replaced by a pseudomorphic assemblage rich in opaque minerals.

The biotite-rich lamprophyre

One sample of biotite-rich lamprophyre (JB-19-36) was collected in a meter-sized lense embedded in migmatites, close to the Olan formations. It mostly contains biotite, clinopyroxene, hornblende and actinolite, with subordinate K-feldspar and plagioclase, and accessory apatite. No zircon was observed. A strong metamorphic foliation is marked by oriented biotite and clinopyroxene augens -[Figure 7.6](#). Clinopyroxene has been heavily retrogressed and partially replaced by amphibole.

7.4.2 Mineral compositions

Preliminary mineral composition data were acquired in one sample of the pyroxene-biotite facies (JB-19-30), collected in the Olan intrusion, in order to perform thermobarometry. Electron probe microanalyses were done following the standard procedure for silicates described in Chapters [3](#), [4](#) and [6](#). A selected set of representative analyses is provided in [Table 7.1](#).

Clinopyroxene is an augite with low Al and Na content < 0.02 p.f.u (per formula unit) and molar $\text{Mg}/(\text{Mg}+\text{Fe})$ ($\text{Mg}\#$) between 0.68 and 0.71. Multiple analyses made in a single

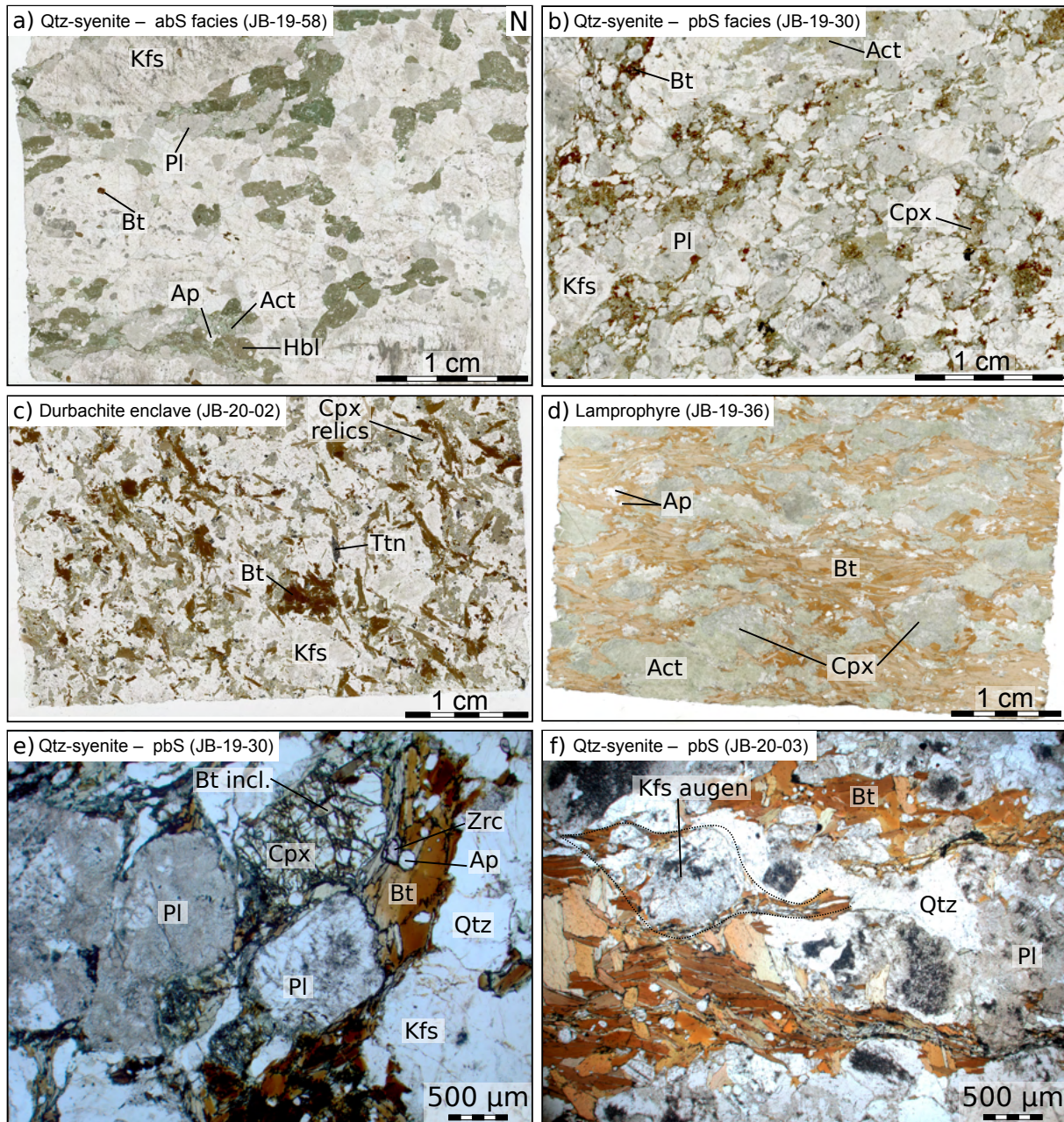


FIGURE 7.6 – Thin section scans and microphotographies of representative samples. a) Olan quartz-syenite, abS facies. b) Olan quartz-syenite, pbS facies. c) mafic enclave in the Rochail granite. d) Lamprophyric enclave in the migmatitic series of the internal Oisans-Peloux. e) Mineral assemblage in a Cpx-bearing quartz-syenite (pbS). Note the inclusions of apatite and zircon in biotite, and the inclusion of biotite in Cpx. f) Deformed quartz-syenite (pbS facies). Foliation is marked by oriented biotite and pressure shadows around K-feldspar augens.

grain have not revealed any significant core-rim zoning. Biotite is homogeneous throughout the sample and phlogopite-rich, with Mg# ranging between 0.53 and 0.58 and Ti content of

0.22 p.f.u. It contains some chromium (0.07-0.09 wt% Cr₂O₃). K-feldspar is an orthoclase (Or₉₁₋₉₆), and plagioclase has composition ranging from An₆₈ to An₈₃.

Label Position	Pl-5 Core	Pl-2 Rim	Kfs-5 Rim	Cpx-6 Core	Cpx-9 Rim	Amp-2 Core	Amp-3 Rim	Bt-9 Core
wt% oxide								
SiO ₂	61.74	61.27	64.43	52.80	53.13	51.79	53.10	37.63
TiO ₂	0.00	0.00	0.00	0.06	0.07	0.55	0.26	4.16
Al ₂ O ₃	24.24	24.18	18.61	0.50	0.46	3.46	2.88	14.03
Cr ₂ O ₃	-	-	-	0.00	0.03	0.00	0.00	0.09
FeO	0.14	0.15	0.05	10.50	10.78	13.88	13.37	17.77
MnO	-	-	-	0.58	0.65	0.48	0.40	0.25
MgO	0.00	0.00	0.00	12.40	12.50	14.84	15.01	12.85
CaO	5.45	5.82	0.00	23.11	23.16	11.87	12.46	0.00
Na ₂ O	8.38	8.21	0.56	0.22	0.18	0.73	0.44	0.14
K ₂ O	0.45	0.28	15.42	-	-	0.33	0.18	9.36
Total	100.40	99.90	99.06	100.17	100.96	97.93	98.10	96.28
Oxygen	8	8	8	6	6	23	23	11
Si	2.73	2.73	2.99	1.99	1.98	7.45	7.62	2.82
Ti	0.00	0.00	0.00	0.00	0.00	0.06	0.03	0.23
Al	1.27	1.27	1.02	0.02	0.02	0.58	0.49	1.24
Cr	-	-	-	0.00	0.00	0.00	0.00	0.01
Fe ³⁺	0.01	0.01	-	0.02	0.02	0.48	0.23	1.11
Fe ²⁺	-	-	0.00	0.31	0.32	1.19	1.37	-
Mn	-	-	-	0.02	0.02	0.06	0.05	0.02
Mg	0.00	0.00	0.00	0.70	0.70	3.18	3.21	1.44
Ca	0.26	0.28	0.00	0.93	0.93	1.83	1.91	0.00
Na	0.72	0.71	0.05	0.02	0.01	0.20	0.12	0.02
K	0.03	0.02	0.91	-	-	0.06	0.03	0.89
Total cation	5.01	5.00	4.98	4.00	4.00	17.09	17.07	7.78
Mg#	-	-	-	0.69	0.69	0.73	0.70	0.56
Ab	0.26	0.28	0.00	-	-	-	-	-
An	0.72	0.71	0.05	-	-	-	-	-
Or	0.03	0.02	0.95	-	-	-	-	-
En	-	-	-	0.36	0.36	-	-	-
Fs	-	-	-	0.16	0.16	-	-	-
Wo	-	-	-	0.48	0.48	-	-	-

TABLE 7.1 – Selected mineral analyses in sample JB-19-30 (Olan Qtz-syenite, pbS facies)

7.5 Whole rock geochemistry and Sr-Nd isotopes

The eight samples were analyzed for major and trace elements and for Sr-Nd isotopes at the SARM in Nancy, following the same procedures as described in Chapter 6. Results are summarized in Tables 7.2 and 7.3. In addition, a compilation of existing data on durbachites from the ECM of Belledonne, Grandes-Rousses and Oisans-Pelvoux has been done, which is provided in the supplements. These data come from several PhD and master thesis done at the Dolomieu institute in Grenoble between 1971 and 1994. The detailed list of references is given in the caption of Figure 7.7. This compilation contains mostly geochemical analyses of durbachitic enclaves in different granitoids, including the Sept-Laux, Roche-Noire, Rochail

and Grun plutons (localization on [Figure 7.2](#)). It also contains geochemical analyses of durbachite plutons, including the Lauzière monzosyenite in the northeast of Belledonne, the Quatre-Tours diorite (a satellite intrusion of the Rochail granite), and a few analyses of the Olan quartz-syenites. Screening for low MgO content (<3 wt.%) was applied for the enclaves in granitoids to remove samples that display a high K₂O content due to normal differentiation processes that may not imply a potassic nature of the source ([Peccerillo, 1992](#)). This screening was however not applied for the plutonic rocks, because the (ultra)-potassic nature of the source is already evidenced by the least differentiated, Mg–K rich terms in the respective intrusions, and the low-MgO samples within these plutons obviously represent the differentiated terms of the same (ultra)-potassic series. Diagrams were plotted using the R-based software GCDKit ([Janoušek *et al.*, 2016](#)).

7.5 Whole rock geochemistry and Sr-Nd isotopes

Sample Formation Type	JB-19-36 Basement mafic lamprophyre	JB-20-01 Rochail mafic enclave	JB-20-02 Rochail mafic enclave	JB-19-26 Olan abS	JB-19-30 Olan pbS	JB-19-58 Olan abS	JB-20-03 Olan pbS	JB-20-04 Olan pbS
Long°	6.222562	6.06082	6.06082	6.237605	6.237201	6.249193	6.201165	6.201165
Lat°	44.853761	44.974636	44.974636	44.839934	44.838616	44.844237	44.849214	44.849214
wt.% ox								
SiO ₂	45.49	50.62	50.05	57.35	60.48	61.95	56.39	63.89
TiO ₂	1.33	1.72	1.87	1.08	0.89	0.86	1.33	0.87
Al ₂ O ₃	11.51	13.15	13.04	14.69	14.28	14.11	14.98	14.44
FeO	8.90	7.02	6.39	5.31	5.05	4.21	6.35	3.88
MnO	0.18	0.14	0.21	0.14	0.10	0.09	0.11	0.07
MgO	14.84	7.17	4.79	3.99	3.78	3.21	5.16	2.79
CaO	6.80	5.58	6.64	4.32	3.79	3.33	4.21	3.33
Na ₂ O	0.82	1.90	1.71	2.44	2.72	2.49	2.91	2.90
K ₂ O	5.38	6.04	6.86	6.40	5.12	6.56	4.49	5.74
P ₂ O ₅	0.38	1.29	1.37	0.83	0.67	0.56	1.13	0.62
LOI	2.27	3.74	5.67	1.59	1.71	1.37	1.48	1.08
Total	98.89	99.15	99.31	98.72	99.16	99.20	99.24	100.03
ppm								
As	1.10	1.81	1.23	3.51	3.47	2.31	11.87	3.14
Ba	880	3823	3088	2579	1801	2161	1279	2231
Be	1.97	3.80	3.91	3.42	4.98	5.92	3.62	3.54
Bi	0.06	0.11	0.11	0.17	0.16	0.18	0.06	0.06
Cd	0.41	0.08	0.08	0.26	0.21	0.11	0.18	0.15
Co	46.64	31.67	27.31	16.12	15.50	13.68	20.13	10.67
Cr	1501.1	388.6	295.7	127.7	149.0	87.2	159.4	86.0
Cs	13.52	7.60	12.19	1.90	5.87	2.65	10.35	2.18
Cu	4.13	28.81	44.38	21.69	21.04	21.37	14.92	11.38
Ga	28.82	22.54	23.44	20.87	20.13	19.07	24.79	19.29
Ge	2.05	1.94	1.83	2.14	1.68	1.90	1.87	1.65
Hf	2.46	11.15	15.31	11.77	8.75	9.86	11.88	11.58
In	0.15	0.06	0.08	0.13	0.08	0.07	0.06	0.06
Nb	22.61	23.04	28.95	24.03	12.16	22.45	24.20	17.95
Ni	609.20	204.50	142.68	53.58	55.00	40.35	68.92	38.07
Pb	31.69	18.15	23.14	27.04	29.90	30.65	16.14	28.27
Rb	362.50	233.14	312.23	162.93	183.74	194.37	250.45	156.92
Sb		0.56	0.72	0.22	0.25	0.24	0.33	0.18
Sc	34.10	22.51	24.35	28.63	18.74	18.15	21.35	14.29
Sn	17.98	8.06	11.56	13.63	3.88	12.77	6.26	10.52
Sr	100.32	960.51	920.29	575.08	536.32	478.97	487.69	632.54
Ta	1.81	1.92	2.46	2.95	0.87	2.68	2.32	2.19
Th	6.15	28.24	40.35	29.44	25.16	43.05	12.00	27.14
U	1.69	6.61	8.74	5.25	3.37	8.54	3.80	4.26
V	166.62	138.04	153.65	98.60	90.71	73.85	122.03	72.19
W			1.09		4.63	6.78		
Y	27.41	24.18	27.62	72.67	18.08	29.14	47.10	27.35
Zn	213.2	105.2	94.3	98.7	89.7	67.5	91.1	66.5
Zr	91.2	430.1	582.3	448.0	346.5	343.4	448.3	410.8
La	21.79	78.57	61.85	50.87	35.41	43.17	33.19	45.81
Ce	50.44	178.84	152.82	133.32	85.02	117.65	104.41	116.03
Pr	6.77	23.72	21.36	19.99	11.82	17.12	17.24	16.10
Nd	29.04	97.33	93.99	92.44	52.58	76.98	84.63	69.36
Sm	7.61	17.37	19.38	23.18	10.91	16.56	21.01	14.35
Eu	0.79	3.41	3.53	3.47	2.27	2.63	3.11	2.41
Gd	6.51	9.84	11.40	14.80	6.02	8.67	13.02	7.82
Tb	1.01	1.14	1.34	2.20	0.72	1.07	1.77	0.98
Dy	5.47	5.42	6.48	13.33	3.79	5.77	9.62	5.23
Ho	0.89	0.91	1.09	2.57	0.67	1.06	1.75	0.98
Er	1.88	2.23	2.66	6.53	1.63	2.80	4.21	2.61
Tm	0.23	0.31	0.36	0.92	0.22	0.41	0.56	0.39
Yb	1.19	1.93	2.27	5.28	1.32	2.64	3.11	2.45
Lu	0.16	0.27	0.33	0.68	0.18	0.37	0.41	0.34
(La/Yb) _N	12.46	27.70	18.50	6.56	18.20	11.13	7.25	12.74
(Th/Nb) _N	2.25	10.14	11.54	10.14	17.13	15.87	4.10	12.52

TABLE 7.2 – Whole rock major and trace element composition of the collected samples.

7.5.1 Major elements composition

All data, including old and new analyses have been plotted on several discrimination diagrams. The red field on each diagram represents the distribution of composition of Carboniferous (K-rich alkali-calcic) granitoids in the ECM, based on our own compilation of data from various sources. This compilation is also provided in an excel file in the supplements. The high Mg# and low Mg# granitoid groups of Debon et Lemmet (1999) significantly overlap, and are therefore not distinguished.

The durbachitic enclaves and intrusions form a group of mafic to intermediate, K₂O-rich compositions, which is clearly distinct from the granitoids (Figure 7.7-a,b), with however large dispersion. SiO₂ content ranges from 46 to 65 wt.% and K₂O from <3.0 to 8.7 wt.%. K₂O/Na₂O ratios are nearly all above 1 and reach values >5 in some samples. Hence, both the enclaves and the plutonic intrusions fall within the group of highly potassic rocks (K₂O/Na₂O>1), and a large part can be classified as ultrapotassic (K₂O/Na₂O>2) following Foley *et al.* (1987). The multicationic B–Mg# and B–A diagrams of Debon et Le Fort (1983) show a clear relation between maficity (B), Mg# and Al saturation (A). Some enclaves present very high maficity (B>350) and larger dispersion in Mg# than the rest of samples, which may be controlled by cumulative processes. It is in particular the case for the lamprophyric sample JB-19-36, which presents very high maficity (B>500) and displays a mineral assemblage consistent with a biotite-clinopyroxene-rich cumulate.

The durbachites in a whole define a highly magnesian (Mg# = 0.50–0.76), metaluminous series with negative B–A correlation (Figure 7.7-c,d). On Harker diagrams, this series is characterized by decreasing MgO, FeO and CaO with increasing SiO₂. The trend for MgO is inflexed concave up, which reflects the early crystallization and settling of Mg-rich minerals (olivine, pyroxene). Al₂O₃ is positively correlated with SiO₂ and present a concave down trend, although considerably scattered. These features are in agreement with fractionation

trends determined experimentally by Parat *et al.* (2010) on mafic durbachites from the Bohemian Massif.

The Olan quartz-syenites slightly depart from the trend defined by the bulk of durbachites. On the B-A plot, they define their own trend at lower Mg# (Figure 7.7). On Harker plots, they define a linear trend, which marks an angle with the rest of the durbachite series (Figure 7.8). This is especially the case for Al_2O_3 , where the trend defined by the Olan samples is nearly orthogonal to the durbachite trend.

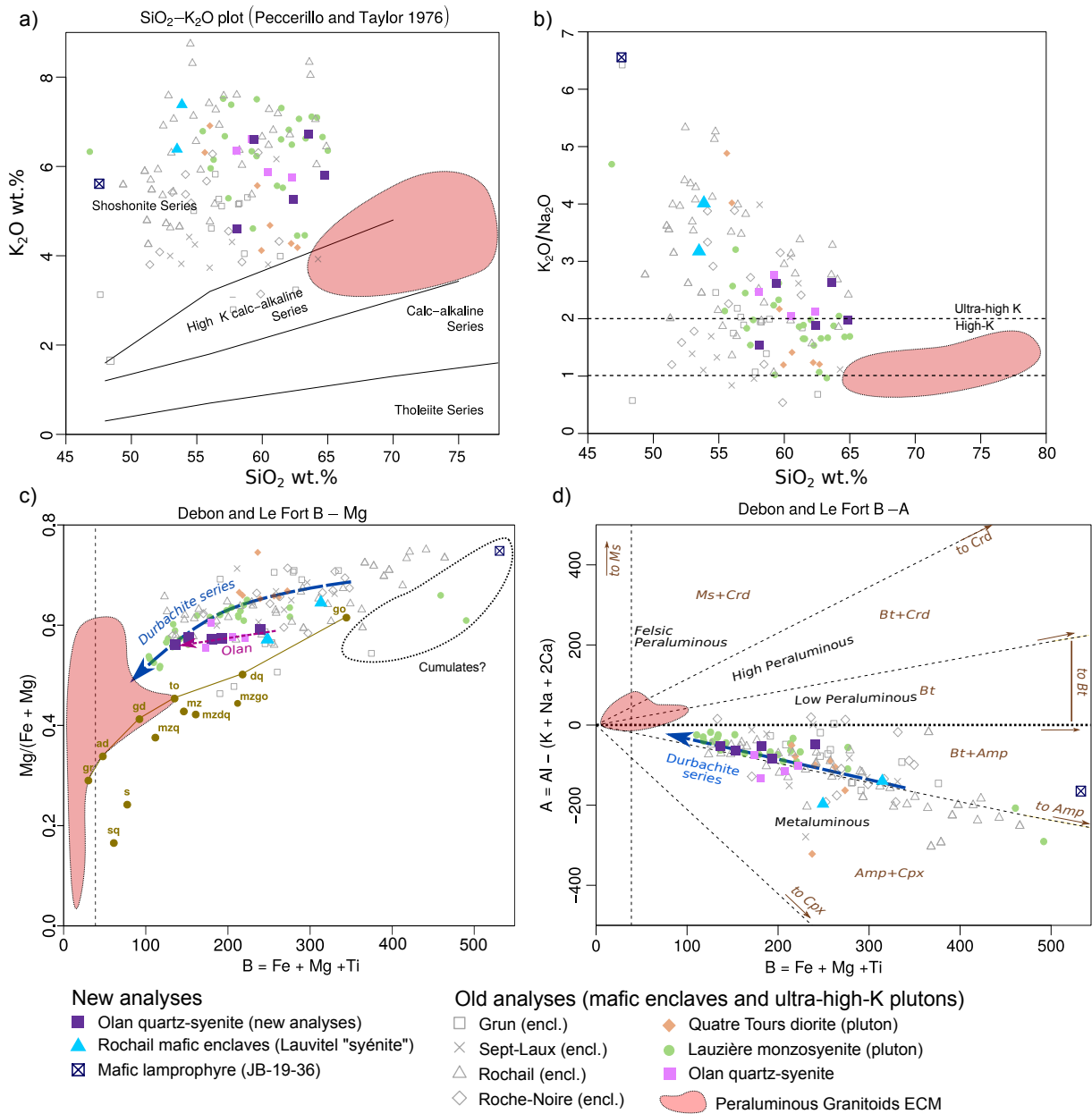


FIGURE 7.7 – Compilation of whole rock geochemical data plotted on several discrimination diagrams. a) $\text{SiO}_2 - \text{K}_2\text{O}$ diagram of Peccerillo et Taylor (1976) used to discriminate low-medium-high-ultra-high K series. b) $\text{SiO}_2 - \text{K}_2\text{O}/\text{Na}_2\text{O}$ diagram. $\text{K}_2\text{O}/\text{Na}_2\text{O} > 1$ is indicative of high-K series, and $\text{K}_2\text{O}/\text{Na}_2\text{O} > 2$ represents true ultrapotassic rocks (Foley et al., 1987). c-d) B – Mg# and B – A diagrams of Debon et Le Fort (1983), which discriminate between magnesian / ferroan and peraluminous / metaluminous series. A, B and Mg# are multicationic parameters based on "millications" (1000 gram.atom per 100 grams). $A = \text{Al} - (\text{K} + \text{Na} + 2\text{Ca})$; $B = \text{Fe} + \text{Mg} + \text{Ti}$, $\text{Mg}\# = \text{Fe}/(\text{Fe} + \text{Mg})$. B is a measure of maficity, correlated with the degree of differentiation of the rock. A is a measure of Al-saturation, similar to the A/CNK parameter of Shand (1947). The compilation includes our new analyses and data from old PhD and master works (Aumaitre et al., 1985; De Boisset, 1986; Gasquet, 1979; Le Fort, 1971; Negga, 1984; Oliver, 1994; Poncerry, 1981; Simeon, 1979; Verjat, 1981). The red field on each diagram indicate the distribution of composition of granitoids in the ECM, based on our own compilation of data.

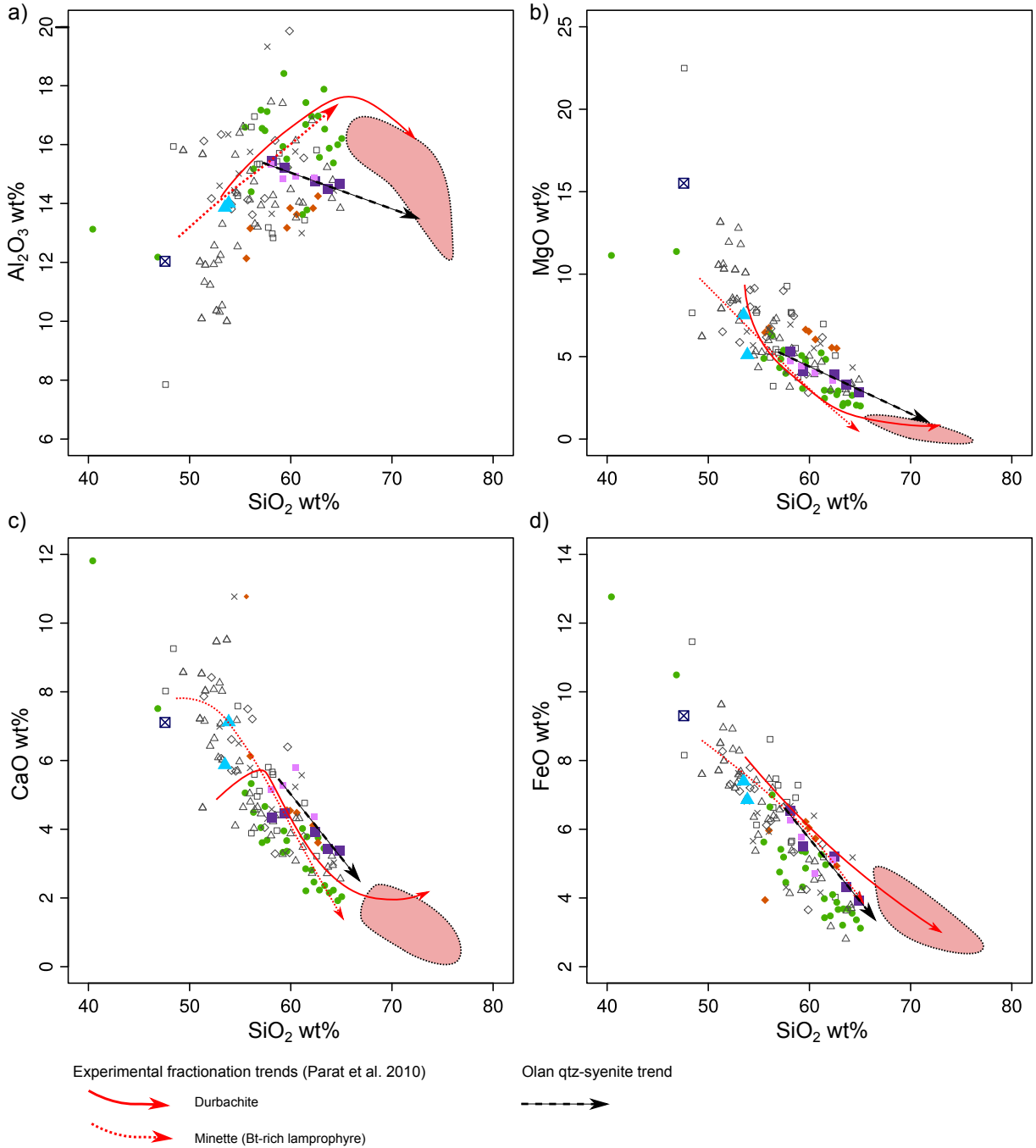


FIGURE 7.8 – Harker plots showing evolution trends of the durbachites in ECM. Experimental fractionation trends of Parat *et al.* (2010) are shown for comparison. The Olan samples are well aligned on a mixing line with a felsic – leucogranitic – component. Legend is the same as on Figure 7.7.

7.5.2 Trace elements composition

The trace element patterns normalized to the primitive mantle composition (Sun et McDonough, 1989) are plotted on Figure 7.9. Variation of trace element composition in surrounding granitoids of the ECM (data from Fréville (2016)) are plotted for comparison. The Olan quartz-syenites and the mafic enclaves both present strong enrichment in LILE (Cs, Rb, Ba, Pb), Th and U relative to the primitive mantle. They display high LREE/HREE ($(La/Yb)_N=6.6-27.7$) and high LILE/HFSE ($(Th/Nb)_N=4.1-17.1$), with negative anomalies in Nb, Ta and Ti and weaker negative anomalies in Sr and Eu. All samples are rich in compatible transition metals (85–392 ppm Cr and 38–206 ppm Ni). These characteristics are typical of Variscan durbachites (Couzinié *et al.*, 2016; Janoušek *et al.*, 2019). Cumulative sample JB-19-36 is very rich in transition metals (1518 ppm Cr, 616 ppm Ni). It presents strong enrichment in some LILE (Cs, Rb, Pb), high LILE/HFSE ($(Th/Nb)_N=2.3$) and high LREE/HREE ($(La/Yb)_N=12.5$), but enrichment is less pronounced in Ba, U and Th. Sr and Eu anomalies are stronger than in other samples, and negative anomalies are observed in Zr and Hf in addition to other HFSE. These characteristics are consistent with the composition of a clinopyroxene-biotite-rich cumulate poor in feldspar (low Ba, Sr, Eu) and zircon (low Zr, Hf).

With the exception of cumulative sample JB-19-36, all the durbachite are richer in LILE, REE and HFSE than the surrounding granitoids. This enrichment is independent of maficity and trace element content may reach five to ten time that of the granitoids for Th, U and most of REE.

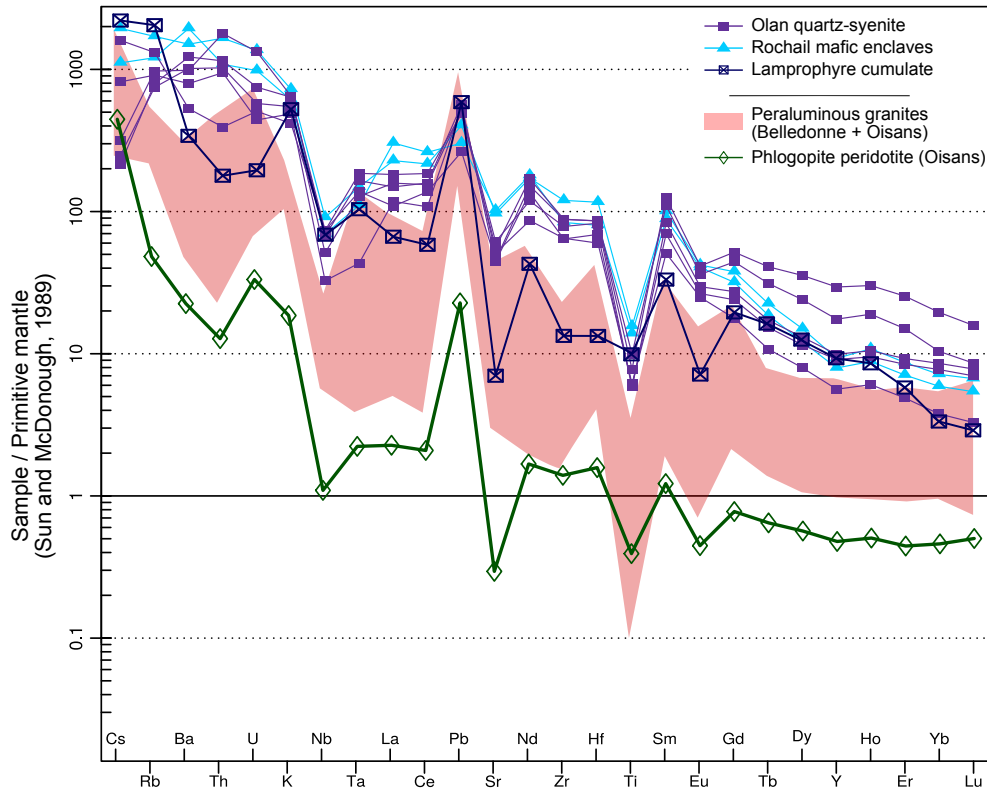


FIGURE 7.9 – Trace element composition of the durbachites normalized to the primitive mantle composition after Sun et McDonough (1989). Trace element composition of peraluminous granitoids (from Fréville, 2016) and an enclave of phlogopite-bearing peridotite found in the Oisans–Pelvoux massif (Chapter 6) are shown for comparison.

7.5.3 Sr-Nd isotopes

Whole rock Sr–Nd isotopes data have been acquired on four samples of the Olan plutonic formation, one mafic enclave (JB-19-01) and on cumulative sample JB-19-36. Isotopic data from the surrounding peraluminous granites Fréville (2016) have been added for comparison, as well as data on mantle enclaves from the Oisans–Pelvoux and Belledonne massifs (Chapter 6). The initial isotopic ratios of plutonic rocks have been recalculated at the age of emplacement of each intrusion, specified in Table 7.3. For the mafic enclave JB-20-01, the emplacement age of the host Rochail granite (after Fréville (2016)) is taken as the initial age. For ultramafic samples, cumulative sample JB-19-36 and migmatite sample MCE140b, isotopic ratios are given at 330 Ma, which is supposed to be the mean age of emplacement

of the durbachites in the ECM according to our geochronological data and other published data (Bussy *et al.*, 2000; Schaltegger *et Corfu*, 1992).

All the durbachites contain highly radiogenic Sr ($0.7068 < {}^{87}\text{Sr}/{}^{86}\text{Sr}_{(t)} < 0.7162$) and unradiogenic Nd ($-4.28 < \epsilon\text{Nd}_{(t)} < -5.97$). In comparison, the peraluminous granitoids and migmatites generally present less radiogenic Sr ($0.7007 < {}^{87}\text{Sr}/{}^{86}\text{Sr}_{(t)} < 0.7070$, with one outlier at 0.7126) and more radiogenic Nd ($-0.98 < \epsilon\text{Nd}_{(t)} < -5.69$). A negative correlation between MgO and $\epsilon\text{Nd}_{(t)}$ is observed for the durbachites. In particular, the most mafic – cumulative – sample JB-19-36 presents the most radiogenic Sr and the most unradiogenic Nd signature (${}^{87}\text{Sr}/{}^{86}\text{Sr}_{(t)} = 0.7162$ and $\epsilon\text{Nd}_{(t)} = -6.0$).

Sample	Unit	Rock type	Age (Ma)	Element ppm				Sr isotopes				Nd isotopes				
				Rb	Sr	Nd	Sm	$\frac{87Sr}{86Sr}$	σ .10 ⁶	$\frac{87Sr}{86Sr}$	$\frac{87Sr}{86Sr}(t)$	$\frac{143Nd}{144Nd}$	σ .10 ⁶	$\frac{147Sm}{144Nd}$	$\frac{143Nd}{144Nd}(t)$	cNd(t)
JB-19-30	Olan	qs(pbs)	324	184	536	52.6	10.9	0.713469	9	0.992162	0.708880	0.512218	4	0.125450	0.511952	-5.12
JB-19-58	Olan	qs(abs)	324	194	479	77.0	16.6	0.712939	6	1.175160	0.707503	n.a.		n.a.	0.511979	-4.39
JB-20-01	Olan	Lpr	337	233	961	97.3	17.4	0.710138	4	0.702684	0.706767	0.512217	6	0.107907	0.511939	-5.36
JB-20-03	Olan	qs(pbs)	324	250	488	84.6	21.0	0.716225	4	1.487598	0.709344	0.512258	5	0.150081	0.511969	-4.79
JB-20-04	Olan	qs(pbs)	324	157	633	69.4	14.3	0.711184	8	0.718303	0.708517	0.512234	7	0.125055	0.511902	-6.10
JB-19-36	Dyke	Lpr	330	362	100	29.0	7.6	0.765695	5	10.517696	0.716293	0.512243	8	0.158373	0.512244	0.59
JB-19-20	Mantle	Gt-Prd	330	1.0	8.6	0.9	0.3	0.708949	5	0.324450	0.707425	0.512609	9	0.169378	0.511925	-5.64
JB-19-21	Mantle	Phi-Prd	330	31.1	6.3	2.3	0.5	0.767705	9	14.446003	0.699852	0.512236	6	0.144258	0.512071	-2.78
JB-19-22	Mantle	Spl-Prd	330	15.2	13.3	2.0	0.4	0.721851	7	3.304820	0.706328	0.512302	7	0.107129	n.a.	
JB-19-33	Mantle	Gt-Prd	330	2.1	9.0	0.7	0.3	0.704401	11	0.689829	0.701161	n.a.		n.a.	0.512144	-1.37
JB-19-48	Mantle	Srp	330	0.3	4.9	0.7	0.2	0.717273	6	0.151137	0.716563	0.512463	12	0.148163	n.a.	
JB-19-49	Mantle	Srp	330	0.2	5.7	0.4	0.1	0.717834	5	0.121045	0.717265	n.a.		n.a.		
JB-20-12	Mantle	Gt-Prd	330	3.8	10.3	0.7	0.3	0.710165	5	1.056448	0.705203	n.a.		n.a.		
JB-20-13	Mantle	Gt-Prd	330	2.3	8.7	0.8	0.3	0.705715	4	0.759682	0.702147	n.a.		n.a.		
JB-20-14	Mantle	Gt-Prd	330	7.1	27.2	2.8	0.8	0.714424	3	0.751378	0.710895	0.512163	7	0.169239	0.511798	-8.12
MCE301	Bans	gd	307	138	183	25.0	4.2	0.715523	1	2.176359	0.706015	0.512322	2	0.100351	0.512121	-2.39
MCE167C	Bérarde	g	303	89	23.6	5.0	5.0	0.723541	2	5.155596	0.701311	0.512355	2	0.128079	0.512102	-2.87
MCE168	Bérarde	g	303	169	62	17.7	3.5	0.73454	1	7.836119	0.700752	0.512427	2	0.118859	0.512192	-1.10
JB-20-07	Boung	g	319	182	363	32.6	5.8	0.71355	7	1.450879	0.706963	0.512153	10	0.106962	0.511930	-5.81
JB-20-11	C-B	qz	330	149	866	46.7	8.1	0.708778	5	0.497989	0.706439	0.512224	5	0.104351	0.512015	-3.87
MCE183A	Cray	g	272	352	78	29.3	5.8	0.763513	2	13.166641	0.712560	0.512339	2	0.119461	0.512127	-3.15
MCE140B	Migmatite	Mig	298	143	111	19.6	3.8	0.721253	1	3.737445	0.703698	0.512350	2	0.115971	0.512100	-1.20
MCE315	R-B	ad	302	164	609	36.8	5.9	0.709999	1	0.779598	0.706649	0.512380	1	0.097251	0.512188	-1.20
MCE181	Rochail	ad	337	225	392	21.9	4.2	0.714977	2	1.662464	0.707002	0.512217	2	0.115658	0.511962	-4.73
MCE182	Rochail	a	337	261	448	22.7	4.3	0.714704	2	1.687356	0.706610	0.512221	2	0.113978	0.511970	-4.58
MCE150	R-N	g	308	172	349	31.4	4.5	0.712197	1	1.422907	0.705960	0.512258	2	0.087020	0.512083	-3.10
MCE152	R-N	qz	308	330	207	39.1	7.1	0.721014	2	4.620145	0.700763	0.512302	1	0.110082	0.512081	-3.15
MCE42	R-N	ad	308	143	242	13.1	2.1	0.712082	2	1.705031	0.704609	0.512268	2	0.096908	0.512073	-3.29
MCE33	7L (inner)	ad	324	182	397	23.2	3.8	0.712843	2	1.323888	0.706738	0.512169	1	0.097971	0.511962	-5.07
MCE39	7L (outer)	ad	348	146	650	24.1	3.8	0.709369	2	0.650215	0.706148	0.512239	1	0.096070	0.512021	-3.31

TABLE 7.3 – Sr-Nd isotope data on rocks from the Oisans-Pelvoux and Belledonne massifs. Data from this thesis (samples JB-xx-xx) and from Fréville (2016) (samples MCE-xx). Abbreviations for geological units : C-B – Colle-Blanche plutonic complex; R-B – Rieou-Blanc granite; R-N – Roche-Noire Granite; 7L – Sept-Laux granite (inner and outer facies). Lithologies : ad – quartz-monzonite; g – granite; gd – granodiorite; qz – quartz-monzonite; qs – quartz-syenite (abs/pbs facies); lpr – lamprophyre; Mig – migmatite; Grt/Phl/Spl-Prd – garnet/phlogopite/spinel-peridotite; srp – serpentinite

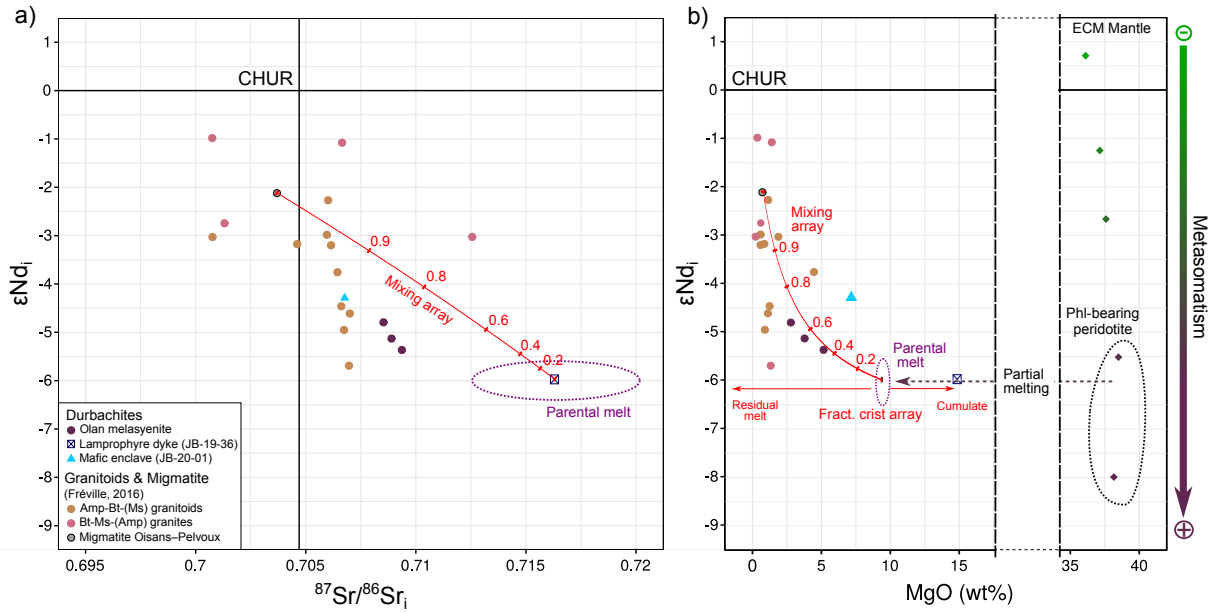


FIGURE 7.10 – a) $\epsilon Nd(t)$ plotted in function of $^{87}Sr/^{86}Sr$ time corrected ratios. Data on durbachites (plus a few granitoids) are from this work, data on granitoids are from Fréville (2016) and data on ultramafic enclaves are from Chapter 6. b) $\epsilon Nd(t)$ in function of MgO. Theoretical trends of mixing with a crustal component (Migmatite MCE140b) and fractional crystallization are drawn in red, assuming a parental melt with 8 wt.% MgO and the same isotopic composition as mafic sample JB-19-36. See explanation in the discussion section.

7.6 U-Pb geochronology

The emplacement age of the Olan intrusion has been determined by U–Pb dating on separated zircon. After crushing and mineral separation, extracted zircon grains were mounted in epoxy resin and polished to expose the grain center. Cathodoluminescence (CL) images were obtained on a Tescan Vega 3 scanning electron microscope at ISTERre, and U–Pb dating was performed with a Laser-Ablation ICP-MS system installed at the GeOHeLiS platform at Géosciences Rennes. Operating conditions are provided in Table 7.6 in the appendix. The IsoplotR package (Vermeesch, 2018) was employed to plot the diagrams and calculate ages. Individual uncertainties are quoted at 2σ level and the confidence level for weighted average is 95%.

Dated samples JB-19-30 and JB-19-58 come respectively from the fine-grained pyroxene-biotite facies (pbS) and the coarse-grained amphibole-biotite facies (abS) of the intrusion (Figure 7.3). Both samples contain abundant zircon grains, which form a remarkably homogeneous population in terms of shape, internal texture and composition. The grains are usually 100-300 μm long and form euhedral prisms with aspect ratios between 1.3 and 2.5, and contain numerous inclusions of apatite. CL imaging reveals common concentric oscillatory and/or sector zoning. There are no discernible textures indicating subsequent overgrowth or (re)crystallization by dissolution-precipitation processes. Th/U ratios measured on dated spots are all above 0.1 (0.13–0.35) and U content ranges from 740 to 2850 ppm. Chondrite-normalized REE patterns are characterized by a strong positive Ce anomaly, a negative Eu anomaly and moderate enrichment in HREE relative to LREE ($(\text{Lu}/\text{Gd})_N=10\text{--}20$). About thirty grains were analyzed for each samples, which all yielded concordant U–Pb dates within uncertainty. $^{238}\text{U}/^{206}\text{Pb}$ dates are consistent with single-age populations in each sample. Weighted mean $^{238}\text{U}/^{206}\text{Pb}$ ages are estimated at 328 ± 3 Ma (MSWD=0.85) and 323 ± 3 Ma (MSWD = 0.77) respectively for sample JB-19-30 and JB-19-58, and are indistinguishable from concordia ages within uncertainty.

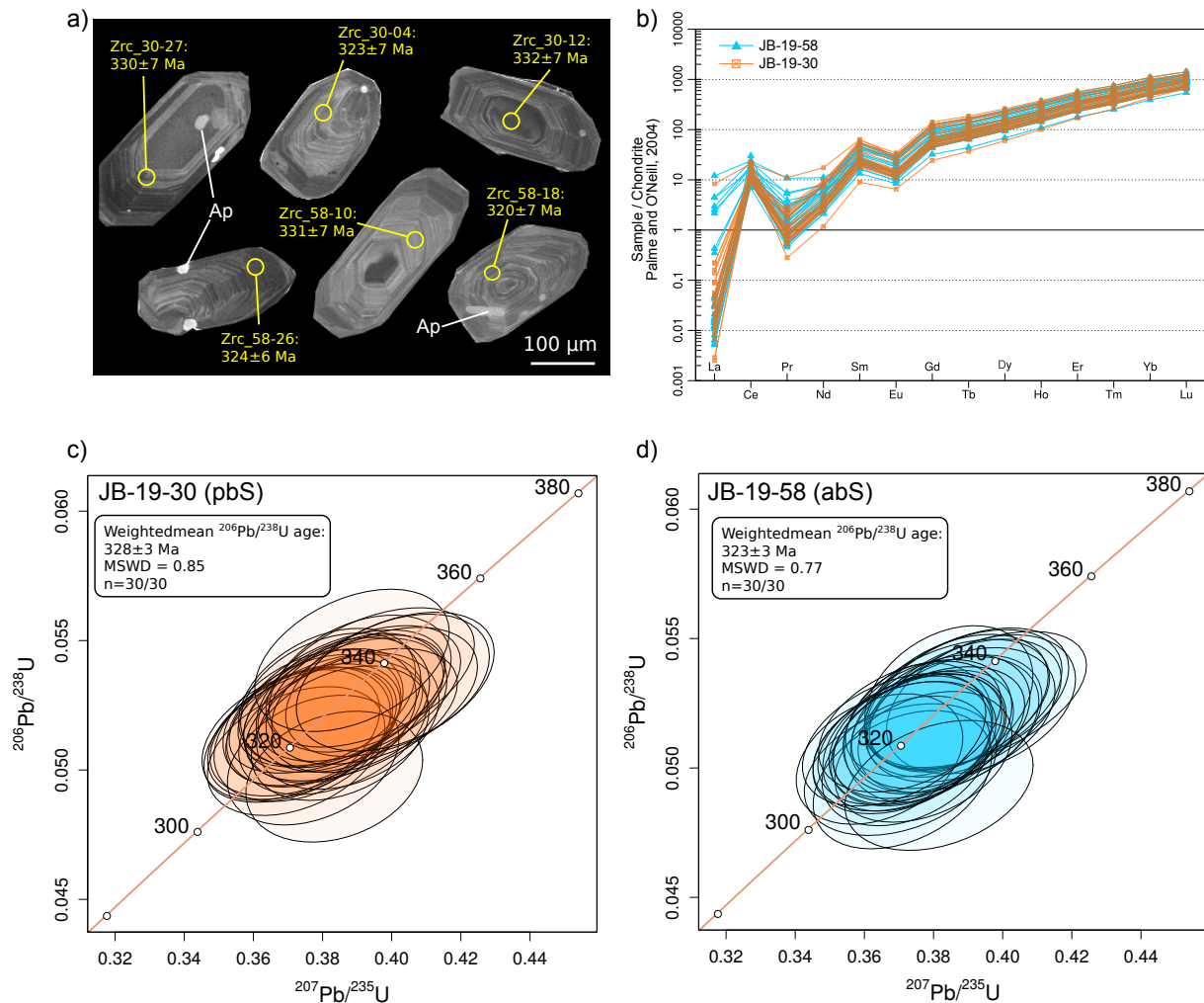


FIGURE 7.11 – U-Pb dating of the Olan quartz-syenite. a) Cathodoluminescence images of representative zircon grains, with marked the position of Laser ablation spots. b) REE patterns of dated zircon grains normalized to chondrite composition after [Palme et O’Neill \(2004\)](#). REE and U-Pb were acquired on the same laser ablation spots. c-d) Wetherill concordia plots for the two dated samples.

7.7 Thermobarometry

The diverse assemblage of both rock-forming and accessory minerals of the Olan quartz-syenites, in particular in the pbS facies, allows the use of multiple independent thermobarometers to constrain the P-T conditions of emplacement of the intrusion. We applied several thermometers and barometers using mineral and whole rock compositions of sample JB-19-30. All the results are summarized in [Tables 7.4 and 7.5](#) and on [Figure 7.12](#), with appropriate

reference to the equations used. Tables of result are reported as average of multiple measurements. The complete set of P-T estimates is available in the supplementary material. Standard deviations indicate dispersion resulting only from electron probe analytical uncertainties and/or variation in mineral composition within a sample. They are generally very small (± 4 - 7°C and ± 0.2 - 1 kbar) and do not represent the absolute uncertainty on T or P, which is dominated by internal uncertainty of the thermobarometric calibrations. According to [Putirka \(2008\)](#), the latter is around ± 20 - 50°C for T and ± 2 - 3 kbar for P depending on the equation.

7.7.1 Thermobarometry of rock forming minerals

Several thermobarometers have been used to estimate the P-T conditions at which rock forming minerals crystallized from the melt. We mostly used equations from [Putirka \(2008\)](#) and [Putirka *et al.* \(2003\)](#) for feldspar and clinopyroxene. These thermobarometers rely either on mineral-liquid equilibria, mineral composition alone, or liquid composition alone (*ie* they provide saturation temperature of a given mineral in a given melt composition), allowing independent comparison between independent methods. In addition, we also estimated the crystallization temperature of biotite using the thermometer of [Richter et Carmichael \(1996\)](#) based on partition of TiO_2 between biotite and liquid. The whole rock composition was considered representative of the liquid composition.

Based on whole rock composition, clinopyroxene has a saturation temperature of 1118°C at 8 kbar (Eq. [34]). This estimate is consistent with clinopyroxene thermometry (Eq. 32d]), which yields $T = 1156^\circ\text{C}$ ($1\sigma = \pm 6^\circ\text{C}$) at the same pressure. Clinopyroxene-liquid thermometers yield $T = 1074^\circ\text{C}$ ($1\sigma = \pm 7^\circ\text{C}$) for the calibration of [Putirka *et al.* \(2003\)](#) and $T = 1019^\circ\text{C}$ ($1\sigma = \pm 5^\circ\text{C}$) for Eq. [33]. The latter is a bit off relative to other independent thermometers (Eq [34] and [32d]), and therefore the question of [Putirka *et al.* \(2003\)](#) is

Method	Reference	Putirka Eq n°	n	T(°C)	1 σ	P (kbar)	1 σ
Cpx saturation	1	[34]	-	1118	-	[8]	-
Cpx-Liq	1	[33]	15	1019	± 5	[8]	-
Cpx-Liq	2	[2003a]	15	1074	± 7	[8]	-
Cpx-Liq	2	[2003b]	15	[1100]	-	6.1	± 1
Cpx-Liq	1	[32c]	15	[1100]	-	4.5	± 0.2
Cpx only	1	[32d]	15	1156	± 6	[8]	-
Pl saturation	1	[26]	-	1039	-	[8]	-
Pl-Liq	1	[23]	8	1009	± 7	-	-
Pl-Liq	1	[24a]	8	958	± 8	-	-
Phl-Liq	3	-	11	1021	± 5	-	-

TABLE 7.4 – Summary of clinopyroxene, plagioclase and biotite thermobarometry for sample JB-19-30 (Olan pbS). Results are reported as average of n analyses, with 1- σ standard deviation. Values in bracket correspond to assumed P or T for thermometric or barometric estimates. The P-T relation for each equation is better visible on [Figure 7.12](#). References for thermobarometric equations : 1 – [Putirka \(2008\)](#); 2 – [Putirka et al. \(2003\)](#); 3 – [Righter et Carmichael \(1996\)](#)

preferred. All these equations have a very small dependency in P, and thus clinopyroxene crystallization T is constrained between 1050 and 1150°C. Eq. 32c and [2003]b have a greater dependency in pressure and are therefore used as barometers. Assuming T = 1100°C, they yield respectively P = 6.1 kbar (1 σ = ± 1 kbar) and P = 4.5 kbar (1 σ = ± 0.2 kbar). However, there is a large uncertainty due to the strong dependence in T. Assuming T between 1050 and 1150°C, the pressure range during clinopyroxene crystallization is estimated between 4 and 9 kbar.

Plagioclase saturation is estimated at 1039°C (at 8 kbar) using Eq. [26]. Pl-Liq thermometers yield slightly lower and mutually consistent T at 1009°C (1 σ = ± 7 °C) for Eq. [23] and 995°C (1 σ = ± 4 °C) for Eq. [24a] at the same pressure. Therefore, crystallization T is estimated at 1000 ± 50 °C.

The TiO₂ content in biotite ranges from 3.79 to 4.07 wt.%, which yields T = 1021°C (1 σ = ± 5 °C) for the given liquid composition. The Bt-Liq thermometer of [Righter et Carmichael \(1996\)](#) is insensitive to P, f_{O₂} and H₂O content of the liquid. Therefore, it supports crystallization of biotite at high T, which is consistent with presence of biotite inclusions in clinopyroxene ([Figure 7.6](#)).

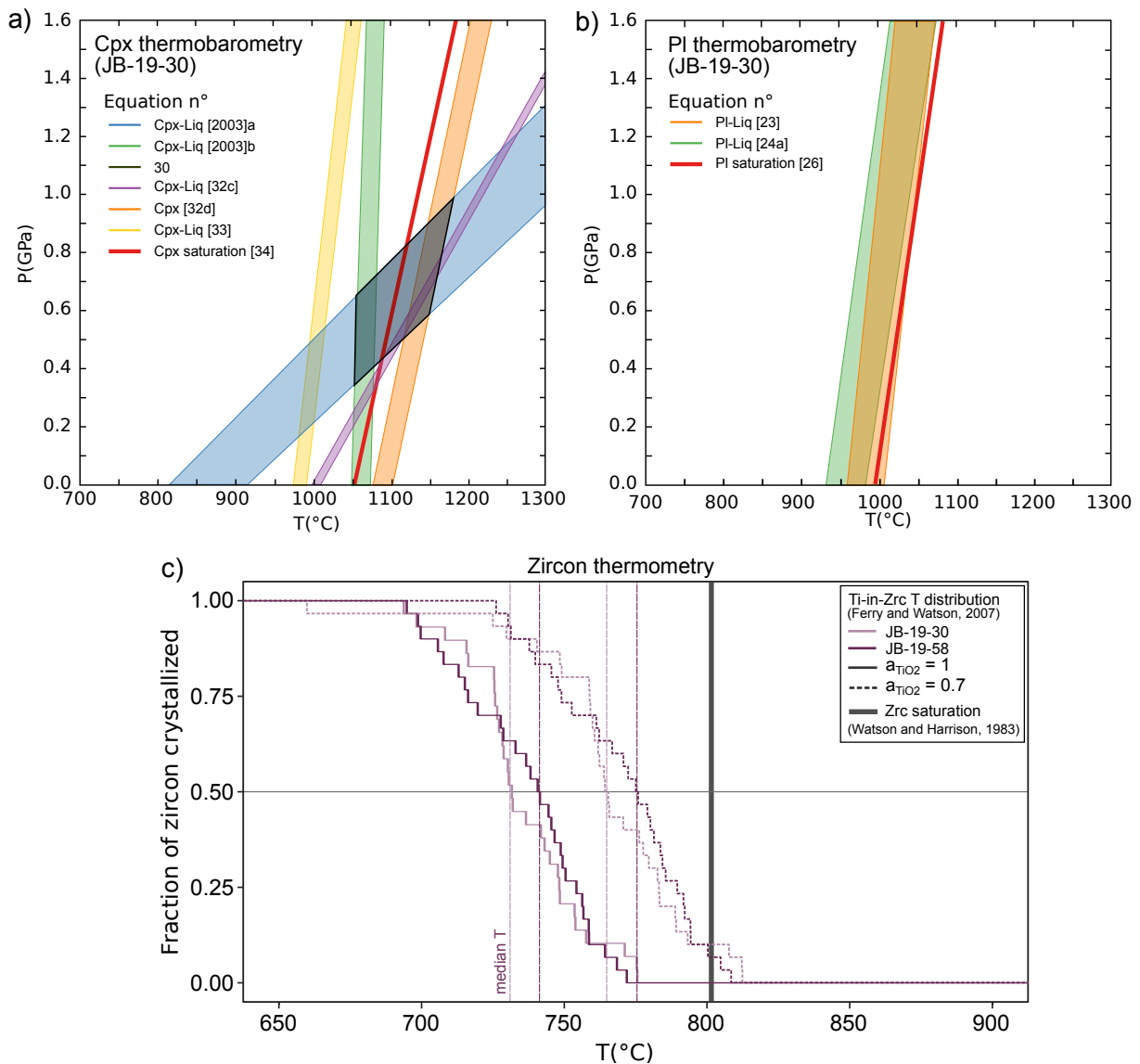


FIGURE 7.12 – Compilation of thermobarometric results obtained on Olan quartz-syenite samples using various thermometers and barometers. Clinopyroxene (a) and plagioclase (b) thermobarometry on sample JB-19-30, based on equations from Putirka *et al.* (2003); Putirka (2008). c) Ti-in-zircon thermometry on dated zircon grains (samples JB-19-30 and JB-19-58) based on the calibration of Ferry *et Watson* (2007). The cumulative distribution of zircon analyses is reported in function of T for each sample, zero meaning that no zircon has crystallized and one meaning that all zircon has crystallized. Different distributions have been calculated assuming either TiO_2 saturation or $a_{TiO_2} = 0.7$ (see discussion in text).

7.7.2 Apatite and zircon saturation

Apatite and zircon saturation temperatures have been calculated for all the collected samples, except cumulative sample JB-19-36, whose composition is unlikely to reflect that

Sample	Zircon saturation			Apatite saturation		
	M	Zr (ppm)	T(°C)	A/CNK	P ₂ O ₅ wt.%)	T(°C)
JB-19-26	2.32	448	807	0.867	1.13	1070
JB-19-30	2.04	346	806	0.782	0.83	1030
JB-19-58	2.07	343	803	0.845	0.67	1035
JB-20-03	2.15	448	821	0.818	0.56	1025
JB-20-04	1.96	411	828	0.848	0.62	1062
JB-20-01	1.54	430	867	0.585	1.37	1015
JB-20-02	1.90	582	867	0.663	1.29	1013

TABLE 7.5 – Summary of zircon and apatite saturation temperatures, obtained respectively with the calibrations of [Watson et Harrison \(1983\)](#) and [Harrison et Watson \(1984\)](#). $M = 100 \cdot (\text{Na} + \text{K} + 2 \cdot \text{Ca}) / (\text{Al} + \text{Si})$ and $A/\text{CNK} = \text{Al} / (2 \cdot \text{Ca} + \text{Na} + \text{K})$, all expressed in atomic proportions in the melt.

of a magmatic liquid. The calibration of [Watson et Harrison \(1983\)](#) was used for zircon, and the calibration of [Harrison et Watson \(1984\)](#) was used for apatite. Whole rock compositions are assumed to approximate the melt composition during crystallization of these minerals. Apatite saturation temperatures (T_{Ap}) in the Olan quartz-syenites are high and display significant dispersion among samples (1025–1070°C). The two mafic enclaves in the Rochail granite slightly lower T_{Ap} at 1013–1015°C. Zircon presents much lower saturation temperatures (T_{zrc}) than apatite, with again some dispersion. The Olan samples yields $T_{zrc} = 806$ – 828 °C, and the two mafic enclaves both yield $T_{zrc} = 867$ °C.

7.7.3 Ti-in-zircon (TiZ) thermometry

TiZ temperatures have been estimated for the two dated samples JB-19-30 and JB-19-58, using the calibration of [Ferry et Watson \(2007\)](#). These two samples contain homogeneous zircon populations with similar Ti-content, which ranges between 2.6 and 13.6 ppm in sample JB-19-30 and between 5.6 and 13.1 ppm in sample JB-19-58. As recently pointed out in [Schiller et Finger \(2019\)](#), simply assuming saturation in TiO₂ and SiO₂ may result in temperatures underestimated by up to 70-80°C, mainly due to reduced a_{TiO_2} , which may be as low as 0.1-0.5 in some types of granitic melts. Thermodynamic calculations have been performed with PerpleX 6.9.0 ([Connolly, 2009](#)) using the melt model of [Holland et al. \(2018\)](#)

(see details in the appendix), which suggest SiO_2 saturation of the liquid was reached at the onset of zircon crystallization ($a_{\text{SiO}_2}=1$). In contrast, TiO_2 was undersaturated and a_{TiO_2} evolved mainly around 0.6-0.8 during cooling below the liquidus. Therefore, calculation of temperatures has been made assuming either $a_{\text{TiO}_2}=1$ or $a_{\text{TiO}_2}=0.7$ to show the resulting variation in T. The cumulative distribution of TiZ temperatures in each sample is reported on [Figure 7.12-c](#). According to [Schiller et Finger \(2019\)](#), the median-T value of a series of zircon analyses should be ca. 30 to 50°C lower than peak-T of the magma or T_{zrc} in case of complete zircon dissolution. Assuming TiO_2 saturation (plain lines) yields median TiZ of 727°C and 736°C respectively for samples JB-19-30 and JB-19-58, with a large spread between ca. 630°C and 770°C, which is much lower than saturation T for zircon in these two samples (respectively 806°C and 803°C). Assuming a_{TiO_2} reduced to 0.7 (dashed lines) yields median T of 764°C and 775°C respectively, with a large spread between ca. 660°C and 812°C, which is in perfect agreement with the calculated saturation T.

7.8 Discussion

7.8.1 Emplacement of the Olan plutonic formation

7.8.1.1 Crystallization sequence and P-T conditions of emplacement

Mineral-liquid and saturation thermometry applied to rock-forming and accessory minerals (clinopyroxene, plagioclase, biotite, apatite) of the Olan quartz-syenite consistently yield high T between 950 and 1150°C. In detail, clinopyroxene yields the highest T ($1100\pm 50^\circ\text{C}$), shortly followed by apatite ($1025\text{-}1070^\circ\text{C}$) and biotite ($1021\pm 50^\circ\text{C}$). Plagioclase then appears at slightly lower T ($1000\pm 50^\circ\text{C}$). Early crystallization of biotite and apatite together with clinopyroxene is further evidenced by petrographic relationships, in particular by inclusions of biotite in clinopyroxene and inclusions of apatite in biotite ([Figure 7.6](#)). Tem-

perature has not been constrained for K-feldspar, quartz and hornblende, but petrographic relationships on thin sections suggest they appeared later in the crystallization sequence. In particular, lack of fresh clinopyroxene in the hornblende-rich facies suggests development of hornblende at the expense of clinopyroxene during cooling. Then, actinolite and chlorite appeared in replacement of clinopyroxene and biotite respectively. This crystallization sequence is consistent with experimental results of Parat *et al.* (2010) on durbachites from the Bohemian massif, which indicate that mafic durbachites have a near-liquidus assemblage of olivine+augite+Ti-rich phlogopite+apatite+zircon, followed by K-feldspar and plagioclase at lower T. Olivine has not been observed but some relics are mentioned by Laurent (1992) in mafic lamprophyres of the Oisans–Pelvoux massif. According to Parat *et al.* (2010), amphibole (both hornblende and actinolite) did not crystallize directly from the melt. They rather result from sub-solidus reactions, which in the case of the Olan formations has been enhanced by intense solid-state deformation following magmatic crystallization.

Zircon saturation temperatures are significantly lower (806-828°C) than that obtained for other minerals. This temperature is consistent with Ti-in-zircon thermometry, which yields median T around 764-775°C assuming reduced TiO₂ activity ($a_{TiO_2}=0.7$). Thus, this lower T is not an artifact caused by an unrealistic melt composition (for instance, if the bulk rock composition used to approximate the melt composition is partly controlled by cumulative processes, *e.g.* Janoušek *et al.* (2019)). We therefore conclude that zircon appeared lately in the residual melt. The large spread of Ti-in-zircon T down to ca. 690°C suggests zircon growth occurred from the onset of Zr saturation in the melt (at ca. 800-830°C) to the last increment of melt crystallization close to the solidus.

Pressure estimates obtained by clinopyroxene-liquid barometry are subject to large uncertainty, mainly due to the strong dependence in T of the barometric equations. Overall, barometric estimates yield P between 4 and 9 kbar, which is consistent with emplacement

of the Olan pluton in the middle to lower crust (15-32 km depth assuming purely lithostatic pressure with a crustal density of 2800 kg.m^{-3}).

7.8.1.2 Age of emplacement

High Th/U, HREE-enriched patterns, concentric oscillatory CL zoning and homogeneity in composition and texture of the zircon grains all point toward crystallization of zircon from a melt (Corfu *et al.*, 2003; Hoskin *et al.*, 2003). Lack of inherited grains is consistent with thermometric estimates, which indicate the near-liquidus T of the melt exceeded by far the Zr saturation threshold, which resulted in complete dissolution of inherited grains. Hence, the two U–Pb ages obtained on samples JB-19-30 and JB-19-58 (respectively 328 ± 3 Ma and 323 ± 3 Ma) are interpreted to date crystallization of zircon from the residual melt below 830-800°C.

Cross-cutting relationships between deformed / undeformed domains within the Olan pluton indicate that the magmatic history is more complex than one single intrusion event. The Olan pluton was rather formed by accumulation of multiple batches of magma emplaced syn-tectonically in the lower crust. The two zircon U-Pb ages obtained on samples collected in different domains of the Olan intrusion barely overlap considering a 95% threshold for the confidence interval on the weighted mean ages. This suggests that the two samples date the emplacement of two different batches of magma of slightly different age. However, resolving precisely the internal magmatic history of the pluton goes beyond the analytical limits of LA-ICPMS dating, and would require more precise ID-TIMS data. Overall, we consider the Olan pluton emplaced over the time interval 328–323 Ma.

7.8.1.3 Tectonic setting of emplacement

Because of its short emplacement time and its clearly syn-tectonic nature, the Olan pluton is a good tectonic marker. Intense solid state deformation in the pluton is correlated with the metamorphic foliation S2h observed in the inner zone of Oisans–Pelvoux. This foliation is interpreted to have formed by N–S directed horizontal flow of the migmatitic lower crust during regional transpression D2 (Chapter 4), which followed a nappe-stacking phase D1 associated with crustal thickening. Therefore, this horizontal flow was already active at ca. 328 Ma when the Olan pluton started to emplace. Timing of HP metamorphism resulting from crustal thickening has been constrained around 340–330 Ma in the Oisans–Pelvoux massif (Chapter 4 and Fréville *et al.* (2022)) and throughout the ECM (Jacob *et al.*, 2021a; Vanardois *et al.*, 2021; Rubatto *et al.*, 2010). Therefore, a transition probably occurred around 330 Ma, from nappe stacking and crustal thickening to horizontal flow of partially molten material in the lower crust.

An interesting link can be made with the P-T-t evolution of the surrounding metamorphic units. These units contain rarely preserved bodies of mafic HP granulites (Figure 7.2), which recorded exhumation from HP conditions (1.5-1.7 GPa and 650-730°C) to a MP-HT stage at 0.6-0.9 GPa and 800-870°C, followed by subsequent exhumation and cooling in the amphibolite-facies (690-450°C. This decompressional evolution has been poorly dated between ca. 337 and 294 Ma based on scattering U-Pb dates of metamorphic zircon rims. P estimated for the MP-HT stage is in good agreement with barometric estimates in the Olan quartz-syenites (Figure 7.12). Therefore, it is probable that this MP-HT stage in the granulites was concomitant with the emplacement of the Olan intrusion in the middle/lower crust, meaning that a significant part of exhumation of the deeper crustal units (from ca. 1.6 to < 0.9 GPa) occurred before ca. 328–323 Ma.

7.8.2 A petrogenetic model for the durbachites in the ECM

7.8.2.1 Crust vs Mantle sources

The high T of emplacement of the durbachites ($>1000^{\circ}\text{C}$), the elevated content in compatible transition metals (Cr, Ni), and the high proportion of mafic to intermediate components clearly indicate that the parental melts derived from a mantle source. Two types of processes may thus be proposed to explain the elevated content in incompatible crustal elements (LILE, U, Th, LREE) and the “crustal” isotopic Sr–Nd signatures : (i) fractionation of a basaltic parental melt poor in incompatible elements, combined with assimilation of crustal lithologies, following an assimilation-fractional crystallization model ((AFC, [DePaolo, 1981](#)); (ii) melting of a mantle source already enriched in incompatible elements and presenting a “crustal” (radiogenic Sr, unradiogenic Nd) isotopic signature.

The surrounding granitoids and migmatites, which we consider as representative of the bulk ECM crust, display lower incompatible element content than the durbachites. In addition, the enrichment in incompatible elements in the durbachites is not correlated with the degree of differentiation, as it would be expected with an AFC model. Similar observations are made for the Sr–Nd isotopes, in particular with Sr, which is consistently more radiogenic in the durbachites than in the surrounding granitoids and migmatites. We therefore discard the AFC scenario to explain the crust-like characteristics of the durbachites, following the same conclusion as [Couzinié *et al.* \(2016\)](#) for similar rocks of the French Massif Central.

Furthermore, the presence of enclaves of metasomatized peridotite embedded in migmatites in the Oisans–Pelvoux massif (Chapter 6) makes a very strong argument for the second scenario. These metasomatized peridotites present negative $\epsilon\text{Nd}_{(t)}$, and their trace element patterns are similar to that of the durbachites but shifted toward lower values. The trace element pattern of a highly-metasomatized phlogopite-bearing peridotite is shown on [Figure 7.9](#) for comparison. This sample is interpreted as a portion of subcontinental mantle

that was percolated by the durbachitic melts, which imprinted their signature to the peridotite (Chapter 6). In detail, the peridotite enclaves display important variation in composition and $\epsilon\text{Nd}_{(330)}$, reflecting heterogeneity of the Variscan mantle.

Despite the clear mantle origin of the durbachites, the presence of intermediate to felsic components marks subsequent evolution of the magmas in the crust, resulting either from fractional crystallization or mixing/assimilation processes. The clear cumulative nature of some mafic enclaves (e.g. JB-19-36) is an evidence that fractional crystallization has occurred. Furthermore, the trends defined by the whole durbachite dataset on Harker diagrams are consistent with fractional crystallization trends obtained experimentally by Parat *et al.* (2010) for mafic durbachites and minettes. In particular, the curvature observed on Al_2O_3 – SiO_2 and MgO – SiO_2 diagrams is typical (Figure 7.8).

However, mixing or assimilation of continental crust did certainly occur, in particular in the Olan quartz-syenites. The Olan samples display indeed a trend that departs from that of the bulk durbachites in ECM, and is almost orthogonal to it for Al_2O_3 . These trends fit well with a mixing line between the more mafic terms of the pluton and a felsic crustal component. Mixing/assimilation in the Olan samples is further evidenced by Nd isotopes. Variations in $\epsilon\text{Nd}_{(t)}$ are indeed observed, which are negatively correlated with the MgO content. These variations cannot result from fractional crystallization, because this process does not fractionate isotopes. They are therefore interpreted to reflect assimilation of a MgO-poor wall-rock component. The effect of pure mixing (*ie.*, without coupled fractional crystallization) between a mantle-derived parental melt and a crustal contaminant and the effect of fractional crystallization (MgO decrease at constant ϵNd) are shown in red on Figure 7.10. These trends are only indicative, as there is not a unique possibility for the composition of the parental melt and the crustal contaminant, considering the large spread in ϵNd of both mantle and crustal rocks. The most likely scenario probably involved coupled assimilation and fractional crystallization (AFC). In any case, the Olan quartz-syenites

likely derived from a primary melt presenting more radiogenic Sr (higher $^{87}\text{Sr}/^{86}\text{Sr}$) and less radiogenic Nd (lower ϵNd).

7.8.2.2 Mechanism of mantle enrichment and geodynamic implications

The trend defined by the durbachites on [Figure 7.10](#) is rather uncommon, as incorporation of crustal contaminant in the mantle-derived magma shifts its composition toward less “crustal” isotopic signature. This observation is in line with zircon data of [Schaltegger et Corfu \(1992\)](#) on durbachites from the Aar-Gothard massif, which present negative $\epsilon\text{Hf}(t)$ that are consistently lower than that of other Variscan granitoids of the massif.

This implies that the mantle source of the durbachites had a more “crustal” isotopic signature than that of the basement in which these magmas intruded, which is in agreement with strongly negative ϵNd_{330} in enclaves of metasomatized peridotite from the Oisans–Peloux massif ([Figure 7.10](#)). Negative $\epsilon\text{Nd}(t)$ and $\epsilon\text{Hf}(t)$ in the mantle source are unlikely to result from a long maturation period following an old (Precambrian) metasomatic contamination (by any material having low $^{176}\text{Lu}/^{177}\text{Hf}$ or $^{147}\text{Sm}/^{144}\text{Nd}$), because unradiogenic Nd–Hf signatures are not observed in older, Ordovician or even Devonian magmatic rocks ([Paquette et al., 1989](#); [Pin et Paquette, 1997](#)). Therefore, this metasomatism must have taken place shortly before the peak of durbachitic magmatism and necessarily implied contamination by material with strongly negative $\epsilon\text{Nd}/\text{Hf}$ and high $^{87}\text{Sr}/^{86}\text{Sr}$ (*ie.* mature continental material) to shift the mantle isotopic composition from positive to negative $\epsilon\text{Nd}/\text{Hf}$.

This continental material is arguably not derived from the ECM crustal basement, which presents relatively juvenile isotope signatures, and must be derived from more mature continental domains. Therefore, Mg–K magmatism in the ECM does not reflect the subduction of a local crustal domain, but rather contamination of the mantle below the ECM by exotic crustal material derived from the subduction of more distant crustal units. This material

may have contained portions of (Neo)-proterozoic crust, which is absent in the ECM but forms part of the Saxo-Thuringian and Armorican domains located further north (?). Hence, the situation in the ECM may be analogue to the Moldanubian zone of the Bohemian Massif, where such crustal reamination processes have been documented and are considered to be at the origin of syn/pos-collisional ultrapotassic magmatism (Janoušek et Holub, 2007; Schulmann *et al.*, 2014).

7.9 Conclusion

The durbachites provide interesting insight in the Variscan geodynamic evolution of the ECM. In the Oisans–Pelvoux massif, the Olan quartz-syenites represent a hot, mantle-derived magmatic intrusion emplaced in the middle to lower crust (4-9 kbar) during a period of ductile horizontal flow, following crustal thickening by underthrusting of crustal nappes. Emplacement of the intrusion is constrained between 328 and 323 Ma, and indicates that lower crustal flow had begun before 328 Ma. The geochemical and isotopic composition of the durbachites reflect derivation from a metasomatized mantle source, although they have been subsequently modified by fractionation and crustal assimilation processes. A clear link is established between the durbachite intrusions and metasomatized peridotite enclaves discovered in the Oisans–Pelvoux massif, which present striking similarities in trace element and Nd isotopic composition. The latter presumably represent portions of mantle percolated by the ultrapotassic durbachitic melts, which derived from a deeper and hotter mantle source. The unradiogenic Nd and highly radiogenic Sr signature of the durbachites imply that the mantle source was contaminated by exotic, mature continental material characterized by strongly negative ϵNd and high $^{87}\text{Sr}/^{86}\text{Sr}$, which contrasts with the crustal basement exposed in the ECM. We suggest this material may be derived from the subduction of (Neo)proterozoic crust forming the Peri-Gondwanian blocks (Saxo-Thuringian, Armorican blocks) involved in the Variscan collision.

APPENDIX

1 – Determination of component activities in durbachitic melts

Activity of components SiO₂ and TiO₂ have been constrained along isobaric cooling profiles by thermodynamic calculations with PerpleX 6.9.0 (Connolly, 2009), using the TC-633 thermocalc database (Holland et Powell, 2011) and the universal melt model of Holland *et al.* (2018), which includes a TiO₂ end-member and applies to a wide range of melt compositions from basaltic to granitic. Calculations have been performed in the composition space NCKFMASHTO, using bulk composition of sample JB-19-30 in input and assuming a water content in the melt of 3 wt.%. The oxygen fugacity was set to the value of the Nickel-Nickel-Oxide (NNO) buffer, following experimental results obtained on durbachitic melts by Parat *et al.* (2010). PerpleX does not return directly activities of components but provides instead chemical potentials μ_i . Activity a_i of a component i can be obtained with an additional calculation step using the relation :

$$a_i = \exp\left(\frac{\mu_{i(P,T)} - \mu_{i(P,T)}^*}{R.T}\right) \quad (7.1)$$

where $\mu_{i(P,T)}^*$ and $\mu_{i(P,T)}$ are the chemical potentials of respectively pure component i and component i in the system at given P and T, and R the gas constant.

The modeled crystallization sequence is reported on Figure 7.13 for P = 6 kbar. a_{SiO_2} and a_{TiO_2} are reported along the same cooling profile at 6, 8 and 10 kbar to show the effect of pressure on activities. This modeled crystallization sequence should however be taken with caution, first because the validity of the melt model of Holland *et al.* (2018) has not been tested for peculiar, alkalic compositions such as that of the durbachites, and second because this modeling implicitly assumes an oversimplified, batch crystallization scenario, which completely overlooks complexity related to fractionation and assimilation

processes. It however allows to investigate the effect of crystallization of a given mineral on component activities. Liquidus T is predicted around 1050°C, which is slightly lower than our estimations based on Cpx thermometry but reasonable considering all the simplifications made in this model. The modeled crystallization sequence is $\text{Opx} + \text{Pl} \rightarrow \text{Cpx} \rightarrow \text{Bt} \rightarrow \text{Qtz} \rightarrow \text{Kfs}$, with no Ol predicted, which does not perfectly agree with experimental results of Parat *et al.* (2010). Amphibole is not predicted in the crystallization sequence, which is in line with results of Parat *et al.* (2010) and petrographic observations suggesting it is a secondary phase formed after Cpx below the solidus. Ilmenite is the main Ti-bearing accessory phase, which is replaced by titanite during cooling.

As long as T remains above the liquidus, both a_{SiO_2} and a_{TiO_2} increase with decreasing T. SiO_2 becomes saturated around ca. 810-850°C for P between 6 and 10 kbar. This temperature is higher than T_{zrc} (800-806°C), and therefore SiO_2 is considered to be saturated at the onset of zircon crystallization ($a_{\text{SiO}_2}=1$). TiO_2 may shortly reach saturation at high P (> 8kbar) and crystallize as rutile, but significant drop in a_{TiO_2} (down to ca. 0.8) is observed when ilmenite starts crystallizing. An even larger drop in a_{TiO_2} down to ca. 0.4-0.6 to is associated with crystallization of biotite due to substantial incorporation of TiO_2 in this phase. Then, a_{TiO_2} increases, and drops again when titanite appears.

The real evolution of a_{TiO_2} during crystallization may be different, because the modeled sequence is different from that observed in the samples, but the effect of ilmenite, titanite and biotite crystallization are expected to be the same. At 6 kbar, a_{TiO_2} evolves between 0.6 and 0.8 during most of the cooling path, with lower extreme around 0.3 and higher extreme around 0.9. Therefore, assuming mean $a_{\text{SiO}_2} = 0.7$ during crystallization is expected to provide realistic TiZ T estimates.

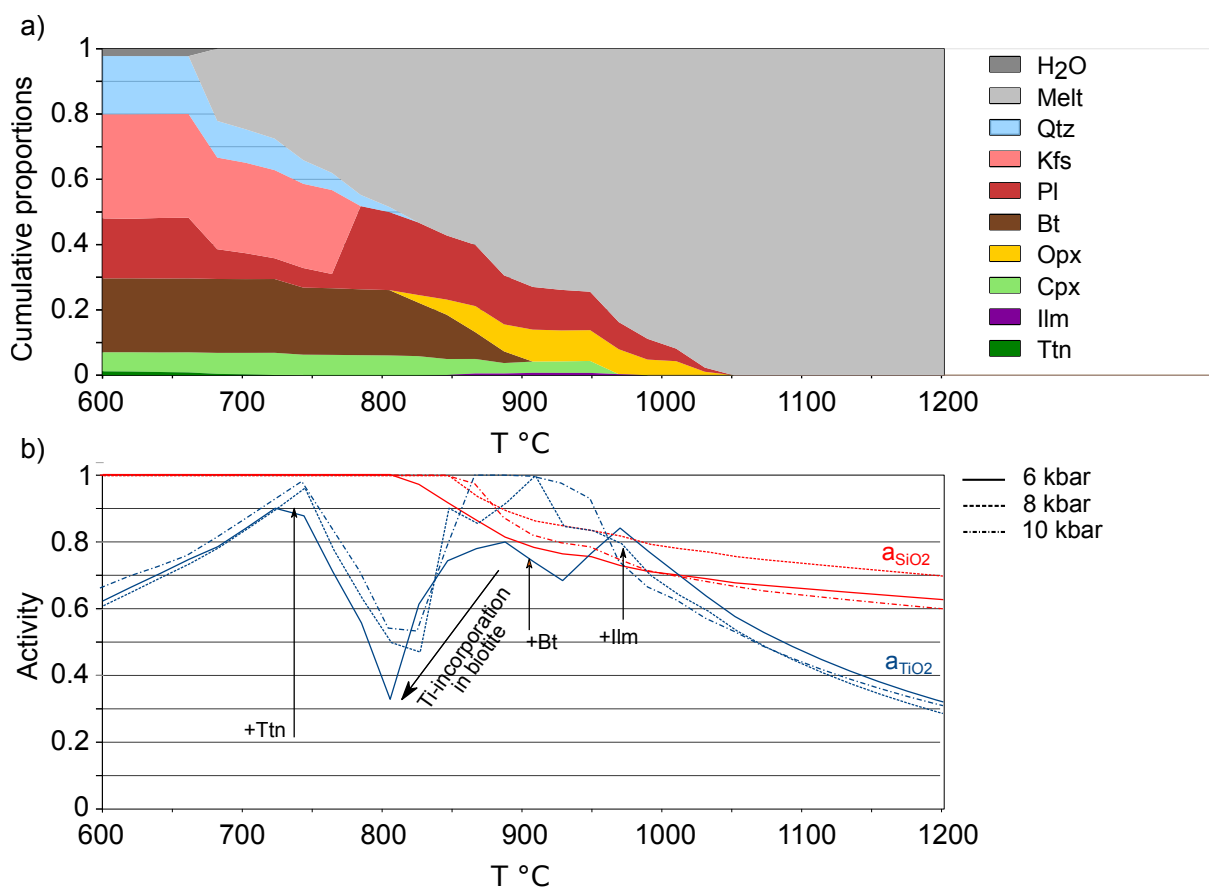


FIGURE 7.13 – Crystallization sequence (a) and component activities (b) modeled with PerpleX during batch crystallization of an ultrapotassic melt, using the melt model of Holland *et al.* (2018). The model assumes batch crystallization, and does not take into account fractionation and assimilation effects.

2 – Operating conditions for zircon U-Pb dating

Laboratory & Sample Preparation	
Laboratory name	GeOHeLiS Analytical Platform, OSUR, Univ Rennes 1, France
Sample type/mineral	Zircon
Sample preparation	1 zircon mount
Imaging	Cathodoluminescence, Tescan Vega 3 SEM (ISTerre, Grenoble)
Laser ablation system	
Make, Model & type	ESI NWR193UC, Excimer
Ablation cell	ESI NWR TwoVol2
Laser wavelength	193 nm
Pulse width	<5 ns
Fluence	6.2 J/cm ²
Repetition rate	3Hz
Spot size	25 μm
Sampling mode / pattern	Single spot
Carrier gas	100% He, Ar make-up gas and N ₂ (3 ml/min) combined using in-house smoothing device
Background collection	20 seconds
Ablation duration	60 seconds
Wash-out delay	15 seconds
Cell carrier gas flow (He)	0.76 l/min
ICP-MS Instrument	
Make, Model & type	Agilent 7700x, Q-ICP-MS
Sample introduction	Via conventional tubing
RF power	1350W
Sampler, skimmer cones	Ni
Extraction lenses	X type
Make-up gas flow (Ar)	0.75 l/min
Detection system	Single collector secondary electron multiplier
Data acquisition protocol	Time-resolved analysis
Scanning mode	Peak hopping, one point per peak
Detector mode	Pulse counting, dead time correction applied, and analog mode when signal intensity >~10 ⁶ cps
Masses measured	204(Hg + Pb), 206Pb, 207Pb, 208Pb, 232Th, 238U
Integration time per peak	10-30 ms (207Pb)
Sensitivity / Efficiency	23000 cps/ppm Pb (50m, 10Hz)
Data Processing	
Gas blank	20 seconds on-peak
Calibration strategy	GJ1 zircon standard used as primary reference material, Plešovice used as secondary reference material (quality control)
Common-Pb correction, composition and uncertainty	No common-Pb correction.
Reference Material info	GJ1 (Jackson et al., 2004), Plešovice (Slama et al., 2008)
Data processing package	Iolite (Paton et al., 2010)
Uncertainty level and propagation	Ages are quoted at 2 sigma absolute, propagation is by quadratic addition according to Horstwood et al. (2016). Reproducibility and age uncertainty of reference material are propagated.
Quality control / Validation	Plešovice : concordia age = 335.5 ± 2.8 Ma (N=15; MSWD=1.5)

TABLE 7.6 – Analytical conditions and procedures for zircon U-Pb dating

CHAPITRE 8

Discussion Générale

Présentée dans l'introduction, la place des MCE au sein de la chaîne varisque est controversée. Les résultats obtenus au cours de ce travail de thèse et leur comparaison avec les travaux existant apportent de nouvelles contraintes sur l'évolution varisque dans les Alpes externes occidentales. Ce chapitre vise à replacer ces résultats dans un cadre géodynamique plus général, et proposer un modèle géodynamique varisque intégrant les MCE. Une première partie présente une synthèse des données existantes sur l'évolution varisque des MCE, incluant les résultats de ce travail de thèse ainsi que d'autres travaux antérieurs ou réalisés conjointement dans le cadre du programme RGF Alpes (thèse de Jonas Vanardois dans les Aiguilles-Rouges). Ces résultats sont utilisés dans un second temps pour proposer un modèle d'évolution géodynamique varisque pour les MCE. Enfin, une troisième partie est dédiée aux corrélations avec les autres domaines varisques en Europe (Massif Central, Vosges-Forêt-Noire et massif de Bohême en particulier), en vue de proposer une reconstitution géodynamique de ce segment de la chaîne varisque intégrant les MCE.

Sommaire

8.1 Synthèse des données pétrologiques, géochronologiques et structurales	292
8.1.1 Enregistrement des roches métamorphiques de haute pression dans les MCE	292
8.1.2 Les péridotites orogéniques des MCE	294
8.1.3 Âge et nature du magmatisme varisque	296
8.2 Évolution géodynamique varisque dans les MCE	300
8.2.1 Signification géodynamique de la haute pression dans les MCE : subduction ou collision ?	300
8.2.2 Y a-t-il une suture océanique dans les MCE ?	303
8.2.3 Phases post-collisionnelles et exhumation des unités de HP dans les MCE	305
8.2.4 Magmatisme mantellique et évolution de la composition du manteau	307
8.3 Place des MCE dans les système varisque	310
8.3.1 Domaine varisque occidental vs oriental	310
8.3.2 Place des MCE : une portion du domaine varisque oriental décalée par la tectonique décrochante tardi-varisque	314
8.3.3 Redéfinition de la branche sud-est varisque	317

8.1 Synthèse des données pétrologiques, géochronologiques et structurales

8.1.1 Enregistrement des roches métamorphiques de haute pression dans les MCE

Les reliques d'éclogites et de granulites HP affleurent sous forme de lentilles de taille variable (métrique à hectométrique) au sein de larges bandes de cisaillement décrochantes, où elles sont parfois mélangées avec des roches de plus basse pression ([chapitre 3](#)). C'est en particulier les cas des éclogites rétro-morphosées des lacs de la Tempête dans le massif de Belledonne, mais aussi des éclogites des Aiguilles Rouges ([Vanardois et al., 2021](#)) ou de l'Argentera ([Ferrando et al., 2008](#); [Jouffray et al., 2020](#)). Les granulites HP du massif de l'Oisans-Pelvoux affleurent dans un autre contexte, et forment plutôt des lentilles hectométriques emballées dans des unités très migmatitiques de la croûte inférieure ([chapitre 4](#)).

Les protolithes mafiques des roches HP varisques des MCE présentent des signatures de type N/E-MORB, marquées par un enrichissement en éléments lithophiles de la croûte continentale (LILE, Th, U), et présentant des signatures isotopiques de manteau appauvri ($+5.9 < \epsilon Nd_i < +8.0$, [Paquette et al., 1989](#)). Les âges obtenus par datation U-Pb des cœurs hérités de zircons indiquent clairement une mise en place des protolithes des roches HP à l'Ordovicien (485-445 Ma, [chapitre 5](#)), lors du magmatisme associé à l'extension de la marge nord gondwanienne ([Von Raumer et Stampfli, 2008](#)).

Les estimations P-T du stade métamorphique HP varisque sont cohérentes sur l'ensemble des MCE. Elles indiquent un stade de HP estimé à 1.4-1.8 GPa et 650-750°C ([Ferrando et al., 2008](#); [Jouffray et al., 2020](#); [Vanardois et al., 2021](#), ce travail de thèse). En particulier, il n'y

8.1 Synthèse des données pétrologiques, géochronologiques et structurales

a pas de différence significative pour ce stade de HP entre les éclogites rétrotransformées du massif de Belledonne (>1.4 GPa, $690-740^{\circ}\text{C}$) et les granulites HP de l'Oisans ($1.5-1.7$ GPa, $650-730^{\circ}\text{C}$). Les granulites HP de l'Oisans enregistrent en outre un stade prograde précoce à $460-550^{\circ}\text{C}$ et $0.4-1.0$ GPa. On observe en revanche un contraste important lors de la décompression entre les granulites HP de l'Oisans et les éclogites rétrotransformées des massifs voisins. Alors que la plupart des éclogites enregistrent des chemins d'exhumation isothermes ou en refroidissement, les granulites HP de l'Oisans enregistrent un pic de température à $0.6-0.9$ GPa et $800-870^{\circ}\text{C}$, soit 100 à 200°C plus chaud que le pic de pression (Figure 8.1). Cette élévation de température pourrait résulter soit d'un réchauffement progressif lors de l'exhumation, soit d'un pic thermique bref après une première phase d'exhumation.

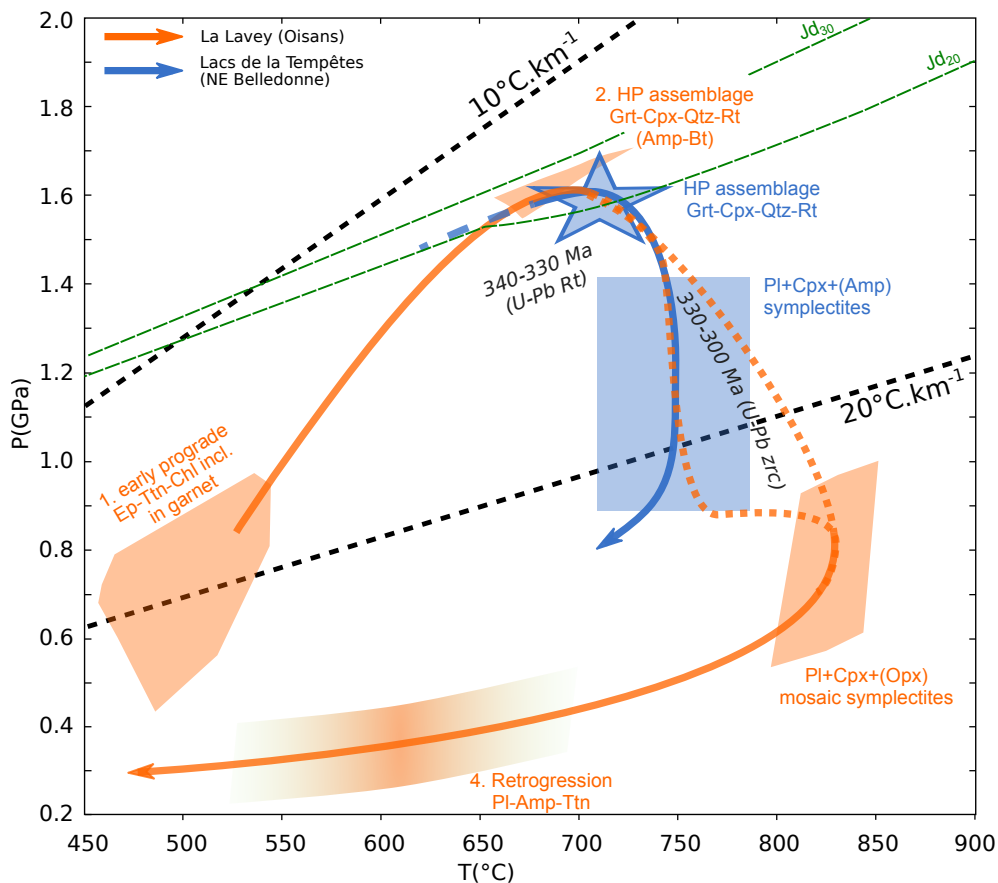


FIGURE 8.1 – Evolution P-T-t comparée des roches HP varisques dans les massifs de l'Oisans (orange) et de Belledonne (bleu), à partir des données des chapitres 3 et 4.

Les datations U-Pb sur zircon et rutile réalisées sur les éclogites et les granulites HP

pointent vers un âge du métamorphisme de HP entre 345 et 330 Ma dans les massifs de Belledonne et de l'Oisans-Pelvoux (chapitres 3 et 4). Ces âges sont identiques à ceux obtenus par Rubatto *et al.* (2010) en Argentera et par Vanardois *et al.* (2021) dans les Aiguilles Rouges. L'âge de l'exhumation est contraint entre \sim 330 et 300 Ma par les âges U-Pb sur zircon, mais ces données géochronologiques sont difficiles à interpréter en raison de leur importante dispersion. Les zircons métamorphiques enregistrent en effet une distribution d'âges très étalée avec un pic principal autour de 325-320 Ma, aussi bien pour les éclogites rétro-morphosées du massif de Belledonne que pour les granulites HP de l'Oisans, et ce malgré des évolutions P-T très contrastées. La dispersion des âges U-Pb pourrait résulter d'une croissance étalée du zircon sur une longue période, de manière continue ou par "pulses", ou bien de phénomènes de remplacement partiels à l'échelle nanométrique lié à des circulations fluides (*e.g.* Grand'Homme *et al.*, 2016), intervenant après une phase principale de croissance. Dans tous les cas, les phases tardives de l'exhumation dans les conditions du faciès schistes-verts / amphibolites se terminent vers 300 Ma, comme en atteste la présence de sédiments stéphaniens (\sim 305-300 Ma, Ballèvre *et al.*, 2018; Fernandez *et al.*, 2002) déposés en discordance sur les unités de HP. Par ailleurs, un âge U-Pb sur sphène à 298 ± 10 Ma a été obtenu par Vanardois *et al.* (2021) dans des éclogites rétro-morphosées du massif des Aiguilles Rouges, et date aussi le refroidissement tardif.

8.1.2 Les péridotites orogéniques des MCE

Les péridotites découvertes dans le cadre de ce travail de thèse affleurent sous forme d'enclaves décimétriques à métriques dans les unités de croûte inférieure migmatitique du massif de l'Oisans-Pelvoux. Elles présentent une diversité lithologique importante, incluant des lherzolites à grenat rétro-morphosées, des harzburgites à spinelle, à phlogopite-chromite ou bien des enclaves totalement serpentinisées (chapitre 6). On retrouve aussi des lentilles ultramafiques totalement serpentinisées au coeur des zones de cisaillement décrochantes dans

le massif des Aiguilles Rouges (Von Raumer et Bussy, 2004) et dans le massif de Belledonne (chapitre 6). Par ailleurs, des enclaves de péridotites similaires à celles découvertes en Oisans ont été observées dans les massifs de l'Aar et du Gothard (*comm. Pers.* Edwin Gnos, Muséum d'histoire naturelle de Genève).

Ces enclaves se retrouvent systématiquement dans les domaines structuraux profonds (ou au sein de bandes de cisaillement exhumant du matériel profond), et sont absentes des niveaux structuraux supérieurs. Elles présentent des caractéristiques géochimiques de manteau appauvri, refertilisé par un ou plusieurs épisodes métasomatiques mantelliques. Une part de ce métasomatisme est probablement liée à une contamination du manteau par du matériel d'origine continentale, enrichi en éléments lithophiles (LILE, LREE, Th, U), appauvri en HFSE (Nb,Ta,Ti), et présentant une signature isotopique "crustale" ($-8.12 < \epsilon Nd_i < +0.59$). Les données P-T acquises sur un échantillon de lherzolite à grenat indiquent une équilibration à ultra-haute pression (UHP) à 3.0 ± 0.5 GPa et $973 \pm 50^\circ\text{C}$, suivie d'une décompression à 0.8-1.4 GPa et $800-850^\circ\text{C}$, associée à la déstabilisation du grenat en kélyphites à Spl+Opx(+Cpx). Les conditions UHP sont bien supérieures à celles des éclogites et les granulites crustales. Aucun assemblage métamorphique de UHP (à coésite par exemple) n'a été décrit pour l'instant dans ces roches. Les enclaves de péridotites n'enregistrent donc pas le même pic de pression que les roches HP crustales, et représentent probablement d'anciennes portions de manteau lithosphérique sous-continentale incorporées tardivement dans la croûte. Les courones réactionelles autour du grenat marquent en revanche une rééquilibration dans la croûte inférieure, à des conditions P-T similaires à celles enregistrées par les granulites mafiques, ce qui suggère une incorporation dans la croûte inférieure lors des stades syn à post-collisionnels.

8.1.3 Âge et nature du magmatisme varisque

Une première phase magmatique précédant à la collision varisque a lieu dans les MCE entre le Dévonien supérieur et le Carbonifère inférieur (370-350 Ma). Elle se caractérise par le dépôt de séries volcano-sédimentaires et par un magmatisme bimodal d'affinité calco-alcaline faiblement potassique, probablement en contexte d'arrière-arc (Guillot et Ménot, 2009; Ménot, 1987a; Carme et Pin, 1987). On retrouve ces séries sur un large secteur sud-ouest du massif de Belledonne ainsi que dans la zone externe (corticale) du massif de l'Oisans-Pelvoux. Ce magmatisme est daté entre ~370 et 350 Ma (Fréville *et al.*, 2018; Guillot et Ménot, 2009; Ménot *et al.*, 1987). En particulier, un âge particulièrement jeune (352 ± 1 Ma) a été obtenu par Fréville *et al.* (2018) sur un sill de trondjémites dans les séries magmatiques bimodales du sud de Belledonne, qui montre que cette phase magmatique se poursuit jusqu'au Carbonifère inférieur. Un âge similaire a par d'ailleurs été obtenu sur des formations équivalentes dans le massif des Aiguilles Rouges (*comm. pers.* Jonas Vanardois). Ces séries ont par la suite été affectées par un métamorphisme barrovien lors de la collision, entre 340 et 330 Ma (Fréville *et al.*, 2018, 2022; Guillot et Menot, 1999).

Les séries magmatiques syn à post-collisionnelles se mettent en place entre le Viséen et le Permien inférieur. La compilation des données géochronologiques sur les granitoïdes de Belledonne, des Grandes Rousses et de l'Oisans-Pelvoux fait clairement apparaître deux pics principaux à 345-330 Ma et 310-295 Ma (Figure 8.2), même si certaines intrusions présentant des âges intermédiaires (granite du Bourg par exemple). Ces deux pics sont bien corrélés avec les âges métamorphiques dans ces domaines (chapitre 4), et reflètent donc deux pics thermiques dans la croûte au Carbonifère moyen (Viséen) et au Carbonifère supérieur – Permien inférieur. Ces granitoïdes sont accompagnés des roches Mg–K métalumineuses de la série des durbachites, qui se retrouvent fréquemment en enclave, notamment dans les granitoïdes viséens, ou forment des plutons distincts. En considérant que les enclaves de durbachites

sont contemporaines des granitoïdes dans lesquelles elles se trouvent, le magmatisme Mg–K débiterait vers 345 Ma dans les MCE. Il se prolonge au moins jusqu'à ~ 323 –328 Ma, âge de la mise en place du pluton de l'Olan ([chapitre 7](#)). Ensuite, ce magmatisme semble devenir plus sporadique mais se prolonge néanmoins, car des enclaves de durbachites sont retrouvées dans des granitoïdes stéphaniens comme celui de Roche-Noire (Grandes Rousses) ou le granite du Mont-Blanc ([Bussy, 1990](#); [Debon et Lemmet, 1999](#)). Le pic d'activité magmatique Mg-K dans les MCE se situe donc entre 345 et 323 Ma. Des datations supplémentaires des nombreuses enclaves mafiques dans les granitoïdes et des dykes de lamprophyres seraient néanmoins nécessaires pour préciser la distribution temporelle du magmatisme Mg-K dans les MCE.

La distribution des roches magmatiques syn/post-collisionnelles dans les MCE forme deux pôles distincts ([chapitre 7](#)); l'un composé des roches mafiques à intermédiaires (ultra)-potassiques de la série des durbachites; l'autre composé des granitoïdes subalcalins potassiques magnésiens ou ferro-magnésiens ([Debon et Lemmet, 1999](#)). Cette distribution bimodale reflète l'implication à la fois d'une source mantellique métagénérée, à l'origine des durbachites, et d'une source crustale liée à l'anatexie. Cette dichotomie se retrouve lorsque l'on compare les températures de mise en place de ces séries. Les estimations thermométriques réalisées sur les durbachites montrent clairement que ces roches dérivent de magmas chauds ($>1000^\circ\text{C}$), ce qui se traduit par une absence ou quasi absence de zircon hérités, puisque la saturation du magma en Zr est atteinte vers 800 – 850°C ([Figure 8.3](#)). En comparaison, les granitoïdes présentent des proportions de zircon hérités variables, marquant une dissolution incomplète et donc des températures inférieures au seuil de saturation du zircon. Ces températures de saturation varient entre 760 et 840°C , ce qui implique que la température maximale du magma granitique n'a pas pu être très supérieure à cette gamme de température. On observe néanmoins une différence entre les granitoïdes viséens et les granitoïdes tardi-carbonifères : ces derniers contiennent de manière générale une propor-

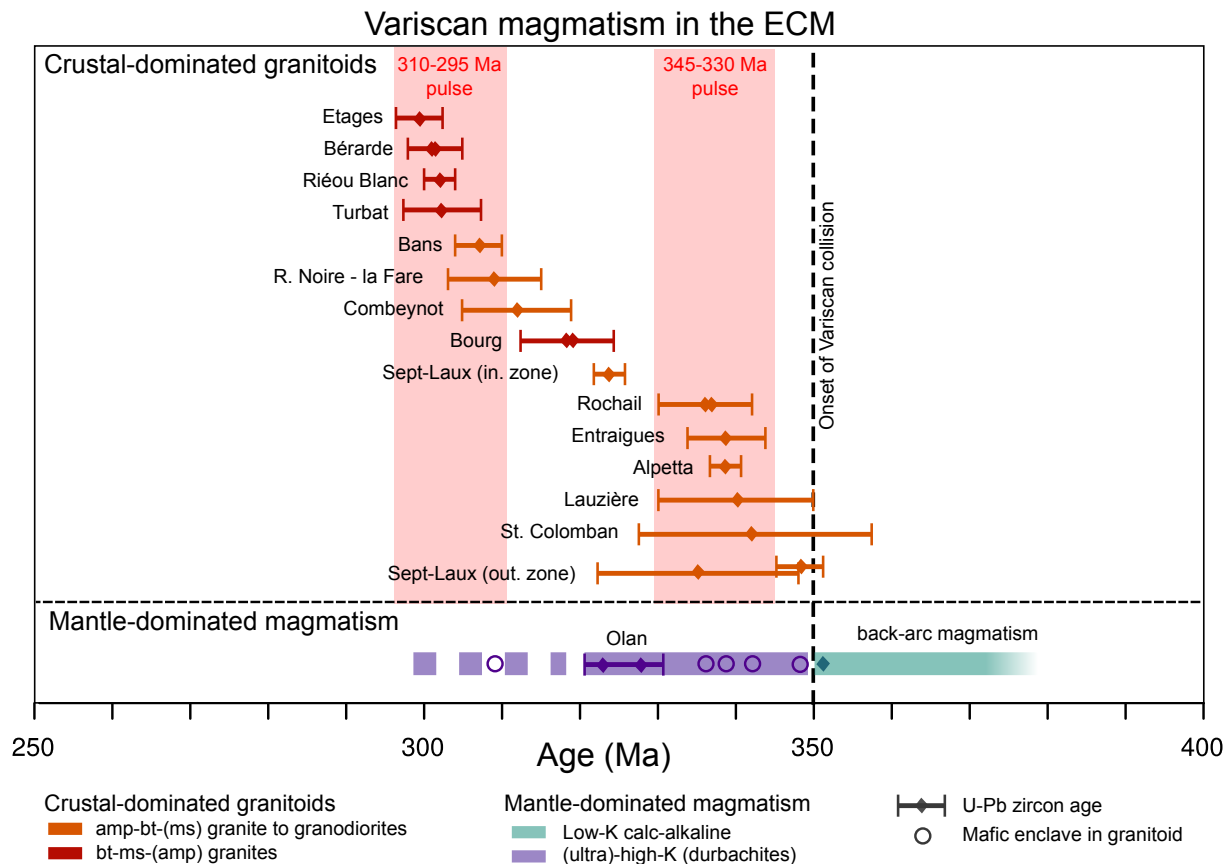


FIGURE 8.2 – Compilation des âges de mise en place des granitoïdes et autres roches magmatiques dans les MCE (Belledonne, Oisans-Pelvoux, Grande-Rousses). Les losanges indiquent les âges obtenus par datation U-Pb sur zircon, avec leur barre d'incertitude (intervalle de confiance à 95%). Pour la série (ultra)-potassique des durbachites, seul le pluton de l'Olan est daté avec précision. Les cercles violets indiquent les âges déduits de la présence d'enclaves de durbachites dans les granitoïdes, en supposant que ces enclaves aient le même âge que le granitoïde encaissant. Données issues de *Debon et al. (1998)*; *Fréville (2016)* et de ce travail de thèse.

tion plus faible de zircons hérités, pour des températures de saturation similaires à celles des granitoïdes viséens. Ceci semble donc marquer une mise en place de ces magmas à une température légèrement plus élevée que celle des granitoïdes viséens, lors du pic thermique tardi-carbonifère.

Ainsi, les durbachites dériveraient d'un magma primaire mantellique, alors que les granitoïdes seraient plutôt issus de la fusion crustale. Cependant, la composition des magmas primaires mantelliques ou crustaux a été plus ou moins fortement modifiée par des processus de mélange de magmas ou d'assimilation, et la plupart des roches magmatiques varisques

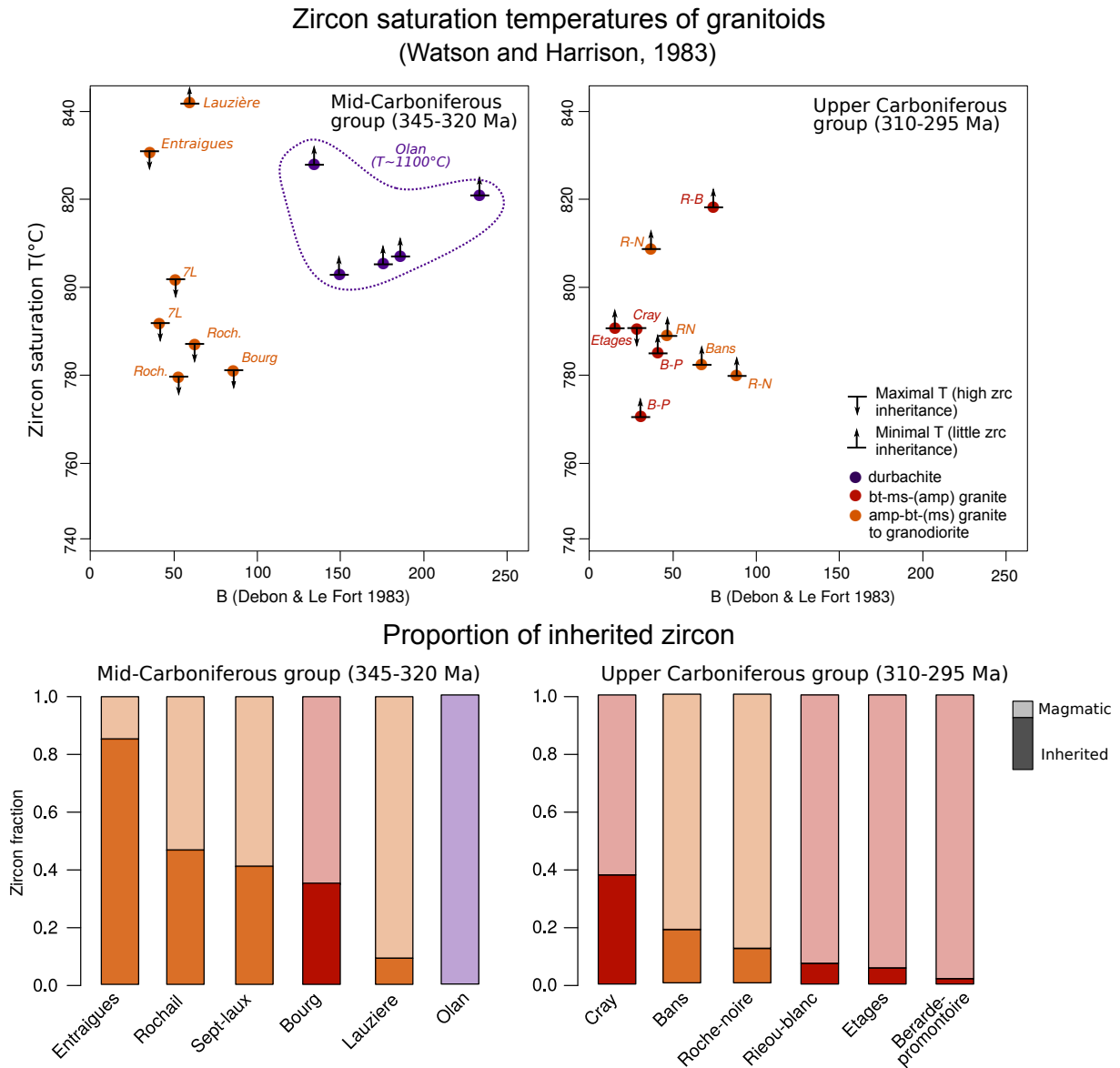


FIGURE 8.3 – Température de saturation et héritage des zircons dans les granitoïdes des MCE. La température de saturation du zircon est déduite de la relation de [Watson et Harrison \(1983\)](#), qui permet d'estimer la quantité de Zr pouvant être dissout dans le magma en fonction de sa composition et de sa température. La solubilité de Zr dans le magma étant une fonction croissante de T, plus T augmente, plus le magma peut incorporer de Zr. Lorsque la quantité de Zr pouvant être incorporée au magma dépasse la teneur en Zr de la roche, on atteint la température de saturation du zircon T_{zrc} , à laquelle tout le zircon devrait en théorie se retrouver dissout dans le magma. Une forte proportion de zircon hérité dans la roche indique donc une température maximale du magma inférieure à T_{zrc} (flèches vers le bas), alors que l'absence ou quasi absence de zircons hérités est indicateur de magmas de température supérieure à T_{zrc} (flèche vers le haut). On constate une différence significative entre les durbachites (Olan), ne préervant pas de zircons hérités malgré une T_{zrc} élevée ($>800^{\circ}\text{C}$), et les granitoïdes subalcalins potassiques, qui montrent parfois un héritage important malgré des températures de saturation généralement plus basses. La proportion plus faible de zircons érités dans les granitoïdes tardi-carbonifères semble marquer une mise en place des magmas à une température légèrement plus élevée que celle des granitoïdes viséens.

dans les MCE résultent de degrés d'hybridation divers entre source crustale et mantellique. Ces processus d'hybridation ont pu être mis en évidence dans les durbachites de l'Olan, où la différenciation du magma primaire mantellique semble avoir été contrôlée par des processus couplés d'assimilation et de cristallisation fractionnée (AFC). Dans les granitoïdes subcalcaïques potassiques, les formes et textures des enclaves mafiques marquent clairement des interactions chimiques avec le granite. Par ailleurs, [Banzet \(1987\)](#) et [Debon *et al.* \(1998\)](#) reportent des teneurs particulièrement élevées en Ba, Sr, Th, U et en terres rares légères dans les granitoïdes viséens (Sept-Laux, Saint Colomban, Lauzière, Rochail), ce qui semble marquer une contamination de ces derniers par des magmas (ultra)-potassiques, qui sont particulièrement riches en ces éléments. Enfin, les termes très peralumineux à grenat / cordiérite sont relativement rares dans les MCE, et se retrouvent essentiellement dans les domaines migmatitiques fortement mobilisés ou bien dans de petits plutons tardifs.

Les contributions relatives des sources crustales et mantelliques dans chaque série restent néanmoins difficiles à déterminer, en raison 1) de la forte hétérogénéité de la croûte et du manteau dont sont issus les magmas, et 2) des contrastes assez faibles de signature isotopique (Sr-Nd) entre les deux sources, lié au fait que le manteau a été contaminé par du matériel crustal et présente déjà des signatures isotopiques typiques de la croûte continentale.

8.2 Évolution géodynamique varisque dans les MCE

8.2.1 Signification géodynamique de la haute pression dans les MCE : subduction ou collision ?

Les éclogites et granulites HP varisques des MCE ont longtemps été interprétées comme des marqueurs de la subduction d'un bassin océanique ouvert lors du rifting cambro-ordovicien (*e.g.* [Fréville *et al.*, 2018](#); [Guillot et Ménot, 2009](#)). Cette interprétation repose : 1) sur l'étude

géochronologique réalisée par [Paquette *et al.* \(1989\)](#) sur les éclogites des MCE, qui indique que ces roches dérivent de protolithes de type MORB mis en place à l'Ordovicien (475-450 Ma), métamorphisés en conditions éclogitiques entre 425 et 395 Ma ; 2) sur la présence du complexe ophiolitique de Chamrousse, daté au Cambrien supérieur (~ 500 Ma) par [Ménot *et al.* \(1988\)](#) et [Pin et Carme \(1987\)](#).

Les données de ce travail de thèse invitent à revoir ce modèle. Premièrement, l'âge de la haute pression n'est pas Dévonien. Toutes les études récentes réalisées dans les MCE, incluant ce travail de thèse, convergent vers un âge viséen (345-330 Ma) pour la phase de HP, et aucun événement métamorphique antérieur à 350 Ma n'a pu être identifié dans les MCE. Cette gamme d'âge coïncide par ailleurs parfaitement avec les phases tectoniques compressives. En particulier, elle correspond à l'âge du métamorphisme barrovien enregistré dans le domaine sud-ouest du massif de Belledonne et dans la zone externe (corticale) du massif de l'Oisans-Pelvoux ([Fréville *et al.*, 2018, 2022](#)), qui marque l'enfouissement au sein d'un édifice de nappes des séries volcano-sédimentaires dévono-tournaisiennes. Ainsi, l'ensemble du cycle métamorphique enregistré par les roches de HP se déroule après la phase d'extension et le magmatisme dévono-tournaisien, et ne peut pas correspondre à une subduction dévonienne.

Deuxièmement, l'évolution prograde enregistrée par les éclogites et des granulites HP correspond à un régime thermique relativement chaud, avec un gradient géothermique apparent de 12 à 19°C.km⁻¹ lors du stade prograde précoce enregistré dans les granulites HP en Oisans (460-550°C et 0.4-1.0 GPa, [Figure 8.1](#)), et un gradient de l'ordre de 11 à 14°C.km⁻¹ pour le stade de HP dans les MCE (1.4-1.8 GPa et 650-750°C). Ce régime thermique est comparable avec les gradients thermiques les plus chauds enregistrés dans les contextes de subductions phanérozoïques ([Penniston-Dorland *et al.*, 2015](#)), et est incompatible avec les gradients froids (<10°C.km⁻¹) associés à la subduction de lithosphère océanique âgée ou

bien de subduction continentale rapide (Figure 8.4). Ce régime thermique est donc plutôt compatible avec un contexte de subduction chaude ou de collision continentale.

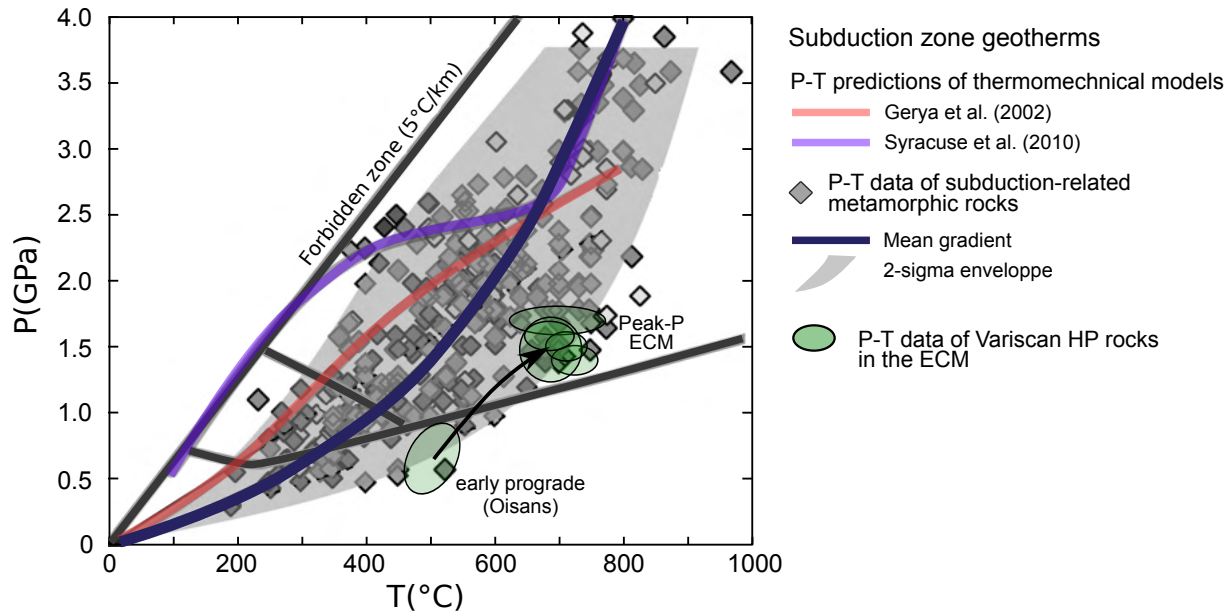


FIGURE 8.4 – Compilation d’estimations P-T de roches métamorphique exhumées en contexte de subduction (Penniston-Dorland *et al.*, 2015), comparée avec les éclogites et granulites HP varisques des MCE (en vert).

Enfin, ce régime thermique chaud lors de la phase de HP viséenne est en accord avec l’enregistrement magmatique dans les MCE. En effet, si l’on considère que la collision débute vers 350 Ma, les premiers granitoïdes seraient produits seulement ~ 5 Ma après l’initiation de la collision. En partant d’une lithosphère initiale présentant un profil thermique de domaine continental stable, et en considérant uniquement une source de chaleur radiogénique crustale, ce laps de temps est très insuffisant pour générer une fusion crustale importante (Moyen, 2019). Une source de chaleur additionnelle provient vraisemblablement de la mise en place des magmas ultra-potassiques, qui dérivent du manteau et sont significativement plus chauds ($\sim 1100^\circ\text{C}$) que la croûte encaissante. Ils sont par ailleurs étroitement associés aux granitoïdes, ce qui semble confirmer leur implication dans les processus de fusion crustale. Cependant, la quantité de magma crustal pouvant être généré grâce à la chaleur libérée par la cristallisation du magma mantellique est limitée par l’enthalpie des réactions

de fusion/cristallisation : un système dont la source de chaleur principale est l'advection de magmas mantelliques devrait être dominé par les termes mantelliques (Annen *et al.*, 2006), ce qui ne correspond pas à ce qui est observé dans les MCE, où le magmatisme viséen est dominé par les roches différenciées (granitoïdes) et présente peu de roches mafiques à intermédiaires. Le seul mécanisme restant pour expliquer ce magmatisme précoce est que l'épaississement a eu lieu dans une croûte continentale initialement chaude, dans laquelle il ne manquait qu'une quantité incrémentale de chaleur pour provoquer la fusion. Ceci qui s'accorde bien avec un contexte d'extension en arrière-arc précédant la collision, mais est en revanche incompatible avec la subduction d'une vieille marge passive froide.

Ainsi, le métamorphisme HP dans les MCE n'enregistre pas la subduction d'un vieil océan ouvert lors du rifting cambro-ordovicien, comme cela avait été initialement proposé par Guillot et Ménot (2009), mais correspond plutôt à une phase d'inversion tectonique du système arc-arrière-arc dévono-tournaisien, qui débute vers 350 Ma. Cette évolution est représentée sur les schémas 1 et 2 de la Figure 8.6. Nous proposons que l'ancien bassin dévono-tournaisien représente une zone de faiblesse mécanique dans la lithosphère, qui aurait permis de localiser la déformation dans ce domaine lors des phases tectoniques compressives viséennes. La lithosphère non amincie située en arrière du bassin agirait alors comme un backstop rigide lors de la compression (Figure 8.6-2). Au vu de la zonation métamorphique générale des MCE de Belledonne et de l'Oisans-Pelvoux, qui marquent un gradient du nord-ouest vers le sud-est, les unités de l'ancien bassin arrière-arc ont probablement été enfouies dans un système à vergence sud-est.

8.2.2 Y a-t-il une suture océanique dans les MCE ?

Les protolithes mafiques des roches HP présentent tous des âges ordoviciens (480-450 Ma), et forment des lentilles disséminées dans des unités felsiques du même âge (Bussy *et al.*,

2011), composées majoritairement de métasédiments et d'orthoigneiss (migmatitiques). Les unités HP enfouies lors de la fermeture du bassin d'arrière-arc sont donc d'anciennes unités continentales cambro-ordoviciennes de la marge nord du Gondwana, sur lesquelles se sont déposés les formations volcano-sédimentaires dévono-tournaisiennes du bassin d'arrière-arc, et ne marquent donc pas une zone de suture océanique. On notera par ailleurs que les roches HP associées aux zones de suture affleurent en générale en position structurale supérieure (Guillot *et al.*, 2008; Lardeaux *et al.*, 2006), ce qui n'est pas le cas des roches HP varisques des MCE. Aucune ophiolite d'âge dévoniens, qui pourrait marquer une éventuelle océanisation du bassin d'arrière-arc, n'a pour l'instant été décrite, et ce bassin est donc à priori continental (Guillot et Ménot, 2009).

Cependant, les MCE se caractérisent par la présence, en position structurale supérieure, du complexe ophiolitique de Chamrousse, qui correspond bien à une portion de lithosphère océanique ou de transition océan-continent obductée (Guillot et Ménot, 2009), et marquerait donc une suture. L'âge du magmatisme associé à l'océanisation est estimé à ~500 Ma (Pin et Carme, 1987; Ménot *et al.*, 1988), mais ces datations sont mises en doute par des observations récentes faites sur des zircons extraits de tonalites de ce complexe ophiolitique, et par la distribution des âges U-Pb sur zircons hérités dans le socle des MCE, qui ne montre aucun signal d'âge à 500 Ma (chapitre 5). De nouvelles datations sont nécessaires pour pouvoir proposer une interprétation géologique de ce complexe. Néanmoins, on peut formuler plusieurs hypothèses compte tenu du contexte varisque en Europe :

- Hypothèse n°1. L'ophiolite de Chamrousse est bien d'âge cambrien à ordovicien, et s'est formée lors de la phase d'extension affectant la marge nord du Gondwana. Elle correspondrait alors à un bassin océanique ouvert au Paléozoïque inférieur, obducté lors d'une phase précoce de la collision. Cependant, cette phase précoce n'est pas enregistrée dans les MCE, puisque le métamorphisme HP ne correspond pas à une subduction dévoniens. La corrélation avec les océans paléozoïques (Rhéique, Saxo-

Thuringien) situés plus au nord est par ailleurs difficile à établir, vu la position très méridionale des MCE dans le système varisque.

- Hypothèse n°2. L’ophiolite de Chamrousse est dévonienne. Cette hypothèse semble plausible, car un bon nombre d’ophiolites varisques ont un âge dévonien. En particulier, les ophiolites du rift de la Brévenne, au nord du Massif Central (Faure *et al.*, 2005) et la ligne des klippes au sud du massif des Vosges (Skrzypek *et al.*, 2012) pourraient alors correspondre à des équivalents latéraux du complexe de Chamrousse. Selon cette hypothèse, le complexe de Chamrousse aurait alors la même signification que les séries magmatiques dévono-tournaisiennes, et marquerait une phase d’océanisation du bassin d’arrière-arc.

8.2.3 Phases post-collisionnelles et exhumation des unités de HP dans les MCE

A partir de la fin du Viséen (330 Ma), la phase d’épaississement crustal et d’empilement de nappes laisse place à un contexte tectonique transpressif, marqué par le développement de la zone de cisaillement est-varisque, un grand système décrochant dextre traversant les MCE (Guillot *et al.*, 2009a; Jacob *et al.*, 2021a; Simonetti *et al.*, 2018, 2020). L’exhumation des unités de HP entre 330 et 300 Ma se fait dans ce contexte globalement décrochant. On observe un contraste important entre les granulites HP de l’Oisans, qui marquent un fort réchauffement lors de l’exhumation, et les éclogites rétromorphosées des massifs voisins (Belledonne et Aiguilles Rouges en particulier), qui sont exhumées de manière isotherme ou en refroidissement. Ceci implique des trajectoires d’exhumation différentes entre les deux domaines. Les chemins de décompression isothermes seraient associés à une exhumation relativement rapide des unités HP vers des niveaux crustaux supérieurs, alors que le chemin de décompression en réchauffement serait associé à une exhumation plus lente (Figure 8.6-3,4), enregistrant le réchauffement de la croûte inférieure. Ce réchauffement est lié en partie à

la maturation thermique de la croûte, mais pourrait aussi résulter d'épisodes tardifs de retrait / rupture de slab, entraînant une élévation du flux thermique basal lié à une remontée de matériel asthénosphérique chaud sous la croûte. Dans le second cas, le pic de température correspondrait alors à un échauffement rapide, intervenant après une première phase d'exhumation (trajet en pointillés sur la [Figure 8.1](#)).

Ces chemins contrastés sont en accord avec la position structurale des roches HP dans les différents massifs : les éclogites rétro-morphosées se retrouvent systématiquement dans des bandes cisailantes décrochantes qui correspondent aux domaines fortement déformés du cœur de la zone de cisaillement est-varisque (EVSZ), en association avec des séries migmatitiques. Nous proposons qu'elles aient été exhumées à la faveur de ces décrochements, par extrusion verticale de matériel crustal partiellement fondu en régime transpressif, au cœur de la zone de cisaillement ([Cao et Neubauer, 2016](#)). Les granulites HP de l'Oisans auraient été quant à elles exhumées plus tardivement au sein d'un dôme migmatitique formé en contexte décrochant ([Figure 8.6-4](#)), marquant une contribution plus importante des forces gravitaires lors des phases post-collisionnelles tardives (*e.g.* [Gerbault et al., 2018](#)). Cette phase tardive est associée à un second pic d'activité magmatique entre 310 et 295 Ma, qui pourrait résulter d'un épisode de délamination lithosphérique / retrait de slab lors du stade post-collisionnel, comme cela a pu être proposé dans différents segments de la chaîne varisque (*e.g.* [Laurent et al., 2017](#); [Vanderhaeghe et al., 2020](#); [Žák et al., 2014](#)). Ce type de contexte tectonique marqué par l'exhumation de domaines profonds en régime transpressif se retrouve dans les domaines périphériques de la chaîne varisque, en particulier dans les Maures-Taneron ([Gerbault et al., 2018](#)), dans les Pyrénées ([Cochelin et al., 2021](#)) ou en Montagne Noire ([Rabin et al., 2015](#)).

8.2.4 Magmatisme mantellique et évolution de la composition du manteau

Les magmas calco-alcalins faiblement potassiques mises en place en contexte d'arrière-arc (370-350 Ma) et les roches (ultra)-potassiques (durbachites) syn-collisionnelles (345-323 Ma) dérivent de magmas primaires mantelliques, et apportent donc des informations sur l'évolution de la composition du manteau varisque au cours du temps. Les roches de la série calco-alcalines présentent une signature caractéristique d'un manteau de type "arc" (Zheng, 2019), qui contraste fortement avec la signature des durbachites (Figure 8.5), qui dérivent d'une source fortement enrichie en éléments lithophiles (LILE, LREE, Th, U) et marquent l'incorporation de matériel dérivé de croûte continentale mature dans la source mantellique. La transition entre ces deux séries magmatiques s'opère rapidement entre 350 et 345 Ma, et reflète une évolution brusque de la composition de la source mantellique, qui passe en 5 Ma d'un manteau de type "arc" à du manteau métasomatisé par du matériel continental. Par ailleurs, la diversité de composition des enclaves de péridotites échantillonnées dans la croûte inférieure suggère une forte hétérogénéité du manteau, entre des domaines peu métasomatisés présentant une signature de manteau appauvri en LREE, et des domaines fortement métasomatisés riches en phlogopite, pargasite, et fortement enrichis en LILE, LREE, etc. Ceci souligne le caractère largement hétérogène du métasomatisme à l'origine de la source des magmas ultra-potassiques, susceptible de générer de fortes hétérogénéités de composition mantellique à l'échelle du km à la dizaine de km.

Le métasomatisme mantellique à l'origine du magmatisme (ultra)-potassique des MCE ne résulte donc pas d'une interaction prolongée et pervasive du manteau asthénosphérique avec des fluides/liquides silicatés issus d'une plaque en subduction. Il s'agirait plutôt d'un mécanisme brusque et chaotique, dans lequel du matériel continental (partiellement fondu) se retrouve incorporé au manteau source, qui fond ensuite rapidement pour former les magmas

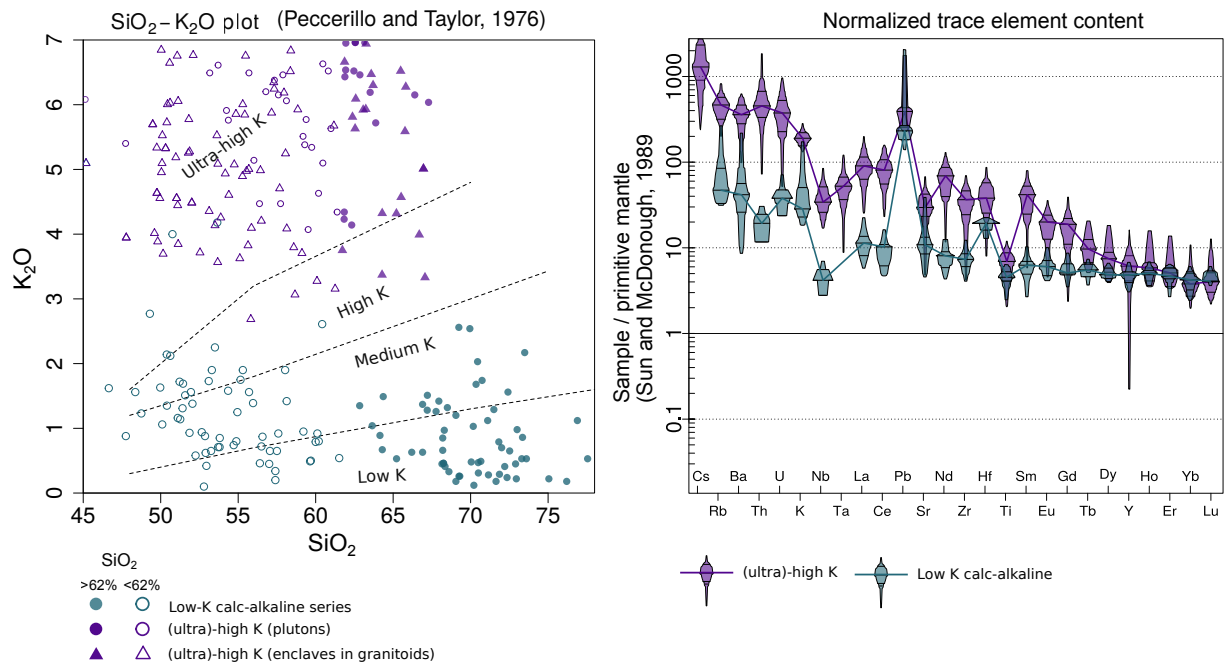
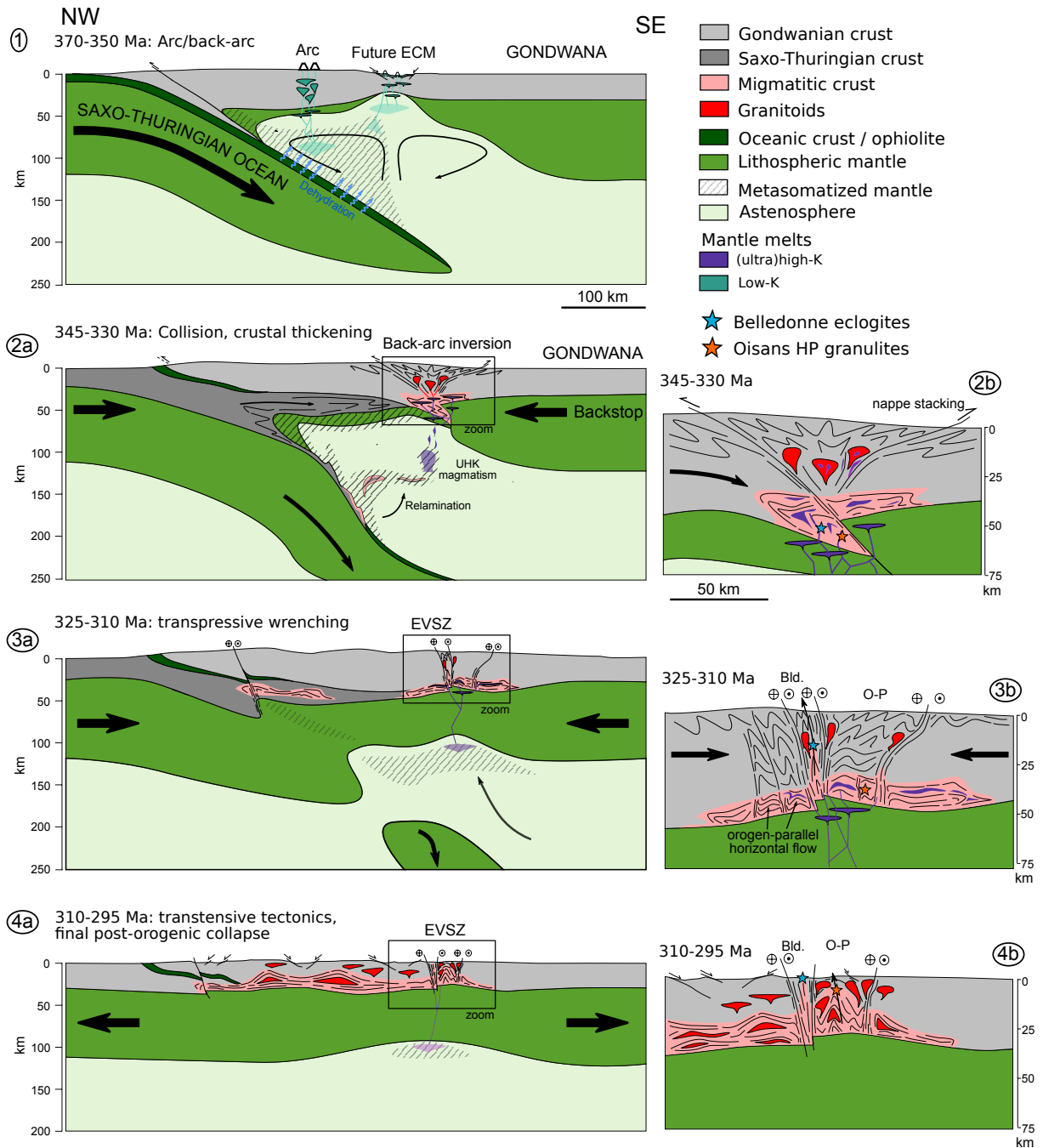


FIGURE 8.5 – Comparaison géochimique entre les durbachites syn/post-collisionnelles (violet) et la série calco-alkaline faiblement potassique formée en contexte d’arrière arc (vert-gris). On constate une différence de premier ordre entre ces deux séries, marquant une évolution de la composition de la source mantellique lors de la collision. Données issues de Ménot (1987b) pour la série la série calco-alkaline sodique. Voir chapitre 7 pour la séries des durbachites.

(ultra)-potassiques. Ce type d’interaction semble compatible avec des mécanismes de re-lamination lithosphérique (Maierová *et al.*, 2018, 2021), dans lesquels du matériel continental subduit peu dense remonte sous forme de diapir, et se mélange de façon chaotique avec les péridotites du coin mantellique, entraînant la formation de domaines très hétérogènes dans le manteau (Figure 8.6). Ces remontées diapiriques pourraient par ailleurs expliquer l’exhumation d’enclaves mantelliques équilibrées à ultra-haute pression (~ 3 GPa) et leur incorporation au sein de la croûte inférieure.

8.2 Évolution géodynamique varisque dans les MCE



Légende page suivante

FIGURE 8.6 – Schémas de synthèse et proposition d'un modèle de l'évolution géodynamique varisque dans les MCE. 1 – au Dévonien, les futurs MCE se situent sur la plaque supérieure (Gondwana), plusieurs centaines de km en amont de la zone de subduction saxo-thuringienne. Une phase d'extension affectant la plaque supérieure entraîne l'ouverture d'un bassin arrière-arc et un magmatisme calco-alcalin faiblement potassique, à l'origine des sérimes magmatiques bimodales et des séries volcano-sédimentaires du sud du massif de Belledonne. 2 – Au Viséen, la collision succédant à la fermeture de l'océan saxo-thuringien entraîne la fermeture du bassin arrière arc, qui forme une zone de faiblesse localisant la déformation compressive. Les unités crustales les plus profondes sont enfouies à >50 km de profondeur et sont métamorphisées en faciès éclogitique (2b). La subduction du bloc continental saxo-thuringien entraîne l'enfouissement de matériel continental dans le manteau, qui est alors enrichi en éléments lithophiles (LILE, LREE). Ce manteau métagénéré fond à son tour, et génère des magmas (ultra)-potassiques à l'origine des durbachites. Ce flux magmatique mantellique combiné à la chaleur résiduelle liée à l'extension arrière-arc entraîne une fusion crustale importante, à l'origine des granites viséens. Dans la croûte inférieure, la zone partiellement fondue s'étend et flue horizontalement. 3 – Mise en place des décrochements, et poursuite de la compression en contexte transpressif. Dans les MCE, cette période correspond au début du fonctionnement de la zone de cisaillement est-varisque (EVSZ), dans la quelle sont exhumées les éclogites de Belledonne. 4 – Effondrement post-collisionnel, associé à une fusion importante de la croûte inférieure dans tous les domaines de la chaîne. Dans les MCE, les mouvements décrochants se poursuivent, dans un régime qui évolue de la transpression à la transtension. Des unités migmatitiques profondes sont exhumées au sein de structures en dôme, formées par une combinaison de forces gravitaires (diapirisme) et tectoniques.

8.3 Place des MCE dans les système varisque

8.3.1 Domaine varisque occidental vs oriental

Les MCE enregistrent une succession de phases géodynamiques typique de l'orogénèse varisque en europe occidentale et centrale :

- une phase d'extension et de magmatisme en contexte d'arrière-arc au Dévonien supérieur – Tournaisien (370-350 Ma) ;
- une phase de collision au Viséen (350-330 Ma), marquée par l'enfouissement des séries volcano-sédimentaires dévono-tournaisiennes et des unités crustales du socle cambro-ordovicien sous-jacent ;
- une évolution vers un régime décrochant transpressif dextre au Carbonifère moyen (~ 330 -325 Ma). Ce régime se prolonge jusqu'au Carbonifère supérieur (~ 300 Ma) et est associé à l'exhumation d'unités crustales profondes partiellement éclogitisées, en particulier au sein des zones de cisaillement décrochantes.

Le magmatisme syn à post-collisionnel est lui aussi typique des domaines varisques. Il se caractérise par l'implication combinée d'une source crustale (anatexie) et d'une source mantellique métasomatisée, produisant des roches mafiques à intermédiaires (ultra)-potassiques (durbachites), associée à des granitoïdes subalcalins potassiques hybrides (type KCG, [Barbarin, 1999](#)). On note en revanche la rareté des granitoïdes très peralumineux (type MPG/CPG de [Barbarin, 1999](#)) dans les MCE. Cette évolution est au premier ordre assez similaire à celle des massifs voisins, en particulier du massif des Vosges–Forêt-Noire, de la Bohême et de la bordure Est du Massif Central ([Faure et al., 2009](#); [Lardeaux et al., 2014](#); [Schulmann et al., 2009](#); [Skrzypek et al., 2012](#)). Une étude comparative de ces domaines montre néanmoins des différences assez nettes entre les massifs situés à l'est (Vosges – Forêt-Noire, Bohême) et les massifs situés plus à l'ouest (Massif Central, Massif Armoricain), ce qui a conduit [Lardeaux et al. \(2014\)](#) à les séparer en un domaine varisque oriental et un domaine varisque occidental ([Figure 8.7](#)). Sur la carte varisque générale ([Figure 8.9](#)), ces domaines correspondent respectivement à l'*Eastern Variscan Domain* (EVD) et au *Central Variscan Domain* (CVD), le *Western Variscan Domain* (WVD) correspondant au bloc ibérique.

Le domaine oriental (EVD) s'inscrit globalement dans un système marqué par la subduction vers le sud du domaine océanique saxo-thuringien au cours du Dévonien ([Figure x](#)), associée à la formation d'un arc magmatique actif entre ~ 375 et 335 Ma sur la plaque supérieure ([Schulmann et al., 2009](#); [Žák et al., 2014](#)). La collision a lieu à partir de ~ 350 Ma, et succède à une phase de subduction continentale entre ~ 380 et 350 Ma ([Schulmann et al., 2009, 2014](#)).

Le domaine occidental (CVD) est quant à lui marqué par une évolution polycyclique. Une première phase *éo-varisque* a lieu au Dévonien, et est associée à la subduction vers le nord d'un petit domaine océanique médio-européen ([Faure et al., 2005](#)). Cette première phase est bien enregistrée par les données géochronologiques, et scellée par le dépôt de sé-

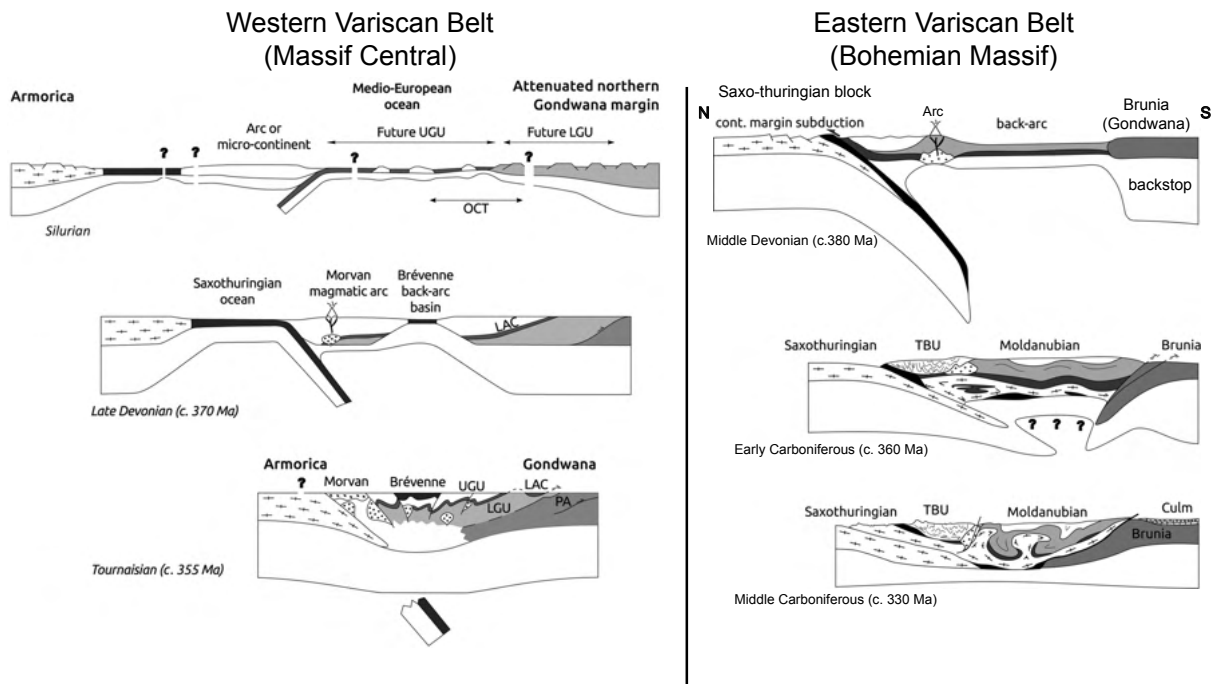


FIGURE 8.7 – Coupes synthétiques des modèles d'évolution géodynamique dans le domaine varisque occidental (Massif Central) et le domaine varisque oriental (Massif de Bohême), d'après [Lardeaux et al. \(2014\)](#). Voir détails dans le texte. UGU – Upper Gneiss Unit ; LGU – Lower Gneiss Unit ; LAC – Leptyno-Amphibolitic Complex ; PA – Para-autochtonous ; TBU – Teplà-Barrandian Unit

ries sédimentaires dévono-tournaisiennes en discordance sur les unités métamorphiques plus anciennes ([Faure et al., 2005, 2008](#)). Elle est suivie de la subduction vers le sud de l'océan saxo-thuringien, associée à la formation d'un arc magmatique de durée assez brève (370-360 Ma) au nord du massif (Morvan), et à l'ouverture du rift de la Brévenne en arrière-arc. La seconde phase collisionnelle a lieu à partir du Carbonifère (~ 360 Ma). Cependant, [Vanderhaeghe et al. \(2020\)](#) propose une évolution géodynamique différente : Après la fermeture du bassin médio-européen par subduction vers le nord, un retrait progressif de la plaque inférieure s'initie au sud de la Brévenne vers 370 Ma et se propage ensuite vers le sud, entraînant une propagation de la déformation, du métamorphisme et du magmatisme vers le sud tout au long du Carbonifère ([Figure 8.8](#)).

En ce qui concerne de magmatisme syn à post-collisionnel, le domaine varisque oriental se caractérise par l'abondance des termes (ultra)-potassiques mafiques à intermédiaires

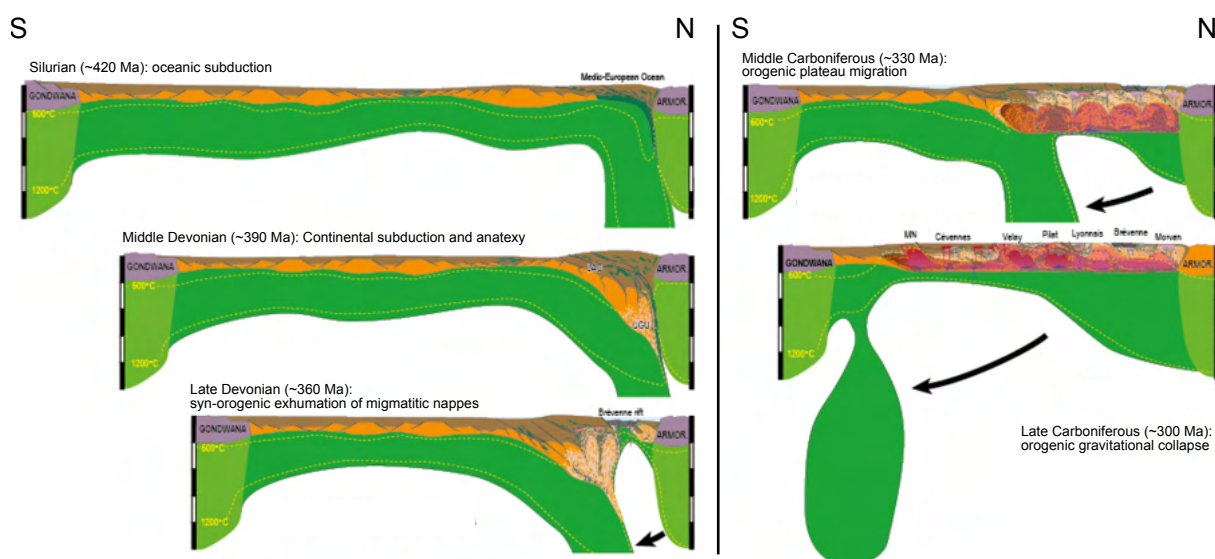


FIGURE 8.8 – Schéma géodynamique alternatif proposé par [Vanderhaeghe et al. \(2020\)](#) pour le domaine occidental (Massif Central), qui implique la subduction vers le nord du bassin médio-européen, suivie d'un retrait de la plaque inférieure vers le sud associé à la formation d'un plateau orogénique à partir du Carbonifère.

(durbachites) et des granitoïdes hybrides (KCG), qui se mettent en place principalement sur une courte période entre ~ 345 et 330 Ma, avec néanmoins quelques manifestations plus récentes jusque vers 320 Ma ([Janoušek et al., 2019](#); [Soder et Romer, 2018](#); [Tabaud et al., 2015](#); [Žák et al., 2014](#)). Les durbachites laissent ensuite place à des granitoïdes plus peralumineux, qui se mettent en place plus tardivement entre 329 et 322 Ma dans les Vosges ([Tabaud et al., 2015](#)) et entre ~ 330 et 300 Ma en Bohême ([Žák et al., 2014](#)). Dans le Massif Central, on observe en revanche une activité magmatique prolongée entre ~ 340 et 300 Ma qui se propage vers le sud, marquée par la mise en place simultanée des séries (ultra)-potassiques à dominante mantellique (durbachites) ou hybride (KCG), et des granites peralumineux (MPG,CPG) à cordiérite \pm grenat \pm muscovite plus franchement crustaux ([Laurent et al., 2017](#)).

8.3.2 Place des MCE : une portion du domaine varisque oriental décallée par la tectonique décrochante tardi-varisque

Les MCE présentent une évolution similaire à celle du domaine varisque oriental. Premièrement, il n'y a pas de phase éo-varisque dévonienne dans les MCE. L'ensemble des phases collisionnelles a lieu au Carbonifère et correspond à la fermeture du bassin d'arrière-arc dévono-tournaisien.

Ensuite, la collision est relativement jeune, avec un premier pic de métamorphisme barrovien vers 340-330 Ma. Ceci est aussi plutôt en accord avec l'enregistrement tectono-métamorphique des massifs des Vosges et de Bohême, où le pic de température associé au métamorphisme barrovien est daté vers 340 Ma (*e.g.* Skrzypek *et al.*, 2012; Štípská *et al.*, 2016). En comparaison, au niveau de la bordure nord-est du Massif Central, le pic métamorphique associé à la collision varisque *sensu-stricto* a plutôt lieu vers 350-360 Ma (Faure *et al.*, 2009; Vanderhaeghe *et al.*, 2020, et références associées).

Enfin, le magmatisme syn à post-collisionnel varisque dans les MCE est très similaire à celui des Vosges ou de la zone moldanubienne de Bohême, aussi bien en terme de composition des magmas que de chronologie de mise en place. Comme dans ces massifs, on retrouve dans les MCE une abondance des termes (ultra)-potassiques (durbachites, granitoïdes hybrides), qui se mettent en place essentiellement entre 340 et 323 Ma. La rareté des granites très peralumineux à cordiérite \pm grenat contraste en revanche avec le magmatisme de la bordure est du Massif Central, où ces magmas sont très abondants (Laurent *et al.*, 2017; Moyen *et al.*, 2017). En ce qui concerne l'âge du magmatisme, les deux pics d'activité magmatique enregistrés dans les MCE se retrouvent dans les Vosges et en Bohême, et contrastent avec le magmatisme prolongé de la bordure est du Massif Central, qui se propage vers le sud entre le Viséen et le Carbonifère supérieur. L'âge du premier pic viséen est très similaire dans les trois massifs (\sim 345-335 Ma), mais l'âge du second pic diffère un peu et est significativement

plus jeune dans les MCE (310-295 Ma) que dans les Vosges (329-332 Ma, [Tabaud et al., 2015](#)) et dans la zone moldanubienne de Bohême (\sim 330-310 Ma, [Žák et al., 2014](#)).

Ainsi, l'évolution tectono-métamorphique et magmatique des MCE s'inscrit assez nettement dans le système varisque oriental. Ceci peut paraître contre-intuitif étant donné leur proximité actuelle avec la bordure est du Massif Central, qui n'est séparée des MCE que d'une petite centaine de kilomètres. Il faut néanmoins tenir compte des importants mouvements décrochants tardi-varisques et de la collision alpine. Les MCE sont en effet traversés par la zone de cisaillement est-varisque (EVSZ), qui est une structure décrochante majeure à l'échelle de la chaîne ([Guillot et al., 2009a](#); [Simonetti et al., 2018, 2020](#)), et qui aurait pu décaler ces massifs vers le sud-ouest de plusieurs centaines de kilomètres entre la fin du Viséen et le Permien inférieur. Ainsi, les études tomographiques récentes réalisées sur l'arc alpin font apparaître une discontinuité nette à l'ouest des MCE, qui pourrait correspondre à la trace d'une ancienne discontinuité varisque majeure résultant de ces mouvements décrochants ([Nouibat et al., 2021](#)). Par ailleurs, la compression alpine a elle aussi entraîné un déplacement vers l'ouest de ces massifs, d'ampleur néanmoins plus limitée (\sim 28 à 66 km, [Bellahsen et al., 2014](#)).

Les MCE correspondent donc probablement à un ancien bassin d'arrière arc associé à la subduction vers le sud-est de l'océan saxo-thuringien. Ce bassin était initialement localisé dans le domaine varisque oriental, et été décalé vers le sud-ouest par la tectonique décrochante tardi-varisque. Ils seraient donc des équivalents latéraux de la zone moldanubienne de Bohême et sud du massif des Vosges ([Figure 8.9](#)), appartenant à la zone est-moldanubienne définie par [Lardeaux et al. \(2014\)](#). Cette position, plusieurs centaines de kilomètres en arrière du front de subduction saxo-thuringien, expliquerait le caractère assez tardif des phases tectono-métamorphiques et magmatiques associées à la collision varisque dans les MCE.

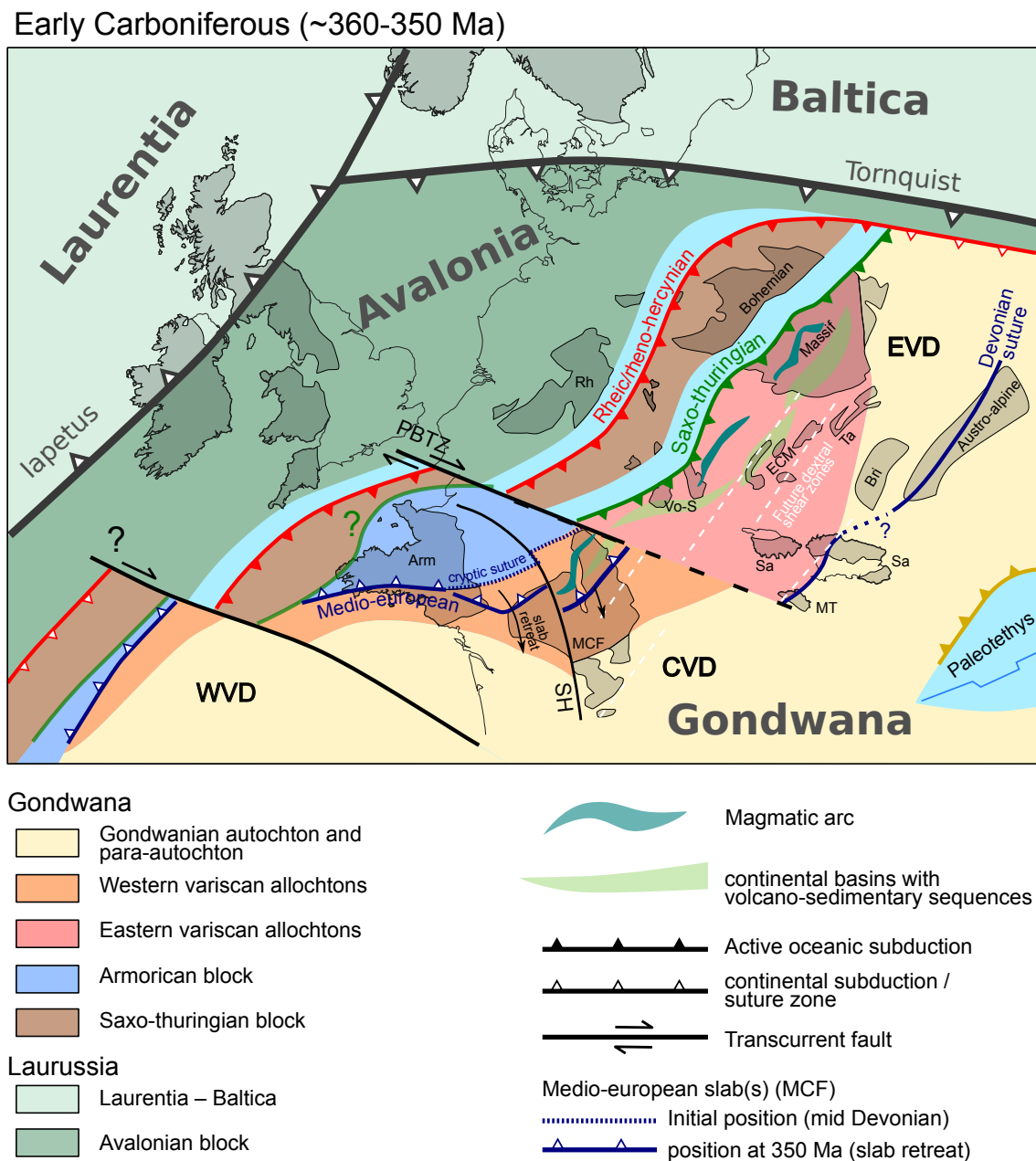


FIGURE 8.9 – Situation géodynamique de la chaîne varisque européenne au Carbonifère inférieur. Une distinction est faite entre le domaine est-varisque et le domaine central (MCF, Massif Armoricain). Le domaine oriental est marqué par la subduction vers le sud du domaine saxo-thuringien (Schulmann *et al.*, 2009), alors que le domaine central est marqué par la subduction vers le nord du domaine médio-européen, potentiellement suivie d'une phase de retrait de slab vers le sud (Vanderhaeghe *et al.*, 2020). EVD – East Variscan Domain ; CVD – Central Variscan Domain ; WVD – Western Variscan Domain ; PBTZ – Pays de Bray Transfert Zone ; SH – Sillon Houiller. La position du bloc Corso-Sarde est reprise de Edel *et al.* (2018). L'ouverture de la Paléotéthys au sud est reprise du modèle de Stampfli *et al.* (2013).

8.3.3 Redéfinition de la branche sud-est varisque

Plusieurs travaux regroupent les MCE et les autres éléments de socle alpin avec le massif des Maures-Tanneron et le bloc Corso-Sarde, qui forment ensemble la branche « sud-est varisque » (Corsini et Rolland, 2009). Cette corrélation repose essentiellement sur l'importance de la tectonique décrochante transpressive dans ces domaines, et plusieurs reconstructions corrélient l'EVSZ dans les MCE avec la faille de Joyeuse-Grimaud dans le massif des Maures-Tanneron et avec la zone de cisaillement de Posada-Asinara en Sardaigne (*e.g.* Carosi *et al.*, 2020; Corsini et Rolland, 2009; Guillot *et al.*, 2009a; Rossi *et al.*, 2009). Si la corrélation entre le bloc Corso-Sarde et le massif des Maures-Tanneron semble bien établie (*e.g.* Corsini et Rolland, 2009; Faure, 2014), la corrélation de ce bloc avec les domaines alpins est moins claire. Par ailleurs, la relation entre les MCE et les autres domaines de socle alpin de la marge européenne distale, du bloc Briançonnais et ceux dérivés de la microplaque apulienne (domaines sud-alpin et nappes austro-alpines) reste aussi à préciser.

Pour les Alpes en général, ce travail a été esquissé dans le [chapitre 2](#) et est présenté plus en détail dans Jacob *et al.* (2022). La comparaison des différents domaines de socle alpin montre des différences de premier ordre entre les domaines issus de la marge européenne (MCE et marge distale) d'une part, et les domaines issus de la plaque apulienne et le bloc Briançonnais d'autre part. Les domaines de la marge européenne enregistrent un métamorphisme de HP assez jeune (345-330 Ma) et de type HP-MT, un métamorphisme barrovien varisque de moyen à haut grade (faciès amphibolitique à granulitique) et un magmatisme d'âge principalement carbonifère, marqué en outre par l'importance de la série des durbachites (Von Raumer *et al.*, 2014).

Les autres domaines alpins enregistrent un métamorphisme de HP plus vieux (360-350 Ma, voire ~400 Ma pour le complexe de Speik dans les nappes austro-alpines, Faryad *et al.*, 2002; Thöni, 2006) et plus froid (type HP-BT). On peut d'ailleurs noter que les éclogites

de Speik enregistrent des conditions P-T relativement froides (700°C à 1.8-2.2 GPa, ce qui correspond à un gradient apparent de l'ordre de 9-10°C.km⁻¹) et font partie d'un complexe formé d'éclogites partiellement amphibolitisées emballées dans des serpentinites (Faryad *et al.*, 2002). Elles présentent donc toutes les caractéristiques d'éclogites exhumées dans un chenal de serpentinite au niveau d'une zone de subduction (Guillot *et al.*, 2009b), et marquent vraisemblablement une ancienne suture (éo)-varisque. Ces domaines sont en outre marqués par un métamorphisme barrovien varisque plus faible que dans les MCE (voire inexistant), et présentent un magmatisme varisque principalement d'âge permien (chapitre 2). Par ailleurs, plusieurs travaux récents montrent la présence de reliques de socle néoprotozoïque et d'un fort héritage paléoprotozoïque à archéen dans le domaine austro-alpin (Chang *et al.*, 2021; Neubauer *et al.*, 2020), qui semblerait se retrouver aussi en partie dans le domaine Briançonnais (*données non publiées*, Thiéblemont *et al.*). Ces domaines semblent donc correspondre à des portions plus externes de la chaîne varisque, présentant une forte affinité gondwanienne.

Ces caractéristiques se retrouvent dans le socle Corso-Sarde. On y retrouve en effet des reliques de socle néoprotozoïque (Faure, 2014; Rossi *et al.*, 2009). Le métamorphisme de HP varisque enregistre des gradients apparents légèrement plus froids que dans les MCE (de l'ordre de 10°C.km⁻¹, Cruciani *et al.*, 2012; Franceschelli *et al.*, 2007) et semble être plus ancien. En Sardaigne, un âge à 352±3 Ma sur des éclogites à disthène (Giacomini *et al.*, 2005) date l'exhumation dans le faciès amphibolique, et la haute pression est donc antérieure. Cet âge est cohérent avec les données de Faure (2014) en Corse, qui enregistre une phase principale d'épaississement vers 360 Ma. Un âge autour de 400-410 Ma a été suggéré pour la phase de HP (Cortesogno *et al.*, 2004; Franceschelli *et al.*, 2007), mais reste néanmoins incertain au vu de la méthode utilisée (datation de fractions multi-grains de zircon par ID-TIMS). Bien que l'on retrouve des granitoïdes viséens de composition similaire aux granitoïdes subalpins potassiques des MCE (granitoïdes U1, 345-340 Ma), l'essentiel du

magmatisme est représenté par les granitoïdes calco-alkalins tardi-carbonifères à permien (U2, 305-285 Ma), et un magmatisme alcalin tardif (U3, 290-260 Ma) se met en place au Permien (Rossi et Cocherie, 1991; Gattacceca *et al.*, 2004).

Ainsi, nous proposons de séparer cette branche sud-est varisque en deux domaines différents (Figure 8.9) :

- domaine *moldanubien*, formé des MCE et de la marge distale européenne, qui se situe en arrière du système de subduction saxo-thuringien dans le domaine varisque oriental (EVD);
- un domaine sud-varisque sensu-stricto, qui regroupe le bloc Maures-Tanneron – Corse – Sardaigne, le bloc Briançonnais et les unités dérivées de la plaque apulienne, et forme un ensemble d’affinité gondwanienne, affecté par un système de subduction différent du système saxo-thuringien. Les éclogites de ces domaines semblent marquer une zone de suture ancienne, qui pourrait être analogue à la suture éo-varisque dans le Massif Central.

Le collage final entre les domaines de la marge européenne, le domaine Briançonnais et les domaines apuliens (sud-alpin et austro-alpin) résulterait des migrations de blocs crustaux associées à l’ouverture et à la fermeture des océans Valaisan et Liguro-Piémontais au cours du Mésozoïque (Stampfli et Hochard, 2009; van Hinsbergen *et al.*, 2019).

Conclusions et perspectives

Le socle des Alpes Externes occidentales enregistre une succession d'événements tectono-métamorphiques et magmatiques associée à l'orogénèse varisque entre le Dévonien supérieur et le Permien inférieur. Cette succession d'événements correspond à l'ouverture d'un bassin d'arrière-arc au cours du Dévonien supérieur, puis à sa fermeture lors de la collision à partir du Carbonifère inférieur (350 Ma). A partir du Carbonifère moyen (~325 Ma), une tectonique décrochante se met en place, qui contrôle l'exhumation des unités crustales profondes contenant des reliques d'éclogites et de granulites HP, et est à l'origine de la structuration finale de ces massifs. L'enfouissement puis l'exhumation des reliques de HP a lieu au cours du Carbonifère (entre 350 et 300 Ma), avec un pic de pression probablement atteint entre 345 et 330 Ma. Ainsi, le métamorphisme de HP varisque dans les MCE n'est pas un marqueur d'un cycle de subduction ancien, mais correspond plutôt aux phases d'épaississement associées à l'inversion du bassin d'arrière-arc lors de la collision.

L'enregistrement magmatique marque un régime thermique assez chaud lors de la collision, qui est lié d'une part à l'héritage thermique de l'ancien bassin d'arrière-arc, et d'autre part à la présence d'un flux magmatique mantellique associé à la mise en place de séries (ultra)-potassiques (UHK) syn à post-collisionnelles. Ce magmatisme UHK dérive de la fusion partielle de manteau métasomaté par du matériel d'origine continental. Ce manteau métasomaté est par ailleurs échantillonné sous forme d'enclaves incorporées dans la croûte inférieure lors de la collision. Le métasomatisme du manteau par du matériel continental intervient de manière relativement rapide lors des phases précoces de la collision, et pourrait être le marqueur de phénomènes de relamination similaires à ceux décrits dans les massifs de Bohême et des Vosges.

Au vu des fortes similitudes entre l'évolution varisque des MCE et celle des massifs des Vosges-Forêt-Noire et de la Bohême, les MCE se rattacheraient à la branche varisque orien-

tale. Il correspondraient à un ancien domaine d'arrière-arc, initialement situé plusieurs centaines de kilomètres en arrière de la subduction saxo-thuringienne, dans la continuité du sud des Vosges et de la zone moldanubienne de Bohême. La position finale de ces massifs à proximité de la bordure est du Massif Central résulterait des importants mouvements associées à la tectonique décrochante tardi-varisque.

Plusieurs points mériteraient néanmoins une étude plus approfondie :

Premièrement, l'interprétation géodynamique du complexe ophiolitique de Chamrousse reste toujours à éclaircir, et de nouvelles données géochronologiques sont indispensables pour lever les incertitudes sur son origine.

Un second point concerne l'évolution temporelle du magmatisme mantellique, et en particulier l'âge et la durée de mise en place des durbachites dans les MCE. La datation des syénites quartziques de l'Olan à 323-328 Ma vient compléter les données existantes dans le massif de l'Aar-Gothard des Aiguilles Rouges, et apporte un nouveau point d'ancrage. Il reste cependant des incertitudes sur la durée totale de ce magmatisme dans les MCE, et son éventuelle prolongation au Carbonifère supérieur. Par ailleurs, la période 350-340 Ma est une période charnière, au cours de laquelle le flux magmatique mantellique passe de séries calco-alcalines sodiques d'arrière-arc aux séries UHK. Cette transition marque une profonde modification de la nature des sources mantelliques, et une étude géochronologique, géochimique et isotopique fine des magmas mis en place durant cet intervalle pourrait permettre de préciser les mécanismes associés à cette transition.

En parallèle, une étude plus poussée des enclaves de péridotites métasomatisées découvertes lors de ce travail de thèse pourrait permettre de préciser l'évolution du manteau et les différents flux métasomatiques associés au cycle orogénique varisque, et de les corrélés à l'évolution des magmas.

Enfin, un parallèle a été fait entre l'évolution varisque des MCE et celles des massifs des Vosges et de la Bohême. Ces massifs sont marqués par des phénomènes de relamination crustale, qui se caractérisent par la présence au sein de la plaque supérieure (Gondwana) de granulites felsiques de (ultra)-HP, qui correspondent à du matériel dérivé de la plaque inférieure et incorporé à la croûte inférieure lors de la collision. Si les MCE correspondent bien à la continuité des massifs des Vosges et de la Bohême, on devrait s'attendre à retrouver ces granulites felsiques (U)HP dans les unités crustales profondes. De telles roches n'ont pour l'instant jamais été décrites dans les MCE, mais des investigations de terrain plus poussées pourraient permettre de les identifier.

Bibliographie

- ALTHERR, R. et KALT, A. (1996). Metamorphic evolution of ultrahigh-pressure garnet peridotites from the Variscan Vosges Mts. (France). *Chemical Geology*, 134(1):27–47.
- ANNEN, C., BLUNDY, J. D. et SPARKS, R. S. J. (2006). The Genesis of Intermediate and Silicic Magmas in Deep Crustal Hot Zones. *J. Petrol.*, 47(3):505–539.
- ARGAND, E., BLOESCH, E. et HEIM, A. (1911). Les nappes de recouvrement des Alpes pennines et leurs prolongements structuraux. *Komm. Bei Francke Vorm Schmidt Franke*, (31-33).
- AUMAITRE, P. R., GIRAUD, P., PONCERRY, E. et VIVIER, G. (1985). Les granitoïdes subalcalins potassiques de la Lauzière, Massif Cristallin Externe de Belledonne (Alpes Françaises). page 16.
- AVIGAD, D., ROSSI, P., GERDES, A. et ABBO, A. (2018). Cadomian metasediments and Ordovician sandstone from Corsica : Detrital zircon U–Pb–Hf constrains on their provenance and paleogeography. *Int J Earth Sci (Geol Rundsch)*, 107(8):2803–2818.
- AXELSSON, E., PAPE, J., BERNDT, J., CORFU, F., MEZGER, K. et RAITH, M. M. (2018). Rutile R632 - A New Natural Reference Material for U–Pb and Zr Determination. *Geostand Geoanal Res*, 42(3):319–338.
- BALLÈVRE, M., BOSSE, V., DUCASSOU, C. et PITRA, P. (2009). Palaeozoic history of the Armorican Massif : Models for the tectonic evolution of the suture zones. *Comptes Rendus Geoscience*, 341(2):174–201.
- BALLÈVRE, M., CAMONIN, A., MANZOTTI, P. et POUJOL, M. (2020). A step towards unraveling the paleogeographic attribution of pre-Mesozoic basement complexes in the Western Alps based on U–Pb geochronology of Permian magmatism. *Swiss J Geosci*, 113(1):12.

- BALLÈVRE, M., FOURCADE, S., CAPDEVILA, R., PEUCAT, J.-J., COCHERIE, A. et FANNING, C. M. (2012). Geochronology and geochemistry of Ordovician felsic volcanism in the Southern Armorican Massif (Variscan belt, France) : Implications for the breakup of Gondwana. *Gondwana Res.*, 21(4):1019–1036.
- BALLÈVRE, M., LE GOFF, E. et HÉBERT, R. (2001). The tectonothermal evolution of the Cadomian belt of northern Brittany, France : A Neoproterozoic volcanic arc. *Tectonophysics*, 331(1):19–43.
- BALLÈVRE, M., MANZOTTI, P. et PIAZ, G. V. D. (2018). Pre-Alpine (Variscan) Inheritance : A Key for the Location of the Future Valaisan Basin (Western Alps). *Tectonics*, 37(3):786–817.
- BALLÈVRE, M., MARTÍNEZ CATALÁN, J. R., LÓPEZ-CARMONA, A., PITRA, P., ABATI, J., FERNÁNDEZ, R. D., DUCASSOU, C., ARENAS, R., BOSSE, V., CASTIÑEIRAS, P., FERNÁNDEZ-SUÁREZ, J., GÓMEZ BARREIRO, J., PAQUETTE, J.-L., PEUCAT, J.-J., POUJOL, M., RUFFET, G. et SÁNCHEZ MARTÍNEZ, S. (2014). Correlation of the nappe stack in the Ibero-Armorican arc across the Bay of Biscay : A joint French–Spanish project. *Geol. Soc. Lond. Spec. Publ.*, 405(1):77–113.
- BANZET, G. (1987). Interactions croûte-manteau et genèse du plutonisme subalcalin du haut-dauphiné occidental. page 23.
- BARBARIN, B. (1999). A review of the relationships between granitoid types, their origins and their geodynamic environments. *Lithos*, 46(3):605–626.
- BARFÉTY, J., GIDON, M., MÉNOT, R. P., DEBON, F., PÊCHER, A., GUILLOT, S., FOURNEAU, J. et GAMOND, J. (2000). Notice de la carte géologique de la France au 1/50 000, feuille de Domène.
- BATANOVA, V. G., SOBOLEV, A. V. et KUZMIN, D. V. (2015). Trace element analysis of olivine : High precision analytical method for JEOL JXA-8230 electron probe microanalyser. *Chemical Geology*, 419:149–157.
- BATANOVA, V. G., THOMPSON, J. M., DANYUSHEVSKY, L. V., PORTNYAGIN, M. V., GARBE-SCHÖNBERG, D., HAURI, E., KIMURA, J.-I., CHANG, Q., SENDA, R., GOEMANN, K., CHAUVEL, C., CAMPILLO, S., IONOV, D. A. et SOBOLEV, A. V. (2019). New Olivine Reference Material for In Situ Microanalysis. *Geostand. Geoanalytical Res.*, 43(3):453–473.

- BEA, F. (2012). The sources of energy for crustal melting and the geochemistry of heat-producing elements. *Lithos*, 153:278–291.
- BELLAHSEN, N., JOLIVET, L., LACOMBE, O., BELLANGER, M., BOUTOUX, A., GARCIA, S., MOUTHEREAU, F., LE POURHIET, L. et GUMIAUX, C. (2012). Mechanisms of margin inversion in the external Western Alps : Implications for crustal rheology. *Tectonophysics*, 560–561:62–83.
- BELLAHSEN, N., MOUTHEREAU, F., BOUTOUX, A., BELLANGER, M., LACOMBE, O., JOLIVET, L. et ROLLAND, Y. (2014). Collision kinematics in the western external Alps. *Tectonics*, 33(6):1055–1088.
- BELLANGER, M., AUGIER, R., BELLAHSEN, N., JOLIVET, L., MONIÉ, P., BAUDIN, T. et BEYSSAC, O. (2015). Shortening of the European Dauphinois margin (Oisans Massif, Western Alps) : New insights from RSCM maximum temperature estimates and $^{40}\text{Ar}/^{39}\text{Ar}$ in situ dating. *Journal of Geodynamics*, 83:37–64.
- BELLANGER, M., BELLAHSEN, N., JOLIVET, L., BAUDIN, T., AUGIER, R. et BOUTOUX, A. (2014). Basement shear zones development and shortening kinematics in the Ecrins Massif, Western Alps. *Tectonics*, 33(2):84–111.
- BERGER, J., FÉMÉNIAS, O., OHNENSTETTER, D., BRUGUIER, O., PLISSART, G., MERCIER, J.-C. C. et DEMAIFFE, D. (2010). New occurrence of UHP eclogites in Limousin (French Massif Central) : Age, tectonic setting and fluid–rock interactions. *Lithos*, 118(3-4):365–382.
- BEYSSAC, O., GOFFÉ, B., CHOPIN, C. et ROUZAUD, J. N. (2002). Raman spectra of carbonaceous material in metasediments : A new geothermometer. *J. Metamorph. Geol.*, 20(9):859–871.
- BLACK, L. P., KAMO, S. L., ALLEN, C. M., ALEINIKOFF, J. N., DAVIS, D. W., KORSCH, R. J. et FOUDOULIS, C. (2003). TEMORA 1 : A new zircon standard for Phanerozoic U–Pb geochronology. *Chemical Geology*, 200(1):155–170.
- BORDET, P. et BORDET, C. (1963). Belledonne-Grandes Rousses et Aiguilles Rouges-Mont Blanc : Quelques données nouvelles sur leurs rapports structuraux. *Mém. H.s. Soc. Géol. Fr.*, 2:309–316.
- BOUSQUET, R., OBERHÄNSLI, R., GOFFÉ, B., WIEDERKEHR, M., KOLLER, F., SCHMID, S. M., SCHUSTER, R., ENGI, M., BERGER, A. et MARTINOTTI, G. (2008). Metamorphism

BIBLIOGRAPHIE

- of metasediments at the scale of an orogen : A key to the Tertiary geodynamic evolution of the Alps. *Geol. Soc. Lond. Spec. Publ.*, 298(1):393–411.
- BOUVIER, A., VERVOORT, J. D. et PATCHETT, P. J. (2008). The Lu–Hf and Sm–Nd isotopic composition of CHUR : Constraints from unequilibrated chondrites and implications for the bulk composition of terrestrial planets. *Earth Planet. Sci. Lett.*, 273(1-2):48–57.
- BREY, G. P. et KÖHLER, T. (1990). Geothermobarometry in Four-phase Lherzolites II. New Thermobarometers, and Practical Assessment of Existing Thermobarometers. *J Petrology*, 31(6):1353–1378.
- BROUWER, F. M., BURRI, T., ENGI, M. et BERGER, A. (2005). Eclogite relics in the Central Alps : PT - evolution, Lu–Hf ages and implications for formation of tectonic mélange zones. *Schweiz. Mineral. Petrogr. Mitteilungen*, 85:147–174.
- BURG, J. P. et MATTE, P. J. (1978). A cross section through the French Massif Central and the scope of its Variscan geodynamic evolution. *Z. Dtsch. Geol. Ges.*, pages 429–460.
- BUSSY, F. (1990). *Pétrogenèse des enclaves microgrenues associées aux granitoïdes calcoalcalins : exemple des massifs varisque du Mont Blanc (Alpes occidentales) et miocène du Monte Capanne (Ile d'Elbe, Italie)*. Thèse de doctorat, Université de Lausanne.
- BUSSY, F., HERNANDEZ, J. et VON RAUMER, J. (2000). Bimodal magmatism as a consequence of the post-collisional readjustment of the thickened Variscan continental lithosphere (Aiguilles Rouges-Mont Blanc Massifs, Western Alps). *Earth Environ. Sci. Trans. R. Soc. Edinb.*, 91(1-2):221–233.
- BUSSY, F., PÉRONNET, V., ULIANOV, A., EPARD, J. L. et RAUMER, J. (2011). Ordovician magmatism in the external French Alps : Witness of a peri-gondwanan active continental margin. *In International Symposium on the Ordovician System (11 ; 2011 ; Alcalá de Henares, Madrid)*.
- CAGNARD, F., DURRIEU, N., GAPAIS, D., BRUN, J.-P. et EHLERS, C. (2006). Crustal thickening and lateral flow during compression of hot lithospheres, with particular reference to Precambrian times. *Terra Nova*, 18(1):72–78.
- CAO, S. et NEUBAUER, F. (2016). Deep crustal expressions of exhumed strike-slip fault systems : Shear zone initiation on rheological boundaries. *Earth-Science Reviews*, 162:155–176.

- CARIGNAN, J., HILD, P., MEVELLE, G., MOREL, J. et YEGHICHEYAN, D. (2001). Routine Analyses of Trace Elements in Geological Samples using Flow Injection and Low Pressure On-Line Liquid Chromatography Coupled to ICP-MS : A Study of Geochemical Reference Materials BR, DR-N, UB-N, AN-G and GH. *Geostand. Newsl.*, 25(2-3):187–198.
- CARME, F. et PIN, C. (1987). Vue d'ensemble sur le magmatisme pré-orogénique et l'évolution métamorphique et tectonique varisques dans le sud de la chaîne de Belledonne (Massifs cristallins externes, Alpes françaises). *Comptes Rendus Académie Sci. Sér. 2 Mécanique Phys. Chim. Sci. Univers Sci. Terre*, 304(19):1177–1181.
- CAROSI, R., PETROCCIA, A., IACCARINO, S., SIMONETTI, M., LANGONE, A. et MONTOMOLI, C. (2020). Kinematics and Timing Constraints in a Transpressive Tectonic Regime : The Example of the Posada-Asinara Shear Zone (NE Sardinia, Italy). *Geosciences*, 10(8):288.
- CHANG, R., NEUBAUER, F., LIU, Y., YUAN, S., GENSER, J., HUANG, Q., GUAN, Q. et YU, S. (2021). Hf isotopic constraints and detrital zircon ages for the Austroalpine basement evolution of Eastern Alps : Review and new data. *Earth-Science Reviews*, 221:103772.
- CHANTRAINE, J., EGAL, E., THIÉBLEMONT, D., LE GOFF, E., GUERROT, C., BALLÈVRE, M. et GUENNOG, P. (2001). The Cadomian active margin (North Armorican Massif, France) : A segment of the North Atlantic Panafrican belt. *Tectonophysics*, 331(1-2):1–18.
- CHAPPELL, B. W. et WHITE, A. J. R. (2001). Two contrasting granite types : 25 years later. *Aust. J. Earth Sci.*, 48(4):489–499.
- CHARDON, D., GAPAIS, D. et CAGNARD, F. (2009). Flow of ultra-hot orogens : A view from the Precambrian, clues for the Phanerozoic. *Tectonophysics*, 477(3):105–118.
- CHARDON, D., JAYANANDA, M. et PEUCAT, J.-J. (2011). Lateral constrictional flow of hot orogenic crust : Insights from the Neoproterozoic of south India, geological and geophysical implications for orogenic plateaux : Lateral constrictional flow of orogens. *Geochem. Geophys. Geosyst.*, 12(2).
- CHELLE-MICHO, C., LAURENT, O., MOYEN, J.-F., BLOCK, S., PAQUETTE, J.-L., COUZINIÉ, S., GARDIEN, V., VANDERHAEGHE, O., VILLAROS, A. et ZEH, A. (2017). Pre-Cadomian to late-Variscan odyssey of the eastern Massif Central, France : Formation of the West European crust in a nutshell. *Gondwana Research*, 46:170–190.

BIBLIOGRAPHIE

- CHERNIAK, D. J. (2000). Pb diffusion in rutile. *Contrib Mineral Petrol*, 139(2):198–207.
- CHEW, D. M., PETRUS, J. A. et KAMBER, B. S. (2014). U–Pb LA–ICPMS dating using accessory mineral standards with variable common Pb. *Chemical Geology*, 363:185–199.
- CHOPIN, C. (1984). Coesite and pure pyrope in high-grade blueschists of the Western Alps : A first record and some consequences. *Contr. Mineral. and Petrol.*, 86(2):107–118.
- CHU, Y., LIN, W., FAURE, M. et WANG, Q. (2016). Detrital zircon U-Pb ages and Hf isotopic constraints on the terrigenous sediments of the Western Alps and their paleogeographic implications. *Tectonics*, 35(11):2734–2753.
- CLARK, C., FITZSIMONS, I. C. W., HEALY, D. et HARLEY, S. L. (2011). How Does the Continental Crust Get Really Hot? *Elements*, 7(4):235–240.
- COCHELIN, B., CHARDON, D., DENÈLE, Y., GUMIAUX, C. et BAYON, B. L. (2017). Vertical strain partitioning in hot Variscan crust : Syn-convergence escape of the Pyrenees in the Iberian-Armorican syntax. *Bull. Soc. géol. Fr.*, 188(6):39.
- COCHELIN, B., LEMIRRE, B., DENÈLE, Y. et BLANQUAT, M. D. S. (2021). Strain partitioning within bending orogens, new insights from the Variscan belt (Chiroulet-Lesponne domes, Pyrenees). *Tectonics*, n/a(n/a).
- COCKS, L. R. M. et TORSVIK, T. H. (2002). Earth geography from 500 to 400 million years ago : A faunal and palaeomagnetic review. *Journal of the Geological Society*, 159(6):631–644.
- CONNOLLY, J. (2005). Computation of phase equilibria by linear programming : A tool for geodynamic modeling and its application to subduction zone decarbonation. *Earth and Planetary Science Letters*, 236(1-2):524–541.
- CONNOLLY, J. A. D. (2009). The geodynamic equation of state : What and how. *Geochemistry, Geophysics, Geosystems*, 10(10):n/a–n/a.
- COOK, K. L. et ROYDEN, L. H. (2008). The role of crustal strength variations in shaping orogenic plateaus, with application to Tibet. *J. Geophys. Res. Solid Earth*, 113(B8).
- CORFU, F., HANCHAR, J. M., HOSKIN, P. W. et KINNY, P. (2003). Atlas of zircon textures. *Rev. Mineral. Geochem.*, 53(1):469–500.

- CORSINI, M. et ROLLAND, Y. (2009). Late evolution of the southern European Variscan belt : Exhumation of the lower crust in a context of oblique convergence. *Comptes Rendus Geoscience*, 341(2):214–223.
- CORTESOGNO, L., GAGGERO, L., OGGIANO, G. et PAQUETTE, J.-L. (2004). Different tectono-thermal evolutionary paths in eclogitic rocks from the axial zone of the Variscan chain in Sardinia (Italy) compared with the Ligurian Alps. page 21.
- COUZINIÉ, S. (2017). *Evolution of the Continental Crust and Significance of the Zircon Record, a Case Study from the French Massif Central*. Thèse de doctorat, Lyon.
- COUZINIÉ, S., BOUILHOL, P., LAURENT, O., MARKO, L. et MOYEN, J.-F. (2021). When zircon drowns : Elusive geochronological record of water-fluxed orthogneiss melting in the Velay dome (Massif Central, France). *Lithos*, 384–385:105938.
- COUZINIÉ, S., LAURENT, O., MOYEN, J.-F., ZEH, A., BOUILHOL, P. et VILLAROS, A. (2016). Post-collisional magmatism : Crustal growth not identified by zircon Hf–O isotopes. *Earth and Planetary Science Letters*, 456:182–195.
- COUZINIÉ, S., LAURENT, O., POUJOL, M., MINTRONE, M., CHELLE-MICHOU, C., MOYEN, J.-F., BOUILHOL, P., VEZINET, A. et MARKO, L. (2017). Cadomian S-type granites as basement rocks of the Variscan belt (Massif Central, France) : Implications for the crustal evolution of the north Gondwana margin. *Lithos*, 286–287:16–34.
- CROWLEY, Q. G., FLOYD, P. A., WINCHESTER, J. A., FRANKE, W. et HOLLAND, J. G. (2000). Early Palaeozoic rift-related magmatism in Variscan Europe : Fragmentation of the Armorican Terrane Assemblage. *Terra Nova*, 12(4):171–180.
- CRUCIANI, G., FRANCESCHELLI, M., GROppo, C. et SPANO, M. E. (2012). Metamorphic evolution of non-equilibrated granulitized eclogite from Punta de li Tulchi (Variscan Sardinia) determined through texturally controlled thermodynamic modelling. *J. Metamorph. Geol.*, 30(7):667–685.
- DAHL, P. S. (1997). A crystal-chemical basis for Pb retention and fission-track annealing systematics in U-bearing minerals, with implications for geochronology. *Earth and Planetary Science Letters*, 150(3-4):277–290.
- DAVIES, J. H. et VON BLANCKENBURG, F. (1995). Slab breakoff : A model of lithosphere detachment and its test in the magmatism and deformation of collisional orogens. *Earth Planet. Sci. Lett.*, 129(1-4):85–102.

BIBLIOGRAPHIE

- DE BOISSET, T. (1986). *Les Enclaves Basiques Du Granite Du Rochail (Syénite Du Lauvitel) - Haut Dauphiné , Alpes Françaises . Pétrographie et Minéralogie*. Theses, Université Scientifique et Médicale de Grenoble.
- DEBON, F., GUERROT, C. et MÉNOT, R.-P. (1998). Late Variscan granites of the Belledonne massif (French Western Alps) : An Early Visean magnesian plutonism. *Schweiz. Mineral. Petrogr. Mitteilungen*, 78:67–85.
- DEBON, F. et LE FORT, P. (1983). A chemical–mineralogical classification of common plutonic rocks and associations. *Earth Environ. Sci. Trans. R. Soc. Edinb.*, 73(3):135–149.
- DEBON, F. et LEMMET, M. (1999). Evolution of Mg/Fe Ratios in Late Variscan Plutonic Rocks from the External Crystalline Massifs of the Alps (France, Italy, Switzerland). *J Petrology*, 40(7):1151–1185.
- DEMEULEMEESTER, P. (1982). *Contribution à l'étude radiométrique à l'argon et au strontium des massifs cristallins externes (Alpes Françaises) - Distribution cartographique des âges sur biotites et amphiboles*. Thèse de doctorat, Université Scientifique et Médicale de Grenoble.
- DEPAOLO, D. J. (1981). Trace element and isotopic effects of combined wallrock assimilation and fractional crystallization. *Earth and Planetary Science Letters*, 53(2):189–202.
- DESCHAMPS, F., GODARD, M., GUILLOT, S. et HATTORI, K. (2013). Geochemistry of subduction zone serpentinites : A review. *Lithos*, 178:96–127.
- DIJKSTRA, A. H., BARTH, M. G., DRURY, M. R., MASON, P. R. D. et VISSERS, R. L. M. (2003). Diffuse porous melt flow and melt-rock reaction in the mantle lithosphere at a slow-spreading ridge : A structural petrology and LA-ICP-MS study of the Othris Peridotite Massif (Greece). *Geochem. Geophys. Geosystems*, 4(8).
- DUCROT, J., LANCELOT, J. R. et MARCHAND, J. (1983). Datation U-Pb sur zircons de l'éclogite de la Borie (Haut-Allier, France) et conséquences sur l'évolution antehercynienne de l'Europe occidentale. *Earth Planet. Sci. Lett.*, 62(3):385–394.
- DUESTERHOEFT, E. et LANARI, P. (2020). Iterative thermodynamic modelling—Part 1 : A theoretical scoring technique and a computer program (Bingo-Antidote). *J. Metamorph. Geol.*, 38(5):527–551.

- DUMONT, T., SIMON-LABRIC, T., AUTHEMAYOU, C. et HEYMES, T. (2011). Lateral termination of the north-directed Alpine orogeny and onset of westward escape in the Western Alpine arc : Structural and sedimentary evidence from the external zone. *Tectonics*, 30(5).
- EDEL, J. B., SCHULMANN, K., LEXA, O. et LARDEAUX, J. M. (2018). Late Palaeozoic palaeomagnetic and tectonic constraints for amalgamation of Pangea supercontinent in the European Variscan belt. *Earth-Science Reviews*, 177:589–612.
- EDEL, J. B. et WEBER, K. (1995). Cadomian terranes, wrench faulting and thrusting in the central Europe Variscides : Geophysical and geological evidence. *Geol Rundsch*, 84(2):412–432.
- ELLIOTT, T., PLANK, T., ZINDLER, A., WHITE, W. et BOURDON, B. (1997). Element transport from slab to volcanic front at the Mariana arc. *J. Geophys. Res. Solid Earth*, 102(B7):14991–15019.
- ENGLAND, P. C. et THOMPSON, A. B. (1984). Pressure—temperature—time paths of regional metamorphism I. Heat transfer during the evolution of regions of thickened continental crust. *J. Petrol.*, 25(4):894–928.
- EWING, T. A., HERMANN, J. et RUBATTO, D. (2013). The robustness of the Zr-in-rutile and Ti-in-zircon thermometers during high-temperature metamorphism (Ivrea-Verbano Zone, northern Italy). *Contrib Mineral Petrol*, 165(4):757–779.
- FARYAD, S. W., MELCHER, F., HOINKES, G., PUHL, J., MEISEL, T. et FRANK, W. (2002). Relics of eclogite facies metamorphism in the Austroalpine basement, Hochgrössen (Speik complex), Austria. *Mineralogy and Petrology*, 74(1):49–73.
- FAURE, M. (1995). Late orogenic carboniferous extensions in the Variscan French Massif Central. *Tectonics*, 14(1):132–153.
- FAURE, M. (2014). Le substratum de la France métropolitaine : De la formation du Gondwana à la constitution de la Pangée, une histoire de 600 Ma. *Géologues*, (180).
- FAURE, M., BÉ MÉZÈME, E., COCHERIE, A., ROSSI, P., CHEMENDA, A. et BOUTELIER, D. (2008). Devonian geodynamic evolution of the Variscan Belt, insights from the French Massif Central and Massif Armoricain. *Tectonics*, 27(2):n/a–n/a.
- FAURE, M., BÉ MÉZÈME, E., DUGUET, M., CARTIER, C. et TALBOT, J.-Y. (2005). Paleozoic tectonic evolution of medio-Europa from the example of the French Massif Central and Massif Armoricain. *J. Virtual Explor.*, 19.

BIBLIOGRAPHIE

- FAURE, M., LARDEAUX, J.-M. et LEDRU, P. (2009). A review of the pre-Permian geology of the Variscan French Massif Central. *Comptes Rendus Geosci.*, 341(2-3):202–213.
- FERNANDEZ, A., GUILLOT, S., MÉNOT, R.-P. et LEDRU, P. (2002). Late Paleozoic poly-phased tectonics in the SW Belledonne massif (external crystalline massifs, French Alps). *Geodin. Acta*, 15(2):127–139.
- FERRANDO, S., LOMBARDO, B. et COMPAGNONI, R. (2008). Metamorphic history of HP mafic granulites from the Gesso-Stura terrain (Argentera Massif, western Alps, Italy). *Eur. J. Mineral.*, 20(5):777–790.
- FERRY, J. M. et WATSON, E. B. (2007). New thermodynamic models and revised calibrations for the Ti-in-zircon and Zr-in-rutile thermometers. *Contrib Mineral Petrol.*, 154(4):429–437.
- FOLEY, S. F., VENTURELLI, G., GREEN, D. H. et TOSCANI, L. (1987). The ultrapotassic rocks : Characteristics, classification, and constraints for petrogenetic models. *Earth-Science Reviews*, 24(2):81–134.
- FORTEY, R. A. et COCKS, L. R. M. (2003). Palaeontological evidence bearing on global Ordovician–Silurian continental reconstructions. *Earth-Science Reviews*, 61(3):245–307.
- FRANCESCHELLI, M., PUXEDDU, M., CRUCIANI, G. et UTZERI, D. (2007). Metabasites with eclogite facies relics from Variscides in Sardinia, Italy : A review. *Int. J. Earth Sci.*, 96(5):795–815.
- FRANKE, W. (2000). The mid-European segment of the Variscides : Tectonostratigraphic units, terrane boundaries and plate tectonic evolution. *Geol. Soc. Lond. Spec. Publ.*, 179(1):35–61.
- FRANKE, W., COCKS, L. R. M. et TORSVIK, T. H. (2017). The Palaeozoic Variscan oceans revisited. *Gondwana Res.*, 48:257–284.
- FRÉVILLE, K. (2016). *L'orogénèse varisque dans les massifs cristallins externes de Belledonne et du Pelvoux (Alpes occidentales françaises) : rôle de la fusion partielle et du plutonisme dans la structuration de la croûte continentale*. Thèse de doctorat, Université d'Orléans.
- FRÉVILLE, K., TRAP, P., FAURE, M., MELLETON, J., LI, X.-H., LIN, W., BLEIN, O., BRUGUIER, O. et POUJOL, M. (2018). Structural, metamorphic and geochronological insights

- on the Variscan evolution of the Alpine basement in the Belledonne Massif (France). *Tectonophysics*, 726:14–42.
- FRÉVILLE, K., TRAP, P., MELLETON, J., VANARDOIS, J., FAURE, M., BRUGUIER, O. et POUJOL, M. (2022). Carboniferous tectono-thermal evolution of the Variscan crust in the Belledonne-Pelvoux area. *Accept. Bull. Société Géologique Fr.*
- FUHRMAN, M. L. et LINDSLEY, D. H. (1988). Ternary-feldspar modeling and thermometry. *Am. Mineral.*, 73(3-4):201–215.
- GALE, A., DALTON, C. A., LANGMUIR, C. H., SU, Y. et SCHILLING, J.-G. (2013). The mean composition of ocean ridge basalts. *Geochem. Geophys. Geosystems*, 14(3):489–518.
- GARDIEN, V., TEGYEY, M., LARDEAUX, J. M., MISSERI, M. et DUFOUR, E. (1990). Crust-mantle relationships in the French Variscan chain : The example of the Southern Monts du Lyonnais unit (eastern French Massif Central). *J. Metamorph. Geol.*, 8(5):477–492.
- GARFUNKEL, Z. (2015). The relations between Gondwana and the adjacent peripheral Cadomian domain—constraints on the origin, history, and paleogeography of the peripheral domain. *Gondwana Res.*, 28(4):1257–1281.
- GASQUET, D. (1979). *Etude pétrologique, géochimique et structurale des terrains cristallins de Belledonne et du Grand Chatelard traversés par les galeries E.D.F. Arc-Isère- Alpes Françaises*. Thèse de doctorat, Université Scientifique et Médicale de Grenoble.
- GATTACCECA, J., ORSINI, J.-B., BELLOT, J.-P., HENRY, B., ROCHETTE, P., ROSSI, P. et CHERCHI, G. (2004). Magnetic fabric of granitoids from Southern Corsica and Northern Sardinia and implications for Late Hercynian tectonic setting. *Journal of the Geological Society*, 161(2):277–289.
- GERBAULT, M., SCHNEIDER, J., REVERSO-PEILA, A. et CORSINI, M. (2018). Crustal exhumation during ongoing compression in the Variscan Maures-Tanneron Massif, France—Geological and thermo-mechanical aspects. *Tectonophysics*, 746:439–458.
- GIACOMINI, F., BOMPAROLA, R. M. et GHEZZO, C. (2005). Petrology and geochronology of metabasites with eclogite facies relics from NE Sardinia : Constraints for the Palaeozoic evolution of Southern Europe. *Lithos*, 82(1):221–248.
- GIRARDEAU, J., DUBUISSON, G. et MERCIER, J.-C. C. (1986). Cinématique de mise en place des ophiolites et nappes crystallophiliennes du Limousin, Ouest du Massif Central français. *Bull. Société Géologique Fr.*, 2(5):849–860.

BIBLIOGRAPHIE

- GODARD, G., MARTIN, S., PROSSER, G., KIENAST, J. R. et MORTEN, L. (1996). Variscan migmatites, eclogites and garnet-peridotites of the Ulten zone, Eastern Austroalpine system. *Tectonophysics*, 259(4):313–341.
- GRAND'HOMME, A., JANOTS, E., SEYDOUX-GUILLAUME, A.-M., GUILLAUME, D., BOSSE, V. et MAGNIN, V. (2016). Partial resetting of the U-Th-Pb systems in experimentally altered monazite : Nanoscale evidence of incomplete replacement. *Geology*, 44(6):431–434.
- GRANDJEAN, V., GUILLOT, S. et PECHER, A. (1996). A new record of the LP-HT late-Variscan metamorphism : The Peyre-Arguet unit (Haut-Dauphine). *Comptes Rendus Académie Sci.*, 322(3):189–195.
- GREEN, E., HOLLAND, T. et POWELL, R. (2007). An order-disorder model for omphacitic pyroxenes in the system jadeite-diopside-hedenbergite-acmite, with applications to eclogitic rocks. *Am. Mineral.*, 92(7):1181–1189.
- GREEN, E. C. R., WHITE, R. W., DIENER, J. F. A., POWELL, R., HOLLAND, T. J. B. et PALIN, R. M. (2016). Activity–composition relations for the calculation of partial melting equilibria in metabasic rocks. *J. Metamorph. Geol.*, 34(9):845–869.
- GRÉGOIRE, M., BELL, D. R. et LE ROEX, A. P. (2003). Garnet Lherzolites from the Kaapvaal Craton (South Africa) : Trace Element Evidence for a Metasomatic History. *Journal of Petrology*, 44(4):629–657.
- GROS, Y. (1974). *Etude Pétrologique et Structurale Du Beaufortin (Nord de Belledonne). Alpes Françaises*. Theses, Université Scientifique et Médicale de Grenoble.
- GUILLOT, F., AVERBUCH, O., DUBOIS, M., DURAND, C., LANARI, P. et GAUTHIER, A. (2020). Zircon age of vaugnerite intrusives from the Central and Southern Vosges crystalline massif (E France) : Contribution to the geodynamics of the European Variscan belt. *BSGF - Earth Sci. Bull.*, 191:26.
- GUILLOT, S., DI PAOLA, S., MÉNOT, R.-P., LEDRU, P., SPALLA, M. I., GOSSO, G. et SCHWARTZ, S. (2009a). Suture zones and importance of strike-slip faulting for Variscan geodynamic reconstructions of the External Crystalline Massifs of the western Alps. *Bull. Société Géologique Fr.*, 180(6):483–500.
- GUILLOT, S., HATTORI, K., AGARD, P., SCHWARTZ, S. et VIDAL, O. (2009b). Exhumation processes in oceanic and continental subduction contexts : A review. *Subduction Zone Geodyn.*, pages 175–205.

- GUILLOT, S., MAHÉO, G., DE SIGOYER, J., HATTORI, K. et PÊCHER, A. (2008). Tethyan and Indian subduction viewed from the Himalayan high- to ultrahigh-pressure metamorphic rocks. *Tectonophysics*, 451(1-4):225–241.
- GUILLOT, S. et MENOT, R. (1999). Nappe stacking and first evidence of Late Variscan extension in the Belledonne Massif (External Crystalline Massifs, French Alps). *Geodin. Acta*, 12(2):97–111.
- GUILLOT, S. et MÉNOT, R.-P. (2009). Paleozoic evolution of the External Crystalline Massifs of the Western Alps. *Comptes Rendus Geosci.*, 341(2-3):253–265.
- GUILLOT, S., MÉNOT, R.-P. et LARDEAUX, J.-M. (1992). Tectonique intra-océanique distensive dans l'ophiolite paléozoïque de Chamrousse (Alpes occidentales). *Bull Soc Geol Fr.*, 163:229–240.
- GUILLOT, S., SCHWARTZ, S., REYNARD, B., AGARD, P. et PRIGENT, C. (2015). Tectonic significance of serpentinites. *Tectonophysics*, 646:1–19.
- HAAS, I., EICHINGER, S., HALLER, D., FRITZ, H., NIEVOLL, J., MANDL, M., HIPPLER, D. et HAUZENBERGER, C. (2020). Gondwana fragments in the Eastern Alps : A travel story from U/Pb zircon data. *Gondwana Research*, 77:204–222.
- HANDY, M. R., SCHMID, S., BOUSQUET, R., KISSLING, E. et BERNOULLI, D. (2010). Reconciling plate-tectonic reconstructions of Alpine Tethys with the geological–geophysical record of spreading and subduction in the Alps. *Earth-Science Reviews*, 102(3):121–158.
- HARRISON, T. M. et WATSON, E. B. (1984). The behavior of apatite during crustal anatexis : Equilibrium and kinetic considerations. *Geochim. Cosmochim. Acta*, 48(7):1467–1477.
- HASTIE, A. R., KERR, A. C., PEARCE, J. A. et MITCHELL, S. F. (2007). Classification of Altered Volcanic Island Arc Rocks using Immobile Trace Elements : Development of the Th–Co Discrimination Diagram. *Journal of Petrology*, 48(12):2341–2357.
- HERMANN, J. et RUBATTO, D. (2009). Accessory phase control on the trace element signature of sediment melts in subduction zones. *Chemical Geology*, 265(3):512–526.
- HOLLAND, T. et BLUNDY, J. (1994). Non-ideal interactions in calcic amphiboles and their bearing on amphibole-plagioclase thermometry. *Contr. Mineral. and Petrol.*, 116(4):433–447.

BIBLIOGRAPHIE

- HOLLAND, T. J., GREEN, E. C. et POWELL, R. (2018). Melting of peridotites through to granites : A simple thermodynamic model in the system KNCFMASHTOCr. *J. Petrol.*, 59(5):881–900.
- HOLLAND, T. J. B. et POWELL, R. (1998). An internally consistent thermodynamic data set for phases of petrological interest. *J. Metamorph. Geol.*, 16(3):309–343.
- HOLLAND, T. J. B. et POWELL, R. (2011). An improved and extended internally consistent thermodynamic dataset for phases of petrological interest, involving a new equation of state for solids. *J. Metamorph. Geol.*, 29(3):333–383.
- HORA, J. M., TABAUD, A.-S., JANOUŠEK, V. et ERBAN KOCHERGINA, Y. V. (2021). Potassic magmas of the Vosges Mts. (NE France) delimit the areal extent and nature of long-gone Variscan orogenic mantle domains. *Lithos*, page 106304.
- HOSKIN, P. W. O. et SCHALTEGGER, U. (2003). The Composition of Zircon and Igneous and Metamorphic Petrogenesis. *Reviews in Mineralogy and Geochemistry*, 53(1):27–62.
- IONOV, D. A. et WOOD, B. J. (1992). The oxidation state of subcontinental mantle : Oxygen thermobarometry of mantle xenoliths from central Asia. *Contrib. Mineral. Petrol.*, 111(2):179–193.
- JACOB, J.-B., GUILLOT, S., RUBATTO, D., JANOTS, E., MELLETON, J. et FAURE, M. (2021a). Carboniferous high pressure metamorphism and deformation in the Belledonne Massif (Western Alps). *J. Metamorph. Geol.*, n/a(n/a).
- JACOB, J.-B., GUILLOT, S., THIÉBLEMONT, D., VANARDOIS, J., TRAP, P., FAURE, M. et MARQUER, D. (2022). Paleozoic evolution and Variscan inheritance in the Alps. *In Geodynamics of the Alps*. ISTE.
- JACOB, J.-B., MOYEN, J.-F., FIANNACCA, P., LAURENT, O., BACHMANN, O., JANOUŠEK, V., FARINA, F. et VILLAROS, A. (2021b). Crustal melting vs. fractionation of basaltic magmas : Part 2, Attempting to quantify mantle and crustal contributions in granitoids. *Lithos*, page 106292.
- JAGOUTZ, E., PALME, H., BADDENHAUSEN, H., BLUM, K., CENDALES, M., DREIBUS, G., SPETTEL, B., LORENZ, V. et WÄNKE, H. (1979). The abundances of major, minor and trace elements in the earth's mantle as derived from primitive ultramafic nodules. *In Lunar and Planetary Science Conference Proceedings*, pages 2031–2050.

- JANOŠEK, V. et HOLUB, F. V. (2007). The causal link between HP-HT metamorphism and ultrapotassic magmatism in collisional orogens : Case study from the Moldanubian Zone of the Bohemian Massif. *Proceedings of the Geologists' Association*, 118(1):75–86.
- JANOŠEK, V., HOLUB, F. V., VERNER, K., ČOPJAKOVÁ, R., GERDES, A., HORA, J. M., KOŠLER, J. et TYRRELL, S. (2019). Two-pyroxene syenitoids from the Moldanubian Zone of the Bohemian Massif : Peculiar magmas derived from a strongly enriched lithospheric mantle source. *Lithos*, 342–343:239–262.
- JANOŠEK, V., MOYEN, J.-F., MARTIN, H., ERBAN, V. et FARROW, C. (2016). Classical Plots. In JANOUŠEK, V., MOYEN, J.-F., MARTIN, H., ERBAN, V. et FARROW, C., éditeurs : *Geochemical Modelling of Igneous Processes – Principles And Recipes in R Language : Bringing the Power of R to a Geochemical Community*, Springer Geochemistry, pages 27–43. Springer, Berlin, Heidelberg.
- JAROSEWICH, E., NELEN, J. A. et NORBERG, J. A. (1980). Reference samples for electron microprobe analysis. *Geostand. Newsl.*, 4(1):43–47.
- JENNINGS, E. S. et HOLLAND, T. J. B. (2015). A Simple Thermodynamic Model for Melting of Peridotite in the System NCFMASOCr. *J Petrology*, 56(5):869–892.
- JOCHUM, K. P., NOHL, U., HERWIG, K., LAMMEL, E., STOLL, B. et HOFMANN, A. W. (2005). GeoReM : A New Geochemical Database for Reference Materials and Isotopic Standards. *Geostand. Geoanalytical Res.*, 29(3):333–338.
- JOCHUM, K. P., WEIS, U., STOLL, B., KUZMIN, D., YANG, Q., RACZEK, I., JACOB, D. E., STRACKE, A., BIRBAUM, K., FRICK, D. A., GÜNTHER, D. et ENZWEILER, J. (2011). Determination of Reference Values for NIST SRM 610–617 Glasses Following ISO Guidelines. *Geostand. Geoanalytical Res.*, 35(4):397–429.
- JOLIVET, L. et BRUN, J.-P. (2010). Cenozoic geodynamic evolution of the Aegean. *Int J Earth Sci (Geol Rundsch)*, 99(1):109–138.
- JOLIVET, L. et FACCENNA, C. (2000). Mediterranean extension and the Africa-Eurasia collision. *Tectonics*, 19(6):1095–1106.
- JOUFFRAY, F., SPALLA, M., LARDEAUX, J., FILIPPI, M., REBAY, G., CORSINI, M., ZANONI, D., ZUCALI, M. et GOSSO, G. (2020). Variscan eclogites from the Argentera–Mercantour Massif (External Crystalline Massifs, SW Alps) : A dismembered cryptic suture zone. *Int J Earth Sci (Geol Rundsch)*.

BIBLIOGRAPHIE

- KALT, A. et ALTHERR, R. (1996). Metamorphic evolution of garnet-spinel peridotites from the Variscan Schwarzwald (Germany). *Geol Rundsch*, 85(2):211–224.
- KIRBY, S. H., WANG, K. et BROCHER, T. M. (2014). A large mantle water source for the northern San Andreas fault system : A ghost of subduction past. *Earth, Planets and Space*, 66(1):67.
- KOHN, M. J. (2020). A refined zirconium-in-rutile thermometer. *American Mineralogist*, 105(6):963–971.
- KOOIJMAN, E., SMIT, M. A., MEZGER, K. et BERNDT, J. (2012). Trace element systematics in granulite facies rutile : Implications for Zr geothermometry and provenance studies. *J. Metamorph. Geol.*, 30(4):397–412.
- KOSSMAT, F. (1927). Gliederung des varistischen Gebirgsbaues : Abhandlungen Sächsischen Geologischen Landesamts, v. 1.
- KOTKOVÁ, J., O'BRIEN, P. J. et ZIEMANN, M. A. (2011). Diamond and coesite discovered in Saxony-type granulite : Solution to the Variscan garnet peridotite enigma. *Geology*, 39(7):667–670.
- KRONER, U. et ROMER, R. L. (2013). Two plates—many subduction zones : The Variscan orogeny reconsidered. *Gondwana Res.*, 24(1):298–329.
- KUNZ, B. E., MANZOTTI, P., VON NIEDERHÄUSERN, B., ENGI, M., DARLING, J. R., GIUNTOLI, F. et LANARI, P. (2018). Permian high-temperature metamorphism in the Western Alps (NW Italy). *Int J Earth Sci (Geol Rundsch)*, 107(1):203–229.
- LADENHAUF, C., ARMSTRONG, R., KONZETT, J. et MILLER, C. (2001). The timing of pre-Alpine high pressure metamorphism in the Eastern Alps : Constraints from U–Pb SHRIMP dating of eclogite zircons from the Austroalpine Silvretta nappe. *In Journal of Conference Abstracts*, volume 6, page 600.
- LANARI, P., VHO, A., BOVAY, T., AIRAGHI, L. et CENTRELLA, S. (2018). Quantitative compositional mapping of mineral phases by electron probe micro-analyser. *Geol. Soc. Lond. Spec. Publ.*, 478:SP478.4.
- LANARI, P., VIDAL, O., DE ANDRADE, V., DUBACQ, B., LEWIN, E., GROSCH, E. G. et SCHWARTZ, S. (2014). XMapTools : A MATLAB©-based program for electron microprobe X-ray image processing and geothermobarometry. *Computers & Geosciences*, 62:227–240.

- LARDEAUX, J. M., SCHULMANN, K., FAURE, M., JANOUŠEK, V., LEXA, O., SKRZYPEK, E., EDEL, J. B. et ŠTÍPSKÁ, P. (2014). The moldanubian zone in the French Massif Central, Vosges/Schwarzwald and Bohemian Massif revisited : Differences and similarities. *Geol. Soc. Lond. Spec. Publ.*, 405(1):7–44.
- LARDEAUX, J.-M., SCHWARTZ, S., TRICART, P., PAUL, A., GUILLOT, S., BÉTHOUX, N. et MASSON, F. (2006). A crustal-scale cross-section of the south-western Alps combining geophysical and geological imagery. *Terra Nova*, 18(6):412–422.
- LAURENT, J. C. (1992). *Les Épisodes Magmatiques Filoniens Basiques Du Massif Des Ecrins-Pelvoux Entre Carbonifère et Lias*. Thèse de doctorat, Université Joseph-Fourier-Grenoble I.
- LAURENT, O., COUZINIÉ, S., ZEH, A., VANDERHAEGHE, O., MOYEN, J.-F., VILLAROS, A., GARDIEN, V. et CHELLE-MICHO, C. (2017). Protracted, coeval crust and mantle melting during Variscan late-orogenic evolution : U–Pb dating in the eastern French Massif Central. *Int J Earth Sci (Geol Rundsch)*, 106(2):421–451.
- LE FORT, P. (1971). *Géologie Du Haut-Dauphiné Cristallin (Alpes Française) : Etudes Pétrologique et Structurale de La Partie Occidentale*. Thèse de doctorat, Université Nancy I.
- LE ROUX, V., DASGUPTA, R. et LEE, C. T. A. (2011). Mineralogical heterogeneities in the Earth's mantle : Constraints from Mn, Co, Ni and Zn partitioning during partial melting. *Earth and Planetary Science Letters*, 307(3):395–408.
- LEDRU, P., COURRIOUX, G., DALLAIN, C., LARDEAUX, J. M., MONTEL, J. M., VANDERHAEGHE, O. et VITEL, G. (2001). The Velay dome (French Massif Central) : Melt generation and granite emplacement during orogenic evolution. *Tectonophysics*, 342(3):207–237.
- LELOUP, P. H., LACASSIN, R., TAPPONNIER, P., SCHÄRER, U., ZHONG, D., LIU, X., ZHANG, L., JI, S. et TRINH, P. T. (1995). The Ailao Shan-Red River shear zone (Yunnan, China), Tertiary transform boundary of Indochina. *Tectonophysics*, 251(1-4):3–84.
- LEMOINE, M., BAS, T., ARNAUD-VANNEAU, A., ARNAUD, H., DUMONT, T., GIDON, M., BOURBON, M., DE GRACIANSKY, P.-C., RUDKIEWICZ, J.-L., MEGARD-GALLI, J. et TRICART, P. (1986). The continental margin of the Mesozoic Tethys in the Western Alps. *Marine and Petroleum Geology*, 3(3):179–199.

BIBLIOGRAPHIE

- LEMOINE, M. et TRÜMPY, R. (1987). Pre-oceanic rifting in the alps. *Tectonophysics*, 133(3):305–320.
- LEXA, O., SCHULMANN, K., JANOUŠEK, V., ŠTÍPSKÁ, P., GUY, A. et RACEK, M. (2011). Heat sources and trigger mechanisms of exhumation of HP granulites in Variscan orogenic root : Heat sources and exhumation mechanisms. *J. Metamorph. Geol.*, 29(1):79–102.
- LIATI, A., GEBAUER, D. et FANNING, C. M. (2009). Geochronological evolution of HP metamorphic rocks of the Adula nappe, Central Alps, in pre-Alpine and Alpine subduction cycles. *J. Geol. Soc.*, 166(4):797–810.
- LIÉGEOIS, J.-P. et DUCHESNE, J.-C. (1981). The Lac Cornu retrograded eclogites (Aiguilles Rouges massif, Western Alps, France) : Evidence of crustal origin and metasomatic alteration. *Lithos*, 14(1):35–48.
- LINNEMANN, U., GERDES, A., DROST, K. et BUSCHMANN, B. (2007). The continuum between Cadomian orogenesis and opening of the Rheic Ocean : Constraints from LA-ICP-MS U-Pb zircon dating and analysis of plate-tectonic setting (Saxo-Thuringian zone, northeastern Bohemian Massif, Germany). *Spec. Pap. - Geol. Soc. Am.*, 423:61.
- LOTOUT, C., PITRA, P., POUJOL, M., ANCZKIEWICZ, R. et VAN DEN DRIESSCHE, J. (2018). Timing and duration of Variscan high-pressure metamorphism in the French Massif Central : A multimethod geochronological study from the Najac Massif. *Lithos*, 308–309:381–394.
- LOTOUT, C., POUJOL, M., PITRA, P., ANCZKIEWICZ, R. et VAN DEN DRIESSCHE, J. (2020). From Burial to Exhumation : Emplacement and Metamorphism of Mafic Eclogitic Terranes Constrained Through Multimethod Petrochronology, Case Study from the Lévézou Massif (French Massif Central, Variscan Belt). *J Petrology*, 61(4).
- LUAIS, B., TELOUK, P. et ALBARÉDE, F. (1997). Precise and accurate neodymium isotopic measurements by plasma-source mass spectrometry. *Geochim. Cosmochim. Acta*, 61(22):4847–4854.
- LUGMAIR, G. W. et MARTI, K. (1978). Lunar initial $^{143}\text{Nd}/^{144}\text{Nd}$: Differential evolution of the lunar crust and mantle. *Earth Planet. Sci. Lett.*, 39(3):349–357.
- LUVIZOTTO, G. L., ZACK, T., MEYER, H. P., LUDWIG, T., TRIEBOLD, S., KRONZ, A., MÜNKER, C., STOCKLI, D. F., PROWATKE, S., KLEMME, S., JACOB, D. E. et VON EYNATTEN,

- H. (2009). Rutile crystals as potential trace element and isotope mineral standards for microanalysis. *Chemical Geology*, 261(3):346–369.
- LYU, C., PEDERSEN, H. A., PAUL, A., ZHAO, L. et SOLARINO, S. (2017). Shear wave velocities in the upper mantle of the Western Alps : New constraints using array analysis of seismic surface waves. *Geophys J Int*, 210(1):321–331.
- MAIEROVÁ, P., SCHULMANN, K. et GERYA, T. (2018). Relamination Styles in Collisional Orogens. *Tectonics*, 37(1):224–250.
- MAIEROVÁ, P., SCHULMANN, K., LEXA, O., GUILLOT, S., ŠTÍPSKÁ, P., JANOUŠEK, V. et ČADEK, O. (2016). European Variscan orogenic evolution as an analogue of Tibetan-Himalayan orogen : Insights from petrology and numerical modeling : Variscan and Himalayan Orogenies. *Tectonics*, 35(7):1760–1780.
- MAIEROVÁ, P., SCHULMANN, K., ŠTÍPSKÁ, P., GERYA, T. et LEXA, O. (2021). Trans-lithospheric diapirism explains the presence of ultra-high pressure rocks in the European Variscides. *Commun Earth Environ*, 2(1):56.
- MALASPINA, N., HERMANN, J. et SCAMBELLURI, M. (2009). Fluid/mineral interaction in UHP garnet peridotite. *Lithos*, 107(1):38–52.
- MALUSÀ, M. G., GUILLOT, S., ZHAO, L., PAUL, A., SOLARINO, S., DUMONT, T., SCHWARTZ, S., AUBERT, C., BACCHESCHI, P., EVA, E., LU, Y., LYU, C., PONDRELLI, S., SALIMBENI, S., SUN, W. et YUAN, H. (2021). The Deep Structure of the Alps Based on the CIFALPS Seismic Experiment : A Synthesis. *Geochem. Geophys. Geosystems*, 22(3):e2020GC009466.
- MANTOVANI, E., VITI, M., BABBUCCI, D., TAMBURELLI, C. et CENNI, N. (2020). Geodynamics of the central-western Mediterranean region : Plausible and non-plausible driving forces. *Marine and Petroleum Geology*, 113:104121.
- MANZOTTI, P., BALLÈVRE, M. et POUJOL, M. (2016). Detrital zircon geochronology in the Dora-Maira and Zone Houillère : A record of sediment travel paths in the Carboniferous. *Terra Nova*, 28(4):279–288.
- MANZOTTI, P., RUBATTO, D., ZUCALI, M., KORH, A. E., CENKI-TOK, B., BALLÈVRE, M. et ENGI, M. (2018). Permian magmatism and metamorphism in the Dent Blanche nappe : Constraints from field observations and geochronology. *Swiss J Geosci*, 111(1-2):79–97.

BIBLIOGRAPHIE

- MARQUER, D., CALCAGNO, P., BARFETY, J.-C. et BAUDIN, T. (2006). 3D Modeling and Kinematics of the External Zone of the French Western Alps (Belledonne and Grand Châtelard Massifs, Maurienne Valley, Savoie). *Eclogae geol. Helv.*, 99(2):211–222.
- MARTÍNEZ CATALÁN, J. R., COLLETT, S., SCHULMANN, K., ALEKSANDROWSKI, P. et MAZUR, S. (2020). Correlation of allochthonous terranes and major tectonostratigraphic domains between NW Iberia and the Bohemian Massif, European Variscan belt. *Int J Earth Sci (Geol Rundsch)*, 109(4):1105–1131.
- MARTÍNEZ CATALÁN, J. R., SCHULMANN, K. et GHIENNE, J.-F. (2021). The Mid-Variscan Allochthon : Keys from correlation, partial retrodeformation and plate-tectonic reconstruction to unlock the geometry of a non-cylindrical belt. *Earth-Science Reviews*, 220:103700.
- MARUYAMA, S. (1996). Blueschist/Eclogites of the world and their exhumation. *Int. Geol. Rev.*, 38:490–596.
- MASINI, E., MANATSCHAL, G. et MOHN, G. (2013). The Alpine Tethys rifted margins : Reconciling old and new ideas to understand the stratigraphic architecture of magma-poor rifted margins. *Sedimentology*, 60(1):174–196.
- MATTE, P. (1986). Tectonics and plate tectonics model for the Variscan belt of Europe. *Tectonophysics*, 126(2-4):329–374.
- MATTE, P. (1991). Accretionary history and crustal evolution of the Variscan belt in Western Europe. *Tectonophysics*, 196(3):309–337.
- MATTE, P. (2001). The Variscan collage and orogeny (480–290 Ma) and the tectonic definition of the Armorica microplate : A review. *Terra Nova*, 13(2):122–128.
- MCDONOUGH, W. et SUN, S.-s. (1995). The composition of the Earth. *Chemical Geology*, 120(3-4):223–253.
- MEDARIS, G., ACKERMAN, L., JELÍNEK, E., MICHELS, Z. D., ERBAN, V. et KOTKOVÁ, J. (2015). Depletion, cryptic metasomatism, and modal metasomatism (refertilization) of Variscan lithospheric mantle : Evidence from major elements, trace elements, and Sr-Nd-Os isotopes in a Saxothuringian garnet peridotite. *Lithos*, 226:81–97.
- MEDARIS, G., WANG, H., JELÍNEK, E., MIHALJEVIČ, M. et JAKEŠ, P. (2005). Characteristics and origins of diverse Variscan peridotites in the Gföhl Nappe, Bohemian Massif, Czech Republic. *Lithos*, 82(1):1–23.

- MÉNOT, R.-P. (1986). Les formations plutono-volcaniques dévoniennes de Rioupéroux-Livet (Massifs cristallins externes des Alpes Françaises) : Nouvelles définitions lithostratigraphique et pétrographique. *Schweiz. Mineral. Petrogr. Mitt*, 66(1-2):229–258.
- MÉNOT, R.-P. (1987a). Magmatismes et structuration orogénique paléozoïques de la chaîne de Belledonne (Massifs cristallins externes alpins). Le domaine sud - occidental. *Géol. alp. (Grenoble)*, 63:55–93.
- MÉNOT, R.-P. (1987b). *Magmatismes Paléozoïques et Structuration Carbonifère Du Massif de Belledonne (Alpes Françaises). Contraintes Nouvelles Pour Les Schémas d'évolution de La Chaîne Varisque Ouest-Européenne*. Thèse de doctorat, Université Claude Bernard Lyon 1.
- MÉNOT, R.-P., BONHOMME, M. G. et VIVIER, G. (1987). Structuration tectono-métamorphique carbonifère dans le massif de Belledonne (Alpes Occidentales françaises), apport de la géochronologie K/Ar des amphiboles. *Schweiz. Mineral. Petrogr. Mitteilungen*, 67(3):273–284.
- MÉNOT, R.-P., PEUCAT, J. J., SCARENZI, D. et PIBOULE, M. (1988). 496 My age of plagiogranites in the Chamrousse ophiolite complex (external crystalline massifs in the French Alps) : Evidence of a Lower Paleozoic oceanization. *Earth Planet. Sci. Lett.*, 88(1-2):82–92.
- MILLER, C. et THÖNI, M. (1995). Origin of eclogites from the Austroalpine Ötztal basement (Tirol, Austria) : Geochemistry and Sm-Nd vs. Rb-Sr isotope systematics. *Chemical Geology*, 122(1):199–225.
- MOYEN, J.-F. (2019). Granites and crustal heat budget. *Geol. Soc. Lond. Spec. Publ.*, 491:SP491–2018–148.
- MOYEN, J. F., LAURENT, O., CHELLE-MICHO, C., COUZINIÉ, S., VANDERHAEGHE, O., ZEH, A., VILLAROS, A. et GARDIEN, V. (2017). Collision vs. subduction-related magmatism : Two contrasting ways of granite formation and implications for crustal growth. *Lithos*, 277:154–177.
- NAEMURA, K., HIRAJIMA, T. et SVOJTKA, M. (2009). The Pressure–Temperature Path and the Origin of Phlogopite in Spinel–Garnet Peridotites from the Blanský Les Massif of the Moldanubian Zone, Czech Republic. *Journal of Petrology*, 50(10):1795–1827.

BIBLIOGRAPHIE

- NANCE, R. D., GUTIÉRREZ-ALONSO, G., KEPPIE, J. D., LINNEMANN, U., MURPHY, J. B., QUESADA, C., STRACHAN, R. A. et WOODCOCK, N. H. (2010). Evolution of the Rheic Ocean. *Gondwana Research*, 17(2):194–222.
- NEGGA, H. S. (1984). *Comportement de l'uranium lors des métamorphismes tardi-hercinien et alpin dans les massifs des Aiguilles rouges et de Belledone (Vallorcine, Lauzière). Alpes occidentales*. Thèse de doctorat, Université de Lorraine.
- NEUBAUER, F. (1989). Pre-Alpine terranes and tectonic zoning in the eastern Alps. *Terranes Circum-Atl. Paleoz. Orogens*, 230:91.
- NEUBAUER, F., FRIED, G., GENSER, J., HANDLER, R., MADER, D. et SCHNEIDER, D. (2007). Origin and tectonic evolution of the Eastern Alps deduced from dating of detrital white mica : A review. *Austrian J. Earth Sci.*, 100.
- NEUBAUER, F., FRISCH, W., SCHMEROLD, R. et SCHLÖSER, H. (1989). Metamorphosed and dismembered ophiolite suites in the basement units of the Eastern Alps. *Tectonophysics*, 164(1):49–62.
- NEUBAUER, F., LIU, Y., CHANG, R., YUAN, S., YU, S., GENSER, J., LIU, B. et GUAN, Q. (2020). The Wechsel Gneiss Complex of Eastern Alps : An Ediacaran to Cambrian continental arc and its Early Proterozoic hinterland. *Swiss Journal of Geosciences*, 113(1): 21.
- NICKEL, K. et GREEN, D. (1985). Empirical geothermobarometry for garnet peridotites and implications for the nature of the lithosphere, kimberlites and diamonds. *Earth and Planetary Science Letters*, 73(1):158–170.
- NIMIS, P. et GRÜTTER, H. (2010). Internally consistent geothermometers for garnet peridotites and pyroxenites. *Contrib Mineral Petrol*, 159(3):411–427.
- NOUBAT, A., STEHLY, L., PAUL, A., BROSSIER, R., BODIN, T., SCHWARTZ, S. et ALPARRAY WORKING GROUP (2021). First step towards an integrated geophysical-geological model of the W-Alps : A new Vs model from transdimensional ambient-noise tomography. pages EGU21–3197.
- NOWLAN, E. U., SCHERTL, H.-P. et SCHREYER, W. (2000). Garnet–omphacite–phengite thermobarometry of eclogites from the coesite-bearing unit of the southern Dora-Maira Massif, Western Alps. *Lithos*, 52(1-4):197–214.

- OBATA, M. (2011). Kelyphite and symplectite : Textural and mineralogical diversities and universality, and a new dynamic view of their structural formation. *In* SHARKOV, E., éditeur : *New Frontiers in Tectonic Research - General Problems, Sedimentary Basins and Island Arcs*. InTech.
- O'BRIEN, P. J. (2000). The fundamental Variscan problem : High-temperature metamorphism at different depths and high-pressure metamorphism at different temperatures. *Geol. Soc. Lond. Spec. Publ.*, 179(1):369–386.
- O'BRIEN, P. J. (2019). Eclogites and other high-pressure rocks in the Himalaya : A review. *Geol. Soc. Lond. Spec. Publ.*, 483(1):183–213.
- O'BRIEN, P. J. et RÖTZLER, J. (2003). High-pressure granulites : Formation, recovery of peak conditions and implications for tectonics. *J. Metamorph. Geol.*, 21(1):3–20.
- OLIVER, R. A. (1994). *Géologie et Géochimie Des Granitoïdes et Des Roches Basique Associées Du Valsenestre : Place Dans La Province Magmatique Varisque Des Massifs Crystallins Externes Du Haut Dauphiné (Alpes Occidentales Françaises)*. Theses, Université Joseph-Fourier - Grenoble I.
- PALME, H. et O'NEILL, H. S. (2004). C. 2014. Cosmochemical estimates of mantle composition. *Treatise Geochem. Oxf. Elsevier-Pergamon*, pages 1–39.
- PAPE, J., MEZGER, K. et ROBYR, M. (2016). A systematic evaluation of the Zr-in-rutile thermometer in ultra-high temperature (UHT) rocks. *Contrib Mineral Petrol*, 171(5):44.
- PAQUETTE, J., MENOT, R. et PEUCAT, J. (1989). REE, Sm-Nd and U-Pb zircon study of eclogites from the Alpine External Massifs (Western Alps) : Evidence for crustal contamination. *Earth Planet. Sci. Lett.*, 96(1-2):181–198.
- PAQUETTE, J.-L., BALLÈVRE, M., PEUCAT, J.-J. et CORNEN, G. (2017). From opening to subduction of an oceanic domain constrained by LA-ICP-MS U-Pb zircon dating (Variscan belt, Southern Armorican Massif, France). *Lithos*, 294–295:418–437.
- PAQUETTE, J.-L., MONCHOUX, P. et COUTURIER, M. (1995). Geochemical and isotopic study of a norite-eclogite transition in the European Variscan belt : Implications for U Pb zircon systematics in metabasic rocks. *Geochim. Cosmochim. Acta*, 59(8):1611–1622.
- PARAT, F., HOLTZ, F., RENE, M. et ALMEEV, R. (2010). Experimental constraints on ultrapotassic magmatism from the Bohemian Massif (durbachite series, Czech Republic). *Contrib Miner. Pet.*, page 17.

BIBLIOGRAPHIE

- PATON, C., HELLSTROM, J., PAUL, B., WOODHEAD, J. et HERGT, J. (2011). Iolite : Free-ware for the visualisation and processing of mass spectrometric data. *J. Anal. At. Spectrom.*, 26(12):2508–2518.
- PAULICK, H., BACH, W., GODARD, M., DE HOOG, J., SUHR, G. et HARVEY, J. (2006). Geochemistry of abyssal peridotites (Mid-Atlantic Ridge, 15 20'N, ODP Leg 209) : Implications for fluid/rock interaction in slow spreading environments. *Chemical Geology*, 234(3-4):179–210.
- PEARCE, J. (1982). Trace element characteristics of lavas from destructive plate boundaries. *Andesites*, 8:525–548.
- PEARCE, J. A. (2008). Geochemical fingerprinting of oceanic basalts with applications to ophiolite classification and the search for Archean oceanic crust. *Lithos*, 100(1):14–48.
- PECCERILLO, A. (1992). Potassic and ultrapotassic rocks : Compositional characteristics, petrogenesis, and geologic significance. *Episodes J. Int. Geosci.*, 15(4):243–251.
- PECCERILLO, A. et TAYLOR, S. R. (1976). Geochemistry of eocene calc-alkaline volcanic rocks from the Kastamonu area, Northern Turkey. *Contr. Mineral. and Petrol.*, 58(1):63–81.
- PECHER, A. (1970). Etude pétrographique de la partie orientale du massif des Ecrins-Pelvoux : le socle ancien - Alpes françaises.
- PENNISTON-DORLAND, S. C., KOHN, M. J. et MANNING, C. E. (2015). The global range of subduction zone thermal structures from exhumed blueschists and eclogites : Rocks are hotter than models. *Earth and Planetary Science Letters*, 428:243–254.
- PEŠIĆ, L., RAMOVŠ, A., SREMAC, J., PANTIĆ-PRODANOVIĆ, S., FILIPOVIĆ, I. et KOVACS, S. . P. (1988). Upper Permian deposits of the Jadar region and their position within the western Palaeotethys. *Mem. Della Soc. Geol. Ital.*, 34 (1986):211–219.
- PIN, C., BRIOT, D., BASSIN, C. et POITRASSON, F. (1994). Concomitant separation of strontium and samarium-neodymium for isotopic analysis in silicate samples, based on specific extraction chromatography. *Anal. Chim. Acta*, 298(2):209–217.
- PIN, C. et CARME, F. (1987). A Sm-Nd isotopic study of 500 Ma old oceanic crust in the Variscan belt of Western Europe : The Chamrousse ophiolite complex, Western Alps (France). *Contrib. Mineral. Petrol.*, 96(3):406–413.

- PIN, C. et MARINI, F. (1993). Early Ordovician continental break-up in Variscan Europe : Nd-Sr isotope and trace element evidence from bimodal igneous associations of the Southern Massif Central, France. *Lithos*, 29(3):177–196.
- PIN, C. et PAQUETTE, J.-L. (1997). A mantle-derived bimodal suite in the Hercynian Belt : Nd isotope and trace element evidence for a subduction-related rift origin of the Late Devonian Brévenne metavolcanics, Massif Central (France). *Contrib Mineral Petrol*, 129(2):222–238.
- PIN, C. et ZALDUEGUI, J. S. (1997). Sequential separation of light rare-earth elements, thorium and uranium by miniaturized extraction chromatography : Application to isotopic analyses of silicate rocks. *Anal. Chim. Acta*, 339(1-2):79–89.
- PITRA, P., POUJOL, M., VAN DEN DRIESSCHE, J., BRETAGNE, E., LOTOUT, C., COGNÉ, N. et HARLEY, S. (2021). Late Variscan (315 Ma) subduction or deceptive zircon REE patterns and U–Pb dates from migmatite-hosted eclogites ? (Montagne Noire, France). *J Metamorph Geol*, page jmg.12609.
- PONCERRY, E. (1981). *Contribution à l'étude géologique des granitoïdes de Vallorcine, Beaufort, Lauzière, de leur encaissant et des minéralisations uranifères associées. Alpes Françaises*. Thèse de doctorat, Université Scientifique et Médicale de Grenoble.
- PUTIRKA, K. D. (2008). Thermometers and Barometers for Volcanic Systems. *Reviews in Mineralogy and Geochemistry*, 69(1):61–120.
- PUTIRKA, K. D., MIKAELIAN, H., RYERSON, F. et SHAW, H. (2003). New clinopyroxene-liquid thermobarometers for mafic, evolved, and volatile-bearing lava compositions, with applications to lavas from Tibet and the Snake River Plain, Idaho. *Am. Mineral.*, 88(10): 1542–1554.
- RABIN, M., TRAP, P., CARRY, N., FRÉVILLE, K., CENKI-TOK, B., LOBJOIE, C., GONCALVES, P. et MARQUER, D. (2015). Strain partitioning along the anatexis front in the Variscan Montagne Noire massif (southern French Massif Central) : Anatexis Front and Strain Partitioning. *Tectonics*, 34(8):1709–1735.
- RIGHTER, K. et CARMICHAEL, I. S. E. (1996). Phase equilibria of phlogopite lamprophyres from western Mexico : Biotite-liquid equilibria and P - T estimates for biotite-bearing igneous rocks. *Contributions to Mineralogy and Petrology*, 123(1):1–21.

BIBLIOGRAPHIE

- ROSSI, P. et COCHERIE, A. (1991). Genesis of a Variscan batholith : Field, petrological and mineralogical evidence from the Corsica-Sardinia batholith. *Tectonophysics*, 195(2):319–346.
- ROSSI, P., OGGIANO, G. et COCHERIE, A. (2009). A restored section of the “southern Variscan realm” across the Corsica–Sardinia microcontinent. *Comptes Rendus Geosci.*, 341(2-3):224–238.
- RUBATTO, D. (2002). Zircon trace element geochemistry : Partitioning with garnet and the link between U–Pb ages and metamorphism. *Chemical Geology*, 184(1):123–138.
- RUBATTO, D. (2017). Zircon : The metamorphic mineral. *Rev. Mineral. Geochem.*, 83(1): 261–295.
- RUBATTO, D., FERRANDO, S., COMPAGNONI, R. et LOMBARDO, B. (2010). Carboniferous high-pressure metamorphism of Ordovician protoliths in the Argentera Massif (Italy), Southern European Variscan belt. *Lithos*, 116(1-2):65–76.
- RUBATTO, D., GEBAUER, D. et COMPAGNONI, R. (1999). Dating of eclogite-facies zircons : The age of Alpine metamorphism in the Sesia–Lanzo Zone (Western Alps). *Earth and Planetary Science Letters*, 167(3):141–158.
- RUBATTO, D., HERMANN, J., BERGER, A. et ENGI, M. (2009). Protracted fluid-induced melting during Barrovian metamorphism in the Central Alps. *Contrib Miner. Pet.*, page 20.
- RUBATTO, D., MÜNTENER, O., BARNHOORN, A. et GREGORY, C. (2008). Dissolution-precipitation of zircon at low-temperature, high-pressure conditions (Lanzo Massif, Italy). *American Mineralogist*, 93(10):1519–1529.
- RUBATTO, D., SCHALTEGGER, U., LOMBARDO, D., COLOMBO, F. et COMPAGNONI, R. (2001). Complex Paleozoic magmatic and metamorphic evolution in the Argentera massif (Western Alps), resolved with U–Pb dating. *Schweiz. Mineral. Petrogr. Mitteilungen*, 81:213–228.
- SANDMANN, S., NAGEL, T. J., HERWARTZ, D., FONSECA, R. O. C., KURZAWSKI, R. M., MÜNKER, C. et FROITZHEIM, N. (2014). Lu–Hf garnet systematics of a polymetamorphic basement unit : New evidence for coherent exhumation of the Adula Nappe (Central Alps) from eclogite-facies conditions. *Contrib Mineral Petrol*, 168(5):1075.

- SANTALLIER, D., BRIAND, B., MENOT, R. P. et PIBOULE, M. (1988). Les complexes leptyno-amphiboliques (CLA) : Revue critique et suggestions pour un meilleur emploi de ce terme. *Bull. Société Géologique Fr.*, 4(1):3–12.
- SCAMBELLURI, M., HERMANN, J., MORTEN, L. et RAMPONE, E. (2006). Melt- versus fluid-induced metasomatism in spinel to garnet wedge peridotites (Ulten Zone, Eastern Italian Alps) : Clues from trace element and Li abundances. *Contrib Mineral Petrol*, 151(4):372–394.
- SCHALTEGGER, U. et CORFU, F. (1992). The age and source of late Hercynian magmatism in the central Alps : Evidence from precise U-Pb ages and initial Hf isotopes. *Contr. Mineral. and Petrol.*, 111(3):329–344.
- SCHALTEGGER, U., NÄGLER, T., CORFU, F., MAGGETTI, M., GALETTI, G. et STOSCH, H. G. (1997). A Cambrian island arc in the Silvretta nappe : Constraints from geochemistry and geochronology. *Schweiz. Mineral. Petrogr. Mitteilungen*, 77(3):337–350.
- SCHANTL, P., HAUZENBERGER, C., FINGER, F., MÜLLER, T. et LINNER, M. (2019). New evidence for the prograde and retrograde PT-path of high-pressure granulites, Moldanubian Zone, Lower Austria, by Zr-in-rutile thermometry and garnet diffusion modelling. *Lithos*, 342–343:420–439.
- SCHILLER, D. et FINGER, F. (2019). Application of Ti-in-zircon thermometry to granite studies : Problems and possible solutions. *Contrib Mineral Petrol*, 174(6):51.
- SCHMID, S. M., FÜGENSCHUH, B., KISSLING, E. et SCHUSTER, R. (2004). Tectonic map and overall architecture of the Alpine orogen. *Eclogae Geol. Helvetiae*, 97(1):93–117.
- SCHULMANN, K., KONOPÁSEK, J., JANOUŠEK, V., LEXA, O., LARDEAUX, J.-M., EDEL, J.-B., ŠTÍPSKÁ, P. et ULRICH, S. (2009). An Andean type Palaeozoic convergence in the Bohemian Massif. *Comptes Rendus Geoscience*, 341(2):266–286.
- SCHULMANN, K., KRÖNER, A., HEGNER, E., WENDT, I., KONOPÁSEK, J., LEXA, O. et ŠTÍPSKÁ, P. (2005). Chronological constraints on the pre-orogenic history, burial and exhumation of deep-seated rocks along the eastern margin of the Variscan Orogen, Bohemian Massif, Czech Republic. *Am J Sci*, 305(5):407–448.
- SCHULMANN, K., LEXA, O., JANOUŠEK, V., LARDEAUX, J.-M. et EDEL, J.-B. (2014). Anatomy of a diffuse cryptic suture zone : An example from the Bohemian Massif, European Variscides. *Geology*, 42(4):275–278.

- SCHULMANN, K., LEXA, O., ŠTÍPSKÁ, P., RACEK, M., TAJČMANOVÁ, L., KONOPÁSEK, J., EDEL, J.-B., PESCHLER, A. et LEHMANN, J. (2008). Vertical extrusion and horizontal channel flow of orogenic lower crust : Key exhumation mechanisms in large hot orogens? *J. Metamorph. Geol.*, 26(2):273–297.
- SHAIL, R. K. et LEVERIDGE, B. E. (2009). The Rhenohercynian passive margin of SW England : Development, inversion and extensional reactivation. *Comptes Rendus Geoscience*, 341(2):140–155.
- SHAND, S. J. (1947). *Eruptive Rocks : Their Genesis, Composition, Classification, and Their Relation to Ore-Deposits, with a Chapter on Meteorites*. T. Murby.
- SIMANCAS, J. F., CARBONELL, R., GONZÁLEZ LODEIRO, F., PÉREZ ESTAÚN, A., JUHLIN, C., AYARZA, P., KASHUBIN, A., AZOR, A., MARTÍNEZ POYATOS, D., ALMODÓVAR, G. R., PASCUAL, E., SÁEZ, R. et EXPÓSITO, I. (2003). Crustal structure of the transpressional Variscan orogen of SW Iberia : SW Iberia deep seismic reflection profile (IBERSEIS). *Tectonics*, 22(6).
- SIMEON, Y. (1979). *Etude pétrologique, géochimique et structurale des terrains cristallins de Belledonne entre l'Arc et l'Isère (Alpes françaises)*. Thèse de doctorat, Université Scientifique et Médicale de Grenoble.
- SIMON-LABRIC, T., ROLLAND, Y., DUMONT, T., HEYMES, T., AUTHEMAYOU, C., CORSINI, M. et FORNARI, M. (2009). $^{40}\text{Ar}/^{39}\text{Ar}$ dating of Penninic Front tectonic displacement (W Alps) during the Lower Oligocene (31–34 Ma). *Terra Nova*, 21(2):127–136.
- SIMONETTI, M., CAROSI, R., MONTOMOLI, C., COTTLE, J. M. et LAW, R. D. (2020). Transpressive Deformation in the Southern European Variscan Belt : New Insights From the Aiguilles Rouges Massif (Western Alps). *Tectonics*, 39(6):e2020TC006153.
- SIMONETTI, M., CAROSI, R., MONTOMOLI, C., LANGONE, A., D'ADDARIO, E. et MAMMOLITI, E. (2018). Kinematic and geochronological constraints on shear deformation in the Ferriere-Mollières shear zone (Argentera-Mercantour Massif, Western Alps) : Implications for the evolution of the Southern European Variscan Belt. *Int J Earth Sci (Geol Rundsch)*, 107(6):2163–2189.
- SIZOVA, E., HAUZENBERGER, C., FRITZ, H., FARYAD, S. W. et GERYA, T. (2019). Late Orogenic Heating of (Ultra)High Pressure Rocks : Slab Rollback vs. Slab Breakoff. *Geosciences*, 9(12):499.

- SKRZYPEK, E., ŠTÍPSKÁ, P. et COCHERIE, A. (2012). The origin of zircon and the significance of U–Pb ages in high-grade metamorphic rocks : A case study from the Variscan orogenic root (Vosges Mountains, NE France). *Contrib Mineral Petrol*, 164(6):935–957.
- SLÁMA, J., KOŠLER, J., CONDON, D. J., CROWLEY, J. L., GERDES, A., HANCHAR, J. M., HORSTWOOD, M. S. A., MORRIS, G. A., NASDALA, L., NORBERG, N., SCHALTEGGER, U., SCHOENE, B., TUBRETT, M. N. et WHITEHOUSE, M. J. (2008). Plešovice zircon — A new natural reference material for U–Pb and Hf isotopic microanalysis. *Chemical Geology*, 249(1):1–35.
- SODER, C. G. et ROMER, R. L. (2018). Post-collisional Potassic–Ultrapotassic Magmatism of the Variscan Orogen : Implications for Mantle Metasomatism during Continental Subduction. *Journal of Petrology*, 59(6):1007–1034.
- SOLARINO, S., MALUSÀ, M. G., EVA, E., GUILLOT, S., PAUL, A., SCHWARTZ, S., ZHAO, L., AUBERT, C., DUMONT, T., PONDRELLI, S., SALIMBENI, S., WANG, Q., XU, X., ZHENG, T. et ZHU, R. (2018). Mantle wedge exhumation beneath the Dora-Maira (U)HP dome unravelled by local earthquake tomography (Western Alps). *Lithos*, 296–299:623–636.
- SPALLA, M. I., ZANONI, D., MAROTTA, A. M., REBAY, G., RODA, M., ZUCALI, M. et GOSSO, G. (2014). The transition from Variscan collision to continental break-up in the Alps : Insights from the comparison between natural data and numerical model predictions. *Geological Society, London, Special Publications*, 405(1):363–400.
- SPEAR, F. S. (1981). Amphibole-plagioclase equilibria : An empirical model for the relation albite+ tremolite= edenite+ 4 quartz. *Contrib. Mineral. Petrol.*, 77(4):355–364.
- SPEAR, F. S. et SPEAR, F. S. (1995). Metamorphic phase equilibria and pressure-temperature-time paths.
- STACEY, J. et KRAMERS, J. (1975). Approximation of terrestrial lead isotope evolution by a two-stage model. *Earth Planet. Sci. Lett.*, 26(2):207–221.
- STAMPFLI, G. M. et HOCHARD, C. (2009). Plate tectonics of the Alpine realm. *Geol. Soc. Lond. Spec. Publ.*, 327(1):89–111.
- STAMPFLI, G. M., HOCHARD, C., VÉRARD, C. et WILHEM, C. (2013). The formation of Pangea. *Tectonophysics*, 593:1–19.

- STAMPFLI, G. M., VON RAUMER, J. et WILHEM, C. (2011). The distribution of Gondwana-derived terranes in the Early Palaeozoic. *In Ordovician of the World*, volume 14, pages 567–574. Instituto Geológico y Minero de España.
- STEIGER, R. et JÄGER, E. (1977). Subcommittee on geochronology : Convention on the use of decay constants in geo- and cosmochronology. *Earth and Planetary Science Letters*, 36(3):359–362.
- STEPHAN, T., KRONER, U. et ROMER, R. L. (2019a). The pre-orogenic detrital zircon record of the Peri-Gondwanan crust. *Geol. Mag.*, 156(2):281–307.
- STEPHAN, T., KRONER, U., ROMER, R. L. et RÖSEL, D. (2019b). From a bipartite Gondwanan shelf to an arcuate Variscan belt : The early Paleozoic evolution of northern Peri-Gondwana. *Earth-Science Reviews*, 192:491–512.
- ŠTÍPSKÁ, P., POWELL, R., HACKER, B. R., HOLDER, R. et KYLANDER-CLARK, A. R. C. (2016). Uncoupled U/Pb and REE response in zircon during the transformation of eclogite to mafic and intermediate granulite (Blanský les, Bohemian Massif). *J. Metamorph. Geol.*, 34(6):551–572.
- ŠTÍPSKÁ, P., SCHULMANN, K. et KRÖNER, A. (2004). Vertical extrusion and middle crustal spreading of omphacite granulite : A model of syn-convergent exhumation (Bohemian Massif, Czech Republic). *J. Metamorph. Geol.*, 22(3):179–198.
- SUESS, E. (1909). *Das Antlitz Der Erde*, volume 3. F. Tempsky.
- SUN, S.-S. et McDONOUGH, W. F. (1989). Chemical and isotopic systematics of oceanic basalts : Implications for mantle composition and processes. *Geol. Soc. Lond. Spec. Publ.*, 42(1):313–345.
- TABAUD, A.-S., JANOUŠEK, V., SKRZYPEK, E., SCHULMANN, K., ROSSI, P., WHITECHURCH, H., GUERROT, C. et PAQUETTE, J.-L. (2015). Chronology, petrogenesis and heat sources for successive Carboniferous magmatic events in the Southern–Central Variscan Vosges Mts (NE France). *J. Geol. Soc.*, 172(1):87–102.
- TALBOT, J.-Y., FAURE, M., CHEN, Y. et MARTELET, G. (2005). Pull-apart emplacement of the Margeride granitic complex (French Massif Central). Implications for the late evolution of the Variscan orogen. *Journal of Structural Geology*, 27(9):1610–1629.

- TANAKA, T., TOGASHI, S., KAMIOKA, H., AMAKAWA, H., KAGAMI, H., HAMAMOTO, T., YUHARA, M., ORIHASHI, Y., YONEDA, S. et SHIMIZU, H. (2000). JNdi-1 : A neodymium isotopic reference in consistency with LaJolla neodymium. *Chem. Geol.*, 168(3-4):279–281.
- TAPPONNIER, P., PELTZER, G. et ARMIJO, R. (1986). On the mechanics of the collision between India and Asia. *Geol. Soc. Lond. Spec. Publ.*, 19(1):113–157.
- TAPPONNIER, P., PELTZER, G., LE DAIN, A. Y., ARMIJO, R. et COBBOLD, P. (1982). Propagating extrusion tectonics in Asia : New insights from simple experiments with plasticine. *Geology*, 10(12):611–616.
- TAYLOR, S. R. et MCLENNAN, S. M. (1995). The geochemical evolution of the continental crust. *Rev. Geophys.*, 33(2):241–265.
- TAYLOR, W. R. (1998). An experimental test of some geothermometer and geobarometer formulations for upper mantle peridotites with application to the thermobarometry of fertile lherzolite and garnet websterite. *Neues Jahrb. Für Mineral. - Abh.*, pages 381–408.
- THOMPSON, A. B. et ENGLAND, P. C. (1984). Pressure—Temperature—Time Paths of Regional Metamorphism II. Their Inference and Interpretation using Mineral Assemblages in Metamorphic Rocks. *Journal of Petrology*, 25(4):929–955.
- THOMPSON, A. B., SCHULMANN, K. et JEZEK, J. (1997). Thermal evolution and exhumation in obliquely convergent (transpressive) orogens. *Tectonophysics*, 280(1-2):171–184.
- THÖNI, M. (2006). Dating eclogite-facies metamorphism in the Eastern Alps—approaches, results, interpretations : A review. *Mineral. Petrol.*, 88(1-2):123–148.
- THÖNI, M., MILLER, C., Blichert-Toft, J., WHITEHOUSE, M. J., KONZETT, J. et ZANNETTI, A. (2008). Timing of high-pressure metamorphism and exhumation of the eclogite type-locality (Kupplerbrunn–Prickler Halt, Saualpe, south-eastern Austria) : Constraints from correlations of the Sm–Nd, Lu–Hf, U–Pb and Rb–Sr isotopic systems. *J. Metamorph. Geol.*, 26(5):561–581.
- TIKOFF, B. et TEYSSIER, C. (1994). Strain modeling of displacement-field partitioning in transpressional orogens. *Journal of Structural Geology*, 16(11):1575–1588.
- TODD, C. S. et ENGI, M. (1997). Metamorphic field gradients in the Central Alps. *J. Metamorph. Geol.*, 15(4):513–530.

BIBLIOGRAPHIE

- TUMIATI, S., THÖNI, M., NIMIS, P., MARTIN, S. et MAIR, V. (2003). Mantle–crust interactions during Variscan subduction in the Eastern Alps (Nonsberg–Ulten zone) : Geochronology and new petrological constraints. *Earth Planet. Sci. Lett.*, 210(3-4):509–526.
- USUKI, T., IIZUKA, Y., HIRAJIMA, T., SVOJTKA, M., LEE, H.-Y. et JAHN, B.-M. (2017). Significance of Zr-in-Rutile Thermometry for Deducing the Decompression P–T Path of a Garnet–Clinopyroxene Granulite in the Moldanubian Zone of the Bohemian Massif. *J. Petrol.*, 58(6):1173–1198.
- VALLI, F., ARNAUD, N., LELOUP, P. H., SOBEL, E. R., MAHÉO, G., LACASSIN, R., GUILLOT, S., LI, H., TAPPONNIER, P. et XU, Z. (2007). Twenty million years of continuous deformation along the Karakorum fault, western Tibet : A thermochronological analysis. *Tectonics*, 26(4):n/a–n/a.
- VALLI, F., LELOUP, P. H., PAQUETTE, J.-L., ARNAUD, N., LI, H., TAPPONNIER, P., LACASSIN, R., GUILLOT, S., LIU, D., DELOULE, E., XU, Z. et MAHÉO, G. (2008). New U-Th/Pb constraints on timing of shearing and long-term slip-rate on the Karakorum fault. *Tectonics*, 27(5):n/a–n/a.
- VAN DER BEEK, P. A., VALLA, P. G., HERMAN, F., BRAUN, J., PERSANO, C., DOBSON, K. J. et LABRIN, E. (2010). Inversion of thermochronological age–elevation profiles to extract independent estimates of denudation and relief history — II : Application to the French Western Alps. *Earth and Planetary Science Letters*, 296(1):9–22.
- VAN HINSBERGEN, D. J. J., TORSVIK, T. H., SCHMID, S. M., MATJENCO, L. C., MAFFIONE, M., VISSERS, R. L. M., GÜRER, D. et SPAKMAN, W. (2019). Orogenic architecture of the Mediterranean region and kinematic reconstruction of its tectonic evolution since the Triassic. *Gondwana Research*.
- VANARDOIS, J., ROGER, F., TRAP, P., GONCALVES, P., LANARI, P., PAQUETTE, J.-L., MARQUER, D., CAGNARD, F., LE BAYON, B., MELLETON, J. et BAROU, F. (2021). Exhumation of deep continental crust in a transpressive regime : The example of 2 Variscan eclogites from the Aiguilles-Rouges Massif (Western Alps). *Journal of Metamorphic Geology*.
- VANDERHAEGHE, O., LAURENT, O., GARDIEN, V., MOYEN, J.-F., GÉBELIN, A., CHELLE-MICHOU, C., COUZINIÉ, S., VILLAROS, A. et BELLANGER, M. (2020). Flow of partially molten crust controlling construction, growth and collapse of the Variscan orogenic belt :

- The geologic record of the French Massif Central. *Bulletin de la Société Géologique de France*, 191(25).
- VERJAT, J. L. (1981). Etude pétrologique et structurale des terrains cristallins du sud-est de Belledonne, à l'ouest du col du Glandon - Alpes françaises.
- VERMEESCH, P. (2018). IsoplotR : A free and open toolbox for geochronology. *Geosci. Front.*, 9(5):1479–1493.
- VIELZEUF, D. et HOLLOWAY, J. R. (1988). Experimental determination of the fluid-absent melting relations in the pelitic system. *Contr. Mineral. and Petrol.*, 98(3):257–276.
- VILLASECA, C., BARBERO, L. et HERREROS, V. (1998). A re-examination of the typology of peraluminous granite types in intracontinental orogenic belts. *Earth Environ. Sci. Trans. R. Soc. Edinb.*, 89(2):113–119.
- VILLASECA, C., MERINO MARTÍNEZ, E., OREJANA, D., ANDERSEN, T. et BELOUSOVA, E. (2016). Zircon Hf signatures from granitic orthogneisses of the Spanish Central System : Significance and sources of the Cambro-Ordovician magmatism in the Iberian Variscan Belt. *Gondwana Research*, 34:60–83.
- VITTOZ, P. (1987). Typologie des granitoïdes hercyniens et zonation magmatique dans le massif du Haut Dauphiné. page 18.
- VIVIER, G., MÉNOT, R.-P. et GIRAUD, P. (1987). Magmatismes et structuration orogénique Paléozoïques de la chaîne de Belledonne (Massifs cristallins externes alpins). Le domaine nord-oriental. *Géologie Alp. Grenoble*, 63:25–53.
- VON RAUMER, J. et BUSSY, F. (2004). Mont Blanc and Aiguilles Rouges geology of their polymetamorphic basement (external massifs, Westerns Alps, France-Switzerland). In *Mémoires de Géologie (Lausanne)*, volume 42, pages 1–210.
- VON RAUMER, J., BUSSY, F., SCHALTEGGER, U., SCHULZ, B. et STAMPFLI, G. (2013). Pre-Mesozoic Alpine basements—their place in the European Paleozoic framework. *Bull. Geol. Soc. Am.*, 125(1-2):89–108.
- VON RAUMER, J., BUSSY, F. et STAMPFLI, G. (2009). The Variscan evolution in the External massifs of the Alps and place in their Variscan framework. *Comptes Rendus Geoscience*, 341(2-3):239–252.

BIBLIOGRAPHIE

- VON RAUMER, J., FINGER, F., VESELÁ, P. et STAMPFLI, G. (2014). Durba-chites–Vaugnerites—a geodynamic marker in the central E uropean Variscan orogen. *Terra Nova*, 26(2):85–95.
- VON RAUMER, J. et STAMPFLI, G. (2008). The birth of the Rheic Ocean—Early Palaeozoic subsidence patterns and subsequent tectonic plate scenarios. *Tectonophysics*, 461(1-4):9–20.
- VON RAUMER, J., STAMPFLI, G., BOREL, G. et BUSSY, F. (2002). Organization of pre-Variscan basement areas at the north-Gondwanan margin. *Int. J. Earth Sci.*, 91(1):35–52.
- WANG, J., SU, B.-X., ROBINSON, P. T., XIAO, Y., BAI, Y., LIU, X., SAKYI, P. A., JING, J.-J., CHEN, C., LIANG, Z. et BAO, Z.-A. (2021). Trace elements in olivine : Proxies for petrogenesis, mineralization and discrimination of mafic-ultramafic rocks. *Lithos*, 388–389:106085.
- WATSON, E. B. et HARRISON, T. M. (1983). Zircon saturation revisited : Temperature and composition effects in a variety of crustal magma types. *Earth and Planetary Science Letters*, 64(2):295–304.
- WATT, G. R., GRIFFIN, B. J. et KINNY, P. D. (2000). Charge contrast imaging of geological materials in the environmental scanning electron microscope. *American Mineralogist*, 85(11-12):1784–1794.
- WHITE, R. W., POWELL, R. et HOLLAND, T. J. B. (2001). Calculation of partial melting equilibria in the system Na₂O–CaO–K₂O–FeO–MgO–Al₂O₃–SiO₂–H₂O (NCKFMASH). *J. Metamorph. Geol.*, 19(2):139–153.
- WHITE, R. W., POWELL, R., HOLLAND, T. J. B., JOHNSON, T. E. et GREEN, E. C. R. (2014). New mineral activity–composition relations for thermodynamic calculations in metapelitic systems. *J. Metamorph. Geol.*, 32(3):261–286.
- WHITE, R. W., POWELL, R., HOLLAND, T. J. B. et WORLEY, B. A. (2000). The effect of TiO₂ and Fe₂O₃ on metapelitic assemblages at greenschist and amphibolite facies conditions : Mineral equilibria calculations in the system K₂O–FeO–MgO–Al₂O₃–SiO₂–H₂O–TiO₂–Fe₂O₃. *J. Metamorph. Geol.*, 18(5):497–511.
- WHITNEY, D. L., HAMELIN, C., TEYSSIER, C., RAIA, N. H., KORCHINSKI, M. S., SEATON, N. C. A., BAGLEY, B. C., von der HANDT, A., ROGER, F. et REY, P. F. (2020). Deep

- crustal source of gneiss dome revealed by eclogite in migmatite (Montagne Noire, French Massif Central). *J. Metamorph. Geol.*, 38(3):297–327.
- WHITNEY, D. L., ROGER, F., TEYSSIER, C., REY, P. F. et RESPAUT, J.-P. (2015). Syn-collapse eclogite metamorphism and exhumation of deep crust in a migmatite dome : The P–T–t record of the youngest Variscan eclogite (Montagne Noire, French Massif Central). *Earth and Planetary Science Letters*, 430:224–234.
- WIEDENBECK, M., HANCHAR, J. M., PECK, W. H., SYLVESTER, P., VALLEY, J., WHITEHOUSE, M., KRONZ, A., MORISHITA, Y., NASDALA, L., FIEBIG, J., FRANCHI, I., GIRARD, J.-P., GREENWOOD, R. C., HINTON, R., KITA, N., MASON, P. R. D., NORMAN, M., OGASAWARA, M., PICCOLI, P. M., RHEDE, D., SATOH, H., SCHULZ-DOBRICK, B., SKÅR, O., SPICUZZA, M., TERADA, K., TINDLE, A., TOGASHI, S., VENNEMANN, T., XIE, Q. et ZHENG, Y.-F. (2004). Further Characterisation of the 91500 Zircon Crystal. *Geostand. Geoanalytical Res.*, 28(1):9–39.
- WIJBRANS, C. H., KLEMME, S., BERNDT, J. et VOLLMER, C. (2015). Experimental determination of trace element partition coefficients between spinel and silicate melt : The influence of chemical composition and oxygen fugacity. *Contrib Mineral Petrol*, 169(4):45.
- ZACK, T. et KOUIJMAN, E. (2017). Petrology and Geochronology of Rutile. *Reviews in Mineralogy and Geochemistry*, 83(1):443–467.
- ŽÁK, J. et SLÁMA, J. (2018). How far did the Cadomian 'terrane' travel from Gondwana during early Palaeozoic? A critical reappraisal based on detrital zircon geochronology. *Int. Geol. Rev.*, 60(3):319–338.
- ŽÁK, J., VERNER, K., JANOUŠEK, V., HOLUB, F. V., KACHLÍK, V., FINGER, F., HAJNÁ, J., TOMEK, F., VONDRŮVÍČEK, L. et TRUBAČ, J. (2014). A plate-kinematic model for the assembly of the Bohemian Massif constrained by structural relationships around granitoid plutons. *Geological Society, London, Special Publications*, 405(1):169–196.
- ZHAO, L., PAUL, A., GUILLOT, S., SOLARINO, S., MALUSÀ, M. G., ZHENG, T., AUBERT, C., SALIMBENI, S., DUMONT, T., SCHWARTZ, S., ZHU, R. et WANG, Q. (2015). First seismic evidence for continental subduction beneath the Western Alps. *Geology*, 43(9):815–818.
- ZHAO, L., PAUL, A., MALUSÀ, M. G., XU, X., ZHENG, T., SOLARINO, S., GUILLOT, S., SCHWARTZ, S., DUMONT, T., SALIMBENI, S., AUBERT, C., PONDRELLI, S., WANG, Q. et ZHU, R. (2016). Continuity of the Alpine slab unraveled by high-resolution P wave tomography. *J. Geophys. Res. Solid Earth*, 121(12):8720–8737.

BIBLIOGRAPHIE

- ZHENG, Y.-F. (2019). Subduction zone geochemistry. *Geoscience Frontiers*, 10(4):1223–1254.
- ZIBERNA, L., KLEMME, S. et NIMIS, P. (2013). Garnet and spinel in fertile and depleted mantle : Insights from thermodynamic modelling. *Contrib Mineral Petrol*, 166(2):411–421.
- ZULAUF, G., DÖRR, W., FISHER-SPURLOCK, S. C., GERDES, A., CHATZARAS, V. et XYPOLIAS, P. (2015). Closure of the Paleotethys in the External Hellenides : Constraints from U–Pb ages of magmatic and detrital zircons (Crete). *Gondwana Research*, 28(2):642–667.
- ZURBRIGGEN, R. (2015). Ordovician orogeny in the Alps : A reappraisal. *Int J Earth Sci (Geol Rundsch)*, 104(2):335–350.
- ZURBRIGGEN, R. (2017). The Cenerian orogeny (early Paleozoic) from the perspective of the Alpine region. *Int J Earth Sci (Geol Rundsch)*, 106(2):517–529.

ANNEXE A

Annexes

Cette section inclut plusieurs articles que j'ai rédigé ou auxquels j'ai participé durant ma thèse, qui n'ont pas été inclus dans le corps du manuscrit. Le premier est un chapitre d'un livre sur la chaîne alpine (*Geodynamics of the Alps, sous presse*). J'ai été chargé de la rédaction du chapitre traitant de l'évolution paléozoïque des domaines alpins. Le second article est un article en deux parties publié dans *Lithos*, qui tente d'unifier les différents paradigmes existant concernant les processus de formation des granitoïdes en contexte de convergence, et présente plusieurs cas concrets incluant la chaîne varisque. Cet article est le fruit de réflexions communes engagées avec les différents co-auteurs au cours des trois dernières années, et auxquelles j'ai activement participé. Ce double article étant particulièrement long, et par ailleurs disponible sur le site de l'éditeur, seule les premières pages de chaque partie sont reportées ici.

A.1 Article #1 : Paleozoic evolution and Variscan inheritance in the Alps

4

Paleozoic evolution and Variscan inheritance in the Alps

Jean-Baptiste Jacob¹, Stéphane Guillot¹, Denis Thiéblemont², Jonas Vanardois³, Pierre Trap³, Michel Faure⁴, Didier Marquer³

1. Univ. Grenoble Alpes, Univ. Savoie Mont Blanc, CNRS, IRD, IFSTTAR, ISTerre, 38000 Grenoble, France

2. Bureau de Recherches Géologiques et Minières, BP 36009, 45060 Orléans Cedex 2, France

3. UMR 6249 Chrono-environnement, Université de Bourgogne-Franche-Comté, 25030, Besançon, France

4. Institut des Sciences de la Terre d'Orléans, Université d'Orléans, CNRS, 45071 Orléans Cedex 2, France

[Book title],

coordinated by [Book coordinator]. © ISTE Ltd 2019.

Abstract

Large outcrops of Paleozoic basement have formed about half of the exposed rock in the Alpine belt. These Paleozoic domains preserve evidence of the long and complex pre-Alpine history, which spanned more than 300 million years, from the Ediacaran to the Permian, and they reflect the general evolution of the European Paleozoic basement. The oldest events recorded correspond to the formation of a Neoproterozoic peri-Gondwanian arc that remained active during the Cambrian before its accretion into Gondwana, presumably during an Ordovician collision. The Cambrian–Ordovician period was marked all over the Alps by tectonic subsidence and widespread magmatic activity, which reflects the general extension that affected North Gondwana prior to the opening of Rheic Ocean and the rifting of Avalonia and the Hun Terranes during the Ordovician. The following Silurian period was relatively calm, marked by crustal subsidence and extension at the margin, and deposition of clastic sediments. These are mostly preserved in the eastern Alps, and they announced the future opening of the Paleotethys from the Late Silurian to the Devonian. Then, convergence between Laurussia and Gondwana started in the Devonian, which marked the closure of Rheic Ocean, followed by the Variscan collision during the Carboniferous. Evidence of this convergence is provided by Devonian HP-LT eclogites preserved in the Austroalpine units, and Devonian–Tournaisian arc-related magmatism in the External Crystalline Massifs (western Alps). The Variscan collision is recorded to various degrees across all of the Alpine basement domains. The main period of nappe-stacking and crustal thickening took place in ca. 350–320 Ma, which was followed by strike-slip tectonics and extension from the Westphalian to the Permian (ca. 315–290 Ma). In the Helvetic domain, the orogen-scale dextral strike-slip East-Variscan shear zone was active from the Late Carboniferous to the Permian, and was responsible for large-scale displacements in the Variscan structure at the end of the orogeny. Following the Variscan orogeny, a high-temperature event occurred during the Permian, which preceded the opening of Tethys Ocean and the initiation of the Alpine cycle. This evolution is in many ways similar to that of other Paleozoic massifs in Europe. However, due to the intense reorganization of the crustal basement during the Alpine orogeny, the Alpine domain does not form a coherent block that can be easily correlated with other Variscan domains in Europe. Replacing the Alpine basement in the European Variscan puzzle remains a challenge to be solved.

4.1. Introduction

Prior to the Alpine cycle, which began with the extension and the opening of the Tethyan oceanic domains during the Lower Jurassic, the Alpine domain underwent a long and complex evolution that can be tracked back to the Late Neoproterozoic. In many places, the basement that preserves this pre-Alpine history has been covered by a thick layer of Mesozoic and Cenozoic sediments, and is therefore not accessible to geologists. However, areas where the pre-Mesozoic basement is exposed represent about half of the Alpine domain (Von Raumer et al., 2013), which makes this one of the largest Paleozoic massifs in Europe, together with the Bohemian Massif, the Massif Central, the Armorican Massif, and the Iberian Massif. This basement is exposed along all of the domains that form the Alpine belt, and was variously overprinted by the Alpine tectonics and metamorphism (Bousquet et al., 2004; Schmid et al., 2004). Like the other Paleozoic massifs of southern and central Europe, the Paleozoic basement of the Alps derives from the northern margin of Gondwana (Stampfli et al., 2011), and has recorded a long and complex history that culminated during the Carboniferous with the Variscan orogeny, during which Gondwana and Laurussia became amalgamated to form the Pangea supercontinent (Matte, 2001). However, this apparently simple history hides great complexity, which is far from being fully understood. This chapter aims to present the current knowledge and outstanding issues concerning the pre-Mesozoic history of the Alpine basement.

4.2. The Paleozoic setting in Europe

4.2.1. General setting: a crustal basement structured by Paleozoic orogenies

The pre-Mesozoic domains of the Alps represent only a small part of the European Paleozoic basement, and form a small piece of the former Variscan belt, a large orogen that can be followed across all of the different Paleozoic massifs of southern and central Europe (Fig. 1). The Variscan belt of Europe itself belongs to a larger orogenic system that extended over about 8000 km, from the Caucasus to the Appalachian and Ouachita mountains of North America (Matte, 1986). It arose from the Devonian to the Permian by progressive closure of the oceanic domains between Laurentia–Baltica to the North, and Gondwana to the South (Figs. 2, 3). Between these two large continental masses, small continental blocks detached from the northern margins of Gondwana during the early Paleozoic, and then from the Late Devonian to the Carboniferous these underwent accretion to form Laurussia and the Variscan orogen (e.g., Franke, 1989; Matte, 2001; Stampfli et al., 2013).

There have been major advances during the last few decades in our understanding of the Paleozoic evolution of the European basement, and most studies have agreed on the first-order structure of the Variscan belt (e.g., Kroner and Romer, 2013; Ballèvre et al., 2014; Lardeaux et al., 2014; Franke et al., 2017). At the European scale, its strongly arcuate shape was acquired more recently in Variscan history (Upper Carboniferous–Early Permian), and this can be subdivided into several lithotectonic domains. On the northern and southern flanks of the Variscan assemblage the basement is formed by the Avalonia and North Gondwana shelves, respectively (Fig. 1), which form the foreland basins of the belt. In between, the Variscan basement is composed of several lithotectonic domains that represent the assemblage of peri-Gondwana terranes that were squeezed between Gondwana and Laurussia during the Variscan orogeny, and then variously overprinted by the associated tectono-metamorphic and magmatic events. The ‘core’ of the European Variscan belt is formed by the Moldanubian zone, which includes a large part of the Bohemian Massif and Massif Central, and extends toward the southern Armorican massif and the northern Iberian massif (Fig. 1). This represents the exhumed crustal root of the belt, and it contains high-grade migmatites and granulites, with relics of high-pressure rock (eclogites, high-temperature eclogites/ high-pressure granulites), and dismembered ophiolites (Lardeaux et al., 2014).

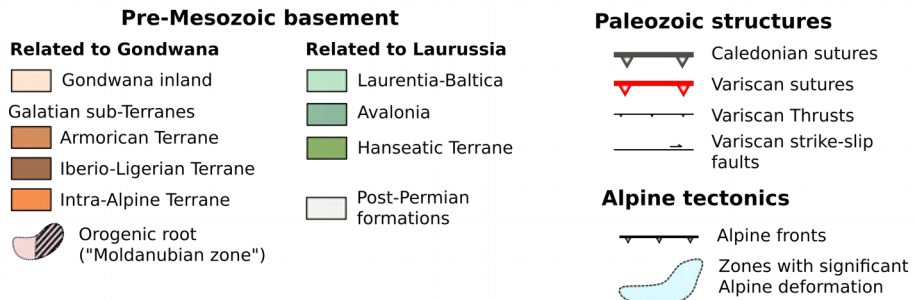
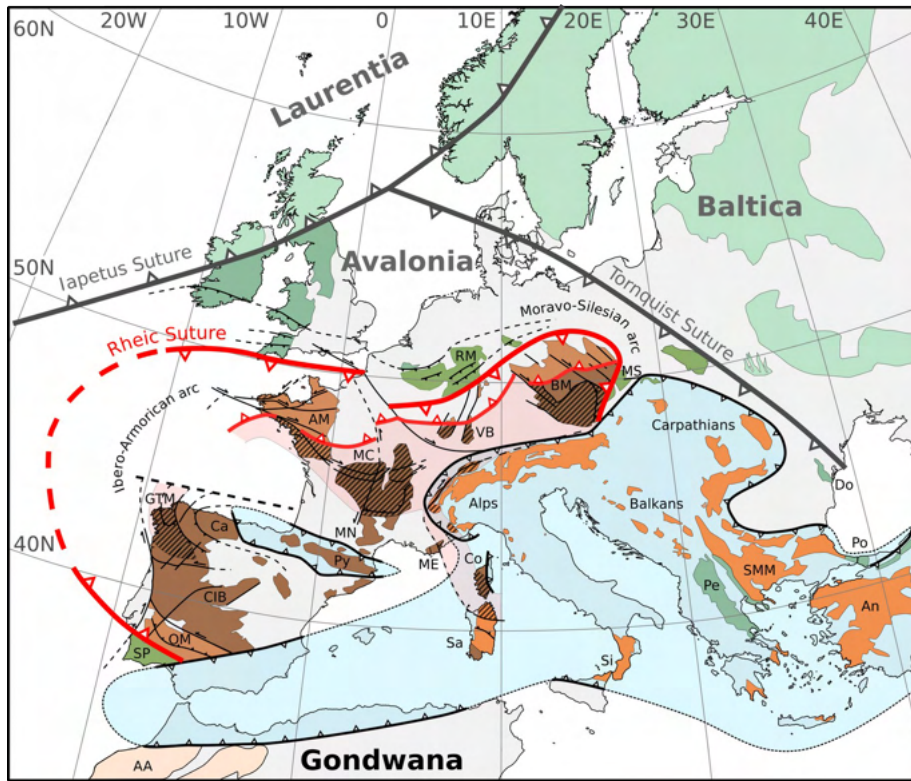


Figure 4.1. Simplified tectonic map of Europe that shows the exposures of the Paleozoic basement and the Paleozoic sutures. The Avalonian crust in the middle of Gondwana-derived domains in southeastern Europe (the Pelagonian zone) is mostly inferred from the study of sedimentary sequences and detrital zircons (Stephan et al., 2019, and references therein), and is not discussed here. AM, Armorican Massif; An, Anatolia; BM, Bohemian Massif; Ca, Cantabrian zone; CIB, Central Iberian zone; Co, Corsica; Do, Dobrogea; GTM, Galicia-Trás-os-Montes; MC, Massif Central; ME, Maures-Esterel; MN, Montagne Noire; MS, Moravo-Silesian zone; OM, Ossa-

Morena zone; Po, Pontides; Pe, Pelagonian zone; Py, Pyrénées; RM, Rhenish Massif; Sa, Sardinia; Si, Sicilia; SMM, Serbo-Macedonian Massif; SP, South Portugese zone; VB, Vosges, Black Forest. Modified from Stephan et al. (2019a), with data from Ballèvre et al. (2014) and Franke et al. (2017).

4.2.2. Pre-Variscan history of the European basement

Prior to the opening of Rheic Ocean during the Ordovician, the future Variscan domains of Europe were located along the northern margin of Gondwana (Matte, 2001; Von Raumer et al., 2002; Stampfli et al., 2011). From the Neoproterozoic to the early Cambrian, a western-Pacific-type accretion zone developed along this margin, which resulted in accretion of various elements to form a consolidated crust (Garfunkel, 2015). This period of accretion peaked during the Late Ediacaran (ca. 600-580 Ma) with the accretion of an arc that had previously rifted off Gondwana, during the Lower Ediacaran. This event is known as the Cadomian orogeny, and it has been poorly preserved in the European basement, except in a few places. These include northern Brittany and the region of Caen in northwestern France (Ballèvre et al., 2001; Chantraine et al., 2001), from which the name ‘Cadomian’ originates (as derived from Cadomus, the Latin name of the city of Caen). Elsewhere, the Cadomian orogeny is mainly inferred from the study of zircons in detrital sediments, which has defined a major peak of zircon crystallization at ca. 600 Ma, which corresponds to the Cadomian orogenic events (e.g., Chu et al., 2016, Chelle-Michou et al., 2017).

The Cambrian–Ordovician period (ca. 540-450 Ma) was characterized by extensional tectonics, with rifting and subsidence over northern Gondwana in a back-arc setting (von Raumer and Stampfli, 2008). This eventually led to the opening of Rheic Ocean (Linnemann et al., 2007; Nance et al., 2010) and the northward drift of the Avalonian microplate (Fig. 2, sketches 1-4). This widespread extension resulted in the formation of a thinned continental shelf on the northern margin of Gondwana, which was associated with the opening of back-arc basins (Kroner and Romer, 2013; Stampfli et al., 2013) and the limited production of some arc or back-arc oceanic crust (e.g., Chamrousse, Fig. 2, sketch 1; Pin and Carne, 1987; Ménot et al., 1988; Guillot et al., 1992). The Cambrian–Ordovician extension was accompanied by widespread bimodal magmatism (Fig. 2, sketch 3), which consisted of alkaline and tholeiitic mafic rock that was associated with alkaline and peralkaline rhyolite (e.g., Pin and Marini, 1993; Crowley et al., 2000). A possible orogenic event occurred during the Ordovician (Fig. 2, sketch 2), which is referred to as the Sardic phase or the Cenerian orogeny; this was inferred from the widespread production of peraluminous granitoids from ca. 500 to 450 Ma

(Valverde-Vaquero and Dunning, 2000; Villaseca et al., 2016; Zurbriggen, 2017). However, the geodynamic setting associated with this peraluminous magmatism remains unclear. Different mechanisms have been proposed, which have included continental rifting associated with the break-up of northern Gondwana (Montes et al., 2010; Ballèvre et al., 2012), back-arc extension in an active arc setting (Valverde-Vaquero and Dunning, 2000; Fernández et al., 2008), thermal relaxation of a thickened arc crust (Villaseca et al., 2016; Soejono et al., 2019), and melting of fore-arc sediments driven by underplating of mafic magma.

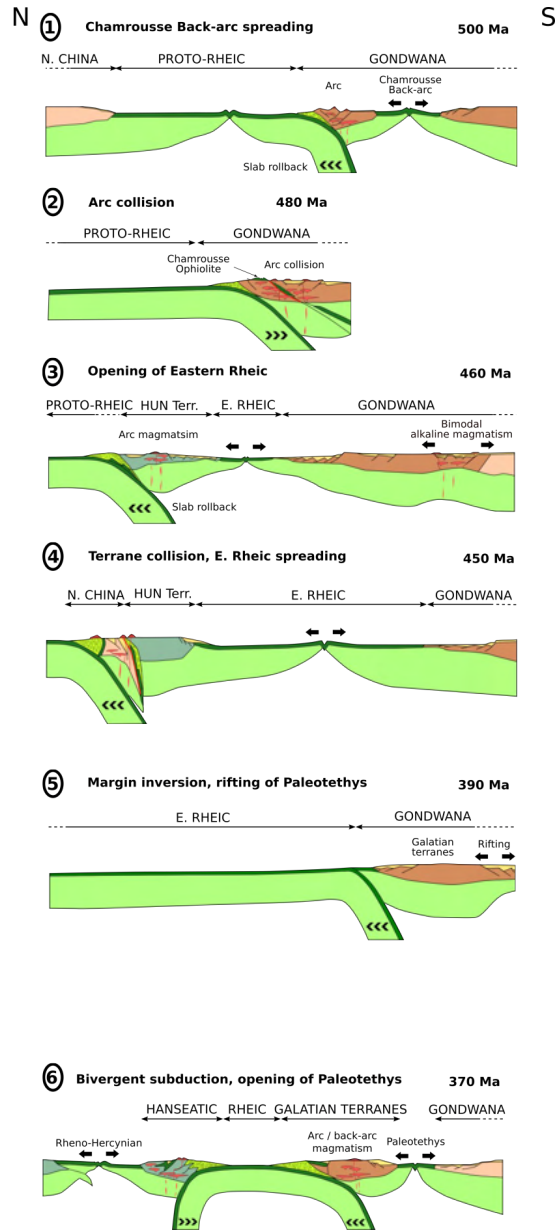
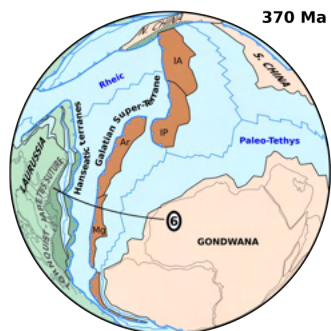
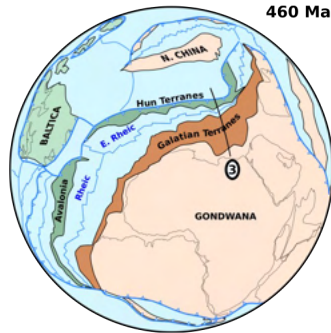


Figure 4.2. *Palinspastic reconstruction that shows the evolution of North Gondwana from the Cambrian to the Devonian, with the associated cross-sections that cut through the northern Gondwana margin. The position of the cross-sections is indicated by the number on the corresponding globe. This period records the progressive opening of the Rheic domain and the drifting of Avalonian and Hun Terrane during the Ordovician, followed by the rifting of Paleo-Tethys during the Silurian and the Devonian, and the progressive closure of Rheic Ocean. Mg, Meguma; Ib, Iberia; Ar, Armorica; IA, Intra-Alpine. Colors of the continents follow the same code as for Figure 1: light green, Laurentia–Baltica; dark green, Avalonia and Hun Terrane; light brown, Gondwana; dark brown, Galatian Terranes. Modified from Stampfli et al. (2011, 2013).*

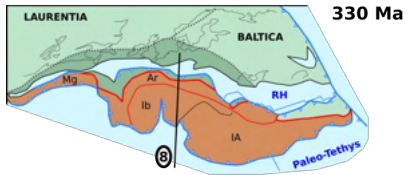
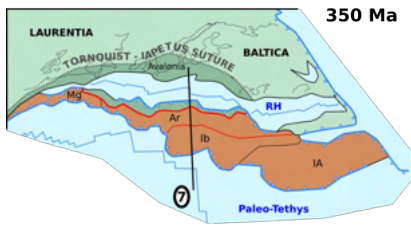
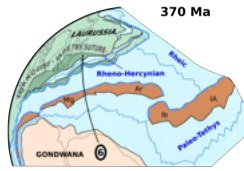
4.2.3. The Variscan orogeny in Europe

From the Late Silurian to the early Devonian, convergence between Gondwana and Laurussia led to the closure of Rheic and Saxo-Thuringian Oceans (Fig. 2, sketches 5-6). This then culminated during the Late Devonian–Carboniferous (360–320 Ma) with the collision between Laurussia, Gondwana, and peri-Gondwanian fragments (Fig. 3). During the Middle-to-Late Carboniferous, two successive stages of post-orogenic extension occurred (Faure and Becq-Giraudon, 1993; Burg et al., 1994). The first of these was associated with lateral East–West extrusion of material in a still convergent setting, and the second was associated with North–South orogenic collapse via the activation of low-angle detachment faults. These were accompanied by development of migmatite complexes, emplacement of large volumes of peraluminous granitoids, and formation of intra-continental, coal-bearing sedimentary basins (e.g., Ledru et al., 2001; Faure et al., 2009; Lardeaux et al., 2014). This general collapse associated with extensive crustal melting might have been driven by the delamination of the sub-continental mantle lithosphere during the late orogenic stages (e.g., Žák et al., 2018)

However, the Variscan orogen has a complex structure that cannot be solely explained by a simple continent–continent collision. In particular, many relics of mafic-ultramafic complexes, mid-ocean ridge basalt (MORB)-type eclogites, and alkalic magmas of the Upper Cambrian–Lower Ordovician can be found within the Variscan domains of western and central Europe, south of the Rheic suture. This disposition suggests that multiple oceanic basins separated the microplates south of Rheic Ocean (Fig. 1). Different tectonic models have been proposed that differ in the numbers of plates and oceans involved, and in the initial pre-Variscan positioning of these blocks along the peri-Gondwana margin (Matte, 2001; Kroner and Romer, 2013; Stampfli et al., 2013; Franke et al., 2017). Moreover, discussion

continues as to the size of the basins that separated the different blocks, and the subduction vergencies. Based on the continuity of the benthic fauna and paleomagnetic data, it is now recognized that these continental fragments were not separated from Gondwana by a large oceanic domain (Cocks and Torsvik, 2002; Fortey and Cocks, 2003). These micro-continents were more likely separated by either small oceanic basins similar to the Mesozoic Alpine Ocean (Franke et al., 2017), or by zones of hyperextended crust that possibly showed continent–ocean transition (Kroner and Romer, 2013; Lardeaux et al., 2014).

Finally, the global picture is further complicated by the noncylindricity of the Variscan belt and its diachronous evolution from West to East, as indicated by palinspastic reconstructions, detrital zircon patterns in the Lower Paleozoic sediments, and lithostratigraphic, tectonic, and magmatic records (Stampfli et al., 2013; Casas and Murphy, 2018; Stephan et al., 2019a). Several recent models now separate the Variscan domains south of the Rheic suture into eastern and western segments that underwent contrasting geodynamic evolution (Stampfli et al., 2013; Stephan et al., 2019a, b). In the western domain, the final collision of Gondwana with Laurussia has been well recorded, and corresponds to indentation of Avalonia by the western Gondwana shelf during the Late Devonian–Carboniferous (ca. 360–340 Ma; Faure et al., 2009; Ballèvre et al., 2014). In the eastern domain, the situation was complicated by the opening of Paleo-Tethys during the Devonian (Fig. 2, sketch 6 and Fig. 3). The main Tournaisian–Visean tectonothermal event corresponded to the accretion of the terranes into a cordillera-like orogen (Fig. 3, sketches 7–8). The final collision of Gondwana with Laurussia occurred later (330–300 Ma; Fig. 3, sketches 9–10) and was less pronounced than for the western domain (Haas et al., 2020). Eastward, the collisional system evolved toward a purely accretionary orogen along the northern Paleo-Tethys, to form the Altaids in central Asia (Wilhem et al., 2012).



N S

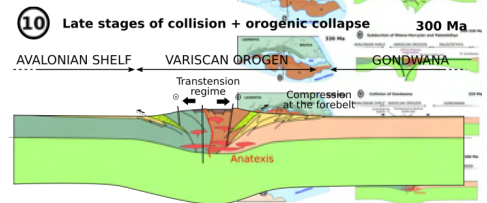
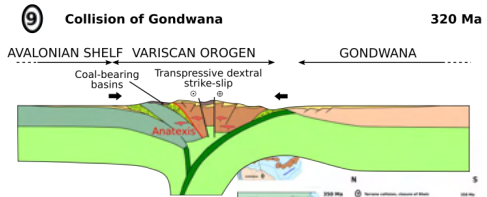
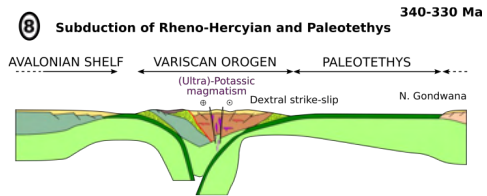
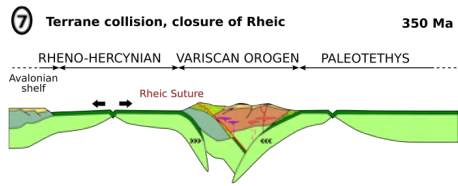


Figure 4.3. *Palinspastic reconstruction of the Variscan domain from the Devonian to the Late Carboniferous, with associated cross-sections through the Variscan collision zone. This period records the closure of Rheic Ocean and other smaller basins, and the collision between Laurussia, Galatian Terranes, and Gondwana. This collision is polyphasic: a first arc–arc collision occurred at ca. 350 Ma between the two sets of Galatian Terranes; a second collision occurred at ca. 320 to 300 Ma with indentation of Gondwana in the Galatia–Laurussia terrane assemblage; this was followed by extension and lateral extrusion of material accommodated by the lithospheric-scale strike–slip faults. See Figure 2 for labels. Modified from Stampfli et al. (2011, 2013).*

The following sections will present an overview of the Paleozoic massifs in the Alps, and discuss their pre-Mesozoic history according to the general setting proposed by Stampfli et al. (2013) for the Paleozoic evolution of northern Gondwana (see Figs. 2, 3). According to this model, the Variscan belt was formed by the amalgamation of terranes derived from Gondwana. Two major sets of ribbon-like peri-Gondwana terranes that extended from the north of South America to southern China drifted from Gondwana at different times during the Lower Paleozoic. A first segment known as the Hun Terrane corresponded to the eastern equivalent of Avalonia, and this detached from the eastern domain of North Gondwana during the Ordovician, with the opening of the eastern Rheic Ocean. This segment then drifted to the northeast and collided with northern China during the Silurian. A second segment known as the Galatian super-terrane detached from Gondwana during the mid-Devonian, synchronous with the opening of Paleo-Tethys, and that comprised most of the European Variscan elements. This ribbon-like micro-continent quickly separated into four sub-terranes. The final collision between Gondwana, Laurussia, and the Galatian Terranes during the Middle-to-Upper Carboniferous (ca. 340-300 Ma) created a complex amalgamation that formed the Variscan belt.

4.3. The basement outcrops in the Alps

The Paleozoic basement is exposed discontinuously all along the Alpine arc, and it forms about half of the Alpine domain (Von Raumer et al., 2013). Pre-Alpine rock is exposed in the four main tectonic domains that have been defined at the lithospheric scale for the Alpine belt (Fig. 4): the Dauphinois–Helvetic; the Penninic; the Austroalpine; and the south Alpine domains. The Dauphinois–Helvetic domain forms the external zone of the European margin west of the Penninic thrust. The Penninic domain is composed of various nappes that derived from the distal European margin (e.g., the Tauern Window basement nappes; Schmid et al., 2013),

the Valaisan basin and the Briançonnais microplate in the western and central Alps. The Austroalpine domain is composed of allochthonous nappes that form the remnants of the southern margin of Piemonte–Liguria Ocean along the Apulian plate, under which the Penninic nappes have been thrust. Finally, the south Alpine domain forms the autochthonous part of the Apulia plate south of the Periadriatic fault.

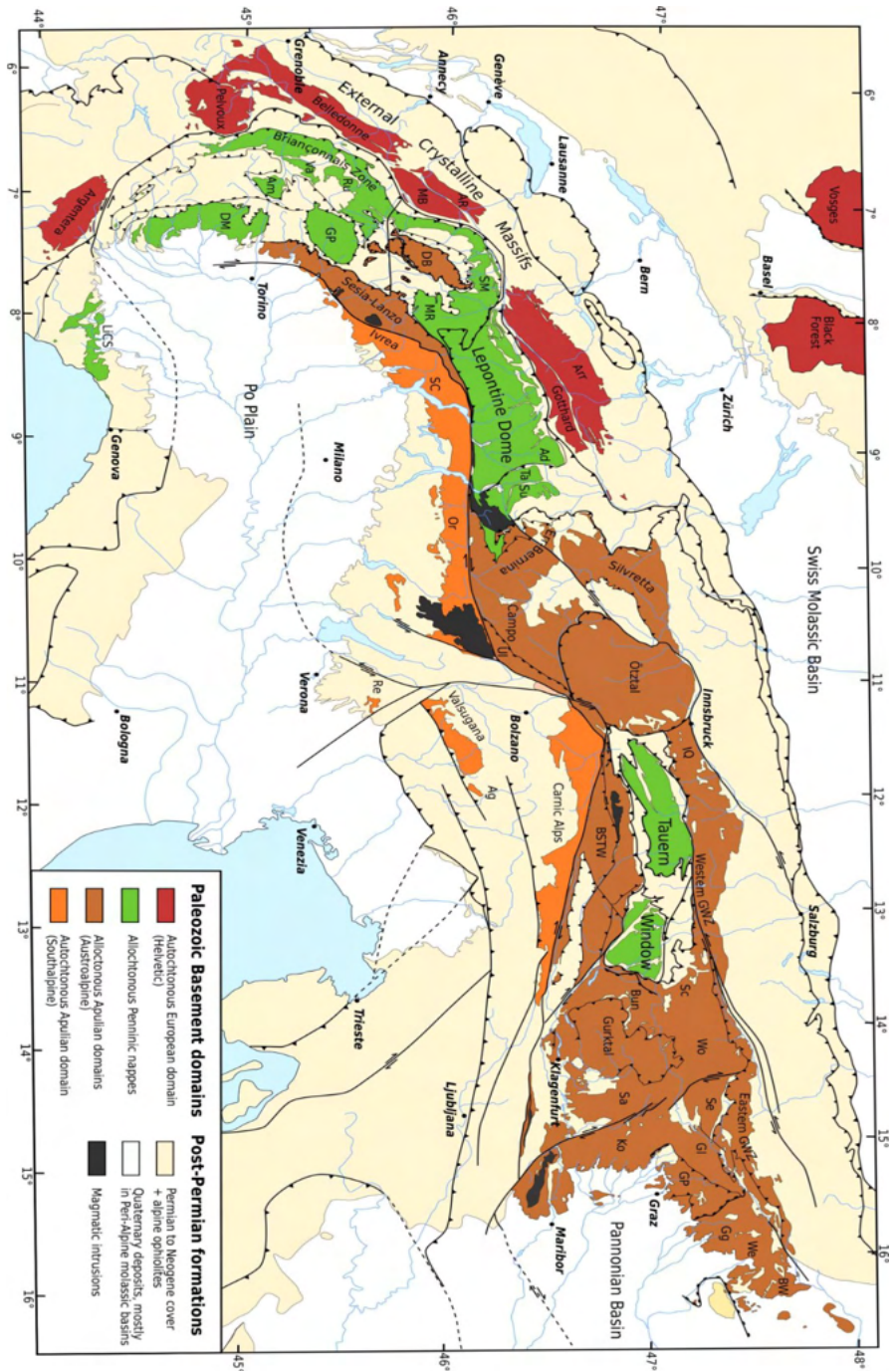


Figure 4.4. *Paleozoic basement units in the Alps in their current tectonic setting and classified according to the Alpine lithotectonic domain to which they belong (i.e., Helvetic, Penninic, Austroalpine, south Alpine). For clarity, no distinction of the lithotectonic domains is made for the post-Permian units, which group the Permian to Neogene sedimentary sequences and the Alpine ophiolites. Dark gray, Cenozoic peri-Adriatic magmatic intrusions. Contours of the massifs were redrawn from Frey et al. (1999). Alpine faults and thrusts are from Bousquet et al. (2004). See legend to Figure 5 for abbreviations.*

The different Paleozoic domains have been variously overprinted by Alpine tectono-metamorphic events, which depended on their location along the Alpine belt (Bousquet et al., 2004; Schmid et al., 2004). In the more external Helvetic and southern Alpine domains, the Alpine metamorphic overprint never exceeds greenschist facies conditions, which indicates that these domains were not deeply buried and belong entirely to the Alpine suprastructure. Between the Penninic thrust and the Periadriatic fault, the Penninic and Austroalpine domains are composed of allochthonous nappes that show various degrees of metamorphic overprint, which range from lower greenschist in the more external units, to high-pressure–ultrahigh-pressure eclogite in the internal units. Re-equilibration along a Barrovian gradient occurred in the central and eastern Alps (Lepontine dome, Tauern Window), and this was characterized by the development of metamorphic assemblages of the amphibolite facies associated with migmatization (Bousquet et al., 2004).

As the Helvetic and south Alpine domains form coherent blocks devoid of pervasive Alpine deformation and metamorphic overprint, they are the ideal places to study pre-Mesozoic evolution in the Alps. In the Penninic and Austroalpine domains, reconstitution of the Paleozoic evolution is more challenging. Difficulties arise from the more pervasive Alpine deformation that has partially or totally obliterated the former structures. Tectonic slicing of these domains into numerous nappes (Fig. 4) that are disconnected from their lower crustal base makes large-scale correlations more speculative. Moreover, in the areas with Alpine metamorphic overprint that exceeds the upper greenschist facies, the interpretation of the successive metamorphic stages is particularly challenging, because the mineral assemblages cannot be unambiguously attributed to one particular Paleozoic or Alpine stage. This is, for instance, the case for the Gruf complex (central Alps), where the age of the ultra-high-temperature metamorphism has been a matter of debate for a long time, as it can be attributed to either a Permian (e.g., Galli et al., 2012) or an Eocene (e.g., Nicollet et al., 2018) high-temperature event. Deciphering the metamorphic history in such complex areas requires very careful investigations using modern petrochronological methods (e.g. Sandmann et al., 2014; Giuntoli et

al., 2018; Kunz et al., 2018). Despite these difficulties, investigations of the Paleozoic basement in the Austroalpine and Penninic units have provided useful constraints on the pre-Mesozoic history of the Alpine domain, especially for the low-grade Austroalpine nappes and for the external Briançonnais (Zone Houillère, and its basement).

4.4. Paleozoic evolution in the Alpine basement

4.4.1. Late Proterozoic evolution: an active margin setting along northern Gondwana

During the Neoproterozoic, the Alpine domains were located on North Gondwana in a Cordillera-like active margin setting, where various terranes underwent accretion to form a consolidated continental crust. This concept of composite terranes was first proposed in the eastern Alps by Neubauer (1989), to explain the apparently unrelated origins of different crustal fragments. This model was further supported by geochronological studies that identified Ediacaran magmatic protoliths at different places in the Austroalpine nappes. The oldest magmatic protoliths of this period are meta-diorites from the Silvretta nappe that became emplaced at 609 ± 3 Ma in an arc-type setting (Schaltegger et al., 1997). Other Neoproterozoic ages have been further identified in the basement of the Tauern (Eichhorn et al., 1995, 2001) and in the basement units south of the Tauern Window, where normal-MORB-type metabasites attributed to subduction-related magmatism were dated at 590 ± 4 Ma (Schulz et al., 2004, 2008). According to these Ediacaran magmatic protoliths, Schulz et al. (2008) defined an eastern Cadomian arc in the eastern Alps that was active from the Late Precambrian to the Cambrian, before undergoing accretion with Gondwana during the Early Ordovician collisional phase (ca. 470 Ma; Fig. 2, sketch 2). Further south, similar fragments of arc-related Cambrian to Neoproterozoic crust have been reported in the Hellenides (Dörr et al., 2015; Zulauf et al., 2015). No sections of preserved Neoproterozoic basement have been identified in the western Alps yet. However, the recent dating of an orthogneiss sampled in crustal fragments embedded within the Mesozoic sediments of the Briançonnais unit close to the city of Briançon yielded an age of 598 ± 4 Ma (our unpublished data, Thiéblemont et al.) (Fig. 6).

Apart from the Cadomian magmatic protoliths, significant information about the pre-Cambrian evolution of the Alpine basement is provided by the inherited zircons in the magmatic rock, and detrital zircons from the Lower Paleozoic sediments. The zircon age spectra here have typically shown a dominant Neoproterozoic age population (ca. 550-650 Ma) for all of the Alpine domains (e.g., Chu et al., 2016;

Manzotti et al., 2016; Haas et al., 2020), which indicates that most of the Alpine basement is made of material recycled from the Cadomian arcs. In addition, the detrital zircon spectra have frequently shown age populations as Mesoproterozoic–Neoproterozoic (ca. 800–1100 Ma) and Mesoproterozoic–Archean (2.0–3.0 Ga), with very few Mesoproterozoic zircons for 1.2–1.6 Ga. This distribution is typical for material derived from the West African and northeast African cratons and proterozoic shields, with possible sources coming from the Arabian–Nubian shield and the southern China block (von Raumer and Stampfli, 2008; Von Raumer et al., 2013; Stephan et al., 2019a).

4.4.2. Cambrian–Ordovician extension and opening of eastern Rheic Ocean

The Cambrian–Ordovician period is marked all across the European Variscides by tectonic subsidence (von Raumer and Stampfli, 2008), widespread magmatic activity that consist mainly of bimodal felsic–mafic igneous associations of alkaline affinity (Pin and Marini, 1993; Crowley et al., 2000), and intrusion of mainly peraluminous granitoids (Montero et al., 2007; Bea et al., 2010; Villaseca et al., 2016; Couzinié et al., 2017; Zurbriggen, 2017). This intense magmatic activity is generally attributed to a regional extensional event that affected the entire margin of North Gondwana (Pin and Marini, 1993; Faure et al., 2009) and that preceded the opening of Rheic Ocean and the separation of Avalonia from Gondwana during the Mid-Ordovician (Matte, 2001; Stampfli et al., 2011). However, the general setting during this period was probably more complex. The evolution along northern Gondwana was dominated by an active margin setting that was accompanied by contemporaneous intra-continental extension (Fig. 2, sketches 1–3) and stretching from west to east (von Raumer and Stampfli, 2008), which was associated with several magmatic pulses.

The Cambrian–Ordovician magmatic records of the Alpine basement provide a good illustration of this complex evolution. Different sets of intrusive and extrusive magmatic rock were emplaced or erupted from the Cambrian to the Early Silurian (ca. 530–430 Ma; Schaltegger and Gebauer, 1999; Bussien et al., 2011; Von Raumer et al., 2013), which was attributed to either intra-continental rifting and back-arc extension, or magmatic accretion and orogenic events that occurred in the arc (Figs. 5, 6).

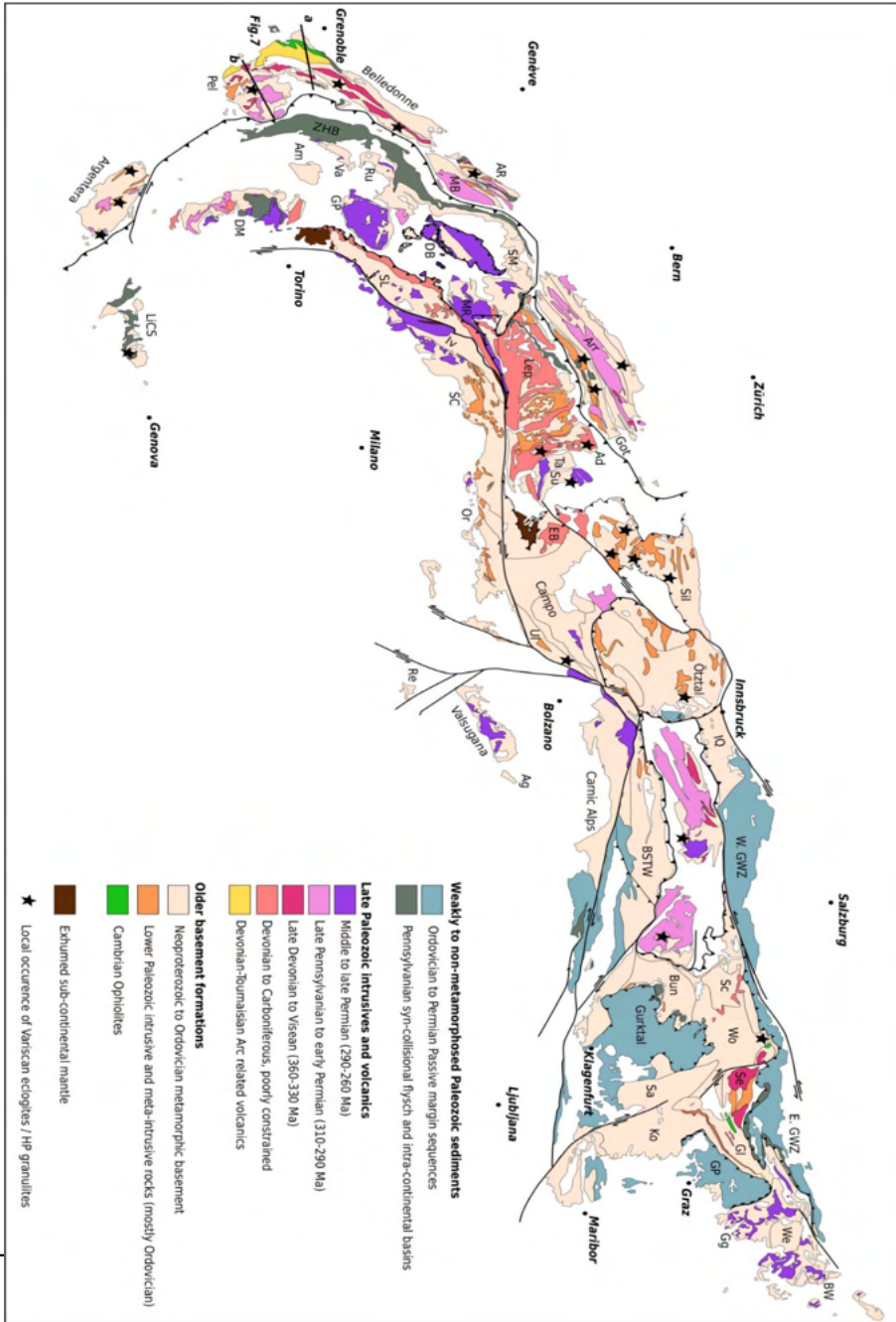


Figure 4.5. Simplified geological map of the lithological units within the pre-Mesozoic basement of the Alps. Contours of the massifs were redrawn from Frey et al. (1999). Alpine faults and thrusts are from Bousquet et al. (2004). The classification of the lithologies is based on geological and geochronological data from the Carte Géologique de la France at 1/1000000 BRGM (2004); Multithematische Geologische Karte von Österreich, GBA; Guillot and Ménot (2009) (Helvetic zone); Ballèvre et al. (2018), and references therein (Briançonnais); Veselà et al. (2011) (Tauern); Schmidt et al. (2013) (Tauern); Mandl et al. (2018) (Seckau plutonic complex). From southwest to northeast: LiCS, Ligurian, Calizzano–Savona; DM, Dora–Maira; Pel, Pelvoux; Am, Ambin massif; ZHB, Zone Houillère Briançonnaise; Va, Vanoise; GP, Gran Paradiso; SL, Sesia–Lanzo; Ru, Ruitor; AR, Aiguilles Rouges; MB, Mont Blanc; DB, Dent Blanche; SM, Siviez–Mischabel; MR, Monte Rosa; Iv, Ivrea Zone; SC, Strona–Ceneri zone; Lep, Lepontine dome; Ad, Adula nappe; Ta, Tambo nappe; Su, Suretta nappe; Got, Gotthard massif; Or, Orobic Alps; EB, Err–Bernina nappe; Sil, Silvretta nappe; Ul, Ulten zone; Re, Recoaro; Ag, Agordo; IQ, Innsbruck Quartzite; BSTW, Basement units south of the Tauern Window; Sc, Schladming nappe; Bun, Bundschuh nappe; Wo, Wölz nappe; Sa, Saualpe; Ko, Koralpe; Se, Seckau nappe; Gl, Gleinalm; GWZ, Grauwacken Zone; GP, Graz Paleozoic; Gg, Grobgneiss; We, Wechsel; BW, Bucklige Welt.

4.4.2.1. Cambro–Ordovician extension magmatism in the Alpine basement

Alkaline and tholeiitic magmatism has been widely recorded for the Alpine basement (Fig. 6), and it has been attributed to back-arc extension and continental rifting that affected North Gondwana (Bussien et al., 2011). In the basement of the Vanoise Massif and the Siviez–Mischabel unit (Penninic domain), A-type alkaline metagranitoids have been dated at 507 ± 9 Ma (Guillot et al., 2002) and 500 ± 4 Ma (Bussy et al., 1996), respectively. In the Silvretta nappe (Austroalpine), two ages at 526 ± 7 Ma and 519 ± 7 Ma have been reported for an alkaline orthogneiss (Müller et al., 1995). These early stages of continental rifting associated with alkaline magmatism were followed by emplacement of tholeiites in a thinned continental crust, with the local production of an oceanic lithosphere in short-lived back-arc basins. This evolution has been well described for the external crystalline massifs of the western Alps (Helvetic domain), where tholeiitic metabasalts with a normal/enriched-MORB signature were emplaced in a thinned continental crust during the Ordovician (ca. 480–450 Ma; Paquette et al., 1989; Rubatto et al., 2001, 2010). In the Belledonne Massif, the ophiolitic complex of Chamrousse (Fig. 5) is a well-

preserved kilometer-scale slab of Cambrian oceanic lithosphere (ca. 500 Ma; Pin and Carme, 1987; Ménot et al., 1988), and it is regarded as the relic of a small marginal basin that spread in a back-arc setting (Guillot et al., 1992) before it closed, presumably during a Mid-Ordovician tectonic phase (Guillot and Ménot, 2009; von Raumer et al., 2009). Such tholeiitic suites have also been described for the Penninic and Austroalpine domains. Dismembered relics of mafic and ultramafic rock from Loderio–Biasca (Ticino, Lower Penninic nappes) that have been dated at 518 ± 11 Ma might represent the relics of an oceanic domain (Schaltegger et al., 2002). In the Tauern Window, the Habach Terrane corresponds to an active continental margin where back-arc spreading occurred during the Cambrian, which was associated with emplacement of diorites, gabbros, and trondhjemite, from ca. 550 Ma to 507 Ma (Neubauer et al., 1989; Eichhorn et al., 2001). Finally, for the Austroalpine domain, oceanic plagiogranites dated at ca. 530 Ma that appear to be emplaced in a back-arc setting were reported by Müller et al. (1996) for the Silvretta nappe, and several dismembered Late Neoproterozoic to Cambrian ophiolites are exposed in different crystalline Austroalpine nappes (Neubauer et al., 1989). This is seen especially in the Speik complex, where a nearly complete ophiolitic sequence dated at ca. 550 Ma is preserved (Melcher and Meisel, 2004).

4.4.2.2. Cambro–Ordovician arc and collisional magmatism in the Alpine basement

Subduction-related magmatism has been recorded contemporaneous to the back-arc rifting. This consists mainly of mafic and felsic meta-igneous rock of calc-alkaline affinity (Fig. 6). In the Silvretta nappe, eclogitized gabbroic and tonalitic melts were emplaced at ca. 530–520 Ma, and are attributed to arc magmatism (Schaltegger et al., 1997). A similar evolution has been described for the basement south of the Tauern Window, where volcanic arc basaltic suites from 550 to 530 Ma have been reported (Schulz et al., 2004, 2008). Additional data that support an Ordovician subduction setting have come from the Aar massif (Helvetic domain), where metagabbros dated at 478 Ma were affected by an Ordovician high-pressure metamorphic event that was followed by a high-temperature overprint accompanied by partial melting, at ca. 450 Ma (Schaltegger et al., 2003).

The active margin setting in the Alpine domain has also been characterized by several pulses of peraluminous and calc-alkaline granitoids that were emplaced between 480 Ma and 450 Ma. These metagranitoids are ubiquitous in the basements of all paleogeographic Alpine domains (Figs. 5, 6), and these attest the wide extension of this magmatism (e.g., Schaltegger and Gebauer, 1999; Bussien et al., 2011; Von Raumer et al., 2013, and references therein). The age of this magmatism is from 470 to 440 Ma in the Helvetic domain (Schaltegger and Gebauer, 1999; Bussy et al., 2011), and from 480 to 450 Ma in the Penninic and Austroalpine

domains (Guillot et al., 2002; Schulz et al., 2008; Liati et al., 2009). In the south Alpine domain, large outcrops of these Ordovician metagranitoids are exposed in the Strona–Ceneri zone, where they represent about 20% of the exposed outcrops of the Paleozoic basement (Zurbriggen, 2015). These consist mainly of peraluminous orthogneisses derived from greywacke source rock, with subordinate amounts of metaluminous calc-alkaline orthogneisses (ca. 90% peraluminous, 10% metaluminous orthogneisses) and rare mafic end-members (Zurbriggen, 2017).

However, the origin of these granitoids has not been well constrained. The predominance of crustal-derived peraluminous granitoids is not expected in a Cordillera-like setting, which typically has a wide variety of mafic to felsic igneous rock derived from both the fractional crystallization of mantle-derived magma and the melting of various igneous and sedimentary crustal components (Barbarin, 1999). This is also not expected in an extensional rift setting, and more generally, in all environments in which the bulk of the heat was advected from the mantle by the ascent of mafic melts, which should be dominated by mantle-derived magmatism (Annen et al., 2006). Zurbriggen (2015, 2017) proposed an alternative model of subduction–accretion complexes, in which the dominant peraluminous magmatism results from the melting of flysh-type sediments in the accretionary prism of an arc fed by a large sedimentary input from the continent. However, this model still involves heat advection from the mantle as the main driver of crustal melting, and attributes the relative scarcity of exposed mafic and intermediate intrusives to exposure bias. Finally, other alternative models proposed for other parts of the European Variscides relate this magmatism to the thermal relaxation of a thickened arc crust (Villaseca et al., 2016; Soejono et al., 2019), which would generate large amounts of peraluminous anatectic granites.

4.4.3. Ordovician to Silurian crustal extension

The Cambrian–Ordovician crustal extension led to detachment of small continental blocks from northern Gondwana during the Ordovician. In the western domain, the Avalonian block detached from Gondwana at ca. 480 Ma, and drifted northward to eventually undergo accretion with Laurentia during the Silurian (Fig. 2). In the eastern domain, the detachment of the Hun Terranes resulted in the opening of the eastern branch of Rheic Ocean, slightly later (ca. 460 Ma) than the western branch (Fig. 2, sketch 3). This opening left a passive margin along North Gondwana (Fig. 2, sketch 4). From the Mid-Ordovician to the Lower Carboniferous, sedimentation occurred along this passive margin. These clastic deposits are mainly exposed in the Austroalpine nappes (Greywacke Zone, Gürktal nappe, Paleozoic of Graz) and in the Carnic Alps (Neubauer et al., 2007), and this provides a record of

the crustal subsidence at the margin (Fig. 5). A few pulses of alkaline magmatism have been recorded for this period; for instance, in basement massifs south of the Tauern Window (Austroalpine), where alkaline within-plate basalts were emplaced at ca. 430 Ma (Schulz et al., 2004). These Late Ordovician–Early Silurian magmatic events might have been related to either late extension after the eastern Rheic opening, or an initial rifting stage that preceded the opening of the Paleo-Tethys (Schulz et al., 2004; Stampfli et al., 2011).

The opening of the Paleo-Tethys has not been well recorded for the European domains, as it was largely obliterated by subsequent Variscan and Alpine events, and parts of the former Paleo-Tethyan margin have been covered under Mesozoic sediments (Von Raumer et al., 2013). In Sardinia, the volcano–sedimentary deposits of the Late Ordovician–Early Silurian (ca. 440 Ma) that consist of alkali basalts and trachyandesites might be associated with the initial rifting that preceded the opening of the Paleo-Tethys (Gaggero et al., 2012). This opening has been better documented in Iran (Bagheri and Stampfli, 2008), and it resulted from two rifting events that occurred during the Late Ordovician (ca. 440 Ma) and the Middle Devonian (ca. 390 Ma). This rifting resulted in separation of the Galatian Terranes from Gondwana, where they contained the Alpine domain (Von Raumer et al., 2013) and most of the crustal fragments that formed the European Variscides (Stampfli et al., 2013).

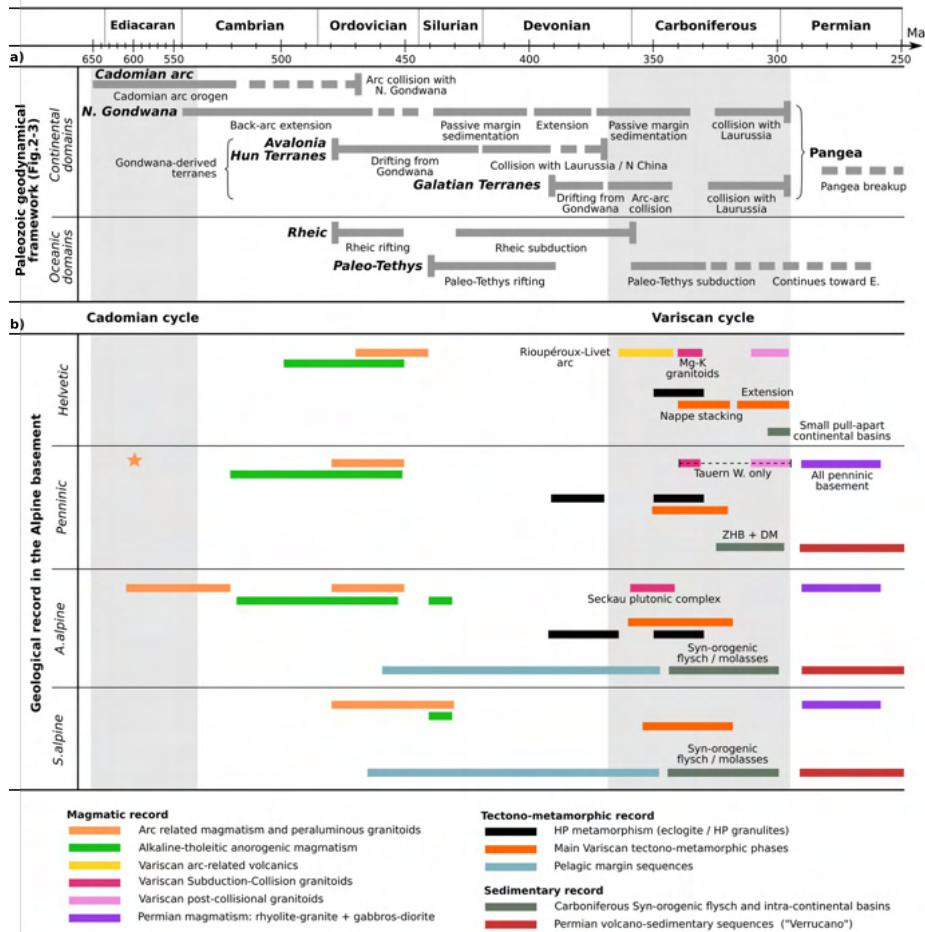


Figure 4.6. (a) Chronological chart for the Neoproterozoic–Paleozoic that summarizes the geodynamical evolution of the European Variscides from the Ediacaran to the Permian. (b) Geological record for the Alpine basement for the same period. The four lithotectonic domains in the Alpine belt (i.e., Helvetic, Penninic, Austroalpine, south Alpine) show contrasted records and are thus treated independently.

4.4.4. Devonian–Carboniferous convergence and Variscan collision

4.4.4.1. A polyphased history during the Variscan collision

From the Mid-Devonian (ca. 390 Ma), Rheic Ocean progressively closed, contemporaneous with the opening of the Paleo-Tethys and the drifting of the Galatian Terranes (Fig. 2, sketches 5-6), which initiated the convergence of Laurussia and Gondwana. The Variscan orogeny corresponds to the succession of collisional events that occurred from the Late Devonian to the Late Carboniferous/ Early Permian (ca. 370-295 Ma). This eventually resulted in the amalgamation of Laurussia, Gondwana, and the peri-Gondwanian terranes (Fig. 3), to form the most recent supercontinent, Pangea. In many basement massifs in the Alps, polymetamorphic assemblages prevail and multiple nappe stacking events have been identified (e.g., Schaltegger and Gebauer, 1999; Raumer and Bussy, 2004; Benciolini et al., 2006; Schulz et al., 2008; Guillot and Ménot, 2009; Fréville et al., 2018), which testifies to the polycyclic evolution during the Variscan orogeny. The intensity of the Variscan deformations and metamorphic overprint varies greatly among the basement areas in the Alps, from lower greenschist to granulite and/or eclogite facies (Frey et al., 1999). These different Paleozoic basement areas with various degrees of Variscan overprint might represent either different structural levels in the crust (Schaltegger et al., 2003) or different paleogeographic domains that were variously affected by the Variscan orogeny and subsequently juxtaposed due to the Late Variscan and Alpine tectonics (Guillot and Ménot, 2009). Two major Variscan tectono-metamorphic events have been identified for the Alpine domain (Von Raumer et al., 2013). The first occurred during the Early-to-Mid Carboniferous (ca. 350-330 Ma) and corresponds to closure of the Rheic domain and amalgamation of the Galatian Terranes to Laurussia (Fig. 3, sketches 7-8). The second event occurred during the Late Carboniferous/ Early Permian (ca. 320-295 Ma), and corresponds to the final collision of Gondwana and the post-collisional collapse of the Variscan belt (Fig. 3, sketches 9-10).

4.4.4.2. Devonian–Visean magmatism

Prior to this collision, early Variscan events can be identified. In the massif of Belledonne (western Alps), the mafic-felsic bimodal suites of volcanic and plutonic rock that were emplaced at ca. 360-350 Ma (Figs. 5, 6, 7) have been attributed to continental extension in a back-arc setting (Guillot and Ménot, 2009; Fréville et al., 2018), similar to the Brévenne unit in the French Massif Central (Faure et al., 2005) and the central part of the Moldanubian zone (Lardeaux et al., 2014). The magmatic evolution suggests a transition from an extensional to a compressional regime, which marks the beginning of the Visean collision. A similar evolution took place along the margin of Laurussia, where the Devonian back-arc extension resulted in

opening of the Rheno-Hercynian domain, which separated ribbon-like terranes from the Laurussian plate (Franke et al., 2017). Volcano–sedimentary deposits of an early Visean age overlie the older gneisses in the basement of the Helvetic domain (Guillot and Ménot, 2009; von Raumer et al., 2009). These present an arc-related tholeiitic geochemical signature with contamination from a continental crust component (Carme and Pin, 1987). It is therefore believed that these formations were deposited in a continental arc setting, to mark the subduction of the Rheic/Paleo-Tethyan domains during the Lower Carboniferous (Guillot and Ménot, 2009; Fréville et al., 2018). In the Seckau nappe (Austroalpine domain), the Hintertal plutonic suite is composed of Late Devonian to Visean (ca. 365–340 Ma) granites and granodiorites (Figs. 5, 6), which were possibly emplaced in a continental arc setting (Mandl et al., 2018).

4.4.4.3. Variscan high-pressure metamorphism

Relics of high-pressure rock, as eclogites and high-pressure granulites, have been reported for many basement areas in the Alpine domain (Fig. 5), where they formed small bodies embedded within felsic lithologies (orthogneisses, metasediments). These high-pressure assemblages have been documented in the external crystalline massifs (Liégeois and Duchesne, 1981; Paquette et al., 1989; Ferrando et al., 2008; Guillot and Ménot, 2009), in the Penninic nappe of Adula in the Lepontine Alps (Liati et al., 2009; Herwartz et al., 2011; Sandmann et al., 2014), and in several crystalline nappes of the Austroalpine domain (Thöni, 2006, and references therein). For most of these bodies, the age of the high-pressure stage has been estimated at ca. 350 to 330 Ma (Fig. 6; Miller and Thöni, 1995; Ladenhauf et al., 2001; Tumiatì et al., 2003; Thöni, 2006; Liati et al., 2009; Rubatto et al., 2010; Jacob et al., 2021). In the eclogites from the Adula nappe (Penninic domain), both U-Pb zircon and garnet Lu-Hf geochronology have indicated a Mid-Carboniferous age for the high-pressure metamorphism (ca. 330–340 Ma). In addition, some zircon rims that were dated by Liati et al. (2009) yielded a Devonian age, at ca. 370 Ma, which might indicate an earlier metamorphism. Finally, an eclogite body from the Hochgrössen Massif (eastern Austroalpine nappes) yielded an age of 397 ± 8 Ma for the high-pressure stage, with peak pressure conditions estimated at ca. 1.8 to 2.2 GPa and 700 °C (Faryad et al., 2002). These ages suggest a Mid-to-Late Devonian subduction cycle that preceded the more widely recorded 350 to 330 Ma high-pressure stage. Paquette et al. (1989) reported a U-Pb zircon age of 395 ± 2 Ma in the external crystalline massifs, but this age was obtained about 30 years ago by multigrain isotope-dilution thermal-ionization mass spectrometry, and it more probably reflects mixing between the Ordovician magmatic cores and the metamorphic rims of the zircons (Paquette et al., 2017). More recent dating in Argentera (Rubatto et al., 2010) and Belledonne (Jacob et al., 2021) have yielded ages between 340 and 320 Ma, which are more consistent with other U-Pb data from the Alpine basement.

4.4.4.4. Variscan nappe-stacking events in the Alpine basement

The Tournaisian–Visean collision was recorded in most basement domains in the Alps by successive episodes of nappe stacking, Barrovian-type metamorphism, emplacement of granitoids, and detrital zircon and mica records in the Carboniferous–Permian basins (Figs. 5, 6; Schulz et al., 2008; Guillot and Ménot, 2009; Von Raumer et al., 2013; Manzotti et al., 2016; Zanoni and Spalla, 2018; Haas et al., 2020). Due to the intense post-Permian reworking of the Alpine basement, regional geometric correlations at the scale of the Alpine domain are particularly challenging, in contrast to other Variscan massifs in Europe (e.g., Faure et al., 2009; Ballèvre et al., 2014; Lardeaux et al., 2014). Such correlations have nevertheless been carried out for the external domains of the western Alps, which underwent very limited reworking by Alpine tectonics (Guillot et al., 2009; Guillot and Ménot, 2009; von Raumer et al., 2009). In these domains, two successive Visean nappe-stacking events have been identified (Fig. 7). The first corresponds to the development of North–North-20-degrees trending transpressive shear zones, which led to the thrusting of the internal high-pressure unit towards the northwest. This deformation was associated with the emplacement of granitoids at ca. 340 Ma (Debon et al., 1998; Debon and Lemmet, 1999; Bussy et al., 2000; Guillot and Ménot, 2009). The second deformation is associated with a top to the East shearing and northeast thrusting of the Chamrousse ophiolitic complex over the Devonian–Tournaisian magmatic complex. This second nappe-stacking event is associated with crustal thickening, and is characterized by a Barrovian metamorphic gradient that increases from West to East (from ca. 0.6 GPa and 600 °C, to ca. 0.8 GPa and 680 °C; Guillot and Ménot, 2009; Fréville et al., 2018).

4.4.4.5. The Visean magnesio-potassic magmatism

The Visean granitoids are of particular significance in the Variscan belt. These form a series of potassic calc-alkaline rock that is enriched in K_2O and MgO . The Visean granitoids are considered to be derived from a mixed source that combined an enriched sub-continental lithospheric mantle and a continental crust (Debon et al., 1998; Debon and Lemmet, 1999). This series is documented for the entire Helvetic domain (Debon and Lemmet, 1999; Bussy et al., 2000; von Raumer et al., 2014), as well as for the basement of the Tauern Window (Lammerer, 1986; Veselà et al., 2011), and it was emplaced at ca. 340 to 330 Ma (Figs. 5, 6). Similar rock of Visean age can be found in other parts of the European basement in Corsica, French Central Massif, Black Forest, Vosges, and the Bohemian Massif (von Raumer et al., 2014). These granitoids are probably related to collisional processes that involved both mantle and crustal melting (Schaltegger, 1997; von Raumer et al., 2013, 2014), although it has not been excluded that they were emplaced in a Cordillera-like setting. Based on their spatial distribution and their emplacement along sinistral

strike-slip shear zones (Debon and Lemmet, 1999; Guillot et al., 2009), it has been suggested that the Mg-K granitoids define a major linear structure in the Variscan belt, and possibly mark an orogen-wide strike-slip fault rooted in the lithospheric mantle or a major suture zone (Schaltegger, 1997; Corsini and Rolland, 2009; Guillot et al., 2009; Veselà et al., 2011; von Raumer et al., 2014).

4.4.5. Crustal extension and post-orogenic collapse

The Mid-Carboniferous to Permian corresponds to the final collision of Gondwana with the peri-Gondwanian crustal blocks that were previously assembled as Laurussia. This period records a complex tectonic history (Fig. 6) that was dominated by strike-slip tectonics and extension from the Late Carboniferous, and was associated with the opening of intra-continental basins (Ballèvre et al., 2018). This was accompanied by a generalized low-pressure and high-temperature metamorphism, which led to migmatization in the lower-to-mid crustal levels, and the production of subalkaline peraluminous granitoids. This series corresponds to the ferriferous low-Mg suite of Debon and Lemmet (1999), which was emplaced at 310 to 295 Ma (Bonin et al., 1993; Schaltegger, 1997; Debon and Lemmet, 1999; Schaltegger and Gebauer, 1999; Bussy et al., 2000 Veselà et al., 2011; Fréville, 2016).

The Late Variscan extension is well documented in the external zone of the western Alps, where two phases of extension have been identified (Fig. 7). The first corresponds to northeast–southwest extension from the Westphalian to the Mid-Stephanian (310–305 Ma), contemporaneous with migmatization in the deeper crustal levels. The second phase corresponds to roughly North–South extension with East–West shortening, accommodated by northeast–southwest-trending dextral shear zones and brittle strike-slip faults that were active from the Stephanian to the Early Permian (ca. 305–295 Ma; Guillot et al., 2009). This strike-slip system that runs from the Aar massif to the northeast to the Belledonne massif has possible connection in the Bohemian massif and in the Corsica–Sardinia block, and would thus define an orogen-wide structure known as the east Variscan shear zone, with a lateral offset of at least 300 km (Corsini and Rolland, 2009; Guillot et al., 2009; Rossi et al., 2009; Duchesne et al., 2013; Ballèvre et al., 2018; Simonetti et al., 2018).

Intra-continental basins with coal-bearing deposits developed during the Late Carboniferous. The largest of these corresponds to the Zone Houillère basin in the Briançonnais domain (Fig. 5), which extends over at least 150 to 200 km from North to South, and has a width of ca. 20 km. Even without accounting for the Alpine shortening, this is one of the largest Carboniferous basins in Europe (Ballèvre et al.,

2018). Sedimentation in the Zone Houillère mainly took place from the Namurian to the Westphalian (ca. 325-315 Ma; Ballèvre et al., 2018, and references therein). There are also smaller Carboniferous basins in other parts of the Alpine belt (Figs. 5, 6). In the internal zone of the Penninic domain, Carboniferous deposits are exposed for the Dora Maira and Gran Paradiso massifs (Ballèvre et al., 2018). Late Carboniferous molasse basins are also known for the Austroalpine nappes of the eastern Alps (Neubauer et al., 2007). In the Helvetic domain, rather small, elongated narrow basins of Westphalian–Stephanian age (305-300 Ma) probably opened when they were pulled apart during the dextral strike-slip tectonic phase (Guillot et al., 2009; Ballèvre et al., 2018, and references therein).

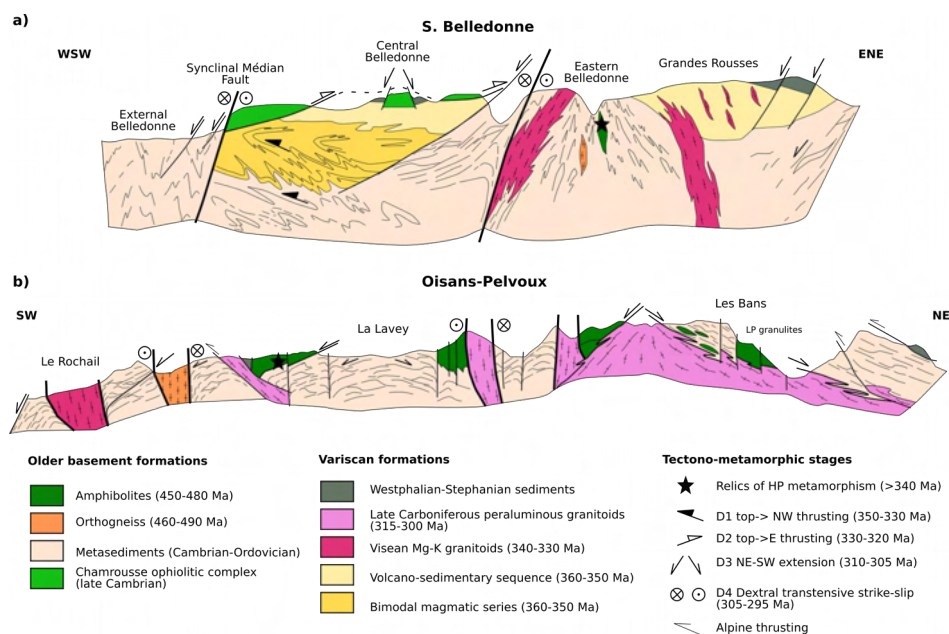


Figure 4.6. Schematic cross-sections showing the structural relationships for the massifs of Belledonne–Grandes Rousses (a) and Oisans–Pelvoux (b). Modified from Guillot and Ménot (2009).

This general evolution that consisted of strike–slip tectonics, extension, opening of the intra–continental basins, and low–pressure–high–temperature metamorphism that was associated with production of large amounts of peraluminous granitoids has been observed for all of the western European Variscides (Catalán et al., 2007; Faure et al., 2009; Faure, 2014), and it attests to the general collapse of the Variscan belt during the Late Carboniferous–Early Permian. For the eastern domain, and particularly for the Austroalpine domain, this late tectonic phase was relatively mild and was not associated with significant crustal thickening and melting (Haas et al., 2020). Following the Variscan orogeny, Mid–to–Late Permian (ca. 280–250 Ma) metamorphic and magmatic activity was recorded for the Alpine basement (Figs. 5, 6). Traces of this episode are scarce in the basement of the Helvetic domain (Fréville, 2016; Ballèvre et al., 2018), although they are ubiquitous for other parts of the Alpine basement, where Permian high–temperature metamorphism and the associated magmatism were widespread (Schaltegger and Gebauer, 1999; Schulz et al., 2008; Spalla et al., 2014; Ballèvre et al., 2018; Kunz et al., 2018; Manzotti et al., 2018). This high–temperature episode might be related either to the latest stages of the Variscan post–orogenic collapse or to the earliest events of the lithospheric

extension and the thinning that preceded the break-up of Pangea (Spalla et al., 2014).

4.5. Discussion

4.5.1. Place of the Alpine domain in the Variscan puzzle

During the last decade, important effort has been devoted to the correlation between the different Variscan massifs in Europe, and to the reconstruction of the general structure of the belt (Schulmann et al., 2014). The exploitation of large geochronological and geochemical datasets that have been collected from all over the European Paleozoic basement has significantly improved the geodynamic reconstructions, through more precise identification of the different crustal blocks that form the Variscan puzzle, and their initial positions along the northern Gondwana margin, prior to the Ordovician rifting (Blichert-Toft et al., 2016; Stephan et al., 2019a, b).

Although there are large portions of well-preserved Paleozoic basement in the Alpine domain, this has not been an important focus for the Variscan community, and it has been a bit left out from such large-scale correlations. This lack of interest in the Alpine basement is mostly due to the extremely complex tectonic setting in the Mediterranean region, where Alpine tectonics have largely perturbed the original pre-Mesozoic position of the crustal blocks. The Alpine domain is composed of a juxtaposition of crustal blocks with different pre-Mesozoic positions that were stacked during the Alpine orogeny (van Hinsbergen et al., 2019). Only the Helvetic domain has been relatively preserved from this complex tectonic reworking, and it remained located on the European margin of Piemonte–Ligurian Ocean during the Mesozoic. In their current configuration, the Alpine basement massifs can therefore be seen as a mosaic of different pieces of the Paleozoic crust that correspond to different domains of the Variscan belt and that record different tectono-metamorphic and magmatic events. An illustration of this point is given by the western Alps, where the basement of the Helvetic and Briançonnais domains underwent very contrasted igneous and metamorphic histories (Figs. 5, 6). The Helvetic basement shows similarities with the Moldanubian core of the Variscan belt (Bohemian Massif, Vosges-Schwarzwald, Massif Central): it has a strong amphibolite/ granulite facies Variscan overprint (Grandjean et al., 1996; Raumer and Bussy, 2004; Guillot and Ménot, 2009), abundant Carboniferous granitic magmatism at ca. 340 to 330 Ma and 310 to 300 Ma (Debon and Lemmet, 1999), and very little Permian magmatism. In contrast, with a few exceptions, the basement of the Briançonnais domain has very weak Variscan metamorphic overprint (Guillot et al., 2002; Ballèvre et al., 2018),

and is mainly devoid of Carboniferous granitoids, but is characterized by abundant Permian magmatism (Ballèvre et al., 2018).

This striking difference in terms of pre-Triassic history was regarded by Ballèvre et al. (2018) as the consequence of a major strike-slip displacement along the eastern Variscan shear zone during the Late Carboniferous–Early Permian, that cut through the large-scale zonation of the Variscan belt, and brought internal and external domains into contact. However, this view does not take into account the displacements that occurred during the Alpine cycle. Indeed, it is widely recognized that the Briançonnais domain has connection with the Corsica–Sardinia block (e.g., Stampfli and Hochard, 2009; van Hinsbergen et al., 2019), which was in a more southern position during the Triassic. It is generally assumed that this Corsica–Sardinia–Briançonnais block was positioned close to the Iberian plate during the Triassic, south of the Pyrenees (Stampfli and Hochard, 2009), or facing the Gulf of Lion and the Maures-Esterel massif in southern France (van Hinsbergen et al., 2019). In any case, these reconstructions emphasize the southern origin of the Briançonnais domain. The sharp differences in terms of tectono-metamorphic history with the Helvetic domain may therefore result from an Alpine collage that brought the Briançonnais block (which belongs to the southern foreland of the Variscan belt) into contact with the internal domains that form the Helvetic margin.

Toward the East, the Southalpine and Austroalpine domains were in a southern position during the Triassic, south of the Pyrénées and east of the Iberian plate (van Hinsbergen et al., 2019). This replaces the Austroalpine units close to the southern foreland of the Variscan belt, which is consistent with the weak overprint recorded during the Late Carboniferous for the final stage of the Variscan orogeny (Haas et al., 2020).

Finally, the basement exposed in the Tauern Window is interpreted as derived from the distal European margin (Schmid et al., 2004), and can be seen as the eastward prolongation of the Helvetic basement. This view is supported by the similar Variscan magmatic evolution in these two domains (Eichhorn et al., 2000; Veselà et al., 2011), and by the similarities in the pre-Variscan magmatic and metamorphic records (Eichhorn et al., 2001). However, these domains are not actually identical. The Permian magmatism recorded in the Tauern Window is not seen for the Helvetic basement (Figs. 5, 6), and the Variscan metamorphic imprint in the Tauern basement reaches a lower grade than in the western domains. Given the relative proximity of the Tauern basement to the Bohemian massif, it is also tempting to see this as the southern continuation of the Moldanubian zone, which forms the core of the Variscan belt. However, there are significant differences between these two domains, in terms of both magmatic and metamorphic history

(e.g., Finger et al., 1997). In particular, the Tauern basement completely lacks ultrahigh-temperature granulites that are typically exposed in the adjacent Moldanubian zone. The Tauern basement therefore corresponds to a more external domain of the Variscan belt. Eichhorn et al. (2001) came to similar conclusions, and suggested that the Tauern basement occupied an intermediate position between the Helvetic basement, which forms parts of the Moldanubian zone, and the more external zones of the Variscan belt, possibly represented by the basement nappes of the Austroalpine domain. In contrast with the Briançonnais zone in the western Alps, Alpine displacement cannot be invoked here to explain the discontinuity with the Moldanubian zone. This latter more probably results from the Late Variscan strike-slip tectonics, which might be related to the east Variscan shear zone that cut through the Variscan zonation and put the lower grade Tauern basement in contact with the high-grade Moldanubian core.

4.5.2 Pre-Variscan position of the Alpine basement units

Prior to the Variscan cycle, the crustal fragments that formed the Paleozoic basement were located along the northern Gondwana margin. The restoration of the pre-Variscan architecture of this continental margin and the reconstitution of its Late Proterozoic–Early Cambrian evolution is under active research, as it has implications for the crustal growth models and the formation of the European continental crust (von Raumer and Stampfli, 2008; Stampfli et al., 2013; von Raumer et al., 2015; Villaseca et al., 2016; Chelle-Michou et al., 2017; Couzinié et al., 2017, 2019). Due to the strong displacement associated with the Late Carboniferous strike-slip tectonics, the replacement of the different crustal blocks in their pre-Ordovician position is not straightforward.

The detrital U-Pb age patterns of zircons from the Paleozoic sediments have proven to be a powerful proxy to unravel their provenance and to infer the relative positions of the crustal fragments in their pre-Variscan setting. Stephan et al. (2019a) used a large compilation of these data from all across Europe and the surrounding cratonic areas to classify the different Paleozoic domains according to their pre-Ordovician positions. Combined with other types of data (e.g., age of magmatism, stratigraphic and paleontological records), this large meta-analysis allowed the identification of three different domains in the Variscan basement, which are related to the Avalonian, the eastern Gondwana, and the western Gondwana shelves. In the main, most of the Moldanubian zone and the Armorican Massif derive from the western Gondwana shelf, while a large part of southeastern Europe, which includes Sardinia and Corsica, derives from the eastern Gondwana shelf. A large part of the Iberian massif also derives from eastern Gondwana, which

appears to be counter-intuitive given its westward position in the Variscan assemblage.

The position of the Alpine domains was unfortunately not assessed in the study of Stephan et al. (2019a). However, based on the pre-Alpine southern position of the Austroalpine and south Alpine domains near the Iberian plate (van Hinsbergen et al., 2019), and the connection of the Briançonnais domain with Corsica–Sardinia, it appears reasonable to also attribute an eastern Gondwana origin to these domains. This initial position has been confirmed by recent U-Pb zircon data from metasediments sampled in the eastern Alps, which attributed these to an origin on the northeastern Gondwana margin for the Austroalpine nappes, next to Anatolia and the Iranian Luth-Tabas blocks (Haas et al., 2020). In contrast, the Helvetic domain shows strong similarities with the Moldanubian zone, which would indicate a more western origin along the northern margin of Gondwana. However, this inference is very speculative because of the lack of detrital zircon data from the Lower Paleozoic sediments in the western Alps.

4.5.3 Significance of Variscan high-pressure metamorphism in the Alps

Eclogite and high-pressure granulites are exposed in different domains of the Alpine basement, mainly for the external crystalline massifs and the Austroalpine nappes (Fig. 5). Such high-pressure assemblages are not rare for the European Variscides, especially in the internal (Moldanubian) zone of the orogen. Many such occurrences have been reported for northern Iberian and southern Armorican massifs, French Massif Central, Vosges-Schwarzwald, Bohemian Massif, Sardinia and in the Alpine Paleozoic basement (Paquette et al., 2017; Regorda et al., 2019).

The high-pressure metamorphic records in the European Variscides is best understood within a model that involves two distinct high-pressure stages (O'Brien, 2000). A Devonian (390-360 Ma) subduction stage produced middle-temperature eclogites ($T < 650$ °C) and blueschists by subduction of the oceanic lithosphere and the hyperextended continental margins of the former Ordovician basins, with these now incorporated into gneiss–metabasite complexes (also known as leptyno–amphibolic complexes in the French part of the Variscides). These rocks were already exhumed by the Late Devonian, as shown by the occurrence of the Devonian sediments that contain high-pressure detritus and/or overlie the gneiss–metabasite complexes (e.g., Schäfer et al., 1997). A second mid-Carboniferous (ca. 340 Ma) high-pressure–high-temperature event (1.5-2.2 GPa, 700-1000 °C) produced granulitic complexes that contained high-temperature eclogites and pyroxenites, and different types of mantle peridotites, which then underwent very rapid exhumation to the lower crustal levels (e.g., Schantl et al., 2019). This was soon followed by

mid-to-low pressure and high-temperature regional metamorphism and granitic magmatism from the Middle-to-Late Carboniferous (335-300 Ma). In contrast with the middle-temperature eclogites, this group rarely preserves prograde metamorphic evolution, and only records exhumation from the deep lower crustal levels, together with the peridotites (O'Brien, 2000). These granulitic complexes might represent deep portions of the orogenic lower crust that were extruded to higher crustal levels during the collision (Schulmann et al., 2005). Alternatively, they might also mark a second subduction stage during the mid-Carboniferous, that might be related to the emplacement of the Mg-K granitoids (Finger et al., 2007).

The Variscan high-pressure rock exposed in the Alps can (with very few exceptions) be related to the mid-Carboniferous group according to the following:

- They mainly consist of small bodies of eclogites and mafic high-pressure granulites embedded within high-grade gneiss (Paquette et al., 1989; Raumer and Bussy, 2004; Ferrando et al., 2008), and they are associated with ultramafic bodies (e.g., garnet-spinel-bearing peridotites, pyroxenites, serpentinites), especially in the external crystalline massifs (Le Fort, 1971; Raumer and Bussy, 2004) and in the Ulten zone (Godard et al., 1996; Tumiati et al., 2003).

- The high-pressure stage is dated at ca. 350 to 330 Ma (Miller and Thöni, 1995; Ladenhauf et al., 2001; Tumiati et al., 2003; Thöni, 2006; Liati et al., 2009; Rubatto et al., 2010).

- Peak pressure conditions occur at relatively high temperatures (>700 °C), although no ultrahigh-temperature conditions have ever been reported for the Alpine basement. In the Helvetic domain, peak pressure conditions are estimated at ca. 1.3 to 1.6 GPa and 650-750 °C, followed by an amphibolitic overprint at ca. 1.0 to 1.2 GPa and 750 °C (Ferrando et al., 2008; Jouffray et al., 2020; Jacob et al., 2021). In the Ulten zone (Austroalpine), eclogites undergo similar equilibration conditions, at ca. 1.4 to 1.5 GPa and 700 °C (Godard et al., 1996; Hauzenberger et al., 1996). Eclogites from the Silvretta and Ötztal nappes (Austroalpine) indicate higher pressure, with peak conditions estimated at ca. 2.7 to 2.8 GPa and 700-763 °C (Miller and Thöni, 1995; Ladenhauf et al., 2001; Thöni, 2006).

The only reported exception here relates to the Devonian eclogites exposed in the Hochgrössen Massif (eastern Austroalpine nappes), at a metamorphic age of 397 ± 8 Ma for the high-pressure stage, with peak pressure conditions estimated at ca. 1.8 to 2.2 GPa and 700 °C (Faryad et al., 2002). This metamorphism is more consistent with the mid-Devonian subduction cycle recorded elsewhere for the Variscan belt.

The geodynamic significance of the Variscan eclogites in the Alps remains under debate. According to Jouffray et al. (2020), the pressure and temperature conditions estimated for the Variscan eclogites in the external crystalline massifs are consistent with a warm subduction geotherm and might represent a dismembered cryptic suture zone. This view is supported by recent thermomechanical modeling (Regorda et al., 2019), which suggested that the pressure and temperature paths and metamorphic ages of the Variscan high-pressure rocks are better reproduced with a two-stage subduction model. However, a subduction process does not necessarily have to be invoked to explain the formation of some Variscan eclogites. For instance, the Montagne Noire migmatite dome, south of the Massif Central, exposes eclogite bodies at ages and under pressure and temperature conditions very similar to those of the eclogites exposed in the external crystalline massifs (Whitney et al., 2015, 2020). They therefore appear on a warm subduction geotherm, despite being exposed in an external domain of the Variscan belt, far from any recognized paleo-subduction zone. Extrusion of the orogenic lower crust during the formation of the Montagne Noire dome is therefore the favored model to explain the exhumation of these eclogites. Discrimination between the different possible geodynamical scenarios requires the use of thermomechanical models. However, as Regorda et al. (2019) indicated, the large uncertainties on the pressure and temperature data, and even more critically, the age data available for the Variscan eclogites, make it difficult to draw any clear conclusions from these models. Refining of these data using all of the modern analytical and modeling tools developed for petrochronology will therefore be essential to build a comprehensive geodynamic model of the Variscan orogeny.

Finally, it can be noted here that two-stage evolution that involves two successive high-pressure stages is also seen for modern orogens, and in particular in the Tibet–Himalaya collisional system that shows striking similarities to the European Variscan belt (Maierová et al., 2016). The earliest metamorphism related to the subduction of the Indian plate is dated at ca. 55 to 45 Ma, and this reached ultrahigh-pressure conditions of ca. 2.7 GPa at 700–770 °C (Guillot et al., 2008, and references therein). This was followed by the Late Eocene (ca. 37–33 Ma) with high-pressure–high-temperature metamorphism at 2.0 to 1.4 GPa and 800 °C recorded for eclogites and granulites from the south Tibetan Neogene migmatitic domes (Kali et al., 2010; Guilmette et al., 2011; Lanari et al., 2013), which were subsequently re-equilibrated at mid-pressure–high-temperature conditions with the surrounding migmatites at 28 to 10 Ma. There are also similarities between the Cenozoic Tibet–Himalaya and Paleozoic Variscan orogens relative to the duration of the convergence and the spatial extension of the collisional events (Maierová et al., 2016). All of these similarities have led to the recognition of the Variscan belt as an ancient analog of the Tibet–Himalaya system.

Conclusion

The Paleozoic domains exposed in the Alps have had a long and complex pre-Alpine history that spanned over more than 300 million years, from the Ediacaran to the Permian. This history is in many ways similar to that of other Paleozoic massifs in Europe, and reflects the general evolution at the northern margin of Gondwana during the Lower Paleozoic, followed by the Variscan collision during the Devonian and the Carboniferous. However, in contrast to other Paleozoic domains in Europe, the Alpine domain does not form a coherent block. Instead, it represents a collage of several lithotectonic units that were amalgamated during the Alpine orogeny. These blocks comprise different portions of the former Variscan orogen, and therefore show contrasting Paleozoic evolution. The autochthonous European margin of Tethys Ocean that currently forms the Helvetic domain has a strong Variscan overprint and exposes deep crustal domains that have been affected by high-grade metamorphism. This probably belongs to the internal Moldanubian zone of the Variscan belt, and possibly corresponds to a domain that was initially located close to the Bohemian massif that was displaced southward during the Upper Carboniferous–Early Permian by the dextral strike-slip east Variscan shear zone. In contrast, the Briançonnais block and the Apulia-derived units (Austroalpine, south Alpine domains) were located in a more southern position prior to the Alpine tectonic cycle, close to the current Pyrenees and the Iberia plate. They therefore represent portions of the southern foreland of the Variscan belt, and have much lower levels of Variscan overprint, although they were more affected by the Permian high-temperature event.

The place of the Alpine Paleozoic domains in the Variscan puzzle is at the current state of knowledge relatively speculative, and still needs to be precisely defined. For this purpose, the succession of pre-Variscan and Variscan tectono-metamorphic, magmatic, and sedimentary events in the Alpine basement need to be better characterized. Correlation with other Paleozoic domains in Europe is not an easy task, given that the Paleozoic massifs in the Alps represent an assemblage of small tectonic blocks that do not preserve a complete section across the Variscan orogen. There remains the need, therefore, to be very careful when considering large-scale Variscan zonation in the Alpine basement massifs. Apart from the Late Variscan strike-slip faults, it appears unlikely that large-scale Variscan zonation can still be unambiguously identified in such a complex assemblage of blocks. In particular, the geodynamic significance of high-pressure relics and their correlation with Variscan suture zones in other parts of the belt are highly speculative.

Acknowledgments

This work was supported by the BRGM through the Référentiel Géologique de la France program (RGF). We are grateful to Michel Ballèvre and an anonymous reviewer for their insightful suggestions and comments. We would also like to thank Christopher Berrie for his careful rereading and correction of the manuscript, which significantly improved the general quality of English.

References

- Bagheri, S., Stampfli, G.M., 2008. The Anarak, Jandaq and Posht-e-Badam metamorphic complexes in central Iran: New geological data, relationships and tectonic implications. *Tectonophysics, Asia out of Tethys: Geochronologic, Tectonic and Sedimentary Records* 451, 123–155. <https://doi.org/10.1016/j.tecto.2007.11.047>
- Ballèvre, M., Le Goff, E., Hébert, R., 2001. The tectonothermal evolution of the Cadomian belt of northern Brittany, France: a Neoproterozoic volcanic arc. *Tectonophysics* 331, 19–43. [https://doi.org/10.1016/S0040-1951\(00\)00234-1](https://doi.org/10.1016/S0040-1951(00)00234-1)
- Ballèvre, M., Manzotti, P., Piazz, G.V.D., 2018. Pre-Alpine (Variscan) Inheritance: A Key for the Location of the Future Valaisan Basin (Western Alps). *Tectonics* 37, 786–817. <https://doi.org/10.1002/2017TC004633>
- Ballèvre, M., Fourcade, S., Capdevila, R., Peucat, J.-J., Cocherie, A., Fanning, C.M., 2012. Geochronology and geochemistry of Ordovician felsic volcanism in the Southern Armorican Massif (Variscan belt, France): Implications for the breakup of Gondwana. *Gondwana Res.* 21, 1019–1036.
- Ballèvre, M., Martínez Catalán, J.R., López-Carmona, A., Pitra, P., Abati, J., Fernández, R.D., Ducassou, C., Arenas, R., Bosse, V., Castiñeiras, P., Fernández-Suárez, J., Gómez Barreiro, J., Paquette, J.-L., Peucat, J.-J., Poujol, M., Ruffet, G., Sánchez Martínez, S., 2014. Correlation of the nappe stack in the Ibero-Armorican arc across the Bay of Biscay: a joint French–Spanish project. *Geol. Soc. Lond. Spec. Publ.* 405, 77–113. <https://doi.org/10.1144/SP405.13>
- Barbarin, B., 1999. A review of the relationships between granitoid types, their origins and their geodynamic environments. *Lithos* 46, 605–626. [https://doi.org/10.1016/S0024-4937\(98\)00085-1](https://doi.org/10.1016/S0024-4937(98)00085-1)

Bea, F., Montero, P., Talavera, C., Abu Anbar, M., Scarrow, J.H., Molina, J.F., Moreno, J.A., 2010. The palaeogeographic position of Central Iberia in Gondwana during the Ordovician: evidence from zircon chronology and Nd isotopes. *Terra Nova* 22, 341–346.

Benciolini, L., Poli, M.E., Visonà, D., Zanferrari, A., 2006. Looking inside Late Variscan tectonics: structural and metamorphic heterogeneity of the Eastern Southalpine Basement (NE Italy). *Geodin. Acta* 19, 17–32.

Blichert-Toft, J., Delile, H., Lee, C.-T., Stos-Gale, Z., Billström, K., Andersen, T., Hannu, H., Albarède, F., 2016. Large-scale tectonic cycles in Europe revealed by distinct Pb isotope provinces: Mapping out Europe with Pb isotopes. *Geochem. Geophys. Geosystems* 17, 3854–3864. <https://doi.org/10.1002/2016GC006524>

Bonin, B., Brändlein, P., Bussy, F., Desmons, J., Eggenberger, U., Finger, F., Graf, K., Marro, C., Mercogli, I., Oberhänsli, R., 1993. Late Variscan magmatic evolution of the Alpine basement, in: *Pre-Mesozoic Geology in the Alps*. Springer, pp. 171–201.

Bousquet, R., Engi, M., Gosso, G., Berger, A., Spalla, M.I., Zucali, M., Goffè, B., 2004. Explanatory notes to the map: metamorphic structure of the Alps. *Cent. Alps Mitt Österr Min. Ges* 157–173.

BRGM, 2004. Carte géologique de la France.

Burg, J.-P., Driessche, J.V. den, Brun, J.-P., 1994. Syn- to post-thickening extension in the Variscan belt of Western Europe: Modes and structural consequences. *Géologie Fr.* 3, 33–51.

Bussien, D., Bussy, F., Magna, T., Masson, H., 2011. Timing of Palaeozoic magmatism in the Maggia and Sambuco nappes and paleogeographic implications (Central Lepontine Alps). *Swiss J. Geosci.* 104, 1–29.

Bussy, F., Hernandez, J., Von Raumer, J., 2000. Bimodal magmatism as a consequence of the post-collisional readjustment of the thickened Variscan continental lithosphere (Aiguilles Rouges-Mont Blanc Massifs, Western Alps). *Earth Environ. Sci. Trans. R. Soc. Edinb.* 91, 221–233.

Bussy, F., Derron, M.-H., Jacquod, J., Sartori, M., Thelin, P., 1996. The 500 Ma-old Thyon metagranite: a new A-type granite occurrence in the western Penninic Alps (Wallis, Switzerland). *Eur. J. Mineral.* 565–576.

Bussy, F., Péronnet, V., Ulianov, A., Epard, J.L., Raumer, J., 2011. Ordovician magmatism in the external French Alps: witness of a peri-gondwanan active continental margin, in: *International Symposium on the Ordovician System* (11; 2011; Alcalá de Henares, Madrid).

Carme, F., Pin, C., 1987. Vue d'ensemble sur le magmatisme péri-orogénique et l'évolution métamorphique et tectonique varisque dans le Sud de la chaîne de Belledonne (Massifs cristallins externes, Alpes françaises). *CR Acad Sci Paris II*, 1177–1180.

Casas, J.M., Murphy, J.B., 2018. Unfolding the arc: The use of pre-orogenic constraints to assess the evolution of the Variscan belt in Western Europe. *Tectonophysics* 736, 47–61.

Catalán, J.M., Arenas, R., García, F.D., Cuadra, P.G., Gómez-Barreiro, J., Abati, J., Castiñeiras, P., Fernández-Suárez, J., Martínez, S.S., Andonaegui, P., 2007. Space and time in the tectonic evolution of the northwestern Iberian Massif: Implications for the Variscan belt, in: *4-D Framework of Continental Crust*. Geological Society of America Memoir Boulder, Colorado, pp. 403–423.

Chantraine, J., Egal, E., Thiéblemont, D., Le Goff, E., Guerrot, C., Ballèvre, M., Guennoc, P., 2001. The Cadomian active margin (North Armorican Massif, France): a segment of the North Atlantic Panafrican belt. *Tectonophysics* 331, 1–18. [https://doi.org/10.1016/S0040-1951\(00\)00233-X](https://doi.org/10.1016/S0040-1951(00)00233-X)

Chelle-Michou, C., Laurent, O., Moyen, J.-F., Block, S., Paquette, J.-L., Couzinié, S., Gardien, V., Vanderhaeghe, O., Villaros, A., Zeh, A., 2017. Pre-Cadomian to late-Variscan odyssey of the eastern Massif Central, France: Formation of the West European crust in a nutshell. *Gondwana Res.* 46, 170–190. <https://doi.org/10.1016/j.gr.2017.02.010>

Chu, Y., Lin, W., Faure, M., Wang, Q., 2016. Detrital zircon U-Pb ages and Hf isotopic constraints on the terrigenous sediments of the Western Alps and their paleogeographic implications. *Tectonics* 35, 2734–2753.

Cocks, L.R.M., Torsvik, T.H., 2002. Earth geography from 500 to 400 million years ago: a faunal and palaeomagnetic review. *J. Geol. Soc.* 159, 631–644. <https://doi.org/10.1144/0016-764901-118>

Corsini, M., Rolland, Y., 2009. Late evolution of the southern European Variscan belt: Exhumation of the lower crust in a context of oblique convergence. *Comptes Rendus Geosci.* 341, 214–223. <https://doi.org/10.1016/j.crte.2008.12.002>

Couzinié, S., Laurent, O., Chelle-Michou, C., Bouilhol, P., Paquette, J.-L., Gannoun, A.-M., Moyen, J.-F., 2019. Detrital zircon U–Pb–Hf systematics of Ediacaran metasediments from the French Massif Central: Consequences for the crustal evolution of the north Gondwana margin. *Precambrian Res.* 324, 269–284. <https://doi.org/10.1016/j.precamres.2019.01.016>

Couzinié, S., Laurent, O., Poujol, M., Mintrone, M., Chelle-Michou, C., Moyen, J.-F., Bouilhol, P., Vezinet, A., Marko, L., 2017. Cadomian S-type granites as basement rocks of the Variscan belt (Massif Central, France): Implications for the crustal evolution of the north Gondwana margin. *Lithos* 286–287, 16–34. <https://doi.org/10.1016/j.lithos.2017.06.001>

Crowley, Q.G., Floyd, P.A., Winchester, J.A., Franke, W., Holland, J.G., 2000. Early Palaeozoic rift-related magmatism in Variscan Europe: fragmentation of the Armorican Terrane Assemblage. *Terra Nova* 12, 171–180. <https://doi.org/10.1046/j.1365-3121.2000.00290.x>

Debon, F., Lemmet, M., 1999. Evolution of Mg/Fe Ratios in Late Variscan Plutonic Rocks from the External Crystalline Massifs of the Alps (France, Italy, Switzerland). *J. Petrol.* 40, 1151–1185. <https://doi.org/10.1093/petroj/40.7.1151>

Debon, F., Guerrot, C., Ménot, R.-P., 1998. Late Variscan granites of the Belledonne massif (French Western Alps): an Early Visean magnesian plutonism. *Bis 1977 Leemann Ab 1978 Stäubli*. <https://doi.org/10.5169/seals-59275>

Dörr, W., Zulauf, G., Gerdes, A., Lahaye, Y., Kowalczyk, G., 2015. A hidden Tonian basement in the eastern Mediterranean: Age constraints from U–Pb data of magmatic and detrital zircons of the External Hellenides (Crete and Peloponnesus). *Precambrian Res.* 258, 83–108. <https://doi.org/10.1016/j.precamres.2014.12.015>

Eichhorn, R., Schärer, U., Höll, R., 1995. Age and evolution of scheelite-hosting rocks in the Felbertal deposit (Eastern Alps): U–Pb geochronology of zircon and titanite. *Contrib. Mineral. Petrol.* 119, 377–386. <https://doi.org/10.1007/BF00286936>

Eichhorn, R., Loth, G., Kennedy, A., 2001. Unravelling the pre-Variscan evolution of the Habach terrane (Tauern Window, Austria) by U–Pb SHRIMP zircon data. *Contrib. Mineral. Petrol.* 142, 147–162. <https://doi.org/10.1007/s004100100284>

Faryad, S.W., Melcher, F., Hoinkes, G., Puhl, J., Meisel, T., Frank, W., 2002. Relics of eclogite facies metamorphism in the Austroalpine basement, Hochgrössen (Speik

complex), Austria. *Mineral. Petrol.* 74, 49–73. <https://doi.org/10.1007/s710-002-8215-9>

Faure, M., 2014. Le substratum de la France métropolitaine : de la formation du Gondwana à la constitution de la Pangée, une histoire de 600 Ma. *Géologues*.

Faure, M., Becq-Giraudon, J.-F., 1993. Sur la succession des épisodes extensifs au cours du désépaissement carbonifère du Massif central français. *Comptes Rendus Académie Sci. Sér. 2 Mécanique Phys. Chim. Sci. Univers Sci. Terre* 316, 967–973.

Faure, M., Lardeaux, J.-M., Ledru, P., 2009. A review of the pre-Permian geology of the Variscan French Massif Central. *Comptes Rendus Geosci.* 341, 202–213.

Faure, M., Bé Mézème, E., Duguet, M., Cartier, C., Talbot, J.-Y., 2005. Paleozoic tectonic evolution of medio-Europa from the example of the French Massif Central and Massif Armoricaïn. *J. Virtual Explor.* 19. <https://doi.org/10.3809/jvirtex.2005.00120>

Fernández, C., Becchio, R., Castro, A., Viramonte, J.M., Moreno-Ventas, I., Corretgé, L.G., 2008. Massive generation of atypical ferrosilicic magmas along the Gondwana active margin: Implications for cold plumes and back-arc magma generation. *Gondwana Res.* 14, 451–473. <https://doi.org/10.1016/j.gr.2008.04.001>

Ferrando, S., Lombardo, B., Compagnoni, R., 2008. Metamorphic history of HP mafic granulites from the Gesso-Stura terrain (Argentera Massif, western Alps, Italy). *Eur. J. Mineral.* 20, 777–790.

Finger, F., Roberts, M.P., Haunschmid, B., Schermaier, A., Steyrer, H.-P., 1997. Variscan granitoids of central Europe: their typology, potential sources and tectonothermal relations. *Mineral. Petrol.* 61, 67–96.

Finger, F., Gerdes, A., Janoušek, V., René, M., Riegler, G., 2007. Resolving the Variscan evolution of the Moldanubian sector of the Bohemian Massif: the significance of the Bavarian and the Moravo-Moldanubian tectonometamorphic phases. *J. Geosci.* 9–28. <https://doi.org/10.3190/jgeosci.005>

Fortey, R.A., Cocks, L.R.M., 2003. Palaeontological evidence bearing on global Ordovician–Silurian continental reconstructions. *Earth-Sci. Rev.* 61, 245–307. [https://doi.org/10.1016/S0012-8252\(02\)00115-0](https://doi.org/10.1016/S0012-8252(02)00115-0)

Franke, W., 1989. Variscan plate tectonics in Central Europe—current ideas and open questions. *Tectonophysics* 169, 221–228. [https://doi.org/10.1016/0040-1951\(89\)90088-7](https://doi.org/10.1016/0040-1951(89)90088-7)

Franke, W., Cocks, L.R.M., Torsvik, T.H., 2017. The Palaeozoic Variscan oceans revisited. *Gondwana Res.* 48, 257–284.

Fréville, K., 2016. L'orogénèse varisque dans les massifs cristallins externes de Belledonne et du Pelvoux (Alpes occidentales françaises) : rôle de la fusion partielle et du plutonisme dans la structuration de la croûte continentale (PhD Thesis). Université d'Orléans.

Fréville, K., Trap, P., Faure, M., Melleton, J., Li, X.-H., Lin, W., Blein, O., Bruguier, O., Poujol, M., 2018. Structural, metamorphic and geochronological insights on the Variscan evolution of the Alpine basement in the Belledonne Massif (France). *Tectonophysics* 726, 14–42.

Frey, M., Desmons, J., Neubauer, F., 1999. The new metamorphic maps of the Alps: Introduction. *Schweiz. Mineral. Petrogr. Mitteilungen* 1–4.

Gaggero, L., Oggiano, G., Funedda, A., Buzzi, L., 2012. Rifting and Arc-Related Early Paleozoic Volcanism along the North Gondwana Margin: Geochemical and Geological Evidence from Sardinia (Italy). *J. Geol.* 120, 273–292. <https://doi.org/10.1086/664776>

Galli, A., Le Bayon, B., Schmidt, M.W., Burg, J.-P., Reusser, É., Sergeev, S.A., Larionov, A., 2012. U–Pb zircon dating of the Gruf Complex: disclosing the late Variscan granulitic lower crust of Europe stranded in the Central Alps. *Contrib. Mineral. Petrol.* 163, 353–378.

Garfunkel, Z., 2015. The relations between Gondwana and the adjacent peripheral Cadomian domain—constraints on the origin, history, and paleogeography of the peripheral domain. *Gondwana Res.* 28, 1257–1281.

GBA, n.d. Multithematische geologische Karte von Österreich.

Giuntoli, F., Lanari, P., Engi, M., 2018. Deeply subducted continental fragments – Part 1: Fracturing, dissolution–precipitation, and diffusion processes recorded by garnet textures of the central Sesia Zone (western Italian Alps). *Solid Earth* 9, 167–189. <https://doi.org/10.5194/se-9-167-2018>

Godard, G., Martin, S., Prosser, G., Kienast, J.R., Morten, L., 1996. Variscan migmatites, eclogites and garnet-peridotites of the Ulten zone, Eastern Austroalpine system. *Tectonophysics* 259, 313–341. [https://doi.org/10.1016/0040-1951\(95\)00145-X](https://doi.org/10.1016/0040-1951(95)00145-X)

Grandjean, V., Guillot, S., Pecher, A., 1996. A new record of the LP-HT late-Variscan metamorphism: The Peyre-Arguet unit (Haut-Dauphine). *Comptes Rendus Académie Sci.* 322, 189–195.

Guillot, F., Schaltegger, U., Bertrand, J.-M., Deloule, É., Baudin, T., 2002. Zircon U–Pb geochronology of Ordovician magmatism in the polycyclic Rutor Massif (Internal W Alps). *Int. J. Earth Sci.* 91, 964–978. <https://doi.org/10.1007/s00531-002-0280-0>

Guillot, S., Ménot, R.-P., 2009. Paleozoic evolution of the External Crystalline Massifs of the Western Alps. *Comptes Rendus Geosci.* 341, 253–265. <https://doi.org/10.1016/j.crte.2008.11.010>

Guillot, S., Ménot, R.-P., Lardeaux, J.-M., 1992. Tectonique intra-océanique distensive dans l’ophiolite paléozoïque de Chamrousse (Alpes occidentales). *Bull Soc Geol Fr.* 163, 229–240.

Guillot, S., Mahéo, G., de Sigoyer, J., Hattori, K.H., Pêcher, A., 2008. Tethyan and Indian subduction viewed from the Himalayan high- to ultrahigh-pressure metamorphic rocks. *Tectonophysics* 451, 225–241. <https://doi.org/10.1016/j.tecto.2007.11.059>

Guillot, S., di Paola, S., Ménot, R.-P., Ledru, P., Spalla, M.I., Gosso, G., Schwartz, S., 2009. Suture zones and importance of strike-slip faulting for Variscan geodynamic reconstructions of the External Crystalline Massifs of the western Alps. *Bull. Société Géologique Fr.* 180, 483–500.

Guilmette, C., Indares, A., Hébert, R., 2011. High-pressure anatectic paragneisses from the Namche Barwa, Eastern Himalayan Syntaxis: Textural evidence for partial melting, phase equilibria modeling and tectonic implications. *Lithos, Granulite facies metamorphism and the rheology of the lower crust* 124, 66–81. <https://doi.org/10.1016/j.lithos.2010.09.003>

Haas, I., Eichinger, S., Haller, D., Fritz, H., Nievoll, J., Mandl, M., Hippler, D., Hauzenberger, C., 2020. Gondwana fragments in the Eastern Alps: A travel story from U/Pb zircon data. *Gondwana Res.* 77, 204–222. <https://doi.org/10.1016/j.gr.2019.07.015>

Hauzenberger, C.A., Höller, W., Hoinkes, G., 1996. Transition from eclogite to amphibolite-facies metamorphism in the Austroalpine Ulten Zone. *Mineral. Petrol.* 58, 111–130. <https://doi.org/10.1007/BF01172092>

Herwartz, D., Nagel, T.J., Münker, C., Scherer, E.E., Froitzheim, N., 2011. Tracing two orogenic cycles in one eclogite sample by Lu–Hf garnet chronometry. *Nat. Geosci.* 4, 178–183. <https://doi.org/10.1038/ngeo1060>

van Hinsbergen, D.J.J., Torsvik, T.H., Schmid, S.M., Maçenco, L.C., Maffione, M., Vissers, R.L.M., Gürer, D., Spakman, W., 2019. Orogenic architecture of the Mediterranean region and kinematic reconstruction of its tectonic evolution since the Triassic. *Gondwana Res.* <https://doi.org/10.1016/j.gr.2019.07.009>

Jacob, J.-B., Guillot, S., Rubatto, D., Janots, E., Melleton, J., & Faure, M. (2021). Carboniferous high pressure metamorphism and deformation in the Belledonne Massif (Western Alps). *Journal of Metamorphic Geology.* <https://doi.org/10.1111/jmg.12600>

Jouffray, F., Spalla, M.I., Lardeaux, J.M., Filippi, M., Rebay, G., Corsini, M., Zanoni, D., Zucali, M., Gosso, G., 2020. Variscan eclogites from the Argentera–Mercantour Massif (External Crystalline Massifs, SW Alps): a dismembered cryptic suture zone. *Int. J. Earth Sci.* <https://doi.org/10.1007/s00531-020-01848-2>

Kali, E., Leloup, P.H., Arnaud, N., Mahéo, G., Liu, D., Boutonnet, E., Woerd, J.V. der, Liu, X., Liu Zeng, J., Li, H., 2010. Exhumation history of the deepest central Himalayan rocks, Ama Drime range: Key pressure-temperature-deformation-time constraints on orogenic models. *Tectonics* 29. <https://doi.org/10.1029/2009TC002551>

Kroner, U., Romer, R.L., 2013. Two plates—many subduction zones: the Variscan orogeny reconsidered. *Gondwana Res.* 24, 298–329.

Kunz, B.E., Manzotti, P., von Niederhäusern, B., Engi, M., Darling, J.R., Giuntoli, F., Lanari, P., 2018. Permian high-temperature metamorphism in the Western Alps (NW Italy). *Int. J. Earth Sci.* 107, 203–229. <https://doi.org/10.1007/s00531-017-1485-6>

Ladenhauf, C., Armstrong, R., Konzett, J., Miller, C., 2001. The timing of pre-Alpine high pressure metamorphism in the Eastern Alps: constraints from U–Pb SHRIMP dating of eclogite zircons from the Austroalpine Silvretta nappe, in: *Journal of Conference Abstracts.* p. 600.

Lammerer, B., 1986. Das autochthon im westlichen tauernfenster. *Jahrb. Geol. Bundesanst.* 129, 51–67.

Lanari, P., Riel, N., Guillot, S., Vidal, O., Schwartz, S., Pêcher, A., Hattori, K.H., 2013. Deciphering high-pressure metamorphism in collisional context using microprobe mapping methods: Application to the Stak eclogitic massif (northwest Himalaya). *Geology* 41, 111–114. <https://doi.org/10.1130/G33523.1>

Lardeaux, J.M., Schulmann, K., Faure, M., Janoušek, V., Lexa, O., Skrzypek, E., Edel, J.B., Štípská, P., 2014. The moldanubian zone in the French Massif Central, Vosges/Schwarzwald and Bohemian Massif revisited: differences and similarities. *Geol. Soc. Lond. Spec. Publ.* 405, 7–44.

Le Fort, P., 1971. *Géologie du Haut-Dauphiné cristallin (Alpes Française): Etudes pétrologique et structurale de la partie occidentale* (PhD Thesis). Université Nancy I.

Ledru, P., Courrioux, G., Dallain, C., Lardeaux, J.M., Montel, J.M., Vanderhaeghe, O., Vitel, G., 2001. The Velay dome (French Massif Central): melt generation and granite emplacement during orogenic evolution. *Tectonophysics, Partial Melting of Crust and Flow of Orogens* 342, 207–237. [https://doi.org/10.1016/S0040-1951\(01\)00165-2](https://doi.org/10.1016/S0040-1951(01)00165-2)

Liatì, A., Gebauer, D., Fanning, C.M., 2009. Geochronological evolution of HP metamorphic rocks of the Adula nappe, Central Alps, in pre-Alpine and Alpine subduction cycles. *J. Geol. Soc.* 166, 797–810.

Liégeois, J.-P., Duchesne, J.-C., 1981. The Lac Cornu retrograded eclogites (Aiguilles Rouges massif, Western Alps, France): evidence of crustal origin and metasomatic alteration. *Lithos* 14, 35–48. [https://doi.org/10.1016/0024-4937\(81\)90035-9](https://doi.org/10.1016/0024-4937(81)90035-9)

Linnemann, U., Gerdes, A., Drost, K., Buschmann, B., 2007. The continuum between Cadomian orogenesis and opening of the Rheic Ocean: Constraints from LA-ICP-MS U-Pb zircon dating and analysis of plate-tectonic setting (Saxo-Thuringian zone, northeastern Bohemian Massif, Germany). *Spec. Pap.-Geol. Soc. Am.* 423, 61.

Maierová, P., Schulmann, K., Lexa, O., Guillot, S., Štípská, P., Janoušek, V., Čadek, O., 2016. European Variscan orogenic evolution as an analogue of Tibetan-Himalayan orogen: Insights from petrology and numerical modeling: Variscan and Himalayan Orogenies. *Tectonics* 35, 1760–1780. <https://doi.org/10.1002/2015TC004098>

Mandl, M., Kurz, W., Hauzenberger, C., Fritz, H., Klötzli, U., Schuster, R., 2018. Pre-Alpine evolution of the Seckau Complex (Austroalpine basement/Eastern Alps): Constraints from in-situ LA-ICP-MS UPb zircon geochronology. *Lithos* 296–299, 412–430. <https://doi.org/10.1016/j.lithos.2017.11.022>

Manzotti, P., Ballèvre, M., Poujol, M., 2016. Detrital zircon geochronology in the Dora-Maira and Zone Houillère: a record of sediment travel paths in the Carboniferous. *Terra Nova* 28, 279–288. <https://doi.org/10.1111/ter.12219>

Manzotti, P., Rubatto, D., Zucali, M., Korh, A.E., Cenko-Tok, B., Ballèvre, M., Engi, M., 2018. Permian magmatism and metamorphism in the Dent Blanche nappe: constraints from field observations and geochronology. *Swiss J. Geosci.* 111, 79–97. <https://doi.org/10.1007/s00015-017-0284-1>

Matte, P., 1986. Tectonics and plate tectonics model for the Variscan belt of Europe. *Tectonophysics* 126, 329–374. [https://doi.org/10.1016/0040-1951\(86\)90237-4](https://doi.org/10.1016/0040-1951(86)90237-4)

Matte, P., 2001. The Variscan collage and orogeny (480–290 Ma) and the tectonic definition of the Armorica microplate: a review. *Terra Nova* 13, 122–128. <https://doi.org/10.1046/j.1365-3121.2001.00327.x>

Melcher, F., Meisel, T., 2004. A metamorphosed early Cambrian crust–mantle transition in the Eastern Alps, Austria. *J. Petrol.* 45, 1689–1723.

Ménot, R.-P., Peucat, J.J., Scarenzi, D., Piboule, M., 1988. 496 My age of plagiogranites in the Chamrousse ophiolite complex (external crystalline massifs in the French Alps): evidence of a Lower Paleozoic oceanization. *Earth Planet. Sci. Lett.* 88, 82–92.

Miller, C., Thöni, M., 1995. Origin of eclogites from the Austroalpine Ötztal basement (Tirol, Austria): geochemistry and Sm Nd vs. Rb Sr isotope systematics. *Chem. Geol.* 122, 199–225. [https://doi.org/10.1016/0009-2541\(95\)00033-I](https://doi.org/10.1016/0009-2541(95)00033-I)

Montero, P., Bea, F., González-Lodeiro, F., Talavera, C., Whitehouse, M.J., 2007. Zircon ages of the metavolcanic rocks and metagranites of the Ollo de Sapo Domain in central Spain: implications for the Neoproterozoic to Early Palaeozoic evolution of Iberia. *Geol. Mag.* 144, 963–976.

Montes, A.D., Catalán, J.R.M., Mulas, F.B., 2010. Role of the Ollo de Sapo massive felsic volcanism of NW Iberia in the Early Ordovician dynamics of northern Gondwana. *Gondwana Res., The Rheic Ocean: Palaeozoic Evolution from*

Gondwana and Laurussia to Pangaea 17, 363–376.
<https://doi.org/10.1016/j.gr.2009.09.001>

Müller, B., Klötzli, U.S., Flisch, M., 1995. U-Pb and Pb-Pb zircon dating of the older orthogneiss suite in the Silvretta nappe, eastern Alps: Cadomian magmatism in the upper Austro-Alpine realm. *Geol. Rundsch.* 84, 457–465.
<https://doi.org/10.1007/BF00284513>

Müller, B., Schaltegger, U., Klötzli, U., Flisch, M., 1996. Early Cambrian oceanic plagiogranite in the Silvretta Nappe, eastern Alps: geochemical, zircon U-Pb and Rb-Sr data from garnet-hornblende-plagioclase gneisses. *Geol. Rundsch.* 85, 822–831. <https://doi.org/10.1007/BF02440113>

Nance, R.D., Gutiérrez-Alonso, G., Keppie, J.D., Linnemann, U., Murphy, J.B., Quesada, C., Strachan, R.A., Woodcock, N.H., 2010. Evolution of the Rheic Ocean. *Gondwana Res., The Rheic Ocean: Palaeozoic Evolution from Gondwana and Laurussia to Pangaea* 17, 194–222. <https://doi.org/10.1016/j.gr.2009.08.001>

Neubauer, F., 1989. Pre-Alpine terranes and tectonic zoning in the eastern Alps. *Terranes Circum-Atl. Paleoz. Orogens* 230, 91.

Neubauer, F., Frisch, W., Schmerold, R., Schlöser, H., 1989. Metamorphosed and dismembered ophiolite suites in the basement units of the Eastern Alps. *Tectonophysics* 164, 49–62. [https://doi.org/10.1016/0040-1951\(89\)90233-3](https://doi.org/10.1016/0040-1951(89)90233-3)

Neubauer, F., Fried, G., Genser, J., Handler, R., Mader, D., Schneider, D., 2007. Origin and tectonic evolution of the Eastern Alps deduced from dating of detrital white mica: a review. *Austrian J. Earth Sci.* 100.

Nicollet, C., Bosse, V., Spalla, M.I., Schiavi, F., 2018. Eocene ultra-high temperature (UHT) metamorphism in the Gruf complex (Central Alps): constraints by LA-ICPMS zircon and monazite dating in petrographic context. *J. Geol. Soc.* 175, 774–787. <https://doi.org/10.1144/jgs2018-017>

O'Brien, P.J., 2000. The fundamental Variscan problem: high-temperature metamorphism at different depths and high-pressure metamorphism at different temperatures. *Geol. Soc. Lond. Spec. Publ.* 179, 369–386. <https://doi.org/10.1144/GSL.SP.2000.179.01.22>

Paquette, J.L., Menot, R.P., Peucat, J.J., 1989. REE, Sm-Nd and U-Pb zircon study of eclogites from the Alpine External Massifs (Western Alps): evidence for crustal contamination. *Earth Planet. Sci. Lett.* 96, 181–198.

Paquette, J.-L., Ballèvre, M., Peucat, J.-J., Cornen, G., 2017. From opening to subduction of an oceanic domain constrained by LA-ICP-MS U-Pb zircon dating (Variscan belt, Southern Armorican Massif, France). *Lithos* 294–295, 418–437. <https://doi.org/10.1016/j.lithos.2017.10.005>

Pin, C., Carme, F., 1987. A Sm-Nd isotopic study of 500 Ma old oceanic crust in the Variscan belt of Western Europe: the Chamrousse ophiolite complex, Western Alps (France). *Contrib. Mineral. Petrol.* 96, 406–413.

Pin, C., Marini, F., 1993. Early Ordovician continental break-up in Variscan Europe: Nd Sr isotope and trace element evidence from bimodal igneous associations of the Southern Massif Central, France. *Lithos* 29, 177–196. [https://doi.org/10.1016/0024-4937\(93\)90016-6](https://doi.org/10.1016/0024-4937(93)90016-6)

Regorda, A., Lardeaux, J.-M., Roda, M., Marotta, A.M., Spalla, M.I., 2019. How many subductions in the Variscan orogeny? Insights from numerical models. *Geosci. Front.* <https://doi.org/10.1016/j.gsf.2019.10.005>

Rubatto, D., Ferrando, S., Compagnoni, R., Lombardo, B., 2010. Carboniferous high-pressure metamorphism of Ordovician protoliths in the Argentera Massif (Italy), Southern European Variscan belt. *Lithos* 116, 65–76.

Rubatto, D., Schaltegger, U., Lombardo, D., Colombo, F., Compagnoni, R., 2001. Complex Paleozoic magmatic and metamorphic evolution in the Argentera massif (Western Alps), resolved with U-Pb dating. *Schweiz. Mineral. Petrogr. Mitteilungen* 81, 213–228.

Sandmann, S., Nagel, T.J., Herwartz, D., Fonseca, R.O.C., Kurzawski, R.M., Münker, C., Froitzheim, N., 2014. Lu-Hf garnet systematics of a polymetamorphic basement unit: new evidence for coherent exhumation of the Adula Nappe (Central Alps) from eclogite-facies conditions. *Contrib. Mineral. Petrol.* 168, 1075. <https://doi.org/10.1007/s00410-014-1075-6>

Schäfer, J., Neuroth, H., Ahrendt, H., Dörr, W., Franke, W., 1997. Accretion and exhumation at a Variscan active margin, recorded in the Saxothuringian flysch. *Geol. Rundsch.* 86, 599–611.

Schaltegger, U., 1997. Magma pulses in the Central Variscan Belt: episodic melt generation and emplacement during lithospheric thinning. *Terra Nova* 9, 242–245. <https://doi.org/10.1111/j.1365-3121.1997.tb00021.x>

Schaltegger, U., Gebauer, D., 1999. Pre-Alpine geochronology of the central, western and southern Alps. *Schweiz. Mineral. Petrogr. Mitteilungen* 79, 79–87.

Schaltegger, U., Gebauer, D., von Quadt, A., 2002. The mafic–ultramafic rock association of Loderio–Biasca (lower Pennine nappes, Ticino, Switzerland): Cambrian oceanic magmatism and its bearing on early Paleozoic paleogeography. *Chem. Geol.* 186, 265–279.

Schaltegger, U., Abrecht, J., Corfu, F., 2003. The Ordovician orogeny in the Alpine basement: constraints from geochronology and geochemistry in the Aar Massif (Central Alps). *Swiss Bull. Mineral. Petrol.* 83, 183–239.

Schaltegger, U., Nægler, T., Corfu, F., Maggetti, M., Galetti, G., Stosch, H.G., 1997. A Cambrian island arc in the Silvretta nappe: constraints from geochemistry and geochronology. *Schweiz. Mineral. Petrogr. Mitteilungen* 77, 337–350.

Schantl, P., Hauzenberger, C., Finger, F., Müller, T., Linner, M., 2019. New evidence for the prograde and retrograde PT-path of high-pressure granulites, Moldanubian Zone, Lower Austria, by Zr-in-rutile thermometry and garnet diffusion modelling. *Lithos* 342–343, 420–439. <https://doi.org/10.1016/j.lithos.2019.05.041>

Schmid, S.M., Fügenschuh, B., Kissling, E., Schuster, R., 2004. Tectonic map and overall architecture of the Alpine orogen. *Eclogae Geol. Helvetiae* 97, 93–117.

Schmid, S.M., Scharf, A., Handy, M.R., Rosenberg, C.L., 2013. The Tauern Window (Eastern Alps, Austria): a new tectonic map, with cross-sections and a tectonometamorphic synthesis. *Swiss J. Geosci.* 106, 1–32. <https://doi.org/10.1007/s00015-013-0123-y>

Schulmann, K., Catalán, J.R.M., Lardeaux, J.M., Janoušek, V., Oggiano, G., 2014. The Variscan orogeny: extent, timescale and the formation of the European crust. *Geol. Soc. Lond. Spec. Publ.* 405, 1–6. <https://doi.org/10.1144/SP405.15>

Schulmann, K., Kröner, A., Hegner, E., Wendt, I., Konopásek, J., Lexa, O., Štípská, P., 2005. Chronological constraints on the pre-orogenic history, burial and exhumation of deep-seated rocks along the eastern margin of the Variscan Orogen, Bohemian Massif, Czech Republic. *Am. J. Sci.* 305, 407–448. <https://doi.org/10.2475/ajs.305.5.407>

Schulz, B., Steenken, A., Siegesmund, S., 2008. Geodynamic evolution of an Alpine terrane—the Austroalpine basement to the south of the Tauern window as a part of the Adriatic Plate (eastern Alps). *Geol. Soc. Lond. Spec. Publ.* 298, 5–44.

Schulz, B., Bombach, K., Pawlig, S., Brätz, H., 2004. Neoproterozoic to Early-Palaeozoic magmatic evolution in the Gondwana-derived Austroalpine basement to the south of the Tauern Window (Eastern Alps). *Int. J. Earth Sci.* 93, 824–843.

Simonetti, M., Carosi, R., Montomoli, C., Langone, A., D’Addario, E., Mammoliti, E., 2018. Kinematic and geochronological constraints on shear deformation in the Ferriere-Mollières shear zone (Argentiera-Mercantour Massif, Western Alps): implications for the evolution of the Southern European Variscan Belt. *Int. J. Earth Sci.* 107, 2163–2189. <https://doi.org/10.1007/s00531-018-1593-y>

Soejono, I., Machek, M., Sláma, J., Janoušek, V., Kohút, M., 2019. Cambro-Ordovician anatexis and magmatic recycling at the thinned Gondwana margin: new constraints from the Kouřim Unit, Bohemian Massif. *J. Geol. Soc.* <https://doi.org/10.1144/jgs2019-037>

Spalla, M.I., Zanoni, D., Marotta, A.M., Rebay, G., Roda, M., Zucali, M., Gosso, G., 2014. The transition from Variscan collision to continental break-up in the Alps: insights from the comparison between natural data and numerical model predictions. *Geol. Soc. Lond. Spec. Publ.* 405, 363–400. <https://doi.org/10.1144/SP405.11>

Stampfli, G.M., Hochard, C., 2009. Plate tectonics of the Alpine realm. *Geol. Soc. Lond. Spec. Publ.* 327, 89–111.

Stampfli, G.M., Von Raumer, J., Wilhem, C., 2011. The distribution of Gondwana-derived terranes in the Early Palaeozoic, in: *Ordovician of the World*. Instituto Geológico y Minero de España, pp. 567–574.

Stampfli, G.M., Hochard, C., Vérard, C., Wilhem, C., 2013. The formation of Pangea. *Tectonophysics* 593, 1–19.

Stephan, T., Kroner, U., Romer, R.L., 2019a. The pre-orogenic detrital zircon record of the Peri-Gondwanan crust. *Geol. Mag.* 156, 281–307. <https://doi.org/10.1017/S0016756818000031>

Stephan, T., Kroner, U., Romer, R.L., Rösel, D., 2019b. From a bipartite Gondwanan shelf to an arcuate Variscan belt: The early Paleozoic evolution of northern Peri-Gondwana. *Earth-Sci. Rev.* 192, 491–512. <https://doi.org/10.1016/j.earscirev.2019.03.012>

Thöni, M., 2006. Dating eclogite-facies metamorphism in the Eastern Alps—approaches, results, interpretations: a review. *Mineral. Petrol.* 88, 123–148.

Tumiati, S., Thöni, M., Nimis, P., Martin, S., Mair, V., 2003. Mantle–crust interactions during Variscan subduction in the Eastern Alps (Nonsberg–Ulten zone): geochronology and new petrological constraints. *Earth Planet. Sci. Lett.* 210, 509–526.

Valverde Vaquero, P., Dunning, G.R., 2000. New U–Pb ages for Early Ordovician magmatism in Central Spain. *J. Geol. Soc.* 157, 15–26. <https://doi.org/10.1144/jgs.157.1.15>

Veselà, P., Söllner, F., Finger, F., Gerdes, A., 2011. Magmato-sedimentary Carboniferous to Jurassic evolution of the western Tauern window, Eastern Alps (constraints from U-Pb zircon dating and geochemistry). *Int. J. Earth Sci.* 100, 993–1027.

Villaseca, C., Merino Martínez, E., Orejana, D., Andersen, T., Belousova, E., 2016. Zircon Hf signatures from granitic orthogneisses of the Spanish Central System: Significance and sources of the Cambro-Ordovician magmatism in the Iberian Variscan Belt. *Gondwana Res.* 34, 60–83. <https://doi.org/10.1016/j.gr.2016.03.004>

Von Raumer, J.F., Bussy, F., 2004. Mont Blanc and Aiguilles Rouges geology of their polymetamorphic basement (external massifs, Western Alps, France–Switzerland), in: *Mémoires de Géologie (Lausanne)*. pp. 1–210.

Von Raumer, J.F., Stampfli, G.M., 2008. The birth of the Rheic Ocean—Early Palaeozoic subsidence patterns and subsequent tectonic plate scenarios. *Tectonophysics* 461, 9–20.

Von Raumer, J.F., Bussy, F., Stampfli, G.M., 2009. The Variscan evolution in the External massifs of the Alps and place in their Variscan framework. *Comptes Rendus Geosci.* 341, 239–252. <https://doi.org/10.1016/j.crte.2008.11.007>

Von Raumer, J., Stampfli, G., Borel, G., Bussy, F., 2002. Organization of pre-Variscan basement areas at the north-Gondwanan margin. *Int. J. Earth Sci.* 91, 35–52.

Von Raumer, J.F., Finger, F., Veselá, P., Stampfli, G., 2014. Durbachites–Vaugnerites—a geodynamic marker in the central European Variscan orogen. *Terra Nova* 26, 85–95.

Von Raumer, J.F., Stampfli, G.M., Arenas, R., Martínez, S.S., 2015. Ediacaran to Cambrian oceanic rocks of the Gondwana margin and their tectonic interpretation. *Int. J. Earth Sci.* 104, 1107–1121.

Von Raumer, J.F., Bussy, F., Schaltegger, U., Schulz, B., Stampfli, G.M., 2013. Pre-Mesozoic Alpine basements—their place in the European Paleozoic framework. *Bulletin* 125, 89–108.

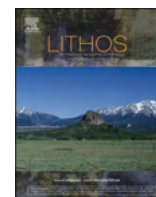
Whitney, D.L., Roger, F., Teyssier, C., Rey, P.F., Respaut, J.-P., 2015. Syn-collapse eclogite metamorphism and exhumation of deep crust in a migmatite dome: The P–T–t record of the youngest Variscan eclogite (Montagne Noire, French Massif Central). *Earth Planet. Sci. Lett.* 430, 224–234. <https://doi.org/10.1016/j.epsl.2015.08.026>

Whitney, D.L., Hamelin, C., Teyssier, C., Raia, N.H., Korchinski, M.S., Seaton, N.C.A., Bagley, B.C., Handt, A. von der, Roger, F., Rey, P.F., 2020. Deep crustal source of gneiss dome revealed by eclogite in migmatite (Montagne Noire, French Massif Central). *J. Metamorph. Geol.* 38, 297–327. <https://doi.org/10.1111/jmg.12523>

Wilhem, C., Windley, B.F., Stampfli, G.M., 2012. The Altaids of Central Asia: a tectonic and evolutionary innovative review. *Earth-Sci. Rev.* 113, 303–341.

Žák, J., Svojtka, M., Opluštil, S., 2018. Topographic inversion and changes in the sediment routing systems in the Variscan orogenic belt as revealed by detrital zircon and monazite UPb geochronology in post-collisional continental basins. *Sediment. Geol.* 377, 63–81. <https://doi.org/10.1016/j.sedgeo.2018.09.008>

A.2 Article #2 : Crustal melting vs. fractionation of basaltic magmas – Parts 1 and 2



Research Article

Crustal melting vs. fractionation of basaltic magmas: Part 1, granites and paradigms



Jean-François Moyen^{a,b,*}, Vojtěch Janoušek^{c,d}, Oscar Laurent^{e,f}, Olivier Bachmann^e, Jean-Baptiste Jacob^g, Federico Farina^h, Patrizia Fiannaccaⁱ, Arnaud Villaros^j

^a Univ. Lyon, UJM, UCBL, ENSL, CNRS, LGL-TPE, 23 rue Dr. Paul Michelon, F-42023 Saint Etienne, France

^b on sabbatical at School of Earth, Environment and Atmosphere Sciences, Monash University, Clayton, VIC 3168, Australia

^c Czech Geological Survey, Klárov 3, 118 21, Prague 1, Czech Republic

^d Institute of Petrology and Structural Geology, Faculty of Science, Charles University, Albertov 6, 128 43 Prague 2, Czech Republic

^e Institute of Geochemistry and Petrology, ETH Zürich, Clausiusstrasse 25, 8092 Zürich, Switzerland

^f CNRS, Observatoire Midi-Pyrénées, Géosciences Environnement Toulouse UMR5563-UPS-CNRS-IRD-CNES, 14 avenue Edouard Belin, 31400 Toulouse, France

^g Univ. Grenoble Alpes, Univ. Savoie Mont Blanc, CNRS, IRD, UGE, ISTerre, 38000 Grenoble, France

^h Dipartimento di Scienze della Terra, Università degli Studi di Milano, Via Botticelli, 23, 20133 Milano, Italy

ⁱ Dipartimento di Scienze Biologiche, Geologiche e Ambientali, Università degli Studi di Catania, Corso Italia 57, 95129 Catania, Italy

^j 4 route de Treignac, 19260 Peyrissac, France

A B S T R A C T

Granitoids are a major component of the continental crust. They play a pivotal role in its evolution, either by adding new material (continental growth), or by reworking older continental crust. These two roles correspond to two main ways of forming granitic magmas, either by partial melting of pre-existing crustal rocks yielding granitic melts directly, or by fractionation of mantle-derived mafic to intermediate magmas. Both models represent endmembers, or paradigms that have shaped the way the geological community envisions granitoids, their occurrence, features, formation and meaning for crustal evolution and differentiation of the whole planet.

In this paper, we expose the two competing paradigms and their implications. We explore the evidence on which each model is based, and how each school of thought articulates a comprehensive view of granitic magmatism based on field geological, petrological, geochemical (including isotopes) and physical constraints; and how, in turn, each view shapes the thinking on crustal growth and evolution, and the interpretation of proxies such as age and Hf isotopic patterns in detrital zircon databases. We emphasize that both schools of thought build a different, but internally consistent view based on a large body of evidence, and we propose that each of them is, or has been, relevant to some portions of the Earth. Thus, the key question is not so much “which” model applies, but “where, when and to which extent”.

1. Introduction

“This question of the origin of granite is perhaps the most lively of geological topics today—but we should remember that it always has been. About every twenty years or so, the problem has been firmly settled, and a sort of uneasy peace has broken out. This indicates to my mind that there is no unique solution of the problem—there are granites and granites.” – Read, 1948 (p. 1)

These words, by H. Read, then one of the most influential granite¹ petrologists, neatly express the nature of the debates that structure, and perhaps polarize the granite community to this day. In Read’s time, the

main controversy was between transformists and magmatists. Transformists (Perrin and Roubault, 1937; Raguin, 1976; Sederholm, 1923; Wegmann, 1935) proposed that granites were the product of solid-state, fluid-induced transformation of country rocks (“metasomatism”, in modern terms). Magmatists, who in the 1940s were winning the argument, held the view now universally admitted that granites are igneous rocks, crystallized from magmas. But this only displaced the controversy, as Read also wrote that “Certain authorities consider therefore that a primary granitic magma could arise by melting, pure or partial, of the sialic crust, once it has been separated from the simatic layer. This magma is independent and not derived from a primary basaltic magma. This classic two-magma view that agrees with the distribution of rock types in the crust

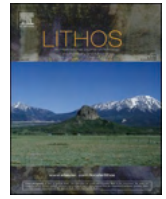
* Corresponding author.

E-mail address: jean.francois.moyen@univ-st-etienne.fr (J.-F. Moyen).

¹ This paper deals with granitoids (i.e. quartz-rich plutonic rocks, irrespective of the relative proportions of plagioclase to alkali feldspar, as implied by the IUGS classification). But for concision we often use the term “granite” as a synonym. We use “granite s.s.” when we need to refer to the exact rock type as defined in IUGS classification.

Contents lists available at [ScienceDirect](https://www.sciencedirect.com)

LITHOS

journal homepage: www.elsevier.com/locate/lithos

Research Article

Crustal melting vs. fractionation of basaltic magmas: Part 2, Attempting to quantify mantle and crustal contributions in granitoids

Jean-Baptiste Jacob^a, Jean-François Moyen^{b,c,*}, Patrizia Fiannacca^d, Oscar Laurent^{e,f}, Olivier Bachmann^e, Vojtěch Janoušek^{g,h}, Federico Farinaⁱ, Arnaud Villaros^j^a Univ. Grenoble Alpes, Univ. Savoie Mont Blanc, CNRS, IRD, UGE, ISTerre, 38000 Grenoble, France^b Univ. Lyon, UJM, UCBL, ENSL, CNRS, LGL-TPE, 23 rue Dr. Paul Michelon, F-42023 Saint Etienne, France^c on sabbatical at School of Earth, Environment and Atmosphere Sciences, Monash University, Clayton, VIC 3168, Australia^d Dipartimento di Scienze Biologiche, Geologiche e Ambientali, Università degli Studi di Catania, Corso Italia 57, 95129 Catania, Italy^e Institute of Geochemistry and Petrology, ETH Zürich, Clausiusstrasse 25, 8092 Zürich, Switzerland^f CNRS, Observatoire Midi-Pyrénées, Géosciences Environnement Toulouse UMR5563-UPS-CNRS-IRD-CNES, 14 avenue Edouard Belin, 31400 Toulouse, France^g Czech Geological Survey, Klárov 3, 118 21 Prague 1, Czech Republic^h Institute of Petrology and Structural Geology, Faculty of Science, Charles University, Albertov 6, 128 43 Prague 2, Czech Republicⁱ Dipartimento di Scienze della Terra, Università degli Studi di Milano, Via Botticelli, 23, 20133 Milano, Italy^j 4 route de Treignac, 19260 Peyrissac, France

A B S T R A C T

Granitic melts may form either directly, by melting of pre-existing crustal rocks, or by fractionation of mafic to intermediate magmas, typically mantle-derived. Each model is applicable to distinct portions of the Earth at different times. Whenever there is an important flux of mafic magmas from the mantle, differentiation of basaltic magmas dominates. In contrast, locations with a lower mafic magma flux, elevated thermal gradients and/or a fertile, thick crust are dominated by crustal melting and reworking. This only partly overlaps with the dichotomy between magmatic arcs and collision zones, as places like e.g. inverted back-arcs also feature large-scale crustal melting, whereas post-collisional domains include a sizeable mantle-derived component. Petrogenesis of individual granitic suites probably cannot be accounted for by pure, end-member models, as these suites typically feature a fair proportion of hybrid or ambiguous granitoids. Thus, we explore various petrogenetic and geological scenarios leading to the formation of hybrid granitoids at various scales. Finally, we outline possibilities to quantify the respective contributions of crust and mantle involved in their formation – hopefully, paving the way for a better understanding and more rigorous discussion of the mechanisms of crustal growth and recycling.

1. Introduction

“I believe that we can look forward to a general unifying thesis concerning the production of granitic rocks. The basis of such a thesis must be that magmas reflect differences in source and process in response to changing geological environment.” – Pitcher, 1987 (p. 68).

More than thirty years ago, W.S. Pitcher, reflecting on the then state of the art on granite thinking, concluded that the long-standing granite controversy, that harked back to the famous Read vs. Bowen debate of the 1940s and beyond, stated that there are “granites and yet more granites forty years on”. He concluded that granites are diverse, and that there is little point in trying to explain them all with a single model (Pitcher, 1987). It is, perhaps, disheartening to realize that to this day, the controversy still stands and is still very much structured along the same lines: are granites the product of melting of older crust, or of

fractionation of mantle-derived basalts? Although Pitcher (1987) presented a very good case for the existence of both possibilities, his holistic view has not been fully accepted by the community, which to this day remains split into two largely disconnected sub-communities, the “(crustal) melting” and the “(basaltic magma) fractionation” ones. The former is connected to the study of migmatites and high-grade metamorphic terrains, mainly – but not exclusively – in former continental collisions. The latter is rooted in volcanic–plutonic terranes of magmatic arcs above active subduction zones.

Perhaps the only place of interaction between these two views is in the realm of crustal growth and crustal evolution through time, and in particular of reading the zircon record – as zircons chiefly form in granitic igneous rocks. The melting paradigm leads to consider that zircons come from granites, themselves principally reflecting reworking of older crust. Thus, the age of zircons tells little on crustal extraction

* Corresponding author at: Univ. Lyon, UJM, UCBL, ENSL, CNRS, LGL-TPE, 23 rue Dr. Paul Michelon, F-42023 Saint Etienne, France.
E-mail address: jean.francois.moyen@univ-st-etienne.fr (J.-F. Moyen).

<https://doi.org/10.1016/j.lithos.2021.106292>

Received 5 June 2021; Accepted 7 June 2021

Available online 10 June 2021

0024-4937/© 2021 Published by Elsevier B.V.

